The international journal of science / 28 January 2021

nature

EXPOSING BIAS

Machine learning helps to detect discrimination on hiring websites

Psychedelic revival
Can hallucinogens finally make it as psychiatric drugs?

Mapping cancer
Track cell vulnerabilities not just sequences to tackle tumours

Alpha bettered
Exotic atoms place constraints on size of α-particle

Vol. 589 No. 7840
nature.com

Nature.2021.01.30

[Sat, 30 Jan 2021]

- Donation
- This Week
- News in Focus
- Books & Arts
- Opinion
- Work
- Research
- Amendments & Corrections

Donation

- **-> 打赏 - Donation**

打赏 - JUST FOR FUN

支持分享! 一杯咖啡钱, 打赏金额随意，感谢大家~ :)

经济学人2020年全集(含epub、mobi、高清pdf, 音频下载地址)已经整理完毕, 有需要的同学可以点击 emagazines.site 查看.

本书来自: www.emagazines.site

This article was downloaded by **calibre** from https://emagazines.site/donate.html

This Week

- **How epidemiology has shaped the COVID pandemic** [27 January 2021]
  Editorial • Nature's third progress report, coming at the end of the pandemic's first year, highlights key findings from epidemiology — from sounding the early alarm to following the impact of new variants.
- **Heed blame for extreme weather** [26 January 2021]
  World View • Now that specific floods, heatwaves and more can be attributed to our actions, decision makers can act.
- **Ground-breaking films show RNA's complex curves take shape** [19 January 2021]
  Research Highlight • Experimental data and predictive algorithms combine to reveal the essential biomolecule's shape-shifting.
- **The moon that made Saturn a pushover** [25 January 2021]
  Research Highlight • Scientists have a new theory for how the ringed planet got its tilt.
- **A material cracks barriers to asymmetrical toughness** [22 January 2021]
  Research Highlight • Precise engineering generates a structure that fractures more easily in one direction than the other.
- **Data helps an anti-rabies campaign go to the dogs** [22 January 2021]
  Research Highlight • A plan uses real-time monitoring to vaccinate more than two-thirds of a city's canines at low cost.
- **Massive water projects leave a parched landscape high and dry** [20 January 2021]
  Research Highlight • Ambitious irrigation schemes are planned for sub-Saharan Africa — but those already built have a dismal track record.
- **Chemists' riff on melanin makes a rainbow** [22 January 2021]
  Research Highlight • An adaptation to the body's pigment formula produces particles that outshine melanin.

- **A deep-sea trench is a plastic dump — and a biodiversity hotspot** [21 January 2021]
  Research Highlight • Plastic bags and wrappers host a thriving community of ocean creatures.

| Next section | Main menu | Previous section |

EDITORIAL
27 January 2021

How epidemiology has shaped the COVID pandemic

Nature's third progress report, coming at the end of the pandemic's first year, highlights key findings from epidemiology — from sounding the early alarm to following the impact of new variants.

Measures such as mask-wearing have been used around the world to try to stop the spread of coronavirus.Credit: Chine Nouvelle/SIPA/Shutterstock

Epidemiology is essential to the fight against any disease. The study of how diseases spread, and why, has loomed large in the struggle to understand, contain and respond to COVID-19. Analyses of data on infections and deaths, and projections from studies that model the virus's spread, have

driven policy decisions all over the world. Many of these, such as locking down countries, imposing quarantines, and mandating social distancing and mask-wearing, are now commonplace.

This editorial — the third instalment in *Nature*'s series of pandemic progress reports — explores some of the key research developments that have helped to illuminate the nature of the infection and the scale of the pandemic.

We also highlight how epidemiology will be important as the pandemic progresses — for example, in understanding the potential impact of the new variants that are currently wreaking havoc around the world. Epidemiology is changing the course of the pandemic, but the coronavirus has stress-tested epidemiology, too, and this report briefly explores how the field is changing as a result.

Epidemiology's early role

It is now more than a year since reports began to emerge of a previously unknown coronavirus causing pneumonia-like symptoms. By 5 January 2020, the virus was reported to have infected 59 people in the city of Wuhan in China's Hubei province; 7 were in a critical condition. By 20 January, the Chinese authorities had reported more than 200 infections and 3 deaths.

Initially, little was known about the virus's transmissibility, but that quickly changed. By about the middle of January, epidemiologists began reporting the results of modelling studies, which indicated that case numbers were likely to be much higher[1] than had initially been documented.

These studies found, for example, that the 'R_0' rate — which describes the number of people an infected person will pass the virus on to, on average, if the virus is allowed to spread uncontrolled — to be between 2 and 4[2,3] Studies also estimated crucial parameters for understanding the virus's epidemic potential. This included its mean incubation period[4] — the time between a person getting infected and the onset of symptoms — and the proportion of people for whom the infection will be fatal[5]. Even early on, it was evident that the risk to people aged over 60 was substantially higher

than that for younger age groups. Some estimates suggested that more than 1 in 10 of those over the age of 80 who became infected would not survive[5].

In these first weeks, researchers were working with limited patient data. However, as more data became available, epidemiologists were able to confirm that the virus could be transmitted by people showing no symptoms[6] and that it had high pandemic potential[1].

Taken together, these studies helped to alert many governments to the fact that the situation might be much more severe than they had anticipated. The findings suggested that hospitals worldwide needed to prepare for a high number of admissions to intensive care.

At the end of January, the World Health Organization declared a Public Health Emergency of International Concern, which included advice for countries on implementing public-health measures, including testing and isolating infected people, and tracing and quarantining their contacts. These moves were based, in part, on research done by epidemiologists after previous infectious-disease outbreaks[7]. But few countries followed this advice.

At the same time, the epidemiological community also began turning its attention to evaluating measures that might help to contain the virus.

Lockdowns and masks

As case numbers started to soar, countries' options for reducing infections and deaths were very limited. It was hard to know what drug regimes might help to combat the disease, and there were no vaccines. In the absence of such tools, researchers began modelling the effectiveness of what are called non-pharmaceutical interventions.

Their models suggested that infections and deaths could be reduced if people wore face masks and maintained a degree of distance from one another, and if more people stayed at home[8,9].

Wuhan went into lockdown on 23 January, and by the middle of February movement was being restricted in about 80 other cities in China. Some months later, researchers would confirm that a range of public-health measures, including closing schools, restricting travel and reducing mixing to within households, brought transmission rates in Wuhan down[3].

Studies from outside China also later affirmed that transmission dropped considerably after educational institutions were closed, gatherings limited and essential businesses closed[10,11]. Moreover, researchers predicted that cities that delayed enacting restrictions would have to keep restrictions in place for longer periods before the virus could be controlled[12].

Although mask-wearing is known to help combat the spread of many infectious respiratory diseases, the lack of controlled trials and direct data meant more time would be required before researchers were able to establish the effectiveness of the measure against the coronavirus. But by the summer of 2020, a number of studies had found that masks contribute to slowing the spread of coronavirus[13,14].

New unknowns

As the virus continues to surge across much of the world, new variants have emerged, and are prompting new questions for epidemiologists. Researchers say that these newer variants, such as B.1.1.7 (also known as VOC 202012/01), first identified in the United Kingdom, are more transmissible and potentially more severe than earlier lineages of the virus (go.nature.com/3a9i9p4). Such findings have implications for policy interventions that were based on earlier data on transmission. Epidemiologists will need to re-evaluate, on the basis of more recent data, whether guidelines on interventions such as social distancing need to be revised and made more stringent to account for the different ways the new variants behave.

Another new challenge for epidemiologists is measuring how the vaccines currently being rolled out around the world affect the virus's spread. Countries where rollouts have already begun might soon be looking to relax restrictions, especially if cases and deaths fall to levels seen before the start

of the second wave. But they should not do so before epidemiologists have established the extent to which vaccines are contributing to increased immunity and the extent to which a fall in cases is the result of the effects of restrictions.

Epidemiology is changing

The pandemic has changed epidemiology. As with many fields that are directly involved in the study of COVID-19, epidemiologists are collaborating across borders and time zones. They are sharing their data using online platforms — preprint servers are giving scientists early access to results — and journals are publishing at a faster rate.

Epidemiology itself is expanding, with the involvement of researchers from other fields, such as physics, mathematics, computer science and network science, who have been contributing their ideas and expertise. The US government has announced that it will establish a National Center for Epidemic Forecasting and Outbreak Analytics. We hope that this will be the epidemiological equivalent of a central meteorological office, an independent body that provides forecasts using advanced computational power, and the best available data. Other countries should consider doing the same.

With many more researchers joining the field from different disciplines — and more people using epidemiological data, including the public, policymakers and the media — researchers must find ways to make sure that their data and findings are communicated transparently, and to ensure the highest standards of research and data ethics.

Communication challenge

The pandemic has thrust epidemiologists and epidemiological models into the policy and media spotlight like never before, and they have faced many challenges. Epidemiology — in particular, epidemic modelling and forecasting — relies on statistical methods to make probabilistic predictions from real-time data. These initial predictions are often not accurate, in part because the underlying data can be incomplete and inconsistently

categorized. Over time, as the data improve and more research groups become involved, results start to look more certain. But often, decisions such as whether to impose restrictions on movement need to be made before there is certainty. Epidemiologists need to communicate both the certainty and the uncertainty of their findings so that the best decisions can be reached.

This has meant that researchers have had to learn how to communicate the inherent uncertainty in their models and predictions in such a way that people can understand that an inaccurate prediction does not invalidate the model and that a general conclusion can still stand. It has also meant that people and policymakers have been exposed to new terminology — words and phrases that help to explain and visualize uncertainty — and models providing a range of probabilistic forecasts from best- to worst-case scenarios.

These challenges also represent an opportunity. They provide a chance to showcase science as it is happening, in real time — something that only researchers normally see. The pandemic has helped people to understand that science, by its very nature, needs to be continually corrected and refined, its conclusions changing as the balance of evidence changes. This contrasts with the way many may have previously viewed science — as a body of knowledge that is fixed and unchanging. The change in how science is perceived might give the impression that scientists are changing their minds, but to do so when the facts change can only be a good thing.

If the past year has taught us anything, it is that knowledge of public-health tools and access to data are not enough to control a pandemic. People have a natural desire for certainty in the face of something as alarming as a pandemic, yet the science informing the pandemic response, by its nature, operates through probabilities. This does not diminish the impact of epidemiology, but, rather, highlights the importance of maintaining a continuous and transparent conversation between researchers, policymakers and the public.

Nature **589**, 491-492 (2021)

doi: https://doi.org/10.1038/d41586-021-00183-z

References

1. 1.

   Wu, J. T., Leung, K. & Leung, G. M. *Lancet* **395**, 689–697 (2020).

2. 2.

   Li, Q. *et al. N. Engl. J. Med.* **382**, 1199–1207 (2020).

3. 3.

   Hao, X. *et al. Nature* **584**, 420–424 (2020).

4. 4.

   Wu, J. T. *et al. Nature Med.* **26**, 506–510 (2020).

5. 5.

   Verity, R. *et al. Lancet Infect. Dis.* **20**, 669–677 (2020).

6. 6.

   He, X. *et al. Nature Med.* **26**, 672–675 (2020).

7. 7.

   Fraser, C., Riley, S., Anderson, R. M. & Ferguson, N. M. *Proc. Natl Acad. Sci. USA* **101**, 6146–6151 (2004).

8. 8.

   Davies, N. G. *et al. Lancet Public Health* **5**, e375–e385 (2020).

9. 9.

   Ferguson, N. M. *et al. COVID-19 Report 9* https://doi.org/10.25561/77482 (Imperial Coll. Lond., 2020).

10. 10.

Flaxman, S. *et al. Nature* **584**, 257–261 (2020).

11. 11.

Hsiang, S. *et al. Nature* **584**, 262–267 (2020).

12. 12.

Du, Z. *et al. Emerg. Infect. Dis.* **26**, 2267–2269 (2020).

13. 13.

Lyu, W. & Wehby, G. L. *Health Aff.* https://doi.org/10.1377/hlthaff.2020.00818 (2020).

14. 14.

IHME COVID-19 Forecasting Team. *Nature Med.* **27**, 94–105 (2021).

Jobs from Nature Careers

-
  -
    - All jobs
  -
    - **Postdoctoral Fellow - Zoubeidi Lab, Vancouver Prostate Centre**

      The University of British Columbia (UBC)

      Vancouver, Canada

      JOB POST

    - **Laser Scientist**

German Electron Synchrotron (DESY)

Hamburg, Germany

JOB POST

- **Fachinformatiker/in Systemintegration (w/m/d)**

  Karlsruhe Institute of Technology (KIT)

  Karlsruhe, Germany

  JOB POST

- **Intership/Bachelor or Master Thesis: "Digitization of land-based shrimp farming in Germany using AI-based evaluation of imaging and acoustic systems"**

  Alfred Wegener Institute - Helmholtz Centre for Polar and Marine Research (AWI)

  Bremerhaven, Germany

  JOB POST

This article was downloaded by **calibre** from https://www.nature.com/articles/d41586-021-00183-z

WORLD VIEW
26 January 2021

Heed blame for extreme weather

Now that specific floods, heatwaves and more can be attributed to our actions, decision makers can act.

Richard A. Betts

Richard A. Betts is head of climate-impacts research at the Met Office Hadley Centre and chair in climate impacts at the University of Exeter Global Systems Institute, UK.
Contact

Search for this author in:

- Pub Med
- Nature.com
- Google Scholar

In 2019, daily maximum temperatures met or broke historical records in more than 24 cities in southwest China. In Yunnan province, a severe drought from March to June caused drinking-water shortages for 2 million people and crop failures over at least 13,500 square kilometres of farmland, with a direct economic loss of about 6.6 billion yuan (about US$1 billion). The chances of those extreme levels of hot and dry conditions occurring concurrently are an estimated 43% higher owing to anthropogenic climate change. A forest fire in the region killed 31 firefighters. The conditions favouring such fires have been made around 7 times more likely by climate change.

In Canada that year, heavy rainfall led to floods that caused thousands of people to evacuate and about Can$200 million (US$157 million) in insured losses; this event was up to 3 times more likely owing to climate change. That August, Hurricane Dorian dropped half a metre of rain on the Bahamas; climate change increased the chances of such precipitation by 5–10%.

These are just a few of the specific heatwaves, floods and events that my colleagues who work on 'climate attribution' can now show were made more likely by human impact (these and more are showcased this week in a special issue of *Bulletin of the American Meteorological Society*; S. C. Herring *et al. Bull. Am. Meteorol. Soc.* **102**, S1–S112; 2021). Now, these techniques should be applied routinely to help governments, organizations and communities to act on their responsibilities and improve resilience to extreme weather.

For too long, weather's randomness has kept events such as these from being blamed squarely on climate change. Reporters in the late 1990s and early 2000s would ask climate scientists about climate change's role in a weather-related disaster. All we could say was that we'd expect to see more of these events. Now, we can specify increased chances for specific events. This extends to forecasts: we can identify the places that are more likely to see wildfires, mudslides and fish die-offs. Such calculations dent both climate denial and a false sense of security. They take away the argument that 'extreme weather happens anyway, so we don't need to worry about it'.

Extreme weather happens — and these metrics pinpoint what is becoming more likely, by how much and why.

The randomness of weather is still a challenge, but physics-based calculations of the workings of the global atmosphere can simulate numerous ways in which the weather could have played out, and compare that with versions of how the weather would have looked in the ‘world that might have been’ without human influence. This lets us estimate how anthropogenic climate change shifted the odds of a drought, heatwave or heavy rain event.

The most crucial use of this information is to make planning more pragmatic. Putting numbers on the increased likelihood of weather extremes increasingly informs my work on climate-change risk assessments, which in turn helps policymakers and planners to apply these methods to saving lives and livelihoods.

Knowing how much more likely heavy rains or heatwaves are can help those who manage grids, roads and rivers to prepare for events that are no longer too improbable to worry about. After major flooding in 2007, UK electricity-transmission and electricity-distribution companies implemented flood-protection measures for substations; quantifying how climate change is increasing flood risk helped to convince the industry regulator that the investment was necessary.

This sort of planning needs to happen as a matter of course. One thing I have found particularly frustrating is that, although houses in my area are now rightly made to be energy-efficient, many are not yet able to cope with hotter weather. (Happily, the UK government launched a consultation related to the topic this month.) Building codes and highway designs are set locally, and are often based on past weather patterns. Drains are built to cope with a certain level of heavy rainfall, say, the highest seen in the past century. Railways and electricity-distribution networks are designed to withstand certain temperatures. For example, in the United Kingdom, a well-maintained railway track should not be vulnerable to buckling below 39°C. Poorly maintained tracks buckle at lower temperatures. As yet, the highest UK temperature officially on record is 38.7°C on 25 July 2019 in the Cambridge Botanic Garden, but exceeding 35°C is now a one-in-5-year

event rather than one in 10–15 years, and the chances of 40°C are no longer negligible.

Such evidence is also useful for legal proceedings when citizens call corporations or governments to account for their role in climate change, or are on trial for taking the law into their own hands. Although the courts, not climate scientists, make judgements on these matters, the legal process needs to be informed by objective, authoritative scientific evidence; published, peer-reviewed science is crucial. I relied on this to provide an expert-witness statement for the trial of an Extinction Rebellion activist arrested after obstructing the main road on Waterloo Bridge in London. For a case against 33 European countries brought by 6 Portuguese youth applicants, the non-profit science and policy institute Climate Analytics prepared an expert report (see go.nature.com/3qmv) centring on the evidence for climate change's rising threat to their lives.

The latest set of extreme-event attribution studies provides yet more evidence, and a reminder that these risks will continue to rise until emissions fall to net zero. We must also learn to adapt, and fast.

Nature **589**, 493 (2021)

doi: https://doi.org/10.1038/d41586-021-00185-x

Jobs from Nature Careers

-
  -
    - All jobs
  -
    - **Postdoctoral Fellow - Zoubeidi Lab, Vancouver Prostate Centre**

      The University of British Columbia (UBC)

      Vancouver, Canada

JOB POST

- **Laser Scientist**

  German Electron Synchrotron (DESY)

  Hamburg, Germany

  JOB POST

- **Fachinformatiker/in Systemintegration (w/m/d)**

  Karlsruhe Institute of Technology (KIT)

  Karlsruhe, Germany

  JOB POST

- **Intership/Bachelor or Master Thesis: "Digitization of land-based shrimp farming in Germany using AI-based evaluation of imaging and acoustic systems"**

  Alfred Wegener Institute - Helmholtz Centre for Polar and Marine Research (AWI)

  Bremerhaven, Germany

  JOB POST

This article was downloaded by **calibre** from https://www.nature.com/articles/d41586-021-00185-x

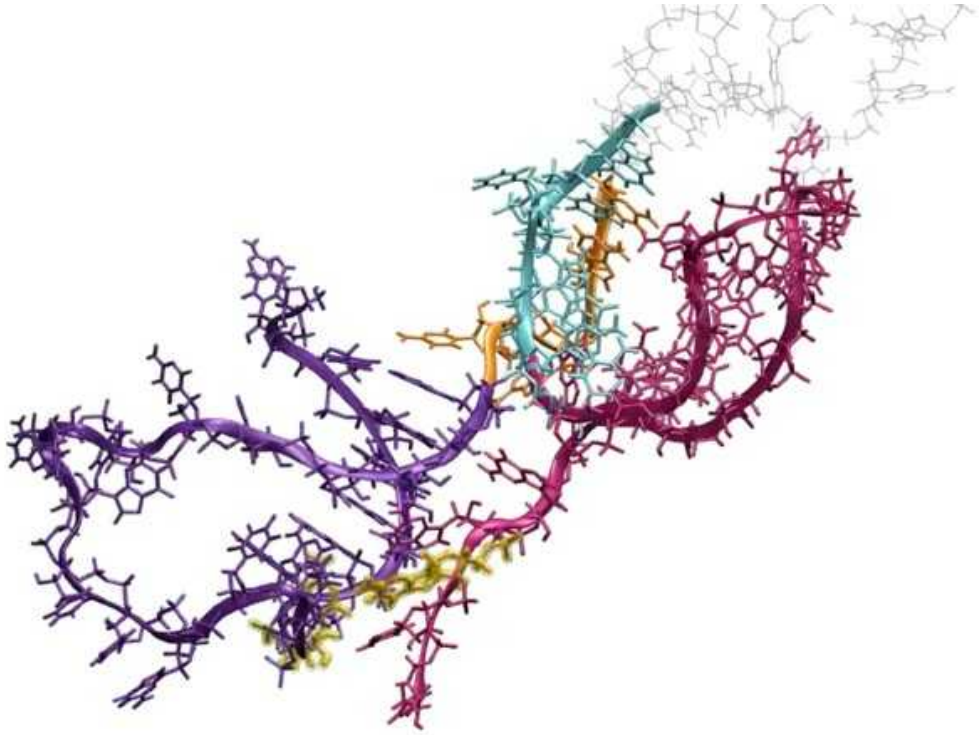

A still from a film of a common type of RNA molecule folding into its signature hairpin shape. Credit: Northwestern Univ./Univ. at Albany

Molecular biology

19 January 2021

Ground-breaking films show RNA's complex curves take shape

Experimental data and predictive algorithms combine to reveal the essential biomolecule's shape-shifting.

Every second, a myriad of shapeless strands of RNA fold, origami-style, into intricate structures inside living cells. Now, researchers can watch the first

data-driven video of this folding as RNA molecules are made by the cellular machinery.

The 3D structure of an RNA molecule is tailored to its function, such as regulating gene expression. To visualize how RNA takes shape, Alan Chen at the University at Albany in New York, Julius Lucks at Northwestern University in Evanston, Illinois, and their colleagues ran experiments to examine how RNA folds as it is synthesized, then fed the data into models that predict RNA folding. This allowed the researchers to generate videos that reconstruct the folding of a type of RNA molecule whose final shape resembles a hairpin.

The footage shows that as the RNA strand grows, it twists, forming knot-like structures. But as more RNA building blocks are added to the strand, the knots unravel, allowing the molecule's structure to emerge.

The findings could help researchers to develop therapies that target RNA molecules, including treatments for a genetic disorder that causes muscular weakness and wasting.

Mol. Cell (2021)

- Molecular biology

This article was downloaded by **calibre** from https://www.nature.com/articles/d41586-021-00126-8

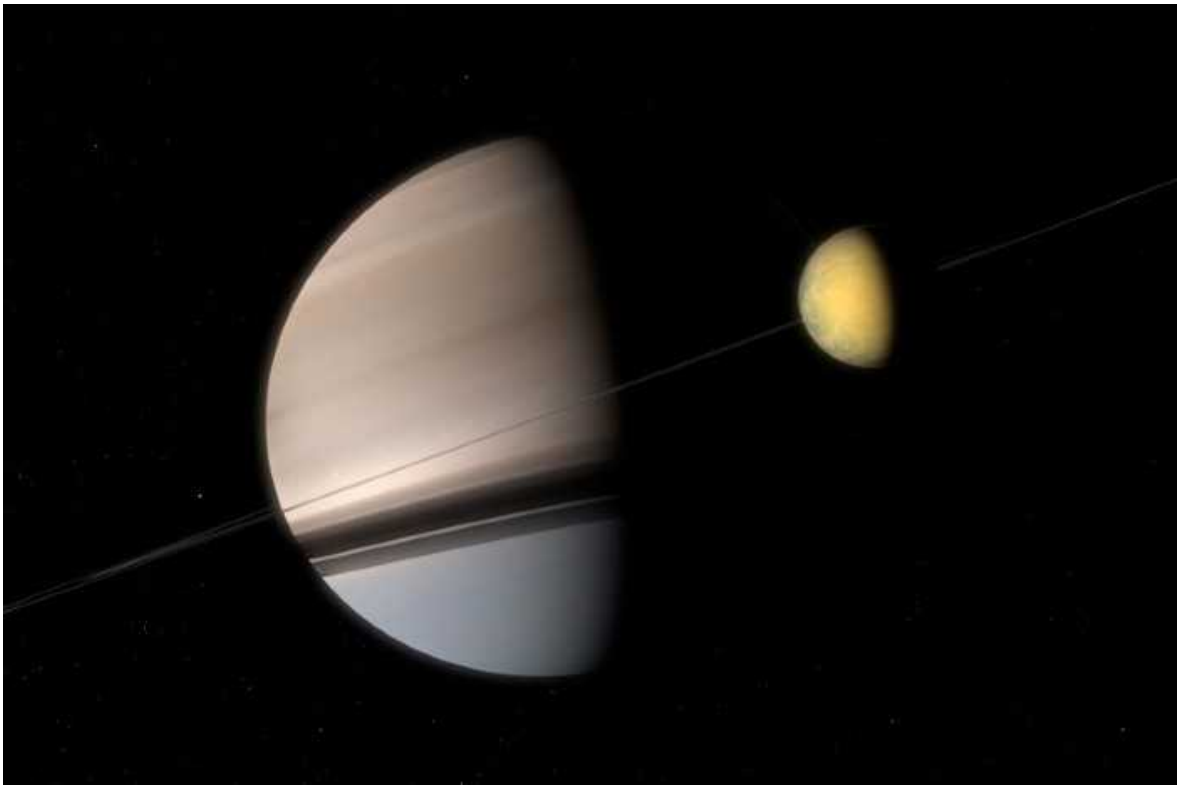

Saturn (left) might have the migration of its moon Titan (right) to thank for its conspicuous tilt. Credit: Mark Garlick/Science Photo Library

Planetary science

25 January 2021

The moon that made Saturn a pushover

Scientists have a new theory for how the ringed planet got its tilt.

Titan, Saturn's biggest moon, probably helped to cause the ringed planet to start tipping off-kilter long ago.

Saturn is tilted with respect to its orbit around the Sun, by a little bit more than Earth is. Planetary scientists had thought that Saturn acquired its tilt more than 4 billion years ago, thanks to the gravitational influence of Neptune.

But recent measurements made with NASA's Cassini spacecraft show that Titan is moving relatively rapidly away from Saturn. Melaine Saillenfest at the Paris Observatory and his colleagues capitalized on that finding to suggest that Titan is to blame for Saturn's tilt.

Their calculations suggest that, around one billion years ago, Titan was migrating away from Saturn and led the planet into a gravitational interaction with Neptune — which steadily tilted Saturn over.

Big migrating moons could similarly cause giant planets in other solar systems to keel over.

Correction 27 January 2021: An earlier version of this article incorrectly used the gender pronoun 'her' for Melaine Saillenfest. It also misstated the journal that published the paper.

Correction 28 January 2021: This article has been changed to correctly describe how Titan influenced Saturn and how Saturn's motion responded to that influence.

Nature Astron. (2021)

- Planetary science

This article was downloaded by **calibre** from https://www.nature.com/articles/d41586-021-00174-0

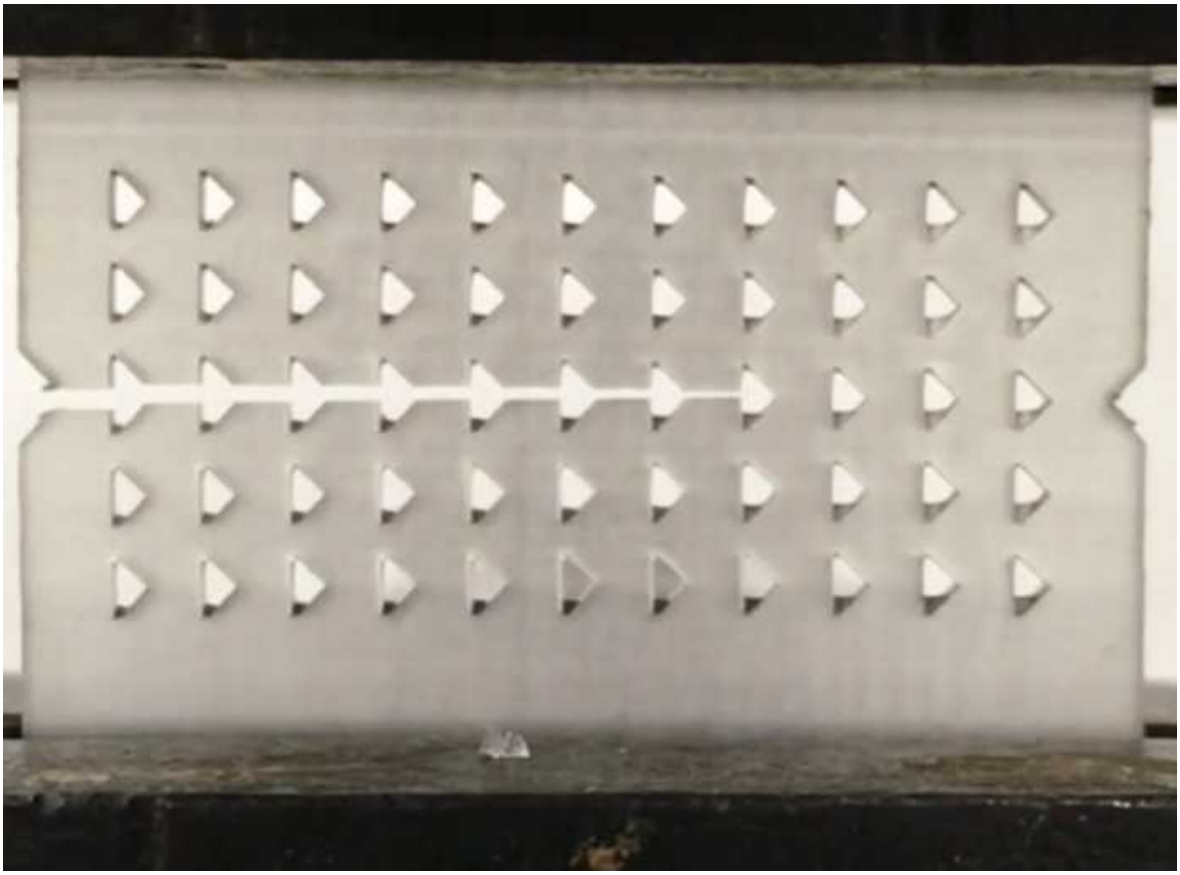

The triangular holes in this material make it more likely to crack from left to right than vice versa. Credit: N. R. Brodnik *et al.*/*Phys. Rev. Lett.*

Materials science

22 January 2021

A material cracks barriers to asymmetrical toughness

Precise engineering generates a structure that fractures more easily in one direction than the other.

Researchers have demonstrated a material that is more resistant to cracks that propagate in one direction than in the opposite direction.

Katherine Faber and Kaushik Bhattacharya at the California Institute of Technology in Pasadena and their colleagues 3D-printed rectangular plates containing a regular array of triangular holes. The holes generally made the material tougher than it would have been without them. That's because it is easier for an existing fracture to propagate than for a new fracture to form; each time a fracture reached a hole, the cracking had to start anew.

But when pulled from its edges, the material tended to break in a specific pattern: if the triangles pointed towards the right, a crack first formed on the left and propagated rightwards, because each triangle's vertex focused the stress into one point and eased a new crack's formation. This cracking sequence revealed that the patterning caused an asymmetrical improvement in toughness.

The authors say that their technique could help to steer cracks in a prescribed direction. In situations in which a failure is inevitable, this could help to protect critical components, they write.

Phys. Rev. Lett. (2021)

- Materials science

This article was downloaded by **calibre** from https://www.nature.com/articles/d41586-021-00158-0

A dog is marked after receiving a rabies jab as part of a drive to inoculate at least 70% of the dogs in Blantyre, Malawi. Credit: Mission Rabies

Public health

22 January 2021

Data helps an anti-rabies campaign go to the dogs

A plan uses real-time monitoring to vaccinate more than two-thirds of a city's canines at low cost.

Build a rabies vaccination station close enough and people will bring their dogs to get the jab. That lesson helped a data-driven vaccination drive to

nearly halve the time and workforce necessary to immunize enough dogs to eliminate rabies in one city.

Dogs and people in a specific location are protected from rabies if 70% or more of its dogs are vaccinated. Vaccination campaigns in Blantyre, Malawi, reached that target, but the campaigns required labour-intensive door-to-door vaccinating teams and fixed vaccination stations. Stella Mazeri at the University of Edinburgh, UK, and her colleagues scoured demographic data and questionnaires collected during those campaigns to understand why dogs were not brought to the fixed stations. They found that people were willing to travel, on average, only 812 metres.

In 2018, the team set up fixed stations so that 77% of dog owners in Blantyre were within that range. The researchers also added roaming stations that moved from street to street in areas where modelling predicted that vaccination would remain low. The campaign vaccinated the same number of dogs as in previous years without door-to-door campaigns.

Proc. Natl Acad. Sci. USA (2020)

- Public health

This article was downloaded by **calibre** from https://www.nature.com/articles/d41586-021-00154-4

Ghana's Tono scheme (pictured) provides water to only about 60% of its original target area, but is still more successful than most large-scale irrigation projects in sub-Saharan Africa. Credit: Timothy Foster, Sarah Redicker and Roshan Adikhari

Sustainability

20 January 2021

Massive water projects leave a parched landscape high and dry

Ambitious irrigation schemes are planned for sub-Saharan Africa — but those already built have a dismal track record.

Most large-scale irrigation projects built in sub-Saharan Africa over the past six decades have failed to work as advertised.

Local governments and international agencies are once again investing in massive irrigation projects, such as dams and canals, in sub-Saharan Africa. To inform such efforts, Thomas Higginbottom and his colleagues at the University of Manchester, UK, compiled data from 79 irrigation schemes built in the region since the 1940s. The researchers then used satellite data to assess the land area irrigated by each project.

The researchers found that irrigation schemes overwhelmingly fell short of their billing: the median irrigated land area across all projects was just 16% of their proposed goals. A scheme's failure risk was not linked to either its size or local climate-change fluctuations, although projects in countries with more stable governance were less likely to fail. The data show no improvement in success rates over the 60-year period.

Because massive irrigation schemes are hugely expensive and have significant impacts on local communities, the authors advise that more research is needed to make these projects cost-effective and sustainable.

Nature Sustain. (2021)

- Sustainability

This article was downloaded by **calibre** from https://www.nature.com/articles/d41586-021-00137-5

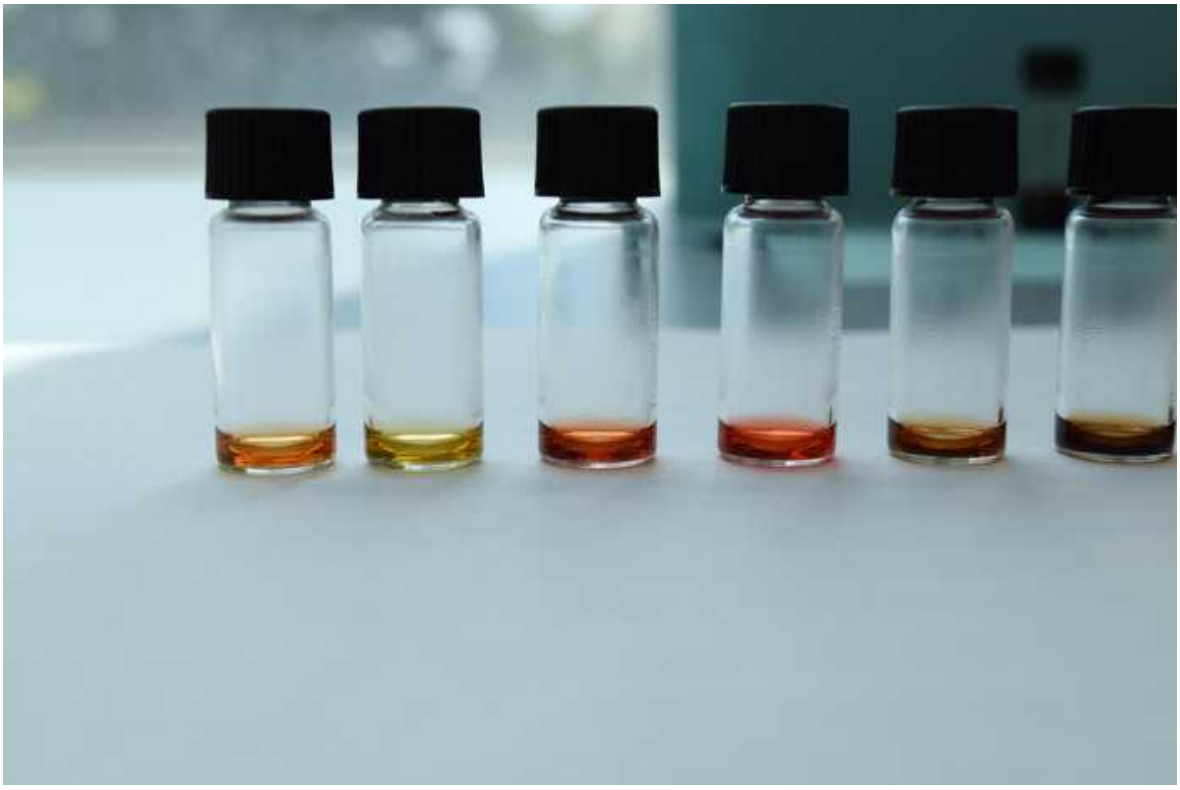

A melanin-like pigment (far left) can assume a range of colours depending on the specific amino acid added to it. Credit: Ayala Lampel

Chemistry

22 January 2021

Chemists' riff on melanin makes a rainbow

An adaptation to the body's pigment formula produces particles that outshine melanin.

A laboratory method that mimics how melanin is made in the skin yields pigments in a wide range of brilliant colours.

Just one pigment — melanin — serves as the basis for the diversity of hair, skin and eye colour in humans. The most abundant form of melanin is black or brown and is made from a single chemical building block, the amino acid tyrosine.

To synthesize similar pigments that outperform melanin, Ayala Lampel at Tel Aviv University in Israel, Rein Ulijn at City University of New York and their colleagues started with a peptide — a short string of amino acids — containing tyrosine, lysine and phenylalanine. The researchers adjusted the peptide's pH to induce its organization into tiny fibres. Then, the researchers added an enzyme to facilitate the same key chemical reaction that triggers melanin formation in the body. As a result, the fibres slowly reconfigured into melanin-like particles.

As the particles grew, they took on a colour when the authors added another amino acid: yellow with cysteine, deep red with phenylalanine and greenish brown with isoleucine.

The researchers hope that these melanin-inspired pigments could one day colour paints and cosmetics.

Angew. Chem. Int. Ed. (2021)

- Chemistry

This article was downloaded by **calibre** from https://www.nature.com/articles/d41586-021-00156-2

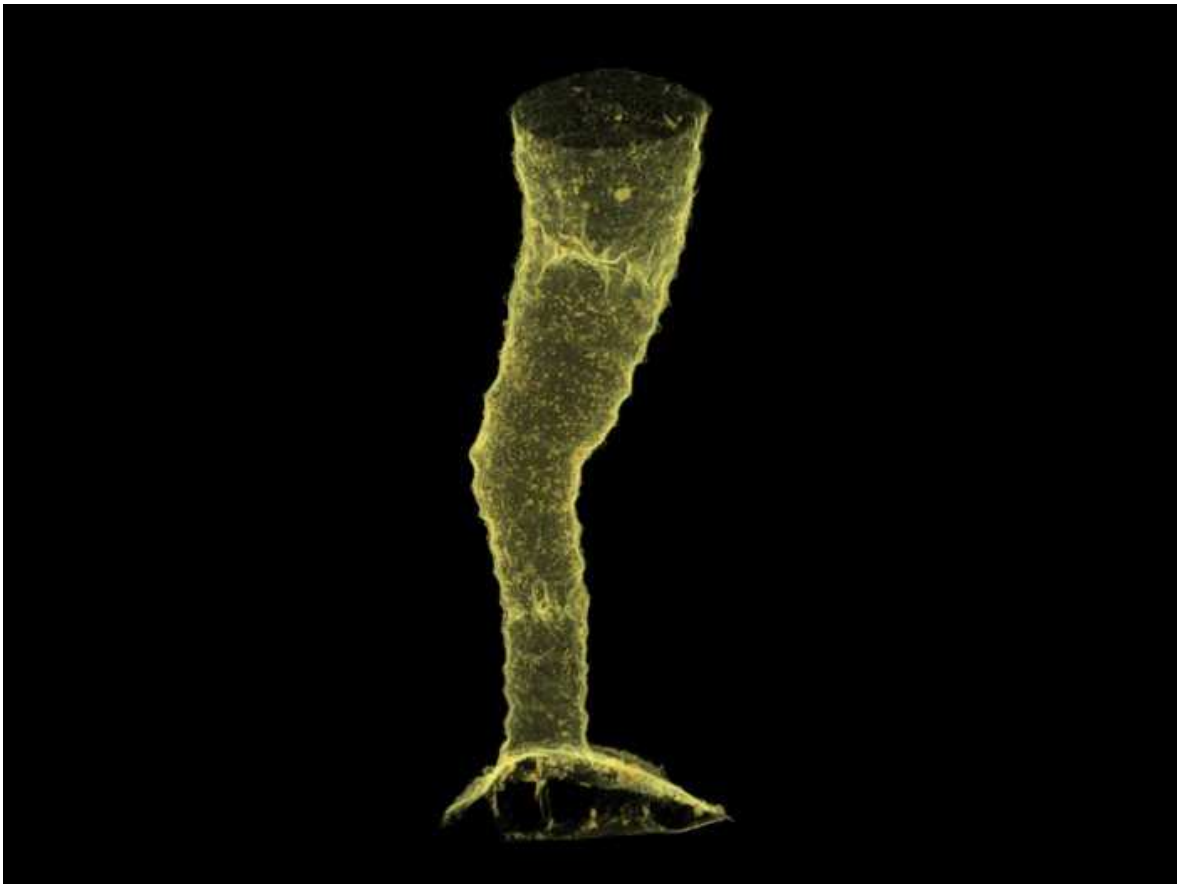

The immobile ‘polyp’ form (pictured) of certain jellyfish has colonized bits of plastic found in a deep-sea rubbish field. Credit: Xikun Song

Ocean sciences

21 January 2021

A deep-sea trench is a plastic dump — and a biodiversity hotspot

Plastic bags and wrappers host a thriving community of ocean creatures.

Discarded plastic is a marine menace, entangling whales and filling seabirds’ stomachs. But deep-ocean plastic dumps can be havens of

biodiversity.

Xikun Song at Xiamen University in China, Xiaotong Peng at the Chinese Academy of Sciences in Sanya and their colleagues dispatched crew members in a submersible to study plastic debris that had accumulated deep in a trench in the South China Sea. Previously described debris ‘dumps’ in the trough held as many as 52,000 pieces of plastic — such as bags, bottles and food wrappers — per square kilometre.

The researchers collected 33 pieces of plastic at depths of 820–3,200 metres. A survey of the items found that they were carrying nearly 1,200 individual organisms representing 49 species of bottom-dwelling organism. Prominent among them were jellyfish polyps — a stage of the animal’s life cycle in which it is fixed to a surface — and the juveniles of shelled organisms called brachiopods, but the team also found free-living creatures such as deep-sea snails and parasitic flatworms.

The authors suggest that these plastic dumps provide refuge for a variety of sea-floor organisms. The effects of this habitat expansion could cascade up the marine food chain.

Environ. Sci. Technol. Lett. (2021)

- Ocean sciences

This article was downloaded by **calibre** from https://www.nature.com/articles/d41586-021-00138-4

News in Focus

- **COVID variants test immunity, NIH chief and China's mixed vaccine data** [27 January 2021]
  News Round-Up • The latest science news, in brief.
- **Why did the world's pandemic warning system fail when COVID hit?** [23 January 2021]
  News • Nearly one year ago, the World Health Organization sounded the alarm about the coronavirus, but was ignored.
- **Fast-spreading COVID variant can elude immune responses** [21 January 2021]
  News • Evidence that a variant of the coronavirus identified in South Africa might compromise immunity sparks concerns about vaccine effectiveness.
- **'Inspired choice': Biden appoints sociologist Alondra Nelson to top science post** [21 January 2021]
  News • Scientists praise US president's selection of the bioethics and social inequality specialist to help lead the Office of Science and Technology Policy.
- **What new COVID variants mean for schools is not yet clear** [21 January 2021]
  News • Children are no more susceptible to these lineages than adults are — and closing schools on the basis of incomplete information could have repercussions.
- **Are COVID vaccination programmes working? Scientists seek first clues** [22 January 2021]
  News • Vaccinated people in Israel are less likely to test positive for SARS-CoV-2, but a population-wide effect will take time to become clear.
- **Science family of journals announces change to open-access policy** [15 January 2021]
  News • Subscription journals will let some Plan S funded researchers share accepted manuscripts under open licences.
- **How ecstasy and psilocybin are shaking up psychiatry** [27 January 2021]

News Feature • Regulators will soon grapple with how to safely administer powerful psychedelics for treating depression and post-traumatic stress disorder.

| Next section | Main menu | Previous section |

NEWS ROUND-UP
27 January 2021

- Correction 28 January 2021

COVID variants test immunity, NIH chief and China's mixed vaccine data

The latest science news, in brief.

Vials of CoronaVac are inspected in Sao Paulo, Brazil.Credit: Amanda Perobelli/Reuters

COVID vaccines might be less potent against new viral variants

Emerging, fast-spreading variants of the coronavirus might reduce the protective effects of two leading vaccines.

Michel Nussenzweig at the Rockefeller University in New York City and his colleagues analysed blood from 20 volunteers who received 2 doses of either the Moderna or the Pfizer–BioNTech vaccines (Z. Wang *et al*. Preprint at bioRxiv https://doi.org/frdn; 2021). Both vaccines carry RNA instructions that prompt human cells to make the spike protein that the virus uses to infect cells. This causes the body to generate antibodies that recognize the spike protein.

Between 3 and 14 weeks after the second jab, study participants developed several types of antibody, including some that block SARS-CoV-2 from infecting cells. Some of these neutralizing antibodies were as effective against viruses carrying certain mutations in the spike protein as they were against widespread forms. But some were only one-third as effective at blocking the mutated variants.

Some of the mutations that the team tested have been seen in coronavirus variants that were first identified in the United Kingdom, Brazil and South Africa. The findings, which haven't been peer reviewed, suggest that vaccine-resistant variants might emerge.

A health worker in Israel prepares a dose of COVID-19 vaccine.Credit: Jack Guez/AFP/Getty

Mixed results for COVID shot

Long-awaited results on the effectiveness of a leading Chinese COVID-19 vaccine were tinged with disappointment. But researchers say the vaccine could still help to reduce deaths from the disease.

Scientists in Brazil reported on 12 January that CoronaVac, developed by Beijing-based Sinovac, was 50.4% effective at preventing severe and mild COVID-19 in late-stage trials. That's significantly lower than the 90% efficacies of several leading vaccines.

The CoronaVac figures were also much lower than those from early trials of the same vaccine in Turkey and Indonesia, and below the efficacy first reported by the Brazil trial team. Researchers at the Butantan Institute in São Paulo had announced on 7 January that the vaccine was 78% effective at

preventing the disease — but later revealed that the figure was based on the narrow criterion of people needing medical attention.

Nevertheless, if the latest results check out — they have not been peer reviewed — the two-dose vaccine could be immediately beneficial in countries where outbreaks are raging, such as Brazil, say researchers. “When you’ve got communities that are absolutely desperate, and have no other choice, then this is a really great thing to have,” says Hilda Bastian, who studies evidence-based medicine at Bond University in Gold Coast, Australia.

Francis Collins is best known for leading the Human Genome Project.Credit: Michael Reynolds/Getty

Francis Collins to stay on at NIH Under Biden

Geneticist Francis Collins will continue in his role as the head of the US National Institutes of Health (NIH), President Joe Biden announced on 15 January.

Former president Barack Obama appointed Collins to lead the biomedical-research agency in 2009, and his successor, Donald Trump, extended Collins's term as director in 2017.

With an annual budget of just over US$40 billion, the NIH has prioritized funding for research on the coronavirus in the past year, as well as efforts to find treatments and vaccines for COVID-19.

"I will do my best to continue to lead this great agency, especially when NIH's role in fighting this pandemic is so critical," Collins said on Twitter after Biden's announcement.

Collins is best known for leading the Human Genome Project, the massive public effort to sequence the human genome that was declared complete in 2003. Trained as a physician, he focused his early research on disease-causing genes, and co-discovered the gene for cystic fibrosis. He was director of the NIH's National Human Genome Research Institute between 1993 and 2008.

Nature **589**, 497 (2021)

doi: https://doi.org/10.1038/d41586-021-00186-w

Updates & Corrections

- **Correction 28 January 2021**: The item entitled 'Francis Collins to stay on at NIH Under Biden' erred in stating that Donald Trump extended Collins's term as director in 2012. He did this in 2017.

Jobs from Nature Careers

-
  -
    - All jobs
  -
    -

Postdoctoral Fellow - Zoubeidi Lab, Vancouver Prostate Centre

The University of British Columbia (UBC)

Vancouver, Canada

JOB POST

- **Laser Scientist**

  German Electron Synchrotron (DESY)

  Hamburg, Germany

  JOB POST

- **Fachinformatiker/in Systemintegration (w/m/d)**

  Karlsruhe Institute of Technology (KIT)

  Karlsruhe, Germany

  JOB POST

- **Intership/Bachelor or Master Thesis: "Digitization of land-based shrimp farming in Germany using AI-based evaluation of imaging and acoustic systems"**

  Alfred Wegener Institute - Helmholtz Centre for Polar and Marine Research (AWI)

  Bremerhaven, Germany

  JOB POST

This article was downloaded by **calibre** from https://www.nature.com/articles/d41586-021-00186-w

NEWS
23 January 2021

- Update 23 January 2021

Why did the world's pandemic warning system fail when COVID hit?

Nearly one year ago, the World Health Organization sounded the alarm about the coronavirus, but was ignored.

Amy Maxmen

Search for this author in:

- Pub Med
- Nature.com
- Google Scholar

WHO director-general Tedros Adhanom Ghebreyesus is reviewing how the world responded to the early days of the COVID-19 pandemic during an executive board meeting this week.Credit: Fabrice Coffrini/Reuters

The World Health Organization (WHO) sounded its highest alarm on 30 January 2020 — a declaration called a ‘public health emergency of international concern’, or PHEIC, signalling that a pandemic might be imminent. Few countries heeded the WHO’s call for testing, tracing and social distancing to curb the coronavirus. By mid-March, it had spread around the world. Now, health officials and researchers are evaluating why the organization’s warning system failed and how to overhaul it.

Many say the organization should have declared a PHEIC about a week earlier than it did. But the largest failing, researchers agree, is that so many countries ignored it. Two new preliminary investigations — one from the WHO and another from an independent panel responsible for assessing the organization — attempt to unravel why.

What a US exit from the WHO means for COVID-19 and global health

“The biggest issue to me is that for six to eight weeks after the PHEIC declaration, countries, except for in Asia, sat on their hands,” says Joanne Liu, a former president of Médecins Sans Frontières (also known as Doctors without Borders), who serves on the independent panel.

World health officials are evaluating potential improvements to the system during the WHO’s executive board meeting, being held 18–26 January. Talks will continue in advance of the annual World Health Assembly in May, when any changes would occur. Some of the proposals include modifying the PHEIC alarm to have colour-coded warning levels, and having countries sign on to a new treaty on preparing for pandemics.

The thorniest problem for the WHO, though, is how to persuade countries to heed its warnings. Liu says: “The real question is, what would it take for people to do something when a declaration happens?”

What's in a name?

The PHEIC alarm originated in 2005, when the WHO overhauled its decades-old regulations about international health emergencies: 196 countries and territories agreed to alert the organization when outbreaks emerged, and gave it the power to declare a PHEIC. The WHO can sound this alarm if it deems an emergency extraordinary, if the emergency poses a risk to countries outside where it originated and if it requires an international response — meaning, in some cases, that it could have pandemic potential. Since the revision, the WHO has declared a PHEIC six times (see 'Sound the alarm').

Sound the alarm

The WHO has declared a 'public health emergency of international concern,' or PHEIC, six times since the alarm system originated in 2005.

2009: H1N1 (swine flu) originates in Mexico and spreads to the United States.

2014: Polio resurges in Afghanistan, Pakistan and Nigeria.

2014: Ebola virus infections spread throughout Guinea, Sierra Leone and Liberia.

2016: A Zika virus epidemic causes microcephaly and other neurological disorders in the Americas.

2019: An Ebola outbreak spreads in a conflict zone in the Democratic Republic of the Congo.

2020: The COVID-19 pandemic originates in China and spreads to 18 other countries.

At each declaration, the WHO advises governments on how to respond to the situation at hand. For example, last January, the WHO director-general Tedros Adhanom Ghebreyesus said of the COVID-19 outbreak, "It is still possible to interrupt virus spread, provided that countries put in place strong

measures to detect disease early, isolate and treat cases, trace contacts and promote social-distancing measures."

Liu admits that the term PHEIC isn't as sexy as an emotive word, such as 'pandemic' or 'emergency'. But researchers and health officials chose it partly because they wanted to avoid panic while encouraging world leaders to act according to WHO advice to contain a threat, says Gian Luca Burci, an international law specialist at the Graduate Institute of International and Development Studies in Geneva, Switzerland. Burci helped to revise the regulations in 2005.

Nature's 10: ten people who helped shape science in 2020

In hindsight, that reasoning appears to be flawed. Several reports note that politicians and the public mainly ignored the PHEIC declaration and Tedros's corresponding recommendations in January 2020, but started listening when the organization used the unofficial term 'pandemic' to describe COVID-19 in March, once it was spreading in multiple continents. Unlike the PHEIC, 'pandemic' is not a defined declaration, and countries haven't agreed to take any actions once it's used.

Despite the disproportionate response to the word pandemic, many scholars argue that changing the name of the WHO's highest alarm wouldn't be useful. "I don't care for the term PHEIC," says Alexandra Phelan, a global-health lawyer at Georgetown University in Washington DC, "but I worry that if we get too into the words, we miss the point that countries need to act appropriately when there is a declaration."

Fixing flaws

Researchers are, however, critical of the process for declaring a PHEIC. On 22 January 2020, Tedros convened a closed-door meeting of virologists, public-health researchers and certain government representatives — as the process dictates. They decided that a PHEIC wasn't warranted, but a week later, the committee flipped its position, resulting in a delay that might have cost the world time to contain the virus.

Global health scholars debate the timing of PHEICs after every declaration. To improve the system, Phelan and an international consortium of researchers argue, in a white paper published in November, that it should be made more transparent. The reason, they say, is so that scholars can better evaluate how these decisions are made by weighing scientific evidence, as well as social, political and economic concerns.

What the data say about border closures and COVID spread

Still, a one-week lag in declaring a global emergency isn't even the most concerning action that took place in the early days of the COVID-19 pandemic, critics say. When Tedros declared the PHEIC, he advised governments to move fast with public-health measures including tests and social distancing. He also asked them to resist bans on travel and trade because, historically, they are of limited utility and are potentially harmful.

But governments around the world ignored those calls. For example, the United States did not roll out testing across the country until late February; did not bar large gatherings until March; ditched contact-tracing; and banned some travel from China, where the virus was first discovered.

Praising and shaming

Countries appear to agree that to improve the world's ability to respond to pandemics, the WHO should be transformed and bolstered. Speaking as a representative of the United States, infectious-disease scientist Anthony Fauci told the WHO this week that the country will reverse its withdrawal from the organization, initiated by former president Donald Trump, and "work constructively with partners to strengthen and importantly reform the WHO".

One change suggested by a former US government official, speaking with *Nature* on background because he is advising US President Joe Biden's administration, is to empower the WHO to act on unofficial data on social media and elsewhere despite questions of accuracy, so that the organization can respond rapidly to emerging diseases without waiting for governments that might withhold information.

Exclusive: Behind the front lines of the Ebola wars

The WHO could also be strengthened through a new treaty on pandemics that countries would need to sign onto. On 20 January, Tedros said he would assemble a working group to explore this proposal from the president of the European Council, Charles Michel. Steven Solomon, principal legal officer at the WHO, says a pandemic treaty might be helpful for world leaders who don't understand the technical details of a PHEIC. Still, the WHO probably wouldn't have the ability to penalize countries that don't comply. "There's no silver bullet here since you're dealing with a community of nations, all of whom guard their sovereignty very closely," says Solomon.

The WHO therefore relies on diplomacy, which often boils down to praising or shaming countries. But the WHO's appetite for criticism is limited by its reliance on donations from its member countries and on countries openly offering access and information — which could be withheld if leaders felt insulted. A case in point is that the WHO spent weeks gently persuading China to permit an international team of scientists to visit Wuhan after the outbreak was reported there. On the financing front, researchers say that a larger, reliable budget for the WHO would give the organization greater autonomy because it wouldn't be dependent on fundraising amid a disaster.

To address communication concerns, Tedros has suggested adding a gradient of warnings to the PHEIC, coded by colour. The colours could separate emergencies that might evolve into a pandemic from those that are serious but won't affect nations across the globe. Countries with outbreaks — or threatening coronavirus variants — might more willingly share information if there were a low-grade alarm that was less likely to result in disruptions to people's livelihoods or the economy.

Reforms won't come until the World Health Assembly in May — at the earliest. The possibility of solutions being delayed or forgotten fills Liu with dread, because she recalls dozens of panels assessing failures in the response to the Ebola outbreak in West Africa in 2014–2016. "Less than 10% of the recommendations were followed up on," she says. "We have an amazing talent to outrage ourselves about a situation, but when it comes time to deliver any change, there is very little traction, and people go back to doing whatever they had done before."

Nature **589**, 499-500 (2021)

doi: https://doi.org/10.1038/d41586-021-00162-4

Updates & Corrections

- **Update 23 January 2021**: This story was updated to include explicit references to preliminary investigations conducted by the WHO and an independent panel about how the world responded to the COVID-19 pandemic.

Jobs from Nature Careers

-
  -
    - All jobs
  -
    - **Postdoctoral Fellow - Zoubeidi Lab, Vancouver Prostate Centre**

The University of British Columbia (UBC)

Vancouver, Canada

JOB POST

- **Laser Scientist**

  German Electron Synchrotron (DESY)

  Hamburg, Germany

  JOB POST

- **Fachinformatiker/in Systemintegration (w/m/d)**

  Karlsruhe Institute of Technology (KIT)

  Karlsruhe, Germany

  JOB POST

- **Intership/Bachelor or Master Thesis: "Digitization of land-based shrimp farming in Germany using AI-based evaluation of imaging and acoustic systems"**

  Alfred Wegener Institute - Helmholtz Centre for Polar and Marine Research (AWI)

  Bremerhaven, Germany

  JOB POST

This article was downloaded by **calibre** from https://www.nature.com/articles/d41586-021-00162-4

NEWS
21 January 2021

Fast-spreading COVID variant can elude immune responses

Evidence that a variant of the coronavirus identified in South Africa might compromise immunity sparks concerns about vaccine effectiveness.

Ewen Callaway

Search for this author in:

- Pub Med
- Nature.com
- Google Scholar

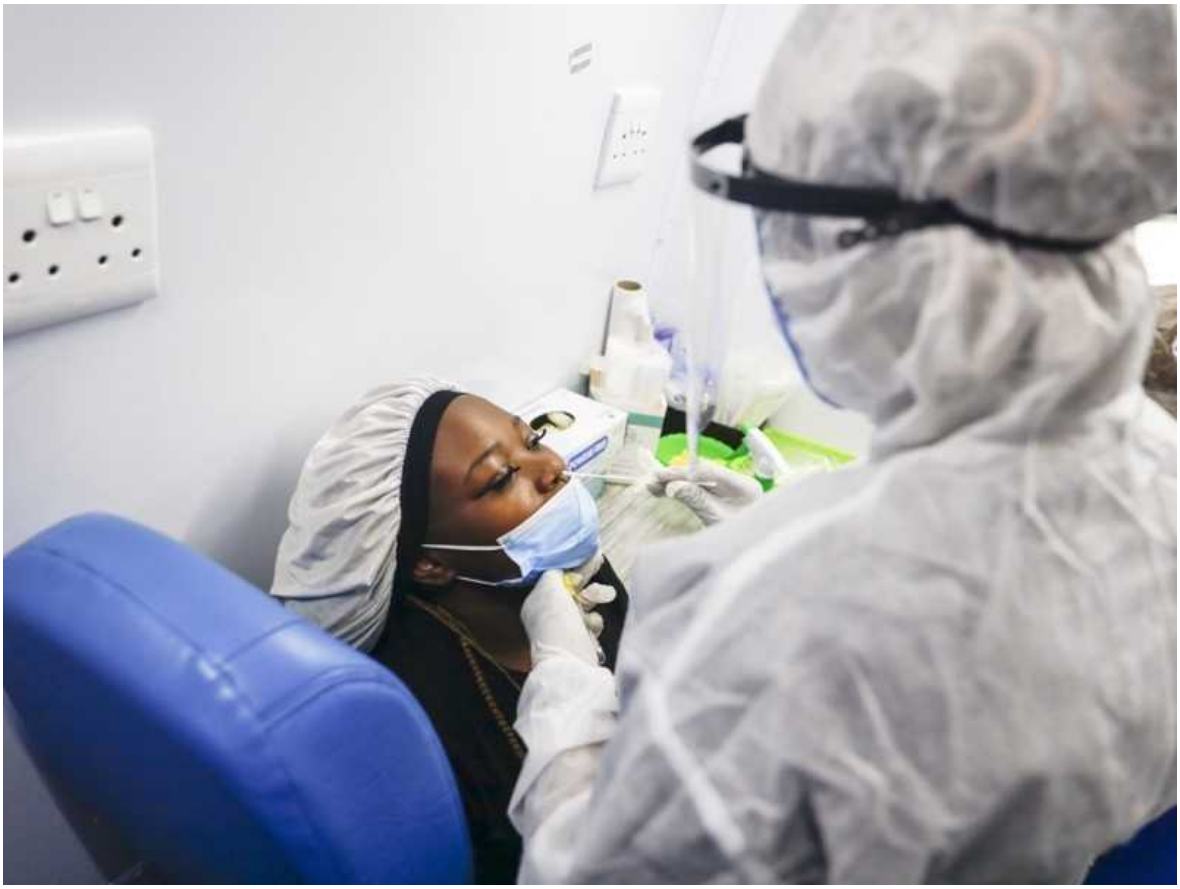

A mobile coronavirus testing unit in South Africa, where the 501Y.V2 variant was detected in late 2020.Credit: Guillem Sartorio/Bloomberg/Getty

Evidence is growing that some coronavirus variants could evade immune responses triggered by vaccines and previous infections. Researchers are trying to make sense of a tsunami of lab studies released this week that raise concerns about some emerging variants and mutations.

“Some of the data I’ve seen in the last 48 hours have really scared me,” says Daniel Altmann, an immunologist at Imperial College London, who worries that some of results could portend a reduction in the effectiveness of COVID-19 vaccines.

Could new COVID variants undermine vaccines? Labs scramble to find out

But the picture is murky, Altmann and other scientists emphasize. The studies — which examined the blood of small numbers of people who had recovered from COVID-19 or received a vaccine — probed only their antibodies' capacity to 'neutralize' variants in laboratory tests, and not the wider effects of other components of their immune response.

Neither do the studies indicate whether the changes in antibody activity make any difference to the real-world effectiveness of vaccines or the likelihood of reinfection. "Are these changes going to be important? I really don't know," says Paul Bieniasz, a virologist at the Rockefeller University in New York City, who co-led one of the studies.

Fast-spreading lineage

Much of the concern centres around a variant that researchers identified in South Africa in late 2020. A team led by Tulio de Oliveira, a bioinformatician at the University of KwaZulu-Natal in Durban, South Africa, linked the variant — called 501Y.V2 — to a fast-growing epidemic in Eastern Cape province that has since spread across South Africa and into other countries[1]. The lineage carries many mutations in the SARS-CoV-2 spike protein — the immune system's prime target, which allows the virus to identify and infect host cells — including some changes linked to weakened antibody activity against the virus[2,3].

The Eastern Cape was hit hard by South Africa's first COVID-19 wave, and researchers wondered whether the rapid spread of 501Y.V2 could be partly explained by its ability to elude previously established immune responses.

To investigate this, de Oliveira, virologist Alex Sigal at the Africa Health Research Institute in Durban and other colleagues isolated 501Y.V2 viruses from people infected with the variant[4]. They then tested the variant samples against serum — the antibody-containing portion of blood — taken from six people who had recovered from COVID-19 caused by other versions of the virus. This convalescent serum tends to contain neutralizing, or virus-blocking, antibodies that can prevent infection. The researchers found that the convalescent serum was much worse at neutralizing 501Y.V2 than at neutralizing variants that circulated earlier in the pandemic. Some people's plasma performed better against 501Y.V2 than did others', but in all cases, the neutralizing power was substantially weakened, says de Oliveira. "It's extremely worrying."

‘A bloody mess’: Confusion reigns over naming of new COVID variants

In a separate study[5], a team led by virologist Penny Moore at the National Institute for Communicable Diseases and the University of the Witwatersrand in Johannesburg, South Africa, probed the effects of convalescent serum on various combinations of spike mutations found in 501Y.V2. They did this using a ‘pseudovirus’ — a modified form of HIV that infects cells using the SARS-CoV-2 spike protein.

These experiments showed that 501Y.V2 contains mutations that blunt the effects of neutralizing antibodies that recognize two key regions of spike: its receptor-binding and N-terminal domains. Pseudoviruses with the full package of 501Y.V2 mutations were fully resistant to convalescent serum from 21 out of 44 participants, and were partly resistant to the vast majority of people’s sera, Moore’s team found.

There is now proof of several reinfections with 501Y.V2 in South Africa, says de Oliveira. It seems increasingly likely that the variant’s ability to spread in places hit hard by earlier waves of COVID-19 is being driven, in part, by its capacity to evade immune responses that developed in response to earlier versions of the virus.

“It becomes virtually inescapable that that’s what’s happening,” says Bieniasz, noting that variants identified in Brazil and the United Kingdom carry some of the same spike mutations.

Impacts on immunity

Both South African teams will soon test the 501Y.V2 variant with serum from people who participated in COVID-19 vaccine trials, and similar studies are under way at labs worldwide. A team co-led by Bieniasz found that mutations in the receptor-binding domain of 501Y.V2 caused a modest

drop in the potency of antibodies from people who had received either the Pfizer or Moderna mRNA vaccines[6]. That's "a reassuring finding", says Moore, but it will be important to test the consequences of other mutations in 501Y.V2.

Vaccine makers in Asia rush to test jabs against fast-spreading COVID variant

Whether these could lessen the effectiveness of vaccines is still uncertain, says Volker Thiel, an RNA virologist at the University of Bern in Switzerland. Most COVID-19 vaccines elicit high levels of antibodies that target diverse regions of the spike protein, so some of the molecules are likely to be able to block variants of the virus. And other components of the immune response, such as T cells, might not be affected by 501Y.V2. "Although the vaccines target only the spike gene, they should still mount an immune response that is diverse enough that these new variants should be covered," Thiel says. "But experimental studies need to be done."

Data from ongoing efficacy trials and national vaccine rollouts should be able to uncover the effects of the variants. Several vaccines are still being

trialled in South Africa, and researchers will be watching for any drop in their ability to prevent COVID-19 that's linked to the rise of 501Y.V2.

A dampened antibody response to variants such as 501Y.V2 might not be much of a problem in practice, says Marion Koopmans, a virologist at the Erasmus Medical Center in Rotterdam, the Netherlands. "You can see some change in a lab assay, which does not have an effect in a person because that person still has enough antibodies to neutralize the infection." It can also be difficult to disentangle whether reinfections are due to waning immune responses triggered by the first infection, or to the effects of a mutation, she adds.

Emerging data

Clues are also beginning to emerge about the behaviour of a fast-spreading variant identified in the United Kingdom, known as B.1.1.7. In pseudovirus experiments, researchers at biotech firm BioNTech in Mainz, Germany, found that B.1.1.7's spike mutations had little effect on sera from 16 people who had received the vaccine the company developed with Pfizer[7]. Meanwhile, a team led by virologist Ravindra Gupta at the University of Cambridge, UK, looked at the sera of 15 people who had received the first of two doses of the same immunization[8]; the team found that 10 people's sera was less effective against B.1.1.7 than against other versions of SARS-CoV-2. These changes shouldn't make a difference to the vaccine's effectiveness now, says Gupta, but they could as antibody levels wane over time.

What this week's results mean for battling the pandemic are not yet clear. It is a top priority for researchers to determine whether mutations in 501Y.V2 are responsible for reinfections. If they are, says de Oliveira, "the whole idea of herd immunity would become a pipe-dream, at least from natural infection".

Nature **589**, 500-501 (2021)

doi: https://doi.org/10.1038/d41586-021-00121-z

References

1. 1.

   Tegally, H. *et al.* Preprint at medRxiv https://doi.org/10.1101/2020.12.21.20248640 (2020).

2. 2.

   Andreano, E. *et al.* Preprint at bioRxiv https://doi.org/10.1101/2020.12.28.424451 (2020).

3. 3.

   Greaney, A. J. *et al.* Preprint at bioRxiv https://doi.org/10.1101/2020.12.31.425021 (2021).

4. 4.

   Cele, S. *et al.* Preprint at medRxiv https://doi.org/10.1101/2021.01.26.21250224v1 (2021).

5. 5.

   Wibmer, C. W. *et al.* Preprint at bioRxiv https://doi.org/10.1101/2021.01.18.427166 (2021).

6. 6.

   Wang, Z. *et al.* Preprint at bioRxiv https://doi.org/10.1101/2021.01.15.426911 (2021).

7. 7.

   Muik, A. *et al.* Preprint at bioRxiv https://doi.org/10.1101/2021.01.18.426984 (2021).

8. 8.

Collier, D. et al. Preprint at medRxiv https://doi.org/10.1101/2021.01.19.21249840 (2021).

Jobs from Nature Careers

-
  -
    - All jobs
  -
    - **Postdoctoral Fellow - Zoubeidi Lab, Vancouver Prostate Centre**

      The University of British Columbia (UBC)

      Vancouver, Canada

      JOB POST

    - **Laser Scientist**

      German Electron Synchrotron (DESY)

      Hamburg, Germany

      JOB POST

    - **Fachinformatiker/in Systemintegration (w/m/d)**

      Karlsruhe Institute of Technology (KIT)

      Karlsruhe, Germany

      JOB POST

    - **Intership/Bachelor or Master Thesis: "Digitization of land-based shrimp farming in Germany using**

AI-based evaluation of imaging and acoustic systems"

Alfred Wegener Institute - Helmholtz Centre for Polar and Marine Research (AWI)

Bremerhaven, Germany

JOB POST

This article was downloaded by **calibre** from https://www.nature.com/articles/d41586-021-00121-z

NEWS
21 January 2021

‘Inspired choice’: Biden appoints sociologist Alondra Nelson to top science post

Scientists praise US president’s selection of the bioethics and social inequality specialist to help lead the Office of Science and Technology Policy.

Nidhi Subbaraman

Search for this author in:

- Pub Med
- Nature.com
- Google Scholar

Alondra Nelson has been appointed deputy director of science and society at the White House Office of Science and Technology Policy.Credit: Alex Wong/Getty

During his presidential campaign, Joe Biden pledged that his administration would address inequality and racism. Now that he's been sworn in as US president, his appointment of a prominent sociologist to the nation's top science office is raising hopes that the changes will extend to the scientific community.

Alondra Nelson, who has studied the societal impacts of emerging technology, as well as racism in science and medicine, will help lead the White House Office of Science and Technology Policy (OSTP) as deputy director for science and society, Biden announced on 15 January. She has spoken and written about divisive and controversial subjects in bioethics, such as gene editing and direct-to-consumer genetic tests.

Scholars say her inclusion on Biden's science team emphasizes the importance of science's effect on society, and vice versa.

The latest on Biden's science team: biologist named as top adviser

"She understands exactly what is needed to ensure that research has maximum impact on policy," says Kate Crawford, a senior principal researcher at Microsoft in New York City who has studied the social implications of artificial intelligence and emerging technologies. "I think that is the real gift that the White House is getting" with Nelson on the team, she says.

Biden's selection is an "inspired choice", says Keith Wailoo, a historian of race and health at Princeton University in New Jersey. Nelson's "scholarship on genetics, social inequality and medical discrimination is deeply insightful and hugely influential across multiple fields, most notably because of its focus on excellence, equity and fairness in scientific and medical innovation", he wrote in an e-mail to *Nature*.

Confronting injustice

Nelson's appointment to the OSTP comes as the United States and its scientific institutions are grappling with their record on equity and inclusion. Although Hispanic and African Americans make up 27.5% of the US

population over the age of 21, these groups constitute only 13% of the US science and engineering workforce. In the past several months, the COVID-19 pandemic has killed nearly three times as many Black Americans as white ones, and it has highlighted gaps in how health care is administered to people of different races and ethnicities.

Universities scrub names of racist leaders — students say it's a first step

During a 16 January event at which Biden introduced his OSTP team, Nelson acknowledged the challenges ahead. "Never before in living memory have the connections between our scientific world and our social world been quite so stark as they are today," she said. "I believe we have a responsibility to work together to make sure that our science and technology reflects us."

On Biden's first day as president, his team announced a government-wide effort to promote equity and dismantle structural racism, led by former US ambassador to the United Nations Susan Rice. The team also noted that confronting inequalities and injustice will be central to how the Biden administration tackles climate change and the COVID-19 pandemic.

Wide-ranging influence

News of Nelson's leadership role at an office that advises the president triggered a wave of praise on Twitter from researchers across disciplines, including computer science, history and American studies.

"I think that that outpouring of support is indicative of her impact, and her impact across a whole bunch of different fields," says Victor Ray, a sociologist who studies race and ethnicity at the University of Iowa in Iowa City. The applause also acknowledged Nelson's generosity to junior scholars, says Ray — something he experienced when meeting her. She had "a genuine interest in me and my ideas, which junior scholars really appreciate from someone of her stature", he adds.

Joe Biden names top geneticist Eric Lander as science adviser

Nelson has been president of the Social Science Research Council, a non-profit organization that supports research in the social sciences, and a professor at the Institute for Advanced Study in Princeton. She is an elected member of the National Academy of Medicine, where she co-chairs the

committee on emerging science technology and innovation in health and medicine. In her 2016 book *The Social Life of DNA*, she documented how Black American descendants of enslaved people are tracing their ancestry using DNA tests. In *Body and Soul*, published in 2011, she chronicled the Black Panther Party's campaign for equal access to health care after its founding in the late 1960s.

"I think that if we want to understand anything about science and technology, we need to begin with the people who have been the most damaged, the most subjugated by it, but who also, out of that history, are often able to be early adopters and innovators," Nelson told *The Believer* magazine in a January 2020 interview.

In a statement, the American Society of Human Genetics commended the Biden administration for naming Nelson as a member of the OSTP team, calling her "a distinguished scholar and thought leader on the intersection of science, technology, and social inequalities".

Nelson is not the first social scientist to have a top job at the OSTP — Thomas Kalil, a political scientist, was deputy director for policy at the agency under former president Barack Obama.

Nature **589**, 502 (2021)

doi: https://doi.org/10.1038/d41586-021-00159-z

Jobs from Nature Careers

-
  -
    - All jobs
  -
    - **Postdoctoral Fellow - Zoubeidi Lab, Vancouver Prostate Centre**

      The University of British Columbia (UBC)

Vancouver, Canada

JOB POST

- **Laser Scientist**

  German Electron Synchrotron (DESY)

  Hamburg, Germany

  JOB POST

- **Fachinformatiker/in Systemintegration (w/m/d)**

  Karlsruhe Institute of Technology (KIT)

  Karlsruhe, Germany

  JOB POST

- **Intership/Bachelor or Master Thesis: "Digitization of land-based shrimp farming in Germany using AI-based evaluation of imaging and acoustic systems"**

  Alfred Wegener Institute - Helmholtz Centre for Polar and Marine Research (AWI)

  Bremerhaven, Germany

  JOB POST

This article was downloaded by **calibre** from https://www.nature.com/articles/d41586-021-00159-z

NEWS
21 January 2021

What new COVID variants mean for schools is not yet clear

Children are no more susceptible to these lineages than adults are — and closing schools on the basis of incomplete information could have repercussions.

Dyani Lewis

Search for this author in:

- Pub Med
- Nature.com
- Google Scholar

Researchers say more testing in children is needed.Credit: Justin Tallis/AFP via Getty

The emergence of fast-spreading coronavirus variants has once again put a spotlight on the role of children in the COVID-19 pandemic. Early data on one new variant had suggested that it was spreading more in children than in adults compared with other lineages. But researchers now suggest the variant is spreading more efficiently in all age groups, allaying those fears.

Still, a year into the pandemic, much remains unknown about the spread of SARS-CoV-2 in children, prompting calls for increased surveillance and testing to inform decisions about school closures. “We still don’t really know how much schools and children actually contribute to spread,” says Catherine Bennett, an epidemiologist at Deakin University in Melbourne.

Children seem to be less susceptible to SARS-CoV-2 than adults are, possibly because of inherent biological differences, says Calum Semple, an outbreak specialist at the University of Liverpool, UK. And studies in schools in several countries last year suggested that campuses were not hot spots for transmission, provided they took precautions such as maintaining

hygiene and social distancing. However, data often aren't easily comparable between countries because of the variation in practices.

But if the new variant is increasing infection rates in children, then the dynamics of transmission in schools should be reinvestigated, says Bennett. Better data are needed because cases in children — who more often experience asymptomatic infections — are probably being missed. Countries often test only people with symptoms.

Many researchers caution against closing schools before other parts of society, noting the harm to children from missed learning. Other scientists think that governments should act quickly when there is a rise in infections, including closing schools. George Milne, who leads COVID-19 modelling at the University of Western Australia in Perth says: "It's better to go hard early and [then] relax."

A changing picture

The new variant, now called B.1.1.7, was first detected in the United Kingdom in November. Data collected between late November and mid-December suggested that children were being infected with B.1.1.7, compared with other known lineages, more-so than people in other age groups. This prompted suggestions the variant was spreading in children more easily than in adults.

But a January report from Public Health England, a government public-health agency, found that the variant, which has spread to dozens of countries, transmits more easily in all age groups. It also found that children — especially those under the age of ten — are about half as likely as adults to transmit the variant to others.

A similar picture is emerging about another fast-spreading variant, which was first detected in South Africa and is known as 501Y.V2, says Richard Lessells, an infectious-diseases specialist at the University of KwaZulu-Natal in Durban. "There's nothing jumping out at us that there's different outcomes in the younger group[s]," he says.

If children do account for a greater proportion of new COVID-19 infections in the United Kingdom, that could be partly because schools stayed open when workplaces and retail outlets were closed at the end of last year, says Semple.

Biological differences?

Estimates suggest that children are half as susceptible to SARS-CoV-2 infection as adults[1,2] — and some researchers suggest their biology could be one reason why. Semple says this could be because of differences in the number and location of ACE2 receptors in the respiratory tract; these receptors are used by the virus to latch on to host cells. Children are thought to have fewer ACE2 receptors than adults have. And whereas adults have these receptors throughout their airways, children might have them only in the upper respiratory tract, says Semple. This could explain why the virus doesn't seem to take hold in young children.

Three recently identified variants have been found with mutations to the spike protein, which the virus uses to latch onto cells, making the variants better able to infect host respiratory cells[3]. But Semple says children might always be less susceptible than adults to an infection that uses the ACE2 receptor, although that needs to be investigated.

Other researchers have suggested that children might be better protected against unfamiliar pathogens than are adults, because they have a more responsive innate immune system and higher numbers of naive immune T cells. But more evidence is needed to establish whether this is the case.

Better data

In light of the increased infections in children, more accurate data on how they transmit the virus is needed, including how many close contacts children infect compared to adults, says Bennett.

Seroprevalence surveys could also check for evidence of previous infection, says Kim Mulholland, a paediatrician at the Murdoch Children's Research Institute in Melbourne, Australia. There has been at least one report[4] of

children developing antibodies to SARS-CoV-2 despite not testing positive in a standard diagnostic test that detects viral RNA. The finding suggests that the children mounted a rapid, local immune response, but that their viral shedding was too low for tests to pick up, says Mulholland, who co-authored the report.

But Mulholland cautions against knee-jerk reactions to early and incomplete information about increased transmission of recent variants in children. The cost of school closures — in terms of lost education, potential exposure to abuse, and, in some countries, the premature end to schooling in favour of work or marriage — could have devastating social impacts that blight a generation of children. A report last October by the charity Save the Children predicted that, by the end of 2020, half a million more children globally than usual would have been forced into marriage, and one million more would have become pregnant, as an indirect result of COVID-19. “These social problems are going to be persisting,” he says.

Bennett, too, says closing schools can have unintended consequences. Keeping kids at home can increase household transmission if parents bring babysitters into their homes, she says.

Nature **589**, 503 (2021)

doi: https://doi.org/10.1038/d41586-021-00139-3

References

1. 1.

   Davies, N. G. *et al. Nature Med.* **26**, 1205–1211 (2020).

2. 2.

   Viner, R. M. *et al. JAMA Pediatr.* https://doi.org/10.1001/jamapediatrics.2020.4573 (2020).

3. 3.

Chan, K. K., Tan, T. J. C., Narayanan, K. K. & Procko, E. Preprint at bioRxiv https://doi.org/10.1101/2020.10.18.344622 (2020).

4. 4.

Tosif, S. *et al. Nature Commun*. **11**, 5703 (2020).

Jobs from Nature Careers

-
  -
    - All jobs
  -
    - **Postdoctoral Fellow - Zoubeidi Lab, Vancouver Prostate Centre**

      The University of British Columbia (UBC)

      Vancouver, Canada

      JOB POST

    - **Laser Scientist**

      German Electron Synchrotron (DESY)

      Hamburg, Germany

      JOB POST

    - **Fachinformatiker/in Systemintegration (w/m/d)**

      Karlsruhe Institute of Technology (KIT)

      Karlsruhe, Germany

      JOB POST

- **Intership/Bachelor or Master Thesis: "Digitization of land-based shrimp farming in Germany using AI-based evaluation of imaging and acoustic systems"**

  Alfred Wegener Institute - Helmholtz Centre for Polar and Marine Research (AWI)

  Bremerhaven, Germany

  JOB POST

This article was downloaded by **calibre** from https://www.nature.com/articles/d41586-021-00139-3

NEWS
22 January 2021

Are COVID vaccination programmes working? Scientists seek first clues

Vaccinated people in Israel are less likely to test positive for SARS-CoV-2, but a population-wide effect will take time to become clear.

Smriti Mallapaty

Search for this author in:

- Pub Med
- Nature.com
- Google Scholar

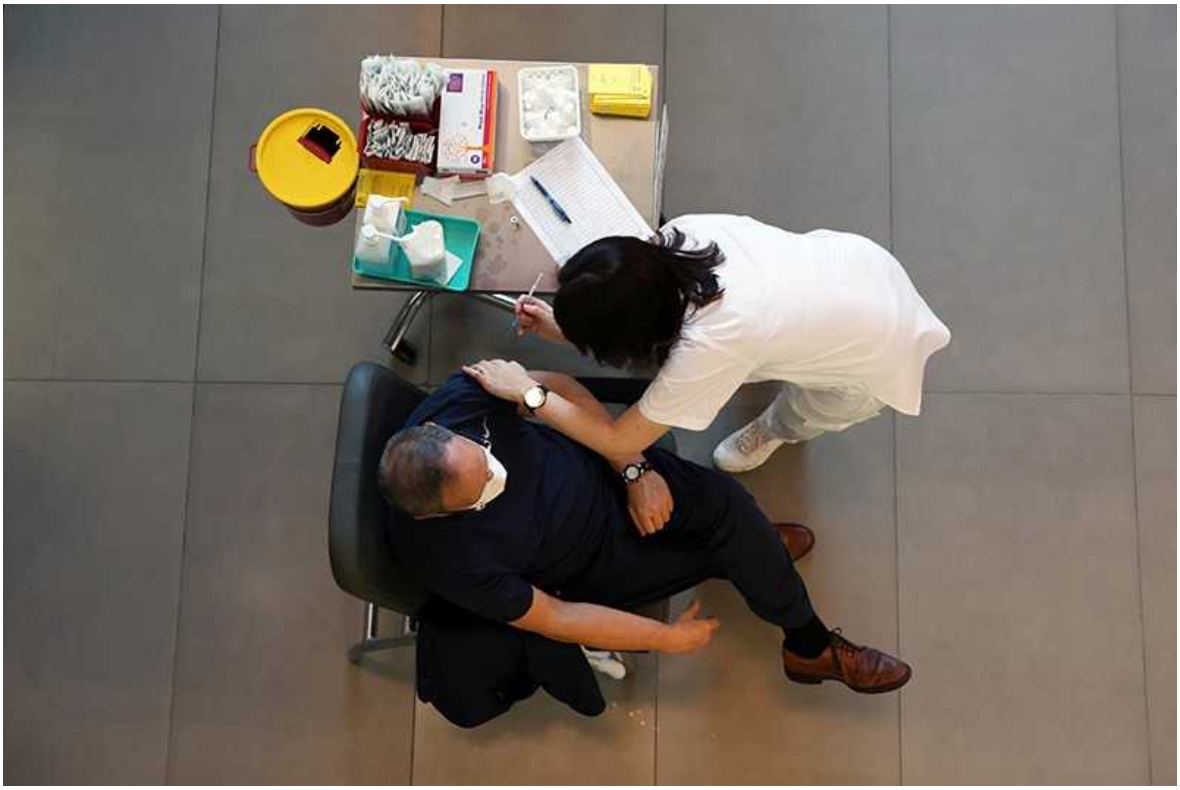

Vaccines are being rolled out and scientists are looking for signs they are reducing infections.Credit: Ronen Zvulun/Reuters

As countries worldwide roll out COVID-19 vaccines, researchers are eagerly watching for early signs that they are having an impact on the pandemic. Last week, researchers in Israel reported preliminary figures suggesting that people vaccinated there were about one-third less likely to test positive for SARS-CoV-2 than people who had not received a shot. But scientists say that population-wide effects of immunization will take time to become clear.

Many factors will determine how soon scientists can detect the impact of vaccines on the pandemic. Among them are the extent of vaccine coverage, the effectiveness of shots at preventing disease and infection, and the rate of viral transmission.

Israel and the United Arab Emirates are leading the world in vaccine coverage. The two nations have vaccinated roughly one-quarter of their populations — more than two million people each. Other nations, such as the United Kingdom and Norway, have targeted their vaccination programmes at high-risk groups. Britain has vaccinated more than 4 million

people, mostly health-care workers and older people, including those living in care homes; Norway has immunized all residents living in nursing homes, some 40,000 people.

First signs

The results from Israel are among the first to report the impact of vaccines administered to people outside clinical trials. They provide an early indication that the two-dose RNA-based vaccine developed by Pfizer–BioNTech can prevent infection or limit its duration in some vaccinated people.

In a preliminary analysis of 200,000 people older than 60 who received the vaccine, compared with a matched group of 200,000 who did not, researchers found that the chances of testing positive for the virus were 33% lower two weeks after the first injection.

“We were happy to see this preliminary result that suggests a real-world impact in the approximate timing and direction we would have expected,” says Ran Balicer, an epidemiologist at Israel’s largest health-care provider, Clalit Health Services, in Tel Aviv. He expects to get more conclusive results several weeks after people receive their second shot.

Another analysis, by Maccabi Healthcare Services, found a similar trend, although neither study has been peer-reviewed.

Clinical trials of the Pfizer–BioNTech vaccine show it to be around 90% effective at preventing COVID-19, and the preliminary data suggest it can also provide some protection from infection. But it will take longer to establish whether vaccinated people no longer spread the virus to unvaccinated people, says Balicer.

As more than 75% of older people in Israel have been vaccinated, Balicer says he expects to see a drop in hospitalizations among vaccinated older people over the coming weeks.

Most countries are prioritizing COVID-19 vaccinations for people who have a high risk of getting severe disease and dying. So, the first evidence that

shots are working in those countries will probably be reductions in hospitalizations, and then in deaths, says Alexandra Hogan, an infectious-disease modeller at Imperial College London.

Indirect effects

If vaccines are effective at preventing infections, then their indirect benefit — protecting unvaccinated people — will be visible only once enough people have been immunized, says Natalie Dean, a biostatistician at the University of Florida in Gainesville.

Israel will probably be the first country to see this kind of population-wide impact, say researchers. This is because it is using a high-efficacy vaccine and aiming for wide coverage with the explicit goal of achieving herd immunity, when enough people are immune to a virus for its spread to be controlled.

In some places, the first signs of indirect protection might emerge in specific groups who have been widely vaccinated, such as health-care and long-term-care workers and their families, says Dean.

But teasing apart the population-level effects of vaccines on a drop in COVID-19 cases from the impacts of other public-health interventions, such as social distancing and lockdowns, will be tricky. “Infectious diseases are very unpredictable — so you end up needing a lot of data to smooth out a lot of unpredictability,” says Dean.

Challenges ahead

The effect of vaccines on reducing overall COVID-19 infections will be more difficult to ascertain in regions such as Norway, which have largely brought the virus under control, says Hogan.

Yet rampant transmission also complicates such investigations, until countries reach high vaccine coverage, adds Dean. Vaccinated health-care workers, for example, might be able to protect their families from infection,

but when the virus is everywhere, there will be lots of opportunities for it to enter a household, she says.

Israel aside, vaccines will not have an impact on viral spread any time soon, says Raina MacIntyre, an epidemiologist at the University of New South Wales in Sydney, Australia. “Many other countries are using much lower-efficacy vaccines, which are unlikely to control infection,” she says.

Modelling work by Hogan shows that vaccines that are less effective at preventing infection will have a smaller impact on transmission in the population. “But even with an imperfect vaccine, that population-level impact on deaths could still be quite substantial,” she says.

Nature **589**, 504-505 (2021)

doi: https://doi.org/10.1038/d41586-021-00140-w

Jobs from Nature Careers

-
  -
    - All jobs
  -
    - **Postdoctoral Fellow - Zoubeidi Lab, Vancouver Prostate Centre**

      The University of British Columbia (UBC)

      Vancouver, Canada

      JOB POST

    - **Laser Scientist**

      German Electron Synchrotron (DESY)

      Hamburg, Germany

JOB POST

- **Fachinformatiker/in Systemintegration (w/m/d)**

  Karlsruhe Institute of Technology (KIT)

  Karlsruhe, Germany

  JOB POST

- **Intership/Bachelor or Master Thesis: "Digitization of land-based shrimp farming in Germany using AI-based evaluation of imaging and acoustic systems"**

  Alfred Wegener Institute - Helmholtz Centre for Polar and Marine Research (AWI)

  Bremerhaven, Germany

  JOB POST

This article was downloaded by **calibre** from https://www.nature.com/articles/d41586-021-00140-w

NEWS
15 January 2021

Science family of journals announces change to open-access policy

Subscription journals will let some Plan S funded researchers share accepted manuscripts under open licences.

Richard Van Noorden

Search for this author in:

- Pub Med
- Nature.com
- Google Scholar

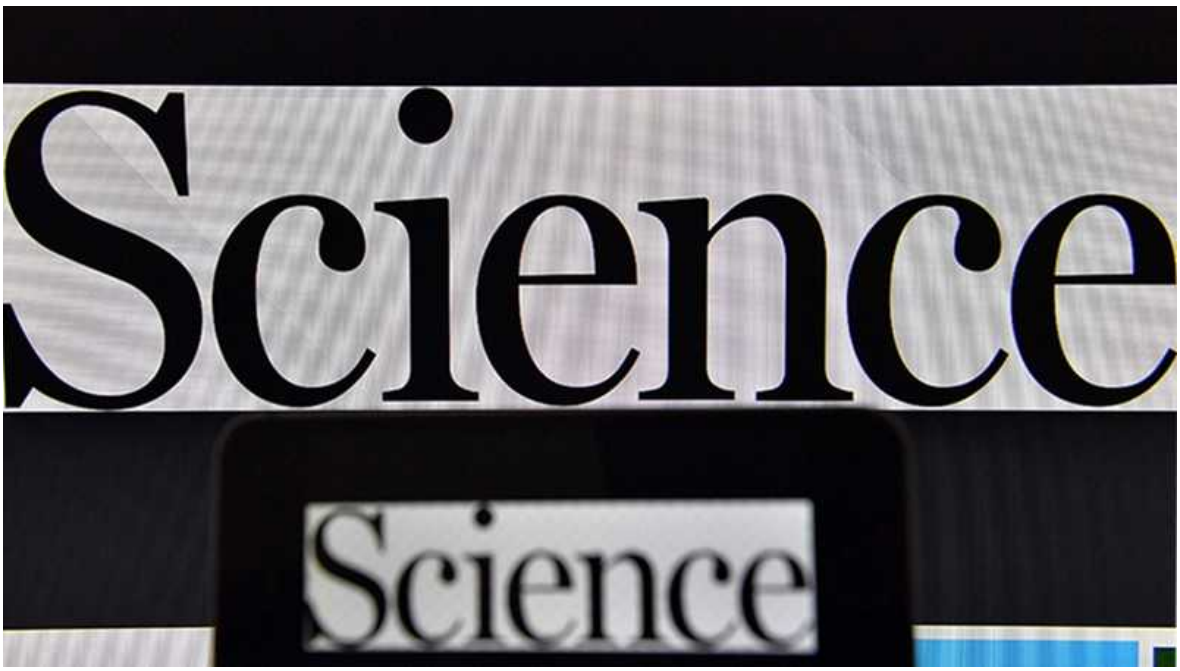

Science and its sister journals will trial a new green open-access policy for some researchers supported by the Plan S group of funders.Credit: Loic Venance/AFP/Getty

In a step towards open access, the publisher of *Science* will start allowing some authors publishing in its high-profile subscription journals to share their accepted manuscripts openly online under liberal terms that mean anyone could reproduce or redistribute the work.

The change ensures that scientists with grants from some funding agencies that insist on open-access (OA) publishing under the bold Plan S initiative can still publish in the Science family of subscription journals. Around two dozen funders have signed up to Plan S, which formally began on 1 January 2021, although individual agencies have different starting dates.

In the past two months, many selective subscription journals have introduced options for authors to pay fees to have their papers published OA, in response to Plan S. But the American Association for the Advancement of Science (AAAS) in Washington DC, which publishes *Science*, says it wants to avoid this because it is concerned about introducing OA-publication charges that could be financially out of reach for authors.

The new AAAS policy instead allows researchers funded by some Plan S agencies to post accepted versions of their articles online freely as soon as their papers appear — and under open licences that let anyone else redistribute or reproduce the manuscripts. (Some Plan S agencies haven't yet finalized their policies over manuscript-sharing, such as the national UK funder, UK Research and Innovation, so the policy doesn't apply to them yet.)

The AAAS already allowed this kind of immediate author-initiated sharing, sometimes called green open access, but its terms stated that the manuscripts could be shared only on personal or institutional web pages, and couldn't be redistributed. Researchers also had to wait six months before they could post manuscripts in repositories such as PubMed Central. That did not satisfy Plan S funders, which say that if scientists can't publish OA in journals (a process sometimes called gold OA), then they must share their accepted manuscripts under fully open licences as soon as they are published.

Legal obligation

In July 2020, some Plan S funders even said that they would make it a legal condition of grants that authors retain the rights to share their accepted manuscripts openly — no matter what a journal's publishing agreement says.

The AAAS now says that scientists funded by Plan S agencies that adopt this 'rights retention scheme' (RRS) will be able to apply open licences to their shared manuscripts. No other scientists publishing in AAAS journals will be able to do this.

Plan S always enabled authors to comply with its policy through this type of green OA, says Johan Rooryck, the executive director of cOAlition S, the group of funders signed up to the initiative. "We are delighted that AAAS is updating its policy to explicitly permit the sharing of these manuscripts," he said in a statement.

The new arrangement, which applies to all research submitted to Science family journals from the start of this year, could see many *Science* manuscripts shared with open licences. According to a report by Clarivate Analytics in Philadelphia, Pennsylvania, 31% of articles published in *Science* in 2017 acknowledged grants from a Plan S funder.

Some other journals have also adopted green OA to comply with Plan S. The *New England Journal of Medicine* told funders in October that it would permit green OA in 2021 for Plan-S funded scientists, for instance. London's Royal Society has allowed green OA in its journals for years and allows this to be done under open licenses if funders require it.

Routes to open access

Other highly selective subscription journals have adapted to Plan S in different ways. In November, publisher Springer Nature said that it would offer OA at Nature-branded journals for a charge of €9,500 (US$11,500) per paper; it is also running trials of a programme to reduce prices at some of its journals. (*Nature* is editorially independent of its publisher.)

And in December, publisher Elsevier in Amsterdam announced a suite of OA options for Cell Press journals, with an €8,500 charge to publish OA in *Cell* and €7,600 for other journals.

But many scientists worry that these prices are too high. Although Plan S funders might pay the fees for their scientists, many other researchers will not be able to afford the OA option. (Elsevier said it would waive OA fees for researchers in the lowest-income countries, and reduce them for some others.) This is why the AAAS has opted for green OA, rather than bringing in gold OA at its subscription journals, the publisher explained.

"This approach reflects AAAS's concern that facilitating open access by gold routes alone puts undue financial obligation on authors, which could freeze in place or further exacerbate longstanding inequities for authors across race, gender, geographies, disciplines, and institutions," it said in a statement.

Publishing privileges

"It's a bold move to go for a green OA solution to meeting Plan S requirements, and notable that they are pointing to the inequities associated with the article-processing-charge business model," says Stephen Curry, a structural biologist at Imperial College London.

The AAAS's approach does mean that most scientists publishing in its journals won't have a fully OA option, notes Lisa Hinchliffe, a librarian at the University of Illinois at Urbana–Champaign. "It is unfortunate that this perpetuates the differentials we see in the ecosystem, where some publishing pathways' privileges are extended to certain scholars but not others — in this case, reflecting the uneven adoption of Plan S policies even within the family of Plan S funders," she says.

How to finance a wholesale switch from a pay-to-read model to an OA one remains hugely contentious. Some journals, hoping to slowly ease their way from subscription to OA business models, have struck agreements in which libraries or institutions pay a lump sum that covers the cost to their authors both of reading subscription content and publishing OA. In December, 11

publishers argued against adopting green OA, saying that it would "undermine progress" towards full OA, and that the version of record of an article, not the accepted manuscript, should be what's made open.

The AAAS wants to try the green OA model for its subscription journals as a "year-long experiment to see if this is sustainable", says Bill Moran, the publisher of the Science family of journals.

Whether green OA can work in the long run for the publisher (which also publishes a gold OA journal, *Science Advances*) is "the biggest question we have wrestled with", he adds. But given that the AAAS already allows manuscripts to be shared — if not as liberally — he hopes the change won't mean that libraries or other communities cut down on subscriptions that support the society.

Nature **589**, 505 (2021)

doi: https://doi.org/10.1038/d41586-021-00103-1

Jobs from Nature Careers

- All jobs

Postdoctoral Fellow - Zoubeidi Lab, Vancouver Prostate Centre

The University of British Columbia (UBC)

Vancouver, Canada

JOB POST

Laser Scientist

German Electron Synchrotron (DESY)

Hamburg, Germany

JOB POST

- **Fachinformatiker/in Systemintegration (w/m/d)**

  Karlsruhe Institute of Technology (KIT)

  Karlsruhe, Germany

  JOB POST

- **Intership/Bachelor or Master Thesis: " Digitization of land-based shrimp farming in Germany using AI-based evaluation of imaging and acoustic systems"**

  Alfred Wegener Institute - Helmholtz Centre for Polar and Marine Research (AWI)

  Bremerhaven, Germany

  JOB POST

This article was downloaded by **calibre** from https://www.nature.com/articles/d41586-021-00103-1

NEWS FEATURE
27 January 2021

How ecstasy and psilocybin are shaking up psychiatry

Regulators will soon grapple with how to safely administer powerful psychedelics for treating depression and post-traumatic stress disorder.

Paul Tullis

Paul Tullis is a journalist based in Amsterdam.

Search for this author in:

- Pub Med
- Nature.com
- Google Scholar

Cartoon showing a patient on couch with a therapist taking notes and a vivid coloured background.

Illustration by Gizem Vural

On a sunny day in London in 2015, Kirk Rutter rode the Tube to Hammersmith Hospital in hopes of finally putting an end to his depression.

Rutter had lived with the condition off and on for years, but the burden had grown since the death of his mother in 2011, followed by a relationship break-up and a car accident the year after. It felt as if his brain was stuck on what he describes as “an automatic circuit”, repeating the same negative thoughts like a mantra: “‘ Everything I do turns to crap.’ I actually believed that,” he recalls.

The visit to Hammersmith was a preview. He would be returning the next day to participate in a study, taking a powerful hallucinogen under the guidance of Robin Carhart-Harris, a psychologist and neuroscientist at Imperial College London. Years of talking therapy and a variety of anti-anxiety medications had failed to improve Rutter's condition, qualifying him for the trial.

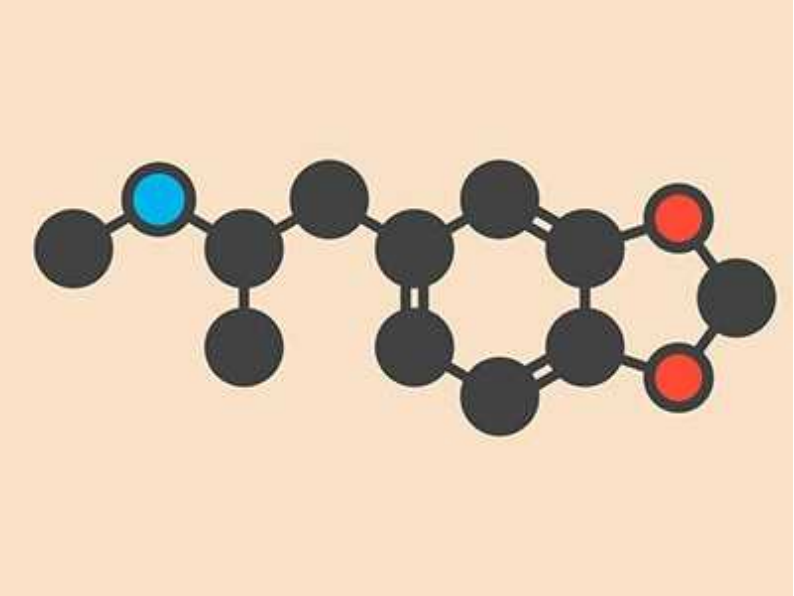

Psychedelics move from agents of rebellion towards therapeutics

"Everyone was super nice, like really lovely, and especially Robin," Rutter recalls. Carhart-Harris led him to a room with a magnetic resonance imaging (MRI) machine, so researchers could acquire a baseline of his brain activity. Then he showed Rutter where he would spend his time while on the drug. Carhart-Harris asked him to lie down and played him some of the music that would accompany the session. He explained that he would have on hand a drug that could neutralize the hallucinogen, if necessary. Then the two practised a grounding technique, to help calm Rutter in the event that he became overwhelmed. Without warning, Rutter burst into tears.

“I think I knew this was going to be unpacking a lot — I was carrying a bit of a load at the time,” Rutter says.

When Rutter returned the next day, one of the researchers handed him two pills containing a synthetic form of psilocybin, the psychoactive ingredient found in magic mushrooms. Rutter lay down on the bed and put on headphones and an eye mask. Soon, images of Sanskrit text appeared to him. Later, he saw golden bejewelled structures. Then his mind went to work on his grief.

The Imperial study was one of a spate of clinical trials launched over the past few years using illicit psychedelic drugs such as psilocybin, lysergic acid diethylamide (LSD) and MDMA (3,4-methylenedioxymethamphetamine, also known as molly or ecstasy) to treat mental-health disorders, generally with the close guidance of a psychiatrist or psychotherapist. The idea has been around for decades — or centuries in some cultures — but the momentum has picked up drastically over the past few years as investors and scientists have begun to champion the approach again (see ‘Psychedelics take flight’).

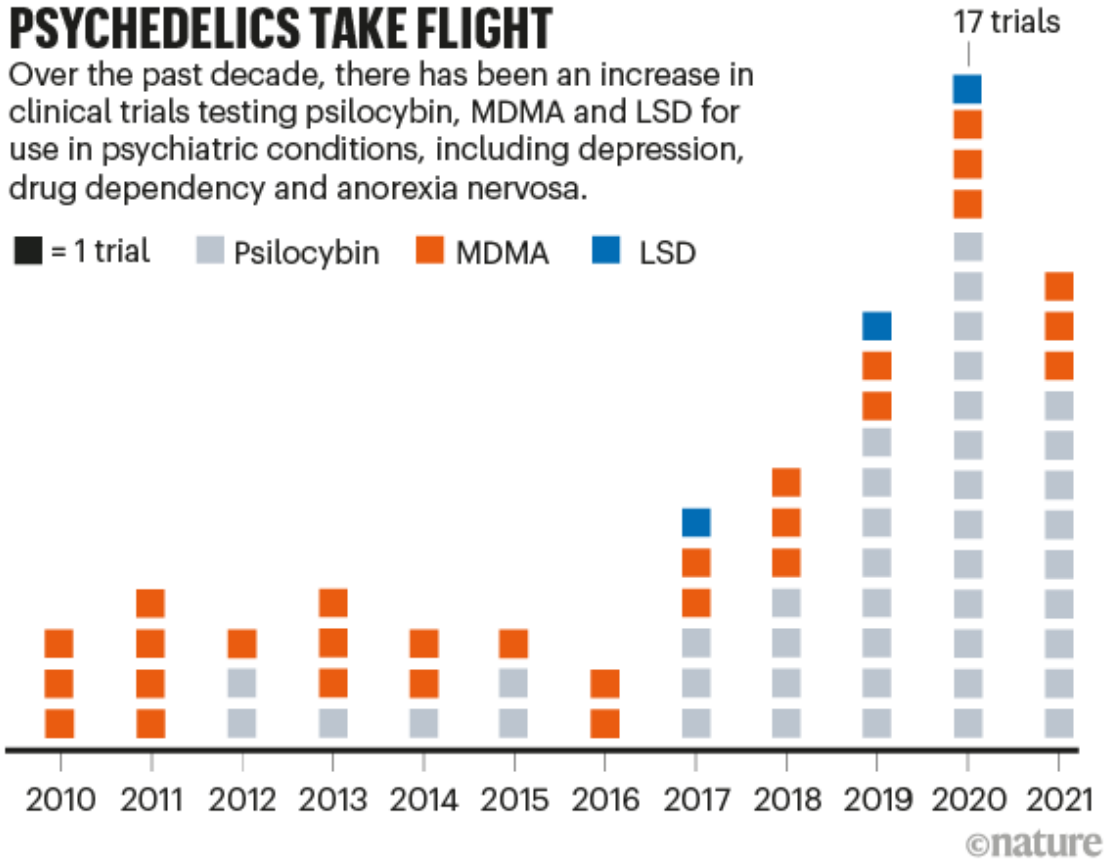

Source: Dimensions

Once dismissed as the dangerous dalliances of the counterculture, these drugs are gaining mainstream acceptance. Several states and cities in the United States are in the process of legalizing or decriminalizing psilocybin for therapeutic or recreational purposes. And respected institutions such as Imperial; Johns Hopkins University in Baltimore, Maryland; the University of California, Berkeley; and the Icahn School of Medicine at Mount Sinai in New York City have opened centres devoted to studying psychedelics. Several small studies suggest the drugs can be safely administered and might have benefits for people with intractable depression and other psychological problems, such as post-traumatic stress disorder (PTSD). One clinical trial involving MDMA has recently ended, with results expected to be published soon. Regulators will then be considering whether to make the treatment available with a prescription.

Psychedelic-assisted psychotherapy could provide needed options for debilitating mental-health disorders including PTSD, major depressive disorder, alcohol-use disorder, anorexia nervosa and more that kill thousands every year in the United States, and cost billions worldwide in lost productivity.

But the strategies represent a new frontier for regulators. “This is unexplored ground as far as a formally evaluated intervention for a psychiatric disorder,” says Walter Dunn, a psychiatrist at the University of California, Los Angeles, who sometimes advises the US Food and Drug Administration (FDA) on psychiatric drugs. Most drugs that treat depression and anxiety can be picked up at a neighbourhood pharmacy. These new approaches, by contrast, use a powerful substance in a therapeutic setting under the close watch of a trained psychotherapist, and regulators and treatment providers will need to grapple with how to implement that safely.

Antidepressant based on party drug gets backing from FDA advisory group

“The clinical trials that have been reported on depression have been done under highly circumscribed and controlled conditions,” says Bertha Madras, a psychobiologist at Harvard Medical School who is based at McLean Hospital in Belmont, Massachusetts. That will make interpreting results difficult. A treatment might show benefits in a trial because the experience is carefully coordinated, and everyone is well trained. Placebo controls pose another challenge because the drugs have such powerful effects.

And there are risks. In extremely rare instances, psychedelics such as psilocybin and LSD can evoke a lasting psychotic reaction, more often in people with a family history of psychosis. Those with schizophrenia, for example, are excluded from trials involving psychedelics as a result. MDMA, moreover, is an amphetamine derivative, so could come with risks for abuse.

But many researchers are excited. Several trials show dramatic results: in a study published in November 2020, for example, 71% of people who took psilocybin for major depressive disorder showed a greater than 50% reduction in symptoms after four weeks, and half of the participants entered remission[1]. Some follow-up studies after therapy, although small, have shown lasting benefits[2,3].

“Sometimes with a therapeutic, you look at the data and think, ‘It slightly moved the needle,’” says Jennifer Mitchell, a neurologist at the Weill Institute for Neurosciences at the University of California, San Francisco, who worked on the recently finished MDMA trial. “Then you see MDMA and you’re like, ‘Never mind that.’ It’s a very different effect size.” Rutter was so moved by his experience with psilocybin that he has consulted for one of the companies sponsoring trials of the compound.

Rave new world

The current wave of interest in the therapeutic potential of psychedelics is something of a renaissance. In the 1950s and 1960s, scientists published more than 1,000 articles on using psychedelics as a psychiatric treatment; the drugs were tested on around 40,000 people in total[4]. Then, as recreational use of the drugs spread, they were banned and the FDA

constricted supplies for research. Only recently have neuroscientists and psychopharmacologists such as Carhart-Harris had the technology to start unpicking how they work in the brain. That has given them some insights as to how these compounds might help in psychiatric disease.

Researchers started exploring the biological effects of psychedelics in the late 1990s, using neuroimaging techniques such as positron emission tomography[5] before and after volunteers used the drugs, or in conjunction with antagonists that dampen some of their effects. The studies show similarities in how brains respond to psychedelics such as psilocybin and LSD, as well as to N,N-dimethyltryptamine (DMT), the active ingredient in ayahuasca, and to mescaline, a psychedelic compound derived from the peyote cactus. They all act on receptors for serotonin, a neurotransmitter that affects mood.

Serotonin is also the target of the predominant class of psychiatric drugs known as selective serotonin reuptake inhibitors, or SSRIs. It is now thought that these antidepressants work not by flooding the brain with the neurotransmitter, as was initially assumed, but by stimulating neuroplasticity — the brain's ability to forge new neuronal connections. There is some evidence that psychedelic drugs, such as psilocybin, enhance neuroplasticity in animals[6], and limited evidence suggests that the same might happen in human brains[7,8]. Clinical studies also suggest that the biological effects work best in concert with human guidance.

The setting for a psilocybin therapy session (shown in this mock-up) must be carefully replicated for clinical trials.Credit: COMPASS Pathways

The drugs “activate a therapeutic, dreamlike state, intensifying sensory perception, and memories pop up like little films”, says Franz Vollenweider, a psychiatrist and neurochemist at the University Hospital of Psychiatry in Zurich, Switzerland, and one of the pioneers of the modern era of psychedelic research. He thinks that this receptive state of mind provides an opportunity to help people escape from rigid patterns of thought, not unlike Rutter’s automatic circuit.

“People get locked into disorders like depression because they develop this system of thinking which is efficient, but wrong,” says David Nutt, a psychopharmacologist at Imperial College London and an outspoken supporter of evidence-based reforms to government policies concerning illegal drugs. Psychiatry has a term for such thinking: rumination. The idea behind psychedelic therapy is that the receptive state that the drug confers opens the door to fresh ideas about how to think about the past and future, which the therapist can reinforce. “There is a growing evidence base to the principle that this is very much about a synergy between drug-induced

hyper-plasticity and therapeutic support," says Carhart-Harris, who trained with Nutt.

Psychedelic compound in ecstasy moves closer to approval to treat PTSD

Rutter says his journey with Carhart-Harris was focused, but flexible. When Rutter first removed a pair of eye shades after the drug took effect, the therapist appeared "fractured" and seemed to have another eye in the centre of his forehead. "I should imagine I look quite strange to you now," Carhart-Harris said. Rutter burst out laughing and Carhart-Harris joined him. When the laughter stopped, the two men started talking. Rutter wanted to discuss his resentments, which led to pondering about the word 'relent' and its etymology. Carhart-Harris looked it up for him on his laptop. "That was a lovely moment, actually," Rutter says. He returned for a second session with a stronger dose of the drug, followed by a second MRI and an 'integration' session, to discuss the experiences.

The treatment “made me look at grief differently”, Rutter says. “It was a realization that actually it wasn’t helping, and letting go wasn’t a betrayal.”

Clinical hurdles

Testing these drugs effectively and translating the clinical research into actual treatments will prove challenging, however. Two of the most closely watched studies have grappled with this. One is the recently completed MDMA trial, which was testing the approach in people with severe PTSD. It was a phase III study, usually the final stage before drug regulators decide whether to approve a treatment, and it involved 90 participants at 15 sites around the world. The Multidisciplinary Association for Psychedelic Studies (MAPS), a non-profit organization in San Jose, California, sponsored the study, but has not so far released the results.

Meanwhile, the mental-health-care company COMPASS Pathways in London is running a phase IIb trial — testing different dosages of psilocybin for treatment-resistant depression.

Evaluating the results won’t be simple. One concern revolves around controls. Most individuals given a placebo will know that they are not receiving a powerful hallucinogen. Some studies evaluating psychedelics have attempted to address this by giving people in the control group a pill containing niacin, which elicits a physical sensation — usually a flushing response in the skin. Mitchell says that some participants in her MDMA study who’ve been given the drug thought they received the placebo, while some taking the placebo believed that they had been given the drug.

The studies’ designers must also tackle how important the non-drug aspects of the trial are to the results. These include the mindset of the individual going into the experience, and the environment in which it takes place.

The vibe is definitely hotel spa at the treatment rooms for the COMPASS study at Utrecht University Medical Centre in the Netherlands. There’s a Mexican-style blanket folded at the foot of a twin-size bed. Beanbag chairs hug a potted palm in the corner. And a poster of Van Gogh’s *Almond Blossom* adorns one wall. All 24 sites in the study are similarly decorated.

Synthetic psilocybin, the psychoactive ingredient found in magic mushrooms.Credit: Paul Taggart/Bloomberg/Getty

Then there's the training and experience of the therapists guiding both the dosing sessions and the drug-free integration sessions. COMPASS, which became a public company in September and earned a stock-market valuation exceeding US$1 billion, developed a five-tier training programme for therapists in its trial. Company co-founder and chief innovation officer Ekaterina Malievskaia says site investigators must adhere to the training if the company expects to win regulators' approval.

Madras goes further to say that the conditions of the trial will have to be replicated for any wider roll-out of the drugs. They "have to be approved

under the stringent conditions in which they were investigated", she says. But the path forward for mandating such conditions is unclear. For the US FDA, there is a mechanism to ensure that drugs are administered in a specific way: Risk Evaluation and Mitigation Strategies, or REMS. Through REMS, the agency can require prescribing physicians and pharmacists to be certified for a treatment strategy designed to mitigate the risks associated with a drug — such as addiction and dependency for opiate prescription. REMS could be used with psychedelics, Dunn says. The effect would be to bundle the delivery of the drug with the therapy component, and potentially certify practitioners. A source working on one of the trials says that discussions are under way with the FDA over whether therapists who administer the drugs ought to be trained, what that training might involve and whether therapist certification should be required.

Certification could mean legitimizing therapists who have been 'treating' individuals with the drugs illegally for as long as 30 years. But some of these therapists might resist the advice, or the involvement, of a government that has driven them underground.

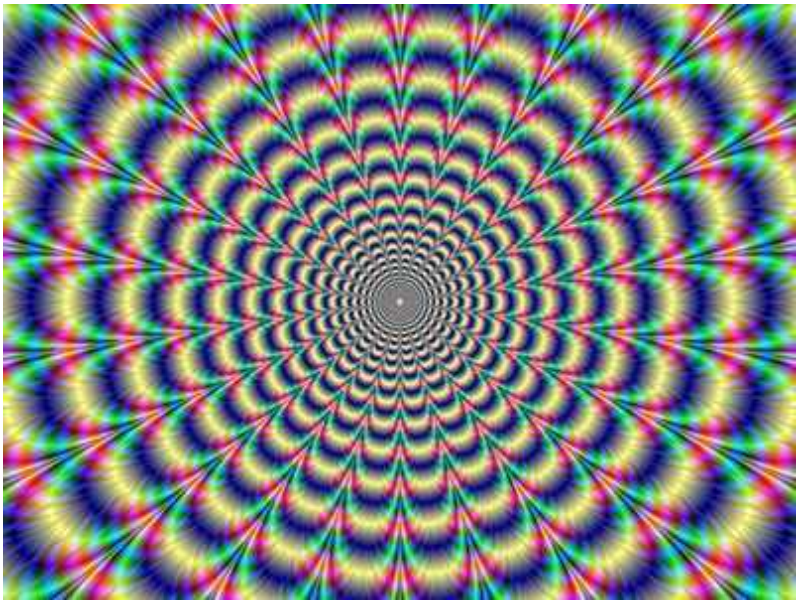

First look at LSD in action reveals acid-trip biochemistry

Approvals still have a long way to go. Towards the end of 2020, MAPS reported in a news release that there are statistically significant differences in the response between the control and placebo groups in its MDMA trial (see go.nature.com/362xsvp). But the company won't say more about the results until it releases the full data some time this year. It is also recruiting for a second phase III study using MDMA therapy for people with moderate-to-severe PTSD, which it aims to complete before the end of the year. COMPASS expects to have results from its phase IIb study on psilocybin by that time, and the company says it is planning a phase III study.

Robert Malenka, a psychiatrist and neuroscientist at Stanford University in California who has studied MDMA's effects on rodents, says he thinks that some psychedelic drugs will eventually earn approval as treatments for certain conditions. "They have potential to be — I want to use the right analogy — a part of our toolset for treating patients," he says. But he warns against overzealousness, particularly a brand of evangelism he's seen among some of the underground purveyors of psychedelic-assisted psychotherapy. "I don't think they're going to be miracle cures," he says.

Magic-mushroom drug lifts depression in first human trial

He argues that the hypotheses for how the drugs might be working in the brain still need further research, and that investigating compounds that provide the same benefits without the hallucinatory effects could prove worthwhile in the long run. Others point out that SSRIs work for many individuals without clinicians fully understanding their mechanism.

Regarding the clinical work, however, Madras says she's concerned by the studies' size and design. She noted that many of them recruit people who have had previous experience taking psychedelics. Those who are attracted to this type of experience, she argues, might be more likely to say positive things about it. Nutt has said that working with experienced users of the drugs minimizes the chance of adverse events. But there are other potential confounders, according to Madras. "The consent forms tell you what the expectations are," she says. "So there's bias on the part of the subjects."

Rutter says that despite all that, he is convinced that the treatment he received in 2015 changed his life for the better. In the weeks after his sessions, he found himself wondering whether the automatic circuit would return. "I was terrified," he says, "and I realized I've got a little bit of control over this, right?" The thought had never occurred to him before.

A week or so later, he was out with friends at a shopping centre and sensed the return of optimism and openness. "It felt like somebody had opened a window in a stuffy room." Five years later, his depression has not returned.

Nature **589**, 506-509 (2021)

doi: https://doi.org/10.1038/d41586-021-00187-9

References

1. 1.

   Davis, A. K. *et al. JAMA Psychiatry* http://doi.org/10.1001/jamapsychiatry.2020.3285 (2020).

2. 2.

Agin-Liebes, G. I. *et al. J. Psychopharmacol.* **34**, 155–166 (2020).

3. 3.

Carhart-Harris, R. L. *et al. Psychopharmacology* **235**, 399–408 (2018).

4. 4.

Vollenweider, F. X. & Preller, K. H. *Nature Rev. Neurosci.* **21**, 611–624 (2020).

5. 5.

Vollenweider, F. X. *et al. Neuropsychopharmacology* **16**, 357–372 (1997).

6. 6.

Zhang, G. *et al. Neuropharmacology* **64**, 403–413 (2013).

7. 7.

Hutten, N. R. P. W. *et al. ACS Pharmacol. Transl. Sci*. https://doi.org/10.1021/acsptsci.0c00099 (2020).

8. 8.

Lebedev, A. V. *et al. Hum. Brain Mapp.* **37**, 3203–3213 (2016).

Jobs from Nature Careers

-
  -
    - All jobs
  -
    - **Postdoctoral Fellow - Zoubeidi Lab, Vancouver Prostate Centre**

The University of British Columbia (UBC)

Vancouver, Canada

JOB POST

- **Laser Scientist**

  German Electron Synchrotron (DESY)

  Hamburg, Germany

  JOB POST

- **Fachinformatiker/in Systemintegration (w/m/d)**

  Karlsruhe Institute of Technology (KIT)

  Karlsruhe, Germany

  JOB POST

- **Intership/Bachelor or Master Thesis: "Digitization of land-based shrimp farming in Germany using AI-based evaluation of imaging and acoustic systems"**

  Alfred Wegener Institute - Helmholtz Centre for Polar and Marine Research (AWI)

  Bremerhaven, Germany

  JOB POST

This article was downloaded by **calibre** from https://www.nature.com/articles/d41586-021-00187-9

Books & Arts

- **Meteorites: ‘a story written across light years down the barrel of a microscope’** [25 January 2021]
  Book Review • Chemical clues reveal stories from the birth of the Solar System.

BOOK REVIEW
25 January 2021

Meteorites: ‘a story written across light years down the barrel of a microscope’

Chemical clues reveal stories from the birth of the Solar System.

Meenakshi Wadhwa

Meenakshi Wadhwa is director and professor in the School of Earth and Space Exploration at Arizona State University in Tempe. Asteroid 8356 Wadhwa is named in recognition of her contributions to meteoritics and planetary science.
Contact

Search for this author in:

- Pub Med
- Nature.com
- Google Scholar

Karakul Lake in Tajikistan formed inside a meteorite impact crater.Credit: USGS/NASA Landsat/Orbital Horizon/Gallo Images/Getty

Meteorite: The Stones From Outer Space That Made Our World *Tim Gregory* John Murray (2020)

On the afternoon of 13 December 1795, three ploughmen in Yorkshire saw something astonishing. A stone plummeted from the sky and buried itself deep into the ground near the village of Wold Newton. Neighbours came running at what sounded like pistol fire. In the earth, they found a warm stone about the size of a loaf of bread.

This unusual rock — unlike any known in England at the time — eventually found its way into the hands of several scientists, including the chemist Edward Howard. He analysed it and several other stones that had been seen to fall from the sky across Europe. In a landmark 1802 paper, Howard linked all these rocks into a new class — the extraterrestrial objects that have come to be known as meteorites (E. C. Howard *Phil. Trans. R. Soc.* **92**, 168–212; 1802).

NASA ‘fist bumps’ an asteroid to reveal Solar System’s secrets

Meteorites are like cosmic time capsules. They carry details of events from the earliest days of the Solar System. Scientific sleuths carefully analyse cosmochemical evidence, such as variations in the ratios of the three naturally occurring isotopes of oxygen in the rock — data that can seem esoteric to the uninitiated. I usually recommend the book *Meteorites and Their Parent Planets*, by Harry McSween, as an approachable text for anyone wishing to learn more. But its most recent edition was published in 1999, and much has transpired in the field in the two decades since. Happily, I have a new book to recommend.

In *Meteorite*, chemist and geoscientist Tim Gregory weaves a colourful tapestry of historical and scientific stories with an eye towards the latest developments. A passionate communicator, Gregory conjures environments and events far outside the human experience. Consider this description of the infant Sun, 4.5 billion years ago: “Turbulent winds and eddies in the thin wisps of gas further concentrated dust into whirling clouds like cosmic tumbleweeds.”

Out of thin air

He begins with the extraordinary circumstances surrounding several historic meteorite finds and falls, including the Wold Newton stone. But humanity's fascination with meteorites stretches back much earlier: he describes how an iron dagger found in the tomb of the Egyptian pharaoh Tutankhamun, from around 1350 bc, was fashioned from a fallen meteorite.

Next comes the history of how clusters of meteorites were discovered in Antarctica and the hot deserts of the world, where low rates of precipitation mean there is little of the erosion that could otherwise degrade the fallen stones. Meteorite-hunting expeditions from countries including the United States and Japan regularly travel to Antarctica, where the movement of ice sheets carries meteorites like a conveyor belt, concentrating them in certain regions.

Researchers with the Antarctic Search for Meteorites programme collect a sample.Credit: Christine Floss/ANSMET/NSF/NASA

Gregory explains how modern analytical tools measure the chemical compositions of meteorites with unprecedented precision and accuracy. He describes “drops of fiery rain” that formed when clumps of primordial dust flash-heated to make round droplets, which quickly solidified and then accreted with other solids into asteroid-sized bodies and planetary embryos. These solidified droplets, or chondrules, are found in some of the most common types of meteorite, called chondrites; understanding the processes that formed them gives insights into how planets came together in the early Solar System.

Radiocarbon revolution: the story of an isotope

And meteorites can reveal information even older than our Solar System. They contain clues to the nature of the space between the stars and the dense molecular clouds that can form there, as well as how newborn stars fuse elements. Studies of meteorites and their components have revealed that the

place in our Galaxy where the Solar System arose was a much more active star-forming region than our current astrophysical environment.

Gregory also delves into meteorites from the Moon and Mars, as well as significant terrestrial impacts (particularly the one 66 million years ago that extinguished almost three-quarters of plant and animal species on Earth, including the non-avian dinosaurs). Along the way, he provides some of the most lucid explanations of the physical and chemical principles of meteoritics and cosmochemistry that I have come across in a popular book. He explains how gravitational tugs between Jupiter and asteroids in the asteroid belt lead to orbital resonances that throw asteroids off course and help to deliver meteorites to Earth. He discusses how scientists can use the oxygen-isotope compositions of meteorites as a ‘ fingerprint’ to discover where in the solar nebula they formed, or use rare isotopes of other elements to determine how long a rock has been exposed to cosmic rays in interplanetary space.

Villagers pose around the crater of a meteorite that landed in Bihar state, India, in 2019.Credit: AFP via Getty

A couple of prominent figures who shaped the field are not mentioned. One is Harvey Nininger: self-taught, his extensive research and collection efforts laid the foundations of modern meteoritics in the 1930s. (Amateur collectors continue to have an important role in advancing the field, by making new types of meteorite more readily accessible to researchers.) Another is William Cassidy, who helped to establish systematic meteorite-collection efforts in Antarctica.

This exemplary book deserves a second edition — with more illustrations, photographs, references and citations. After all, meteorites offer a way to unravel the mysteries of our planet, the Solar System and beyond. By studying them, Gregory writes, "We have discovered a story written across light years down the barrel of a microscope, and come face to face with the grandest of timescales."

Nature **589**, 510-511 (2021)

doi: https://doi.org/10.1038/d41586-021-00188-8

Jobs from Nature Careers

- All jobs

- **Postdoctoral Fellow - Zoubeidi Lab, Vancouver Prostate Centre**

  The University of British Columbia (UBC)

  Vancouver, Canada

  JOB POST

- **Laser Scientist**

  German Electron Synchrotron (DESY)

Hamburg, Germany

JOB POST

- **Fachinformatiker/in Systemintegration (w/m/d)**

  Karlsruhe Institute of Technology (KIT)

  Karlsruhe, Germany

  JOB POST

- **Intership/Bachelor or Master Thesis: " Digitization of land-based shrimp farming in Germany using AI-based evaluation of imaging and acoustic systems"**

  Alfred Wegener Institute - Helmholtz Centre for Polar and Marine Research (AWI)

  Bremerhaven, Germany

  JOB POST

This article was downloaded by **calibre** from https://www.nature.com/articles/d41586-021-00188-8

Opinion

- **Akito Arima (1930–2020)** [22 January 2021]
  Obituary • Theoretician who simplified nuclear physics and revamped Japan's science.
- **Cancer research needs a better map** [26 January 2021]
  Comment • It is time to move beyond tumour sequencing data to identify vulnerabilities in cancers.

OBITUARY
22 January 2021

Akito Arima (1930–2020)

Theoretician who simplified nuclear physics and revamped Japan's science.

David Swinbanks

David Swinbanks is chairman of Springer Nature in Australia and New Zealand. From 1986 to 1995, he was *Nature*'s Tokyo correspondent and was then the journal's Asia-Pacific editor until 2000.
Contact

Search for this author in:

- Pub Med
- Nature.com
- Google Scholar

Credit: RIKEN

The Japanese theoretical physicist Akito Arima helped to create a model that radically simplified the representation of the atomic nucleus. As president of Japan's University of Tokyo and of RIKEN, and as a government adviser and minister, he modernized Japanese science and promoted centres of excellence in advanced research. He has died, aged 90.

Arima's 1974 model, created jointly with Italian colleague Francesco Iachello, treated each pair of protons and neutrons, collectively called nucleons, as one particle — a boson with an angular momentum of either 0 or 2. Arima and Iachello refined the shell model, in which the binding energy of each nucleon is affected by the number of nucleons. Using that model, calculating the binding energy or spin for nucleons at low energies becomes intractable for heavier nuclei, because of the sheer number of possible states. Arima and Iachello's interacting-boson model collapsed the number of possible states by orders of magnitude.

Born in Osaka in 1930, Arima was educated at a private secondary school in Tokyo that accelerated students who were achieving ahead of their age group. He got his doctorate in 1958 from the University of Tokyo, where he became a full professor in 1975, having started his career in 1956 at the university's Institute for Nuclear Studies.

He and Iachello extended their ideas on nuclear structure, and in 1987, co-authored *The Interacting Boson Model*, which presents the mathematical techniques used to analyse the structure of the model. The book also collects in a single, easily accessible reference all the formulae that had been developed over the years to account for collective properties of nuclei.

A research position at Argonne National Laboratory in Chicago, Illinois, a visiting professorship at Rutgers University in New Jersey and a full professorship at Stony Brook University in New York showed Arima "the zeal for education at American universities … as well as the rigorous evaluation system". He felt that facilities for physics in Japan were poor by comparison, and that the level of government funding bore little relation to the quality of the work produced.

In 1991, As president of the University of Tokyo, he confronted the minister of education and other politicians about the conditions in his public university, in breach of Japanese conventions of deference. In a further radical act, he invited a panel of overseas scientists to review the buildings and resources of the physics department, which highlighted their deficiencies (see *Nature* **362**, 387; 1993). By the end of his four-year term, he had won funding for new buildings and equipment. Reviews by international scientists soon became standard in Japan.

In 1993, Arima became president of RIKEN, Japan's multi-campus scientific research institute. He continued to lobby the government, with other forward-looking colleagues, for a law to inject substantial funding into Japanese science through 5-year plans. Japan's Basic Law for Science and Technology came into force on 15 November 1995, and was implemented in the budget of 1997. As part of the first 5-year plan, he doubled the number of postdoctoral fellows in Japan to 10,000 by the end of the 1990s.

After five years as a government adviser, Arima was elected as a member of the upper house of the Diet (parliament) in 1998. He was both minister for education and state minister of science and technology under Prime Minister Keizo Obuchi (1998–2000). On his watch, Japanese universities moved towards incorporation as semi-public corporate agencies with some degree of independence from government. He published proposals for shorter weeks and lighter curricula for schoolchildren, and introduced a system for high-achieving secondary schoolchildren to jump ahead a year. But his greatest achievements were in university reform, including the strengthening of graduate programmes and corporate sponsorship of research.

Having met resistance from faculty and government officials to the internationalization of Japan's institutions, he collaborated with politician Omi Kōji from 2001 to set up the Okinawa Institute of Science and Technology Graduate University (OIST) to create a truly international university in a green field site. The president of the OIST Promotion Corporation that led to the establishment of OIST in 2011 was the Nobel prizewinner and molecular biologist Sydney Brenner. Now helming OIST is

Peter Gruss, former president of Germany's Max Planck Society. More than half of the faculty and students who pursue interdisciplinary PhD programmes at OIST are international, and the language of instruction is English. Arima also promoted scientific cooperation between Japan and China; he held honorary posts at several Chinese universities.

From an early age, Arima studied the Japanese poetic form haiku. He published numerous poetry books, including *Einstein's Century* (in English translation). Speaking in 2012 at the Fifth Haiku Pacific Rim Conference, he explained to fellow poet Michele Root-Bernstein that when stuck on a physics problem, he would turn his mind to gigantic scenery or the beautiful song of an insect. "I write a haiku," he said, "then I can suddenly find the heart of a secret of nature."

In the same interview, he commented that his interest in many-body problems in physics did not translate well when the bodies were human beings. "Don't go into administration," he joked, "there's no reward at all."

Nature **589**, 513 (2021)

doi: https://doi.org/10.1038/d41586-021-00189-7

Jobs from Nature Careers

-
  -
    - All jobs
  -
    - **Postdoctoral Fellow - Zoubeidi Lab, Vancouver Prostate Centre**

      The University of British Columbia (UBC)

      Vancouver, Canada

      JOB POST

- **Laser Scientist**

  German Electron Synchrotron (DESY)

  Hamburg, Germany

  JOB POST

- **Fachinformatiker/in Systemintegration (w/m/d)**

  Karlsruhe Institute of Technology (KIT)

  Karlsruhe, Germany

  JOB POST

- **Intership/Bachelor or Master Thesis: "Digitization of land-based shrimp farming in Germany using AI-based evaluation of imaging and acoustic systems"**

  Alfred Wegener Institute - Helmholtz Centre for Polar and Marine Research (AWI)

  Bremerhaven, Germany

  JOB POST

This article was downloaded by **calibre** from https://www.nature.com/articles/d41586-021-00189-7

COMMENT
26 January 2021

Cancer research needs a better map

It is time to move beyond tumour sequencing data to identify vulnerabilities in cancers.

Jesse S. Boehm,

Jesse S. Boehm is a leader of the Cancer Dependency Map project at the Broad Institute in Cambridge, Massachusetts, USA.
Contact

Search for this author in:

- Pub Med
- Nature.com
- Google Scholar

Mathew J. Garnett,

Mathew J. Garnett is a leader of the Cancer Dependency Map project at the Wellcome Sanger Institute in Hinxton, UK.
Contact

Search for this author in:

- Pub Med
- Nature.com
- Google Scholar

David J. Adams,

David J. Adams is a leader of the Cancer Dependency Map project at the Wellcome Sanger Institute in Hinxton, UK.

Search for this author in:

- Pub Med
- Nature.com
- Google Scholar

Hayley E. Francies,

Hayley E. Francies is a leader of the Cancer Dependency Map project at the Wellcome Sanger Institute in Hinxton, UK.

Search for this author in:

- Pub Med
- Nature.com
- Google Scholar

Todd R. Golub,

Todd R. Golub is a leader of the Cancer Dependency Map project at the Broad Institute in Cambridge, Massachusetts, USA; and a cancer biologist at the Dana-Farber Cancer Research Institute in Boston, Massachusetts, USA.

Search for this author in:

- Pub Med
- Nature.com
- Google Scholar

William C. Hahn,

William C. Hahn is a leader of the Cancer Dependency Map project at the Broad Institute in Cambridge, Massachusetts, USA; and a cancer biologist at

the Dana-Farber Cancer Research Institute in Boston, Massachusetts, USA.

Search for this author in:

- Pub Med
- Nature.com
- Google Scholar

Francesco Iorio,

Francesco Iorio is a leader of the Cancer Dependency Map project at the Wellcome Sanger Institute in Hinxton, UK; and a computational cancer biologist at the Human Technopole in Milan, Italy.

Search for this author in:

- Pub Med
- Nature.com
- Google Scholar

James M. McFarland,

James M. McFarland is a leader of the Cancer Dependency Map project at the Broad Institute in Cambridge, Massachusetts, USA.

Search for this author in:

- Pub Med
- Nature.com
- Google Scholar

Leopold Parts &

Leopold Parts is a leader of the Cancer Dependency Map project at the Wellcome Sanger Institute in Hinxton, UK.

Search for this author in:

- Pub Med
- Nature.com
- Google Scholar

Francisca Vazquez

Francisca Vazquez is a leader of the Cancer Dependency Map project at the Broad Institute in Cambridge, Massachusetts, USA.

Search for this author in:

- Pub Med
- Nature.com
- Google Scholar

A coloured scanning electron micrograph of a spheroid pancreatic cancer cell covered in nodules

There are few models to study rare cancers. Credit: Steve Gschmeissner/SPL

Almost 15 years ago, scientists and clinicians set out to characterize genomes of tumours from thousands of patients. The result? The Cancer Genome Atlas (TCGA) and International Cancer Genome Consortium (ICGC). Nearly every targeted cancer drug approved over the past decade has drawn from the data sets generated by these efforts. This information is now also providing clues to triangulate which individuals can benefit from new types of drug, such as pembrolizumab and nivolumab, which help the immune system to fight cancer. TCGA generated more than 2.5 petabytes of data measuring mutations, gene expression and protein levels across 33 cancer types. It catalysed innovation in DNA sequencing technology and genome analysis. It ultimately collected data from some 11,000 patients — data that thousands of researchers use. This work redefined cancers on the molecular level, and painted a picture of the mutations that occur in common tumour types.

Nonetheless, less than one-quarter of people with the most common cancers benefit from precision medicine today[1,2]. For most patients, there's a long way to go before clinicians will be able to predict drug activity and mechanism on the basis of a mutation (or other molecular marker) in an individual tumour. In 2018, an estimated 10 million people worldwide died from cancer. Too many endured invasive, toxic treatments because physicians had no way to know what would work.

Improving the odds requires another ambitious project, one we call the Cancer Dependency Map. This would systematically map cancer vulnerabilities by perturbing genes and proteins across many cancer types as well as across clinical stages and settings. The Cancer Dependency Map would collect different data and ask different questions from sequencing projects by looking at the experimental effects of perturbations (see 'Big projects, big insights').

BIG PROJECTS, BIG INSIGHTS

The Cancer Genome Atlas revealed cancer mutations. A new project to find weak points in many cancer types using systematic experiments can suggest how to exploit these vulnerabilities for treatments.

Project	**The Cancer Genome Atlas** Focus on comparing DNA in healthy tissues and tumours.	**The Cancer Dependency Map** Focus on laboratory experiments to find tumour vulnerabilities.
Input	Tumours and healthy tissues from thousands of individuals across 33 cancer types.	Experiments to knock out genes and screen drug libraries in thousands of cancer models, representing diverse cancer types at different clinical stages and from people of various ethnicities.
Data	• DNA sequence • Epigenetic marks • Gene expression • Protein levels and modifications.	After perturbation: • Cell growth • Cell death • Gene expression • Cellular morphology.
Insights	Identified changes (such as mutations or deletions) specific to certain cancer types. Found genes implicated in many cancers, but did not directly explore gene functions.	How manipulating a given target in a given tumour type might affect tumour growth, including when the best targets are not in the altered genes themselves.

©nature

Our goal is audacious — some might even say naive. The aim is to evaluate every gene and drug perturbation in every possible type of cancer in laboratory experiments, and to make the data accessible to researchers and machine-learning experts worldwide. To put some ballpark numbers on this ambition, we think it will be necessary to perturb 20,000 genes and assess the activity of 10,000 drugs and drug candidates in 20,000 cancer models, and measure changes in viability, morphology, gene expression and more. Technologies from CRISPR genome editing to informatics now make this possible, given enough resources and researchers to take on the task.

We are investigators at two leading genomics-research institutes — the Wellcome Sanger Institute in Hinxton, UK, and the Broad Institute in Cambridge, Massachusetts. Our organizations have led and supported large international initiatives that produced reference genomics data sets (the Human Genome Project, 1000 Genomes, TCGA, ICGC, gnomAD, the Human Cell Atlas and more). We started a pilot project for the Cancer Dependency Map several years ago[3,4,5] to assess the basic feasibility of this effort. Data from these pilot efforts are now accessed daily by 1,500 researchers across more than 100 countries. Tens of highly validated drug targets have been discovered, and clinical trials have already been launched. But the scale and complexity of this challenge means that we need more than the Broad and Sanger institutes alone.

Now is the time to follow in the footsteps of other large scientific projects to expand these efforts beyond our two institutes into a communal initiative coordinated and built by many hands.

More than mutations

In oncology, a ‘dependency’ is a gene, protein or other molecular feature that a tumour depends on for growth. It could also be called a vulnerability. The simplest type of dependency is an addiction[6]: a gene that spurs tumour growth when mutated, copied or overexpressed, and which becomes essential for the cells’ continued proliferation. There are therapies that can suppress such gene products directly. Relevant drugs include vemurafenib (which blocks the cell-signalling enzyme B-RAF to treat melanoma and other cancers), osimertinib (which blocks the cell receptor EGFR to treat certain lung cancers) and, more recently, sotorasib (which blocks a mutant form of the K-Ras cell-signalling protein)[7]. The addictions involving mutant genes are the type of vulnerability most readily revealed by the tumour sequencing projects.

Remember why we work on cancer

Another type of vulnerability is more complicated, and hard to find using tumour sequence data: a protein becomes indispensable for a tumour's growth because of alterations in other genes; this situation is known as synthetic lethality[8]. For example, some people with breast and ovarian cancers have mutations in the gene *BRCA1*. Drugs for these individuals target a protein involved in the DNA-repair mechanism that these cancers need to survive, not the BRCA1 protein itself. Discovering and understanding more vulnerabilities, and more kinds of them, could transform cancer treatment.

The roots of the Cancer Dependency Map began with the intersection of two lines of research. One aimed to assess the effects of known drugs across hundreds of cancer lines[5,9,10,11,12]. The other sought to disrupt nearly every gene in hundreds of cancer models[3,4,13].

Our estimate is that this pilot represents just a small proportion, probably less than 10%, of a 'complete' Cancer Dependency Map. Much remains to be done.

Mega mapping

The easiest step is to expand the range of drugs and genetic manipulations used in screens. CRISPR genome-editing tools can knock out genes, turn expression on and off and even manipulate combinations of genes. These perturbations can be performed across many tumour types and cellular contexts (such as in the presence of immune and other non-cancerous cells). Existing collections of drugs and other molecules with specific activity against known proteins can be used to inhibit or even modify proteins' function. Classes of compounds that have other types of activity, such as promoting protein degradation, should be included in screens as our understanding of them matures.

The most challenging expansion will be in the number of cancer models (cell lines and organoids), to represent all of the diversity in cancer. Our pilot project screened about 1,000 cancer cell lines. These included few of the 'driver genes' that individually are found in less than 10% of tumours (but which together constitute the majority of cancer mutations). For common tumour types, populations of non-European descent are under-represented in the bulk of data collected, as are drug-resistant tumours and early stages of disease. (Projects such as TracerX show how individuals' cancers evolve over time, but not how to treat different stages.) Rare cancers collectively represent 25% of all cancers. Most, including paediatric cancers, are under-represented in or completely absent from existing models.

Cancer geneticists tackle troubling ethnic bias in studies

The range of data that must be collected is substantial. The pilot phase of the dependency map mainly measured proxies for proliferation, so further measurements would be extremely informative. For example, identifying drug targets that promote senescence, a condition in which cells live but no longer divide, would open routes to new forms of therapeutics. Measuring gene expression in response to drugs could reveal which ones might be combined into more-effective therapies. Single-cell measurements, such as cell imaging[14] or sequencing to determine RNA levels at various time points (RNA-seq), could identify differences in the responses of tumour cell populations. This information could be used to target drug-tolerant cells.

Some of the essential work for comprehensive screening is under way. Curated collections of thousands of drug-like and tool compounds have been assembled by the US National Institutes of Health (NIH), and chemical probes to new targets have been developed by the Structural Genomics Consortium. Efforts such as the Human Cancer Models Initiative are creating biobanks of new cancer cell lines, organoids and other models that are genetically and clinically annotated. Such crucial efforts will not produce

a Cancer Dependency Map, however. That will take multiple, large-scale data generation and analysis centres, as well as resources and coordination.

Data standards

Data from the Cancer Dependency Map must be accessible and flow easily into analysis pipelines for academic and pharmaceutical scientists, artificial-intelligence experts and clinicians.

Data sets generated at different sites using varying technologies will be difficult or impossible to aggregate without careful advance planning. Care must be taken so that the data will be maximally useful, and can be readily integrated with databases such as the US National Cancer Institute's Genomics Data Commons, cBioPortal and the Catalogue Of Somatic Mutations In Cancer (COSMIC), as well as new dedicated data portals. For the past 20 years, various scientific communities have crafted 'minimal information' standards to enable interpretation and replication of experiments. The best known of these, MIAME (minimum information about a microarray experiment), was set up so that researchers could effectively compare gene-expression experiments in different laboratories. The Cancer Dependency Map will need something similar to support annotation, integration, reproducibility and computation.

Money and collaboration

This project is ambitious but possible. Past examples of large, successful, global projects include the ICGC and the Human Cell Atlas[15], a project to categorize gene expression, lineage and the location of hundreds of cell types. The NIH and Wellcome Trust were major funders of these, and the Chan Zuckerberg Initiative also funded the Human Cell Atlas. At least half a dozen countries came together to support the Human Genome Project.

Our best weapons against cancer are not magic bullets

The first step forward is to assemble scientific thought leaders as well as funders to clearly define the scope and scale of data needed. The next step is to establish working groups around standards, technology, data access and cancer types. This follows the example of the Human Cell Atlas, in which research is led by independent laboratories with coordination at the level of the organ. Its working groups set data standards that enable sharing and integration.

Similar to the Human Cell Atlas, data and technologies arising from the Cancer Dependency Map will provide huge resources for science, as will the networking and technology development spurred by the umbrella project. Just gearing up to collect measurements for the Cancer Dependency Map could drive innovation: in automation, miniaturization and in new co-culturing techniques that mimic physiological conditions.

It is true that the cell-based experiments we propose will miss many complexities of cancer biology. Still, most drugs available today arose from *in vitro* screens. As the technologies mature, we expect that experiments will

extend towards new types of target, including those involving the tumour microenvironment or immune system. Early concerns about reproducibility[16] seem to now be largely overcome[12,13]. The precision of CRISPR technologies and the statistical power that comes from large-scale experiments strongly benefit reproducible experimentation.

We estimate that a thorough Cancer Dependency Map project will require an annual commitment of US$30 million to $50 million over a decade. (The TCGA pilot launched by the NIH cost $100 million during its first 3 years, and continued for 12 years.) For comparison, the US National Cancer Institute's 2020 budget was$6.4 billion, and the 2019–20 research budget for the funder Cancer Research UK was £511 million (US$694 million). Industry, government agencies and philanthropists should contribute.

One in six deaths worldwide are due to cancer. Although more targets and therapeutic approaches are published every day, systematic investigation will enable more and faster discoveries. By testing thousands of genetic and chemical perturbations in thousands of cancer models in rigorous, coordinated experiments, the Cancer Dependency Map can reveal the cellular wiring underlying a breadth of tumours, with data accessible to individual researchers' queries and computational approaches. In the same way that large-scale, systematic genome sequencing transformed our understanding of cancer, the Cancer Dependency Map will enable researchers to explore questions and identify routes to therapies that are currently unimaginable.

Nature **589**, 514-516 (2021)

doi: https://doi.org/10.1038/d41586-021-00182-0

References

1. 1.

   Zehir, A. *et al. Nature Med.* **23**, 703–713 (2017).

2. 2.

Stockley, T. L. *et al. Genome Med.* **8**, 109 (2016).

3. 3.

Tsherniak, A. *et al. Cell* **170**, 564–576 (2017).

4. 4.

Behan, F. M. *et al. Nature* **568**, 511–516 (2019).

5. 5.

Corsello, S. M. *et al. Nature Cancer* **1**, 235–248 (2020).

6. 6.

Weinstein, I. B. & Joe, A. *Cancer Res.* **68**, 3077–3080 (2008).

7. 7.

Hong, D. S. *et al. N. Engl. J. Med.* **383**, 1207–1217 (2020).

8. 8.

Luo, J., Solimini, N. L. & Elledge, S. *J. Cell* **136**, 823–837 (2009).

9. 9.

Garnett, M. J. *et al. Nature* **483**, 570–575 (2012).

10. 10.

Iorio, F. *et al. Cell* **166**, 740–754 (2016).

11. 11.

Barretina, J. *et al. Nature* **483**, 603–607 (2012).

12. 12.

Haverty, P. M. *et al. Nature* **533**, 333–337 (2016).

13. 13.

Dempster, J. M. *et al. Nature Commun.* **10**, 5817 (2019).

14. 14.

Feldman, D. *et al. Cell* **179**, 787–799 (2019).

15. 15.

Rozenblatt-Rosen, O., Stubbington, M. J. T., Regev, A. & Teichmann, S. A. *Nature* **550**, 451–453 (2017).

16. 16.

Haibe-Kains, B. *et al. Nature* **504**, 389–393 (2013).

Jobs from Nature Careers

-
  -
    - All jobs
  -
    - **Postdoctoral Fellow - Zoubeidi Lab, Vancouver Prostate Centre**

      The University of British Columbia (UBC)

      Vancouver, Canada

      JOB POST

    - **Laser Scientist**

      German Electron Synchrotron (DESY)

Hamburg, Germany

JOB POST

- **Fachinformatiker/in Systemintegration (w/m/d)**

  Karlsruhe Institute of Technology (KIT)

  Karlsruhe, Germany

  JOB POST

- **Intership/Bachelor or Master Thesis: " Digitization of land-based shrimp farming in Germany using AI-based evaluation of imaging and acoustic systems"**

  Alfred Wegener Institute - Helmholtz Centre for Polar and Marine Research (AWI)

  Bremerhaven, Germany

  JOB POST

This article was downloaded by **calibre** from https://www.nature.com/articles/d41586-021-00182-0

Work

- **Let the dog in: how institutions and colleagues can help scientists who require support animals** [27 January 2021]
  Career Feature • University policies often present barriers to bringing assistance dogs into the lab or on campus.
- **Seven technologies to watch in 2021** [26 January 2021]
  Technology Feature • COVID considerations unsurprisingly dominate the tech developments that could have a big impact in the coming year.
- **The bird librarian** [25 January 2021]
  Where I Work • Leah Tsang helps to bring bird poisoners to justice as part of her role at Australia's oldest museum.

CAREER FEATURE
27 January 2021

- Correction 28 January 2021

Let the dog in: how institutions and colleagues can help scientists who require support animals

University policies often present barriers to bringing assistance dogs into the lab or on campus.

Nina Notman

Nina Notman is a freelance writer in Salisbury, UK.

Search for this author in:

- Pub Med
- Nature.com
- Google Scholar

Find a new job

Sampson wore protective equipment when working in the lab with Joey Ramp during her undergraduate degree.Credit: Doris Dahl

When Joey Ramp enrolled in science classes in 2012 at a local community college, she was surprised that she could not bring her assistance dog, Theo, into institutional laboratories. College regulations barred the practice, saying that labs were unsafe environments for support animals. Going it alone wasn't an option; she needs the help of an assistance dog for tasks such as balancing on stairs and retrieving dropped items. The dog also alerts her to emotional overload.

Ramp had a choice: leave the course or demand access. She chose to stay.

Ramp, whose assistance dog provides support for her physical disability and complex post-traumatic stress disorder, the results of a horse-riding accident in 2006, says that she hadn't thought to mention Theo in advance of her first classes at the college in Champaign, Illinois. Disability anti-discrimination laws in many nations, including the United States, mandate that assistance dogs have access to most public spaces.

In retrospect, Ramp admits, she was naive to remain silent. Still, she quickly resolved the problem after a two-hour conversation with her lab manager and the college's director of disability services. She agreed to garb Theo in protective equipment, including goggles and a lab coat, before taking him into the lab.

But Ramp faced more obstacles when she transferred to the University of Illinois Urbana-Champaign, where she earned an undergraduate degree in neuroscience in 2019. She says that it took more than a year of discussions with university administrators and disability-services representatives for her to win the right to bring Theo to particular lab classes. A spokesperson says that the university cannot comment on specific situations and that it has robust accommodations for campus members with disabilities. Eventually, Theo and his successor, Sampson, were able to enter all of Ramp's lab classes, save one that involved live rodents.

Although she was largely successful in her quest to gain access for her canine supporters, Ramp says that she felt battered by the process, particularly around the need to argue her case again every semester with new professors. "It left me wanting to change the landscape for the people that followed me," she says.

Today, Ramp is chief executive of Empower Ability Consulting in Champaign, Illinois, which she launched in 2018 to advise universities, other scientific workplaces and people with disabilities on hosting assistance dogs in laboratories. She estimates that her clients number more than 100 individuals and at least a dozen universities.

Increasing numbers

Assistance or support dogs perform a specific task, or tasks, that mitigate their users' disability in some way. Categories differ, according to Melissa Winkle, an occupational therapist and assistance-dog trainer at Dogwood Therapy Services in Albuquerque, New Mexico. They include guide dogs that work with people who are blind or visually impaired, dogs that support the deaf or hearing-impaired, mobility-assistance dogs, medical-alert assistance dogs and psychiatric-assistance dogs.

Between 2009 and 2019, the number of support-dog users increased by 42%, according to Assistance Dogs International (ADI), a global coalition of 133 non-profit programmes in North America, Europe, Australia and New Zealand.

The proportion of dogs that help their handlers with disabilities other than vision and hearing has been increasing for at least a decade, says an ADI spokesperson. In 2019, 49% of handlers who were registered with ADI programmes had guide dogs, 7% had hearing dogs and 44% had other types of assistance dog.

Despite rising numbers, many universities remain unprepared for the presence of assistance dogs on campus. Institutional policies often do not mention bringing dogs into lab spaces, for example. “There is this roadblock where it’s often just assumed that it would be too hard,” says Jade Simon, an assistance-dog user who is a palaeobiology PhD student at the Royal Ontario Museum and the University of Toronto in Canada.

Basil, Simon’s current dog, helps her with balance and alerts her to changes in her pulse rate and blood pressure related to a connective-tissue disorder and associated complications. Neither the museum nor the university has robust written guidelines on hosting assistance dogs in the lab. A spokesperson says that the university prefers to address situations individually.

Basil now has access to a lab at the institute where her handler Jade Simon is a PhD student.Credit: Jade Simon

After reading stories about Ramp's experience, Simon worked with the university on a plan for Charlie, Basil's predecessor. She can take Basil into the museum's microscopy lab and is negotiating access to the histology lab where she prepares thin sections from fossil samples.

Simon thinks that institutions need to be better prepared for researchers with assistance dogs who require access to labs. "They need to tackle it like they do any other equity issue and have a comprehensive plan in place ahead of time," she says.

These guidelines should include considerations of lab-member safety, says Patricia Redden, a chemist at Saint Peter's University in Jersey City, New Jersey, and a member of the American Chemical Society's Committee on Chemists with Disabilities. As a volunteer for Canine Companions for Independence in Santa Rosa, California, she fosters future assistance puppies at her home, teaching and socializing each for 18 months in preparation for their transition to a professional trainer. Redden says that support dogs in labs should be positioned so as to not pose a trip hazard — lying down at the back, or in vacant wheelchair spaces — and should not present a hindrance to safe emergency evacuation.

Institutional guidelines should also consider the safety of the dogs, Redden adds. The amount and type of protective equipment needed will vary depending on the type of lab and the person writing the rules.

Ramp says that dogs should wear the same level of protective equipment as their handler. Sampson, for example, wore goggles designed for military and police dogs and one of Ramp's lab coats under his harness. Redden recommends that support dogs in wet labs wear a bespoke full-coverage chemical-resistant suit. Many handlers agree that dogs should wear booties and lie on a suitable mat in the lab.

Pliable policies

Establishing guidelines around support animals is a positive move towards inclusion, says Sharon Rozovsky, a chemist at the University of Delaware, Newark, who adds that those guidelines must stay flexible. She helps to

coordinate a summer research programme for undergraduates with disabilities who want to pursue chemistry or biochemistry. “There can’t be a rigid standard operating procedure,” she says. Every assistance-dog user has different requirements, every dog is different and every lab has a different set of hazards, she adds.

Scientists with support dogs say that universities should involve them in discussions around their dogs’ presence in campus labs. “Researchers can advocate very well for themselves — it won’t be the first time that they have had to explain to people what they need,” says Rozovsky. Debbie Decker, who retired last year from her role as safety manager for the chemistry department at the University of California (UC) Davis, says that she always aimed to collaborate with support-dog users and to prioritize safety for the researcher and their dog.

Guide dog Bing at work in the field. Bing supports Katherine Brafford, a PhD student in ecology at the University of California, Davis.Credit: Katherine Brafford

Discussions should cover whether bringing the dog into the lab is always the best solution, says Redden. Some scientists' support needs might be better met by another person. Katherine Brafford, a guide-dog user and PhD student in ecology, at UC Davis, leaves her dog, Bing, outside the lab. "A cane, or a sighted guide, just works much better [for me] in a lab setting," she says. Still, she notes, leaving the dog outside the lab creates other challenges, such as identifying an appropriate location for the dog during lab time. That could be an office space, a crate or a quiet corridor. Brafford leaves Bing in a corridor with a laminated sign asking people to leave him alone. These conversations should begin several months before the researcher will be on campus, says Rozovsky (see 'Canines at conferences').

Colleague considerations

Simon says that it is hugely helpful if others on campus do not distract working animals. Those who are around a support dog should not touch, feed or talk to them. "Our dogs are working, and often they are monitoring us for changes in our physiology," says Simon. Distraction might cause a support dog to miss an alert, which can be life threatening for the scientist, who might have diabetes, cardiac issues or a seizure illness. "It can be downright dangerous [for me] to have people distracting Bing when we're crossing a street," says Brafford. She estimates that people try to pet her guide dog at least ten times during an average day on campus.

Isabel Rutten, who studies animal science and management at UC Davis, gets annoyed when people try to sneak photos of her psychiatric and mobility-assistance dog, Winston. "This happened a lot outside my chemistry lab when he was in his boots and lab coat," she says. "They are taking pictures of my medical equipment." Brafford says that she feels disappointed when people talk to Bing and not to her, although she concedes that Bing can act as a useful communication tool. "It gives people a good, safe way to talk to me about my disability if they need to," she says. "They can talk to me about my dog first and then go into other things."

Isabel Rutten, who studies animal science and management at the University of California, Davis, with Winston, her psychiatric and mobility-assistance dog.Credit: Paula Rutten

Lieke van Putten, a postdoc who studies optoelectronics at the University of Southampton, UK, got her mobility-assistance dog, Nell, from the UK charity Canine Partners in Midhurst. The organization e-mailed details about the support animal to van Putten's colleagues before she and Nell arrived on campus. "In short, it said, 'Don't distract the dog'," van Putten explains, it also asked colleagues to allow her support dog to help her. "Once I got Nell, I didn't need people to pick up a dropped phone or press a door release button any more," says van Putten, who uses a wheelchair. "I feel a lot more independent if Nell does that for me."

Nell provides mobility assistance to postdoc Lieke van Putten, who uses a wheelchair.Credit: Lieke van Putten

Some students and colleagues might be uncomfortable with or afraid of dogs, particularly in certain geographical locations. “There is a widespread fear of dogs in South Africa,” says Juan Erwee, a disability officer at the University of Pretoria, who adds that the use of aggressive police dogs during apartheid, between 1948 and the mid-1990s, might have contributed to the cultural fear. The university runs awareness campaigns, which include information on service animals, to boost understanding of disabilities among students and staff, he says.

Brafford recommends that colleagues who fear a support dog communicate their concerns to its user. When Brafford is aware of such fears, she says, she ensures that Bing keeps his distance from that person.

Although the presence of support dogs on university campuses can still be a challenge for both users and their institutions, researchers who depend on the animals are optimistic that administrators, faculty members and safety officers will eventually smooth the bumps. “My hope,” says Brafford, “is that one day, it won’t be so weird that there are people with disabilities and service animals in science.”

Canines at conferences

Most conferences worldwide have become virtual while the pandemic continues, but many will eventually return to on-site schedules. Conference organizers who aim for inclusivity will want to consider how they can help attendees and speakers who rely on assistance animals to successfully navigate the event.

Initiate the conversation. “An option on the registration form to enter accessibility requirements is helpful,” says Lieke van Putten, an assistance-dog user and postdoc at the University of Southampton, UK. This can be as simple as ‘Please tick here and you will be contacted to discuss your specific needs’. Or it could be a comprehensive list of questions about the full range of needs that attendees who have disabilities might have.

Make space available at sessions. Assistance-dog users need the same amount of manoeuvring space as wheelchair users, says Joey Ramp, an assistance-dog user and chief executive of Empower Ability Consulting in

Champaign, Illinois. In the United States, this requirement is 0.9 metres down a corridor and a 1.5-metre turning circle. Space between rows of seats should also be considered. A support dog will also require rest space next to the scientist-user, both in the audience and on the stage if the scientist is presenting.

Provide comfort information and time. Ensure that the conference map or welcome pack includes locations of and clear directions to nearby grassy areas for assistance dogs to go to the toilet. These areas should be easy to find. Organizers might consider walking the route in advance and ensuring that fire and other doors do not lock after a person has left the building. "Breaks should allow sufficient time for the handler to use the restroom and take their dog out for relief," says Ramp.

Clarify support-dog protocols. Organizers should educate all conference staff and volunteers about proper service-dog etiquette in advance. Crucial information includes ignoring the support dog unless its owner indicates otherwise, says Patricia Redden, a chemist at Saint Peter's University in Jersey City, New Jersey. She adds that it's also important to understand that a support-dog user will need the dog with them at all times. Organizers might consider adding a service-dog fact sheet to the conference welcome pack, suggests Ramp.

Show respect. Organizers should emphasize on the conference website and registration form that they will work with support-dog users to accommodate their accessibility requirements. At the event, conference staff members can offer assistance to users by asking what they need. "If someone asks me how they can help, I can decline the offer if I'm fine or ask for specific help," says van Putten. "I usually find that if people try to help me without asking first, they unintentionally make the situation harder."

Nature **589**, 627-629 (2021)

doi: https://doi.org/10.1038/d41586-021-00190-0

Updates & Corrections

- **Correction 28 January 2021**: An earlier version of the caption for the photo of Jade Simon's assistance dog implied that Basil is male.

Jobs from Nature Careers

-
  -
    - All jobs
  -
    - **Postdoctoral Fellow - Zoubeidi Lab, Vancouver Prostate Centre**

      The University of British Columbia (UBC)

      Vancouver, Canada

      JOB POST

    - **Laser Scientist**

      German Electron Synchrotron (DESY)

      Hamburg, Germany

      JOB POST

    - **Fachinformatiker/in Systemintegration (w/m/d)**

      Karlsruhe Institute of Technology (KIT)

      Karlsruhe, Germany

      JOB POST

    - **Intership/Bachelor or Master Thesis: "Digitization of land-based shrimp farming in Germany using**

AI-based evaluation of imaging and acoustic systems"

Alfred Wegener Institute - Helmholtz Centre for Polar and Marine Research (AWI)

Bremerhaven, Germany

JOB POST

This article was downloaded by **calibre** from https://www.nature.com/articles/d41586-021-00190-0

TECHNOLOGY FEATURE
26 January 2021

Seven technologies to watch in 2021

COVID considerations unsurprisingly dominate the tech developments that could have a big impact in the coming year.

Esther Landhuis

Esther Landhuis is a science journalist based near San Francisco, California.

Search for this author in:

- Pub Med
- Nature.com
- Google Scholar

Two workers in white lab coats inspect a large electronic system behind a glass screen

Biopharmaceutical firm CureVac's RNA printer can rapidly supply mRNA vaccine candidates. Credit: CureVac

This year looks to be a promising one for technology development. From advances in vaccines to olfaction, neuroscience to mass spectrometry, researchers describe the tools and techniques generating excitement in their disciplines.

NICK JACKSON: Thermally stable vaccines

Head of programmes and technology for research and development at CEPI in London.

At the Coalition for Epidemic Preparedness Innovations (CEPI), a global coalition launched in 2017 to develop vaccines against emerging infectious diseases, we're interested in vaccine technologies that drive speed, scale and access. That includes the speed at which vaccines are proven safe and effective, and how they can be manufactured at scale and delivered to vulnerable populations so that everyone has access.

At no other time has that proven more urgent than in the continuing COVID-19 pandemic, during which messenger RNA vaccines inside lipid nanoparticles have gone from sequence to clinical proof-of-concept to interim analysis in record time. It took less than four months for the biotechnology company Moderna and the drug firm Pfizer to go from sequence to phase I trial, which is incredible when development typically takes years or decades. These vaccines are already being rolled out to the public for emergency use.

But they could be made to work even better. One powerful recent innovation has been the use of ionizable lipids in the nanoparticles that deliver mRNA into cells[1]. The particles remain neutral at physiological pH but when they enter a cell's endosome, they build up charge in the organelle's acidic environment, which then aids the release of its mRNA payload. The next generation of ionizable lipid nanoparticles under development would use a receptor-binding process to target the particles to specific tissues or cell types.

Other innovations are improving access. Some technologies, for example, use sugar molecules to allow efficient freeze-drying without damaging the vaccines' refined structure or formulation, making them easier to store and transport.

Another avenue for increasing vaccine access is developing portable RNA-printing technology. Few countries have the capital and expertise to produce high-quality vaccines at scale, but in February 2019, CEPI invested US$34 million in the biopharmaceutical company CureVac's efforts to develop a fully transportable unit that could enable low-resource areas to produce their own mRNA vaccines. This sort of innovation is going to make vaccines even more accessible. And it provides a glimpse of the future: it means more countries will be better prepared for the inevitable next outbreak.

OFER YIZHAR: Holograms in the brain

Systems neuroscientist at the Weizmann Institute of Science in Rehovot, Israel.

Optogenetics — techniques for controlling the activity of defined brain cells and circuits — has generated excitement in the neuroscience field since it emerged in 2005. In 2021, I anticipate these tools will have an even bigger impact.

With optogenetics, researchers can shine light into a tissue, and all neurons that express the tool will respond. Yet in reality, brain activity is much more nuanced. Neurons respond only to particular stimuli. The timing matters; the sequence matters; the neurons rarely fire all together. From 2005, optogenetics allowed us to manipulate specific types of neurons, but still couldn't recapitulate the language cells use to communicate with each other.

To address this shortcoming, some neuroscientists developed new light-responsive proteins — for example, by changing the colour of light that activates the channel, or making the channel stay open for longer. Some of these modified proteins allowed us to stimulate neurons more precisely using two-photon excitation, a technique for high-resolution imaging of living tissue. However, there are limits to how fast a laser beam can activate individual neurons, and this constrained how reliably we could design stimulation patterns to mimic natural activity.

The lightning-fast quest for COVID vaccines — and what it means for other diseases

At the same time, others made advances in optics. Over the past few years, holography and other optical approaches for single-neuron manipulation have matured enough to be adopted by non-specialist labs. By splitting laser light into many beamlets that form the shape of neurons, it's possible to generate holograms to stimulate neurons precisely, in complex temporal patterns, in three dimensions[2].

Whereas a single laser beam might take 10–20 milliseconds to stimulate a neuron, holography lets you stimulate that cell in less than a millisecond — considerably faster than the 4–5 milliseconds it generally takes to transmit a signal from one neuron to another. You can also generate multiple holograms at the same time, or in a particular sequence.

This type of experiment used to be limited to specialized labs with the know-how to build custom microscopes. Now, microscope companies such as Bruker and 3i have incorporated holography in their two-photon imaging

systems. Neuroscientists can take a picture through the microscope, mark the neurons they want to activate, and the software generates holograms to match these activation patterns. With converging developments in optogenetic tools and optical techniques, we can begin to explore the neural code with single-neuron precision.

ALICIA CHENOWETH: Building better antibodies

Cancer immunologist at King's College London and co-chair of the 2022 Antibody Biology and Engineering Gordon Research Conference.

Antibodies have been used as therapies since the mid-1990s. However, it's only in the past couple of years, as scientists have worked out how the structure of antibodies influences their function, that we've really started to uncover their potential. Amid the continuing pandemic, antibody therapeutics have taken on new urgency.

Most antibody therapies are just regular, unmodified antibodies that bind to a particular target — for instance, a protein on the surface of a virus or tumour cell. However, many of these antibodies are ineffective at engaging immune cells to get rid of the targeted material. With advances in molecular biology, we can quickly modify antibodies to make them better at harnessing the immune system to fight disease[3].

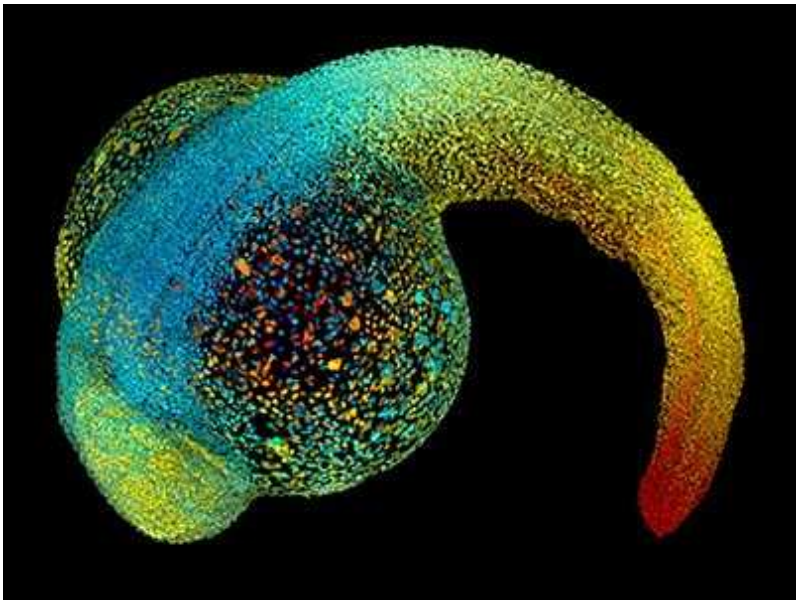

The secret forces that squeeze and pull life into shape

My laboratory has been using two different strategies for doing that. Using the PIPE (polymerase incomplete primer extension) platform, a rapid and efficient molecular-cloning method developed at the Genomics Institute of the Novartis Research Foundation in San Diego, California, we have introduced point mutations into antibodies to make it easier for them to interact with natural killer cells, which increases the death of cancer cells in a breast cancer model in mice.

Separately, we have started investigating antibodies based on immunoglobulin E (IgE). Most therapeutic antibodies are based on an immunoglobulin G backbone. People typically think of IgE as this really awful antibody associated with allergic reactions. Yet in fact, if you use IgE antibodies to unleash that powerful inflammation, it could be a great way for targeting cancer cells for killing[4].

The beauty of engineered antibodies is that, because of their versatile nature, they can be applied to almost any disease as long as you have something to target. So, while we're looking into cancer, other scientists are engineering

antibodies to shut down the immune system to treat autoimmunity and allergies, or to aid the immune response against infectious diseases, including COVID-19. The possibilities really are endless.

CORAL ZHOU: The single-cell power of three

Cell and developmental biologist at the University of California, Berkeley and co-chair of the 2021 Chromosome Dynamics Gordon Research Conference.

The body's cells have many different functions. Yet they all derive from a single cell and a single genome. How does one cell give rise to all these different types?

I'm excited about three new single-cell sequencing technologies that can help to address this question at the earliest stages of embryonic development. One uses Hi-C — a method for studying the 3D architecture of the genome — to examine maternal and paternal chromosomes in single cells of mouse embryos at distinct stages of early development. Using this approach, researchers reported last March that parental genomes do not mix immediately after fertilization — there is a moment between the 1- and 64-cell stage when the structure of the maternal genome looks different to that of the paternal genome[5]. Although we don't know exactly why this brief asymmetry exists, the authors speculate that it has a role in establishing sex-specific gene expression programs later in development. Until then, I don't think we had the technology to discover something like this.

Another technique called CUT&Tag tracks specific biochemical 'marks' on the genome to help scientists study how these chemical modifications switch genes on and off in individual live cells[6], while SHARE-seq combines two sequencing methods to identify regions of the genome that are accessible to transcription-activating molecules[7].

By applying these tools to the developing embryo, we can create a roadmap for how specific features of genomic architecture determine cell fate as an embryo develops.

TAKANARI INOUE: Feeling the force

Synthetic cell biologist at the Johns Hopkins School of Medicine, Baltimore, Maryland, and was a co-organizer of the Tools and Devices for Cell Biology subgroup for the American Society for Cell Biology 2019 conference.

Besides growth factors and other molecules, cells also sense physical force. Force sensation can regulate gene expression, proliferation, development and possibly cancer.

Force is hard to study because you only see its effects — when you push something, there's deformation or movement. But now, using two cutting-edge tools to visualize and manipulate force in living cells, scientists can probe causal relationships between physical force and cellular functions as never before.

GenEPi, developed at Imperial College London, fuses two molecules. One, called Piezo1, is an ion channel that conducts calcium ions through its pores when it senses tension on the cell membrane. These ions are detected by the second molecule — which fluoresces more brightly when it binds to calcium.

Previous studies used physical probes or other invasive devices to study the impact of force on cells. With GenEPi you can study intact cells in physiologically relevant conditions. And unlike previous sensors that broadly monitor cytoplasmic calcium, GenEPi measures only calcium activity linked to force sensation through Piezo1. As proof of principle, the researchers altered GenEPi fluorescence by stimulating heart muscle cells with the tip of an atomic force microscope cantilever[8].

The second tool, ActuAtor, is one that we generated using ActA, a protein from the pathogenic bacterium *Listeria monocytogenes*. When the bacterium infects a mammalian host cell, ActA hijacks the host's machinery to trigger actin polymerization on the microbe's surface. This generates force that pushes the bacterium through the cytoplasm.

We repurpose this hijacking by engineering ActA to polymerize actin at specific sites inside cells when given a light or chemical stimulus[9]. With

ActuAtor we can exert force deep inside cells. For example, we liberated ActuAtor on the surface of mitochondria, causing the organelles to get chopped up in minutes. We found that these damaged mitochondria are more susceptible to degradation by mitophagy but that key mitochondrial functions such as ATP synthesis were unaffected.

Previously it was hard to address such processes because we lacked tools to deform organelles specifically and non-invasively in living cells. ActuAtor is one of the first tools to be able to do that, to our knowledge.

Genio Technologies' MasSpec Pen is designed to detect tumour tissues and their boundaries.Credit: Dr. James Suliburk/Baylor College of Medicine

LIVIA SCHIAVINATO EBERLIN: Mass spec in the clinic

Analytical chemist at the University of Texas at Austin, co-founder and chief scientific officer at Genio Technologies, Tulsa, Oklahoma, and vice co-chair of the 2021 Chemical Imaging Gordon Research Conference.

Mass spectrometry can rapidly analyse hundreds to thousands of molecules from complex samples with high sensitivity and chemical specificity. Biomedical research on these methods proceeds largely at two extremes. Some scientists are developing high-performance technologies to probe biological tissues more deeply. Researchers in our lab are simplifying mass spectrometry tools so physicians can use them for clinical decisions.

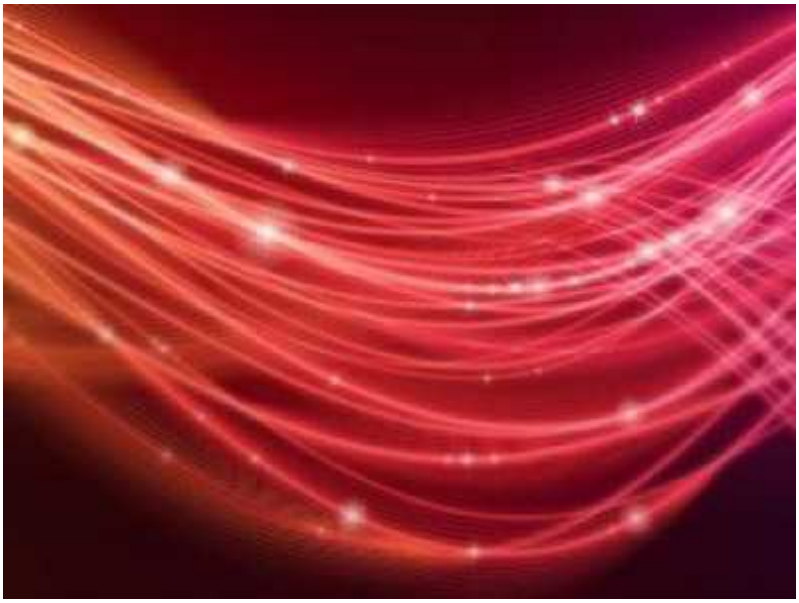

NatureTech hub

MALDI (matrix-assisted laser desorption/ionization) is a mass spectrometry imaging technology that has been used to analyse biological tissues. But releasing molecules from tissues and ionizing them under vacuum conditions can be cumbersome. In 2017, researchers developed a MALDI system that allowed them to manipulate ions in the open air, rather than

under vacuum conditions[10]. That development simplified the MALDI process and allowed it to be combined with other technologies, including fluorescence *in situ* hybridization microscopy, bioluminescent imaging, blockface imaging and magnetic resonance imaging. These multimodal capabilities have enabled researchers to, for instance, probe host–microbe interactions and metabolic changes with greater molecular and histological precision than previously possible[11,12].

On the clinical side, our lab has created MasSpec Pen, a handheld mass spectrometry system that helps surgeons to identify tumour tissues and their boundaries[13]. Our device focuses on metabolites — end products of enzymatic reactions in the body that can distinguish normal tissue from tumour tissue. The process delivers a water droplet onto the tissue, dissolving the metabolites and then sending the molecular contents to the mass spectrometer for analysis. We already know the molecular profiles that characterize metabolism in normal tissue versus tumour tissue in the lab. Now we are testing the tool in the operating room[14].

This year, we plan to continue evaluating the MasSpec Pen in people undergoing surgery for breast, ovarian and pancreatic cancer, or robotic prostate-cancer surgery. We've licensed the technology to Genio Technologies.

JONG-HEUN LEE: Sniffing out sickness

Materials scientist at Korea University, Seoul, and a steering committee member for the 2021 International Meeting on Chemical Sensors.

To detect mixtures of gases that could indicate environmental risks or diseases, including COVID-19, researchers would like to mimic human olfaction, to know what we are smelling. However, unlike sight, hearing and touch, chemical sensors for smell are complex. They involve detecting mixtures of several hundred or even thousands of chemicals, often at trace concentrations.

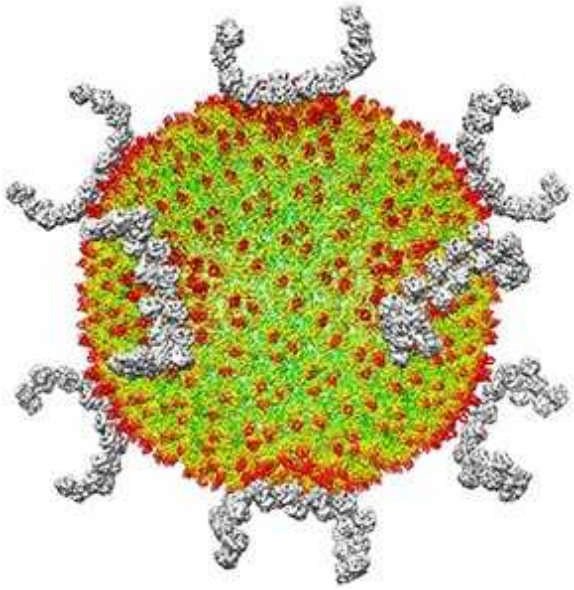

Technologies to watch in 2020

In my lab we are taking several approaches to developing the next generation of artificial olfaction[15]. One involves increasing the diversity of gas-sensing materials using a bilayer design. For example, we could coat each of 10 different sensing materials with 10 catalytic layers that fine-tune each material's gas-sensing characteristics, to make a total of 10x10 or 100 different sensors. This is much easier than separately coating 100 different sensing materials.

We also need to make the sensors respond more rapidly. One strategy is to make the sensing material porous by mimicking nature's hierarchical assemblies, such as trees, which maximize surface area to absorb sunlight for photosynthesis, or lungs, which have a large surface area within a small volume that maximizes transport from main airway vessels to smaller branches.

Artificial olfaction technology can be used for medical diagnosis, for example, to detect higher concentrations of nitric oxide in the breath of people with asthma. Other applications include monitoring air pollution, evaluating food quality and smart farming based on signals from plant hormones.

Nature **589**, 630-632 (2021)

doi: https://doi.org/10.1038/d41586-021-00191-z

These interviews have been edited for length and clarity.

References

1. 1.

   Zeng, C., Zhang, C., Walker, P. G. & Dong, Y. 'Formulation and Delivery Technologies for mRNA Vaccines' in *Current Topics in Microbiology and Immunology*. https://doi.org/10.1007/82_2020_217 (Springer, 2020).

2. 2.

   Papagiakoumou, E., Ronzitti, E. & Emiliani, V. *Nature Methods* **17**, 571–581 (2020).

3. 3.

   Chenoweth, A. M., Wines, B. D., Anania, J. C. & Hogarth, P. M. *Immunol. Cell Biol.* **98**, 287–304 (2020).

4. 4.

   Chauhan, J. *et al. Antibodies* **9**, 55 (2020).

5. 5.

   Collombet, S. *et al. Nature* **580**, 142–146 (2020).

6. 6.

   Kaya-Okur, H. S. *et al. Nature Commun.* **10**, 1930 (2019).

7. 7.

Ma, S. *et al. Cell* **183**, 1103–1116 (2020).

8. 8.

Yaganoglu, S. *et al.* Preprint at bioRxiv https://doi.org/10.1101/702423 (2019).

9. 9.

Nakamura, H. *et al.* Preprint at bioRxiv https://doi.org/10.1101/2020.03.30.016360 (2020).

10. 10.

Kompauer, M., Heiles, S. & Spengler, B. *Nature Methods* **14**, 90–96 (2017).

11. 11.

Cassat, J. E. *et al. Sci. Transl. Med.* **10**, eaan6361 (2018).

12. 12.

Geier, B. *et al. Nature Microbiol.* **5**, 498–510 (2020).

13. 13.

Zhang, J. *et al. Sci. Transl. Med.* **9**, eaan3968 (2017).

14. 14.

Zhang, J. *et al.* Preprint at medRxiv https://doi.org/10.1101/2020.12.14.20248101 (2020).

15. 15.

Jeong, S.-Y., Kim, J.-S. & Lee, J.-H. *Adv. Mater.* **32**, 2002075 (2020).

Jobs from Nature Careers

-
  -
    - All jobs
  -
    - **Postdoctoral Fellow - Zoubeidi Lab, Vancouver Prostate Centre**

      The University of British Columbia (UBC)

      Vancouver, Canada

      JOB POST

    - **Laser Scientist**

      German Electron Synchrotron (DESY)

      Hamburg, Germany

      JOB POST

    - **Fachinformatiker/in Systemintegration (w/m/d)**

      Karlsruhe Institute of Technology (KIT)

      Karlsruhe, Germany

      JOB POST

    - **Intership/Bachelor or Master Thesis: "Digitization of land-based shrimp farming in Germany using AI-based evaluation of imaging and acoustic systems"**

      Alfred Wegener Institute - Helmholtz Centre for Polar and Marine Research (AWI)

Bremerhaven, Germany

JOB POST

This article was downloaded by **calibre** from https://www.nature.com/articles/d41586-021-00191-z

WHERE I WORK
25 January 2021

The bird librarian

Leah Tsang helps to bring bird poisoners to justice as part of her role at Australia's oldest museum.

James Mitchell Crow

James Mitchell Crow is a freelance writer in Melbourne, Australia.

Search for this author in:

- Pub Med
- Nature.com
- Google Scholar

Leah Tsang photographed in a warehouse at a desk covered in bird skull samples using callipers to measure a bird skull

Leah Tsang is collection manager of ornithology at the Australian Museum in Sydney. Credit: Doug Gimesy/Nature Picture Library

On the table in this photograph are the remains of more than 130 wedge-tailed eagles (*Aquila audax*) — Australia's largest bird of prey. The birds had been poisoned, and I needed to confirm the species for a criminal case.

As collection manager of ornithology at the Australian Museum in Sydney, I not only identify birds, but also give input on exhibits and educational programmes and provide other scientific services. The museum's bird collection is the oldest and largest in Australia, containing about 100,000 specimens of species from all over both the country and the world. The

oldest registered specimen is a northern pintail duck (*Anas acuta*), collected in 1828.

I liken the collection to a bird library. Researchers can come in to study a species or range of species. We've got stuffed specimens; skeletons; animals mounted in lifelike poses; intact birds in ethanol; eggs and nests; and a range of frozen tissues. Every item notes the time and location of collection, as well as the name of the species. Each is a snapshot in time and holds information that can't be replicated.

My passion for birds began when I was young. I liked watching them to work out what they were doing. Why would different birds walk differently, eat different things, be different colours? For me, the collection is brilliant. I can hold the birds in my hand and look at them closely to scrutinize and appreciate their differences.

Specimens usually come in from the public or from staff at the National Parks and Wildlife Service. But in the eagle poisoning case, I had to fly down to a chilly government-department shed in Knoxfield to carry out my analyses.

The whole situation was very sad. The perpetrator was prosecuted for poisoning hundreds of birds on a property in Victoria between 2016 and 2018. He was fined and jailed. It was a great outcome to have him caught and penalized.

Nature **589**, 634 (2021)

doi: https://doi.org/10.1038/d41586-021-00179-9

Jobs from Nature Careers

-
  -
    - All jobs
  -
    -

Postdoctoral Fellow - Zoubeidi Lab, Vancouver Prostate Centre

The University of British Columbia (UBC)

Vancouver, Canada

JOB POST

- **Laser Scientist**

  German Electron Synchrotron (DESY)

  Hamburg, Germany

  JOB POST

- **Fachinformatiker/in Systemintegration (w/m/d)**

  Karlsruhe Institute of Technology (KIT)

  Karlsruhe, Germany

  JOB POST

- **Intership/Bachelor or Master Thesis: "Digitization of land-based shrimp farming in Germany using AI-based evaluation of imaging and acoustic systems"**

  Alfred Wegener Institute - Helmholtz Centre for Polar and Marine Research (AWI)

  Bremerhaven, Germany

  JOB POST

This article was downloaded by **calibre** from https://www.nature.com/articles/d41586-021-00179-9

Research

- **A two-pronged attack on antibiotic-resistant microbes** [11 January 2021]
  News & Views • Isoprenoid molecules are essential in many disease-causing microorganisms, and intermediates made during their synthesis trigger immune-defence responses by γδ T cells. ‘Immunoantibiotics’ exploit this dual vulnerability.
- **Helium nucleus measured with record precision** [27 January 2021]
  News & Views • The size of the helium nucleus has been determined using exotic helium atoms in which one electron has been replaced with its heavier cousin, a muon. The result sheds light on a decade-old puzzle regarding the proton radius.
- **Pain-sensing neurons mobilize blood stem cells from bone marrow** [23 December 2020]
  News & Views • Pain-sensing nerve cells can mobilize blood stem cells in mice, with a component of chilli peppers being one stimulus. The finding holds the promise of improving procedures for stem-cell transplantation.
- **Palaeoclimate puzzle explained by seasonal variation** [27 January 2021]
  News & Views • Scientists have long been baffled by the mismatch of climate simulations of the past 12,000 years with temperature reconstructions from geological records. It now emerges that seasonal biases in the records explain the disparity.
- **Base editor repairs mutation found in the premature-ageing syndrome progeria** [06 January 2021]
  News & Views • No cure exists for the lethal premature-ageing condition Hutchinson–Gilford progeria. A gene-editing tool — adenine base editors — offers a way to treat the condition in mice. Could this approach lead to an effective therapy?
- **Accurate machine learning in materials science facilitated by using diverse data sources** [14 January 2021]
  News & Views • A strategy for machine learning has been developed that exploits the fact that data are often collected in different ways with varying levels of accuracy. The approach was used to build a model that predicts a key property of materials.
- **Measuring the α-particle charge radius with muonic helium-4 ions** [27 January 2021]

Article • The 2S–2P transitions in muonic helium-4 ions are measured using laser spectroscopy and used to obtain an α-particle charge-radius value five times more precise than that from electron scattering.

- **Metastability of diamond ramp-compressed to 2 terapascals** [27 January 2021]
  Article • X-ray diffraction measurements of solid carbon compressed to pressures of about two terapascals (approximately twenty million atmospheres) find that carbon retains a diamond structure even under these extreme conditions.

- **Correlation-driven topological phases in magic-angle twisted bilayer graphene** [18 January 2021]
  Article • Correlation-driven topological phases with different Chern numbers are observed in magic-angle twisted bilayer graphene in modest magnetic fields, indicating that strong electronic interactions can lead to topologically non-trivial phases.

- **Metallaphotoredox aryl and alkyl radiomethylation for PET ligand discovery** [25 November 2020]
  Article • A versatile and rapid metallaphotoredox catalytic method of making 3H- and 11C-labelled tracer compounds for use in positron emission tomography (PET) is reported.

- **Seasonal origin of the thermal maxima at the Holocene and the last interglacial** [27 January 2021]
  Article • Reanalysis of Holocene sea surface temperature records affirms the role of retreating ice and rising greenhouse gases in driving a steady increase in global temperatures over the past 12,000 years.

- **Global and regional drivers of land-use emissions in 1961–2017** [27 January 2021]
  Article • Trends in the rate of region- and sector-specific land-use greenhouse gas emissions in 1961–2017 show an acceleration of about 20% per decade after 2001.

- **A thin mantle transition zone beneath the equatorial Mid-Atlantic Ridge** [27 January 2021]
  Article • Data from ocean bottom seismometers show that the mantle transition zone beneath the equatorial Mid-Atlantic Ridge is thin and warm, which suggests more material transfer than previously thought.

- **Half a century of global decline in oceanic sharks and rays** [27 January 2021]
  Article • The global abundance of oceanic sharks and rays has decreased by 71% since 1970 and 24 species are threatened with extinction owing to a concomitant increase in fishing pressure.

- **Monitoring hiring discrimination through online recruitment platforms** [20 January 2021]
  Article • An analysis of the search behaviour of recruiters on a Swiss online recruitment platform shows that jobseekers from minority ethnic groups are less likely to be contacted by recruiters, and also provides evidence of gender-based discrimination.
- **Neural circuit mechanisms of sexual receptivity in Drosophila females** [25 November 2020]
  Article • In Drosophila melanogaster, female mating decisions are governed by female-specific descending neurons that integrate input from auditory neurons that respond to features of the song of a conspecific male and central neurons that encode the mating status of the female.
- **Availability of food determines the need for sleep in memory consolidation** [02 December 2020]
  Article • Hunger status in a fly is shown to drive either sleep-dependent or sleep-independent memory formation through different mushroom body circuits.
- **An SHR–SCR module specifies legume cortical cell fate to enable nodulation** [09 December 2020]
  Article • Repurposing of an SHR–SCR stem cell program in the legume root cortex enables rhizobial symbiosis.
- **Nociceptive nerves regulate haematopoietic stem cell mobilization** [23 December 2020]
  Article • Stimulation of pain-sensing neurons, which can be achieved in mice by the ingestion of capsaicin, promotes the migration of haematopoietic stem cells from the bone marrow into the blood.
- **IspH inhibitors kill Gram-negative bacteria and mobilize immune clearance** [23 December 2020]
  Article • A class of compounds with a dual mechanism of action—direct targeting of IspH and stimulation of cytotoxic γδ T cells to enhance pathogen clearance—are active against multidrug-resistant bacteria.
- **COVID-19 treatments and pathogenesis including anosmia in K18-hACE2 mice** [09 November 2020]
  Article • Transgenic K18-hACE2 mice are a useful model of COVID-19 including anosmia; infection of these mice resulted in severe pneumonia and, in some cases, infection in the brain, which was prevented by convalescent plasma.
- **In vivo base editing rescues Hutchinson–Gilford progeria syndrome in mice** [06 January 2021]
  Article • In a mouse model of progeria, an adenine base editor delivered with adeno-associated virus corrects the pathogenic mutation in LMNA, rescues vascular pathology and markedly

extends the lifespan of the mice.

- **Capping pores of alphavirus nsP1 gate membranous viral replication factories** [16 December 2020]
  Article • Cryo-electron microscopy structures of non-structural protein 1 (nsP1) of chikungunya virus reveal the mechanisms that underpin the association of viral replication machinery with virus-induced membranous organelles within host cells.

- **Structures of the glucocorticoid-bound adhesion receptor GPR97–Go complex** [06 January 2021]
  Article • The authors report on the structure of a glucocorticoid-bound adhesion G-protein-coupled receptor–G protein complex.

NEWS AND VIEWS
11 January 2021

A two-pronged attack on antibiotic-resistant microbes

Isoprenoid molecules are essential in many disease-causing microorganisms, and intermediates made during their synthesis trigger immune-defence responses by γδ T cells. ‘Immunoantibiotics’ exploit this dual vulnerability.

Youcef Mehellou &

Youcef Mehellou is in the School of Pharmacy and Pharmaceutical Sciences, Cardiff University, Cardiff CF10 3NB, UK.
Contact

Search for this author in:

- Pub Med
- Nature.com
- Google Scholar

Benjamin E. Willcox

Benjamin E. Willcox is at the Institute of Immunology and Immunotherapy, University of Birmingham, Edgbaston, Birmingham B15 2TT, UK.
Contact

Search for this author in:

- Pub Med
- Nature.com
- Google Scholar

The emergence of strains of harmful microorganisms that are resistant to antibiotic treatment is a major global health concern. This has prompted ongoing drug-development efforts, including the identification of possible biological targets linked to essential microbial processes. However, the clinical development of drugs is slow, and the emergence of resistance to newly developed compounds remains a continuing problem. Finding alternative ways to tackle the emergence of antibiotic-resistant bacteria is of paramount importance. Writing in *Nature*, Singh *et al.*[1] outline a two-pronged strategy to address this challenge.

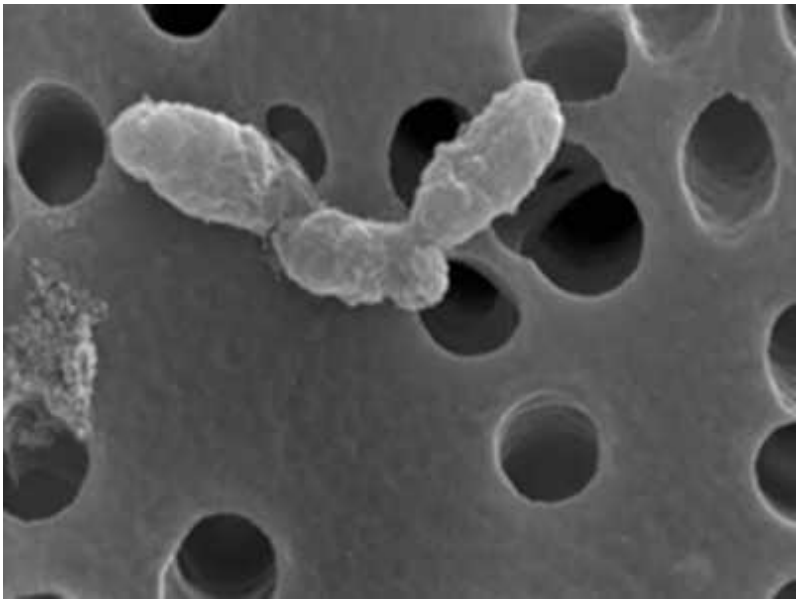

Read the paper: IspH inhibitors kill Gram-negative bacteria and mobilize immune clearance

The authors' approach involved the development of a new class of molecule called immunoantibiotics. These target a key pathway that generates a molecule needed by microbes and, in doing so, stimulate a particular population of immune cells. The cells, from the grouping called γδ T cells, then provide a general (innate-like), potent antimicrobial immune response.

Singh and colleagues focused on inhibition of an enzyme termed IspH (Fig. 1). This catalyses a step in a pathway that makes molecules called isoprenoids. Isoprenoids are key building blocks needed for the synthesis of a diverse range of molecules in prokaryotes (organisms lacking a nucleus, such as bacteria) and eukaryotes (organisms that have a cellular nucleus). However, IspH catalyses a reaction in an arm of the isoprenoid-synthesis pathway, called the methylerythritol 4-phosphate (MEP) pathway, that is found in bacteria and certain protozoa (single-celled eukaryotes), but is absent in animals[2]. Several enzymes in this pathway, which underpins processes such as the synthesis of the bacterial cell wall and energy production, have already attracted interest as potential antimicrobial drug targets[3–7]. These targets include IspH itself[3,6], which is present in a diverse range of disease-causing microorganisms, including Gram-negative bacteria, mycobacteria (a grouping that includes the microbe that causes tuberculosis) and certain protozoa, such as *Plasmodium falciparum* (the microorganism that causes malaria).

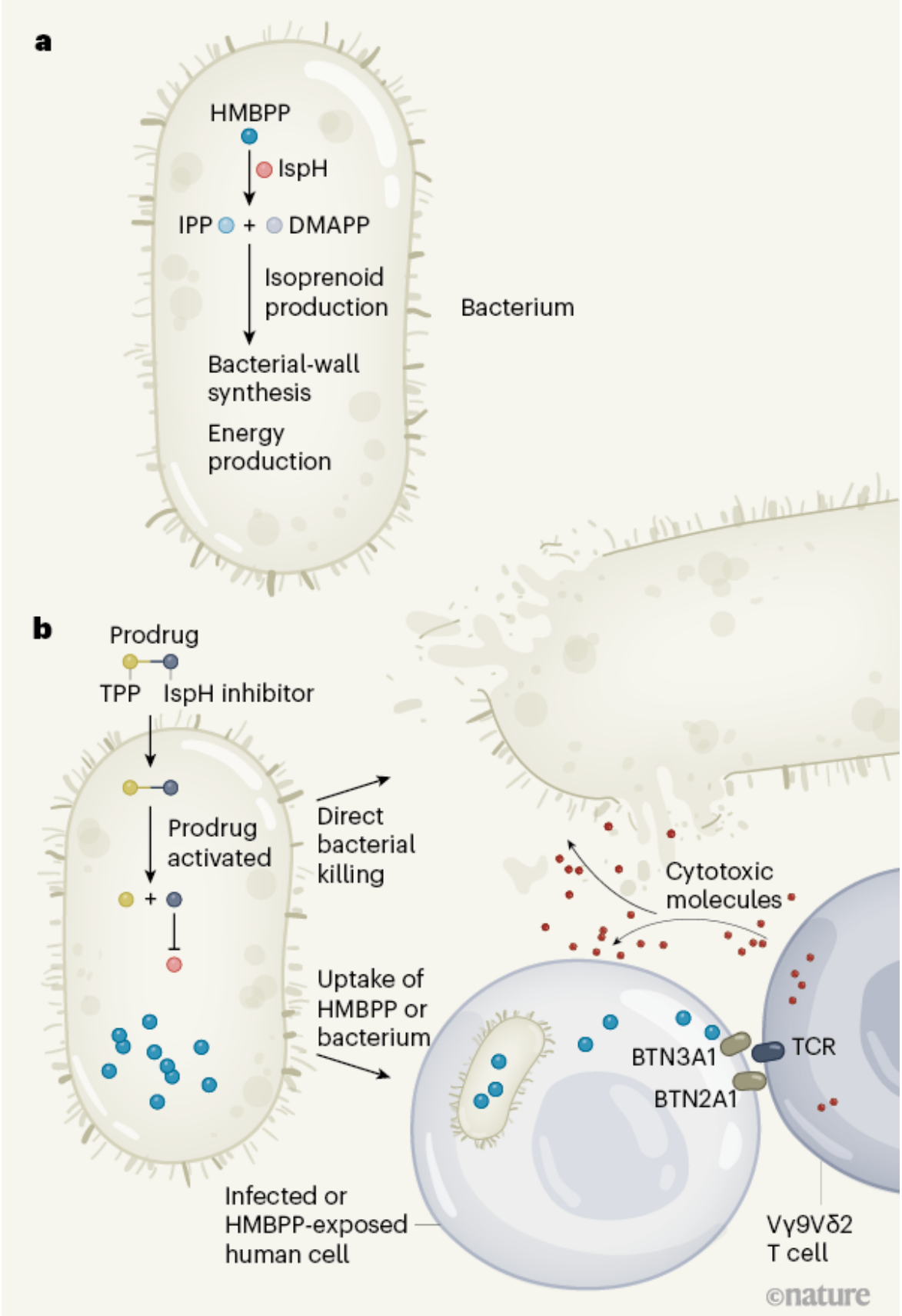
a
HMBPP
IspH
IPP + DMAPP
Isoprenoid production
Bacterium
Bacterial-wall synthesis
Energy production
b
Prodrug
TPP
IspH inhibitor
Prodrug activated
Direct bacterial killing
Cytotoxic molecules
Uptake of HMBPP or bacterium
BTN3A1
TCR
BTN2A1
Infected or HMBPP-exposed human cell
Vγ9Vδ2 T cell
©nature

Figure 1 | Development of an immunoantibiotic. **a**, A microbe-specific pathway uses the enzyme IspH to break down the molecule (*E*)-4-hydroxy-3-methyl-but-2-enyl pyrophosphate (HMBPP) into isopentenyl diphosphate (IPP) and dimethylallyl diphosphate (DMAPP). After other steps in the downstream pathway (not shown), isoprenoid molecules are synthesized; these have essential cellular roles. **b**, Singh *et al*.[1] used a screening method to identify IspH inhibitors. To boost entry into cells, the authors generated a prodrug version of the inhibitor, in the form of a triphenylphosphonium (TPP) ester derivative. Inside the bacterium, the inhibitor is separated from the TPP group and targets IspH. IspH inhibition blocks isoprenoid production, eventually killing the bacterium. It also increases HMBPP levels. HMBPP that is taken up by human cells, or that is present in human cells infected with bacteria, is sensed by an immune cell called a Vγ9Vδ2 T cell. This sensing process requires BTN3A1 and BTN2A1 receptors on the target cell and the immune cell's T-cell receptor (TCR). On sensing HMBPP, these T cells become activated and release molecules that can kill infected human cells or bacteria.

Choosing IspH as a therapeutic target provides a benefit that extends beyond its role in generating the compounds needed for isoprenoid synthesis. This is because the microbial molecule that it breaks down, (*E*)-4-hydroxy-3-methyl-but-2-enyl pyrophosphate (HMBPP), is one that the immune system of primates has evolved the ability to detect[8]. Humans detect HMBPP in the body by using immune cells known as Vγ9Vδ2 T cells, which represent approximately 1–10% of T cells in the blood. After Vγ9Vδ2 T cells recognize[9] cells exposed to HMBPP, through a process that relies on the receptors BTN3A1 and BTN2A1 in exposed cells (Fig. 1), they become activated, proliferate and mediate potent defence responses, including the production of molecules capable of killing cells and the release of signalling molecules called cytokines.

Activated Vγ9Vδ2 T cells can also either directly kill human cells exposed to HMBPP (exposed by, for example, intracellular microbial infection) or kill bacterial cells themselves. Singh and colleagues' strategy of focusing on IspH, therefore, combines rational targeting to inhibit the isoprenoid pathway, and thereby block a source of crucial microbial molecules, with the stimulation of an immune response due to the resulting accumulation of

HMBPP, which is a highly potent signal that drives the activation of Vγ9Vδ2 T cells.

The authors took a structure-directed, *in silico* screening approach to identify possible IspH inhibitors, and tested around ten million compounds. Strikingly, 2 of the 24 most promising compounds inhibited IspH with high potency (at nanomolar concentrations) when tested *in vitro*. Further optimization of the molecular structures of these compounds improved their affinity for IspH compared with the affinity of IspH for its natural substrate, HMBPP.

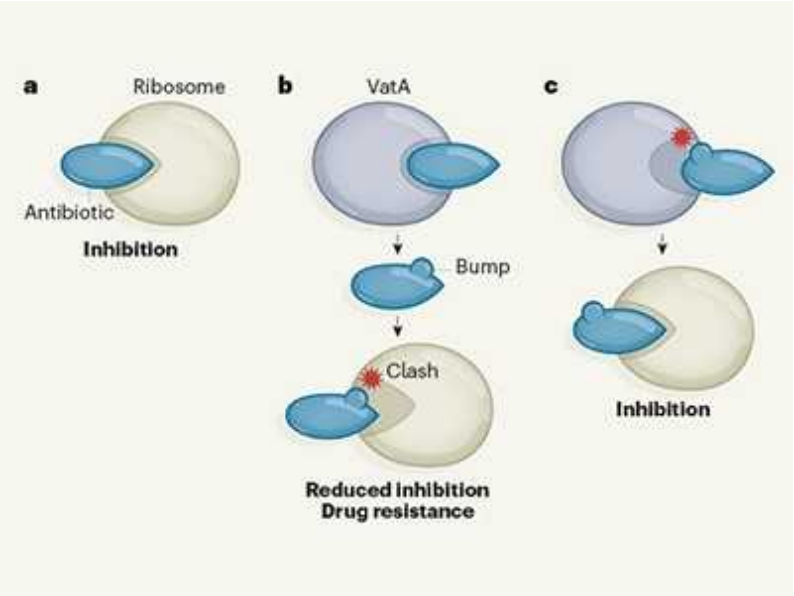

Modular synthesis enables molecular ju-jitsu in the fight against antibiotic resistance

However, the physical characteristics of the inhibitors were expected to limit their entry into bacteria. To circumvent this, Singh *et al.* adopted a strategy previously used to enable drugs to pass through membranes. This method generates what is called a prodrug — an inactive version of the drug (in this case, an ester derivative of the inhibitor) that can be taken up easily by cells

and then metabolized into the active version. Crucially, unlike previous work[3,6] that described IspH inhibitors, this prodrug approach allowed such inhibitors to successfully enter bacteria. The authors confirmed that the drugs inhibited enzyme breakdown of HMBPP, hindering essential microbial processes, and that this resulted in the killing of a range of different bacteria, including *Escherichia coli*, without notable signs of drug toxicity to mammalian cells.

In keeping with the ability to inhibit HMBPP breakdown by IspH, prodrug use also led to the *in vitro* activation and proliferation of HMBPP-responsive Vγ9Vδ2 T cells during bacterial infection of samples of human peripheral blood mononuclear cells. This result indicates the potential of such prodrugs to act as dual-action immunoantibiotics. When tested *in vivo* in mice, the prodrugs induced direct antimicrobial effects and controlled bacterial infection through a process mediated by γδ T cells.

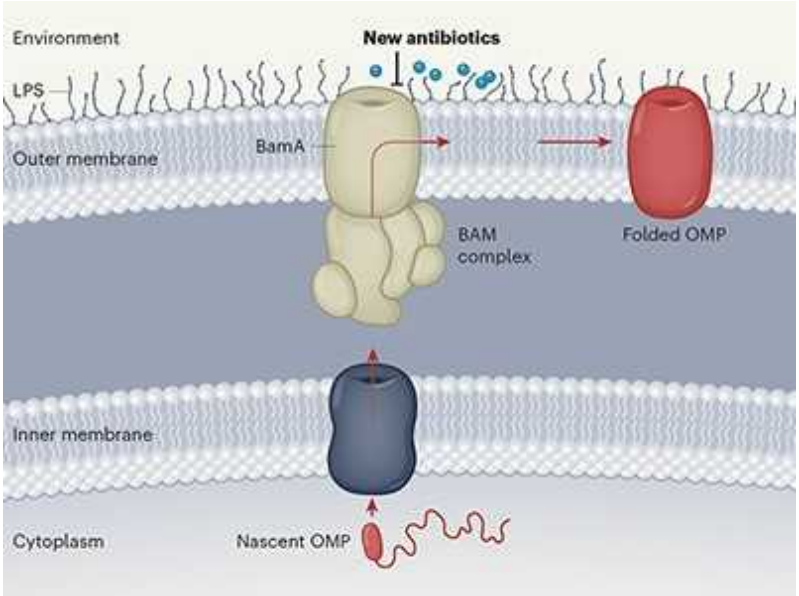

New antibiotics target the outer membrane of bacteria

Singh *et al*. explored two key aspects of the potential of these new compounds to combat antimicrobial resistance. First, the researchers present

in vitro and *in vivo* data indicating direct bactericidal effects on a variety of clinically isolated harmful bacteria that are resistant to current antibiotics, including multidrug-resistant microbes. The authors observed that the IspH inhibitors had greater ability to kill multidrug-resistant microbes than do the current best-in-class antibiotics. Second, using an *in vitro* model system, Singh and colleagues showed that bacteria did not acquire resistance to the IspH inhibitors in the presence of γδ T cells. But in the absence of these T cells, drug resistance occurred over a similar timescale to that observed for conventional antibiotics. These results emphasize the potential advantage that immunoantibiotics might have for tackling the emergence of drug resistance.

Singh and colleagues' study is a highly promising proof-of-concept that a new class of antimicrobial can be developed with a dual mechanism of action. Leveraging Vγ9Vδ2 T cells is appealing because of the therapeutic advantages offered by harnessing this approach. These cells, present in humans from early in life, are capable of highly potent defence functions[10], and, unlike many other types of T cell, don't depend on the recognition of major histocompatibility complex (MHC) molecules, which differ between individuals. Encouragingly, the pathway containing IspH is shared by a diverse range of clinically relevant disease-causing microorganisms, suggesting that such antimicrobial drugs could have broad applicability.

Antibiotic approaches using monotherapy (a single type of drug) have often resulted in the emergence of drug resistance, whereas combination therapies using multiple drugs, operating through different mechanisms of action, have been more fruitful and have met with relatively fewer resistance problems. This 'two-in-one' mechanism underpinning Singh and colleagues' strategy might, therefore, allow the targeting of existing multidrug-resistant microbes, as well as decrease the chances of resistance emerging. Although the subsequent steps on the road to drug development can often be challenging, the progress of this exciting class of compound towards clinical application will undoubtedly be followed with interest.

Nature **589**, 517-518 (2021)

doi: https://doi.org/10.1038/d41586-020-03660-z

References

1. 1.

   Singh, K. S. *et al. Nature* **589**, 597–602 (2021).

2. 2.

   Zhao, L., Chang, W.-C., Xiao, Y., Liu, H. W. & Liu, P. *Annu. Rev. Biochem.* **82**, 497–530 (2013).

3. 3.

   Janthawornpong, K. *et al. J. Am. Chem. Soc.* **135**, 1816–1822 (2013).

4. 4.

   Jomaa, H. *et al. Science* **285**, 1573–1576 (1999).

5. 5.

   McAteer, S., Coulson, A., McLennan, N. & Masters, M. *J. Bacteriol.* **183**, 7403–7407 (2001).

6. 6.

   Wang, K. *et al. J. Am. Chem. Soc.* **132**, 6719–6727 (2010).

7. 7.

   Zinglé, C., Kuntz, L., Tritsch, D., Grosdemange-Billiard, C. & Rohmer, M. *J. Org. Chem.* **75**, 3203–3207 (2010).

8. 8.

   Morita, C. T., Jin, C., Sarikonda, G. & Wang, H. *Immunol. Rev.* **215**, 59–76 (2007).

9. 9.

Willcox, C. R., Mohammed, F. & Willcox, B. E. *Immunol. Rev.* **298**, 25–46 (2020).

10. 10.

Silva-Santos, B., Mensurado, S. & Coffelt, S. B. *Nature Rev. Cancer* **19**, 392–404 (2019).

Jobs from Nature Careers

-
  -
    - All jobs
  -
    - **Postdoctoral Fellow - Zoubeidi Lab, Vancouver Prostate Centre**

      The University of British Columbia (UBC)

      Vancouver, Canada

      JOB POST

    - **Laser Scientist**

      German Electron Synchrotron (DESY)

      Hamburg, Germany

      JOB POST

    - **Fachinformatiker/in Systemintegration (w/m/d)**

      Karlsruhe Institute of Technology (KIT)

      Karlsruhe, Germany

JOB POST

- **Intership/Bachelor or Master Thesis: "Digitization of land-based shrimp farming in Germany using AI-based evaluation of imaging and acoustic systems"**

  Alfred Wegener Institute - Helmholtz Centre for Polar and Marine Research (AWI)

  Bremerhaven, Germany

  JOB POST

This article was downloaded by **calibre** from https://www.nature.com/articles/d41586-020-03660-z

NEWS AND VIEWS
27 January 2021

Helium nucleus measured with record precision

The size of the helium nucleus has been determined using exotic helium atoms in which one electron has been replaced with its heavier cousin, a muon. The result sheds light on a decade-old puzzle regarding the proton radius.

Wilfried Nörtershäuser

Wilfried Nörtershäuser is at the Institute for Nuclear Physics, Technical University of Darmstadt, 64289 Darmstadt, Germany.
Contact

Search for this author in:

- Pub Med
- Nature.com
- Google Scholar

Helium is the second most abundant element in the Universe, after hydrogen. The nucleus of its most common isotope, helium-4, consists of two protons and two neutrons and is called the α-particle. This particle is more compact than other light nuclei — for instance, it is about 20% smaller than the nucleus of the hydrogen isotope deuterium[1], which contains only one proton and one neutron. The exact size of the α-particle is of particular interest because of a decade-old experiment that suggested the radius of the proton is considerably smaller than had been thought[2]. This result led to much speculation about possible missing pieces in the standard model of particle physics[3]. Writing in *Nature*, Krauth *et al.*[4] report a determination of

the α-particle size that strongly restricts such explanations and provides a benchmark for nuclear-structure theory.

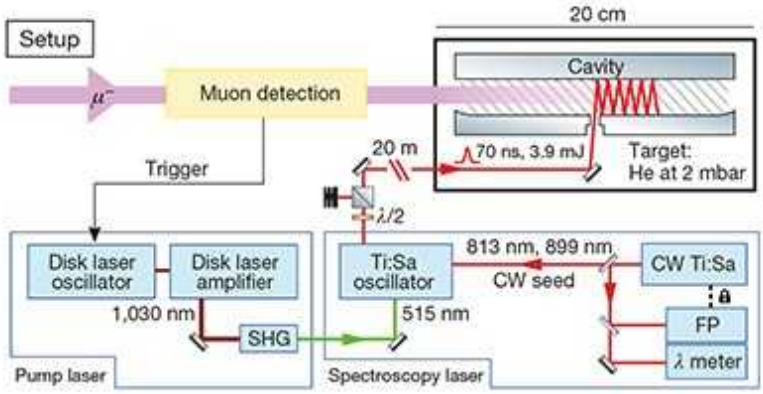

[Read the paper: Measuring the α-particle charge radius with muonic helium-4 ions]

The authors measured the α-particle size using a technique known as laser spectroscopy. This approach is based on the fact that atoms can emit and absorb light only at discrete frequencies, which are determined by the details of the atomic structure — namely, the interaction of the negatively charged electrons with the positively charged nucleus and with each other. Protons make up the charged component of the nucleus. The number of protons dictates the element, and their spatial extent is characterized by a property called the nuclear charge radius, which defines the size of the nucleus.

The exact frequencies of absorption and emission depend slightly on the charge radius. Therefore, this property can be determined if the atomic structure is understood well enough for a sufficiently accurate calculation of all other factors that affect the frequencies. Although there has been

substantial progress in this field, such determinations are currently possible only for two-body systems — namely, a single electron or similar particle bound to a nucleus. Adding another particle leads to an enormous increase in complexity, and the quantum-mechanical calculations are currently unmanageable. Consequently, laser spectroscopy has previously been used to directly extract the sizes of only the proton[2] and the deuterium nucleus[5].

Krauth and colleagues used a clever method to apply this approach to the α-particle. They injected negatively charged muons — heavier cousins of electrons — into a low-density helium gas. Collisions between the muons and the gas caused the muons to lose energy, and allowed a given muon to replace one of the two electrons in a helium atom (Fig. 1). This muon then lost more energy and moved closer to the atomic nucleus. During this process, the second electron was ejected from the atom, generating a positively charged ion composed of an α-particle and a muon.

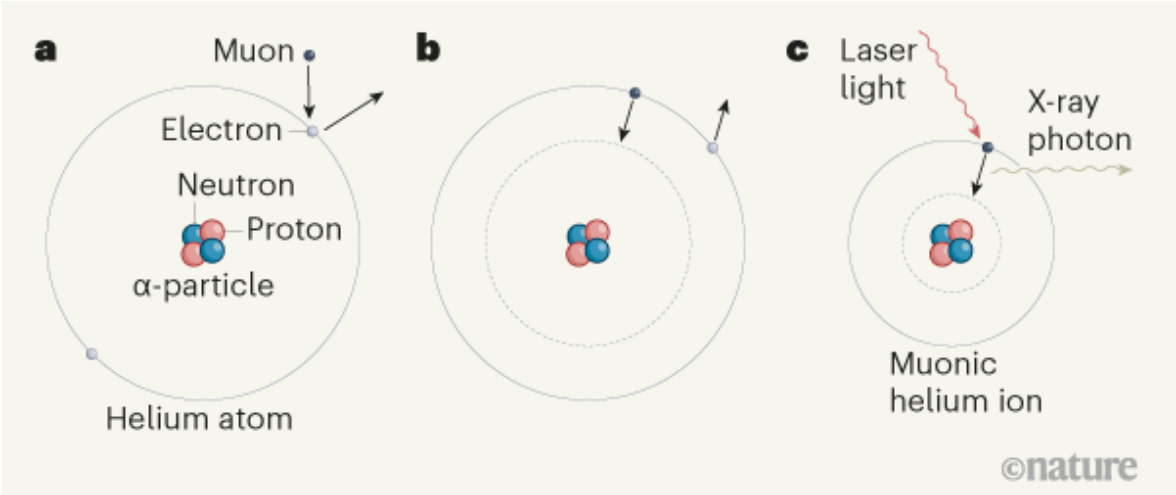

Figure 1 | Measuring the size of the helium nucleus. a, The nucleus of the helium atom, also known as the α-particle, comprises two protons and two neutrons, surrounded by two electrons. Krauth *et al.*[4] carried out an experiment in which a muon (a heavier cousin of the electron) ejected and replaced one electron in a helium atom. **b**, This muon gradually moved closer to the nucleus, and ejected the second electron from the atom. **c**, The result of this process was a muonic helium ion — a positively charged ion composed of an α-particle and a muon. The authors fired laser light at this ion shortly after its formation. In some cases, the muon then moved even closer to the nucleus and produced a single X-ray photon. By analysing this

X-ray emission, the authors determined the size of the helium nucleus with unprecedented precision.

The atomic structure of this muonic helium ion can be determined theoretically with extremely high precision. Moreover, because the muon has approximately 200 times the mass of an electron (go.nature.com/3twyjba), it is bound roughly 200 times closer to the helium nucleus than an electron would be. As a result, laser spectroscopy is about eight million times more sensitive to the α-particle size when a muonic helium ion, rather than an ordinary, singly charged helium ion, is used. This remarkable sensitivity justifies the huge experimental effort that was required for the current work.

A muon exists for only two microseconds before it decays into an electron and elusive particles called neutrinos (go.nature.com/3twyjba). Therefore, Krauth *et al.* had to detect each individual muon that entered their experimental chamber and could potentially lead to the formation of a muonic helium ion. They then needed to fire a laser that had a well-defined frequency within one microsecond of this muonic-helium-ion formation (Fig. 1). Finally, they had to detect a single X-ray photon that was emitted from the ion after successful laser excitation, as well as the electron generated by the decay of the muon. At the correct laser frequency, about 8 of these events were detected per hour, and needed to be distinguished from roughly 50,000 events associated with other atomic processes.

The result of this heroic effort is a determination of the α-particle radius with a precision of just one attometre (10^{-18} m), which is roughly 1,000th the size of the proton radius. The value is about five times more precise than measurements based on electron–helium scattering[6]. Although this finding might sound rather academic, it is important for several areas of fundamental physics. In particular, for the first time, the results from laser spectroscopy of muonic atoms and electron scattering are in excellent agreement, which was not the case for the proton or the deuterium nucleus.

For the proton radius, the value obtained[2] from muonic hydrogen was about 4% smaller than the previously accepted value obtained from other approaches, including electron scattering and laser spectroscopy of ordinary hydrogen. This proton-radius puzzle led to many theories about processes

involved in the interaction between muons and other particles that are not contained in the standard model[3]. However, the agreement in the case of helium rules out several of these speculative processes because there is no reason why they should not occur in muonic helium, as well as in muonic hydrogen and muonic deuterium.

Krauth and colleagues' measurement can also be used to improve *ab initio* nuclear-structure models. Whereas atomic structure is determined by the well-understood electromagnetic interaction, nuclear structure is governed by the strong nuclear force, which is much more complex. The protons and uncharged neutrons in the nucleus, known collectively as nucleons, have a complicated internal structure. Each nucleon is made up of three fundamental particles, called quarks, that are tied together by the strong force. The nucleus itself is bound by the residual strong force that persists beyond the borders of the nucleons and acts only within distances of less than one femtometre (10^{-15} m).

Physicists do not yet have a theory that can explain nuclear structure on the basis of a description at the quark level. Instead, they rely on *ab initio* nuclear-structure models that consider 'effective' forces between individual nucleons. The formulation of these models requires knowledge of some key parameters that describe light nuclear systems. The charge radius of the α-particle that has now been obtained can serve as such a parameter.

The authors' result also provides a benchmark for planned experiments that will enable precise measurements of nuclear charge radii of elements heavier than helium. This goal will be achievable once required quantum-mechanical calculations for two-electron (helium-like) systems are available. Theoretical[7] and experimental[8] efforts in this direction are under way. The measured charge radius of helium will serve as an ideal test case for such calculations. If agreement is obtained, it should then be possible to determine the charge radii of at least all the stable isotopes from lithium to nitrogen by carrying out laser spectroscopy on their respective helium-like ions. Such ions can be produced in small laboratory experiments with much less effort than is required for studies of the corresponding muonic systems at large particle-accelerator facilities.

Nature **589**, 518-519 (2021)

doi: https://doi.org/10.1038/d41586-021-00120-0

References

1. 1.

   Sick, I. J. *Phys. Chem. Ref. Data* **44**, 031213 (2015).

2. 2.

   Pohl, R. *et al. Nature* **466**, 213–216 (2010).

3. 3.

   Pohl, R., Gilman, R., Miller, G. A. & Pachucki, K. *Annu. Rev. Nucl. Part. Sci.* **63**, 175–204 (2013).

4. 4.

   Krauth, J. J. *et al. Nature* **589**, 527–531 (2021).

5. 5.

   Pohl, R. *et al. Science* **353**, 669–673 (2016).

6. 6.

   Sick, I. *Phys. Rev. C* **77**, 041302 (2008).

7. 7.

   Yerokhin, V. A., Patkóš, V. & Pachucki, K. *Phys. Rev. A* **98**, 032503 (2018).

8. 8.

   König, K. *et al. Rev. Sci. Instrum.* **91**, 081301 (2020).

Jobs from Nature Careers

- All jobs

- **Postdoctoral Fellow - Zoubeidi Lab, Vancouver Prostate Centre**

  The University of British Columbia (UBC)

  Vancouver, Canada

  JOB POST

- **Laser Scientist**

  German Electron Synchrotron (DESY)

  Hamburg, Germany

  JOB POST

- **Fachinformatiker/in Systemintegration (w/m/d)**

  Karlsruhe Institute of Technology (KIT)

  Karlsruhe, Germany

  JOB POST

- **Intership/Bachelor or Master Thesis: "Digitization of land-based shrimp farming in Germany using AI-based evaluation of imaging and acoustic systems"**

  Alfred Wegener Institute - Helmholtz Centre for Polar and Marine Research (AWI)

Bremerhaven, Germany

JOB POST

This article was downloaded by **calibre** from https://www.nature.com/articles/d41586-021-00120-0

NEWS AND VIEWS
23 December 2020

Pain-sensing neurons mobilize blood stem cells from bone marrow

Pain-sensing nerve cells can mobilize blood stem cells in mice, with a component of chilli peppers being one stimulus. The finding holds the promise of improving procedures for stem-cell transplantation.

Anastasia N. Tikhonova &

Anastasia N. Tikhonova is at the Princess Margaret Cancer Centre, University Health Network, Toronto, Ontario M5G 1L7, Canada.
Contact

Search for this author in:

- Pub Med
- Nature.com
- Google Scholar

Iannis Aifantis

Iannis Aifantis is in the Department of Pathology and Perlmutter Cancer Center, NYU Grossman School of Medicine, New York 10016, USA.
Contact

Search for this author in:

- Pub Med
- Nature.com
- Google Scholar

The cardinal feature of blood stem cells is their ability to regenerate the body's entire blood and immune systems. The process is known as haematopoiesis, and the cells are better known as haematopoietic stem cells (HSCs). In developing embryos, HSCs shuffle around distinct anatomical sites, with blood circulation enabling their trafficking. After birth, these cells reside in specialized niches in the bone marrow that support their quiescence and self-renewal[1]. Throughout life, HSCs are released from the bone marrow to replenish blood cells in a circadian pattern that is under the control of involuntary nerves[2]. Pain-sensing nerves also make connections with the bone marrow, but can these neurons mobilize HSCs, too? Writing in *Nature*, Gao *et al*.[3] address this question and identify a surprising role for chilli peppers.

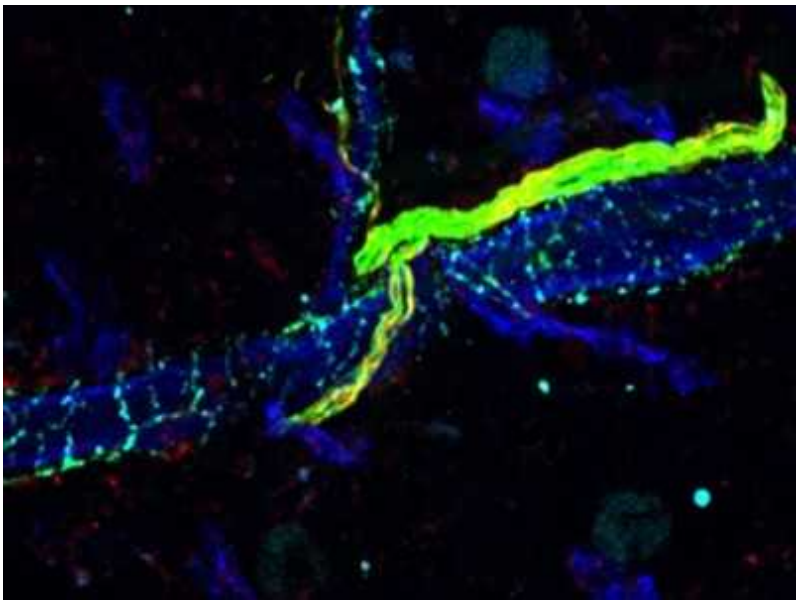

Read the paper: Nociceptive nerves regulate haematopoietic stem cell mobilization

This work is of potential clinical as well as biological importance. For people who have blood cancers such as aggressive leukaemia, lymphomas and multiple myeloma, an essential part of treatment, following high-dose

chemotherapy, is autologous stem-cell transplantation (ASCT)[4] — replacing damaged HSCs with healthy ones. To avoid the possibility of complications, ASCT uses an individual's own stem cells, which are collected from the blood before chemotherapy, then re-infused intravenously afterwards to regenerate damaged bone marrow.

This procedure requires a way to prompt healthy HSCs to leave their bone-marrow niche and enter the bloodstream to be collected. Since the 1990s, a secreted factor known as granulocyte-colony-stimulating factor (G-CSF) has been the most commonly used molecular prompt. The introduction of another prompt came in 2003 in the form of plerixafor, a small molecule that stops HSCs from remaining glued to the bone-marrow scaffold[4]. Since then, advances have included different routes of administration and combining G-CSF with plerixafor. But in a fraction of people, HSCs still do not mobilize sufficiently, with clinical risk factors including age, genetics and the type of cancer (up to 25% of people with lymphoma show poor mobilization), as well as repeated rounds of chemotherapy[5]. So, there is an urgent need to understand the molecular mechanisms of HSC mobilization[4].

Enter Gao and colleagues. The authors began with an immunofluorescent imaging survey of the bone marrow's nerve fibres in mice, revealing most to be 'nociceptive' nerves. These nociceptors are sensory neurons that protect organisms from danger by eliciting pain in response to injury. Nociceptors can be found in any area of the body that senses noxious stimuli[6]. These neurons have been best investigated in barrier tissues such as the skin and gut. The biological role of nociceptors in non-barrier tissues, such as the bone marrow, remains poorly studied with the exception of pain perception.

To examine a possible role of nociceptors in maintaining haematopoiesis, Gao *et al*. used pharmacological and genetic strategies to eliminate these neurons. This had no effect on the maintenance of HSCs in the bone marrow. It did lead to a marked reduction of G-CSF-induced mobilization of HSCs to the bloodstream, which suggests that this class of neuron affects HSC adhesion or migration.

Calcitonin-gene-related peptide (CGRP) is a major neurotransmitter molecule secreted by nociceptor neurons[6]. Gao *et al.* found that

administering CGRP greatly improved HSC mobilization following treatment with G-CSF, plerixafor, or both. They also observed that CGRP affects HSCs directly (rather than acting indirectly through the bone marrow), inducing the formation of a dimeric receptor comprising the CALCRL and RAMP1 proteins on the HSC surface (Fig. 1). Genetically engineering mice to lack either of these in bone-marrow HSCs resulted in defective HSC mobilization.

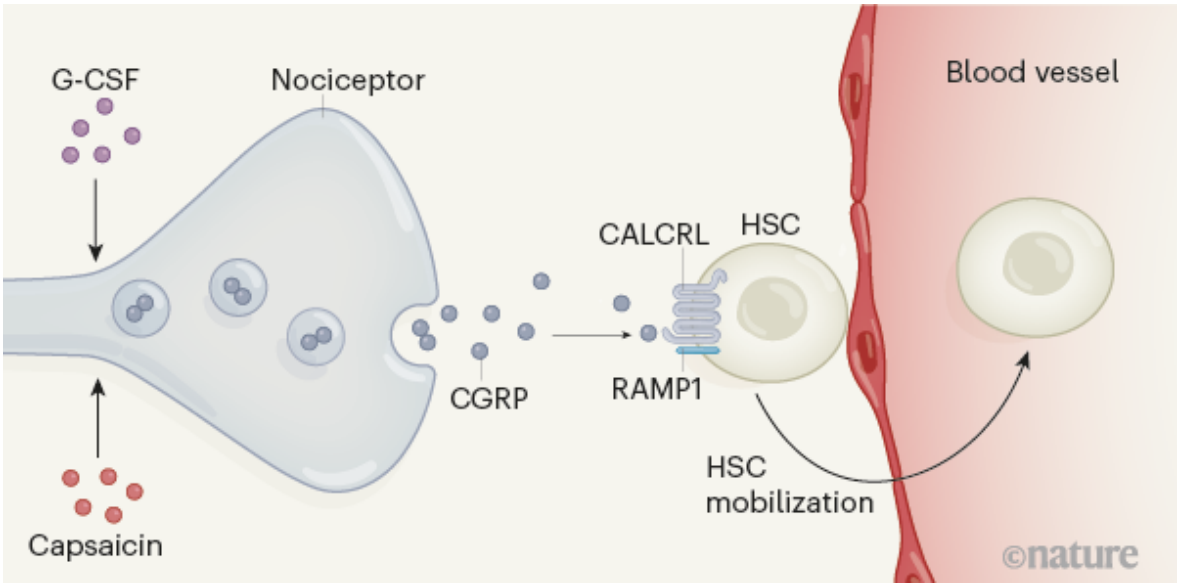

Figure 1 | Pain-sensing nerve cells regulate the mobilization of haematopoietic stem cells. Gao and colleagues[3] report that most nerves in the bone marrow are neurons called nociceptors. They find that stimulation of these nerves by the protein granulocyte-colony-stimulating factor (G-CSF), or by a component of chilli peppers called capsaicin (it is not known whether stimulation was direct or indirect), leads the cells to release the neurotransmitter molecule calcitonin-gene-related peptide (CGRP). In turn, CGRP binds directly to blood stem cells called haematopoietic stem cells (HSCs) through a receptor dimer comprising the CALCRL and RAMP1 proteins. This stimulates the HSCs to move from the bone marrow into blood vessels.

In the clinic, continuous rounds of chemotherapy often lead to a decrease in HSC mobilization — a deficit that Gao *et al.* recapitulated by treating mice with five weekly cycles of the chemotherapy drug cisplatin. Remarkably, administering CGRP restored HSC mobilization in these animals. This is a

potentially crucial finding that could greatly improve protocols for HSC collection in 'poor mobilizer' individuals.

Certain types of spicy food can trigger nociceptor activation, leading Gao *et al.* to wonder whether consuming spicy food might cause HSC mobilization. To test this idea, the authors fed mice a diet rich in capsaicin — an active component of chilli peppers. This spicy fare increased the levels of CGRP in the extracellular fluid of the bone marrow, and increased the CGRP-induced mobilization of HSCs. The effect disappeared when nociceptors were blocked pharmacologically, indicating that these neurons mediated the effect of the capsaicin-rich diet.

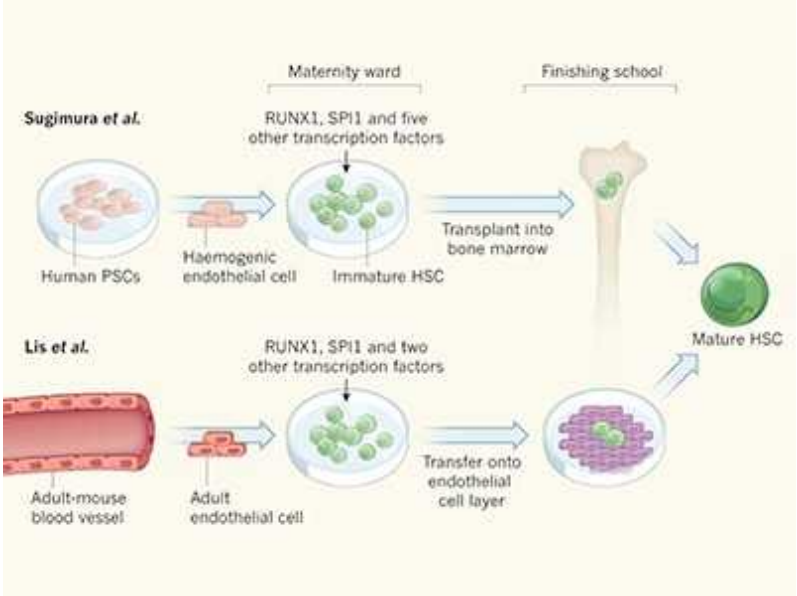

Education for stem cells

This paper adds intriguing pieces to our picture of the connections between the nervous system, bone marrow and blood-cell development. Early studies using photomicrographs of neurons in the bone marrow showed that it is innervated by nerve fibres[7]. During the past decade, surgical, pharmacological and genetic denervation models have established the nervous system's role in regulating the HSC niche[8]. But these studies mainly focused on sympathetic nerve fibres (those involved in involuntary actions of the body), showing that they help to maintain the functional integrity of

the niche[9]. Here, Gao *et al.* have found that the adhesion of HSCs to their bone-marrow niche and their ability to mobilize to the peripheral blood is controlled by nociceptive neurons acting directly on HSCs through secretion of the neurotransmitter CGRP.

Surprisingly, the authors did not detect neuron-induced changes in the cell-surface levels of CXCR4, CD44 and VLA4 — molecules known to be expressed on HSCs and associated with their trafficking. Future studies, then, will need to delineate the precise mechanisms that mediate HSC mobilization following CALCRL–RAMP1 stimulation. It is also not known whether G-CSF affects nociceptors directly or indirectly through other cell types in the marrow. Such questions can be addressed using cell-type-specific gene targeting in animals. Moreover, findings that might be relevant to humans would need to be validated in clinical trials, because human biology is often not perfectly reflected in mice.

Finally, we should also consider stress responses in the bone marrow and their effects on neurons: for example, leukaemia induces nerve damage in the marrow[10], so it will be valuable to study the effects of blood cancers and ageing specifically on bone-marrow nociceptors. These issues notwithstanding, a robust molecular understanding of the neural regulation of haematopoiesis is now beginning to emerge.

Nature **589**, 520-521 (2021)

doi: https://doi.org/10.1038/d41586-020-03577-7

References

1. 1.

   Crane, G. M., Jeffery, E. & Morrison, S. J. *Nature Rev. Immunol.* **17**, 573–590 (2017).

2. 2.

   Méndez-Ferrer, S., Lucas, D., Battista, M. & Frenette, P. S. *Nature* **452**, 442–447 (2008).

3. 3.

Gao, X. *et al. Nature* **589**, 591–596 (2021).

4. 4.

To, L. B., Levesque, J.-P. & Herbert, K. E. *Blood* **118**, 4530–4540 (2011).

5. 5.

Donmez, A., Yilmaz, F., Gokmen, N. & Tombuloglu, M. *Transfus. Apher. Sci.* **49**, 485–488 (2013).

6. 6.

Dubin, A. E. & Patapoutian, A. *J. Clin. Invest.* **120**, 3760–3772 (2010).

7. 7.

Calvo, W. *Am. J. Anat.* **123**, 315–328 (1968).

8. 8.

Agarwala, S. & Tamplin, O. J. *Trends Cell. Biol.* **28**, 987–998 (2018).

9. 9.

Picoli, C. C. *et al. Stem Cells Transl. Med*. https://doi.org/10.1002/sctm.20-0284 (2020).

10. 10.

Hanoun, M. *et al. Cell Stem Cell* **15**, 365–375 (2014).

Jobs from Nature Careers

-
  -

- All jobs
-
- **Postdoctoral Fellow - Zoubeidi Lab, Vancouver Prostate Centre**

  The University of British Columbia (UBC)

  Vancouver, Canada

  JOB POST

- **Laser Scientist**

  German Electron Synchrotron (DESY)

  Hamburg, Germany

  JOB POST

- **Fachinformatiker/in Systemintegration (w/m/d)**

  Karlsruhe Institute of Technology (KIT)

  Karlsruhe, Germany

  JOB POST

- **Intership/Bachelor or Master Thesis: " Digitization of land-based shrimp farming in Germany using AI-based evaluation of imaging and acoustic systems"**

  Alfred Wegener Institute - Helmholtz Centre for Polar and Marine Research (AWI)

  Bremerhaven, Germany

JOB POST

This article was downloaded by **calibre** from https://www.nature.com/articles/d41586-020-03577-7

NEWS AND VIEWS
27 January 2021

Palaeoclimate puzzle explained by seasonal variation

Scientists have long been baffled by the mismatch of climate simulations of the past 12,000 years with temperature reconstructions from geological records. It now emerges that seasonal biases in the records explain the disparity.

Jennifer Hertzberg

Jennifer Hertzberg is in the International Ocean Discovery Program, Texas A&M University, College Station, Texas 77845, USA.
Contact

Search for this author in:

- Pub Med
- Nature.com
- Google Scholar

Understanding past climate change is crucial for putting modern global warming in context. Reconstructions of climate during the Holocene — the current interglacial epoch, which began 11,700 years ago — based on geological evidence suggest that a peak in global mean annual temperatures between 10,000 and 6,000 years ago was followed by a cooling trend, which then reversed in the post-industrial era[1,2]. However, computational simulations of Holocene climate reveal only a long-term warming trend[3]. Writing in *Nature*, Bova *et al*.[4] report an analysis that effectively brings Holocene climate reconstructions in line with computational simulations. This result has important implications for our understanding of the drivers of

climate change during the Holocene and for the context of post-industrial warming.

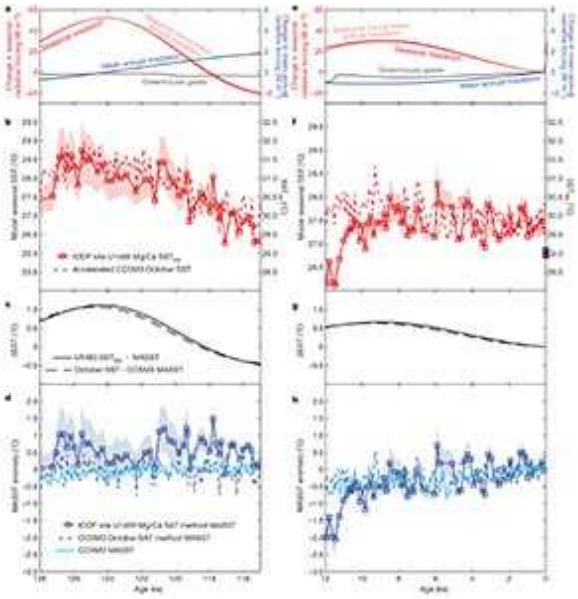

Read the paper: Seasonal origin of the thermal maxima at the Holocene and the last interglacial

To reconstruct past climates, scientists rely on proxies: geological materials that have properties that can be measured and correlated with modern climate parameters. The apparent temperature peak during the early Holocene (known as the Holocene thermal maximum) is a prominent feature in global syntheses of proxy-based climate reconstructions[1,2] (Fig. 1). Its notable absence from computational modelling has been dubbed the Holocene temperature conundrum, and has puzzled climate scientists for years[3]. The disagreement has been attributed to seasonal biases in proxy reconstructions[5] — that is, the proxies reflect the evolution of seasonal temperatures, rather than mean annual ones — and to deficiencies in modelling[6]. Notably, global proxy syntheses are dominated by sea surface

temperature (SST) records (see ref. 2, for example)[2], which are known to be seasonally biased[5].

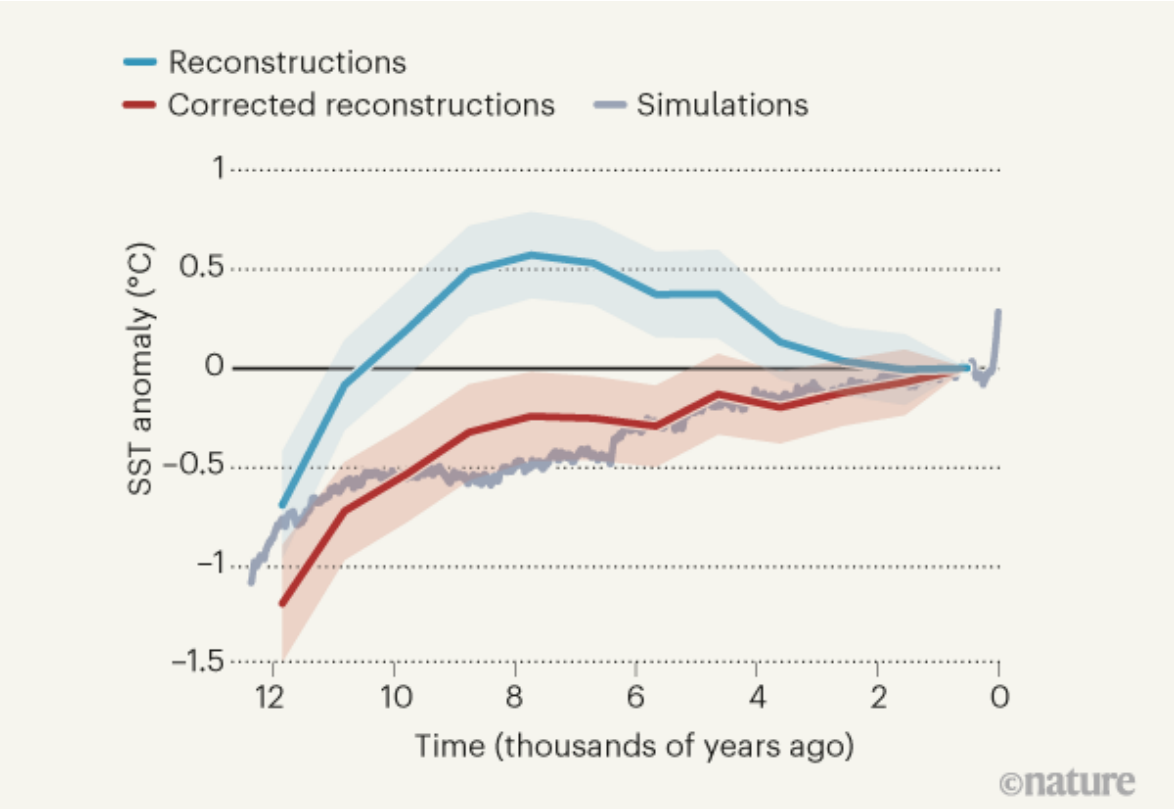

Figure 1 | Correcting seasonal bias in climate reconstructions. Average global temperatures during the Holocene (the current interglacial epoch, which began 11,700 years ago) can be reconstructed from geological records. These reconstructions (blue line) suggest that sea surface temperatures (SSTs) peaked between 10,000 and 6,000 years ago, then declined until the post-industrial period, when temperatures began to rise. However, computational simulations of Holocene SSTs don't match those reconstructions, probably because the geological records are seasonally biased — the records reflect the evolution of seasonal temperatures, rather than mean annual temperatures. Bova *et al.*[4] report a method that quantifies and corrects for seasonal bias in marine geological records, and use it to estimate mean annual SSTs (red line). The corrected data match the computational simulations, thus resolving a long-standing problem in this field. SSTs are shown as anomalies: the difference between the SST of a reference time interval and the average SST between 0 and 1,000 years ago. Shaded areas represent the bounds of one standard error.

Bova and colleagues' new method identifies seasonal biases in SST records and enables the calculation of mean annual SST from seasonal SST. It takes advantage of the characteristics of the last interglacial period (128,000–115,000 years ago), which was marked by mild global temperatures, smaller ice sheets and higher sea levels than those of today[7]. This period is advantageous for the authors' purposes in that the seasonal difference of incoming solar radiation (insolation) was greater than during the Holocene, whereas the effects of other factors that alter climate, such as greenhouse gases and ice, were weaker, making it easier to identify seasonal biases.

More specifically, the authors' method involves identifying seasonal bias in the portion of an SST record that corresponds to the last interglacial, and in which there was a stronger correlation of SST with seasonal insolation than with mean annual insolation. The sensitivity of the SST record to seasonal insolation during this period is then calculated, and used as a benchmark to remove seasonal bias from the entire record, thereby allowing mean annual SST to be determined from that record. The authors first applied their method to an SST reconstruction based on a proxy taken from a marine site located off the northeast coast of Papua New Guinea. The transformed mean annual SST record was independently validated by applying the new method to SST data for the same geographical region produced in computational simulations of the past 300,000 years — the transformed data matched the mean annual SST output from the simulations.

Bova *et al*. went on to create a synthesis of previously published SST records spanning the last interglacial and the Holocene periods. These records are based on two common proxies used for reconstructing SST: the chemical composition of the fossilized calcium carbonate shells of surface-dwelling unicellular marine organisms known as foraminifera; and organic biomarkers known as alkenones, which are synthesized by marine algae and settle into marine sediments. The authors found that the majority of the examined SST records are indeed seasonally biased.

After converting the seasonally biased SST records into mean annual SST records, Bova and colleagues infer that the climate has been warming since the early Holocene — that is, there is no evidence for a Holocene thermal maximum in mean annual temperatures (Fig. 1). They suggest instead that the Holocene thermal maximum is a seasonal feature driven by a peak in

summer insolation in the Northern Hemisphere that occurred during the early Holocene.

The reconstruction of mean annual temperatures produced from the authors' synthesis of proxy records strongly resembles a computational simulation[3] of Holocene climate that also reflects mean annual temperatures — effectively solving the Holocene temperature conundrum. This enabled Bova and colleagues to shed new light on the drivers of Holocene climate change. They find that the increase in global mean annual temperatures that occurred during the early Holocene (12,000–6,500 years ago) was a response to retreating ice sheets, whereas the continued increase in temperatures over the past 6,500 years is due to rising greenhouse-gas concentrations.

The authors also show that mean annual temperatures during the last interglacial period were more stable and higher than their estimates of Holocene temperatures. They attribute this to the near-constant greenhouse-gas concentrations and reduced extent of ice sheets during the last interglacial. Crucially, the researchers find that the current mean annual temperature exceeds those of the past 12,000 years, and probably approaches the warmth of the last interglacial period.

Bova and colleagues' method to identify and correct for seasonal biases in proxy SST reconstructions can now be applied to other temperature records on different timescales. This is a key benefit of their study, because palaeoclimate scientists have long known that temperature reconstructions are probably seasonally biased, but did not have a method for addressing the problem.

One limitation of the findings is that the new synthesis of proxy SST records is limited to the global region between 40° N and 40° S. Proxy records from higher latitudes were deliberately excluded because of the scarcity of such records for the last interglacial, and because of the proximity of those regions to ocean fronts, where ocean dynamics can affect SST. However, the inclusion of these regions might be needed in the future, given that processes at high latitudes have a substantial role in many climate feedback processes. Moreover, the new synthesis examines records based on only two SST proxies. Future work should include more records based on other temperature proxies. Nevertheless, by solving a conundrum that has puzzled

climate scientists for years, Bova and colleagues' study is a major step forward for the field.

Nature **589**, 521-522 (2021)

doi: https://doi.org/10.1038/d41586-021-00115-x

References

1. 1.

   Kaufman, D. *et al. Sci. Data* **7**, 201 (2020).

2. 2.

   Marcott, S. A., Shakun, J. D., Clark, P. U. & Mix, A. C. *Science* **339**, 1198–1201 (2013).

3. 3.

   Liu, Z. *et al. Proc. Natl Acad. Sci. USA* **111**, E3501–E3505 (2014).

4. 4.

   Bova, S., Rosenthal, Y., Liu, Z., Godad, S. P. & Yan, M. *Nature* **589**, 548–553 (2021).

5. 5.

   Marsicek, J., Shuman, B. N., Bartlein, P. J., Shafer, S. L. & Brewer, S. *Nature* **554**, 92–96 (2018).

6. 6.

   Liu, Y. *et al. Sci. Rep.* 8, 4434 (2018).

7. 7.

Hoffman, J. S., Clark, P. U., Parnell, A. C. & He, F. *Science* **355**, 276–279 (2017).

Jobs from Nature Careers

-
  -
    - All jobs
  -
    - **Postdoctoral Fellow - Zoubeidi Lab, Vancouver Prostate Centre**

      The University of British Columbia (UBC)

      Vancouver, Canada

      JOB POST

    - **Laser Scientist**

      German Electron Synchrotron (DESY)

      Hamburg, Germany

      JOB POST

    - **Fachinformatiker/in Systemintegration (w/m/d)**

      Karlsruhe Institute of Technology (KIT)

      Karlsruhe, Germany

      JOB POST

    - **Intership/Bachelor or Master Thesis: "Digitization of land-based shrimp farming in Germany using**

AI-based evaluation of imaging and acoustic systems"

Alfred Wegener Institute - Helmholtz Centre for Polar and Marine Research (AWI)

Bremerhaven, Germany

JOB POST

This article was downloaded by **calibre** from https://www.nature.com/articles/d41586-021-00115-x

NEWS AND VIEWS
06 January 2021

Base editor repairs mutation found in the premature-ageing syndrome progeria

No cure exists for the lethal premature-ageing condition Hutchinson–Gilford progeria. A gene-editing tool — adenine base editors — offers a way to treat the condition in mice. Could this approach lead to an effective therapy?

Wilbert P. Vermeij &

Wilbert P. Vermeij is at the Princess Máxima Center for Pediatric Oncology, Oncode Institute, 3584 CS Utrecht, the Netherlands.
Contact

Search for this author in:

- Pub Med
- Nature.com
- Google Scholar

Jan H. J. Hoeijmakers

Jan H. J. Hoeijmakers is in the Molecular Genetics Department, Erasmus MC, 3015 GD Rotterdam, the Netherlands, and also at the Princess Máxima Center for Pediatric Oncology, Oncode Institute and at the Institute for Genome Stability in Ageing and Disease, CECAD Research Centre, Cologne, Germany.
Contact

Search for this author in:

- Pub Med
- Nature.com
- Google Scholar

Gene-editing technologies raise the possibility of tackling the fundamental cause of certain inherited human diseases. Writing in *Nature*, Koblan *et al*.[1] report their use of such a technology in mice that provide a model for a human accelerated-ageing disorder.

Ageing is influenced by numerous factors — some external, some organ-specific and others systemic, affecting the entire body. It is one of the main biological processes for which the chief cause or causes are not fully known. Often, the mechanisms underlying a biological process are revealed by an analysis of genetic mutants, and mutations in systemic ageing factors are associated with processes of accelerated ageing that affect multiple organs. Most premature-ageing disorders point to problems in DNA maintenance and integrity as the underlying cause. People with Werner or Cockayne syndrome, for example, have defects in different mechanisms that affect genome stability[2].

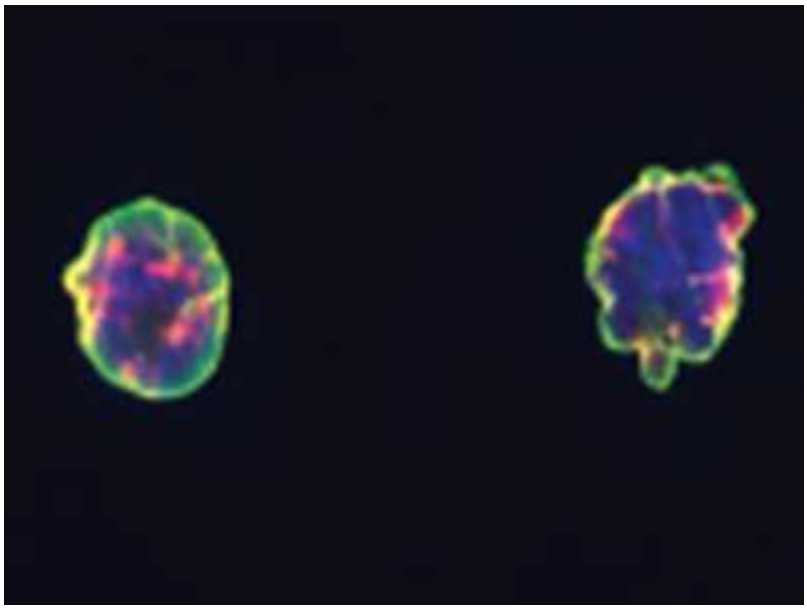

Read the paper: In vivo base editing rescues Hutchinson–Gilford progeria syndrome in mice

Generally, premature-ageing conditions exhibit accelerated ageing of a subset of tissues. The best known of such disorders is Hutchinson–Gilford progeria syndrome, which is often referred to just as progeria. Children with this condition look healthy at birth. But, from around one year of age, symptoms begin to emerge, such as growth failure, skin abnormalities and hearing loss. The features of premature ageing increase over time, resulting in striking hallmarks of old age that include wrinkles, loss of fat under the skin, joint stiffness and musculoskeletal abnormalities. However, these children retain a normally functioning nervous system, underscoring the syndrome's organ-specific nature. No cure exists for progeria, and affected individuals usually die aged around 14 or 15 as a consequence of conditions such as atherosclerosis, severe cardiovascular complications or stroke[3].

Progeria is caused[4] by the mutation of a single base (a cytosine mutated to a thymine) in one of the two copies of the gene encoding the protein lamin A (Fig. 1). This protein is a structural component of the outer rim of the cell nucleus. The mutated version of the gene leads to abnormalities during the splicing process that occurs during gene transcription. As a result, a shorter-than-normal version of lamin A, termed progerin, is produced. Progerin and maturing lamin A undergo a modification termed farnesylation, in which a specific lipid group called farnesyl is attached to the protein. As lamin A matures, this lipid-modified region of the protein is removed in an enzyme-mediated cleavage event. However, progerin remains farnesylated because it lacks the amino-acid residues that provide the usual cleavage site. Farnesylated progerin accumulates and hampers the normal role of lamin A, thereby perturbing nuclear shape, rigidity and function.

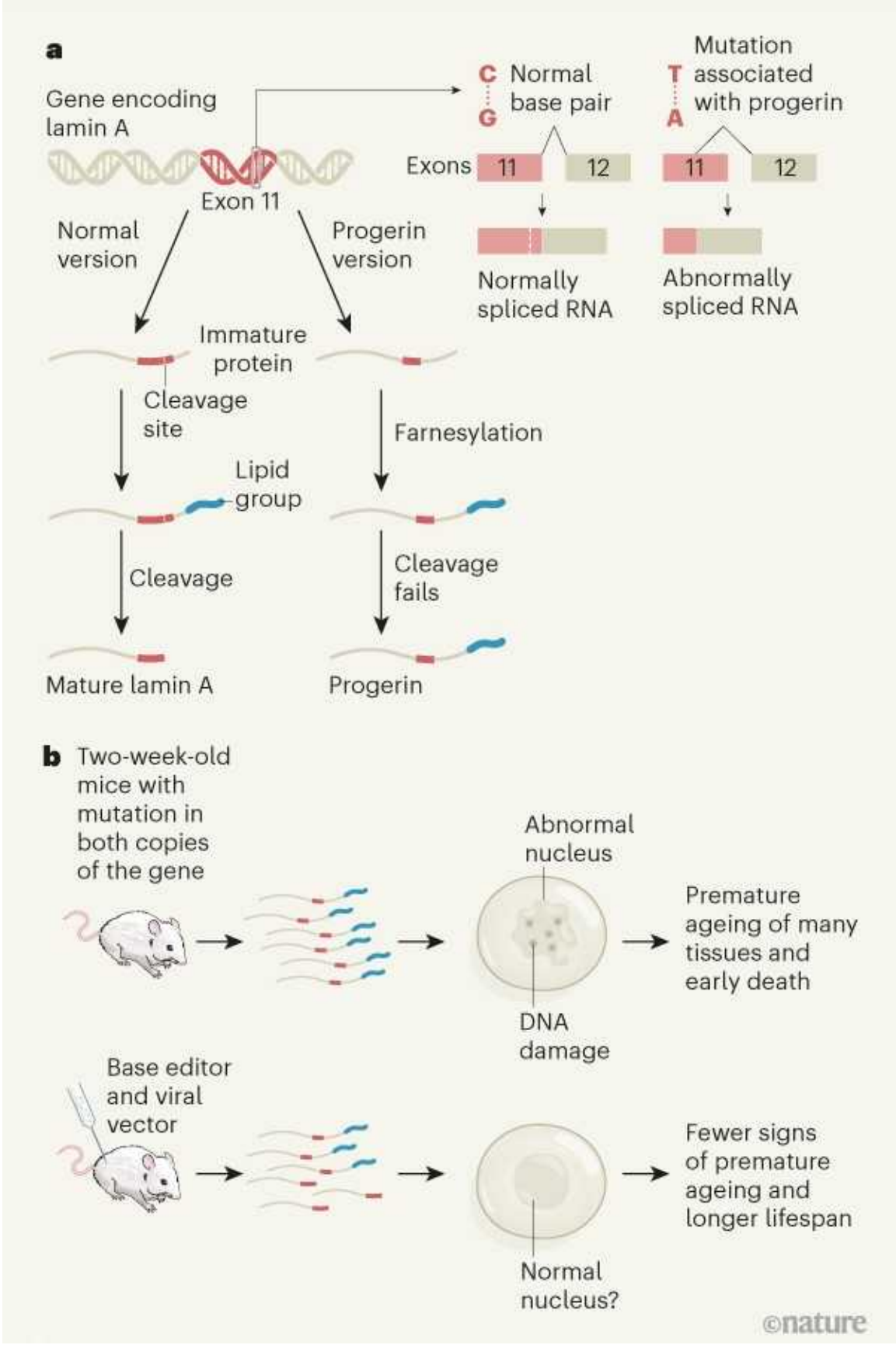
a
Gene encoding lamin A
Exon 11
Normal version
Progerin version
C
G
Normal base pair
T
A
Mutation associated with progerin
Exons
11
12
11
12
Normally spliced RNA
Abnormally spliced RNA
Immature protein
Cleavage site
Farnesylation
Lipid group
Cleavage
Cleavage fails
Mature lamin A
Progerin
b
Two-week-old mice with mutation in both copies of the gene
Abnormal nucleus
DNA damage
Premature ageing of many tissues and early death
Base editor and viral vector
Normal nucleus?
Fewer signs of premature ageing and longer lifespan
©nature

Figure 1 | Repair of a mutation that causes a premature-ageing syndrome. a, The lethal disease Hutchinson–Gilford progeria syndrome, also known as progeria, arises from a mutation in the gene that encodes the protein lamin A. This mutation, in a region of the gene called exon 11, changes a cytosine (C) base that is paired with a guanine (G) to a thymine (T) paired with adenine (A). This causes an abnormal splicing event in which a section of exon 11, including a region that encodes a cleavage site (dotted white line), is absent from the RNA sequence that encodes protein. As lamin A matures, a lipid group is added in an event called farnesylation. Cleavage of the protein at the site encoded by exon 11 produces mature lamin A. The mutated version of the protein, termed progerin, lacks this cleavage site and retains the lipid group. Progerin causes nuclear abnormalities and DNA damage, resulting in accelerated ageing[5,6]. **b**, Mice with two mutant copies of the gene encoding lamin A are a model for human progeria. Koblan *et al.*[1] used gene-editing tools called base editors. When the mice were given a base editor and a viral vector to enable the editing machinery to enter cells, the mutation was corrected in many, but not all, tissues. The reduction in progerin improved the health and lifespan of treated mice, and presumably corrected nuclear abnormalities in their cells.

Nuclear malformations arising from progerin are particularly apparent in organs and tissues that are subject to mechanical stress, including the skin and the cardiovascular system. Parts of the body that are subject to high mechanical stress correspond to the most-affected organs in progeria, and the nuclear deformations that arise from stress activate the DNA-damage response[5,6]. Progerin-induced nuclear weakening might result in genome instability under mechanical stress if various delicate processes in the nucleus are disturbed. This would be consistent with the higher-than--normal levels of DNA damage and chromosome aberrations found in cells from people who have progeria, and in mice that provide a model for the syndrome[7], ranking progeria among other premature-ageing disorders associated with genomic instability.

Attempts to find treatments for progeria initially focused on trying to reduce the accumulation of farnesylated progerin[8]. Compounds that generated interest included those with reported anti-ageing activities, such as

metformin and rapamycin — which might affect splicing and turnover of progerin, respectively. The most-advanced drugs, in terms of clinical use, are inhibitors of the enzyme farnesyl transferase, which reduce the accumulation of farnesylated progerin. One of these, lonafarnib, was approved in November 2020 by the US Food and Drug Administration. This is the first licensed therapy for progeria. However, the treatment only partially alleviates the syndrome[8].

The most rigorous approach for tackling progeria would be to directly correct the genetic defect. In 2019, two teams reported using the gene-editing method CRISPR–Cas9 to repair the associated mutation in the gene encoding lamin A in mice[9,10]. This treatment alleviated the decline in health normally expected in such animals and extended their lifespan, compared with those whose mutation was not corrected. CRISPR–Cas9 targets a specific genome sequence through a process aided by a guide RNA sequence that helps to ensure that editing occurs at the desired location. However, unwanted alterations could arise — either from the formation of the double-stranded DNA breaks that occur during this editing process, or from off-target edits of sequences that are similar to the sequence of interest. The possibility of such unwanted events would demand extreme caution in any potential clinical roll-out.

Koblan *et al*. present their use of an editing approach that could offer a way forwards. The authors harnessed tools known as base editors[11]. Like CRISPR–Cas9, these can alter a single base at a specific genomic location, such as where the mutant thymine is paired with adenine in the gene encoding lamin A. However, one difference is that base editors do not cleave DNA's phosphate backbone when targeting the nucleotide, so double-stranded DNA breaks are not generated. Instead, the approach chemically modifies the targeted nucleotide[12]. Adenine base editors convert adenine, through an intermediate called inosine, to guanine during DNA replication. The need for DNA replication could pose a problem if trying to use this method to target mutations in other diseases in which non-dividing cells, such as those of the nervous system, are the main target of interest.

Koblan and colleagues used an adenine base editor, transferred into cells by means of a virus called a lentivirus, to target the mutation in the gene

encoding lamin A in cells from people with progeria. Repair occurred in 90% of all cells. Correction of the mutation resulted in the normal splicing of lamin A, reduced the expression of progerin and corrected abnormalities in nuclear shape. Minimal off-target editing was observed.

Using a mouse model of progeria, the authors delivered the base editor using adeno-associated virus. Following a single injection of the editor near the eye socket, or in the abdominal cavity, of mice that were up to two weeks old, the authors observed targeted repair of the gene encoding lamin A in many organs. This took place mainly in the liver and heart, but also occurred, to a lesser extent, in muscle, in the aortic artery and in bone tissue.

Although most of the key organs affected in progeria showed only a modest level of genetic correction and reduction in progerin, a striking increase in the level of lamin A was observed as a consequence of the treatment. Crucially, compared with the model animals that did not undergo gene editing, those that received the base editor aged with remarkably fewer abnormalities in the usually lifespan-limiting cardiovascular system. These animals also had greater vitality (a better ability to move and a better overall appearance) and a statistically significant lifespan extension.

By directly addressing the root cause of the disease, base editing could offer great advantages over current drug-based therapeutic strategies. Many key questions remain to be answered, however, before people might benefit from the introduction of this technology. For example, what is the optimal distribution of base editor mediated by adeno-associated virus or by other delivery methods? And which organs can be targeted? The adeno-associated virus injection strategy was less efficient in targeting the skin than in targeting other mouse organs.

To what extent can the genetic defect be corrected? High efficiency of editing might be crucial, particularly for efforts to treat other diseases. Previous attempts[11,12] to use gene editing to address the defects under-lying Duchenne muscular dystrophy and rare liver diseases met with only limited success. However, Koblan and colleagues' work indicates that correction does not need to reach 100% efficiency to provide positive benefits,

opening the possibility of reconsidering this approach for some other diseases, too.

Another important question is whether an immune response might develop that would target components of the editing system. Such a response might result in inefficient treatment if cells harbouring editing components were selectively eliminated[11].

What about long-term considerations? For example, would a single administration of the editors be sufficient? And what would be the best age for treatment to be administered? Progeria is diagnosed relatively early in life compared with many other diseases for which base editing is a possibility. A treatment age of two weeks, for mice, is therefore much lower than the equivalent age, for humans, at which many diseases are diagnosed. Moreover, with animal testing, it is difficult to benchmark the equivalent human age that corresponds to a mouse of a given age. Finally, how would the current drug therapy available for progeria fit with the potential of repair by base editing in a treatment plan?

If base editing is to be used to treat human disease, the safety of such an intervention must be ensured. If it can be, and if this method successfully repairs the progeria-causing alteration in the crucial tissues, such an approach holds tremendous promise as a way of prolonging health, extending lifespan and improving the quality of life of those who have this mutation.

Nature **589**, 522-524 (2021)

doi: https://doi.org/10.1038/d41586-020-03573-x

References

1. 1.

   Koblan, L. W. *et al. Nature* **589**, 608–614 (2021).

2. 2.

Niedernhofer, L. J. *et al. Annu. Rev. Biochem.* **87**, 295–322 (2018).

3. 3.

Merideth, M. A. *et al. N. Engl. J. Med.* **358**, 592–604 (2008).

4. 4.

Eriksson, M. *et al. Nature* **423**, 293–298 (2003).

5. 5.

Kumar, A. *et al. Cell* **158**, 633–646 (2014).

6. 6.

Nava, M. M. *et al. Cell* **181**, 800–817 (2020).

7. 7.

Liu, B. *et al. Nature Med.* **11**, 780–785 (2005).

8. 8.

Harhouri, K. *et al. Nucleus* **9**, 265–276 (2018).

9. 9.

Beyret, E. *et al. Nature Med.* **25**, 419–422 (2019).

10. 10.

Santiago-Fernández, O. *et al. Nature Med.* **25**, 423–426 (2019).

11. 11.

Porto, E. M., Komor, A. C., Slaymaker, I. M. & Yeo, G. W. *Nature Rev. Drug. Discov.* **19**, 839–859 (2020).

12. 12.

Katrekar, D. *et al. Nature Methods* **16**, 239–242 (2019).

Jobs from Nature Careers

-
  -
    - All jobs
  -
    - **Postdoctoral Fellow - Zoubeidi Lab, Vancouver Prostate Centre**

      The University of British Columbia (UBC)

      Vancouver, Canada

      JOB POST
    - **Laser Scientist**

      German Electron Synchrotron (DESY)

      Hamburg, Germany

      JOB POST
    - **Fachinformatiker/in Systemintegration (w/m/d)**

      Karlsruhe Institute of Technology (KIT)

      Karlsruhe, Germany

      JOB POST
    - **Intership/Bachelor or Master Thesis: "Digitization of land-based shrimp farming in Germany using**

AI-based evaluation of imaging and acoustic systems"

Alfred Wegener Institute - Helmholtz Centre for Polar and Marine Research (AWI)

Bremerhaven, Germany

JOB POST

This article was downloaded by **calibre** from https://www.nature.com/articles/d41586-020-03573-x

NEWS AND VIEWS
14 January 2021

Accurate machine learning in materials science facilitated by using diverse data sources

A strategy for machine learning has been developed that exploits the fact that data are often collected in different ways with varying levels of accuracy. The approach was used to build a model that predicts a key property of materials.

Rohit Batra

Rohit Batra is at the Center for Nanoscale Materials, Argonne National Laboratory, Lemont, Illinois 60439, USA.
Contact

Search for this author in:

- Pub Med
- Nature.com
- Google Scholar

Scientists are always hunting for materials that have superior properties. They therefore continually synthesize, characterize and measure the properties of new materials using a range of experimental techniques. Computational modelling is also used to estimate the properties of materials. However, there is usually a trade-off between the cost of the experiments (or simulations) and the accuracy of the measurements (or estimates), which has limited the number of materials that can be tested rigorously. Writing in *Nature Computational Science*, Chen *et al.*[1] report a machine-learning

approach that combines data from multiple sources of measurements and simulations, all of which have different levels of approximation, to learn and predict materials' properties. Their method allows the construction of a more general and accurate model of such properties than was previously possible, thereby facilitating the screening of promising material candidates.

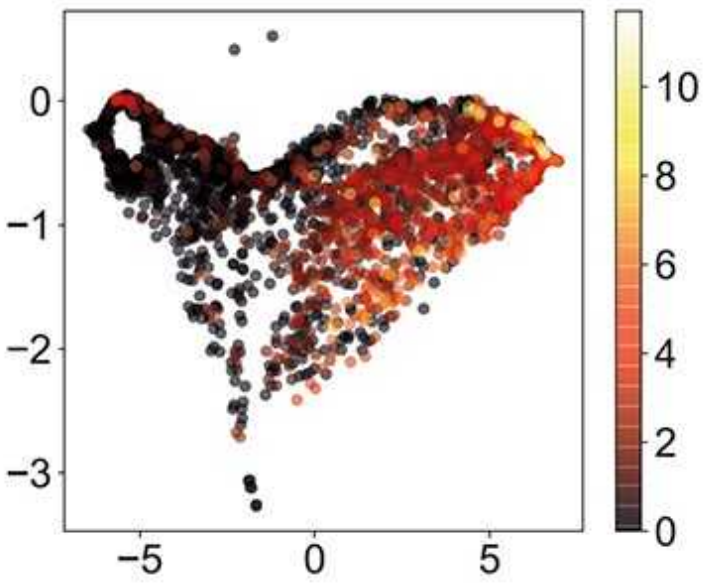

Read the paper: Learning properties of ordered and disordered materials from multi-fidelity data

Materials scientists commonly supplement their own 'chemical intuition' with predictions from machine-learning models, to decide which experiments to conduct next[2,3]. For example, artificial intelligence has been used to identify candidate compounds that act as superconductors at high temperatures[4], electrolyte materials that conduct electric currents using lithium ions[5], and electrically insulating polymers that can withstand large electric fields without breaking down[6]. Artificial intelligence has also been

used to work out ways of synthesizing materials — that is, to suggest which reagents, catalysts and experimental conditions to use[7].

Most of these studies involve supervised learning, in which a machine is exposed to a large volume of historical data about the chemical composition or atomic structure of materials, and their associated properties, to build a model that can predict the properties of other materials. More importantly, almost all of these studies use models built on data obtained from a single, consistent source. Such models are referred to as single-fidelity models.

However, for most real-world applications, measurements of materials' properties have varying levels of fidelity, depending on the resources available. For instance, the most accurate (high-fidelity) measurements of properties of crystalline materials are made using single crystals, which can be laborious to prepare. Approximate (low-fidelity) measurements are therefore often made using easily synthesizable polycrystalline samples. Similarly, a hierarchy of increasingly accurate, but progressively more expensive, computational modelling schemes are used to calculate materials' properties — high-fidelity modelling is therefore often restricted by its cost.

Overall, this variation in measurement and modelling techniques leads to a heterogeneous data structure — low-fidelity measurements are plentiful, whereas high-fidelity data are sparse. Notably, each type of fidelity has its own advantages: low-fidelity data cover a diverse range of compounds, whereas high-fidelity data are more accurate. Single-fidelity models trained using only low- or high-fidelity data therefore miss out on high accuracy or generality, respectively (Fig. 1).

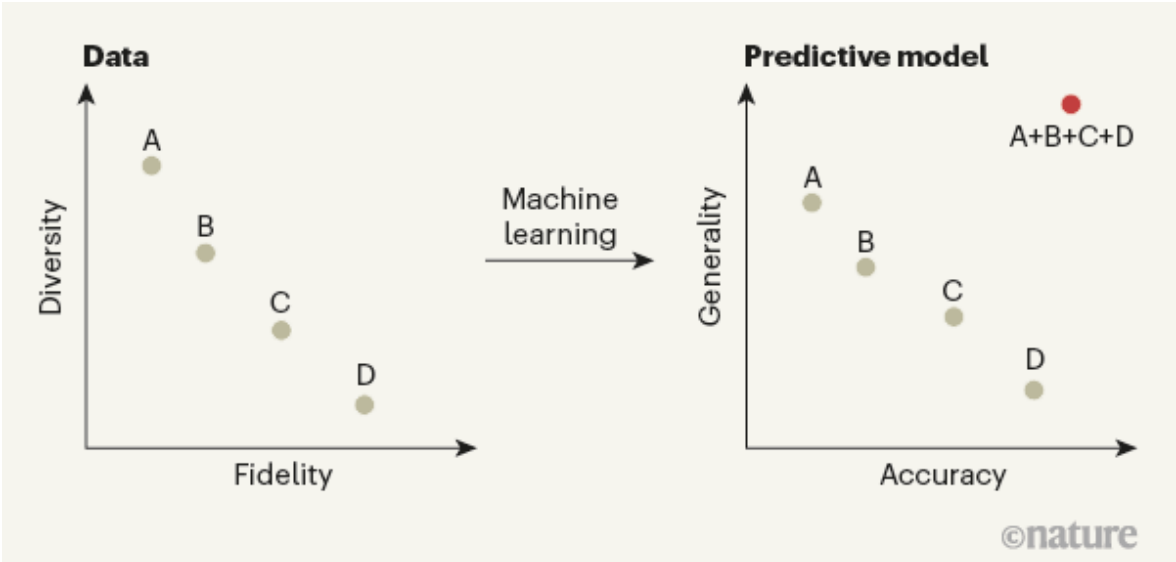

Figure 1 | Multi-fidelity data can improve predictive models developed using machine learning. Accurate (high-fidelity) data about the properties of materials can be difficult or expensive to acquire, and so less-accurate (low-fidelity) data are often obtained instead. Low-fidelity data sets are therefore usually larger than high-fidelity ones, and represent a greater diversity of materials. Machine-learning systems typically use individual data sets to generate predictive models of materials' properties. Diverse low-fidelity data produce general but approximate models, whereas high-fidelity data produce accurate but less-general ones. Here, machine learning based on individual data sets A to D produces four predictive models, the generality and accuracy of which are shown. Chen *et al.*[1] report a machine-learning architecture that can process materials data from multiple sets that have different fidelities, and thereby generates predictive models that are more general and accurate than are those produced using the individual data sets; the red spot indicates the generality and accuracy of a model trained using the combined data sets A to D. Examples are illustrative, and do not depict actual data.

Chen *et al*. now report an adaptation of an artificial neural network (a brain-inspired computer system) that they call a multi-fidelity graph network. This can learn about materials' properties using data acquired from different modelling and experimental techniques. As a proof of principle, the authors trained their graph network to learn about bandgaps — a property that controls several electrical and optical properties of solid materials, such as

their conductivity and colour. They used bandgap data from five sources: four data sets were the results of different types of quantum-mechanical calculation, and the fifth source was experimental data. The data set that had the lowest fidelity level contained about 50,000 data points, roughly 100 times more than the number in each of the other data sets; this is typical of the heterogeneity of available data in materials science.

The authors' graph network takes a materials graph — a mathematical representation of the structure of a material, consisting of nodes that represent atoms and edges that represent bonds — as an input. It then performs a series of mathematical (convolution) operations to exchange information between its nodes and edges. This produces an output vector known as a latent representation, which is passed on to, and further manipulated by, another artificial neural network to predict the property of interest (in this case, the bandgap). One or more historical data sets are used first to simultaneously train the materials graph and the second artificial neural network, priming them to make predictions.

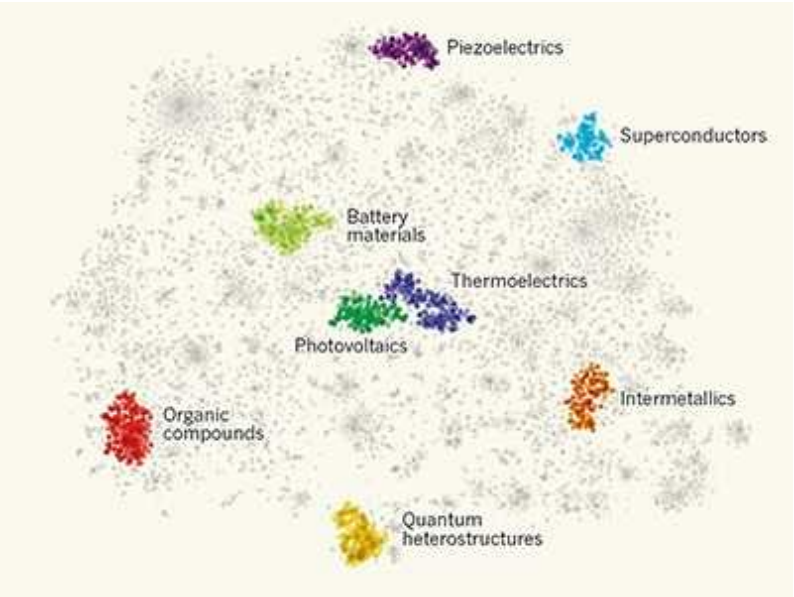

Text mining facilitates materials discovery

Machine-learning techniques based on graph networks are among the top-performing methods for single-fidelity learning of materials properties, and do not require a feature-engineering step (in which a material's composition and/or atomic structure is converted into a string of numbers in a machine-readable format), as is necessary for other machine-learning algorithms[8]. To adapt their graph network for multi-fidelity learning, the authors introduced a new variable, in addition to those used to represent graph nodes and edges, that accounts for the fidelity level of a data point. The authors' graph network therefore exchanges information between the atom nodes, the bond edges and the data-fidelity level represented by the new variable. This means that their approach is applicable to any number of fidelity levels.

A comparison of prediction errors clearly demonstrates the benefit of the multi-fidelity approach. For example, models that had four levels of fidelity reduced errors in predictions of bandgaps by 22–45%, compared with single-fidelity models. Similarly, multi-fidelity models involving two, three or five levels of fidelity performed better than did single-fidelity models.

This improvement can be attributed to two key factors. First, the large volume of low-fidelity data represents a more chemically diverse collection of materials than does a single high-fidelity data set; exposure of the graph network to this diversity results in a better and more-general latent representation. Second, there is a high correlation between the low- and high-fidelity bandgap data — many of the bandgaps in the low-fidelity data set are close in value to the equivalent data points in the high-fidelity data sets. This second factor is evident from the higher prediction accuracy that is achieved when using high-fidelity data sets that correlate more closely with the low-fidelity data set.

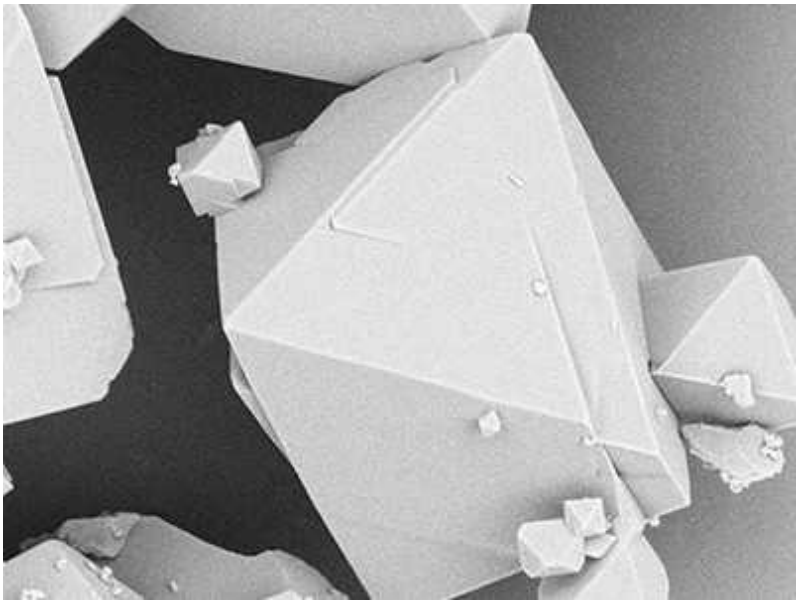

Machine learning speeds up synthesis of porous materials

Chen and colleagues' approach overcomes the limitations of other multi-fidelity approaches[9,10], which are either not easily scalable to large data sets, or cannot handle heterogeneous data or more than two levels of fidelity. The authors' multi-fidelity graph network is therefore a powerful new system for capturing complex relationships between data sets of multiple fidelities. It should be noted, however, that Chen *et al*. did not explore what happens if low- and high-fidelity data points are weighted differently. Such weighting might become necessary when the number of low-fidelity points is so large that it over-represents the full set of multi-fidelity data.

The authors' system is not restricted to materials science, but is generalizable to any problem that can be described using graph structures, such as social networks and knowledge graphs (digital frameworks that represent knowledge as concepts connected by relationships). Furthermore, this approach could, in principle, be used to learn about multiple properties simultaneously (multi-task learning), rather than learning about just one property for which data are available at multiple levels of fidelity.

However, some fundamental questions remain. Are multi-fidelity approaches guaranteed to perform better than single-fidelity models, even when the quality of the low-fidelity data is extremely poor? And what happens when low- and high-fidelity data points are poorly correlated? More research is needed to understand the scenarios for which multi-fidelity learning is most beneficial, balancing prediction accuracy with the cost of acquiring data. In the meantime, the popularity of multi-fidelity methods will surely increase, because they directly exploit the underlying widespread heterogeneity of data in the materials and chemical sciences.

Nature **589**, 524-525 (2021)

doi: https://doi.org/10.1038/d41586-020-03259-4

References

1. 1.

   Chen, C., Zuo, Y., Ye, W., Li, X. & Ong, S. P. *Nature Comput. Sci*. **1**, 46–53 (2021).

2. 2.

   Butler, K. T., Davies, D. W., Cartwright, H., Isayev, O. & Walsh, A. *Nature* **559**, 547–555 (2018).

3. 3.

   Ramprasad, R., Batra, R., Pilania, G., Mannodi-Kanakkithodi, A. & Kim, C. *npjComput. Mater.* **3**, 54 (2017).

4. 4.

   Stanev, V. *et al. npjComput. Mater.* **4**, 29 (2018).

5. 5.

   Sendek, A. D. *et al. Chem. Mater.* **31**, 342–352 (2019).

6. 6.

Mannodi-Kanakkithodi, A. *et al. Mater. Today* **21**, 785–796 (2018).

7. 7.

Huo, H. *et al. npj Comput. Mater.* **5**, 62 (2019).

8. 8.

Chen, C., Ye, W., Zuo, Y., Zheng, C. & Ong, S. P. *Chem. Mater.* **31**, 3564–3572 (2019).

9. 9.

Rohit, B., Pilania, G., Uberuaga, B. P. & Ramprasad, R. *ACS Appl. Mater. Interf.* **11**, 24906–24918 (2019).

10. 10.

Dahl, G. E., Jaitly, N. & Salakhutdinov, R. Preprint at https://arxiv.org/abs/1406.1231 (2014).

Jobs from Nature Careers

-
  -
    - All jobs
  -
    - **Postdoctoral Fellow - Zoubeidi Lab, Vancouver Prostate Centre**

      The University of British Columbia (UBC)

      Vancouver, Canada

      JOB POST

- **Laser Scientist**

  German Electron Synchrotron (DESY)

  Hamburg, Germany

  JOB POST

- **Fachinformatiker/in Systemintegration (w/m/d)**

  Karlsruhe Institute of Technology (KIT)

  Karlsruhe, Germany

  JOB POST

- **Intership/Bachelor or Master Thesis: "Digitization of land-based shrimp farming in Germany using AI-based evaluation of imaging and acoustic systems"**

  Alfred Wegener Institute - Helmholtz Centre for Polar and Marine Research (AWI)

  Bremerhaven, Germany

  JOB POST

This article was downloaded by **calibre** from https://www.nature.com/articles/d41586-020-03259-4

- Article
- Published: 27 January 2021

Measuring the α-particle charge radius with muonic helium-4 ions

- Julian J. Krauth ORCID: orcid.org/0000-0001-7769-650X[1,2] [nAff12],
- Karsten Schuhmann[3,4],
- Marwan Abdou Ahmed[5],
- Fernando D. Amaro[6],
- Pedro Amaro ORCID: orcid.org/0000-0002-5257-6728[7],
- François Biraben[8],
- Tzu-Ling Chen ORCID: orcid.org/0000-0002-2243-5780[9],
- Daniel S. Covita[10],
- Andreas J. Dax[4],
- Marc Diepold[1],
- Luis M. P. Fernandes ORCID: orcid.org/0000-0002-7061-8768[6],
- Beatrice Franke[1] [nAff13],
- Sandrine Galtier[8] [nAff14],
- Andrea L. Gouvea[6],
- Johannes Götzfried[1],
- Thomas Graf ORCID: orcid.org/0000-0002-8466-073X[5],
- Theodor W. Hänsch[1,11],
- Jens Hartmann[11],
- Malte Hildebrandt[4],
- Paul Indelicato[8],
- Lucile Julien ORCID: orcid.org/0000-0001-7010-8314[8],
- Klaus Kirch[3,4],
- Andreas Knecht ORCID: orcid.org/0000-0002-3767-950X[4],
- Yi-Wei Liu ORCID: orcid.org/0000-0002-1090-0665[9],

- Jorge Machado ORCID: orcid.org/0000-0002-0383-4882[7],
- Cristina M. B. Monteiro[6],
- Françoise Mulhauser ORCID: orcid.org/0000-0003-2429-3314[1],
- Boris Naar[4],
- Tobias Nebel[1],
- François Nez ORCID: orcid.org/0000-0002-3478-7521[8],
- Joaquim M. F. dos Santos[6],
- José Paulo Santos ORCID: orcid.org/0000-0002-5890-0971[7],
- Csilla I. Szabo ORCID: orcid.org/0000-0002-6125-7948[8 nAff15],
- David Taqqu[3,4],
- João F. C. A. Veloso ORCID: orcid.org/0000-0002-7107-7203[10],
- Jan Vogelsang ORCID: orcid.org/0000-0002-9664-6265[1 nAff16],
- Andreas Voss[5],
- Birgit Weichelt[5],
- Randolf Pohl ORCID: orcid.org/0000-0001-6435-659X[1,2],
- Aldo Antognini ORCID: orcid.org/0000-0002-1837-0419[3,4] &
- Franz Kottmann[3,4]

Nature **volume 589**, pages527–531(2021)Cite this article

- 275 Accesses
- 182 Altmetric
- Metrics details

Subjects

- Exotic atoms and molecules
- Experimental nuclear physics

Abstract

The energy levels of hydrogen-like atomic systems can be calculated with great precision. Starting from their quantum mechanical solution, they have

been refined over the years to include the electron spin, the relativistic and quantum field effects, and tiny energy shifts related to the complex structure of the nucleus. These energy shifts caused by the nuclear structure are vastly magnified in hydrogen-like systems formed by a negative muon and a nucleus, so spectroscopy of these muonic ions can be used to investigate the nuclear structure with high precision. Here we present the measurement of two 2S–2P transitions in the muonic helium-4 ion that yields a precise determination of the root-mean-square charge radius of the α particle of 1.67824(83) femtometres. This determination from atomic spectroscopy is in excellent agreement with the value from electron scattering[1], but a factor of 4.8 more precise, providing a benchmark for few-nucleon theories, lattice quantum chromodynamics and electron scattering. This agreement also constrains several beyond-standard-model theories proposed to explain the proton-radius puzzle[2,3,4,5], in line with recent determinations of the proton charge radius[6,7,8,9], and establishes spectroscopy of light muonic atoms and ions as a precise tool for studies of nuclear properties.

Access through your institution
Change institution
Buy or subscribe

Access options

Subscribe to Journal

Get full journal access for 1 year

$199.00

only $3.90 per issue

Subscribe

All prices are NET prices.
VAT will be added later in the checkout.

Rent or Buy article

Get time limited or full article access on ReadCube.

from$8.99

Rent or Buy

All prices are NET prices.

Additional access options:

- Log in
- Access through your institution
- Learn about institutional subscriptions

Fig. 1: Energy-level scheme and experimental setup.

Fig. 2: The measured transitions.

Data availability

Reasonable requests for data should be addressed to R.P.

Code availability

Reasonable requests for computer code should be addressed to the corresponding authors.

References

1. 1.

   Sick, I. Precise root-mean-square radius of ^{4}He. *Phys. Rev. C* **77**, 041302 (2008).

   ADS Google Scholar

2. 2.

   Pohl, R. et al. The size of the proton. *Nature* **466**, 213–216 (2010).

   ADS CAS Google Scholar

3. 3.

   Antognini, A. et al. Proton structure from the measurement of 2S–2P transition frequencies of muonic hydrogen. *Science* **339**, 417–420 (2013).

   ADS CAS PubMed Google Scholar

4. 4.

   Pohl, R. et al. Muonic hydrogen and the proton radius puzzle. *Annu. Rev. Nucl. Part. Sci*. **63**, 175–204 (2013).

   ADS CAS Google Scholar

5. 5.

   Carlson, C. E. The proton radius puzzle. *Prog. Part. Nucl. Phys*. **82**, 59–77 (2015).

   ADS CAS Google Scholar

6. 6.

Pohl, R. et al. Laser spectroscopy of muonic deuterium. *Science* **353**, 669–673 (2016).

ADS CAS Google Scholar

7. 7.

Beyer, A. et al. The Rydberg constant and proton size from atomic hydrogen. *Science* **358**, 79–85 (2017).

ADS MathSciNet CAS PubMed MATH Google Scholar

8. 8.

Bezginov, N. et al. A measurement of the atomic hydrogen Lamb shift and the proton charge radius. *Science* **365**, 1007–1012 (2019).

ADS CAS PubMed Google Scholar

9. 9.

Xiong, W. et al. A small proton charge radius from an electron–proton scattering experiment. *Nature* **575**, 147–150 (2019).

ADS CAS PubMed Google Scholar

10. 10.

Sick, I. Elastic electron scattering from light nuclei. *Prog. Part. Nucl. Phys*. **47**, 245–318 (2001).

ADS CAS Google Scholar

11. 11.

Leidemann, W. & Orlandini, G. Modern ab initio approaches and applications in few-nucleon physics with $A \geq 4$. *Prog. Part. Nucl. Phys*. **68**, 158–214 (2013).

ADS CAS Google Scholar

12. 12.

Fleurbaey, H. et al. New measurement of the 1S–3S transition frequency of hydrogen: contribution to the proton charge radius puzzle. *Phys. Rev. Lett*. **120**, 183001 (2018).

ADS CAS PubMed Google Scholar

13. 13.

Shiner, D., Dixson, R. & Vedantham, V. Three-nucleon charge radius: a precise laser determination using ^{3}He. *Phys. Rev. Lett*. **74**, 3553–3556 (1995).

ADS CAS PubMed Google Scholar

14. 14.

Cancio Pastor, P. et al. Frequency metrology of helium around 1083 nm and determination of the nuclear charge radius. *Phys. Rev. Lett*. **108**, 143001 (2012).

ADS CAS PubMed Google Scholar

15. 15.

Lu, Z. T. et al. Laser probing of neutron-rich nuclei in light atoms. *Rev. Mod. Phys*. **85**, 1383–1400 (2013).

ADS CAS Google Scholar

16. 16.

Rengelink, R. J. et al. Precision spectroscopy of helium in a magic wavelength optical dipole trap. *Nat. Phys*. **14**, 1132–1137 (2018).

CAS Google Scholar

17. 17.

Zheng, X. et al. Measurement of the frequency of the 2^3S–2^3P transition of ^4He. *Phys. Rev. Lett*. **119**, 263002 (2017).

ADS CAS PubMed Google Scholar

18. 18.

Huang, Y. J. et al. Precision laser spectroscopy of the 2^1S_0–3^1D_2 two-photon transition in ^3He. *Phys. Rev. A* **101**, 062507 (2020).

ADS CAS Google Scholar

19. 19.

Patkóš, V., Yerokhin, V. A. & Pachucki, K. Nonradiative $\alpha^7 m$ QED effects in Lamb shift of helium triplet states. *Phys. Rev. A* **101**, 062516 (2020).

ADS Google Scholar

20. 20.

Herrmann, M. et al. Feasibility of coherent xuv spectroscopy on the 1S–2S transition in singly ionized helium. *Phys. Rev. A* **79**, 052505 (2009).

ADS Google Scholar

21. 21.

Krauth, J. J. et al. Paving the way for fundamental physics tests with singly-ionized helium. *Proc. Sci*. **353**, 049 (2019).

Google Scholar

22. 22.

Lamb, W. E. & Retherford, R. C. Fine structure of the hydrogen atom by a microwave method. *Phys. Rev*. **72**, 241–243 (1947).

ADS CAS Google Scholar

23. 23.

Diepold, M. et al. Theory of the Lamb shift and fine structure in muonic ^{4}He ions and the muonic ^{3}He–^{4}He isotope shift. *Ann. Phys*. **396**, 220–244 (2018).

ADS CAS Google Scholar

24. 24.

Faustov, R. N. et al. Radiative nonrecoil nuclear finite size corrections of order $\alpha(Z\alpha)^5$ to the Lamb shift in light muonic atoms. *Phys. Lett. B* **775**, 79–83 (2017).

ADS CAS Google Scholar

25. 25.

Sick, I. Zemach moments of ^{3}He and ^{4}He. *Phys. Rev. C* **90**, 064002 (2014).

ADS Google Scholar

26. 26.

Ji, C. et al. Ab initio calculation of nuclear-structure corrections in muonic atoms. *J. Phys. G* **45**, 093002 (2018).

ADS Google Scholar

27. 27.

Pachucki, K., Patkóš, V. & Yerokhin, V. A. Three-photon-exchange nuclear structure correction in hydrogenic systems. *Phys. Rev. A* **97**,

062511 (2018).

ADS CAS Google Scholar

28. 28.

Dittus, F. B. *Experimentelle Untersuchung über Bildung und Zerfall myonischer Heliumionen im metastabilen 2S-Zustand*. PhD thesis, ETH Zurich (1985).

29. 29.

Ludhova, L. et al. Muonic hydrogen cascade time and lifetime of the short-lived 2S state. *Phys. Rev. A* **75**, 040501 (2007).

ADS Google Scholar

30. 30.

von Arb, H. P. et al. Measurement of the lifetime and quenching rate of metastable 2S muonic helium ions. *Phys. Lett. B* **136**, 232–236 (1984).

ADS Google Scholar

31. 31.

Diepold, M. et al. Improved X-ray detection and particle identification with avalanche photodiodes. *Rev. Sci. Instrum*. **86**, 053102 (2015).

ADS PubMed Google Scholar

32. 32.

Amaro, P. et al. Quantum interference effects in laser spectroscopy of muonic hydrogen, deuterium, and helium-3. *Phys. Rev. A* **92**, 022514 (2015).

ADS Google Scholar

33. 33.

Ji, C. et al. Nuclear polarization corrections to the μ^4He^+ Lamb shift. *Phys. Rev. Lett*. **111**, 143402 (2013).

ADS CAS PubMed Google Scholar

34. 34.

Carlson, C. E., Gorchtein, M. & Vanderhaeghen, M. Nuclear-structure contribution to the Lamb shift in muonic deuterium. *Phys. Rev. A* **89**, 022504 (2014).

ADS Google Scholar

35. 35.

Nevo Dinur, N. et al. Zemach moments and radii of $^{2,3}H$ and $^{3,4}He$. *Phys. Rev. C* **99**, 034004 (2019).

ADS CAS Google Scholar

36. 36.

Ji, C. et al. Nuclear polarization effects in muonic atoms. *Few Body Syst*. **55**, 917–921 (2014).

ADS CAS Google Scholar

37. 37.

Bacca, S. Electromagnetic reactions and few-nucleon dynamics. *EPJ Web Conf*. **66**, 01002 (2014).

Google Scholar

38. 38.

Carboni, G. et al. Precise measurement of the $2S_{1/2}$–$2P_{3/2}$ splitting in the $(\mu^{-4}He)^{+}$ muonic ion. *Nucl. Phys. A* **278**, 381–386 (1977).

ADS Google Scholar

39. 39.

Carboni, G. et al. Measurement of the $2S_{1/2}$–$2P_{1/2}$ splitting in the $(\mu^{-4}He)^{+}$ muonic ion. *Phys. Lett. B* **73**, 229–231 (1978).

ADS Google Scholar

40. 40.

Hauser, P. et al. Search for the 2S–2P energy difference in muonic ^{4}He ions. *Phys. Rev. A* **46**, 2363–2377 (1992).

ADS CAS PubMed Google Scholar

41. 41.

Batell, B., McKeen, D. & Pospelov, M. New parity-violating muonic forces and the proton charge radius. *Phys. Rev. Lett*. **107**, 011803 (2011).

ADS PubMed Google Scholar

42. 42.

Tucker-Smith, D. & Yavin, I. Muonic hydrogen and MeV forces. *Phys. Rev. D* **83**, 101702 (2011).

ADS Google Scholar

43. 43.

Miller, G. A. Nonperturbative lepton-sea fermions in the nucleon and the proton radius puzzle. *Phys. Rev. C* **91**, 055204 (2015).

ADS Google Scholar

44. 44.

Wang, L. B. & Ni, W. T. Proton radius puzzle and large extra dimensions. *Mod. Phys. Lett. A* **28**, 1350094 (2013).

ADS Google Scholar

45. 45.

Miller, G. A. Proton polarizability contribution: muonic hydrogen Lamb shift and elastic scattering. *Phys. Lett. B* **718**, 1078–1082 (2013).

ADS CAS Google Scholar

46. 46.

Carlson, C. E. & Freid, M. Extending theories on muon-specific interactions. *Phys. Rev. D* **92**, 095024 (2015).

ADS Google Scholar

47. 47.

Jentschura, U. D. Light sea fermions in electron–proton and muon–proton interactions. *Phys. Rev. A* **88**, 062514 (2013).

ADS Google Scholar

48. 48.

Liu, Y. S., Cloët, I. C. & Miller, G. A. Eta decay and muonic puzzles. *Nucl. Phys. B* **944**, 114638 (2019).

CAS MATH Google Scholar

49. 49.

Marcucci, L. E. et al. Electromagnetic structure of few-nucleon ground states. *J. Phys. G* **43**, 023002 (2016).

ADS Google Scholar

50. 50.

Ekström, A. et al. Accurate nuclear radii and binding energies from a chiral interaction. *Phys. Rev. C* **91**, 051301 (2015).

ADS Google Scholar

51. 51.

Gazit, D., Quaglioni, S. & Navrátil, P. Three-nucleon low-energy constants from the consistency of interactions and currents in chiral effective field theory. *Phys. Rev. Lett*. **103**, 102502 (2009).

ADS PubMed Google Scholar

52. 52.

Karshenboim, S. G. et al. The Lamb shift of the 1s state in hydrogen: two-loop and three-loop contributions. *Phys. Lett. B* **795**, 432–437 (2019).

ADS CAS Google Scholar

53. 53.

Yerokhin, V. A., Pachucki, K. & Patkóš, V. Theory of the Lamb shift in hydrogen and light hydrogen-like ions. *Ann. Phys*. **531**, 1800324 (2019).

Google Scholar

54. 54.

Jentschura, U. D. Muonic bound systems, virtual particles, and proton radius. *Phys. Rev. A* **92**, 012123 (2015).

ADS Google Scholar

55. 55.

Miller, G. A. Defining the proton radius: a unified treatment. *Phys. Rev. C* **99**, 035202 (2019).

ADS CAS Google Scholar

56. 56.

Vogelsang, J. et al. Multipass laser cavity for efficient transverse illumination of an elongated volume. *Opt. Express* **22**, 13050–13062 (2014).

ADS CAS PubMed Google Scholar

57. 57.

Ludhova, L. et al. Planar LAAPDs: temperature dependence, performance, and application in low-energy X-ray spectroscopy. *Nucl. Instrum. Methods Phys. Rev. A* **540**, 169–179 (2005).

ADS CAS Google Scholar

58. 58.

Borie, E. Lamb shift in light muonic atoms – revisited. Preprint at https://arxiv.org/abs/1103.1772 (2014).

59. 59.

Krutov, A. et al. Theory of the Lamb shift in muonic helium ions. *J. Exp. Theor. Phys*. **120**, 73–90 (2015).

ADS CAS Google Scholar

60. 60.

Karshenboim, S. G., Ivanov, V. G. & Korzinin, E. Y. Relativistic recoil corrections to the electron-vacuum-polarization contribution in light muonic atoms. *Phys. Rev. A* **85**, 032509 (2012).

ADS Google Scholar

61. 61.

Korzinin, E. Y., Ivanov, V. G. & Karshenboim, S. G. $\alpha^2(Z\alpha)^4 m$ contributions to the Lamb shift and the fine structure in light muonic atoms. *Phys. Rev. D* **88**, 125019 (2013).

ADS Google Scholar

62. 62.

Jentschura, U. D. & Wundt, B. J. Semi-analytic approach to higher-order corrections in simple muonic bound systems: vacuum polarisation, self-energy and radiative-recoil. *Eur. Phys. J. D* **65**, 357–366 (2011).

ADS CAS Google Scholar

63. 63.

Jentschura, U. D. Proton radius, Darwin–Foldy term and radiative corrections. *Eur. Phys. J. D* **61**, 7–14 (2011).

ADS CAS Google Scholar

64. 64.

Friar, J. L. Nuclear finite-size effects in light muonic atoms. *Ann. Phys*. **122**, 151–196 (1979).

ADS CAS Google Scholar

Download references

Acknowledgements

This work was performed at HIPA at PSI. We thank the accelerator and beamline support groups for excellent conditions. We also thank L. Simons, U. Röser, M. Nüssli, H. v. Gunten, B. Zehr, W. Lustermann, A. Gendotti, A. Müller, F. Barchetti, B. van den Brandt, P. Schurter, M. Horisberger, A. Weber, S. Spielmann-Jäggi, U. Greuter, P.-R. Kettle, S. Ritt, W. Simons, K. Linner, H. Brückner, K. S. E. Eikema and the PSI, ETH and MPQ workshops and support groups for their help. We acknowledge the support of the following grants: European Research Council (ERC) through StG. 279765 and CoG. 725039, Deutsche Forschungsgemeinschaft (DFG, German Research Foundation) under Germany's Excellence Initiative EXC 1098 PRISMA (194673446) and Excellence Strategy EXC PRISMA+ (390831469), EU Horizon 2020 innovation programme STRONG-2020 (grant agreement number 824093), DFG_GR_3172/9–1, MOST of Taiwan under contract number 106-2112-M-007 -021 -MY3, Fundação para a Ciência e a Tecnologia (FCT), Portugal, and FEDER through COMPETE in the framework of project numbers PTDC/FIS-NUC/0843/2012, PTDC/FIS-NUC/1534/2014, PTDC/FIS-AQM/29611/2017, PEstOE/FIS/UI0303/2011, PTDC/FIS/117606/2010 and UID/04559/2020 (LIBPhys), contract numbers SFRH/BPD/92329/2013, SFRH/BD/52332/2013, SFRH/BD/66731/2009 and SFRH/BPD/76842/2011, and by SNF 200021L_138175, SNF 200020_159755 and SNF 200021_165854, as well as the ETH-FAST initiative as part of the NCCR MUST programme.

Author information

Author notes

1. Julian J. Krauth

   Present address: LaserLaB, Department of Physics and Astronomy, Vrije Universiteit, Amsterdam, The Netherlands

2. Beatrice Franke

   Present address: TRIUMF, Vancouver, British Columbia, Canada

3. Sandrine Galtier

   Present address: Institut Lumière Matière, University of Lyon, Université Claude Bernard Lyon 1, CNRS, Villeurbanne, France

4. Csilla I. Szabo

   Present address: Theiss Research, La Jolla, CA, USA

5. Jan Vogelsang

   Present address: Department of Physics, Lund University, Lund, Sweden

Affiliations

1. Max Planck Institute of Quantum Optics, Garching, Germany

   Julian J. Krauth, Marc Diepold, Beatrice Franke, Johannes Götzfried, Theodor W. Hänsch, Françoise Mulhauser, Tobias Nebel, Jan Vogelsang & Randolf Pohl

2. QUANTUM, Institut für Physik & Exzellenzcluster PRISMA, Johannes Gutenberg-Universität Mainz, Mainz, Germany

   Julian J. Krauth & Randolf Pohl

3. Institute for Particle Physics and Astrophysics, ETH Zurich, Zurich, Switzerland

   Karsten Schuhmann, Klaus Kirch, David Taqqu, Aldo Antognini & Franz Kottmann

4. Paul Scherrer Institute, Villigen, Switzerland

Karsten Schuhmann, Andreas J. Dax, Malte Hildebrandt, Klaus Kirch, Andreas Knecht, Boris Naar, David Taqqu, Aldo Antognini & Franz Kottmann

5. Institut für Strahlwerkzeuge, Universität Stuttgart, Stuttgart, Germany

   Marwan Abdou Ahmed, Thomas Graf, Andreas Voss & Birgit Weichelt

6. LIBPhys-UC, Department of Physics, University of Coimbra, Coimbra, Portugal

   Fernando D. Amaro, Luis M. P. Fernandes, Andrea L. Gouvea, Cristina M. B. Monteiro & Joaquim M. F. dos Santos

7. Laboratory for Instrumentation, Biomedical Engineering and Radiation Physics (LIBPhys-UNL), Department of Physics, NOVA School of Science and Technology, NOVA University Lisbon, Caparica, Portugal

   Pedro Amaro, Jorge Machado & José Paulo Santos

8. Laboratoire Kastler Brossel, Sorbonne Université, CNRS, ENS-PSL Research University, Collège de France, Paris, France

   François Biraben, Sandrine Galtier, Paul Indelicato, Lucile Julien, François Nez & Csilla I. Szabo

9. Physics Department, National Tsing Hua University, Hsincho, Taiwan

   Tzu-Ling Chen & Yi-Wei Liu

10. i3N, Universidade de Aveiro, Aveiro, Portugal

    Daniel S. Covita & João F. C. A. Veloso

11. Ludwig-Maximilians-Universität, Fakultät für Physik, Munich, Germany

    Theodor W. Hänsch & Jens Hartmann

Authors

1. Julian J. Krauth
   View author publications

   You can also search for this author in PubMed Google Scholar

2. Karsten Schuhmann
   View author publications

   You can also search for this author in PubMed Google Scholar

3. Marwan Abdou Ahmed
   View author publications

   You can also search for this author in PubMed Google Scholar

4. Fernando D. Amaro
   View author publications

   You can also search for this author in PubMed Google Scholar

5. Pedro Amaro
   View author publications

   You can also search for this author in PubMed Google Scholar

6. François Biraben
   View author publications

   You can also search for this author in PubMed Google Scholar

7. Tzu-Ling Chen
   View author publications

   You can also search for this author in PubMed Google Scholar

8. Daniel S. Covita
   View author publications

You can also search for this author in PubMed Google Scholar

9. Andreas J. Dax
   View author publications

   You can also search for this author in PubMed Google Scholar

10. Marc Diepold
    View author publications

    You can also search for this author in PubMed Google Scholar

11. Luis M. P. Fernandes
    View author publications

    You can also search for this author in PubMed Google Scholar

12. Beatrice Franke
    View author publications

    You can also search for this author in PubMed Google Scholar

13. Sandrine Galtier
    View author publications

    You can also search for this author in PubMed Google Scholar

14. Andrea L. Gouvea
    View author publications

    You can also search for this author in PubMed Google Scholar

15. Johannes Götzfried
    View author publications

    You can also search for this author in PubMed Google Scholar

16. Thomas Graf
    View author publications

You can also search for this author in PubMed Google Scholar

17. Theodor W. Hänsch
View author publications

You can also search for this author in PubMed Google Scholar

18. Jens Hartmann
View author publications

You can also search for this author in PubMed Google Scholar

19. Malte Hildebrandt
View author publications

You can also search for this author in PubMed Google Scholar

20. Paul Indelicato
View author publications

You can also search for this author in PubMed Google Scholar

21. Lucile Julien
View author publications

You can also search for this author in PubMed Google Scholar

22. Klaus Kirch
View author publications

You can also search for this author in PubMed Google Scholar

23. Andreas Knecht
View author publications

You can also search for this author in PubMed Google Scholar

24. Yi-Wei Liu
View author publications

You can also search for this author in PubMed Google Scholar

25. Jorge Machado
View author publications

You can also search for this author in PubMed Google Scholar

26. Cristina M. B. Monteiro
View author publications

You can also search for this author in PubMed Google Scholar

27. Françoise Mulhauser
View author publications

You can also search for this author in PubMed Google Scholar

28. Boris Naar
View author publications

You can also search for this author in PubMed Google Scholar

29. Tobias Nebel
View author publications

You can also search for this author in PubMed Google Scholar

30. François Nez
View author publications

You can also search for this author in PubMed Google Scholar

31. Joaquim M. F. dos Santos
View author publications

You can also search for this author in PubMed Google Scholar

32. José Paulo Santos
View author publications

You can also search for this author in PubMed Google Scholar

33. Csilla I. Szabo
View author publications

You can also search for this author in PubMed Google Scholar

34. David Taqqu
View author publications

You can also search for this author in PubMed Google Scholar

35. João F. C. A. Veloso
View author publications

You can also search for this author in PubMed Google Scholar

36. Jan Vogelsang
View author publications

You can also search for this author in PubMed Google Scholar

37. Andreas Voss
View author publications

You can also search for this author in PubMed Google Scholar

38. Birgit Weichelt
View author publications

You can also search for this author in PubMed Google Scholar

39. Randolf Pohl
View author publications

You can also search for this author in PubMed Google Scholar

40. Aldo Antognini
View author publications

You can also search for this author in PubMed Google Scholar

41. Franz Kottmann
View author publications

You can also search for this author in PubMed Google Scholar

Contributions

J.J.K., K.S., M.A.A., F.B., T.-L.C., M.D., S.G., T.G., T.W.H., L.J., K.K., Y.-W.L., B.N., F.N., D.T., J.V., A.V., B.W., R.P., A.A. and F.K. designed, built and operated parts of the laser system. J.J.K., K.S., F.D.A., M.D., L.M.P.F., B.F., A.L.G., M.H., K.K., A.K., Y.-W.L., J.M., C.M.B.M., F.M., T.N., F.N., J.M.F.S., J.P.S., D.T., J.F.C.A.V., R.P., A.A. and F.K. planned, built and set up the various detectors of the experiment. J.J.K., K.S., F.D.A., P.A., D.S.C., M.D., L.M.P.F., B.F., J.G., J.H., M.H., K.K., A.K., J.M., F.M., J.P.S., C.I.S., D.T., R.P., A.A. and F.K. designed, built, set up and operated the muon beam line. J.J.K., K.S., F.D.A., M.D., L.M.P.F., B.F., A.K., J.M., C.M.B.M., F.M., F.N., J.M.F.S., D.T., R.P., A.A. and F.K. designed and implemented the electronics used in the experiment. J.J.K., P.A., M.D., A.K., J.P.S., J.V., R.P. and A.A. set up the computing infrastructure, wrote software and realized the data acquisition system. J.J.K., K.S., F.D.A., P.A., D.S.C., A.J.D., M.D., L.M.P.F., B.F., S.G., J.G., A.L.G., J.H., P.I., L.J., A.K., Y.-W.L., J.M., C.M.B.M., B.N., F.N., J.M.F.S., J.P.S., C.I.S., D.T., J.F.C.A.V., R.P., A.A. and F.K. took part in the months-long data taking runs. J.J.K., P.A., M.D., B.F., P.I., J.P.S., D.T., R.P., A.A. and F.K. did work on theory. J.J.K., K.S., M.D., L.M.P.F., P.I., C.M.B.M., F.N., J.M.F.S., R.P., A.A. and F.K. analysed the data J.J.K., R.P., A.A. and F.K. drafted this manuscript. The manuscript was then read, improved and finally acknowledged by the other authors.

Corresponding authors

Correspondence to Julian J. Krauth or Randolf Pohl or Aldo Antognini.

Ethics declarations

Competing interests

The authors declare no competing interests.

Additional information

Peer review information *Nature* thanks Wim Ubachs and the other, anonymous, reviewer(s) for their contribution to the peer review of this work. Peer reviewer reports are available.

Publisher's note Springer Nature remains neutral with regard to jurisdictional claims in published maps and institutional affiliations.

Supplementary information

Peer Review File

Rights and permissions

Reprints and Permissions

About this article

Check for updates

Cite this article

Krauth, J.J., Schuhmann, K., Ahmed, M.A. *et al.* Measuring the α-particle charge radius with muonic helium-4 ions. *Nature* **589,** 527–531 (2021). https://doi.org/10.1038/s41586-021-03183-1

Download citation

- Received: 03 July 2020
- Accepted: 24 November 2020
- Published: 27 January 2021
- Issue Date: 28 January 2021
- DOI: https://doi.org/10.1038/s41586-021-03183-1

Comments

By submitting a comment you agree to abide by our Terms and Community Guidelines. If you find something abusive or that does not comply with our terms or guidelines please flag it as inappropriate.

Access through your institution
Change institution
Buy or subscribe

Associated Content

Nature | News & Views

Helium nucleus measured with record precision

- Wilfried Nörtershäuser

This article was downloaded by **calibre** from https://www.nature.com/articles/s41586-021-03183-1

- Article
- Published: 27 January 2021

Metastability of diamond ramp-compressed to 2 terapascals

- A. Lazicki ORCID: orcid.org/0000-0002-9821-6074[1],
- D. McGonegle[2],
- J. R. Rygg ORCID: orcid.org/0000-0002-0605-7847[3,4,5],
- D. G. Braun[1],
- D. C. Swift[1],
- M. G. Gorman[1],
- R. F. Smith[1],
- P. G. Heighway[2],
- A. Higginbotham[6],
- M. J. Suggit[2],
- D. E. Fratanduono[1],
- F. Coppari ORCID: orcid.org/0000-0003-1592-3898[1],
- C. E. Wehrenberg[1],
- R. G. Kraus[1],
- D. Erskine ORCID: orcid.org/0000-0002-7094-458X[1],
- J. V. Bernier[1],
- J. M. McNaney[1],
- R. E. Rudd ORCID: orcid.org/0000-0002-6632-2681[1],
- G. W. Collins[3,4,5],
- J. H. Eggert[1] &
- J. S. Wark ORCID: orcid.org/0000-0003-3055-3223[2]

Nature **volume 589**, pages532–535(2021)Cite this article

- 232 Accesses

- 130 Altmetric
- Metrics details

Subjects

- Exoplanets
- Structure of solids and liquids

Abstract

Carbon is the fourth-most prevalent element in the Universe and essential for all known life. In the elemental form it is found in multiple allotropes, including graphite, diamond and fullerenes, and it has long been predicted that even more structures can exist at pressures greater than those at Earth's core[1,2,3]. Several phases have been predicted to exist in the multi-terapascal regime, which is important for accurate modelling of the interiors of carbon-rich exoplanets[4,5]. By compressing solid carbon to 2 terapascals (20 million atmospheres; more than five times the pressure at Earth's core) using ramp-shaped laser pulses and simultaneously measuring nanosecond-duration time-resolved X-ray diffraction, we found that solid carbon retains the diamond structure far beyond its regime of predicted stability. The results confirm predictions that the strength of the tetrahedral molecular orbital bonds in diamond persists under enormous pressure, resulting in large energy barriers that hinder conversion to more-stable high-pressure allotropes[1,2], just as graphite formation from metastable diamond is kinetically hindered at atmospheric pressure. This work nearly doubles the highest pressure at which X-ray diffraction has been recorded on any material.

Access through your institution
Change institution
Buy or subscribe

Access options

Subscribe to Journal

Get full journal access for 1 year

$199.00

only $3.90 per issue

Subscribe

All prices are NET prices.
VAT will be added later in the checkout.

Rent or Buy article

Get time limited or full article access on ReadCube.

from$8.99

Rent or Buy

All prices are NET prices.

Additional access options:

- Log in
- Access through your institution
- Learn about institutional subscriptions

Fig. 1: Carbon phase diagram summarizing DFT-predicted phase boundaries[46,47,48], Hugoniot data[17] and predicted thermodynamic paths[35,48].

Fig. 2: Summary of experimental data.

Fig. 3: Data compared to theoretical predictions.

Fig. 4: FC8 and BC8 crystal structures.

Data availability

The source data shown in the figures are provided, where not already summarized in Extended Data Table 1. Additional data are available from the corresponding author upon request. Source data are provided with this paper.

Code availability

The data analysis code implementing the methods described in ref. [25] is publicly available at https://github.com/HEXRD.

References

1. 1.

Scandolo, S., Chiarotti, G. L. & Tosatti, E. SC4: a metallic phase of carbon at terapascal pressures. *Phys. Rev. B* **53**, 5051–5054 (1996).

ADS CAS Google Scholar

2. 2.

Sun, J., Klug, D. D. & Martoňák, R. Structural transformations in carbon under extreme pressure: beyond diamond. *J. Chem. Phys*. **130**, 194512 (2009).

ADS PubMed PubMed Central Google Scholar

3. 3.

Martinez-Canales, M., Pickard, C. J. & Needs, R. J. Thermodynamically stable phases of carbon at multiterapascal pressures. *Phys. Rev. Lett*. **108**, 045704 (2012).

ADS PubMed PubMed Central Google Scholar

4. 4.

Madhusudhan, N., Lee, K. K. M. & Mousis, O. A possible carbon-rich interior in super-earth 55 Cancri e. *Astrophys. J*. **759**, L40 (2012).

ADS Google Scholar

5. 5.

Mashian, N. & Loeb, A. CEMP stars: possible hosts to carbon planets in the early universe. *Mon. Not. R. Astron. Soc*. **460**, 2482–2491 (2016).

ADS CAS Google Scholar

6. 6.

Frondel, C. & Marvin, U. B. Lonsdaleite, a hexagonal polymorph of diamond. *Nature* **214**, 587–589 (1967).

ADS CAS Google Scholar

7. 7.

Narayan, J. & Bhaumik, A. Novel phase of carbon, ferromagnetism, and conversion into diamond. *J. Appl. Phys*. **118**, 215303 (2015).

ADS Google Scholar

8. 8.

Johnston, R. L. & Hoffmann, R. Superdense carbon, C8: supercubane or analog of γ-silicon? *J. Am. Chem. Soc*. **111**, 810–819 (1989).

CAS Google Scholar

9. 9.

Mailhiot, C. & McMahan, A. K. Atmospheric-pressure stability of energetic phases of carbon. *Phys. Rev. B* **44**, 11578–11591 (1991).

ADS CAS Google Scholar

10. 10.

Oganov, A. R. & Glass, C. W. Crystal structure prediction using ab initio evolutionary techniques: principles and applications. *J. Chem. Phys*. **124**, 244704 (2006).

ADS PubMed PubMed Central Google Scholar

11. 11.

Oganov, A. R., Hemley, R. J., Hazen, R. M. & Jones, A. P. Structure, bonding, and mineralogy of carbon at extreme conditions. *Rev. Mineral. Geochem*. **75**, 47–77 (2013).

CAS Google Scholar

12. 12.

Yin, M. T. & Cohen, M. L. Will diamond transform under megabar pressures? *Phys. Rev. Lett*. **50**, 2006–2009 (1983).

ADS CAS Google Scholar

13. 13.

Biswas, R. & Martin, R. M., Needs, R. J. & Nielsen, O. H. Stability and electronic proper- ties of complex structures of silicon and carbon under pressure: density-functional calculations. *Phys. Rev. B* **35**, 9559–9568 (1987).

ADS CAS Google Scholar

14. 14.

Fahy, S. & Louie, S. G. High-pressure structural and electronic properties of carbon. *Phys. Rev. B* **36**, 3373–3385 (1987).

ADS CAS Google Scholar

15. 15.

Dubrovinsky, L., Dubrovinskaia, N., Prakapenka, V. B. & Abakumov, A. M. Implementation of micro-ball nanodiamond anvils for high-pressure studies above 6 Mbar. *Nat. Commun*. **3**, 1163 (2012).

ADS PubMed PubMed Central Google Scholar

16. 16.

Wu, H., Luo, X., Wen, L., Sun, H. & Chen, C. Extreme static compression of carbon to terapascal pressures. *Carbon* **144**, 161–170 (2019).

CAS Google Scholar

17. 17.

Eggert, J. H. et al. Melting temperature of diamond at ultrahigh pressure. *Nat. Phys*. **6**, 40–43 (2010).

CAS Google Scholar

18. 18.

Swift, D. C. Numerical solution of shock and ramp compression for general material properties. *J. Appl. Phys*. **104**, 073536 (2008).

ADS Google Scholar

19. 19.

Smith, R. F. et al. Ramp compression of diamond to five terapascals. *Nature* **511**, 330–333 (2014).

ADS CAS PubMed PubMed Central Google Scholar

20. 20.

Knudson, M. D., Desjarlais, M. P. & Dolan, D. H. Shock-wave exploration of the high-pressure phases of carbon. *Science* **322**, 1822–1825 (2008).

ADS CAS PubMed PubMed Central Google Scholar

21. 21.

Barrios, M. A. et al. X-ray area backlighter development at the National Ignition Facility. *Rev. Sci. Instrum*. **85**, 11D502 (2014).

CAS PubMed PubMed Central Google Scholar

22. 22.

Coppari, F. et al. Optimized x-ray sources for x-ray diffraction measurements at the Omega Laser Facility. *Rev. Sci. Instrum*. **90**, 125113 (2019).

ADS CAS PubMed PubMed Central Google Scholar

23. 23.

Wark, J. S., Whitlock, R. R., Hauer, A. A., Swain, J. E. & Solone, P. J. Subnanosecond x-ray diffraction from laser-shocked crystals. *Phys. Rev. B* **40**, 5705–5714 (1989).

ADS CAS Google Scholar

24. 24.

Rygg, J. R. et al. Powder diffraction from solids in the terapascal regime. *Rev. Sci. Instrum*. **83**, 113904 (2012).

ADS CAS PubMed PubMed Central Google Scholar

25. 25.

Rygg, J. R. et al. X-ray diffraction at the National Ignition Facility. *Rev. Sci. Instrum*. **91**, 043902 (2020).

ADS CAS PubMed PubMed Central Google Scholar

26. 26.

Celliers, P. M. et al. Line-imaging velocimeter for shock diagnostics at the OMEGA laser facility. *Rev. Sci. Instrum*. **75**, 4916–4929 (2004).

ADS CAS Google Scholar

27. 27.

Rothman, S. D. et al. Measurement of the principal isentropes of lead and lead–antimony alloy to ~400 kbar by quasi-isentropic

compression. *J. Phys. D* **38**, 733–740 (2005).

ADS CAS Google Scholar

28. 28.

Bradley, D. K. et al. Diamond at 800 GPa. *Phys. Rev. Lett*. **102**, 075503 (2009).

ADS CAS PubMed PubMed Central Google Scholar

29. 29.

Coppari, F. et al. Experimental evidence for a phase transition in magnesium oxide at exoplanet pressures. *Nat. Geosci*. **6**, 926–929 (2013).

ADS CAS Google Scholar

30. 30.

Nelmes, R. J., McMahon, M. I., Wright, N. G., Allan, D. R. & Loveday, J. S. Stability and crystal structure of BC8 germanium. *Phys. Rev. B* **48**, 9883–9886 (1993).

ADS CAS Google Scholar

31. 31.

Kurakevych, O. O. et al. Synthesis of bulk BC8 silicon allotrope by direct transformation and reduced-pressure chemical pathways. *Inorg. Chem*. **55**, 8943–8950 (2016).

CAS PubMed PubMed Central Google Scholar

32. 32.

Turneaure, S. J., Sharma, S. M., Volz, T. J., Winey, J. M. & Gupta, Y. M. Transformation of shock-compressed graphite to hexagonal

diamond in nanoseconds. *Sci. Adv*. **3**, eaao3561 (2017).

PubMed PubMed Central Google Scholar

33. 33.

McWilliams, R. S. et al. Strength effects in diamond under shock compression from 0.1 to 1 TPa. *Phys. Rev. B* **81**, 014111 (2010).

ADS Google Scholar

34. 34.

Orlikowski, D., Correa, A. A., Schwegler, E. & Klepeis, J. E. A Steinberg-Guinan model for high-pressure carbon: diamond phase. *AIP Conf. Proc*. **955**, 247–250 (2007).

ADS CAS Google Scholar

35. 35.

Swift, D. C. et al. Equation of state and strength of diamond in high pressure ramp loading. Preprint at https://arxiv.org/abs/2004.03071 (2020).

36. 36.

Lang, J. M., Winey, J. M. & Gupta, Y. M. Strength and deformation of shocked diamond single crystals: orientation dependence. *Phys. Rev. B* **97**, 104106 (2018).

ADS CAS Google Scholar

37. 37.

Taylor, G. I. & Quinney, H. The latent energy remaining in a metal after cold working. *Proc. R. Soc. Lond. A* **143**, 307–326 (1934).

ADS Google Scholar

38. 38.

Suggit, M. J. et al. Nanosecond white-light Laue diffraction measurements of dislocation microstructure in shock-compressed single-crystal copper. *Nat. Commun*. **3**, 1224 (2012).

ADS PubMed PubMed Central Google Scholar

39. 39.

Heighway, P. G. et al. Nonisentropic release of a shocked solid. *Phys. Rev. Lett*. **123**, 245501 (2019).

ADS CAS Google Scholar

40. 40.

Ping, Y. et al. Solid iron compressed up to 560 GPa. *Phys. Rev. Lett*. **111**, 065501 (2013).

ADS CAS PubMed PubMed Central Google Scholar

41. 41.

Murphy, W. J., Higginbotham, A., Wark, J. S. & Park, N. Molecular dynamics simulations of the Debye-Waller effect in shocked copper. *Phys. Rev. B* **78**, 014109 (2008).

ADS Google Scholar

42. 42.

Ertel, K. et al. DiPOLE: A scalable laser architecture for pumping multi-Hz PW systems. *Proc. SPIE* **8780**, 288–292 (2013).

Google Scholar

43. 43.

Pellegrini, C. X-ray free-electron lasers: from dreams to reality. *Phys. Scr*. **T169**, 014004 (2016).

ADS Google Scholar

44. 44.

McBride, E. E. et al. Setup for meV-resolution inelastic x-ray scattering measurements and x-ray diffraction at the matter in extreme conditions endstation at the Linac Coherent Light Source. *Rev. Sci. Instrum*. **89**, 10F104 (2018)

CAS PubMed PubMed Central Google Scholar

45. 45.

Descamps, A. et al. An approach for the measurement of the bulk temperature of single crystal diamond using an X-ray free electron laser. *Sci. Rep.* **10**, 14564 (2020).

46. 46.

Wang, X., Scandolo, S. & Car, R. Carbon phase diagram from ab initio molecular dynamics. *Phys. Rev. Lett*. **95**, 185701 (2005).

ADS PubMed PubMed Central Google Scholar

47. 47.

Correa, A. A., Bonev, S. A. & Galli, G. Carbon under extreme conditions: phase boundaries and electronic properties from first-principles theory. *Proc. Natl Acad. Sci. USA* **103**, 1204–1208 (2006).

ADS CAS PubMed PubMed Central Google Scholar

48. 48.

Benedict, L. X. et al. Multiphase equation of state for carbon addressing high pressures and temperatures. *Phys. Rev. B* **89**, 224109

(2014).

ADS Google Scholar

49. 49.

Zimmerman, G., Kershaw, D., Bailey, D. & Harte, J. LASNEX code for inertial confinement fusion. *J. Opt. Soc. Am*. **68**, 549 (1978).

ADS Google Scholar

50. 50.

Boettger, J. C. *SESAME Equation Of State For Epoxy*. Report LA-12755-MS (Los Alamos National Laboratory, 1994).

51. 51.

Wild, Ch., Herres, N. & Koidl, P. Texture formation in polycrystalline diamond films. *J. Appl. Phys*. **68**, 973–978 (1990).

ADS CAS Google Scholar

52. 52.

Vedam, K. & Schmidt, E. D. D. Variation of refractive index of MgO with pressure to 7 kbar. *Phys. Rev*. **146**, 548–554 (1966).

ADS CAS Google Scholar

53. 53.

Lazicki, A. et al. X-ray diffraction of solid tin to 1.2 TPa. *Phys. Rev. Lett*. **115**, 075502 (2015).

ADS CAS PubMed PubMed Central Google Scholar

Download references

Acknowledgements

We acknowledge discussions with B. Remington, M. Millot and D. Klug, and we thank the National Ignition Facility staff and the National Ignition Facility Discovery Science programme. This work was performed under the auspices of the US Department of Energy by Lawrence Livermore National Laboratory under contract number DE-AC52-07NA27344. J.S.W. thanks the UK EPSRC for support under grants EP/J017256/1 and EP/S025065/1. D.McG. was supported by LLNS under contract number B595954. Partial funding for G.W.C. and J.R.R. was provided by NSF Physics Frontier Center award PHY-2020249 and DOE NNSA award DE-NA0003856.

Author information

Affiliations

1. Lawrence Livermore National Laboratory, Livermore, CA, USA

   A. Lazicki, D. G. Braun, D. C. Swift, M. G. Gorman, R. F. Smith, D. E. Fratanduono, F. Coppari, C. E. Wehrenberg, R. G. Kraus, D. Erskine, J. V. Bernier, J. M. McNaney, R. E. Rudd & J. H. Eggert

2. Department of Physics, Clarendon Laboratory, University of Oxford, Oxford, UK

   D. McGonegle, P. G. Heighway, M. J. Suggit & J. S. Wark

3. Laboratory for Laser Energetics, University of Rochester, Rochester, NY, USA

   J. R. Rygg & G. W. Collins

4. Department of Mechanical Engineering, University of Rochester, Rochester, NY, USA

   J. R. Rygg & G. W. Collins

5. Department of Physics and Astronomy, University of Rochester, Rochester, NY, USA

   J. R. Rygg & G. W. Collins

6. Department of Physics, University of York, York, UK

   A. Higginbotham

Authors

1. A. Lazicki
   View author publications

   You can also search for this author in PubMed Google Scholar

2. D. McGonegle
   View author publications

   You can also search for this author in PubMed Google Scholar

3. J. R. Rygg
   View author publications

   You can also search for this author in PubMed Google Scholar

4. D. G. Braun
   View author publications

   You can also search for this author in PubMed Google Scholar

5. D. C. Swift
   View author publications

   You can also search for this author in PubMed Google Scholar

6. M. G. Gorman
   View author publications

You can also search for this author in PubMed Google Scholar

7. R. F. Smith
   View author publications

   You can also search for this author in PubMed Google Scholar

8. P. G. Heighway
   View author publications

   You can also search for this author in PubMed Google Scholar

9. A. Higginbotham
   View author publications

   You can also search for this author in PubMed Google Scholar

10. M. J. Suggit
    View author publications

    You can also search for this author in PubMed Google Scholar

11. D. E. Fratanduono
    View author publications

    You can also search for this author in PubMed Google Scholar

12. F. Coppari
    View author publications

    You can also search for this author in PubMed Google Scholar

13. C. E. Wehrenberg
    View author publications

    You can also search for this author in PubMed Google Scholar

14. R. G. Kraus
    View author publications

You can also search for this author in PubMed Google Scholar

15. D. Erskine
    View author publications

    You can also search for this author in PubMed Google Scholar

16. J. V. Bernier
    View author publications

    You can also search for this author in PubMed Google Scholar

17. J. M. McNaney
    View author publications

    You can also search for this author in PubMed Google Scholar

18. R. E. Rudd
    View author publications

    You can also search for this author in PubMed Google Scholar

19. G. W. Collins
    View author publications

    You can also search for this author in PubMed Google Scholar

20. J. H. Eggert
    View author publications

    You can also search for this author in PubMed Google Scholar

21. J. S. Wark
    View author publications

    You can also search for this author in PubMed Google Scholar

Contributions

J.S.W. and J.H.E. conceived the work. A.L., D.McG., J.R.R., R.F.S., M.G.G., P.G.H., A.H. and M.J.S. performed the experiments. D.G.B. designed the laser pulse shapes. A.L. analysed the data with assistance from J.R.R., J.H.E., D.E.F., D.E. and J.V.B. D.C.S., F.C., C.E.W., R.G.K., J.M.McN., R.E.R. and G.W.C. contributed to the design of the work and interpretation of the data. A.L. and J.S.W. wrote the paper. All coauthors commented critically on the manuscript.

Corresponding author

Correspondence to A. Lazicki.

Ethics declarations

Competing interests

The authors declare no competing interests.

Additional information

Peer review information *Nature* thanks Philip Dalladay-Simpson and the other, anonymous, reviewer(s) for their contribution to the peer review of this work. Peer reviewer reports are available.

Publisher's note Springer Nature remains neutral with regard to jurisdictional claims in published maps and institutional affiliations.

Extended data figures and tables

Extended Data Fig. 1 Experimental configuration.

a, Cross-section of diffraction sample: a description of the sample layers for each shot is shown in Extended Data Table 1. **b**, TARDIS diagnostic geometry with X-ray source (XRS) beam and scattered Bragg peaks on the

image plate illustrated by red lines. **c**, Raw data scans of the three TARDIS image plates for shot N160315. Source data

Extended Data Fig. 2 Summary of reported X-ray diffraction data.

Image plates are background-subtracted and projected into azimuthal angle ϕ versus 2θ and stereographic space. The circular opening at the centre is a hole in the diagnostic through which the VISAR laser can pass. **a**, N160315 (about 0.8 TPa) has diffraction peaks from the FC8 sample and B2 MgO window. The model ideal diffraction pattern includes the structure factor, multiplicity, Lorentz polarization factor (for a flat powder sample in transmission), and an instrument broadening tuned to match the data (the peak widths are proportional to the spatial extent of the emitting plasma cloud around the X-ray source, which varies somewhat from shot to shot). The peak width FWHM is between 1° and 1.5°, which is consistent with our source size and typical shot-to-shot variation. We do not attempt to model the effects of texture or temperature, which are both important in this data. The high temperatures are primarily responsible for the intensity mismatch between the real and ideal diffraction data at high angle, owing to the Debye–Waller effect. The square-shaped features on the rectangular plate are an array of Ross-pair filters designed to constrain the spectrum of the background radiation. **b**, N150217 (1.02 TPa): two peaks consistent with the FC8 structure are evident (ideal pattern shown in blue). The large double rectangular feature centred on the VISAR hole (also seen in **c** and **d**) is a pinhole image of a region at the front of the TARDIS box that generates fluorescence when illuminated by the hard X-rays and fast electrons coming from the X-ray source. The diagnostic was redesigned after 2015 to eliminate this feature. The smaller rectangular feature centred around the direct beam spot (also seen in **c** and **d**) is a combination of fluorescence from the front face of a cylindrical shield positioned around the direct beam spot, to block image plate fluorescence, and the shadow of the fixturing holding the shield in place. The design of this shield was also subsequently improved. **c**, N150927 (1.18 TPa): in this shot there is evident overlap between the polycrystalline diamond diffraction, which shows up as continuous rings, and strongly textured diffraction from the single-crystal diamond windows. **d**, N150304 (1.38 TPa). **e**, N161211 (about 1.8 TPa). In

this shot, two spatially and temporally separated X-ray sources were used to yield two separate, easily distinguishable ring patterns, for the purpose of improving image plate calibration (the first pattern is from the undriven target and primarily picks up the scattering from the undriven Au heat shield). On this shot there is also a pattern of Laue spots evident on the image plates because the X-ray source has a broad, high-energy Bremsstrahlung tail that scatters off the windows, which are still undriven single crystals during the earlier X-ray exposure. Laue spots consistent with scattering of 5–25 keV radiation from {001}-oriented single crystal MgO are marked with black squares.

Extended Data Fig. 3 Summary of reported X-ray diffraction data.

a, N170304 (1.74 TPa): two peaks consistent with the FC8 structure are evident. **b**, N180214 (2.01 TPa): 2–3 peaks consistent with the FC8 structure are evident. The background is so high on this shot that diffraction is observed only when the single-crystal-like texture allows it to arise above the background, as is the case for the (111) peak, or the peak falls in a region of the image plate partially shielded from the ablation plasma background by the pinhole (further explained in Extended Data Fig. 7). This shot used a Zr (16.25 keV) X-ray source to measure diffraction at peak compression (XRS 1), so all peaks appear at lower angles compared to the rest of the shots with Ge (10.25 keV) X-ray sources. The second X-ray source (XRS 2) was Ge, and was fired before the compression wave entered the target, to capture diffraction from uncompressed hexagonal close-packed (hcp) Zr and FC8 diamond. These additional diffraction lines were used to improve the image plate angular calibration. The broadband Bremsstrahlung tail of the Ge X-ray source scattered off the uncompressed single-crystal diamond window to produce the Laue spots, marked with black squares in the stereographic projection. These positions are consistent with scattering from a {110}-oriented crystal, with an energy spanning 15–35 keV.

Extended Data Fig. 4 Laser drive intensities and their relationship to sample stress and image plate background.

a, The sample drive for all but the highest-stress shot N180214 used 16 overlapped beams at the National Ignition Facility with phase plates to produce a 0.9 mm × 1.2 mm elliptical spot when projected onto the sample. The transverse uniformity of the stress in the sample degrades with increasing stress. By 1.8 TPa, two-dimensional radiation-hydrodynamic simulations predict that the uniformity is still within 5% out to a radius of 400 μm but at the highest stress it becomes necessary to delay the lateral release waves by increasing the area of the drive initially. To accomplish this, we tile 8 of the beams to form an approximately uniform 1.8 mm × 1.8 mm square drive spot and use these beams to drive the sample to near 0.8 TPa, after which we drive to 2 TPa using 8 overlapped beams (cartoon inset). With this drive, simulations indicate that the stress is uniform to within 5% out to a radius of 300 μm and drops an additional 2–3% by a radius of 400 μm. The maximum sample radius for which an unobstructed ray may pass through the pinhole aperture is about 330 μm by peak compression (the sample has moved 200 μm closer to the aperture), so this transverse uniformity is adequate. For the highest power laser drives, high background levels on the image plates coming from X-rays produced in the laser-ablation process nearly overwhelm the X-ray diffraction data, and subsequent attempts to measure diffraction above 2 TPa were unsuccessful for that reason. The difficulty of achieving stresses of 2 TPa and higher is illustrated in **b**. The longitudinal stress produced from a given drive intensity increases in a sublinear fashion, while the increase in background from the ablation plasma is strongly superlinear. Image plate backgrounds shown in this figure were taken from the same regions on the image plate in each shot and were normalized by the relative transmission through the different sample and filter materials and thicknesses. Source data

Extended Data Fig. 5 VISAR summary and pressure inference.

a, VISAR velocity histories showing the velocity of the rear surface of the diamond window. In all cases the diamond elastic wave shocks the samples to an initial ~0.1 TPa before subsequent slower compression. By 2 TPa, the elastic wave is nearly overtaken by a strong growing shock that forms within the rear diamond tamper. **b**, Experimental diamond window free-surface velocity measurement and stress histories in the diamond sample inferred from characteristics analysis, compared to the LASNEX radiation-

hydrodynamic code predictions for shot N180214 (2.01 TPa). To achieve reasonable agreement with experimental breakout times and peak velocities, it was necessary in the simulation to turn off diamond strength in the sample and window after the elastic wave had reached the free surface. The characteristics method was also used to infer stress from the LASNEX-predicted free-surface velocity, to demonstrate reasonable agreement with the predicted stress histories. The inferred stress from the characteristics analysis of the LASNEX velocities is systematically slightly lower than the LASNEX stress. We consider this apparent underestimate as an additional systematic contribution to the stress uncertainty. Source data

Extended Data Fig. 6 Steps to subtract the X-ray background on the image plates.

A lineout of the image plate from shot N170305 is shown, for illustration. **a**, Raw data, projected into ϕ (angle around the direct beam) versus 2θ (scattering angle) space. **b**, data after the SNIP background subtraction and intensity corrections (which take into account the variable transmission through the sample and image plate filter materials and the changing effective pinhole area depending on the angle of scattered X-rays) are applied. **c**, Image plate lineouts: the SNIP background (B) is subtracted from the raw data (D), yielding (S). Intensity corrections are then applied, yielding (I). At lower pressures (lower ablation-plasma background) this is often sufficient to flatten the background but when the laser power is very high, an additional polynomial background (P) is subtracted from (I) to generate the final result (R). **d** shows the diffraction pattern (R, teal line), a fit with Gaussian peak shapes and constant background (black dashed line), and residual (solid black line). The centroids of the Gaussian peaks were used in a least-squares fitting to infer the FC8 density.

Extended Data Fig. 7 Data extraction for shot N180214.

At 2 TPa, the high drive background results in statistical noise levels that almost overwhelm the X-ray diffraction signal, so spurious features in the background show up clearly in the image plate lineouts. Some of the features are highlighted in this image: a pattern of Laue spots which originates from the broadband (modelled as 15–35 keV) Bremsstrahlung

tail of the backlighter radiation, scattered off the uncompressed { 110} -oriented single-crystal diamond window during the early X-ray source pulse (locations shown in black boxes); a series of bright bands, which are scanning artefacts, are marked with red dashed lines; and an aliasing pattern which arises from low sampling resolution is marked with white dashed lines (the sampling resolution is quite heterogeneous in this projection). As a result of all these spurious features, some diffraction lines that are evident by eye do not rise above the background noise in an average lineout over the entire image plate, and so we have chosen to stitch together narrower lineouts around the apparent diffraction lines. A narrow lineout over a region on the image plate highlighted in blue centred at about −80° is shown as the blue line. A single-crystal-like (111) diffraction line from diamond shows up above the background, because of its strong texture. Based on this texture, the line apparently originates from the single-crystal diamond tamper, which has reached pressure equilibrium with the sample over approximately half its volume by the time of the X-ray exposure. The (200) line and a fragment of the (311) line are largely too weak to register above the background noise from the ablation plasma, but they do show up in some regions of the image plate where the ablation plasma is shielded by the edge of the pinhole aperture, as illustrated by the cartoon inset. The X-rays from the ablation front that comprise the majority of the background are generated further from the pinhole than the Zr He_α X-rays scattered from the sample. There is consequently a narrow region on the image plate where the signal-to-noise ratio of the diffracted X-rays is higher, as shown in the narrow lineout centred near −100° (solid red line). The blue and red lineouts were stitched together, strong spurious features were masked out, and a polynomial background was subtracted, to create the teal-coloured diffraction pattern. The peaks evident by eye were fitted with Gaussian functions and the centroids used in a least-squares fit to infer the density. The residual is shown as the black solid line. The (311) peak position was not used in the least-squares fitting because it is so weak and so limited in azimuthal extent that its existence is questionable.

Extended Data Fig. 8 Ruling out alternate phases.

The observed diffraction peaks easily rule out a high-pressure BC8 or SC1 phase (ideal patterns shown in green and pink, respectively, in **a** for shot

N170209), but the SC4 phase (grey) has peaks that come reasonably close to overlapping those of the FC8 (blue). All model diffraction patterns are plotted at 7.82 g cm^{-3} SC4 and FC8 peak positions are shown in **b**. The 'q_1' diffraction peak angle is several standard deviations away from the expectation for the SC4 phase (shown even more clearly in the plot of the ratio of peak positions q_1/q_2).

Extended Data Fig. 9 MgO data summary.

VISAR data from shots N160315 (**a**) and N160519 (**b**), which used MgO windows. The carbon–MgO interface can be tracked until the compression wave reaches the free surface, although the fringes lose substantial visibility, owing to the B1-to-B2 phase transformation in the MgO window. The ramp equation of state and index of refraction as a function of pressure are not yet well constrained for MgO, so the experimental stress is uncertain. The interface velocity shown here is corrected for the MgO index using an approximate Gladstone–Dale correction of 2.015 from the results of Vedam and Schmidt[52]. **c**, Radiation-hydrodynamic simulations of the stress and density histories across the sample for shot N160315. The X-ray source duration is bracketed by dashed white lines. These simulations show that, at the time of the experiment (that is, the duration of the X-ray source), 1/3 to 1/2 of the MgO window is in a uniform stress state at equilibrium with the diamond window, and the remaining volume is experiencing a strong stress gradient in which no single volume will diffract with sufficient intensity. We therefore report the peak positions in **d** at the same stress as the diamond sample. The pink contours in **d** show the ideal peak angles for B2 MgO as a function of pressure, taken from the equation of state reported by Coppari et al.[29] (data points shown as red triangles) and extrapolated to 2 TPa. The dashed contour, plotted for the B2 (110) peak only, shows the compressibility predicted for the principal adiabat by the Livermore tabulated equation of state model LEOS 219. We also show the peak positions reported to be from the diamond windows in a previous diffraction experiment[53] with open black symbols.

Extended Data Table 1 Summary of experimental parameters and findings

Full size table

Supplementary information

Peer Review File

Source data

Source Data Fig. 1

Source Data Fig. 2

Source Data Extended Data Fig. 4

Source Data Extended Data Fig. 5

Rights and permissions

Reprints and Permissions

About this article

Check for updates

Cite this article

Lazicki, A., McGonegle, D., Rygg, J.R. *et al.* Metastability of diamond ramp-compressed to 2 terapascals. *Nature* **589,** 532–535 (2021). https://doi.org/10.1038/s41586-020-03140-4

Download citation

- Received: 01 June 2020
- Accepted: 26 October 2020
- Published: 27 January 2021
- Issue Date: 28 January 2021
- DOI: https://doi.org/10.1038/s41586-020-03140-4

Comments

By submitting a comment you agree to abide by our Terms and Community Guidelines. If you find something abusive or that does not comply with our terms or guidelines please flag it as inappropriate.

Access through your institution
Change institution
Buy or subscribe

This article was downloaded by **calibre** from https://www.nature.com/articles/s41586-020-03140-4

- Article
- Published: 18 January 2021

Correlation-driven topological phases in magic-angle twisted bilayer graphene

- Youngjoon Choi[1,2,3 na1],
- Hyunjin Kim ORCID: orcid.org/0000-0001-9886-0487[1,2,3 na1],
- Yang Peng[4],
- Alex Thomson[2,3,5],
- Cyprian Lewandowski[2,3,5],
- Robert Polski ORCID: orcid.org/0000-0003-0887-8099[1,2],
- Yiran Zhang ORCID: orcid.org/0000-0002-8477-0074[1,2,3],
- Harpreet Singh Arora ORCID: orcid.org/0000-0002-7674-735X[1,2],
- Kenji Watanabe ORCID: orcid.org/0000-0003-3701-8119[6],
- Takashi Taniguchi[6],
- Jason Alicea[2,3,5] &
- Stevan Nadj-Perge ORCID: orcid.org/0000-0002-2394-9070[1,2]

Nature **volume 589**, pages536–541(2021)Cite this article

- 3059 Accesses
- 32 Altmetric
- Metrics details

Subjects

- Electronic properties and materials

- Phase transitions and critical phenomena

Abstract

Magic-angle twisted bilayer graphene (MATBG) exhibits a range of correlated phenomena that originate from strong electron–electron interactions. These interactions make the Fermi surface highly susceptible to reconstruction when ±1, ±2 and ±3 electrons occupy each moiré unit cell, and lead to the formation of various correlated phases[1,2,3,4]. Although some phases have been shown to have a non-zero Chern number[5,6], the local microscopic properties and topological character of many other phases have not yet been determined. Here we introduce a set of techniques that use scanning tunnelling microscopy to map the topological phases that emerge in MATBG in a finite magnetic field. By following the evolution of the local density of states at the Fermi level with electrostatic doping and magnetic field, we create a local Landau fan diagram that enables us to assign Chern numbers directly to all observed phases. We uncover the existence of six topological phases that arise from integer fillings in finite fields and that originate from a cascade of symmetry-breaking transitions driven by correlations[7,8]. These topological phases can form only for a small range of twist angles around the magic angle, which further differentiates them from the Landau levels observed near charge neutrality. Moreover, we observe that even the charge-neutrality Landau spectrum taken at low fields is considerably modified by interactions, exhibits prominent electron–hole asymmetry, and features an unexpectedly large splitting between zero Landau levels (about 3 to 5 millielectronvolts). Our results show how strong electronic interactions affect the MATBG band structure and lead to correlation-enabled topological phases.

Access through your institution
Change institution
Buy or subscribe

Access options

Subscribe to Journal

Get full journal access for 1 year

$199.00

only $3.90 per issue

Subscribe

All prices are NET prices.
VAT will be added later in the checkout.

Rent or Buy article

Get time limited or full article access on ReadCube.

from$8.99

Rent or Buy

All prices are NET prices.

Additional access options:

- Log in
- Access through your institution
- Learn about institutional subscriptions

Fig. 1: Spectroscopy of MATBG with a magnetic field at 2 K.

Fig. 2: LDOS Landau fan and gaps induced by Chern insulating phases.

Fig. 3: Angle and magnetic-field dependence of the LDOS and identification of Chern insulators.

Fig. 4: Evolution of LLs from charge neutrality.

Data availability

The data that support the findings of this study are available from the corresponding authors on reasonable request.

References

1. 1.

   Cao, Y. et al. Correlated insulator behaviour at half-filling in magic-angle graphene superlattices. *Nature* **556**, 80–84 (2018).

   ADS CAS Article Google Scholar

2. 2.

   Cao, Y. et al. Unconventional superconductivity in magic-angle graphene superlattices. *Nature* **556**, 43–50 (2018).

   ADS CAS Article Google Scholar

3. 3.

   Yankowitz, M. et al. Tuning superconductivity in twisted bilayer graphene. *Science* **363**, 1059–1064 (2019).

   ADS CAS Article Google Scholar

4. 4.

   Lu, X. et al. Superconductors, orbital magnets and correlated states in magic-angle bilayer graphene. *Nature* **574**, 653–657 (2019).

   ADS CAS Article Google Scholar

5. 5.

   Sharpe, A. L. et al. Emergent ferromagnetism near three-quarters filling in twisted bilayer graphene. *Science* **365**, 605–608 (2019).

ADS CAS PubMed Google Scholar

6. 6.

Serlin, M. et al. Intrinsic quantized anomalous Hall effect in a moiré heterostructure. *Science* **367**, 900–903 (2019).

ADS Article Google Scholar

7. 7.

Zondiner, U. et al. Cascade of phase transitions and Dirac revivals in magic-angle graphene. *Nature* **582**, 203–208 (2020).

ADS CAS Article Google Scholar

8. 8.

Wong, D. et al. Cascade of transitions between the correlated electronic states of magic-angle twisted bilayer graphene. *Nature* **582**, 198–202 (2020).

ADS CAS Article Google Scholar

9. 9.

Lopes dos Santos, J. M. B., Peres, N. M. R. & Castro Neto, A. H. Graphene bilayer with a twist: electronic structure. *Phys. Rev. Lett*. **99**, 256802 (2007).

ADS CAS Article Google Scholar

10. 10.

Bistritzer, R. & MacDonald, A. H. Moiré bands in twisted double-layer graphene. *Proc. Natl Acad. Sci. USA* **108**, 12233–12237 (2011).

ADS CAS Article Google Scholar

11. 11.

Hunt, B. et al. Massive Dirac fermions and Hofstadter butterfly in a van der Waals heterostructure. *Science* **340**, 1427–1430 (2013).

ADS CAS Article Google Scholar

12. 12.

Ponomarenko, L. A. et al. Cloning of Dirac fermions in graphene superlattices. *Nature* **497**, 594–597 (2013).

ADS CAS Article Google Scholar

13. 13.

Dean, C. R. et al. Hofstadter's butterfly and the fractal quantum Hall effect in moiré superlattices. *Nature* **497**, 598–602 (2013).

ADS CAS Article Google Scholar

14. 14.

Wang, L. et al. Evidence for a fractional fractal quantum Hall effect in graphene superlattices. *Science* **350**, 1231–1234 (2015).

ADS MathSciNet CAS Article Google Scholar

15. 15.

Hofstadter, D. R. Energy levels and wave functions of Bloch electrons in rational and irrational magnetic fields. *Phys. Rev. B* **14**, 2239–2249 (1976).

ADS CAS Article Google Scholar

16. 16.

Bistritzer, R. & MacDonald, A. H. Moiré butterflies in twisted bilayer graphene. *Phys. Rev. B* **84**, 035440 (2011).

ADS Article Google Scholar

17. 17.

Arora, H. S. et al. Superconductivity in metallic twisted bilayer graphene stabilized by WSe_2. *Nature* **583**, 379–384 (2020).

ADS CAS Article Google Scholar

18. 18.

Brihuega, I. et al. Unraveling the intrinsic and robust nature of van Hove singularities in twisted bilayer graphene by scanning tunneling microscopy and theoretical analysis. *Phys. Rev. Lett*. **109**, 196802 (2012).

ADS CAS Article Google Scholar

19. 19.

Kerelsky, A. et al. Maximized electron interactions at the magic angle in twisted bilayer graphene. *Nature* **572**, 95–100 (2019).

ADS CAS Article Google Scholar

20. 20.

Choi, Y. et al. Electronic correlations in twisted bilayer graphene near the magic angle. *Nat. Phys*. **15**, 1174–1180 (2019); author correction **15**, 1205 (2019).

CAS Article Google Scholar

21. 21.

Xie, Y. et al. Spectroscopic signatures of many-body correlations in magic-angle twisted bilayer graphene. *Nature* **572**, 101–105 (2019).

ADS CAS Article Google Scholar

22. 22.

Jiang, Y. et al. Charge order and broken rotational symmetry in magic-angle twisted bilayer graphene. *Nature* **573**, 91–95 (2019).

ADS CAS Article Google Scholar

23. 23.

Jung, S. et al. Evolution of microscopic localization in graphene in a magnetic field from scattering resonances to quantum dots. *Nat. Phys*. **7**, 245–251 (2011).

CAS Article Google Scholar

24. 24.

Po, H. C., Zou, L., Senthil, T. & Vishwanath, A. Faithful tight-binding models and fragile topology of magic-angle bilayer graphene. *Phys. Rev. B* **99**, 195455 (2019).

ADS CAS Article Google Scholar

25. 25.

Uri, A. et al. Mapping the twist-angle disorder and Landau levels in magic-angle graphene. *Nature* **581**, 47–52 (2020).

ADS CAS Article Google Scholar

26. 26.

Saito, Y. et al. Hofstadter subband ferromagnetism and symmetry broken Chern insulators in twisted bilayer graphene. Preprint at

https://arxiv.org/abs/2007.06115 (2020).

27. 27.

Wu, S., Zhang, Z., Watanabe, K., Taniguchi, T. & Andrei, E. Y. Chern insulators and topological flat-bands in magic-angle twisted bilayer graphene. Preprint at https://arxiv.org/abs/2007.03735 (2020).

28. 28.

Das, I. et al. Symmetry broken Chern insulators and magic series of Rashba-like Landau level crossings in magic angle bilayer graphene. Preprint at https://arxiv.org/abs/2007.13390 (2020).

29. 29.

Wannier, G. H. A result not dependent on rationality for Bloch electrons in a magnetic field. *Phys. Stat. Sol. B* **88**, 757–765 (1978).

ADS Article Google Scholar

30. 30.

Guinea, F. & Walet, N. R. Electrostatic effects, band distortions, and superconductivity in twisted graphene bilayers. *Proc. Natl Acad. Sci. USA* **115**, 13174–13179 (2018).

ADS CAS Article Google Scholar

31. 31.

Goodwin, Z. A. H., Vitale, V., Liang, X., Mostofi, A. A. & Lischner, J. Hartree theory calculations of quasiparticle properties in twisted bilayer graphene. *Electron. Struct.* **2**, 034001 (2020).

32. 32.

Xie, M. & MacDonald, A. H. Nature of the correlated insulator states in twisted bilayer graphene. *Phys. Rev. Lett*. **124**, 097601 (2020).

ADS CAS Article Google Scholar

33. 33.

Bi, Z., Yuan, N. F. Q. & Fu, L. Designing flat bands by strain. *Phys. Rev. B* **100**, 035448 (2019).

ADS CAS Article Google Scholar

34. 34.

Nam, N. N. T. & Koshino, M. Lattice relaxation and energy band modulation in twisted bilayer graphene. *Phys. Rev. B* **96**, 075311 (2017).

ADS Article Google Scholar

35. 35.

Hejazi, K., Liu, C. & Balents, L. Landau levels in twisted bilayer graphene and semiclassical orbits. *Phys. Rev. B* **100**, 035115 (2019).

ADS CAS Article Google Scholar

36. 36.

Zhang, Y.-H., Po, H. C. & Senthil, T. Landau level degeneracy in twisted bilayer graphene: role of symmetry breaking. *Phys. Rev. B* **100**, 125104 (2019).

ADS CAS Article Google Scholar

37. 37.

Carr, S., Fang, S., Po, H. C., Vishwanath, A. & Kaxiras, E. Derivation of Wannier orbitals and minimal-basis tight-binding Hamiltonians for twisted bilayer graphene: first-principles approach. *Phys. Rev. Res*. **1**, 033072 (2019).

CAS Article Google Scholar

38. 38.

Nuckolls, K. P. et al. Strongly correlated Chern insulators in magic-angle twisted bilayer graphene. *Nature* **588**, 610–615 (2020).

39. 39.

Walkup, D. et al. Tuning single-electron charging and interactions between compressible Landau level islands in graphene. *Phys. Rev. B* **101**, 035428 (2020).

ADS CAS Article Google Scholar

40. 40.

Wang, T., Bultinck, N. & Zaletel, M. P. Flat band topology of magic angle graphene on a transition metal dichalcogenide. *Phys. Rev. B* **102**, 235146 (2020).

41. 41.

Yin, J.-X. et al. Quantum-limit Chern topological magnetism in $TbMn_6Sn_6$. *Nature* **583**, 533–536 (2020).

ADS CAS Article Google Scholar

42. 42.

Gusynin, V. P. & Sharapov, S. G. Unconventional integer quantum Hall effect in graphene. *Phys. Rev. Lett*. **95**, 146801 (2005).

ADS CAS Article Google Scholar

43. 43.

Hatsugai, Y., Fukui, T. & Aoki, H. Topological aspects of graphene. *Eur. Phys. J. Spec. Top*. **148**, 133–141 (2007).

Article Google Scholar

Download references

Acknowledgements

We acknowledge discussions with A. Young, G. Refael and S. Mashhadi. The device nanofabrication was performed at the Kavli Nanoscience Institute (KNI) at Caltech. This work was supported by NSF through grants DMR-2005129 and DMR-1723367 and by the Army Research Office under grant award W911NF-17-1-0323. Part of the initial STM characterization was supported by CAREER DMR-1753306. Nanofabrication performed by Y.Z. was supported by the DOE-QIS programme (DE-SC0019166). J.A. and S.N.-P. also acknowledge the support of IQIM (an NSF Physics Frontiers Center with support of the Gordon and Betty Moore Foundation through grant GBMF1250). Y.P. acknowledges support from a startup fund from California State University, Northridge. A.T., C.L. and J.A. are grateful for support from the Walter Burke Institute for Theoretical Physics at Caltech and the Gordon and Betty Moore Foundation's EPiQS Initiative, grant GBMF8682. Y.C. and H.K. acknowledge support from the Kwanjeong fellowship.

Author information

Author notes

1. These authors contributed equally: Youngjoon Choi, Hyunjin Kim

Affiliations

1. T. J. Watson Laboratory of Applied Physics, California Institute of Technology, Pasadena, CA, USA

   Youngjoon Choi, Hyunjin Kim, Robert Polski, Yiran Zhang, Harpreet Singh Arora & Stevan Nadj-Perge

2. Institute for Quantum Information and Matter, California Institute of Technology, Pasadena, CA, USA

   Youngjoon Choi, Hyunjin Kim, Alex Thomson, Cyprian Lewandowski, Robert Polski, Yiran Zhang, Harpreet Singh Arora, Jason Alicea & Stevan Nadj-Perge

3. Department of Physics, California Institute of Technology, Pasadena, CA, USA

   Youngjoon Choi, Hyunjin Kim, Alex Thomson, Cyprian Lewandowski, Yiran Zhang & Jason Alicea

4. Department of Physics and Astronomy, California State University, Northridge, CA, USA

   Yang Peng

5. Walter Burke Institute for Theoretical Physics, California Institute of Technology, Pasadena, CA, USA

   Alex Thomson, Cyprian Lewandowski & Jason Alicea

6. National Institute for Materials Science, Tsukuba, Japan

   Kenji Watanabe & Takashi Taniguchi

Authors

1. Youngjoon Choi
   View author publications

   You can also search for this author in PubMed Google Scholar

2. Hyunjin Kim
   View author publications

   You can also search for this author in PubMed Google Scholar

3. Yang Peng
View author publications

You can also search for this author in PubMed Google Scholar

4. Alex Thomson
View author publications

You can also search for this author in PubMed Google Scholar

5. Cyprian Lewandowski
View author publications

You can also search for this author in PubMed Google Scholar

6. Robert Polski
View author publications

You can also search for this author in PubMed Google Scholar

7. Yiran Zhang
View author publications

You can also search for this author in PubMed Google Scholar

8. Harpreet Singh Arora
View author publications

You can also search for this author in PubMed Google Scholar

9. Kenji Watanabe
View author publications

You can also search for this author in PubMed Google Scholar

10. Takashi Taniguchi
View author publications

You can also search for this author in PubMed Google Scholar

11. Jason Alicea
View author publications

You can also search for this author in PubMed Google Scholar

12. Stevan Nadj-Perge
View author publications

You can also search for this author in PubMed Google Scholar

Contributions

Y.C. and H.K. fabricated samples with the help of R.P., Y.Z. and H.A., and performed STM measurements. Y.C., H.K. and S.N.-P. analysed the data. Y.P. and A.T. implemented the models. Y.P., A.T. and C.L. provided theoretical analysis, supervised by J.A.; K.W. and T.T. provided materials (hBN). S.N-P. supervised the project. Y.C., H.K, Y.P., A.T., C.L., J.A. and S.N-P. wrote the manuscript.

Corresponding author

Correspondence to Stevan Nadj-Perge.

Ethics declarations

Competing interests

The authors declare no competing interests.

Additional information

Peer review information *Nature* thanks Vincent Renard, Yayu Wang and the other, anonymous, reviewer(s) for their contribution to the peer review of this work.

Publisher's note Springer Nature remains neutral with regard to jurisdictional claims in published maps and institutional affiliations.

Extended data figures and tables

Extended Data Fig. 1 Optical image of the device and STM topography of WSe_2/hBN boundary.

a, Optical image of the device. The blue dashed line indicates the region with twisted bilayer graphene (TBG). **b**, STM topography of a WSe_2 boundary underneath twisted bilayer graphene ($V_{bias} = -400$ mV, $I = 20$ pA). **c**, Linecut along the yellow dashed line in **b**. The height difference is around 0.8 nm, which matches the monolayer WSe_2 thickness. Small ripples originate from the moiré pattern.

Extended Data Fig. 2 AA site point spectra versus gate voltage with magnetic field.

a, $B = 0$ T. **b**, $B = 4$ T. **c**, $B = 8$ T. The area (with $\theta = 1.03°$) is the same as that shown in Fig. 1c–e. The VHSs are more pronounced compared to the AB site, making LL features harder to resolve.

Extended Data Fig. 3 Evolution of cascade with magnetic field.

a–**e**, Point spectra versus gate voltage on an AB site ($\theta = 1.03°$) at $B = 4$ T (**a**), $B = 5$ T (**b**), $B = 6$ T (**c**), $B = 7$ T (**d**) and $B = 8$ T (**e**). Coloured dashed lines indicate positions calculated with the corresponding Chern numbers. **f**, Tracking of cascades on the conduction band at different magnetic fields. As the field is increased, the shifting of cascade onsets follows the evolution of Chern insulators. **a** and **e** show the same data as Fig. 1d, e; **b**–**d** are at intermediate fields on the same area.

Extended Data Fig. 4 Quantum Hall ferromagnetic states at the zLL.

a, Point spectra on an AB site at $\theta = 1.01°$ as a function of V_{gate} for magnetic field $B = 7$ T. **b**, Zoom-in around the CNP, where zLLs (0^+ and 0^-) cross the Fermi energy. The fourfold degeneracy of each zLL is broken by exchange interactions at the Fermi energy, creating gaps at $\nu_{LL} = -4, -3, \ldots, +4$. **c**, Linecuts obtained when the 0^- and 0^+ LLs cross the Fermi energy, with vertical offset for clarity. Shifting of the spectral weight of the fourfold-degenerate 0^- and 0^+ LLs cross the Fermi level is clearly visible. Numbers in blue (red) correspond to the number of spin–valley flavours of 0^- (0^+) LLs below and above the Fermi level ($V_{bias} = 0$) as they cross E_F near $\nu_{LL} = 4, 3, 2, 1, 0, -1, -2, -3, -4$.

Extended Data Fig. 5 Chern insulating phases in the valence band.

a, Full gate voltage range of Fig. 2d at $B = 7$ T, from $\nu = -4$ to $\nu = 4$. **b**–**g**, Zoom-in of Extended Data Fig. 5a around $C = -3$ (**b**), $C = -2$ (**d**) and $C = -1$ (**f**), and the corresponding linecuts (**c**, **e**, **g**) at various V_{gate} values with vertical offset. Shifting of the spectral weight across the Fermi level is clearly visible in **c** and **e**. The $C = -1$ state is not visible at this angle ($\theta = 1.02°$) and this magnetic field ($B = 7$ T).

Extended Data Fig. 6 $C = -1$ phase in a high-resolution angle-dependent LDOS map at $B = 7$ T.

Measurements were taken over a 20 nm × 200 nm area in which the twist angle varies continuously from $\theta = 1.01°$ to 1.18° by using $V_{bias} = 0$ mV and changing the spatial position and carrier density (V_{gate}). The signature of the $C = -1$ phase and $\nu_{LL} = \pm1, \pm3$, which are not visible in Fig. 3b, are now observed owing to the enhanced V_{gate} resolution, and the electron–hole asymmetry between Chern phases is even more pronaunced. We note that the visibility of $\nu_{LL} = \pm1, \pm3$ shows strong spatial dependence, whereas the visibility of $\nu_{LL} = \pm2, \pm4$ is high throughout the range.

Extended Data Fig. 7 Spectrum of a continuum model taking into account the effects of a displacement field.

a–**c**, The spectra correspond to twist angles of $\theta = 1.03°$ (**a**), $\theta = 1.06°$ (**b**) and $\theta = 1.09°$ (**c**). The displacement field, expressed as an energy difference between the two graphene monolayers, is 10 meV, and the ratio between AA and AB tunnelling amplitudes, $w_0/w_1 = 0.4$, is the same for all results. A similar spectrum is obtained for larger w_0/w_1 ratios. The simple continuum model, known to predict correct trends, can capture energetically offset Dirac cones by including a displacement field. However, it underestimates the bandwidth of the flat bands (or equivalently the separation between VHSs) and exhibits an unrealistically strong dependence on the twist angle; even at angles slightly far from the magic angle ($\theta = 1.06–1.09°$), the model predicts a 2−4 times smaller bandwidth than that observed in the data. All spectra feature a well separated LL starting from each band edge that moves inwards with the field. This LL originates from the pocket near the centre of the moiré Brillouin zone and was not observed in the experiment. The bandwidth W_e (W_h) corresponding to the conductance (valence) flat VHS sub-band is used for estimating the U/W values in Extended Data Fig. 8.

Extended Data Fig. 8 Estimated ratio between correlation and kinetic-energy scales, *U*/*W*, as a function of twist angle and magnetic field.

a, **b**, Estimates from the continuum model for the conduction (**a**) and valence (**b**) bands for $w_0/w_1 = 0.4$. **c**, **d**, The same calculation for $w_0/w_1 = 0.7$. **e**, Analytical estimate from equation (2). The bandwidth in **a**, **b**,**c**,**d** is evaluated as the total width of all levels that comprise the sub-band that includes the VHS (and carry $C = -1$ Chern number). Points very close to the magic angle are not shown owing to a lack of clear energy separation from adjacent levels. The plotted constant-U/W curves outline regions where U/W exceeds a threshold value, and qualitatively reproduce the structure of the experimental phase diagram in which Chern insulating phases are observed (Fig. 3f). In **e**, the large η values are necessary to

compensate for the crude approximation of the bandwidth from equation (3), which underestimates the bandwidth compared to the numerical simulation in **a**, **b**,**c**,**d**.

Extended Data Fig. 9 Possible MATBG band-structure scenarios obtained using the ten-band model and corresponding LL spectra.

a, **b**, Scenario (i); **c**, **d**, scenario (ii); **e**, **f**, scenario (iii); **g**, **h**, scenario (iv) (see Methods section 'LL spectrum for low fields and MATBG band structure'). The inset in **a** shows the relevant high-symmetry momenta in the moiré Brillouin zone. Colours in **b**, **d**, **f** and **h** represent the normalized density of states (DOS) obtained via Lorentzian broadening of the Landau spectrum by 0.3 meV. **i**, A possible fit to the data in Fig. 4j corresponding to scenario (ii), yielding $v_{D1} = 2.3 \times 10^5$ m s^{-1} and $v_{D2} = 1.9 \times 10^5$ m s^{-1} for the LLs originating from two two Dirac cones (here marked with red and blue solid lines). The dashed lines correspond to expected LLs that were not observed, possibly owing to the relative positions of the Dirac cones with respect to the VHS. We note that this fitting scenario is not unique. However, all analysed scenarios give v_D that exceeds 10^5 m s^{-1}.

Extended Data Fig. 10 Landau fan diagram overlaid on experimental data for different choices of gate voltages corresponding to $\nu = \pm 4$.

a, LDOS Landau fan with the same gate voltages $V_{\nu=-4}$ and $V_{\nu=4}$, corresponding to $\nu = \pm 4$, as in Fig. 2c. The same gate voltages ($V_{\nu=-4} = -5.6$ V and $V_{\nu=4} = 6.2$ V) are used in **b** and **d. b**, **c**, LDOS Landau fan zoomed-in around the hole-side dispersive band with different choice of gate voltages. The choice in **c** ($V_{\nu=-4} = -5.7$ V and $V_{\nu=4} = 6.2$ V) does not reproduce the data well. **d**, **e**, Similar comparison around the CNP, where **e** corresponds to $V_{\nu=-4} = -5.7$ V and $V_{\nu=4} = 6.3$ V. From this comparison, we extract the error in determining $\nu = \pm 4$ to be 0.1 V. All LDOS data are normalized by an average LDOS value for each magnetic field. **f**, Linecut of the LDOS fan in **a** along the LL filling of −2 emanating from $\nu = -2$,

averaged over a V_{gate} window of 0.04 V. The state above $B = 6$ T that we identify as a Chern insulating phase is distinguished from half-filling LLs by the abrupt drop in LDOS.

Supplementary information

Supplementary Information

The file includes the continuum and ten-band model details that are used to calculate the spectrum in Fig. 1g, Extended Data Fig. 7, Extended Data Fig. 8 and Extended Data Fig. 9.

Rights and permissions

Reprints and Permissions

About this article

Check for updates

Cite this article

Choi, Y., Kim, H., Peng, Y. *et al.* Correlation-driven topological phases in magic-angle twisted bilayer graphene. *Nature* **589,** 536–541 (2021). https://doi.org/10.1038/s41586-020-03159-7

Download citation

- Received: 21 August 2020
- Accepted: 13 November 2020
- Published: 18 January 2021

- Issue Date: 28 January 2021
- DOI: https://doi.org/10.1038/s41586-020-03159-7

Comments

By submitting a comment you agree to abide by our Terms and Community Guidelines. If you find something abusive or that does not comply with our terms or guidelines please flag it as inappropriate.

Access through your institution
Change institution
Buy or subscribe

This article was downloaded by **calibre** from https://www.nature.com/articles/s41586-020-03159-7

| Section menu | Main menu |

- Article
- Published: 25 November 2020

Metallaphotoredox aryl and alkyl radiomethylation for PET ligand discovery

- Robert W. Pipal[1],
- Kenneth T. Stout[1],
- Patricia Z. Musacchio[1],
- Sumei Ren ORCID: orcid.org/0000-0002-5163-0489[2],
- Thomas J. A. Graham[3],
- Stefan Verhoog[4],
- Liza Gantert[4],
- Talakad G. Lohith[4],
- Alexander Schmitz[3],
- Hsiaoju S. Lee[3],
- David Hesk[2,5],
- Eric D. Hostetler[4],
- Ian W. Davies ORCID: orcid.org/0000-0001-6936-5540[1] &
- David W. C. MacMillan ORCID: orcid.org/0000-0003-3352-4532[1]

Nature **volume 589**, pages542–547(2021)Cite this article

- 8491 Accesses
- 44 Altmetric
- Metrics details

Subjects

- Diagnostic markers
- Synthetic chemistry methodology
- Photocatalysis

Abstract

Positron emission tomography (PET) radioligands (radioactively labelled tracer compounds) are extremely useful for in vivo characterization of central nervous system drug candidates, neurodegenerative diseases and numerous oncology targets[1]. Both tritium and carbon-11 radioisotopologues are generally necessary for in vitro and in vivo characterization of radioligands[2], yet there exist few radiolabelling protocols for the synthesis of either, inhibiting the development of PET radioligands. The synthesis of such radioligands also needs to be very rapid owing to the short half-life of carbon-11. Here we report a versatile and rapid metallaphotoredox-catalysed method for late-stage installation of both tritium and carbon-11 into the desired compounds via methylation of pharmaceutical precursors bearing aryl and alkyl bromides. Methyl groups are among the most prevalent structural elements found in bioactive molecules, and so this synthetic approach simplifies the discovery of radioligands. To demonstrate the breadth of applicability of this technique, we perform rapid synthesis of 20 tritiated and 10 carbon-11-labelled complex pharmaceuticals and PET radioligands, including a one-step radiosynthesis of the clinically used compounds [^{11}C]UCB-J and [^{11}C]PHNO. We further outline the direct utility of this protocol for preclinical PET imaging and its translation to automated radiosynthesis for routine radiotracer production in human clinical imaging. We also demonstrate this protocol for the installation of other diverse and pharmaceutically useful isotopes, including carbon-14, carbon-13 and deuterium.

Access through your institution
Change institution
Buy or subscribe

Access options

Subscribe to Journal

Get full journal access for 1 year

$199.00

only $3.90 per issue

Subscribe

All prices are NET prices.
VAT will be added later in the checkout.

Rent or Buy article

Get time limited or full article access on ReadCube.

from$8.99

Rent or Buy

All prices are NET prices.

Additional access options:

- Log in
- Access through your institution
- Learn about institutional subscriptions

Fig. 1: General approach to radioligand synthesis.

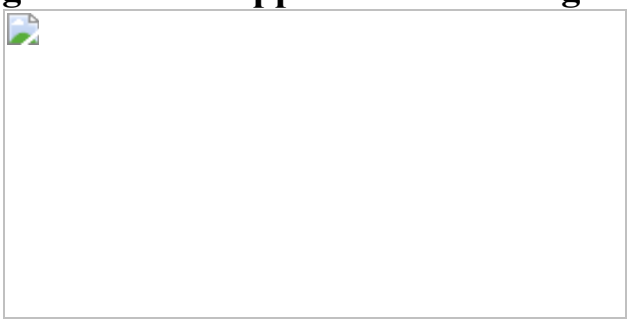

Fig. 2: Scope of high-molar-activity tritiation.

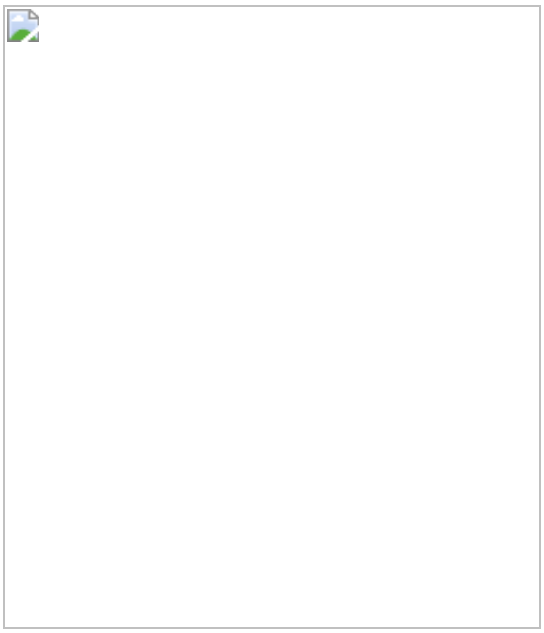

Fig. 3: Scope of carbon-11 radiolabelling.

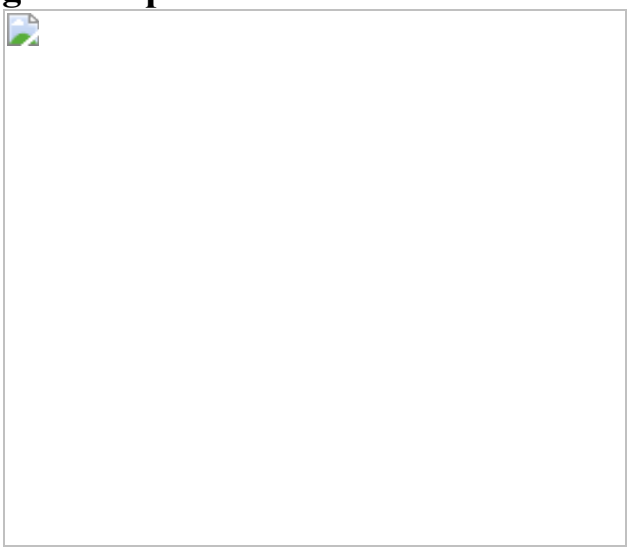

Fig. 4: Synthesis of various carbon and hydrogen isotopologues.

Data availability

The data supporting the findings of this study are available within the paper and its Supplementary Information.

References

1. 1.

   Ametamey, S. M., Honer, M. & Schubiger, P. A. Molecular imaging with PET. *Chem. Rev*. **108**, 1501–1516 (2008).

   CAS Article Google Scholar

2. 2.

   Patel, S. & Gibson, R. In vivo site-directed radiotracers: a mini-review. *Nucl. Med. Biol*. **35**, 805–815 (2008).

   CAS Article Google Scholar

3. 3.

Atzrodt, J., Derdau, V., Kerr, W. J. & Reid, M. Deuterium- and tritium-labelled compounds: applications in the life sciences. *Angew. Chem. Int. Ed*. **57**, 1758–1784 (2018).

CAS Article Google Scholar

4. 4.

Miller, P. W., Long, N. J., Vilar, R. & Gee, A. D. Synthesis of ^{11}C, ^{18}F, ^{15}O, and ^{13}N radiolabels for positron emission tomography. *Angew. Chem. Int. Ed*. **47**, 8998–9033 (2008).

CAS Article Google Scholar

5. 5.

Elmore, C. S. & Bragg, R. A. Isotope chemistry; a useful tool in the drug discovery arsenal. *Bioorg. Med. Chem. Lett*. **25**, 167–171 (2015).

CAS Article Google Scholar

6. 6.

Bar-Shalom, R., Valdivia, A. Y. & Blaufox, M. D. PET imaging in oncology. *Semin. Nucl. Med*. **30**, 150–185 (2000).

CAS Article Google Scholar

7. 7.

Tiepolt, S. et al. Current radiotracers to image neurodegenerative diseases. *EJNMMI Radiopharm. Chem*. **4**, 17 (2019).

Article PubMed PubMed Central Google Scholar

8. 8.

Suridjan, I., Comley, R. A. & Rabiner, E. A. The application of positron emission tomography (PET) imaging in CNS drug

development. *Brain Imaging Behav*. **13**, 354–365 (2019).

Article Google Scholar

9. 9.

Piel, M., Vernaleken, I. & Rösch, F. Positron emission tomography in CNS drug discovery and drug monitoring. *J. Med. Chem*. **57**, 9232–9258 (2014).

CAS Article Google Scholar

10. 10.

Boscutti, G., Huiban, M. & Passchier, J. Use of carbon-11 labelled tool compounds in support of drug development. *Drug Discov. Today Technol*. **25**, 3–10 (2017).

Article Google Scholar

11. 11.

Hargreaves, R. Imaging substance P receptors (NK_1) in the living human brain using positron emission tomography. *J. Clin. Psychiat*. **63**, 18–24 (2002).

CAS Google Scholar

12. 12.

Deng, X. et al. Chemistry for positron emission tomography: recent advances in ^{11}C-, ^{18}F-, ^{13}N-, and ^{15}O-labeling reactions. *Angew. Chem. Int. Ed*. **58**, 2580–2605 (2019).

CAS Article Google Scholar

13. 13.

Dahl, K., Halldin, C. & Schou, M. New methodologies for the preparation of carbon-11 labeled radiopharmaceuticals. *Clin. Transl. Imaging* **5**, 275–289 (2017).

Article Google Scholar

14. 14.

Zarate, C., Yang, H., Bezdek, M. J., Hesk, D. & Chirik, P. J. Ni(i)–X complexes bearing a bulky α-diimine ligand: synthesis, structure, and superior catalytic performance in the hydrogen isotope exchange in pharmaceuticals. *J. Am. Chem. Soc*. **141**, 5034–5044 (2019).

CAS Article Google Scholar

15. 15.

Voges, R., Heys, J. R. & Moenius, T. Preparation of tritium-labeled compounds by chemical synthesis. In *Preparation of Compounds Labeled with Tritium and Carbon-14* 109–209 (John Wiley & Sons, 2009).

16. 16.

Wuest, F., Berndt, M. & Kniess, T. Carbon-11 labeling chemistry based upon [^{11}C]methyl iodide. In *PET Chemistry* (eds Schubiger, P. A., Lehmann, L. & Friebe, M.) 183–213 (Springer, 2007).

17. 17.

McGrath, N. A., Brichacek, M. & Njardarson, J. T. A graphical journey of innovative organic architectures that have improved our lives. *J. Chem. Educ*. **87**, 1348–1349 (2010).

CAS Article Google Scholar

18. 18.

Voges, R., Heys, J. R. & Moenius, T. Introduction. In *Preparation of Compounds Labeled with Tritium and Carbon-14* 1–23 (John Wiley & Sons, 2009).

19. 19.

Sandell, J. et al. Synthesis, radiolabeling and preliminary biological evaluation of radiolabeled 5-methyl-6-nitroquipazine, a potential radioligand for the serotonin transporter. *Bioorg. Med. Chem. Lett*. **12**, 3611–3613 (2002).

CAS Article Google Scholar

20. 20.

Halldin, C. et al. Development of a central nicotinic acetylcholine receptor radioligand, 5-methyl-A-85380, and postmortem autoradiography in human brain. *J. Labelled Comp. Radiopharm.* **44**, S251–S253 (2001).

Article Google Scholar

21. 21.

Twilton, J. et al. The merger of transition metal and photocatalysis. *Nat. Rev. Chem*. **1**, 0052 (2017).

CAS Article Google Scholar

22. 22.

Zhang, P. & Le, C. & MacMillan, D. W. C. Silyl radical activation of alkyl halides in metallaphotoredox catalysis: a unique pathway for cross-electrophile coupling. *J. Am. Chem. Soc*. **138**, 8084–8087 (2016).

CAS Article Google Scholar

23. 23.

Smith, R. T. et al. Metallaphotoredox-catalyzed cross-electrophile C_{sp}^3–C_{sp}^3 coupling of aliphatic bromides. *J. Am. Chem. Soc*. **140**, 17433–17438 (2018).

CAS Article Google Scholar

24. 24.

Li, P. & Olszewski, J. D. Radiosynthesis of [^{3}H]-ABP688 using [^{3}H]-methyl nosylate: a non-volatile alternative methylating agent. *J. Labelled Comp. Radiopharm.* **52**, 512–513 (2009).

CAS Article Google Scholar

25. 25.

Le, C. et al. A general small-scale reactor to enable standardization and acceleration of photocatalytic reactions. *ACS Cent. Sci*. **3**, 647–653 (2017).

CAS Article Google Scholar

26. 26.

Smith, J. R. L. & Masheder, D. Amine oxidation. Part IX. The electrochemical oxidation of some tertiary amines: the effect of structure on reactivity. *J. Chem. Soc. Perkin Trans*. **2**, 47–51 (1976).

CAS Article Google Scholar

27. 27.

Koyama, H. et al. Synthesis of PET probe O^6-[(3-[^{11}C]methyl)benzyl]guanine by Pd^0-mediated rapid *C*-[^{11}C]methylation toward imaging DNA repair protein O^6-methylguanine-DNA methyltransferase in glioblastoma. *Bioorg. Med. Chem. Lett*. **27**, 1892–1896 (2017).

CAS Article Google Scholar

28. 28.

Nabulsi, N. B. et al. Synthesis and preclinical evaluation of ^{11}C-UCB-J as a PET tracer for imaging the synaptic vesicle glycoprotein 2A in the brain. *J. Nucl. Med*. **57**, 777–784 (2016).

CAS Article Google Scholar

29. 29.

Shimoda, Y. et al. Synthesis and evaluation of novel radioligands based on 3-[5-(pyridin-2-yl)-2*H*-tetrazol-2-yl]benzonitrile for positron emission tomography imaging of metabotropic glutamate receptor subtype 5. *J. Med. Chem*. **59**, 3980–3990 (2016).

CAS Article Google Scholar

30. 30.

Hostetler, E. D., Fallis, S., McCarthy, T. J., Welch, M. J. & Katzenellenbogen, J. A. Improved methods for the synthesis of [ω-^{11}C]palmitic acid. *J. Org. Chem*. **63**, 1348–1351 (1998).

CAS Article Google Scholar

31. 31.

Shoup, T. M. et al. Synthesis of the dopamine D_2/D_3 receptor agonist (+)-PHNO via supercritical fluid chromatography: preliminary PET imaging study with [3-^{11}C]-(+)PHNO. *Tetrahedr. Lett*. **55**, 682–685 (2014).

CAS Article Google Scholar

32. 32.

Andries, J., Lemoine, L., Le Bars, D., Zimmer, L. & Billard, T. Synthesis and biological evaluation of potential 5-HT_7 receptor PET radiotracers. *Eur. J. Med. Chem*. **46**, 3455–3461 (2011).

CAS Article Google Scholar

33. 33.

Mintun, M. A. et al. [^{11}C]PIB in a nondemented population: potential antecedent marker of Alzheimer disease. *Neurology* **67**, 446–452 (2006).

CAS Article Google Scholar

34. 34.

International Council for Harmonisation of Technical Requirements for Pharmaceuticals for Human Use (ICH). *Quality Guidelines* https://www.ich.org/page/quality-guidelines.

35. 35.

Isin, E. M., Elmore, C. S., Nilsson, G. N., Thompson, R. A. & Weidolf, L. Use of radiolabeled compounds in drug metabolism and pharmacokinetic studies. *Chem. Res. Toxicol*. **25**, 532–542 (2012).

CAS Article Google Scholar

36. 36.

Gant, T. G. Using deuterium in drug discovery: leaving the label in the drug. *J. Med. Chem*. **57**, 3595–3611 (2014).

CAS Article Google Scholar

37. 37.

Atzrodt, J., Derdau, V., Fey, T. & Zimmermann, J. The renaissance of H/D exchange. *Angew. Chem. Int. Ed*. **46**, 7744–7765 (2007).

CAS Article Google Scholar

Download references

Acknowledgements

Research reported in this publication was supported by the NIH (under award number R35GM134897-01) and the Princeton Catalysis Initiative. We thank L. Wilson (Lotus Separations) and H. Wang for compound purification; I. Mergelsberg, M. Reibarkh and Y. N. J. Chen for discussions; A. Chaudhary and Z. Zhu (Siemens) for high-activity [^{11}C]UCB-J radiotracer synthesis; and C. Liu for assistance in preparing this manuscript.

Author information

Affiliations

1. Merck Center for Catalysis at Princeton University, Princeton, NJ, USA

   Robert W. Pipal, Kenneth T. Stout, Patricia Z. Musacchio, Ian W. Davies & David W. C. MacMillan

2. Labeled Compound Synthesis Group, Department of Process R&D, MRL, Merck & Co., Rahway, NJ, USA

   Sumei Ren & David Hesk

3. Cyclotron Facility, Department of Radiology, University of Pennsylvania, Philadelphia, PA, USA

   Thomas J. A. Graham, Alexander Schmitz & Hsiaoju S. Lee

4. MRL, Merck & Co., West Point, PA, USA

   Stefan Verhoog, Liza Gantert, Talakad G. Lohith & Eric D. Hostetler

5. Department of Isotopic Chemistry, RTI International, Durham, NC, USA

   David Hesk

Authors

1. Robert W. Pipal
   View author publications

   You can also search for this author in PubMed Google Scholar

2. Kenneth T. Stout
   View author publications

   You can also search for this author in PubMed Google Scholar

3. Patricia Z. Musacchio
   View author publications

   You can also search for this author in PubMed Google Scholar

4. Sumei Ren
   View author publications

   You can also search for this author in PubMed Google Scholar

5. Thomas J. A. Graham
   View author publications

   You can also search for this author in PubMed Google Scholar

6. Stefan Verhoog
   View author publications

   You can also search for this author in PubMed Google Scholar

7. Liza Gantert
   View author publications

You can also search for this author in PubMed Google Scholar

8. Talakad G. Lohith
   View author publications

   You can also search for this author in PubMed Google Scholar

9. Alexander Schmitz
   View author publications

   You can also search for this author in PubMed Google Scholar

10. Hsiaoju S. Lee
    View author publications

    You can also search for this author in PubMed Google Scholar

11. David Hesk
    View author publications

    You can also search for this author in PubMed Google Scholar

12. Eric D. Hostetler
    View author publications

    You can also search for this author in PubMed Google Scholar

13. Ian W. Davies
    View author publications

    You can also search for this author in PubMed Google Scholar

14. David W. C. MacMillan
    View author publications

    You can also search for this author in PubMed Google Scholar

Contributions

P.Z.M., S.R., T.J.A.G., D.H., E.D.H., I.W.D. and D.W.C.M. conceived the work. R.W.P., P.Z.M. and S.R. conducted initial optimization. R.W.P., K.T.S. and S.R. synthesized organobromide precursors. R.W.P. and K.T.S. performed and isolated labelling experiments. R.W.P., K.T.S., S.R. and D.H. developed purification conditions. T.J.A.G., S.V. and E.D.H. provided insight into experimental design. L.G. conducted the non-human primate PET imaging study and T.G.L. performed data analysis. A.S. configured and performed the fully automated radiosynthesis and H.S.L. performed data analysis. R.W.P., K.T.S., T.J.A.G. and D.W.C.M. prepared the manuscript with input from all co-authors.

Corresponding author

Correspondence to David W. C. MacMillan.

Ethics declarations

Competing interests

The authors declare no competing interests.

Additional information

Peer review information *Nature* thanks Yu-Shin Ding and the other, anonymous, reviewer(s) for their contribution to the peer review of this work.

Publisher's note Springer Nature remains neutral with regard to jurisdictional claims in published maps and institutional affiliations.

Supplementary information

Supplementary Information

This file contains Supplementary Materials and Methods, Supplementary Text, Supplementary Figures S1–S17, NMR Spectra, and Supplementary References.

Reporting Summary

Supplementary Video 1

: Photoreactor Initiation for Automated Radiosynthesis A brief video demonstrating how the integrated photoreactor is switched on with a Bluetooth-enabled, SwitchBot remote control push button for application to automated carbon-11 radiolabeling.

Rights and permissions

Reprints and Permissions

About this article

Check for updates

Cite this article

Pipal, R.W., Stout, K.T., Musacchio, P.Z. *et al.* Metallaphotoredox aryl and alkyl radiomethylation for PET ligand discovery. *Nature* **589,** 542–547 (2021). https://doi.org/10.1038/s41586-020-3015-0

Download citation

- Received: 29 July 2020
- Accepted: 18 November 2020
- Published: 25 November 2020

- Issue Date: 28 January 2021
- DOI: https://doi.org/10.1038/s41586-020-3015-0

Comments

By submitting a comment you agree to abide by our Terms and Community Guidelines. If you find something abusive or that does not comply with our terms or guidelines please flag it as inappropriate.

Access through your institution
Change institution
Buy or subscribe

This article was downloaded by **calibre** from https://www.nature.com/articles/s41586-020-3015-0

| Section menu | Main menu |

- Article
- Published: 27 January 2021

Seasonal origin of the thermal maxima at the Holocene and the last interglacial

- Samantha Bova ORCID: orcid.org/0000-0002-5064-8775[1],
- Yair Rosenthal ORCID: orcid.org/0000-0002-7546-6011[1,2],
- Zhengyu Liu ORCID: orcid.org/0000-0003-4554-2666[3],
- Shital P. Godad[1] nAff6 &
- Mi Yan ORCID: orcid.org/0000-0003-4730-3781[4,5]

Nature **volume 589**, pages548–553(2021)Cite this article

- 1013 Accesses
- 757 Altmetric
- Metrics details

Subjects

- Climate and Earth system modelling
- Palaeoceanography
- Palaeoclimate

Abstract

Proxy reconstructions from marine sediment cores indicate peak temperatures in the first half of the last and current interglacial periods (the

thermal maxima of the Holocene epoch, 10,000 to 6,000 years ago, and the last interglacial period, 128,000 to 123,000 years ago) that arguably exceed modern warmth[1,2,3]. By contrast, climate models simulate monotonic warming throughout both periods[4,5,6,7]. This substantial model–data discrepancy undermines confidence in both proxy reconstructions and climate models, and inhibits a mechanistic understanding of recent climate change. Here we show that previous global reconstructions of temperature in the Holocene[1,2,3] and the last interglacial period[8] reflect the evolution of seasonal, rather than annual, temperatures and we develop a method of transforming them to mean annual temperatures. We further demonstrate that global mean annual sea surface temperatures have been steadily increasing since the start of the Holocene (about 12,000 years ago), first in response to retreating ice sheets (12 to 6.5 thousand years ago), and then as a result of rising greenhouse gas concentrations (0.25 ± 0.21 degrees Celsius over the past 6,500 years or so). However, mean annual temperatures during the last interglacial period were stable and warmer than estimates of temperatures during the Holocene, and we attribute this to the near-constant greenhouse gas levels and the reduced extent of ice sheets. We therefore argue that the climate of the Holocene differed from that of the last interglacial period in two ways: first, larger remnant glacial ice sheets acted to cool the early Holocene, and second, rising greenhouse gas levels in the late Holocene warmed the planet. Furthermore, our reconstructions demonstrate that the modern global temperature has exceeded annual levels over the past 12,000 years and probably approaches the warmth of the last interglacial period (128,000 to 115,000 years ago).

Access through your institution
Change institution
Buy or subscribe

Access options

Subscribe to Journal

Get full journal access for 1 year

$199.00

only $3.90 per issue

Subscribe

All prices are NET prices.
VAT will be added later in the checkout.

Rent or Buy article

Get time limited or full article access on ReadCube.

from$8.99

Rent or Buy

All prices are NET prices.

Additional access options:

- Log in
- Access through your institution
- Learn about institutional subscriptions

Fig. 1: Application of SAT method at IODP Site U1485.

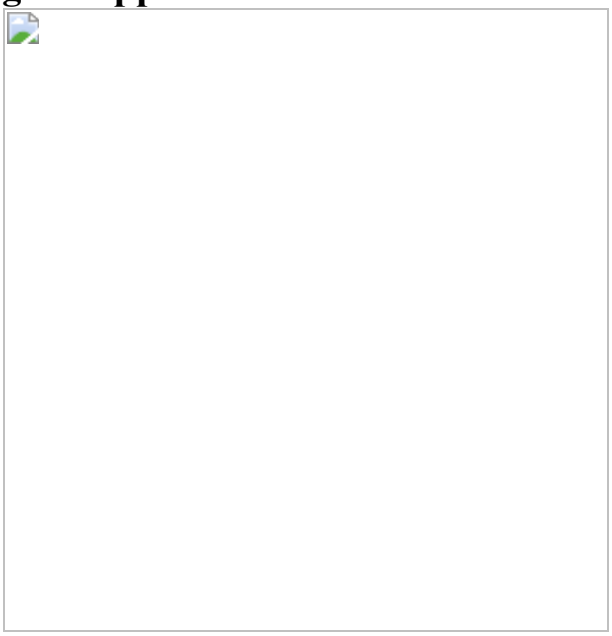

Fig. 2: Regional seasonal and mean annual temperature reconstructions.

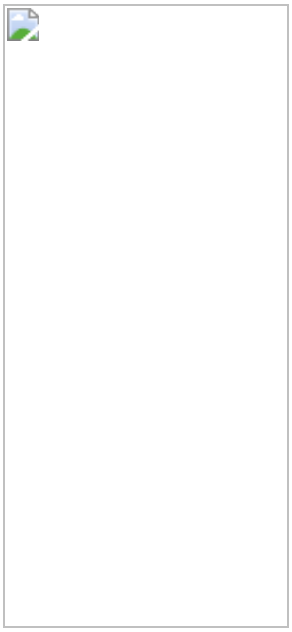

Fig. 3: Holocene warming driven by retreating ice sheets and rising greenhouse gases.

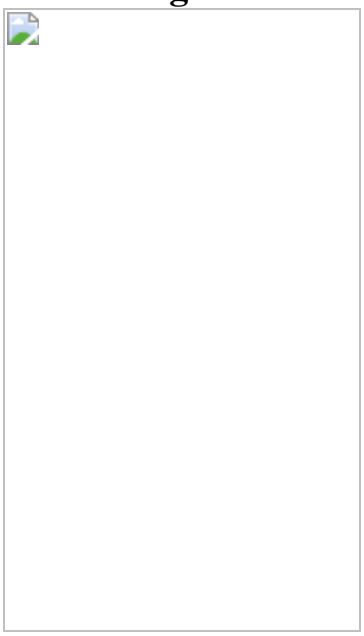

Fig. 4: Evolution and drivers of Holocene and LIG SST.

Data availability

The datasets generated and compiled for this study are available in the NOAA Database, World Data Service for Paleoclimatology at https://www.ncdc.noaa.gov/paleo/study/31752. International Comprehensive Ocean-Atmosphere Data Set data were provided by the National Oceanic and Atmospheric Administration/Oceanic and Atmospheric Research/Earth System Research Laboratories Physical Sciences Laboratory at https://psl.noaa.gov/. Source data are provided with this paper.

Code availability

A MATLAB code that implements the SAT method is available on GitHub (https://github.com/sambova/SAT).

References

1. 1.

   Kaufman, D. et al. Holocene global mean surface temperature, a multi-method reconstruction approach. *Sci. Data* **7**, 201 (2020).

CAS PubMed PubMed Central Google Scholar

2. 2.

Kaufman, D. et al. A global database of Holocene paleotemperature records. *Sci. Data* **7**, 183 (2020).

PubMed PubMed Central Google Scholar

3. 3.

Marcott, S. A., Shakun, J. D., Clark, P. U. & Mix, A. C. A reconstruction of regional and global temperature for the past 11,300 years. *Science* **339**, 1198–1201 (2013).

ADS CAS Google Scholar

4. 4.

Liu, Z. et al. The Holocene temperature conundrum. *Proc. Natl Acad. Sci. USA* **111**, E3501–E3505 (2014).

ADS CAS Google Scholar

5. 5.

Brierley, C. M. et al. Large-scale features and evaluation of the PMIP4-CMIP6 mid-Holocene simulations. *Clim. Past Discuss*. **2020**, 1–35 (2020).

Google Scholar

6. 6.

Varma, V., Prange, M. & Schulz, M. Transient simulations of the present and the last interglacial climate using the Community Climate System Model version 3: effects of orbital acceleration. *Geosci. Model Dev*. **9**, 3859–3873 (2016).

ADS Google Scholar

7. 7.

Lu, Z., Liu, Z., Chen, G. & Guan, J. Prominent precession band variance in ENSO intensity over the last 300,000 years. *Geophys. Res. Lett*. **46**, 9786–9795 (2019).

ADS Google Scholar

8. 8.

Hoffman, J. S., Clark, P. U., Parnell, A. C. & He, F. Regional and global sea-surface temperatures during the last interglaciation. *Science* **355**, 276–279 (2017).

ADS CAS Google Scholar

9. 9.

Mann, M. E. et al. Proxy-based reconstructions of hemispheric and global surface temperature variations over the past two millennia. *Proc. Natl Acad. Sci. USA* **105**, 13252–13257 (2008).

ADS CAS PubMed Google Scholar

10. 10.

PAGES 2k Consortium. Consistent multidecadal variability in global temperature reconstructions and simulations over the Common Era. *Nat. Geosci*. **12**, 643–649 (2019).

ADS CAS PubMed Central Google Scholar

11. 11.

Marsicek, J., Shuman, B. N., Bartlein, P. J., Shafer, S. L. & Brewer, S. Reconciling divergent trends and millennial variations in Holocene temperatures. *Nature* **554**, 92–96 (2018).

ADS CAS Google Scholar

12. 12.

Rodriguez, L. G. et al. Mid-Holocene, coral-based sea surface temperatures in the western tropical Atlantic. *Paleoceanogr. Paleoclimatol*. **34**, 1234–1245 (2019).

ADS Google Scholar

13. 13.

Timmermann, A., Sachs, J. & Timm, O. E. Assessing divergent SST behavior during the last 21 ka derived from alkenones and *G. ruber*-Mg/Ca in the equatorial Pacific. *Paleoceanogr. Paleoclimatol*. **29**, 680–696 (2014).

ADS Google Scholar

14. 14.

Leduc, G., Schneider, R., Kim, J.-H. & Lohmann, G. Holocene and Eemian sea surface temperature trends as revealed by alkenone and Mg/Ca paleothermometry. *Quat. Sci. Rev*. **29**, 989–1004 (2010).

ADS Google Scholar

15. 15.

Liu, Y. et al. A possible role of dust in resolving the Holocene temperature conundrum. *Sci. Rep*. **8**, 4434 (2018).

ADS PubMed PubMed Central Google Scholar

16. 16.

Park, H.-S., Kim, S.-J., Stewart, A. L., Son, S.-W. & Seo, K.-H. Mid-Holocene Northern Hemisphere warming driven by Arctic amplification. *Sci. Adv*. **5**, eaax8203 (2019).

ADS PubMed PubMed Central Google Scholar

17. 17.

Affolter, S. et al. Central Europe temperature constrained by speleothem fluid inclusion water isotopes over the past 14,000 years. *Sci. Adv*. **5**, eaav3809 (2019).

ADS PubMed PubMed Central Google Scholar

18. 18.

Martin, C. et al. Early Holocene Thermal Maximum recorded by branched tetraethers and pollen in Western Europe (Massif Central, France). *Quat. Sci. Rev*. **228**, (2020).

19. 19.

Longo, W. M. et al. Insolation and greenhouse gases drove Holocene winter and spring warming in Arctic Alaska. *Quat. Sci. Rev*. **242**, 106438 (2020).

Google Scholar

20. 20.

Köhler, P., Nehrbass-Ahles, C., Schmitt, J., Stocker, T. F. & Fischer, H. A. 156 kyr smoothed history of the atmospheric greenhouse gases CO_2, CH_4, and N_2O and their radiative forcing. *Earth Syst. Sci. Data* **9**, 363–387 (2017).

ADS Google Scholar

21. 21.

Huybers, P. & Eisenman, I. (eds) *NOAA/NCDC Paleoclimatology Program*, http://eisenman.ucsd.edu/code/daily_insolation.m (IGBP PAGES/World Data Center for Paleoclimatology, 2006).

22. 22.

Berger, A. Long-term variations of daily insolation and Quaternary climatic changes. *J. Atmos. Sci*. **35**, 2362–2367 (1978).

ADS Google Scholar

23. 23.

Freeman, E. et al. ICOADS Release 3.0: a major update to the historical marine climate record. *Int. J. Climatol*. **37**, 2211–2232 (2017).

Google Scholar

24. 24.

Be, A. & Hamilton, W. H. Ecology of recent planktonic foraminifera. *Micropaleontology* **13**, 87–106 (1967).

Google Scholar

25. 25.

De Deckker, P. The Indo-Pacific warm pool: critical to world oceanography and world climate. *Geosci. Lett*. **3**, 20 (2016).

ADS Google Scholar

26. 26.

Moffa-Sanchez, P., Rosenthal, Y., Babila, T. L., Mohtadi, M. & Zhang, X. Temperature evolution of the Indo-Pacific warm pool over the Holocene and the last deglaciation. *Paleoceanogr. Paleoclimatol*. **34**, 1107–1123 (2019).

ADS Google Scholar

27. 27.

Ruddiman, W., He, F., Vavrus, S. & Kutzbach, J. The early anthropogenic hypothesis: a review. *Quat. Sci. Rev*. **240**, 106386 (2020).

Google Scholar

28. 28.

Studer, A. S. et al. Increased nutrient supply to the Southern Ocean during the Holocene and its implications for the pre-industrial atmospheric CO_2 rise. *Nat. Geosci*. **11**, 756–760 (2018).

ADS CAS Google Scholar

29. 29.

Cowtan, K. & Way, R. G. Coverage bias in the HadCRUT4 temperature series and its impact on recent temperature trends. *Q. J. R. Meteorol. Soc*. **140**, 1935–1944 (2014).

ADS Google Scholar

30. 30.

Pausata, F. S. R. et al. The greening of the Sahara: past changes and future implications. *One Earth* **2**, 235–250 (2020).

Google Scholar

31. 31.

Ritchie, J. C., Cwynar, L. C. & Spear, R. W. Evidence from north-west Canada for an early Holocene Milankovitch thermal maximum. *Nature* **305**, 126–128 (1983).

ADS Google Scholar

32. 32.

McKay, N. P., Kaufman, D. S., Routson, C. C., Erb, M. P. & Zander, P. D. The onset and rate of Holocene neoglacial cooling in the Arctic. *Geophys. Res. Lett*. **45**, 12487–12496 (2018).

ADS Google Scholar

33. 33.

Hays, J. D., Imbrie, J. & Shackleton, N. J. Variations in the Earth's orbit: pacemaker of the Ice Ages. *Science* **194**, 1121–1132 (1976).

ADS CAS PubMed Google Scholar

34. 34.

Milankovitch, M. *Kanon Der Erdbestrahlung Und Seine Anwendung Auf Das Eiszeitenproblem* (Mihaila Ćurčića, 1941).

35. 35.

Imbrie, J. et al. On the structure and origin of major glaciation cycles. 1. Linear responses to Milankovitch forcing. *Paleoceanogr. Paleoclimatol*. **7**, 701–738 (1992).

ADS Google Scholar

36. 36.

Wang, P. X. et al. The global monsoon across time scales: mechanisms and outstanding issues. *Earth Sci. Rev*. **174**, 84–121 (2017).

ADS CAS Google Scholar

37. 37.

Clark, P. U. et al. Oceanic forcing of penultimate deglacial and last interglacial sea-level rise. *Nature* **577**, 660–664 (2020).

ADS CAS PubMed Google Scholar

38. 38.

Lambeck, K., Rouby, H., Purcell, A., Sun, Y. & Sambridge, M. Sea level and global ice volumes from the Last Glacial Maximum to the Holocene. *Proc. Natl Acad. Sci. USA* **111**, 15296–15303 (2014).

ADS CAS PubMed Google Scholar

39. 39.

Grant, K. M. et al. Rapid coupling between ice volume and polar temperature over the past 150,000 years. *Nature* **491**, 744–747 (2012).

ADS CAS PubMed Google Scholar

40. 40.

Reimer, P. J. et al. Intcal13 and Marine13 radiocarbon age calibration curves 0-50,000 years cal BP. *Radiocarbon* **55**, 1869–1887 (2013).

CAS Google Scholar

41. 41.

Rafter, P. A., Herguera, J.-C. & Southon, J. R. Extreme lowering of deglacial seawater radiocarbon recorded by both epifaunal and infaunal benthic foraminifera in a wood-dated sediment core. *Clim. Past* **14**, 1977–1989 (2018).

Google Scholar

42. 42.

Galbraith, E. D., Kwon, E. Y., Bianchi, D., Hain, M. P. & Sarmiento, J. L. The impact of atmospheric pCO_2 on carbon isotope ratios of the atmosphere and ocean. *Glob. Biogeochem. Cycles* **29**, 307–324 (2015).

ADS CAS Google Scholar

43. 43.

Haslett, J. & Parnell, A. A simple monotone process with application to radiocarbon-dated depth chronologies. *J. R. Stat. Soc. C* **57**, 399–418 (2008).

MathSciNet MATH Google Scholar

44. 44.

Lisiecki, L. E. & Raymo, M. E. A Pliocene-Pleistocene stack of 57 globally distributed benthic $\delta^{18}O$ records. *Paleoceanogr. Paleoclimatol*. **20**, https://doi.org/10.1029/2004PA001071 (2005).

45. 45.

Shackleton, N. J., Hall, M. A. & Vincent, E. Phase relationships between millennial-scale events 64,000–24,000 years ago. *Paleoceanogr. Paleoclimatol*. **15**, 565–569 (2000).

ADS Google Scholar

46. 46.

Rosenthal, Y., Boyle, E. A. & Slowey, N. Temperature control on the incorporation of magnesium, strontium, fluorine, and cadmium into benthic foraminiferal shells from Little Bahama Bank: prospects for thermocline paleoceanography. *Geochim. Cosmochim. Acta* **61**, (1997).

47. 47.

Rosenthal, Y., Field, M. P. & Sherrell, R. M. Precise determination of element/calcium ratios in calcareous samples using sector field inductively coupled plasma mass spectrometry. *Anal. Chem*. **71**, 3248–3253 (1999).

CAS PubMed Google Scholar

48. 48.

Rosenthal, Y., Holbourn, A. E., Kulhanek, D. K. & Expedition 363 Scientists. Western Pacific Warm Pool. In *Proc. IODP* Vol. 363, https://doi.org/10.14379/iodp.proc.363.2018 (International Ocean Discovery Program, 2018).

49. 49.

Minoshima, K., Kawahata, H. & Ikehara, K. Changes in biological production in the mixed water region (MWR) of the northwestern North Pacific during the last 27 kyr. *Palaeogeogr. Palaeoclimatol. Palaeoecol*. **254**, 430–447 (2007).

Google Scholar

50. 50.

Bard, E. et al. Retreat velocity of the North Atlantic polar front during the last deglaciation determined by ^{14}C accelerator mass spectrometry. *Nature* **328**, 791–794 (1987).

ADS Google Scholar

51. 51.

Bard, E., Rostek, F., Turon, J.-L. & Gendreau, S. Hydrological impact of Heinrich events in the subtropical northeast Atlantic. *Science* **289**, 1321–1324 (2000).

ADS CAS PubMed Google Scholar

52. 52.

Martrat, B. et al. Four climate cycles of recurring deep and surface water destabilizations on the Iberian margin. *Science* **317**, 502–507 (2007).

ADS CAS PubMed Google Scholar

53. 53.

Rodrigo-Gámiz, M., Martínez-Ruiz, F., Rampen, S. W., Schouten, S. & Sinninghe Damsté, J. S. Sea surface temperature variations in the western Mediterranean Sea over the last 20 kyr: a dual-organic proxy ($U^{K'}_{37}$ and LDI) approach. *Paleoceanogr. Paleoclimatol*. **29**, 87–98 (2014).

ADS Google Scholar

54. 54.

Cacho, I. et al. Dansgaard-Oeschger and Heinrich event imprints in Alboran Sea paleotemperatures. *Paleoceanogr. Paleoclimatol*. **14**, 698–705 (1999).

ADS Google Scholar

55. 55.

Isono, D. et al. The 1500-year climate oscillation in the midlatitude North Pacific during the Holocene. *Geology* **37**, 591–594 (2009).

ADS Google Scholar

56. 56.

Yamamoto, M., Yamamuro, M. & Tanaka, Y. The California current system during the last 136,000 years: response of the North Pacific High to precessional forcing. *Quat. Sci. Rev*. **26**, 405–414 (2007).

ADS Google Scholar

57. 57.

Herbert, T. D. et al. Collapse of the California Current during glacial maxima linked to climate change on land. *Science* **293**, 71–76 (2001).

ADS CAS PubMed Google Scholar

58. 58.

Ziegler, M., Nürnberg, D., Karas, C., Tiedemann, R. & Lourens, L. J. Persistent summer expansion of the Atlantic Warm Pool during glacial abrupt cold events. *Nat. Geosci*. **1**, 601–605 (2008).

ADS CAS Google Scholar

59. 59.

Schmidt, M. W., Weinlein, W. A., Marcantonio, F. & Lynch-Stieglitz, J. Solar forcing of Florida Straits surface salinity during the early Holocene. *Paleoceanogr. Paleoclimatol*. **27**, https://doi.org/10.1029/2012PA002284 (2012).

60. 60.

Zhao, M., Beveridge, N. A. S., Shackleton, N. J., Sarnthein, M. & Eglinton, G. Molecular stratigraphy of cores off northwest Africa: sea surface temperature history over the last 80 Ka. *Paleoceanogr. Paleoclimatol*. **10**, 661–675 (1995).

ADS Google Scholar

61. 61.

Schmidt, M. W., Spero, H. J. & Lea, D. W. Links between salinity variation in the Caribbean and North Atlantic thermohaline circulation. *Nature* **428**, 160–163 (2004).

ADS CAS PubMed Google Scholar

62. 62.

Schmidt, M. W. et al. Impact of abrupt deglacial climate change on tropical Atlantic subsurface temperatures. *Proc. Natl Acad. Sci. USA* **109**, 14348–14352 (2012).

ADS CAS PubMed Google Scholar

63. 63.

Lea, D. W., Pak, D. K., Peterson, L. C. & Hughen, K. A. Synchroneity of tropical and high-latitude Atlantic tmperatures over the Last Glacial Termination. *Science* **301**, 1361–1364 (2003).

ADS CAS PubMed Google Scholar

64. 64.

de Garidel-Thoron, T., Beaufort, L., Linsley, B. K. & Dannenmann, S. Millennial-scale dynamics of the east Asian winter monsoon during the last 200,000 years. *Paleoceanogr. Paleoclimatol*. **16**, 491–502 (2001).

ADS Google Scholar

65. 65.

Rosenthal, Y., Oppo, D. W. & Linsley, B. K. The amplitude and phasing of climate change during the last deglaciation in the Sulu Sea, western equatorial Pacific. *Geophys. Res. Lett*. **30**, https://doi.org/10.1029/2002GL016612 (2003).

66. 66.

Zhao, M., Huang, C.-Y., Wang, C.-C. & Wei, G. A millennial-scale U37K′ sea-surface temperature record from the South China Sea (8°N) over the last 150 kyr: monsoon and sea-level influence. *Palaeogeogr. Palaeoclimatol. Palaeoecol*. **236**, 39–55 (2006).

Google Scholar

67. 67.

Pelejero, C., Grimalt, J. O., Heilig, S., Kienast, M. & Wang, L. High-resolution U^{K}_{37} temperature reconstructions in the South China Sea

over the past 220 kyr. *Paleoceanogr. Paleoclimatol*. **14**, 224–231 (1999).

ADS Google Scholar

68. 68.

Benway, H. M., Mix, A. C., Haley, B. A. & Klinkhammer, G. P. Eastern Pacific Warm Pool paleosalinity and climate variability: 0–30 kyr. *Paleoceanogr. Paleoclimatol*. **21**, https://doi.org/10.1029/2005PA001208 (2006).

69. 69.

Dubois, N., Kienast, M., Normandeau, C. & Herbert, T. D. Eastern equatorial Pacific cold tongue during the Last Glacial Maximum as seen from alkenone paleothermometry. *Paleoceanogr. Paleoclimatol*. **24**, https://doi.org/10.1029/2009PA001781 (2009).

70. 70.

Bolliet, T. et al. Mindanao Dome variability over the last 160 kyr: episodic glacial cooling of the West Pacific Warm Pool. *Paleoceanogr. Paleoclimatol*. **26**, https://doi.org/10.1029/2010PA001966 (2011).

71. 71.

Kienast, M., Steinke, S., Stattegger, K. & Calvert, S. E. Synchronous tropical South China Sea SST change and Greenland warming during deglaciation. *Science* **291**, 2132–2134 (2001).

ADS CAS PubMed Google Scholar

72. 72.

Fan, W. et al. Variability of the Indonesian throughflow in the Makassar Strait over the last 30 ka. *Sci. Rep*. **8**, 5678 (2018).

ADS PubMed PubMed Central Google Scholar

73. 73.

Weldeab, S., Lea, D. W., Schneider, R. R. & Andersen, N. 155,000 years of west African monsoon and ocean thermal evolution. *Science* **316**, 1303–1307 (2007).

ADS CAS PubMed Google Scholar

74. 74.

Weldeab, S., Schneider, R. R., Kölling, M. & Wefer, G. Holocene African droughts relate to eastern equatorial Atlantic cooling. *Geology* **33**, 981–984 (2005).

ADS CAS Google Scholar

75. 75.

Lea, D. W., Pak, D. K. & Spero, H. J. Climate impact of Late Quaternary equatorial Pacific sea surface temperature variations. *Science* **289**, 1719–1724 (2000).

ADS CAS PubMed Google Scholar

76. 76.

Lea, D. W. et al. Paleoclimate history of Galápagos surface waters over the last 135,000yr. *Quat. Sci. Rev*. **25**, 1152–1167 (2006).

ADS Google Scholar

77. 77.

Pena, L. D., Cacho, I., Ferretti, P. & Hall, M. A. El Niño–Southern Oscillation–like variability during glacial terminations and interlatitudinal teleconnections. *Paleoceanogr. Paleoclimatol*. **23**, https://doi.org/10.1029/2008PA001620 (2008).

78. 78.

Schröder, J. F., Holbourn, A., Kuhnt, W. & Küssner, K. Variations in sea surface hydrology in the southern Makassar Strait over the past 26 kyr. *Quat. Sci. Rev*. **154**, 143–156 (2016).

ADS Google Scholar

79. 79.

Linsley, B. K., Rosenthal, Y. & Oppo, D. W. Holocene evolution of the Indonesian throughflow and the western Pacific Warm Pool. *Nat. Geosci*. **3**, 578–583 (2010).

ADS CAS Google Scholar

80. 80.

Bova, S. C. et al. Links between eastern equatorial Pacific stratification and atmospheric CO_2 rise during the last deglaciation. *Paleoceanogr. Paleoclimatol*. **30**, 1407–1424 (2015).

ADS Google Scholar

81. 81.

Arz, H. W., Pätzold, J. & Wefer, G. Correlated millennial-scale changes in surface hydrography and terrigenous sediment yield inferred from last-glacial marine deposits off northeastern Brazil. *Quat. Res*. **50**, 157–166 (1998).

CAS Google Scholar

82. 82.

Weldeab, S., Schneider, R. R. & Kölling, M. Deglacial sea surface temperature and salinity increase in the western tropical Atlantic in synchrony with high latitude climate instabilities. *Earth Planet. Sci. Lett*. **241**, 699–706 (2006).

ADS CAS Google Scholar

83. 83.

Visser, K., Thunell, R. & Stott, L. Magnitude and timing of temperature change in the Indo-Pacific warm pool during deglaciation. *Nature* **421**, 152–155 (2003).

ADS CAS PubMed Google Scholar

84. 84.

Lückge, A. et al. Monsoon versus ocean circulation controls on paleoenvironmental conditions off southern Sumatra during the past 300,000 years. *Paleoceanogr. Paleoclimatol*. **24**, https://doi.org/10.1029/2008PA001627 (2009).

85. 85.

Gibbons, F. T. et al. Deglacial $\delta^{18}O$ and hydrologic variability in the tropical Pacific and Indian oceans. *Earth Planet. Sci. Lett*. **387**, 240–251 (2014).

ADS CAS Google Scholar

86. 86.

Xu, J., Holbourn, A., Kuhnt, W., Jian, Z. & Kawamura, H. Changes in the thermocline structure of the Indonesian outflow during Terminations I and II. *Earth Planet. Sci. Lett*. **273**, 152–162 (2008).

ADS CAS Google Scholar

87. 87.

Lawrence, K. T. & Herbert, T. D. Late Quaternary sea-surface temperatures in the western Coral Sea: implications for the growth of the Australian Great Barrier Reef. *Geology* **33**, 677–680 (2005).

ADS Google Scholar

88. 88.

Lopes dos Santos, R. A. et al. Abrupt vegetation change after the Late Quaternary megafaunal extinction in southeastern Australia. *Nat. Geosci*. **6**, 627–631 (2013).

ADS CAS Google Scholar

89. 89.

Lopes dos Santos, R. A. et al. Comparison of organic ($U^{K'}_{37}$, TEXH86, LDI) and faunal proxies (foraminiferal assemblages) for reconstruction of late Quaternary sea surface temperature variability from offshore southeastern Australia. *Paleoceanogr. Paleoclimatol*. **28**, 377–387 (2013).

ADS Google Scholar

90. 90.

Pahnke, K. & Sachs, J. P. Sea surface temperatures of southern midlatitudes 0–160 kyr B.P. *Paleoceanogr. Paleoclimatol*. **21**, https://doi.org/10.1029/2005PA001191 (2006).

91. 91.

Anand, P., Elderfield, H. & Conte, M. H. Calibration of Mg/Ca thermometry in planktonic foraminifera from a sediment trap time series. *Paleoceanogr. Paleoclimatol*. **18**, https://doi.org/10.1029/2002PA000846 (2003).

92. 92.

Tierney, J. E., Malevich, S. B., Gray, W., Vetter, L. & Thirumalai, K. Bayesian calibration of the Mg/Ca paleothermometer in planktic foraminifera. *Paleoceanogr. Paleoclimatol*. **34**, 2005–2030 (2019).

ADS Google Scholar

93. 93.

Gray, W. R. & Evans, D. Nonthermal influences on Mg/Ca in planktonic foraminifera: a review of culture studies and application to the Last Glacial Maximum. *Paleoceanogr. Paleoclimatol*. **34**, 306–315 (2019).

ADS Google Scholar

94. 94.

Prahl, F. G., Muehlhausen, L. A. & Zahnle, D. L. Further evaluation of long-chain alkenones as indicators of paleoceanographic conditions. *Geochim. Cosmochim. Acta* **52**, 2303–2310 (1988).

ADS CAS Google Scholar

95. 95.

Tierney, J. E. & Tingley, M. P. BAYSPLINE: a new calibration for the alkenone paleothermometer. *Paleoceanogr. Paleoclimatol*. **33**, 281–301 (2018).

ADS Google Scholar

96. 96.

Schneider, T. Analysis of incomplete climate data: estimation of mean values and covariance matrices and imputation of missing values. *J. Clim*. **14**, 853–871 (2001).

ADS Google Scholar

97. 97.

Yeager, S. G., Shields, C. A., Large, W. G. & Hack, J. J. The low-resolution CCSM3. *J. Clim*. **19**, 2545–2566 (2006).

ADS Google Scholar

98. 98.

Timmermann, A., Lorenz, S. J., An, S.-I., Clement, A. & Xie, S.-P. The effect of orbital forcing on the mean climate and variability of the tropical Pacific. *J. Clim*. **20**, 4147–4159 (2007).

ADS Google Scholar

99. 99.

Delcroix, T. et al. Sea surface temperature and salinity seasonal changes in the western Solomon and Bismarck seas. *J. Geophys. Res. Oceans* **119**, 2642–2657 (2014).

ADS Google Scholar

100. 100.

Palmer, M. R. & Pearson, P. N. A. 23,000-year record of surface water pH and pCO_2 in the western equatorial Pacific Ocean. *Science* **300**, 480–482 (2003).

ADS CAS PubMed Google Scholar

101. 101.

Sikes, E. L., O'Leary, T., Nodder, S. D. & Volkman, J. K. Alkenone temperature records and biomarker flux at the subtropical front on the Chatham Rise, SW Pacific Ocean. *Deep Sea Res. Part I* **52**, 721–748 (2005).

ADS CAS Google Scholar

102. 102.

King, A. L. & Howard, W. Planktonic foraminiferal $\delta^{13}C$ records from Southern Ocean sediment traps: new estimates of the oceanic Suess Effect. *Glob. Biogeochem. Cycles* **18**, GB2007 (2004).

ADS Google Scholar

103. 103.

Park, E. M. *Variations In GDGT Flux And TEX Thermometry In Three Distinct Oceanic Regimes Of The Atlantic Ocean: A Sediment Trap Study*. https://epic.awi.de/id/eprint/51148/1/EPark_PhDThesis_2019.pdf PhD thesis, University of Bremen (2019).

104. 104.

Amante, C. & Eakins, B. W. *ETOPO1 Global Relief Model Converted To PanMap Layer Format*. https://doi.org/10.1594/PANGAEA.769615 (NOAA-National Geophysical Data Center, PANGAEA, 2009).

105. 105.

Emile-Geay, J., McKay, N. P., Wang, J. & Anchukaitis, K. J. *CommonClimate/PAGES2k_phase2 code: first public release* https://doi.org/10.5281/zenodo.545815 (2017).

Download references

Acknowledgements

This research used samples and data provided by the International Ocean Discovery Program (IODP). We thank the science party, technical staff and crew of IODP Expedition 363, who together ensured the successful recovery of IODP Site U1485. Funding for this research was provided by NSF grants OCE-1834208 and OCE-1810681, the NSF-sponsored US Science Support Program for IODP, the Institute of Earth, Ocean, and Atmospheric Sciences at Rutgers University, the Chinese NSF (grant NSFC41630527), Chinese MOST (grant 2017YFA0603801), the School of Geography, Nanjing Normal University and the USIEF-Fulbright Program.

Author information

Author notes

1. Shital P. Godad

   Present address: Department of Geosciences, National Taiwan University, Taipei, Taiwan

Affiliations

1. Department of Marine and Coastal Sciences, Rutgers, State University of New Jersey, New Brunswick, NJ, USA

   Samantha Bova, Yair Rosenthal & Shital P. Godad

2. Department of Earth and Planetary Sciences, Rutgers University, New Brunswick, NJ, USA

   Yair Rosenthal

3. Atmospheric Science Program, Department of Geography, The Ohio State University, Columbus, OH, USA

   Zhengyu Liu

4. School of Geography, Nanjing Normal University, Nanjing, China

   Mi Yan

5. Open Studio for Ocean-Climate-Isotope Modeling, Pilot National Laboratory for Marine Science and Technology, Qingdao, China

   Mi Yan

Authors

1. Samantha Bova
   View author publications

   You can also search for this author in PubMed Google Scholar

2. Yair Rosenthal
View author publications

You can also search for this author in PubMed Google Scholar

3. Zhengyu Liu
View author publications

You can also search for this author in PubMed Google Scholar

4. Shital P. Godad
View author publications

You can also search for this author in PubMed Google Scholar

5. Mi Yan
View author publications

You can also search for this author in PubMed Google Scholar

Contributions

S.B. and Y.R. derived the empirical form of the SAT method. S.B. compiled and analysed the proxy datasets and wrote the first manuscript draft. S.B. and S.P.G. collected the geochemical data from Site U1485 under the supervision of Y.R. Z.L. and M.Y. provided access to and interpretation of model results, and the theory explaining the SAT method. All authors provided review and editing.

Corresponding author

Correspondence to Samantha Bova.

Ethics declarations

Competing interests

The authors declare no competing interests.

Additional information

Peer review information *Nature* thanks Jeroen Groeneveld, Jennifer Hertzberg, Feng Zhu, and the other, anonymous, reviewer(s) for their contribution to the peer review of this work. Peer reviewer reports are available.

Publisher's note Springer Nature remains neutral with regard to jurisdictional claims in published maps and institutional affiliations.

Extended data figures and tables

Extended Data Fig. 1 Location map of IODP Site U1485.

Bathymetric map of the northern margin of Papua New Guinea showing the location of IODP Site U1485 (yellow circle)[48,104]. Contour interval is 500 m. Map constructed using the M_Map software package for MATLAB.

Extended Data Fig. 2 Age–depth model for Holocene and Termination I section of IODP Site U1485.

a, Reservoir age estimates calculated by measuring co-occurring wood and *G. ruber* ^{14}C ages and subtracting the wood ^{14}C age from planktic foraminifer ^{14}C age. Twelve reservoir age estimates were deemed outliers (see Methods) and are not shown. Shading represents 2σ error estimate. **b**, Final age model for the upper 27.5 m CCSF-A of Site U1485 constructed using the Bchron age modelling software package for R[43]. Sedimentation across the Holocene is approximately constant at a rate of 62 cm kyr^{-1}. Shading represents the 3σ error estimate. The red square indicates an outlying ^{14}C date that is not included in the final age model.

Extended Data Fig. 3 Age–depth model for LIG and Termination II section of IODP Site U1485.

Benthic foraminiferal $\delta^{18}O$ record from Site U1485 (blue) measured on *Cibicidoides pachyderma* (>212 μm) plotted with the LR04 benthic stack (black)[44] and the benthic foraminifer $\delta^{18}O$ record from Site MD95-2042 from the Iberian Margin (purple)[45]. Dashed lines show tie points used to define age control for the LIG and Termination II section of Site U1485. Depth scale for Site U1485 is CCSF-A. Foraminiferal $\delta^{18}O$ for Site U1485 and MD95-2042 are reported relative to the Pee Dee belemnite (PDB) standard.

Extended Data Fig. 4 Mg/Ca-temperature calibration comparison at IODP Site U1485.

a, **d**, SST_{SN} records based on the three different calibrations of Anand et al.[91], Gray and Evans[93] and Tierney et al.[92] (BAYMAG) for the LGM-HL and MIS 6-5 intervals; **b**, **e**, same plotted as SST anomalies; **c**, **f**, calculated mean annual SST anomalies.

Extended Data Fig. 5 SAT method insensitivity to insolation window length.

Application of the SAT method to Mg/Ca SST_{SN} from Site U1485 (**a**–**d**) and October SSTs from the CCSM3 accelerated model simulation (**e**–**h**)[7]. MASST is estimated by regressing seasonal SSTs with insolation averaged over a range of window lengths, from 30 to 270 days, with the same central 30-day interval. Widening the window length changes the slope of the regression between insolation and seasonal SST (**d**, **h**) but has a negligible impact on the SAT calculated MASST anomalies. Shaded region in **b** reflects the 2 s.e. uncertainty.

Extended Data Fig. 6 Locations and temporal availability of proxy records.

a, Map of SST records used in this study showing proxy type and whether the site has a LIG section. See Extended Data Table 1 for a list of records and their citations. **b**, **c**, Temporal availability of records over the Holocene

and LIG intervals, respectively. Figure constructed using MATLAB and code from Emile-Geay et al.[105].

Extended Data Fig. 7 Map of proxy seasonal bias.

Map of SST records used in this study showing the month of best fit between LIG SST_{SN} and insolation closest to the 30-day window identified using the SAT method. See Extended Data Table 1 for a list of records included. Figure constructed using MATLAB and code from Emile-Geay et al.[105].

Extended Data Fig. 8 Application of SAT method to model seasonal SSTs from core locations in the Eastern Equatorial Pacific (EEP), Southern Hemisphere extratropics, Northern Hemisphere extratropics, and tropical Atlantic.

a–**d**, Proxy SST_{SN} anomalies plotted with SST_{SN} output from the nearest grid cell in the CCSM3 accelerated model simulation. **e**–**h**, SAT method MASST (blue) calculated from model SST_{SN} data shown in **a**–**d** plotted with the actual model MASST data (black) for each location. All SST anomalies in this figure are calculated relative to values averaged between 115 ka and 116 ka.

Extended Data Table 1 Records included in SST stacks
Full size table

Supplementary information

Supplementary Methods

This file contains theoretical derivation of the SAT method and its properties.

Source data

Source Data Fig. 1

Source Data Fig. 2

Source Data Fig. 3

Source Data Fig. 4

Rights and permissions

Reprints and Permissions

About this article

Check for updates

Cite this article

Bova, S., Rosenthal, Y., Liu, Z. *et al.* Seasonal origin of the thermal maxima at the Holocene and the last interglacial. *Nature* **589,** 548–553 (2021). https://doi.org/10.1038/s41586-020-03155-x

Download citation

- Received: 18 July 2020
- Accepted: 03 December 2020
- Published: 27 January 2021
- Issue Date: 28 January 2021
- DOI: https://doi.org/10.1038/s41586-020-03155-x

Comments

By submitting a comment you agree to abide by our Terms and Community Guidelines. If you find something abusive or that does not comply with our terms or guidelines please flag it as inappropriate.

Access through your institution
Change institution
Buy or subscribe

Associated Content

Nature | News & Views

Palaeoclimate puzzle explained by seasonal variation

- Jennifer Hertzberg

This article was downloaded by **calibre** from https://www.nature.com/articles/s41586-020-03155-x

- Article
- Published: 27 January 2021

Global and regional drivers of land-use emissions in 1961–2017

- Chaopeng Hong ORCID: orcid.org/0000-0002-8825-9062[1],
- Jennifer A. Burney ORCID: orcid.org/0000-0003-3532-2934[2],
- Julia Pongratz ORCID: orcid.org/0000-0003-0372-3960[3,4],
- Julia E. M. S. Nabel ORCID: orcid.org/0000-0002-8122-5206[4],
- Nathaniel D. Mueller ORCID: orcid.org/0000-0003-1857-5104[5,6],
- Robert B. Jackson ORCID: orcid.org/0000-0001-8846-7147[7,8,9] &
- Steven J. Davis ORCID: orcid.org/0000-0002-9338-0844[1,10]

Nature **volume 589**, pages554–561(2021)Cite this article

- 388 Accesses
- 172 Altmetric
- Metrics details

Subjects

- Carbon cycle
- Climate-change mitigation
- Climate sciences
- Environmental sciences

Abstract

Historically, human uses of land have transformed and fragmented ecosystems[1,2], degraded biodiversity[3,4], disrupted carbon and nitrogen cycles[5,6] and added prodigious quantities of greenhouse gases (GHGs) to the atmosphere[7,8]. However, in contrast to fossil-fuel carbon dioxide (CO_2) emissions, trends and drivers of GHG emissions from land management and land-use change (together referred to as 'land-use emissions') have not been as comprehensively and systematically assessed. Here we present country-, process-, GHG- and product-specific inventories of global land-use emissions from 1961 to 2017, we decompose key demographic, economic and technical drivers of emissions and we assess the uncertainties and the sensitivity of results to different accounting assumptions. Despite steady increases in population (+144 per cent) and agricultural production per capita (+58 per cent), as well as smaller increases in emissions per land area used (+8 per cent), decreases in land required per unit of agricultural production (–70 per cent) kept global annual land-use emissions relatively constant at about 11 gigatonnes CO_2-equivalent until 2001. After 2001, driven by rising emissions per land area, emissions increased by 2.4 gigatonnes CO_2-equivalent per decade to 14.6 gigatonnes CO_2-equivalent in 2017 (about 25 per cent of total anthropogenic GHG emissions). Although emissions intensity decreased in all regions, large differences across regions persist over time. The three highest-emitting regions (Latin America, Southeast Asia and sub-Saharan Africa) dominate global emissions growth from 1961 to 2017, driven by rapid and extensive growth of agricultural production and related land-use change. In addition, disproportionate emissions are related to certain products: beef and a few other red meats supply only 1 per cent of calories worldwide, but account for 25 per cent of all land-use emissions. Even where land-use change emissions are negligible or negative, total per capita CO_2-equivalent land-use emissions remain near 0.5 tonnes per capita, suggesting the current frontier of mitigation efforts. Our results are consistent with existing knowledge—for example, on the role of population and economic growth and dietary choice—but provide additional insight into regional and sectoral trends.

Access through your institution
Change institution

Buy or subscribe

Access options

Subscribe to Journal

Get full journal access for 1 year

$199.00

only $3.90 per issue

Subscribe

All prices are NET prices.
VAT will be added later in the checkout.

Rent or Buy article

Get time limited or full article access on ReadCube.

from$8.99

Rent or Buy

All prices are NET prices.

Additional access options:

- Log in
- Access through your institution
- Learn about institutional subscriptions

Fig. 1: Estimated emissions from land-use change and land management (land-use emissions) over the period 1961–2017.

Fig. 2: Global and regional drivers of land-use emissions in 1961–2017.

Fig. 3: Global distribution of key *Pale* factors in 2017.

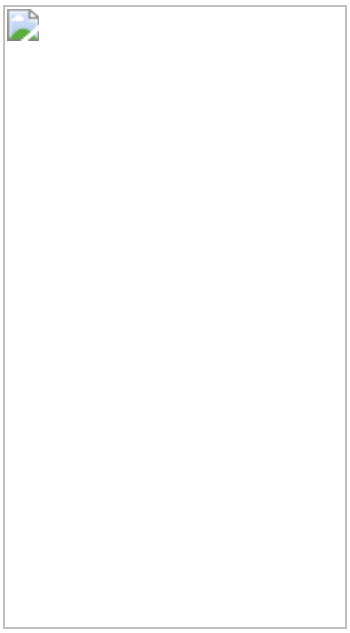

Fig. 4: Intensities of the key *Pale* factors by country and by product.

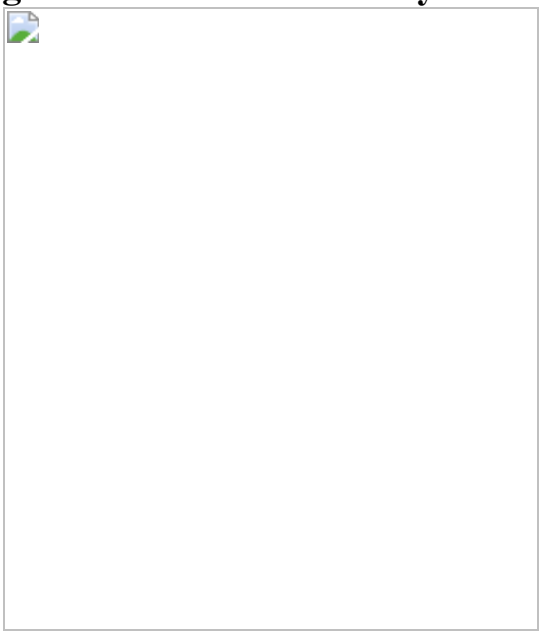

Fig. 5: Trends in per capita land-use emissions.

Data availability

The agricultural emissions data are curated by the FAO and freely available from FAOSTAT at http://faostat.fao.org/. Land-use change emissions (BLUE) data and all of our results are available at https://sustsys.ess.uci.edu/CALUE.html and https://doi.org/10.6084/m9.figshare.12248735.

Code availability

Computer codes or algorithms used to generate results that are reported in the paper and central to the main claims are available at https://github.com/ChaopengHong/Land-use_Emissions.

References

1. 1.

   Foley, J. A. et al. Global consequences of land use. *Science* **309**, 570–574 (2005).

   ADS CAS PubMed PubMed Central Google Scholar

2. 2.

Haddad, N. M. et al. Habitat fragmentation and its lasting impact on Earth's ecosystems. *Sci. Adv*. **1**, e1500052 (2015).

ADS PubMed PubMed Central Google Scholar

3. 3.

Marques, A. et al. Increasing impacts of land use on biodiversity and carbon sequestration driven by population and economic growth. *Nat. Ecol. Evol*. **3**, 628–637 (2019).

PubMed PubMed Central Google Scholar

4. 4.

Newbold, T. et al. Global effects of land use on local terrestrial biodiversity. *Nature* **520**, 45–50 (2015).

ADS CAS PubMed PubMed Central Google Scholar

5. 5.

Houghton, R. A. Land-use change and the carbon cycle. *Glob. Change Biol*. **1**, 275–287 (1995).

ADS Google Scholar

6. 6.

Gruber, N. & Galloway, J. An Earth-system perspective of the global nitrogen cycle. *Nature* **451**, 293–296 (2008).

ADS CAS PubMed PubMed Central Google Scholar

7. 7.

Houghton, R. A. et al. Carbon emissions from land use and land-cover change. *Biogeosciences* **9**, 5125–5142 (2012).

ADS CAS Google Scholar

8. 8.

Carlson, K. M. et al. Greenhouse gas emissions intensity of global croplands. *Nat. Clim. Chang*. **7**, 63–68 (2017).

ADS CAS Google Scholar

9. 9.

Matthews, H. D. & Caldeira, K. Stabilizing climate requires near-zero emissions. *Geophys. Res. Lett*. **35**, L04705 (2008).

ADS Google Scholar

10. 10.

Smith, S. M. et al. Equivalence of greenhouse-gas emissions for peak temperature limits. *Nat. Clim. Chang*. **2**, 535–538 (2012).

ADS CAS Google Scholar

11. 11.

Rogelj, J., Meinshausen, M., Schaeffer, M., Knutti, R. & Riahi, K. Impact of short-lived non-CO2 mitigation on carbon budgets for stabilizing global warming. *Environ. Res. Lett*. **10**, 075001 (2015).

ADS Google Scholar

12. 12.

Collins, W. J. et al. Increased importance of methane reduction for a 1.5 degree target. *Environ. Res. Lett*. **13**, 054003 (2018).

ADS Google Scholar

13. 13.

Peters, G. P. et al. Key indicators to track current progress and future ambition of the Paris Agreement. *Nat. Clim. Chang*. **7**, 118–122 (2017).

ADS Google Scholar

14. 14.

Le Quéré, C. et al. Drivers of declining CO_2 emissions in 18 developed economies. *Nat. Clim. Chang*. **9**, 213–217 (2019).

ADS Google Scholar

15. 15.

FAO. *FAOSTAT* http://faostat.fao.org/ (Food and Agriculture Organization of the United Nations, 2019).

16. 16.

Houghton, R. A. The annual net flux of carbon to the atmosphere from changes in land use, 1850–1990. *Tellus B* **51**, 298–313 (1999).

ADS Google Scholar

17. 17.

Carlson, K. M. et al. Carbon emissions from forest conversion by Kalimantan oil palm plantations. *Nat. Clim. Chang*. **3**, 283–287 (2013).

ADS CAS Google Scholar

18. 18.

Morton, D. C. et al. Cropland expansion changes deforestation dynamics in the southern Brazilian Amazon. *Proc. Natl Acad. Sci. USA* **103**, 14637–14641 (2006).

ADS CAS PubMed PubMed Central Google Scholar

19. 19.

Barona, E., Ramankutty, N., Hyman, G. & Coomes, O. T. The role of pasture and soybean in deforestation of the Brazilian Amazon. *Environ. Res. Lett*. **5**, 024002 (2010).

ADS Google Scholar

20. 20.

Yan, X., Akiyama, H., Yagi, K. & Akimoto, H. Global estimations of the inventory and mitigation potential of methane emissions from rice cultivation conducted using the 2006 Intergovernmental Panel on Climate Change Guidelines. *Glob. Biogeochem. Cycles* **23**, GB2002 (2009).

ADS Google Scholar

21. 21.

Huber, V., Neher, I., Bodirsky, B. L., Hofner, K. & Schellnhuber, H. J. Will the world run out of land? A Kaya-type decomposition to study past trends of cropland expansion. *Environ. Res. Lett*. **9**, 024011 (2014).

ADS Google Scholar

22. 22.

Hosonuma, N. et al. An assessment of deforestation and forest degradation drivers in developing countries. *Environ. Res. Lett*. **7**, 044009 (2012).

ADS Google Scholar

23. 23.

IPCC. *Climate Change and Land* (eds Shukla, P. R. et al.) (IPCC, 2019); https://www.ipcc.ch/srccl/

24. 24.

Hansis, E., Davis, S. J. & Pongratz, J. Relevance of methodological choices for accounting of land use change carbon fluxes. *Glob. Biogeochem. Cycles* **29**, 1230–1246 (2015).

ADS CAS Google Scholar

25. 25.

Davis, S. J., Burney, J. A., Pongratz, J. & Caldeira, K. Methods for attributing land-use emissions to products. *Carbon Manag*. **5**, 233–245 (2014).

CAS Google Scholar

26. 26.

Griscom, B. W. et al. Natural climate solutions. *Proc. Natl Acad. Sci. USA* **114**, 11645–11650 (2017).

ADS CAS PubMed PubMed Central Google Scholar

27. 27.

US EPA. *Global Anthropogenic Non-CO_2 Greenhouse Gas Emissions: 1990–2030*. Report No. 430-R-12-006 (US Environmental Protection Agency, 2012); www.epa.gov/sites/production/files/2016-08/documents/epa_global_nonco2_projections_dec2012.pdf

28. 28.

Janssens-Maenhout, G. et al. EDGAR v4.3.2 Global Atlas of the three major greenhouse gas emissions for the period 1970–2012. *Earth Syst. Sci. Data* **11**, 959–1002 (2019).

ADS Google Scholar

29. 29.

Houghton, R. A. & Nassikas, A. A. Global and regional fluxes of carbon from land use and land cover change 1850–2015. *Glob. Biogeochem. Cycles* **31**, 456–472 (2017).

ADS CAS Google Scholar

30. 30.

Friedlingstein, P. et al. Global carbon budget 2019. *Earth Syst. Sci. Data* **11**, 1783–1838 (2019).

ADS Google Scholar

31. 31.

Gibbs, H. K. et al. Tropical forests were the primary sources of new agricultural land in the 1980s and 1990s. *Proc. Natl Acad. Sci. USA* **107**, 16732–16737 (2010).

ADS CAS PubMed PubMed Central Google Scholar

32. 32.

Sánchez, P. A. Tripling crop yields in tropical Africa. *Nat. Geosci*. **3**, 299–300 (2010).

ADS Google Scholar

33. 33.

Felix, M. & Gheewala, S. H. A review of biomass energy dependency in Tanzania. *Enrgy. Proced*. **9**, 338–343 (2011).

Google Scholar

34. 34.

Sola, P., Ochieng, C., Yila, J. & Iiyama, M. Links between energy access and food security in sub Saharan Africa: an exploratory review. *Food Secur*. **8**, 635–642 (2016).

Google Scholar

35. 35.

Gustavsson, J., Cederberg, C. & Sonesson, U. *Global Food Losses and Food Waste: Extent, Causes and Prevention* (Food and Agriculture Organization of the United Nations, 2011); http://www.fao.org/3/a-i2697e.pdf

36. 36.

D'Odorico, P., Carr, J. A., Laio, F., Ridolfi, L. & Vandoni, S. Feeding humanity through global food trade. *Earths Futur*. **2**, 458–469 (2014).

ADS Google Scholar

37. 37.

Lamb, A. et al. The potential for land sparing to offset greenhouse gas emissions from agriculture. *Nat. Clim. Chang*. **6**, 488–492 (2016).

ADS Google Scholar

38. 38.

Clark, M. & Tilman, D. Comparative analysis of environmental impacts of agricultural production systems, agricultural input efficiency, and food choice. *Environ. Res. Lett*. **12**, 064016 (2017).

ADS Google Scholar

39. 39.

Kanter, D. R. & Searchinger, T. D. A technology-forcing approach to reduce nitrogen pollution. *Nat. Sustain*. **1**, 544–552 (2018); author correction **1**, 719 (2018).

Google Scholar

40. 40.

Paustian, K. et al. Climate-smart soils. *Nature* **532**, 49–57 (2016).

ADS CAS PubMed PubMed Central Google Scholar

41. 41.

Herrero, M. et al. Greenhouse gas mitigation potentials in the livestock sector. *Nat. Clim. Chang*. **6**, 452–461 (2016).

ADS Google Scholar

42. 42.

Ritchie, H., Reay, D. S. & Higgins, P. Beyond calories: a holistic assessment of the global food system. *Front. Sustain. Food Syst*. **2**, 57 (2018).

Google Scholar

43. 43.

Bajželj, B. et al. Importance of food-demand management for climate mitigation. *Nat. Clim. Chang*. **4**, 924–929 (2014).

ADS Google Scholar

44. 44.

Poore, J. & Nemecek, T. Reducing food's environmental impacts through producers and consumers. *Science* **360**, 987–992 (2018); erratum **363**, eaaw9908 (2019).

ADS CAS PubMed PubMed Central Google Scholar

45. 45.

Stehfest, E. Food choices for health and planet. *Nature* **515**, 501–502 (2014).

ADS CAS PubMed PubMed Central Google Scholar

46. 46.

Jiang, Y. et al. Water management to mitigate the global warming potential of rice systems: a global meta-analysis. *Field Crops Res*. **234**, 47–54 (2019).

Google Scholar

47. 47.

Jiang, Y. et al. Higher yields and lower methane emissions with new rice cultivars. *Glob. Change Biol*. **23**, 4728–4738 (2017).

ADS Google Scholar

48. 48.

Roque, B. M. et al. Effect of the macroalgae *Asparagopsis taxiformis* on methane production and rumen microbiome assemblage. *Animal Microbiome* **1**, 3 (2019); correction **1**, 4 (2019).

Google Scholar

49. 49.

Lamb, W. F. & Minx, J. C. The political economy of national climate policy: architectures of constraint and a typology of countries. *Energy Res. Soc. Sci*. **64**, 101429 (2020).

Google Scholar

50. 50.

Clark, M. A. et al. Global food system emissions could preclude achieving the 1.5° and 2° C climate change targets. *Science* **370**, 705–708 (2020).

51. 51.

Hurtt, G. C. et al. Harmonization of global land use change and management for the period 850–2100 (LUH2) for CMIP6. *Geosci. Model Dev*. **13**, 5425–5464 (2020).

ADS Google Scholar

52. 52.

Pongratz, J., Reick, C., Raddatz, T. & Claussen, M. A reconstruction of global agricultural areas and land cover for the last millennium. *Glob. Biogeochem. Cycles* **22**, GB3018 (2008).

ADS Google Scholar

53. 53.

Houghton, R. A. et al. Changes in the carbon content of terrestrial biota and soils between 1860 and 1980: a net release of CO_2 to the atmosphere. *Ecol. Monogr*. **53**, 235–262 (1983).

CAS Google Scholar

54. 54.

Heinimann, A. et al. A global view of shifting cultivation: recent, current, and future extent. *PLoS One* **12**, e0184479 (2017).

PubMed PubMed Central Google Scholar

55. 55.

Leifeld, J., Wust-Galley, C. & Page, S. Intact and managed peatland soils as a source and sink of GHGs from 1850 to 2100. *Nat. Clim. Chang*. **9**, 945–947 (2019).

ADS CAS Google Scholar

56. 56.

Hooijer, A. et al. Current and future CO_2 emissions from drained peatlands in Southeast Asia. *Biogeosciences* **7**, 1505–1514 (2010).

ADS CAS Google Scholar

57. 57.

van der Werf, G. R. et al. Global fire emissions estimates during 1997–2016. *Earth Syst. Sci. Data* **9**, 697–720 (2017).

ADS Google Scholar

58. 58.

Tubiello, F. N. et al. The FAOSTAT database of greenhouse gas emissions from agriculture. *Environ. Res. Lett*. **8**, 015009 (2013).

ADS Google Scholar

59. 59.

Conant, R. T., Berdanier, A. B. & Grace, P. R. Patterns and trends in nitrogen use and nitrogen recovery efficiency in world agriculture. *Glob. Biogeochem. Cycles* **27**, 558–566 (2013).

ADS CAS Google Scholar

60. 60.

IPCC. *Guidelines for National Greenhouse Gas Inventories* Vol. 4 (IPCC, 2006).

61. 61.

FAO. *Global Agro-Ecological Zones (GAEZ v3.0)* http://www.fao.org/nr/gaez/en/ (Food and Agriculture Organization of the United Nations, 2012).

62. 62.

Davis, S. J., Peters, G. P. & Caldeira, K. The supply chain of CO_2 emissions. *Proc. Natl Acad. Sci. USA* **108**, 18554–18559 (2011).

ADS CAS PubMed PubMed Central Google Scholar

63. 63.

Davis, S. J. & Caldeira, K. Consumption-based accounting of CO_2 emissions. *Proc. Natl Acad. Sci. USA* **107**, 5687–5692 (2010).

ADS CAS PubMed PubMed Central Google Scholar

64. 64.

Peters, G. P. & Hertwich, E. G. CO_2 embodied in international trade with implications for global climate policy. *Environ. Sci. Technol*. **42**, 1401–1407 (2008).

ADS CAS PubMed PubMed Central Google Scholar

65. 65.

UN. *World Population Prospects 2019: Highlights*. Report No. ST/ESA/SER.A/423 (United Nations, 2019);

https://population.un.org/wpp/Publications/Files/WPP2019_Highlights.pdf

66. 66.

FAO. *Food Balance Sheets: A Handbook* (Food and Agriculture Organization of the United Nations, 2001); http://www.fao.org/docrep/pdf/011/x9892e/x9892e00.pdf

67. 67.

Robinson, T. P., Franceschini, G. & Wint, W. The Food and Agriculture Organization's gridded livestock of the world. *Vet. Ital*. **43**, 745–751 (2007).

PubMed PubMed Central Google Scholar

68. 68.

Robinson, T. P. et al. Mapping the global distribution of livestock. *PLoS One* **9**, e96084 (2014).

ADS PubMed PubMed Central Google Scholar

69. 69.

Herrero, M. et al. Biomass use, production, feed efficiencies, and greenhouse gas emissions from global livestock systems. *Proc. Natl Acad. Sci. USA* **110**, 20888–20893 (2013).

ADS CAS PubMed PubMed Central Google Scholar

70. 70.

IPCC. *Climate Change 2014: Mitigation of Climate Change* (eds Edenhofer, O. et al.) (Cambridge Univ. Press, 2014).

71. 71.

IPCC. *Climate Change 2013: The Physical Science Basis* (eds Stocker, T. F. et al.) (Cambridge Univ. Press, 2013).

72. 72.

Allen, M. R. et al. A solution to the misrepresentations of CO_2-equivalent emissions of short-lived climate pollutants under ambitious mitigation. *npj Clim. Atmos. Sci* **1**, 16 (2018).

Google Scholar

73. 73.

Cain, M. et al. Improved calculation of warming-equivalent emissions for short-lived climate pollutants. *npj Clim. Atmos. Sci*. **2**, 29 (2019).

PubMed PubMed Central Google Scholar

74. 74.

Le Quéré, C. et al. Global carbon budget 2018. *Earth Syst. Sci. Data* **10**, 2141–2194 (2018).

ADS Google Scholar

75. 75.

Lawrence, D. M. et al. The Land Use Model Intercomparison Project (LUMIP) contribution to CMIP6: rationale and experimental design. *Geosci. Model Dev*. **9**, 2973–2998 (2016).

ADS Google Scholar

Download references

Acknowledgements

A. LoPresti helped with preliminary analysis; E. Hansis made important contributions to the development of the BLUE model. K. Hartung helped with additional BLUE simulations. We thank A. Jain and D. Goll for providing ISAM and ORCHIDEE-CNP data. We thank R. A. Houghton and A. A. Nassikas for providing data from ref. [29]. We thank R. T. Conant for providing crop-specific fertilizer application rates. The manuscript also benefitted from discussions with R. Andrew, L. Chini, H. van Grinsven, K. Hartung, R. A. Houghton, S. Kloster, E. Lambin, D. Lobell, P. Meyfroidt, G. Peters, Y. Qin, T. Raddatz, J. Randerson, M. Raupach, D. Tong and T. West. C.H., J.A.B. and S.J.D. were supported by the US National Science Foundation and US Department of Agriculture (INFEWS grant EAR 1639318). J.P. and J.E.M.S.N. were supported by the German Research Foundation's Emmy Noether Programme (PO1751/1-1). R.B.J. acknowledges support from the Gordon and Betty Moore Foundation (grant GBMF5439).

Author information

Affiliations

1. Department of Earth System Science, University of California, Irvine, Irvine, CA, USA

   Chaopeng Hong & Steven J. Davis

2. School of Global Policy and Strategy, University of California, San Diego, San Diego, CA, USA

   Jennifer A. Burney

3. Department of Geography, Ludwig-Maximilians-Universität, Munich, Germany

   Julia Pongratz

4. Department of Land in the Earth System, Max Planck Institute for Meteorology, Hamburg, Germany

Julia Pongratz & Julia E. M. S. Nabel

5. Department of Ecosystem Science and Sustainability, Colorado State University, Fort Collins, CO, USA

   Nathaniel D. Mueller

6. Department of Soil and Crop Sciences, Colorado State University, Fort Collins, CO, USA

   Nathaniel D. Mueller

7. Department of Earth System Science, Stanford University, Stanford, CA, USA

   Robert B. Jackson

8. Woods Institute for the Environment, Stanford University, Stanford, CA, USA

   Robert B. Jackson

9. Precourt Institute for Energy, Stanford University, Stanford, CA, USA

   Robert B. Jackson

10. Department of Civil and Environmental Engineering, University of California, Irvine, Irvine, CA, USA

    Steven J. Davis

Authors

1. Chaopeng Hong
   View author publications

   You can also search for this author in PubMed Google Scholar

2. Jennifer A. Burney

View author publications

You can also search for this author in PubMed Google Scholar

3. Julia Pongratz
View author publications

You can also search for this author in PubMed Google Scholar

4. Julia E. M. S. Nabel
View author publications

You can also search for this author in PubMed Google Scholar

5. Nathaniel D. Mueller
View author publications

You can also search for this author in PubMed Google Scholar

6. Robert B. Jackson
View author publications

You can also search for this author in PubMed Google Scholar

7. Steven J. Davis
View author publications

You can also search for this author in PubMed Google Scholar

Contributions

S.J.D., C.H., J.A.B. and J.P. conceived the study. C.H., S.J.D. and J.A.B. performed the analyses, with support from J.P. and J.E.M.S.N. on datasets, and from N.D.M and R.B.J. on analytical approaches. C.H. and S.J.D. led the writing with input from all co-authors. All co-authors reviewed and commented on the manuscript.

Corresponding authors

Correspondence to Chaopeng Hong or Jennifer A. Burney or Steven J. Davis.

Ethics declarations

Competing interests

The authors declare no competing interests.

Additional information

Peer review information *Nature* thanks Jan Minx, David Reay, Stefan Wirsenius and the other, anonymous, reviewer(s) for their contribution to the peer review of this work.

Publisher's note Springer Nature remains neutral with regard to jurisdictional claims in published maps and institutional affiliations.

Extended data figures and tables

Extended Data Fig. 1 Differences in global cumulative land-use emissions attributed to processes and products, obtained using different accounting methods.

a–**r**, Estimated global cumulative land-use emissions attributed to processes (**a**–**c**) and products (**d**–**r**) over 1961–2017, using different accounting methods to distribute land-use change emissions over time and to products. Our base results (**a**, **d**) reflect emissions occurring in each year owing to past changes in land use (legacy emissions; left), calculated using GWP_{100}, and allocated among crops and livestock by land area used. Different methods to distribute land-use change emissions over time have also been evaluated, that is, all future emissions from a change in land use are assigned to the year of the change (committed emissions; middle) and committed emissions amortized uniformly over 20 years (uniformly distributed emissions; right). Different methods to distribute land-use

change emissions to products have also been evaluated, that is, allocating among crops and livestock by change in land area (**g**–**i**), calories of production (**j**–**l**), mass of production (**m**–**o**) and change in mass of production (**p**–**r**) (see Methods). Error bars denote uncertainty ranges (68% intervals), determined by uncertainties in land-use change emissions and in agricultural emissions, as well as uncertainties in the GWP_{100} values. Carbon uptake from agriculture abandonment (negative emissions) is not shown.

Extended Data Fig. 2 Global land-use emissions by product group in 2017, with two accountings of the emissions related to feed crops.

Our base case allocates the feed crop emissions to the crops themselves (bars). The results of the other accounting—allocating the feed crop emissions to the livestock that consumed the feed—are shown by dots. Numbers are the emissions related to crops fed to livestock (negative values for crops and positive values for livestock) in units of Mt CO_2-eq.

Extended Data Fig. 3 Uncertainties in global and regional land-use GHG emissions over the period 1961–2017 related to emission metrics.

a–**i**, Curves show trends in CO_2 (orange), CH_4 (green), N_2O (purple) and total GHG emissions (black) for the global total (**a**) and for each region (**b**–**i**). For our base case, we aggregate all GHG emissions (that is, CO_2, CH_4 and N_2O) in units of CO_2-eq using GWP_{100} values of CH_4 and N_2O. Solid curves show trends in CH_4, N_2O and total GHG emissions calculated using GWP_{100}, with the shading reflecting the range of uncertainty in GWP_{100} values. To assess the sensitivity of the results to metric choices, we also estimate emissions using the GWP* method. Dashed curves show trends in CH_4 and total GHG emissions calculated using GWP* (in units of CO_2-e*). For CO_2 and N_2O, CO_2-eq and CO_2-e* emissions are identical. The length

of CO_2-e*emissions records is reduced because interannual variability is smoothed with a 20-year running average.

Extended Data Fig. 4 Comparison of global and regional agricultural emissions between this work, EDGAR and USEPA.

a–**i**, Curves show trends in agricultural emissions for the global total (**a**) and for each region (**b**–**i**), estimated in this work (green; based on FAO data), by EDGAR (orange) and by USEPA (blue). All estimated emissions are converted into CO_2-equivalents, based on the same GWP_{100} values from the IPCC Fifth Assessment Report (34 for CH_4 and 298 for N_2O). The shaded areas reflect the range of uncertainty in agricultural emissions in this work, determined by Monte Carlo analysis (performed by varying activity data, parameter values and emission factors from those used in the FAO database).

Extended Data Fig. 5 Comparison of global and regional land-use change emissions between two bookkeeping models.

a–**i**, Curves show trends in land-use change emissions for the global total (**a**) and for each region (**b**–**i**), estimated by BLUE (black; used in this work) and H&N (orange; available until 2015 only). The average of the bookkeeping models (green line) is also shown. The range from the uncertainty simulations with BLUE is shown as the 68% uncertainty range of our estimates (grey areas), with the five additional simulations using different assumptions indicated by thin lines: different assumptions on land-use transitions (purple) and different assumptions on carbon values (green).

Extended Data Fig. 6 Comparison of global and regional land-use emissions, obtained using different land-use change emissions from two bookkeeping models.

a–**i**, Curves show trends in land-use emissions for the global total (**a**) and for each region (**b**–**i**), obtained using land-use change emissions from BLUE (black; used in this work) and H&N (orange; available until 2015

only). The average of the two bookkeeping models (green line) is also shown. In this work, we combined agricultural emissions from the FAO with land-use change emissions estimated by the BLUE model to calculate total land-use emissions. We performed sensitivity analyses by also combining the agricultural emissions from the FAO with the land-use change emissions estimated by another bookkeeping model (H&N) and with the average of two bookkeeping models (BLUE and H&N). Lighter grey areas represent uncertainty ranges (68% intervals) of our estimates, determined by uncertainties in land-use change emissions and in agricultural emissions, as well as uncertainties in the GWP_{100} values. Darker grey areas show uncertainties only related to land-use change emissions, determined from additional simulations with the BLUE model.

Extended Data Fig. 7 Comparison of global and regional trends in land-use emissions and *Pale* factors, obtained using different land-use change emission inventories.

a–**i**, Curves show trends in land-use emissions (black), emissions intensity of land use (orange) and agricultural production (red) for the global total (**a**) and for each region (**b**–**i**), using land-use change emissions from BLUE (solid lines; used in this work) and the combination of two bookkeeping models (dashed lines; available until 2015 only). In this work, we combined agricultural emissions from the FAO with land-use change emissions estimated by the BLUE model to perform *Pale* analysis of land-use emissions. We also performed an additional *Pale* analysis by using agricultural emissions from the FAO combined with the average of land-use change emissions from two bookkeeping models (BLUE and H&N). Lighter grey areas represent uncertainty ranges (68% intervals) of our estimates, determined by uncertainties in land-use change emissions and in agricultural emissions, as well as uncertainties in the GWP_{100} values. Darker grey areas show uncertainties related only to land-use change emissions, determined from additional simulations with the BLUE model.

Extended Data Fig. 8 Global and regional trends in *Pale* factors contributing to land-use emissions during 1961–2017,

decomposed into land-use change emissions and agricultural emissions.

a–**i**, Curves show changes in the *Pale* factors contributing to land-use change (LUC, solid lines) emissions and agricultural (Ag, dashed lines) emissions over the period 1961–2017 for the global total (**a**) and for each region (**b**–**i**) relative to 1961. Results shown are for our base assumptions (see Extended Data Fig. 1), and different curves are labelled in **a**. Oceania is not shown.

Extended Data Fig. 9 Estimated land-use emissions over the period 1961–2017 for nine world regions.

a–**i**, Estimated land-use emissions for each region (**a**–**i**) by process, product group and GHG emitted. In each panel, net emissions are shown by the bold black line.

Extended Data Fig. 10 Changes in 2007–2017 in *Pale* factors of the 50 country–product sources with the largest annual emissions.

a–**d**, Bars show the per cent change in annual land-use emissions (**a**), per capita production (**b**), land intensity of production (**c**) and emissions intensity of land use (**d**) for each country–product combination.

Extended Data Fig. 11 Trends in emissions intensity of major agricultural products.

a–**c**, Curves show trends in emissions intensity of processes including CH_4 emissions from rice (**a**) and dairy cattle (**b**) production and N_2O emissions from fertilizer use for rice production (**c**). **d**–**i**, Curves show trends in emissions intensity of major agricultural products including rice (**d**), maize (**e**), soybeans (**f**), oil palm (**g**), dairy cattle (**h**) and sheep and goats (**i**). Total emissions per calorie of agricultural production (**d**–**i**) in the six countries

that produce the most of each product tend to decrease over time, but in all cases remain greater than zero.

Extended Data Table 1 Data sources used for the study
Full size table
Extended Data Table 2 169 agricultural products and their categorization
Full size table

Supplementary information

Supplementary Table

Supplementary Table 1: The uncertainty ranges for activity data, parameters and emission factors for agricultural processes.

Rights and permissions

Reprints and Permissions

About this article

Check for updates

Cite this article

Hong, C., Burney, J.A., Pongratz, J. *et al.* Global and regional drivers of land-use emissions in 1961–2017. *Nature* **589,** 554–561 (2021). https://doi.org/10.1038/s41586-020-03138-y

Download citation

- Received: 26 November 2019

- Accepted: 23 October 2020
- Published: 27 January 2021
- Issue Date: 28 January 2021
- DOI: https://doi.org/10.1038/s41586-020-03138-y

Comments

By submitting a comment you agree to abide by our Terms and Community Guidelines. If you find something abusive or that does not comply with our terms or guidelines please flag it as inappropriate.

Access through your institution
Change institution
Buy or subscribe

This article was downloaded by **calibre** from https://www.nature.com/articles/s41586-020-03138-y

| Section menu | Main menu |

- Article
- Published: 27 January 2021

A thin mantle transition zone beneath the equatorial Mid-Atlantic Ridge

- Matthew R. Agius ORCID: orcid.org/0000-0002-2620-295X[1] [nAff3],
- Catherine A. Rychert ORCID: orcid.org/0000-0001-5071-793X[1],
- Nicholas Harmon[1],
- Saikiran Tharimena ORCID: orcid.org/0000-0002-1841-1911[1] [nAff4] &
- J.-Michael Kendall[2]

Nature **volume 589**, pages562–566(2021)Cite this article

- 131 Accesses
- 360 Altmetric
- Metrics details

Subjects

- Geodynamics
- Geophysics
- Seismology

Abstract

The location and degree of material transfer between the upper and lower mantle are key to the Earth's thermal and chemical evolution. Sinking slabs

and rising plumes are generally accepted as locations of transfer[1,2], whereas mid-ocean ridges are not typically assumed to have a role[3]. However, tight constraints from in situ measurements at ridges have proved to be challenging. Here we use receiver functions that reveal the conversion of primary to secondary seismic waves to image the discontinuities that bound the mantle transition zone, using ocean bottom seismic data from the equatorial Mid-Atlantic Ridge. Our images show that the seismic discontinuity at depths of about 660 kilometres is broadly uplifted by 10 ± 4 kilometres over a swath about 600 kilometres wide and that the 410-kilometre discontinuity is depressed by 5 ± 4 kilometres. This thinning of the mantle transition zone is coincident with slow shear-wave velocities in the mantle, from global seismic tomography[4,5,6,7]. In addition, seismic velocities in the mantle transition zone beneath the Mid-Atlantic Ridge are on average slower than those beneath older Atlantic Ocean seafloor. The observations imply material transfer from the lower to the upper mantle—either continuous or punctuated—that is linked to the Mid-Atlantic Ridge. Given the length and longevity of the mid-ocean ridge system, this implies that whole-mantle convection may be more prevalent than previously thought, with ridge upwellings having a role in counterbalancing slab downwellings.

Access through your institution
Change institution
Buy or subscribe

Access options

Subscribe to Journal

Get full journal access for 1 year

$199.00

only $3.90 per issue

Subscribe

All prices are NET prices.
VAT will be added later in the checkout.

Rent or Buy article

Get time limited or full article access on ReadCube.

from$8.99

Rent or Buy

All prices are NET prices.

Additional access options:

- Log in
- Access through your institution
- Learn about institutional subscriptions

Fig. 1: The PI-LAB network, data coverage and mantle transition zone delay time.

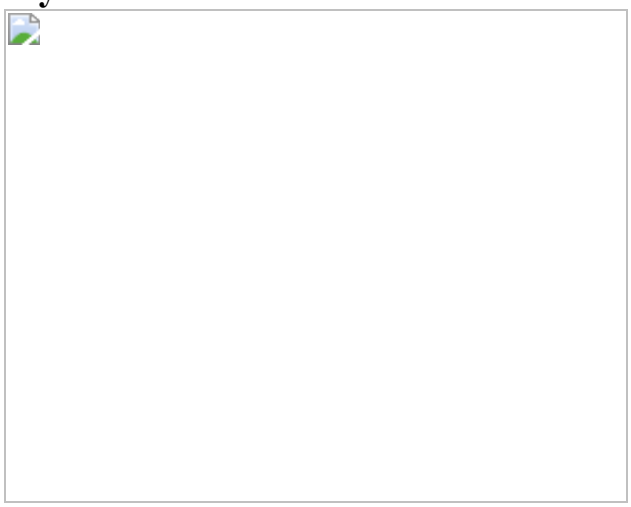

Fig. 2: Vertical cross-section from the 3D depth-migrated receiver functions.

Fig. 3: Horizontal cross-sections from the 3D depth-migrated receiver functions.

Fig. 4: Mantle flow beneath the Mid-Atlantic Ridge.

Data availability

Data are available from the Incorporated Research Institutions for Seismology (IRIS) Data Management Center (DMC) website https://ds.iris.edu/ds/nodes/dmc/ under the XS network for 2016-2017

(https://doi.org/10.7914/SN/XS_2016). Source data are provided with this paper.

Code availability

The methods and codes used are standard and widely used[42] and are detailed in the Methods section. Figures were made using Generic Mapping Tools[61] and MATLAB. Correspondence and requests for materials should be addressed to M.R.A.

References

1. 1.

   van der Hilst, R. D. Complex morphology of subducted lithosphere in the mantle beneath the Tonga trench. *Nature* **374**, 154–157 (1995).

   ADS Google Scholar

2. 2.

   Montelli, R. et al. Finite-frequency tomography reveals a variety of plumes in the mantle. *Science* **303**, 338–343 (2004).

   CAS ADS Google Scholar

3. 3.

   Hofmann, A. W. Mantle geochemistry: the message from oceanic volcanism. *Nature* **385**, 219–229 (1997).

   CAS ADS Google Scholar

4. 4.

   Chang, S. J., Ferreira, A. M., Ritsema, J., van Heijst, H. J. & Woodhouse, J. H. Joint inversion for global isotropic and radially

anisotropic mantle structure including crustal thickness perturbations. *J. Geophys. Res*. **120**, 4278–4300 (2015).

ADS Google Scholar

5. 5.

Ritsema, J., Deuss, A. A., Van Heijst, H. J. & Woodhouse, J. H. S40RTS: a degree-40 shear-velocity model for the mantle from new Rayleigh wave dispersion, teleseismic traveltime and normal-mode splitting function measurements. *Geophys. J. Int*. **184**, 1223–1236 (2011).

ADS Google Scholar

6. 6.

French, S., Lekic, V. & Romanowicz, B. Waveform tomography reveals channeled flow at the base of the oceanic asthenosphere. *Science* **342**, 227–230 (2013).

CAS ADS Google Scholar

7. 7.

Montelli, R., Nolet, G., Dahlen, F. A. & Masters, G. A catalogue of deep mantle plumes: new results from finite-frequency tomography. *Geochem. Geophys. Geosyst*. **7**, https://doi.org/10.1029/2006GC001248 (2006).

8. 8.

Dziewonski, A. M. & Anderson, D. L. Preliminary reference Earth model. *Phys. Earth Planet. Inter*. **25**, 297–356 (1981).

ADS Google Scholar

9. 9.

Rickers, F., Fichtner, A. & Trampert, J. The Iceland–Jan Mayen plume system and its impact on mantle dynamics in the North Atlantic region: evidence from full-waveform inversion. *Earth Planet. Sci. Lett*. **367**, 39–51 (2013).

CAS ADS Google Scholar

10. 10.

French, S. W. & Romanowicz, B. Broad plumes rooted at the base of the Earth's mantle beneath major hotspots. *Nature* **525**, 95–99 (2015).

CAS PubMed PubMed Central ADS Google Scholar

11. 11.

Fukao, Y. & Obayashi, M. Subducted slabs stagnant above, penetrating through, and trapped below the 660 km discontinuity. *J. Geophys. Res*. **118**, 5920–5938 (2013).

ADS Google Scholar

12. 12.

Li, C., van der Hilst, R. D., Engdahl, E. R. & Burdick, S. A new global model for P wave speed variations in Earth's mantle. *Geochem. Geophys. Geosyst*. **9**, https://doi.org/10.1029/2007GC001806 (2008).

13. 13.

Ito, E. & Katsura, T. A temperature profile of the mantle transition zone. *Geophys. Res. Lett*. **16**, 425–428 (1989).

CAS ADS Google Scholar

14. 14.

Lawrence, J. F. & Shearer, P. M. Imaging mantle transition zone thickness with SdS-SS finite-frequency sensitivity kernels. *Geophys. J.*

Int. **174**, 143–158 (2008).

ADS Google Scholar

15. 15.

Houser, C., Masters, G., Flanagan, M. & Shearer, P. Determination and analysis of long-wavelength transition zone structure using SS precursors. *Geophys. J. Int*. **174**, 178–194 (2008).

ADS Google Scholar

16. 16.

Phipps Morgan, J. & Morgan, W. J. Two-stage melting and the geochemical evolution of the mantle: a recipe for mantle plum-pudding. *Earth Planet. Sci. Lett*. **170**, 215–239 (1999).

CAS ADS Google Scholar

17. 17.

Jellinek, A. M. & Manga, M. The influence of a chemical boundary layer on the fixity, spacing and lifetime of mantle plumes. *Nature* **418**, 760–763 (2002).

CAS PubMed PubMed Central ADS Google Scholar

18. 18.

Jellinek, A. M. & Manga, M. Links between long-lived hot spots, mantle plumes, D″, and plate tectonics. *Rev. Geophys*. **42**, https://doi.org/10.1029/2003RG000144 (2004).

19. 19.

McNamara, A. K. & Zhong, S. Thermochemical structures beneath Africa and the Pacific Ocean. *Nature* **437**, 1136–1139 (2005).

CAS PubMed PubMed Central ADS Google Scholar

20. 20.

Kellogg, L. H., Hager, B. H. & van der Hilst, R. D. Compositional stratification in the deep mantle. *Science* **283**, 1881–1884 (1999).

CAS PubMed PubMed Central ADS Google Scholar

21. 21.

Ballmer, M. D., Schmerr, N. C., Nakagawa, T. & Ritsema, J. Compositional mantle layering revealed by slab stagnation at ~1000-km depth. *Sci. Adv*. **1**, e1500815 (2015).

PubMed PubMed Central ADS Google Scholar

22. 22.

Marquardt, H. & Miyagi, L. Slab stagnation in the shallow lower mantle linked to an increase in mantle viscosity. *Nat. Geosci*. **8**, 311–314 (2015).

CAS ADS Google Scholar

23. 23.

Ballmer, M. D., Houser, C., Hernlund, J. W., Wentzcovitch, R. M. & Hirose, K. Persistence of strong silica-enriched domains in the Earth's lower mantle. *Nat. Geosci*. **10**, 236–240 (2017).

CAS ADS Google Scholar

24. 24.

Bercovici, D. & Karato, S. I. Whole-mantle convection and the transition-zone water filter. *Nature* **425**, 39–44 (2003).

CAS PubMed PubMed Central ADS Google Scholar

25. 25.

Lawrence, J. F. & Shearer, P. M. A global study of transition zone thickness using receiver functions. *J. Geophys. Res*. **111**, https://doi.org/10.1029/2005JB003973 (2006).

26. 26.

Shen, Y., Sheehan, A. F., Dueker, K. G., de Groot–Hedlin, C. & Gilbert, H. Mantle discontinuity structure beneath the southern East Pacific Rise from P-to-S converted phases. *Science* **280**, 1232–1235 (1998).

CAS PubMed PubMed Central ADS Google Scholar

27. 27.

Ruan, A. et al. Crustal structure and mantle transition zone thickness beneath a hydrothermal vent at the ultra-slow spreading Southwest Indian Ridge (49° 39′ E): a supplementary study based on passive seismic receiver functions. *Mar. Geophys. Res*. **38**, 39–46 (2017).

Google Scholar

28. 28.

Saki, M., Thomas, C., Nippress, S. E. & Lessing, S. Topography of upper mantle seismic discontinuities beneath the North Atlantic: the Azores, Canary and Cape Verde plumes. *Earth Planet. Sci. Lett*. **409**, 193–202 (2015).

CAS ADS Google Scholar

29. 29.

Courtillot, V., Davaille, A., Besse, J. & Stock, J. Three distinct types of hotspots in the Earth's mantle. *Earth Planet. Sci. Lett*. **205**, 295–308 (2003).

CAS ADS Google Scholar

30. 30.

Le Voyer, M., Cottrell, E., Kelley, K. A., Brounce, M. & Hauri, E. H. The effect of primary versus secondary processes on the volatile content of MORB glasses: an example from the equatorial Mid-Atlantic Ridge (5° N–3° S). *J. Geophys. Res*. **120**, 125–144 (2015).

Google Scholar

31. 31.

Jenkins, J., Cottaar, S., White, R. S. & Deuss, A. Depressed mantle discontinuities beneath Iceland: evidence of a garnet controlled 660 km discontinuity? *Earth Planet. Sci. Lett*. **433**, 159–168 (2016).

CAS ADS Google Scholar

32. 32.

Agius, M. R., Rychert, C. A., Harmon, N. & Laske, G. Mapping the mantle transition zone beneath Hawaii from Ps receiver functions: evidence for a hot plume and cold mantle downwellings. *Earth Planet. Sci. Lett*. **474**, 226–236 (2017).

CAS ADS Google Scholar

33. 33.

Thomson, A. R., Walter, M. J., Kohn, S. C. & Brooker, R. A. Slab melting as a barrier to deep carbon subduction. *Nature* **529**, 76–79 (2016).

CAS ADS Google Scholar

34. 34.

Dalton, C. A., Langmuir, C. H. & Gale, A. Geophysical and geochemical evidence for deep temperature variations beneath mid-ocean ridges. *Science* **344**, 80–83 (2014).

CAS PubMed PubMed Central ADS Google Scholar

35. 35.

Richter, F. M. Convection and the large-scale circulation of the mantle. *J. Geophys. Res*. **78**, 8735–8745 (1973).

ADS Google Scholar

36. 36.

Schilling, J. G., Hanan, B. B., McCully, B., Kingsley, R. H. & Fontignie, D. Influence of the Sierra Leone mantle plume on the equatorial Mid-Atlantic Ridge: a Nd–Sr–Pb isotopic study. *J. Geophys. Res*. **99**, 12005–12028 (1994).

ADS Google Scholar

37. 37.

Bird, P. An updated digital model of plate boundaries. *Geochem. Geophys. Geosyst*. **4**, https://doi.org/10.1029/2001GC000252 (2003).

38. 38.

Agius, M. R., Harmon, N., Rychert, C. A., Tharimena, S. & Kendall, J. M. Sediment characterization at the equatorial Mid-Atlantic Ridge from P-to-S teleseismic phase conversions recorded on the PI-LAB experiment. *Geophys. Res. Lett*. **45**, https://doi.org/10.1029/2018GL080565 (2018).

39. 39.

Harmon, N. et al. Marine geophysical investigation of the chain fracture zone in the Equatorial Atlantic from the PI-LAB experiment.

J. Geophys. Res. **123**, 11030–11016 (2018).

Google Scholar

40. 40.

Crawford, W. C. & Webb, S. C. Identifying and removing tilt noise from low-frequency (<0.1 Hz) seafloor vertical seismic data. *Bull. Seismol. Soc. Am*. **90**, 952–963 (2000).

Google Scholar

41. 41.

Bell, S. W., Forsyth, D. W. & Ruan, Y. Removing noise from the vertical component records of ocean-bottom seismometers: results from year one of the Cascadia Initiative. *Bull. Seismol. Soc. Am*. **105**, 300–313 (2015).

Google Scholar

42. 42.

Helffrich, G. Extended-time multitaper frequency domain cross-correlation receiver-function estimation. *Bull. Seismol. Soc. Am*. **96**, 344–347 (2006).

Google Scholar

43. 43.

Rychert, C. A., Laske, G., Harmon, N. & Shearer, P. M. Seismic imaging of melt in a displaced Hawaiian plume. *Nat. Geosci*. **6**, 657–660 (2013).

CAS ADS Google Scholar

44. 44.

Efron, B. & Tibshirani, R. Statistical data analysis in the computer age. *Science* **253**, 390–395 (1991).

CAS ADS Google Scholar

45. 45.

Schmandt, B., Jacobsen, S. D., Becker, T. W., Liu, Z. & Dueker, K. G. Dehydration melting at the top of the lower mantle. *Science* **344**, 1265–1268 (2014).

CAS ADS Google Scholar

46. 46.

Harmon, N. et al. Evolution of the oceanic lithosphere in the equatorial Atlantic from Rayleigh wave tomography, evidence for small-scale convection from the PI-LAB experiment. *Geochem. Geophys. Geosyst*. **21**, e2020GC009174 (2020).

ADS Google Scholar

47. 47.

Wang, S., Constable, S., Rychert, C. A. & Harmon, N. A lithosphere-asthenosphere boundary and partial melt estimated using marine magnetotelluric data at the central Middle Atlantic Ridge. *Geochem. Geophys. Geosyst*. **21**, e2020GC009177 (2020).

ADS Google Scholar

48. 48.

Bina, C. R. & Helffrich, G. Phase transition Clapeyron slopes and transition zone seismic discontinuity topography. *J. Geophys. Res*. **99**, 15853–15860 (1994).

CAS ADS Google Scholar

49. 49.

Ye, Y., Gu, C., Shim, S. H., Meng, Y. & Prakapenka, V. The postspinel boundary in pyrolitic compositions determined in the laser-heated diamond anvil cell. *Geophys. Res. Lett*. **41**, 3833–3841 (2014).

CAS ADS Google Scholar

50. 50.

Litasov, K. D., Ohtani, E. & Sano, A. Influence of water on major phase transitions in the Earth's mantle. *Geophys. Monogr. Ser*. **168**, 95–111 (2006).

CAS Google Scholar

51. 51.

Lebedev, S., Chevrot, S. & van der Hilst, R. D. Seismic evidence for olivine phase changes at the 410- and 660-kilometer discontinuities. *Science* **296**, 1300–1302 (2002).

CAS PubMed PubMed Central ADS Google Scholar

52. 52.

Akaogi, M., Ito, E. & Navrotsky, A. Olivine-modified spinel–spinel transitions in the system Mg_2SiO_4–Fe_2SiO_4: calorimetric measurements, thermochemical calculation, and geophysical application. *J. Geophys. Res*. **94**, 15671–15685 (1989).

ADS Google Scholar

53. 53.

Ito, E., Akaogi, M., Topor, L. & Navrotsky, A. Negative pressure–temperature slopes for reactions forming $MgSiO_3$ perovskite from calorimetry. *Science* **249**, 1275–1278 (1990).

CAS PubMed PubMed Central ADS Google Scholar

54. 54.

Houser, C. Global seismic data reveal little water in the mantle transition zone. *Earth Planet. Sci. Lett*. **448**, 94–101 (2016).

CAS ADS Google Scholar

55. 55.

Anderson, D. L., Schramm, K. A., Foulger, G. R., Natland, J. H. & Presnall, D. C. Global hotspot maps. *Geol. Soc. Am. Spec. Pap*. **388**, 19–29 (2005).

Google Scholar

56. 56.

Durand, S., Debayle, E., Ricard, Y., Zaroli, C. & Lambotte, S. Confirmation of a change in the global shear velocity pattern at around 1000 km depth. *Geophys. J. Int*. **211**, 1628–1639 (2017).

ADS Google Scholar

57. 57.

French, S. W. & Romanowicz, B. A. Whole-mantle radially anisotropic shear velocity structure from spectral-element waveform tomography. *Geophys. J. Int*. **199**, 1303–1327 (2014).

ADS Google Scholar

58. 58.

Tesoniero, A., Auer, L., Boschi, L. & Cammarano, F. Hydration of marginal basins and compositional variations within the continental lithospheric mantle inferred from a new global model of shear and compressional velocity. *J. Geophys. Res*. **120**, 7789–7813 (2015).

ADS Google Scholar

59. 59.

Moulik, P. & Ekström, G. An anisotropic shear velocity model of the Earth's mantle using normal modes, body waves, surface waves and long-period waveforms. *Geophys. J. Int*. **199**, 1713–1738 (2014).

ADS Google Scholar

60. 60.

Colli, L., Fichtner, A. & Bunge, H. P. Full waveform tomography of the upper mantle in the South Atlantic region: imaging a westward fluxing shallow asthenosphere? *Tectonophysics* **604**, 26–40 (2013).

ADS Google Scholar

61. 61.

Wessel, P. et al. The Generic Mapping Tools version 6. *Geochem. Geophys. Geosyst*. **20**, 5556–5564 (2019).

ADS Google Scholar

62. 62.

Shen, Y., Solomon, S. C., Bjarnason, I. T. & Wolfe, C. J. Seismic evidence for a lower-mantle origin of the Iceland plume. *Nature* **395**, 62 (1998).

CAS ADS Google Scholar

Download references

Acknowledgements

C.A.R. and N.H. acknowledge funding from the Natural Environment Research Council (NE/M003507/1 and NE/K010654/1) and the European Research Council (GA 638665). J.-M.K. was funded by the Natural Environment Research Council (NE/M004643/1). We thank the captain and crew of the R/V *Marcus G. Langseth* and the RRS *Discovery*, and also the scientific technicians.

Author information

Author notes

1. Matthew R. Agius

   Present address: Dipartimento di Scienze, Università degli studi Roma Tre, Rome, Italy

2. Saikiran Tharimena

   Present address: Institute for Meteorology and Geophysics, University of Vienna, Vienna, Austria

Affiliations

1. Ocean and Earth Science, University of Southampton, Southampton, UK

   Matthew R. Agius, Catherine A. Rychert, Nicholas Harmon & Saikiran Tharimena

2. Department of Earth Sciences, University of Oxford, Oxford, UK

   J.-Michael Kendall

Authors

1. Matthew R. Agius
   View author publications

You can also search for this author in PubMed Google Scholar

2. Catherine A. Rychert
   View author publications

   You can also search for this author in PubMed Google Scholar

3. Nicholas Harmon
   View author publications

   You can also search for this author in PubMed Google Scholar

4. Saikiran Tharimena
   View author publications

   You can also search for this author in PubMed Google Scholar

5. J.-Michael Kendall
   View author publications

   You can also search for this author in PubMed Google Scholar

Contributions

M.R.A. processed the data and wrote the manuscript. C.A.R. conceived the experiment, acquired funding, managed the project and wrote the manuscript. N.H. contributed to conceptualization, funding acquisition, project management and writing of the original manuscript. S.T. organized the raw data and assisted in initial data quality control. J.-M.K. contributed to funding acquisition and the writing of the manuscript.

Corresponding author

Correspondence to Matthew R. Agius.

Ethics declarations

Competing interests

The authors declare no competing interests.

Additional information

Peer review information *Nature* thanks Brandon Schmandt and the other, anonymous, reviewer(s) for their contribution to the peer review of this work. Peer reviewer reports are available.

Publisher's note Springer Nature remains neutral with regard to jurisdictional claims in published maps and institutional affiliations.

Extended data figures and tables

Extended Data Fig. 1 Relationship of MTZ shear velocity with distance to ridge.

Distance-binned average velocity of the mantle transition zone for global[4,5,7,56,57,58,59] and regional[9,60] models. Bin averages are shown as cyan circles, with error bars showing the standard error of the mean. Red lines show the averages for distances <300 km and >300 km. Background shading shows a 2D histogram of transition zone velocities. Model name and *t*-statistic are given above each panel. The top two rows are presented in percentage anomaly, whereas the bottom row is in absolute velocity, as reported in the original publications. Probability at 95% occurs when the absolute value of the *t*-statistic is >1.67; 99% occurs at a value >2.37 for the given degrees of freedom. A negative *t*-statistic indicates that the mean of the sub-ridge bin is less than the mean of more distant bins. Map shows the distance to ridge binning as coloured circles, with the MAR shown in black. White circles centred on black dots show the hotspot locations, with the size of the black circle proportional to their deep origin ranking[29,55]. Black box shows our study area. Source data

Extended Data Fig. 2 Global shear-velocity models of the mantle transition zone.

The three models PRI-S05[7], S40RTS[5] and SGLOBE[4] show average MTZ shear velocities beneath the Atlantic Ocean. The MAR is shown in black. White circles centred on black dots show the hotspot locations, with the size of the black circle proportional to their deep origin ranking[29,55]. Black box shows our study area.

Extended Data Fig. 3 Temperature estimates from relationships with respect to the 410 and 660 discontinuity topography, and mantle TZT.

Grey lines are the Clapeyron slopes +2.9 MPa K^{-1} (ref. [48]), −2.5 MPa K^{-1} (ref. [49]) and −0.13 km K^{-1} (ref. [51]) for the 410, 660 and TZT, respectively. Black diamonds, estimates from this study. Other symbols, average estimates from the Azores, the Canary islands, Cape Verde, northwest Africa[28], Iceland (orange[62] and brown[31] pentagons), the Southwest Indian Ridge[27] and Hawaii[32].

Extended Data Fig. 4 Example of waveform corrections and receiver functions.

Left panels, the unfiltered and uncorrected (black) and the tilt- and compliance-corrected (cyan) vertical waveforms (Vert.) of a recorded earthquake on stations I04D and I28D. Middle, zoomed in, filtered waveforms also showing the radial (red) component. Right, receiver functions (RF) from the deconvolution of the vertical uncorrected (black) and corrected (blue) components with the radial component, here essentially identical for corrected and uncorrected data. Top and bottom are examples of waveforms from earthquakes of magnitude 7.4 and 6.6, respectively.

Extended Data Fig. 5 Maps showing the number of waveforms stacked at 410-km and 660-km depths (grey shade).

Dark red line marks the plate boundary[37].

Extended Data Fig. 6 Depth errors of the 410 and 660 discontinuities.

Standard errors are determined from the depth migration of each waveform. Dark red line marks the plate boundary[37].

Extended Data Fig. 7 Migration tests.

Receiver function migration tests using 1D crust-corrected PREM[8], 3D V_S model SEMUM2[6] (using PREM V_P/V_S ratio for V_P) and 3D V_P and V_S model from PRI[7]. Horizontal cross-sections from the 3D depth migration: 410 and 660 discontinuities (top and middle, respectively), and mantle TZT (bottom). The TZT is given as the difference from a thickness of 250 km. Semi-transparent shades are poorly constrained areas. Dark red line marks the plate boundary[37].

Supplementary information

Peer Review File

Source data

Source Data Fig. 2

Source Data Fig. 3

Source Data Fig. 4

Source Data Extended Data Fig. 1

Rights and permissions

Reprints and Permissions

About this article

Check for updates

Cite this article

Agius, M.R., Rychert, C.A., Harmon, N. *et al.* A thin mantle transition zone beneath the equatorial Mid-Atlantic Ridge. *Nature* **589,** 562–566 (2021). https://doi.org/10.1038/s41586-020-03139-x

Download citation

- Received: 05 March 2020
- Accepted: 03 November 2020
- Published: 27 January 2021
- Issue Date: 28 January 2021
- DOI: https://doi.org/10.1038/s41586-020-03139-x

Comments

By submitting a comment you agree to abide by our Terms and Community Guidelines. If you find something abusive or that does not comply with our terms or guidelines please flag it as inappropriate.

Access through your institution
Change institution
Buy or subscribe

This article was downloaded by **calibre** from https://www.nature.com/articles/s41586-020-03139-x

- Article
- Published: 27 January 2021

Half a century of global decline in oceanic sharks and rays

- Nathan Pacoureau ORCID: orcid.org/0000-0002-8363-6332[1],
- Cassandra L. Rigby[2],
- Peter M. Kyne[3],
- Richard B. Sherley ORCID: orcid.org/0000-0001-7367-9315[4],
- Henning Winker[5,6],
- John K. Carlson[7],
- Sonja V. Fordham[8],
- Rodrigo Barreto ORCID: orcid.org/0000-0002-5737-9416[9],
- Daniel Fernando ORCID: orcid.org/0000-0003-2163-1832[10],
- Malcolm P. Francis ORCID: orcid.org/0000-0001-7976-932X[11],
- Rima W. Jabado[12],
- Katelyn B. Herman ORCID: orcid.org/0000-0003-4654-3644[13],
- Kwang-Ming Liu[14],
- Andrea D. Marshall[15],
- Riley A. Pollom ORCID: orcid.org/0000-0001-8260-4614[1],
- Evgeny V. Romanov[16],
- Colin A. Simpfendorfer[2],
- Jamie S. Yin[1,17],
- Holly K. Kindsvater ORCID: orcid.org/0000-0001-7580-4095[18] &
- Nicholas K. Dulvy[1]

Nature **volume 589**, pages567–571(2021)Cite this article

- 771 Accesses

- 3217 Altmetric
- Metrics details

Subjects

- Ecology
- Zoology

Abstract

Overfishing is the primary cause of marine defaunation, yet declines in and increasing extinction risks of individual species are difficult to measure, particularly for the largest predators found in the high seas[1,2,3]. Here we calculate two well-established indicators to track progress towards Aichi Biodiversity Targets and Sustainable Development Goals[4,5]: the Living Planet Index (a measure of changes in abundance aggregated from 57 abundance time-series datasets for 18 oceanic shark and ray species) and the Red List Index (a measure of change in extinction risk calculated for all 31 oceanic species of sharks and rays). We find that, since 1970, the global abundance of oceanic sharks and rays has declined by 71% owing to an 18-fold increase in relative fishing pressure. This depletion has increased the global extinction risk to the point at which three-quarters of the species comprising this functionally important assemblage are threatened with extinction. Strict prohibitions and precautionary science-based catch limits are urgently needed to avert population collapse[6,7], avoid the disruption of ecological functions and promote species recovery[8,9].

Access through your institution
Change institution
Buy or subscribe

Access options

Subscribe to Journal

Get full journal access for 1 year

$199.00

only $3.90 per issue

Subscribe

All prices are NET prices.
VAT will be added later in the checkout.

Rent or Buy article

Get time limited or full article access on ReadCube.

from$8.99

Rent or Buy

All prices are NET prices.

Additional access options:

- Log in
- Access through your institution
- Learn about institutional subscriptions

Fig. 1: Global LPI for 18 oceanic sharks estimated from 1970 to 2018.

Fig. 2: LPI for 18 oceanic sharks from 1970 to 2018 disaggregated for each of the oceans and traits.

Fig. 3: Increase in extinction risk of oceanic sharks.

Fig. 4: Attributing abundance declines to overfishing.

Data availability

Data are available on https://www.sharkipedia.org/ and at https://doi.org/10.5281/zenodo.4135325. Source data are provided with this paper.

References

1. 1.

   Dulvy, N. K. et al. You can swim but you can't hide: the global status and conservation of oceanic pelagic sharks and rays. *Aquat. Conserv.* **18**, 459–482 (2008).

   Google Scholar

2. 2.

   Webb, T. J. & Mindel, B. L. Global patterns of extinction risk in marine and non-marine systems. *Curr. Biol.* **25**, 506–511 (2015).

   CAS Google Scholar

3. 3.

McCauley, D. J. et al. Marine defaunation: animal loss in the global ocean. *Science* **347**, 1255641 (2015).

PubMed Google Scholar

4. 4.

Tittensor, D. P. et al. A mid-term analysis of progress toward international biodiversity targets. *Science* **346**, 241–244 (2014).

CAS ADS Google Scholar

5. 5.

Butchart, S. H. et al. Global biodiversity: indicators of recent declines. *Science* **328**, 1164–1168 (2010).

CAS ADS Google Scholar

6. 6.

Davidson, L. N., Krawchuk, M. A. & Dulvy, N. K. Why have global shark and ray landings declined: improved management or overfishing? *Fish Fish*. **17**, 438–458 (2016).

Google Scholar

7. 7.

Dulvy, N. K. et al. Challenges and priorities in shark and ray conservation. *Curr. Biol*. **27**, R565–R572 (2017).

CAS PubMed PubMed Central Google Scholar

8. 8.

Simpfendorfer, C. A. & Dulvy, N. K. Bright spots of sustainable shark fishing. *Curr. Biol*. **27**, R97–R98 (2017).

CAS PubMed PubMed Central Google Scholar

9. 9.

Sumaila, U. R. et al. Benefits of rebuilding global marine fisheries outweigh costs. *PLoS ONE* **7**, e40542 (2012).

CAS PubMed PubMed Central ADS Google Scholar

10. 10.

Brooks, T. M. et al. Harnessing biodiversity and conservation knowledge products to track the Aichi Targets and Sustainable Development Goals. *Biodiversity (Nepean)* **16**, 157–174 (2015).

Google Scholar

11. 11.

FAO. *The State of World Fisheries and Aquaculture 2016*. *Contributing to Food Security and Nutrition for All* (FAO, 2016).

12. 12.

Hicks, C. C. et al. Harnessing global fisheries to tackle micronutrient deficiencies. *Nature* **574**, 95–98 (2019).

CAS PubMed PubMed Central ADS Google Scholar

13. 13.

Pereira, H. M., Navarro, L. M. & Martins, I. S. Global biodiversity change: the bad, the good, and the unknown. *Annu. Rev. Environ. Resour*. **37**, 25–50 (2012).

Google Scholar

14. 14.

Stein, R. W. et al. Global priorities for conserving the evolutionary history of sharks, rays and chimaeras. *Nat. Ecol. Evol*. **2**, 288–298 (2018).

PubMed PubMed Central Google Scholar

15. 15.

Pimiento, C. et al. Functional diversity of marine megafauna in the Anthropocene. *Sci. Adv*. **6**, eaay7650 (2020).

CAS PubMed PubMed Central ADS Google Scholar

16. 16.

Dulvy, N. K. et al. Extinction risk and conservation of the world's sharks and rays. *eLife* **3**, e00590 (2014).

PubMed PubMed Central Google Scholar

17. 17.

Stuart, S. N. et al. Status and trends of amphibian declines and extinctions worldwide. *Science* **306**, 1783–1786 (2004).

CAS PubMed PubMed Central ADS Google Scholar

18. 18.

Hoffmann, M. et al. The impact of conservation on the status of the world's vertebrates. *Science* **330**, 1503–1509 (2010).

CAS PubMed ADS Google Scholar

19. 19.

Pardo, S. A., Kindsvater, H. K., Reynolds, J. D. & Dulvy, N. K. Maximum intrinsic rate of population increase in sharks, rays, and chimaeras: the importance of survival to maturity. *Can. J. Fish. Aquat. Sci*. **73**, 1159–1163 (2016).

Google Scholar

20. 20.

McClenachan, L., Cooper, A. B. & Dulvy, N. K. Rethinking trade-driven extinction risk in marine and terrestrial megafauna. *Curr. Biol*. **26**, 1640–1646 (2016).

CAS PubMed PubMed Central Google Scholar

21. 21.

Clarke, S. C. et al. Global estimates of shark catches using trade records from commercial markets. *Ecol. Lett*. **9**, 1115–1126 (2006).

PubMed PubMed Central Google Scholar

22. 22.

Brander, K. Disappearance of common skate *Raia batis* from Irish Sea. *Nature* **290**, 48–49 (1981).

ADS Google Scholar

23. 23.

Manire, C. A. & Gruber, S. H. Many sharks may be headed toward extinction. *Conserv. Biol*. **4**, 10–11 (1990).

Google Scholar

24. 24.

Southeast Data, Assessment, and Review (SEDAR). *Update Assessment to SEDAR 21, HMS Dusky Shark* http://sedarweb.org/docs/suar/Dusky_update_report_2016.pdf (SEDAR, 2016).

25. 25.

International Commission for the Conservation of Atlantic Tunas. *Report of the 2019 ICCAT Shortfin Mako Shark Stock Assessment Update Meeting*. (ICCAT, 2019).

26. 26.

Dudley, S. F. & Simpfendorfer, C. A. Population status of 14 shark species caught in the protective gillnets off KwaZulu-Natal beaches, South Africa, 1978–2003. *Mar. Freshw. Res*. **57**, 225–240 (2006).

Google Scholar

27. 27.

Roff, G., Brown, C. J., Priest, M. A. & Mumby, P. J. Decline of coastal apex shark populations over the past half century. *Commun. Biol*. **1**, 223 (2018).

PubMed PubMed Central Google Scholar

28. 28.

Jiao, Y., Cortés, E., Andrews, K. & Guo, F. Poor-data and data-poor species stock assessment using a Bayesian hierarchical approach. *Ecol. Appl*. **21**, 2691–2708 (2011).

PubMed PubMed Central Google Scholar

29. 29.

Cortés, E. et al. Ecological risk assessment of pelagic sharks caught in Atlantic pelagic longline fisheries. *Aquat. Living Resour*. **23**, 25–34

(2010).

Google Scholar

30. 30.

Loh, J. et al. The Living Planet Index: using species population time series to track trends in biodiversity. *Phil. Trans. R. Soc. B* **360**, 289–295 (2005).

Google Scholar

31. 31.

Butchart, S. H. et al. Improvements to the Red List Index. *PLoS ONE* **2**, e140 (2007).

PubMed PubMed Central ADS Google Scholar

32. 32.

Winker, H., Carvalho, F. & Kapur, M. JABBA: Just Another Bayesian Biomass Assessment. *Fish. Res*. **204**, 275–288 (2018).

Google Scholar

33. 33.

Sherley, R. B. et al. Estimating IUCN Red List population reduction: JARA—a decision-support tool applied to pelagic sharks. *Conserv. Lett*. **13**, e12688 (2020).

Google Scholar

34. 34.

Punt, A. E. & Smith, A. D. in *Conservation of Exploited Species* (ed. Reynolds, J. D.) 41–66 (Cambridge Univ. Press, 2001).

35. 35.

Marler, P. N. & Marler, T. E. An assessment of Red List data for the Cycadales. *Trop. Conserv. Sci*. **8**, 1114–1125 (2015).

Google Scholar

36. 36.

Anticamara, J. A., Watson, R., Gelchu, A. & Pauly, D. Global fishing effort (1950–2010): trends, gaps, and implications. *Fish. Res*. **107**, 131–136 (2011).

Google Scholar

37. 37.

Vannuccini, S. *Shark Utilization, Marketing, and Trade* (FAO, 1999).

38. 38.

Salafsky, N. et al. A standard lexicon for biodiversity conservation: unified classifications of threats and actions. *Conserv. Biol*. **22**, 897–911 (2008).

Google Scholar

39. 39.

Juan-Jordá, M. J., Mosqueira, I., Cooper, A. B., Freire, J. & Dulvy, N. K. Global population trajectories of tunas and their relatives. *Proc. Natl Acad. Sci. USA* **108**, 20650–20655 (2011).

ADS Google Scholar

40. 40.

Lawson, J. M. & Fordham, F. *Realizing the Potential of the Convention on Migratory Species to Conserve Elasmobranchs*

https://www.cms.int/sites/default/files/publication/CMS-SAI-76pp-FINAL-5DEC-HIGH%20%281%29-min.pdf (Shark Advocates International, 2018).

41. 41.

Juan-Jordá, M. J., Murua, H., Arrizabalaga, H., Dulvy, N. K. & Restrepo, V. Report card on ecosystem-based fisheries management in tuna regional fisheries management organizations. *Fish Fish*. **19**, 321–339 (2018).

Google Scholar

42. 42.

Gilman, E., Passfield, K. & Nakamura, K. Performance of regional fisheries management organizations: ecosystem-based governance of bycatch and discards. *Fish Fish*. **15**, 327–351 (2014).

Google Scholar

43. 43.

Curtis, T. H. et al. Seasonal distribution and historic trends in abundance of white sharks, *Carcharodon carcharias*, in the western North Atlantic Ocean. *PLoS ONE* **9**, e99240 (2014).

PubMed PubMed Central ADS Google Scholar

44. 44.

Queiroz, N. et al. Global spatial risk assessment of sharks under the footprint of fisheries. *Nature* **572**, 461–466 (2019).

CAS PubMed PubMed Central ADS Google Scholar

45. 45.

Peterson, C. D. et al. Preliminary recovery of coastal sharks in the south-east United States. *Fish Fish*. **18**, 845–859 (2017).

Google Scholar

46. 46.

Jennings, S. Reporting and advising on the effects of fishing. *Fish Fish*. **8**, 269–276 (2007).

Google Scholar

47. 47.

Kitchell, J. F., Essington, T. E., Boggs, C. H., Schindler, D. E. & Walters, C. J. The role of sharks and longline fisheries in a pelagic ecosystem of the central Pacific. *Ecosystems (N. Y.)* **5**, 202–216 (2002).

Google Scholar

48. 48.

Polovina, J. J., Abecassis, M., Howell, E. A. & Woodworth, P. Increases in the relative abundance of mid-trophic level fishes concurrent with declines in apex predators in the subtropical North Pacific, 1996–2006. *Fish Bull*. **107**, 523–531 (2009).

Google Scholar

49. 49.

Jabado, R. W. et al. Troubled waters: threats and extinction risk of the sharks, rays and chimaeras of the Arabian Sea and adjacent waters. *Fish Fish*. **19**, 1043–1062 (2018).

Google Scholar

50. 50.

Costello, C. et al. Global fishery prospects under contrasting management regimes. *Proc. Natl Acad. Sci. USA* **113**, 5125–5129 (2016).

CAS PubMed PubMed Central ADS Google Scholar

51. 51.

Tremblay-Boyer, L., Carvalho, F., Neubauer, P. & Pilling, G. M. *Stock Assessment for Oceanic Whitetip Shark in the Western and Central Pacific Ocean*. Scientific Committee Fifteenth Regular Session Report. No. WCPFC-SC15-2019/SA-WP-06 (WCPFC, 2019).

52. 52.

Cailliet, G. M. & Goldman, K. J. in *Biology of Sharks and their Relatives* (eds Carrier, J. C., Musick, J. A. & Heithaus, M. R.) 404–453 (CRC, 2004).

53. 53.

Cailliet, G. M. Perspectives on elasmobranch life-history studies: a focus on age validation and relevance to fishery management. *J. Fish Biol*. **87**, 1271–1292 (2015).

CAS PubMed PubMed Central Google Scholar

54. 54.

Harry, A. V. Evidence for systemic age underestimation in shark and ray ageing studies. *Fish Fish*. **19**, 185–200 (2018).

Google Scholar

55. 55.

IUCN Standards and Petitions Subcommittee. *Guidelines for using the IUCN Red List Categories and Criteria*. Version 13 (IUCN, 2017).

56. 56.

Pacifici, M. et al. Generation length for mammals. *Nat. Conserv*. **5**, 89–94 (2013).

Google Scholar

57. 57.

Winker, H., Pacoureau, N. & Sherley, R. B. JARA: 'Just Another Red-List Assessment'. Preprint at https://doi.org/10.1101/672899 (2020).

58. 58.

Gelman, A. & Rubin, D. B. Inference from iterative simulation using multiple sequences. *Stat. Sci*. **7**, 457–472 (1992).

MATH Google Scholar

59. 59.

Conn, P. B., Johnson, D. S., Williams, P. J., Melin, S. R. & Hooten, M. B. A guide to Bayesian model checking for ecologists. *Ecol. Monogr*. **88**, 526–542 (2018).

Google Scholar

60. 60.

Gelman, A. et al. *Bayesian Data Analysis* (CRC, 2013).

61. 61.

R Core Team. *R: A Language and Environment for Statistical Computing* (R Foundation for Statistical Computing, 2018).

62. 62.

Su, Y.-S. & Yajima, M. R2jags: using R to run ‘JAGS’. R package version 0.5-7, Vol. 34 https://cran.r-project.org/web/packages/R2jags/index.html (2015).

63. 63.

Plummer, M. *JAGS version 4.3.0 User Manual* (2017).

64. 64.

Pauly, D., Zeller, D. & Palomares, M. L. D. Sea Around Us Concepts, Design and Data. http://www.seaaroundus.org/ (2015).

65. 65.

IUCN. *The IUCN Red List of Threatened Species*. Version 2019-2 http://www.iucnredlist.org (IUCN, 2019).

66. 66.

Takeuchi, Y., Tremblay-Boyer, L., Pilling, G. M. & Hampton, J. *Assessment of Blue Shark in the Southwestern Pacific*. Scientific Committee Twelfth Regular Session Report. No. WCPFC-SC12-2016/SA-WP-08 REV1 (WCPFC, 2016).

Download references

Acknowledgements

We thank all members of the IUCN SSC SSG and other experts who contributed to the data collation and, in particular, A. Aires-da-Silva, F. Carvalho, J. Cheok, S. Clarke, R. Coelho, E. Cortés, T. Driggers, C. Dudgeon, M. Hoffmann, Y. Jiao, T. Kashiwagi, A. Kock, C. Lowe, J. Rice, L. Tremblay-Boyer, W. J. VanderWright and S. Wintner. The scientific results and conclusions, as well as any views or opinions expressed herein, are those of the author(s) and do not necessarily reflect those of institutions or data providers. This project was funded by the Shark Conservation Fund, a philanthropic collaborative pooling expertise and resources to meet the

threats facing the world's sharks and rays. The Shark Conservation Fund is a project of Rockefeller Philanthropy Advisors. This work was funded by the Shark Conservation Fund as part of the Global Shark Trends Project to N.K.D. and C.A.S., and US National Science Foundation grant DEB-1556779 to H.K.K. P.M.K. was supported by the Marine Biodiversity Hub, a collaborative partnership supported through funding from the Australian Government's National Environmental Science Program. N.K.D. was supported by Natural Science and Engineering Research Council Discovery and Accelerator Awards and the Canada Research Chairs Program.

Author information

Affiliations

1. Department of Biological Sciences, Earth to Ocean Research Group, Simon Fraser University, Burnaby, British Columbia, Canada

   Nathan Pacoureau, Riley A. Pollom, Jamie S. Yin & Nicholas K. Dulvy

2. College of Science and Engineering, James Cook University, Townsville, Queensland, Australia

   Cassandra L. Rigby & Colin A. Simpfendorfer

3. Research Institute for the Environment and Livelihoods, Charles Darwin University, Darwin, Northern Territory, Australia

   Peter M. Kyne

4. Centre for Ecology and Conservation, College of Life and Environmental Sciences, University of Exeter, Penryn Campus, Penryn, UK

   Richard B. Sherley

5. Joint Research Centre (JRC), European Commission, Ispra, Italy

Henning Winker

6. Department of Environment, Forestry and Fisheries, Cape Town, South Africa

   Henning Winker

7. NOAA National Marine Fisheries Service, Southeast Fisheries Science Center, Panama City Laboratory, Panama City, FL, USA

   John K. Carlson

8. Shark Advocates International, The Ocean Foundation, Washington, DC, USA

   Sonja V. Fordham

9. Centro Nacional de Pesquisa e Conservação da Biodiversidade Marinha do Sudeste e Sul do Brasil (CEPSUL), Instituto Chico Mendes de Conservação da Biodiversidade (ICMBio), Itajaí, Brazil

   Rodrigo Barreto

10. Blue Resources Trust, Colombo, Sri Lanka

    Daniel Fernando

11. National Institute of Water and Atmospheric Research, Wellington, New Zealand

    Malcolm P. Francis

12. Elasmo Project, Dubai, United Arab Emirates

    Rima W. Jabado

13. Georgia Aquarium, Atlanta, GA, USA

    Katelyn B. Herman

14. Institute of Marine Affairs and Resource Management, George Chen Shark Research Center, National Taiwan Ocean University, Center of Excellence for the Oceans, National Taiwan Ocean University, Keelung, Taiwan

    Kwang-Ming Liu

15. Marine Megafauna Foundation, Truckee, CA, USA

    Andrea D. Marshall

16. CAP RUN — CITEB, Le Port, Île de la Réunion, France

    Evgeny V. Romanov

17. Department of Ecology, Evolution, and Natural Resources, Rutgers University, New Brunswick, NJ, USA

    Jamie S. Yin

18. Department of Fish and Wildlife Conservation, Virginia Polytechnic Institute and State University, Blacksburg, VA, USA

    Holly K. Kindsvater

Authors

1. Nathan Pacoureau
   View author publications

   You can also search for this author in PubMed Google Scholar

2. Cassandra L. Rigby
   View author publications

   You can also search for this author in PubMed Google Scholar

3. Peter M. Kyne
   View author publications

You can also search for this author in PubMed Google Scholar

4. Richard B. Sherley
View author publications

You can also search for this author in PubMed Google Scholar

5. Henning Winker
View author publications

You can also search for this author in PubMed Google Scholar

6. John K. Carlson
View author publications

You can also search for this author in PubMed Google Scholar

7. Sonja V. Fordham
View author publications

You can also search for this author in PubMed Google Scholar

8. Rodrigo Barreto
View author publications

You can also search for this author in PubMed Google Scholar

9. Daniel Fernando
View author publications

You can also search for this author in PubMed Google Scholar

10. Malcolm P. Francis
View author publications

You can also search for this author in PubMed Google Scholar

11. Rima W. Jabado
View author publications

You can also search for this author in PubMed Google Scholar

12. Katelyn B. Herman
    View author publications

    You can also search for this author in PubMed Google Scholar

13. Kwang-Ming Liu
    View author publications

    You can also search for this author in PubMed Google Scholar

14. Andrea D. Marshall
    View author publications

    You can also search for this author in PubMed Google Scholar

15. Riley A. Pollom
    View author publications

    You can also search for this author in PubMed Google Scholar

16. Evgeny V. Romanov
    View author publications

    You can also search for this author in PubMed Google Scholar

17. Colin A. Simpfendorfer
    View author publications

    You can also search for this author in PubMed Google Scholar

18. Jamie S. Yin
    View author publications

    You can also search for this author in PubMed Google Scholar

19. Holly K. Kindsvater
    View author publications

You can also search for this author in PubMed Google Scholar

20. Nicholas K. Dulvy
View author publications

You can also search for this author in PubMed Google Scholar

Contributions

C.L.R., P.M.K., R.A.P. and N.K.D. organized and led the workshop investigation of data quality and facilitated the 2018 Red List assessments. N.P., H.K.K. and N.K.D. conceptualized the analysis. J.S.Y., C.L.R., H.K.K., R.B.S., N.P. and N.K.D. compiled and curated the time-series data. J.K.C., A.D.M. and H.W. provided additional time-series data. N.P., R.B.S. and H.W. conducted the statistical analysis. N.P., H.K.K. and N.K.D. visualized the data and wrote the first draft. N.K.D. and H.K.K. acquired the funding. All authors discussed the time-series data, analysis and results, and contributed to writing the manuscript.

Corresponding authors

Correspondence to Nathan Pacoureau or Richard B. Sherley.

Ethics declarations

Competing interests

The authors declare no competing interests.

Additional information

Peer review information *Nature* thanks Paul Conn, Johann Mourier, Nuno Queiroz and the other, anonymous, reviewer(s) for their contribution to the peer review of this work.

Publisher's note Springer Nature remains neutral with regard to jurisdictional claims in published maps and institutional affiliations.

Extended data figures and tables

Extended Data Fig. 1 Hierarchical building of the global LPI and RLI.

LC, least concern; NT, near threatened; VU, vulnerable; EN, endangered; CR, critically endangered; EX, extinct.

Extended Data Fig. 2 Calculation of the LPI.

a, Schematic example of constructing the observed (black) and projected (blue) LPI. First, year-to-year rates of change (yyrc) (d_t) are averaged between species in the same region (for example, in region 1 (R1), species A with \({ d} _{ { { \rm{ A} } } _{ t} } \) and species B with \({ d} _{ { { \rm{ B} } } _{ t} } \) averaged in \({ d} _{ { { \rm{ R} } 1} _{ t} } \)). In a second step, yyrc are averaged between regions 1, 2 and 3 to give the global yyrc. The observed LPI builds on the yyrc calculated from the estimated abundance index from the state–space population model. The projected LPI builds on the yyrc calculated from the estimated and projected abundance index from the state-space population model. Projections are from the last data point to 2020. **b**, Global LPI for oceanic sharks and rays estimated from 1970 to 2018 in black and extrapolated to 2020 in blue. The black and the thick blue lines denote, respectively, the mean of the estimated and extrapolated LPI. The white and thin blues lines denote, respectively, the 95% credible intervals of the estimated and extrapolated LPI and the grey lines denote each iteration of the estimated LPI. **c**, The annual percentage change was calculated from the posteriors of the estimated LPI (grey) and extrapolated LPI (blue) around the final-assessment year relative to the posteriors for 1970. Vertical bars for the 1970–2018 period denote the median of the estimated and extrapolated LPI.

Extended Data Fig. 3 Global and species-specific LPI for oceanic sharks and rays from 1970 to 2018.

Global original LPI is the mean black line. Faint grey lines show the effect of excluding all data for a single species at a time and recalculating the mean global LPI for all other species. No means from jackknife species trends fall outside the 95% credible interval from the run with all of the datasets included, suggesting that our selection of species did not unduly influence the overall LPI result.

Extended Data Fig. 4 Time-series output for Carcharhinidae.

a–**d**, Observed (black or empty points and stars indicate different time-series) and modelled (black line) abundance indices for silky shark (*Carcharhinus falciformis*) (**a**), oceanic whitetip shark (*C. longimanus*) (**b**), dusky shark (*C. obscurus*) (**c**) and blue shark (*Prionace glauca*) (**d**) obtained from the state–space population model. The thick black line denotes the mean of the estimated abundance index and the shaded regions denote 95% credible intervals.

Extended Data Fig. 5 Time-series output for Sphyrnidae.

a–**c**, Observed (black or empty points and stars indicate different time-series) and modelled (black line) abundance indices for scalloped hammerhead (*S. lewini*) (**a**), great hammerhead (*S. mokarran*) (**b**) and smooth hammerhead (*S. zygaena*) (**c**) obtained from the state–space population model. The thick black line denotes the mean of the estimated abundance index and the shaded regions denote 95% credible intervals.

Extended Data Fig. 6 Time-series output for Alopiidae.

a–**c**, Observed (points) and modelled (black line) abundance indices for pelagic thresher (*A. pelagicus*) (**a**), bigeye thresher (*Alopias superciliosus*) (**b**) and common thresher (*Alopias vulpinus*) (**c**) obtained from the state–space population model. The thick black line denotes the mean of the estimated abundance index and the shaded regions denote 95% credible intervals.

Extended Data Fig. 7 Time-series output for Lamnidae.

a–**d**, Observed (black or empty points and stars indicate different time-series) and modelled (black line) abundance indices for white shark (*C. carcharias*) (**a**), shortfin mako (*I. oxyrinchus*) (**b**), longfin mako (*I. paucus*) (**c**) and porbeagle (*L. nasus*) (**d**) obtained from the state–space population model. The thick black line denotes the mean of the estimated abundance index and the shaded regions denote 95% credible intervals.

Extended Data Fig. 8 Time-series output for Dasyatidae and Mobulidae.

a–**d**, Observed (points) and modelled (black line) abundance indices for pelagic stingray (*P. violacea*) (**a**), reef manta ray (*M. alfredi*) (**b**), giant manta ray (*Mobula birostris*) (**c**) and shortfin devilray (*M. kuhlii*) (**d**) obtained from the state–space population model. The thick black line denotes the mean of the estimated abundance index and the shaded regions denote 95% credible intervals.

Extended Data Fig. 9 Stock assessments for oceanic sharks.

a, Oceanic shark stock status—over time—being at levels of biomass or abundance above MSY (green lines) or below MSY (red lines). Data were obtained from refs. [24,25,28,51], and refs. 81–84,93,94,96,97 in the Supplementary Information. Dotted lines indicate that a stock is above or below the biomass or abundance levels producing MSY following the last stock assessment value. **b**, Number of published stock assessments for oceanic sharks and rays over time. **c**, Presentation of 14 stocks of oceanic sharks (no available stock assessments for oceanic rays), status (biomass or abundance over value at MSY) versus pressure (F/F_{MSY}) in a Kobe plot style, for the last year with available data. Circles represent the unique values of each species if only one stock exists and represent the mean of the values of the different stocks (diamonds) when the species has multiple stocks. The plot is divided into four panels: the red panel (top left), with four stocks and three species, corresponds to stocks that are being overfished and where overfishing is occurring; the orange panel (top right), with one stock and one species, corresponds to stocks that are not overfished but where overfishing is occurring; the yellow panel (bottom

left), with four stocks and three species, corresponds to stocks that are overfished but where overfishing is not occurring; and the green panel (bottom right), with five stocks and one species, corresponds to stocks that are not overfished and where overfishing is not occurring.

Extended Data Fig. 10 Percentage of reported threat categories in the 31 oceanic shark IUCN Red List assessments.

‘Biological resource use’ and, more specifically, ‘fishing and harvesting aquatic resources’ is the major reported threat.

Supplementary information

Supplementary Information

This file contains Supplementary Methods 1 and 2, Supplementary Tables 1-3, Supplementary Discussion 1-3 and Supplementary References. The Supplementary Methods 1 explains the method used to correct fishing effort, using technological efficiency, into an effective fishing effort. The Supplementary Methods 2 describes the nine encountered situations details when selecting generation time of species and describes the quality of data. Supplementary Table 1 describes all the time-series analysed and provides the ecological information used in the analyses. Supplementary Table 2 describes all the available Red List status available for oceanic sharks and rays and the ones used in the analyses. Supplementary Table 3 describes the type of trajectories and gives the source of the 15 stock assessment outputs of 8 species used in the analysis. The Supplementary Discussion 2 discusses the reasons why the Living Planet Index analysis for oceanic sharks and rays is conservative (true abundance trend index values are likely to be lower and the calculated percent declines worse than estimated here). The Supplementary Discussion 2 discusses the declines in devil rays’ time-series in Mozambique and the context suggesting that these declines may have occurred in other Indian Ocean countries. The Supplementary Discussion 3 discusses some additional management details of the regional fishery management organizations focused on tunas, relative to oceanic shark species.

Reporting Summary

Supplementary Data 1

Table of the LPI per oceanic shark and ray species per year: median (Credible Interval 95%).

Supplementary Data 2

Table of compiled time-series of mean oceanic shark stock assessments biomass/abundance trajectories relative to maximum sustainable yield per year.

Source data

Source Data Fig. 2

Source Data Fig. 3

Source Data Fig. 4

Rights and permissions

Reprints and Permissions

About this article

Check for updates

Cite this article

Pacoureau, N., Rigby, C.L., Kyne, P.M. *et al.* Half a century of global decline in oceanic sharks and rays. *Nature* **589,** 567–571 (2021). https://doi.org/10.1038/s41586-020-03173-9

Download citation

- Received: 10 July 2019
- Accepted: 27 November 2020
- Published: 27 January 2021
- Issue Date: 28 January 2021
- DOI: https://doi.org/10.1038/s41586-020-03173-9

Comments

By submitting a comment you agree to abide by our Terms and Community Guidelines. If you find something abusive or that does not comply with our terms or guidelines please flag it as inappropriate.

Access through your institution
Change institution
Buy or subscribe

This article was downloaded by **calibre** from https://www.nature.com/articles/s41586-020-03173-9

- Article
- Published: 20 January 2021

Monitoring hiring discrimination through online recruitment platforms

- Dominik Hangartner ORCID: orcid.org/0000-0002-4511-7507[1,2,3] na1,
- Daniel Kopp ORCID: orcid.org/0000-0002-4023-865X[3,4] na1 &
- Michael Siegenthaler ORCID: orcid.org/0000-0002-9423-4515[3,4] na1

Nature **volume 589**, pages572–576(2021)Cite this article

- 2070 Accesses
- 269 Altmetric
- Metrics details

Subjects

- Economics
- Politics

Abstract

Women (compared to men) and individuals from minority ethnic groups (compared to the majority group) face unfavourable labour market outcomes in many economies[1,2], but the extent to which discrimination is responsible for these effects, and the channels through which they occur,

remain unclear[3,4]. Although correspondence tests[5]—in which researchers send fictitious CVs that are identical except for the randomized minority trait to be tested (for example, names that are deemed to sound 'Black' versus those deemed to sound 'white')—are an increasingly popular method to quantify discrimination in hiring practices[6,7], they can usually consider only a few applicant characteristics in select occupations at a particular point in time. To overcome these limitations, here we develop an approach to investigate hiring discrimination that combines tracking of the search behaviour of recruiters on employment websites and supervised machine learning to control for all relevant jobseeker characteristics that are visible to recruiters. We apply this methodology to the online recruitment platform of the Swiss public employment service and find that rates of contact by recruiters are 4–19% lower for individuals from immigrant and minority ethnic groups, depending on their country of origin, than for citizens from the majority group. Women experience a penalty of 7% in professions that are dominated by men, and the opposite pattern emerges for men in professions that are dominated by women. We find no evidence that recruiters spend less time evaluating the profiles of individuals from minority ethnic groups. Our methodology provides a widely applicable, non-intrusive and cost-efficient tool that researchers and policy-makers can use to continuously monitor hiring discrimination, to identify some of the drivers of discrimination and to inform approaches to counter it.

Access through your institution
Change institution
Buy or subscribe

Access options

Subscribe to Journal

Get full journal access for 1 year

$199.00

only $3.90 per issue

Subscribe

All prices are NET prices.
VAT will be added later in the checkout.

Rent or Buy article

Get time limited or full article access on ReadCube.

from$8.99

Rent or Buy

All prices are NET prices.

Additional access options:

- Log in
- Access through your institution
- Learn about institutional subscriptions

Fig. 1: Effects of the ethnicity of jobseekers on contact rate and time spent by recruiters on jobseekers' profile.

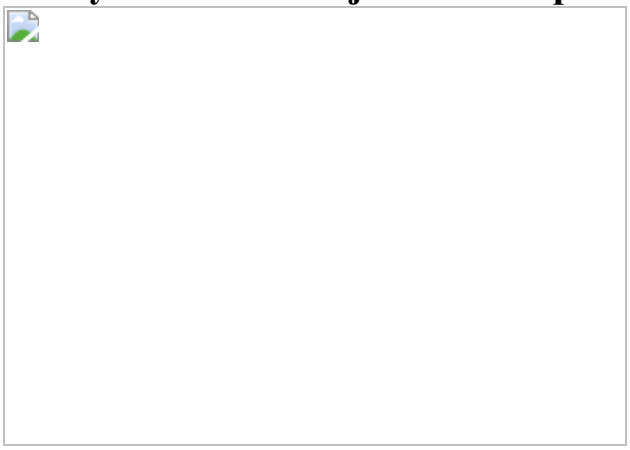

Fig. 2: Variation in the time that recruiters spend on profiles and ethnic penalties during the workday.

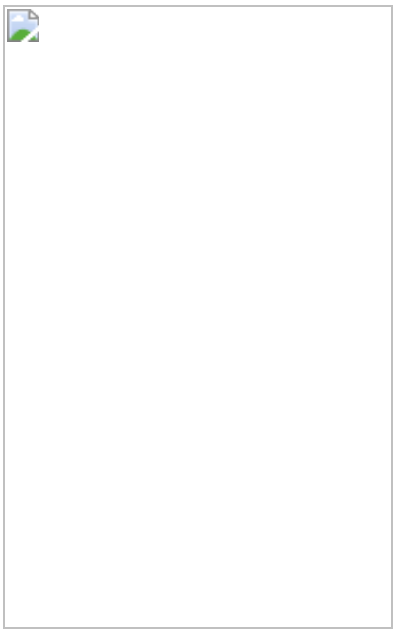

Fig. 3: Gender-based hiring disparities across occupations.

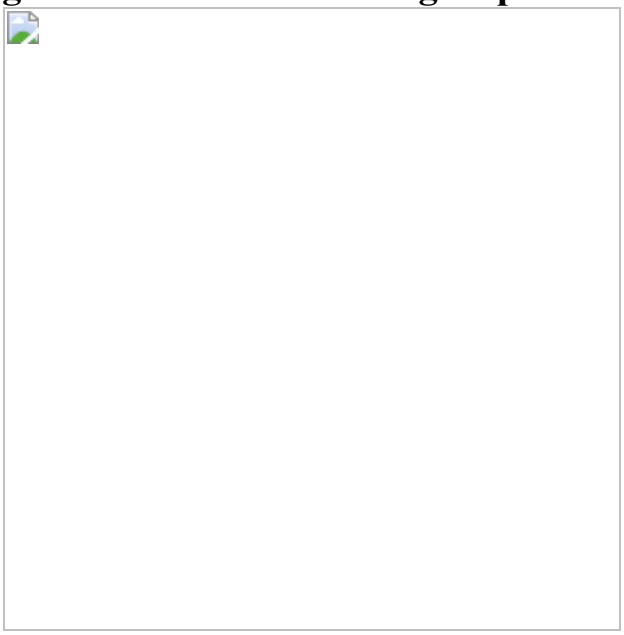

Data availability

To obtain access to the anonymized data, researchers have to sign a data sharing agreement with the KOF Micro Data Centre at ETH Zurich and the Labour Directorate of SECO. Source data are provided with this paper.

Code availability

Code to replicate all analyses presented here is available at the publicly accessible Harvard Dataverse: https://doi.org/10.7910/DVN/GGENFB.

References

1. 1.

   Altonji, J. G. & Blank, R. M. Race and gender in the labor market. *Handbook of Labor Economics* **3**, 3143–3259 (1999).

   Article Google Scholar

2. 2.

   Blau, F. D. & Kahn, L. M. The gender wage gap: extent, trends, and explanations. *J. Econ. Lit*. **55**, 789–865 (2017).

   Article Google Scholar

3. 3.

   Neumark, D. Experimental research on labor market discrimination. *J. Econ. Lit*. **56**, 799–866 (2018).

   Article Google Scholar

4. 4.

   Bartoš, V., Bauer, M., Chytilová, J. & Matějka, F. Attention discrimination: theory and field experiments with monitoring information acquisition. *Am. Econ. Rev*. **106**, 1437–1475 (2016).

   Article Google Scholar

5. 5.

   Bertrand, M. & Mullainathan, S. Are Emily and Greg more employable than Lakisha and Jamal? A field experiment on labor

market discrimination. *Am. Econ. Rev*. **94**, 991–1013 (2004).

Article Google Scholar

6. 6.

Bertrand, M. & Duflo, E. in *Handbook of Economic Field Experiments* Vol. 1 (eds Banerjee, A. V. & Duflo, E.) 309–393 (Elsevier, 2017).

7. 7.

Baert, S. in *Audit Studies: Behind the Scenes with Theory, Method, and Nuance* (ed. Gaddis, S. M.) 63–77 (Springer, 2018).

8. 8.

Kuhn, P. & Shen, K. Gender discrimination in job ads: evidence from China. *Q. J. Econ*. **128**, 287–336 (2013).

Article Google Scholar

9. 9.

Horton, J. J. & Tambe, P. Labor economists get their microscope: big data and labor market analysis. *Big Data* **3**, 130–137 (2015).

Article Google Scholar

10. 10.

Chan, J. & Wang, J. Hiring preferences in online labor markets: evidence of a female hiring bias. *Manage. Sci*. **64**, 2973–2994 (2018).

Article Google Scholar

11. 11.

Eriksson, S. & Lagerström, J. Detecting discrimination in the hiring process: evidence from an internet-based search channel. *Empir. Econ*.

43, 537–563 (2012).

Article Google Scholar

12. 12.

Tibshirani, R. Regression shrinkage and selection via the lasso. *J. R. Stat. Soc. B* **58**, 267–288 (1996).

MathSciNet MATH Google Scholar

13. 13.

Belloni, A., Chernozhukov, V. & Hansen, C. Inference on treatment effects after selection among high-dimensional controls. *Rev. Econ. Stud*. **81**, 608–650 (2014).

MathSciNet Article Google Scholar

14. 14.

Zschirnt, E. & Fibbi, R. *Do Swiss Citizens of Immigrant Origin Face Hiring Discrimination in the Labour Market?* Working paper 20 (Université de Neuchâtel, 2019).

15. 15.

Hainmueller, J. & Hangartner, D. Who gets a Swiss passport? A natural experiment in immigrant discrimination. *Am. Polit. Sci. Rev*. **107**, 159–187 (2013).

Article Google Scholar

16. 16.

Greenwald, A. G. & Banaji, M. R. Implicit social cognition: attitudes, self-esteem, and stereotypes. *Psychol. Rev*. **102**, 4–27 (1995).

CAS Article Google Scholar

17. 17.

Chugh, D. Societal and managerial implications of implicit social cognition: why milliseconds matter. *Soc. Justice Res*. **17**, 203–222 (2004).

Article Google Scholar

18. 18.

Muraven, M. & Baumeister, R. F. Self-regulation and depletion of limited resources: does self-control resemble a muscle? *Psychol. Bull*. **126**, 247–259 (2000).

CAS Article Google Scholar

19. 19.

Pocheptsova, A., Amir, O., Dhar, R. & Baumeister, R. F. Deciding without resources: resource depletion and choice in context. *J. Mark. Res*. **46**, 344–355 (2009).

Article Google Scholar

20. 20.

Danziger, S., Levav, J. & Avnaim-Pesso, L. Extraneous factors in judicial decisions. *Proc. Natl Acad. Sci. USA* **108**, 6889–6892 (2011).

ADS CAS Article Google Scholar

21. 21.

Olivetti, C. & Petrongolo, B. The evolution of gender gaps in industrialized countries. *Annu. Rev. Econ*. **8**, 405–434 (2016).

Article Google Scholar

22. 22.

Azmat, G. & Petrongolo, B. Gender and the labor market: what have we learned from field and lab experiments? *Labour Econ*. **30**, 32–40 (2014).

Article Google Scholar

23. 23.

Riach, P. A. & Rich, J. An experimental investigation of sexual discrimination in hiring in the English labor market. *Adv. Econ. Anal. Policy* **5**, https://doi.org/10.2202/1538-0637.1416 (2006).

24. 24.

Eagly, A. H. & Steffen, V. J. Gender stereotypes stem from the distribution of women and men into social roles. *J. Pers. Soc. Psychol*. **46**, 735–754 (1984).

Article Google Scholar

25. 25.

Pager, D. & Shepherd, H. The sociology of discrimination: racial discrimination in employment, housing, credit, and consumer markets. *Annu. Rev. Sociol*. **34**, 181–209 (2008).

Article Google Scholar

26. 26.

Hagendoorn, L. Intergroup biases in multiple group systems: the perception of ethnic hierarchies. *Eur. Rev. Soc. Psychol*. **6**, 199–228 (1995).

Article Google Scholar

27. 27.

Phelps, E. S. The statistical theory of racism and sexism. *Am. Econ. Rev*. **62**, 659–661 (1972).

Google Scholar

28. 28.

Arrow, K. *The Theory of Discrimination*. Working paper 30A (Princeton University, 1971).

29. 29.

Becker, G. S. *The Economics of Discrimination* (Univ. Chicago Press, 1957).

30. 30.

Greenwald, A. G. & Krieger, L. H. Implicit bias: scientific foundations. *Calif. Law Rev*. **94**, 945–967 (2006).

Article Google Scholar

31. 31.

Bohnet, I., Van Geen, A. & Bazerman, M. When performance trumps gender bias: joint vs. separate evaluation. *Manage. Sci*. **62**, 1225–1234 (2016).

Article Google Scholar

Download references

Acknowledgements

We acknowledge funding from the Swiss National Science Foundation (grant no. 162620). We are grateful to SECO for collaborating on this project and sharing data, and we thank S. Thöni and M. Bannert for programming support.

Author information

Author notes

1. These authors contributed equally: Dominik Hangartner, Daniel Kopp, Michael Siegenthaler

Affiliations

1. Public Policy Group, ETH Zurich, Zurich, Switzerland

   Dominik Hangartner

2. Department of Government, London School of Economics and Political Science, London, UK

   Dominik Hangartner

3. Immigration Policy Lab, ETH Zurich, Zurich, Switzerland

   Dominik Hangartner, Daniel Kopp & Michael Siegenthaler

4. KOF Swiss Economic Institute, ETH Zurich, Zurich, Switzerland

   Daniel Kopp & Michael Siegenthaler

Authors

1. Dominik Hangartner
   View author publications

   You can also search for this author in PubMed Google Scholar

2. Daniel Kopp
   View author publications

   You can also search for this author in PubMed Google Scholar

3. Michael Siegenthaler
View author publications

You can also search for this author in PubMed Google Scholar

Contributions

D.H., D.K. and M.S. designed the research; D.H., D.K. and M.S. performed the research and analysed the data; and D.H., D.K. and M.S. wrote the paper.

Corresponding author

Correspondence to Dominik Hangartner.

Ethics declarations

Competing interests

The authors declare no competing interests.

Additional information

Peer review information *Nature* thanks Philipp Kircher and the other, anonymous, reviewer(s) for their contribution to the peer review of this work.

Publisher's note Springer Nature remains neutral with regard to jurisdictional claims in published maps and institutional affiliations.

Extended data figures and tables

Extended Data Fig. 1 The search process on Job-Room.

The search process on the government-affiliated online recruitment platform of the Swiss public employment service. Left, stylized illustration of the search process; right, screenshots of every step. **a**–**c**, First the recruiter completes the search mask (**a**), typically by entering the occupation for which a vacancy exists and place of work, from which a ranked list of candidates who meet these criteria is generated (**b**). From this list, the recruiter selects the profiles that provide detailed productivity-related information akin to a standard CV about the jobseekers' education, work experience and skills, as well as gender and markers of ethnicity (**c**). The bottom of the profile contains a button that reveals the contact information, typically a jobseeker's phone number and email address, and the contact details of the employment office.

Extended Data Fig. 2 Validation of research design.

a, Percentage point effects and associated cluster-robust 95% confidence intervals of ethnicity on the likelihood that the contact button has been clicked conditional on profile visit (n = 254,975). The sample is restricted to non-registered recruiters who do not observe the nationality and name of jobseekers. Controlling for detailed language skills of jobseekers, these recruiters should not be able to infer candidates' ethnicity. Standard errors are clustered at recruiter level. The null hypothesis that all ethnicity coefficients are jointly zero is not rejected (P = 0.93 (two-sided F-test)). **b**, Comparison of our baseline results that are based on the click on the contact button (in blue) with analogous regressions with outcome variables that are more direct signals of contact attempts by recruiters (n = 3,251,303). Dots with horizontal lines indicate point estimates with cluster-robust 95% confidence intervals from OLS regression. The dependent variable in the model 'mail or print button' is a binary indicator if a recruiter clicked on the hyperlink of the email address of the candidate or on the button 'print candidate profile' available on the profile page (n = 3,251,263 profile views). These click events happen in only 3.3% and 4.8% of profile visits, respectively. The dependent variable in the model 'contact button (60 sec)' is a binary indicator equal to one if a recruiter clicked on the contact button and subsequently stayed on the profile of the respective jobseeker for at least 60 s—a sign that the recruiter contacted the jobseeker immediately, possibly via phone or email. This happens in 27.3% of all contact attempts.

The coefficients are normalized with the mean of the outcome variables to represent percent effects. Source data

Extended Data Fig. 3 Discrimination by type of recruiter.

a, Effects of ethnicity on contact rate estimated separately for recruiters with 1 search (n = 62,081 profile views), 2–10 searches (n = 404,203 profile views), 11–50 searches (n = 546,441 profile views) and more than 50 searches (n = 2,238,538 profile views) in the study period. The coefficients are normalized with the mean contact rate of the respective category. Dots with horizontal lines indicate point estimates with cluster-robust 95% confidence intervals from OLS regression. **b**, Effects of ethnicity on the contact rate estimated separately for registered (n = 2,996,288 profile views) and non-registered (n = 254,975 profile views) recruiters of the platform. Dots with horizontal lines indicate point estimates with cluster-robust 95% confidence intervals from OLS regression. The light red bars indicate minority ethnic groups that are not (or to a lesser extent) identifiable based on their language skills on Job-Room. Supplementary Table 11 provides an overview of the language skills of the different ethnic groups. Source data

Extended Data Fig. 4 Effects by search duration within a session and for slow and fast deciders.

a, Effect of ethnicity on contact rate depending on the length of a session for immigrant jobseekers from Europe (in blue) and from outside of Europe (in red). Dots with horizontal lines indicate point estimates with cluster-robust 95% confidence intervals from OLS regression (n = 1,378,011 profile views). The estimates are derived from interactions between the indicators of ethnicity and indicators of the time elapsed since the start of the session. A session is defined as the time at which the recruiter logs into Job-Room until he or she logs off or closes the browser window. Longer sessions typically encompass several searches. As recruiters vary in their average session length, and these compositional differences can influence our results, the sample is restricted to sessions that take at least 30 min. The regressions control for session instead of search-fixed effects. Swiss jobseekers are used as the reference category. **b**, Effects of ethnicity on

contact rate depending on the average decision time of a recruiter. Dots with horizontal lines indicate point estimates with cluster-robust 95% confidence intervals from OLS regression. The sample is restricted to recruiters who conduct at least 6 searches and view at least 12 profiles. We use a random subset of one third of searches per recruiter to assign recruiters into one of four groups: fast deciders (lowest quartile), rather fast deciders (second quartile), rather slow deciders (third quartile) and slow deciders (highest quartile). The figure shows the ethnic penalties estimated separately for each group of recruiters using the test sample (the remaining two thirds of searches per recruiter). The average time that recruiters are looking at jobseekers' profiles in the test sample are 5.7 s for fast deciders (n = 303,934 profile views), 9.9 s for rather fast deciders (n = 545,538 profile views), 15.4 s for rather slow deciders (n = 690,989 profile views) and 31.7 s for slow deciders (n = 364,018 profile views). Source data

Extended Data Fig. 5 Additional gender analyses.

a, Effect of female gender on the probability of contact (in %) (n = 17,369,372 profiles). The circles show the (dis)advantage that women face compared to men in a given occupation, plotted against the share of women in that occupation. In contrast to Fig. 3 in the main text, the share of women per occupation is calculated from the Swiss earnings structure survey instead of the share of women in the result list. The circumference of the dots denotes the share of searches in each occupation. The solid black line indicates the weighted least squares regression of the estimated gender disparity against the share of female workers in each occupation. The dashed black lines show the associated 95% confidence intervals. The colour of the circles indicates the ISCO-1 level occupation classification. **b**, Relationship between occupational wages and hiring penalties (advantages) for female versus male jobseekers, grouped by two-digit ISCO occupation (n = 17,369,372 profiles). We estimate occupation-specific wages from the October 2016 wave of the Swiss Earnings Structure Survey. The circles show the (dis)advantage that women face compared to men in a given occupation, plotted against the log average wage in the occupation. The circumference of the dots denotes the share of searches in each occupation. The solid black line indicates the weighted least squares regression of the estimated gender disparity against the average log wage in each occupation.

The dashed black lines show the associated 95% confidence intervals. The colour of the circles indicates the ISCO-1 level occupation classification. Source data

Extended Data Fig. 6 Tests for statistical discrimination.

a, Effects of ethnicity on the contact rate estimated separately for jobseekers with low (n = 332,425 profile views), medium (n = 585,979 profile views) or high (n = 501,506 profile views) unobserved employability. Dots with horizontal lines indicate point estimates with cluster-robust 95% confidence intervals from OLS regression. The construction of the index of unobserved employability exploit that we can observe the age, marital status and pre-unemployment wage of jobseekers. These characteristics are unobserved by recruiters on Job-Room. The construction involves several steps. First, we collapse the data at the jobseeker level and split the sample randomly in a training (50% of the searches) and a test sample (the remaining 50%). Second, we interact the three characteristics with nine occupation dummies (according to the Swiss SBN occupational classification). Third, we regress a dummy variable that a jobseeker leaves unemployment within the first four months after registering at the Swiss public employment service on these interactions, controlling for occupation-period and canton fixed effects. On the basis of these occupation-specific estimates, we predict the likelihood that jobseekers in the test sample leave unemployment within four months. We then assign each of these jobseekers to one of three equally sized groups (high, medium and low unobserved employability). The likelihood that a jobseeker with high unobserved employability leaves unemployment within 4 months is 37%, whereas it is 10% for jobseekers with low unobserved employability. The regressions are based on the test sample. **b**, Effects of ethnicity on the contact rate by length of the unstructured text field containing information on additional skills of jobseekers (see Supplementary Table 1 for examples). Dots with horizontal lines indicate point estimates of the interaction between length of skill field and ethnicity with cluster-robust 95% confidence intervals from OLS regression (n = 3,251,263 profile views). The reference categories (the hollow dots on the zero line) are Swiss jobseekers who report no additional skills, a skill field with 1 to 10 words and a skill field with more than 10 words, respectively. Source data

Extended Data Fig. 7 Effect of a click on the contact button on the likelihood of leaving unemployment.

Effect and associated cluster-robust 95% confidence intervals of a click on the contact button on Job-Room on the likelihood that a jobseeker leaves unemployment, exploiting that we can link candidates to the unemployment register. The dependent variables are dummy variables equal to one if a jobseeker leaves unemployment within 30, 60, 90, 120 and 150 days, respectively, after a search. Each coefficient is derived from a separate regression (n = 12,823,811 profiles). The variable of interest is the contact attempt on Job-Room. The sample consists of all individuals that appeared within a result list of a search between March and September 2017. We drop the remaining periods because we observe unemployment exits only up to March 2018. We also exclude all registered unemployed individuals who reach their maximum benefit duration to make sure that exit out of unemployment represents a voluntary decision by the jobseeker. The regressions control for search-specific fixed effects and all variables visible to recruiters on Job-Room including unemployment duration at the time of the search and all relevant first-order interactions. The model contains 2,569 covariates that are predictive for leaving unemployment and the contact button click, selected by the Lasso-based post-double selection method. The regressions thus control for all factors that plausibly influence recruiters' contact attempts on the platform. The coefficients are identified because certain individuals are contacted on the platform whereas observationally equivalent individuals who appear in the same search are not; for example, because of idiosyncrasies in recruiters' decisions or because their candidate profile is not visited (for example, as they are ranked low in the result list). The average likelihood of leaving unemployment after 30 (60, 90, 120, 150) days is 17% (30%, 40%, 48%, 54%). The click on the contact button thus increases the likelihood to leave unemployment within 90 days after the search by 2.1% (0.821/40). Standard errors are clustered at recruiter level. Source data

Extended Data Table 1 Comparison of ethnic penalties with estimates from a contemporaneous correspondence study
Full size table

Extended Data Table 2 Characteristics of candidates with at least one profile visit by nationality
Full size table
Extended Data Table 3 Descriptive sample statistics with and without sample restrictions
Full size table

Supplementary information

Supplementary Information

The Supplementary Information contains supplementary methods and eleven supplementary tables that provide details on the data used in the analysis, the statistical model used to estimate ethnic and gender penalties, robustness and sensitivity analyses for these regressions, and extensions to our main regression results to draw out further implications.

Reporting Summary

Source data

Source Data Fig. 1

Source Data Fig. 2

Source Data Fig. 3

Source Data Extended Data Fig. 2

Source Data Extended Data Fig. 3

Source Data Extended Data Fig. 4

Source Data Extended Data Fig. 5

Source Data Extended Data Fig. 6

Source Data Extended Data Fig. 7

Rights and permissions

Reprints and Permissions

About this article

Check for updates

Cite this article

Hangartner, D., Kopp, D. & Siegenthaler, M. Monitoring hiring discrimination through online recruitment platforms. *Nature* **589,** 572–576 (2021). https://doi.org/10.1038/s41586-020-03136-0

Download citation

- Received: 26 November 2019
- Accepted: 02 December 2020
- Published: 20 January 2021
- Issue Date: 28 January 2021
- DOI: https://doi.org/10.1038/s41586-020-03136-0

Comments

By submitting a comment you agree to abide by our Terms and Community Guidelines. If you find something abusive or that does not comply with our terms or guidelines please flag it as inappropriate.

Access through your institution
Change institution
Buy or subscribe

This article was downloaded by **calibre** from https://www.nature.com/articles/s41586-020-03136-0

- Article
- Published: 25 November 2020

Neural circuit mechanisms of sexual receptivity in *Drosophila* females

- Kaiyu Wang[1 na1],
- Fei Wang ORCID: orcid.org/0000-0002-8646-2411[1 na1],
- Nora Forknall ORCID: orcid.org/0000-0003-2139-7599[1],
- Tansy Yang ORCID: orcid.org/0000-0003-1131-0410[1],
- Christopher Patrick ORCID: orcid.org/0000-0001-8830-1892[1],
- Ruchi Parekh[1] &
- Barry J. Dickson ORCID: orcid.org/0000-0003-0715-892X[1,2]

Nature **volume 589**, pages577–581(2021)Cite this article

- 2835 Accesses
- 1 Citations
- 28 Altmetric
- Metrics details

Subjects

- Auditory system
- Neural circuits
- Sexual behaviour

Abstract

Choosing a mate is one of the most consequential decisions a female will make during her lifetime. A female fly signals her willingness to mate by opening her vaginal plates, allowing a courting male to copulate[1,2]. Vaginal plate opening (VPO) occurs in response to the male courtship song and is dependent on the mating status of the female. How these exteroceptive (song) and interoceptive (mating status) inputs are integrated to regulate VPO remains unknown. Here we characterize the neural circuitry that implements mating decisions in the brain of female *Drosophila melanogaster*. We show that VPO is controlled by a pair of female-specific descending neurons (vpoDNs). The vpoDNs receive excitatory input from auditory neurons (vpoENs), which are tuned to specific features of the *D. melanogaster* song, and from pC1 neurons, which encode the mating status of the female[3,4]. The song responses of vpoDNs, but not vpoENs, are attenuated upon mating, accounting for the reduced receptivity of mated females. This modulation is mediated by pC1 neurons. The vpoDNs thus directly integrate the external and internal signals that control the mating decisions of *Drosophila* females.

Access through your institution
Change institution
Buy or subscribe

Access options

Subscribe to Journal

Get full journal access for 1 year

$199.00

only $3.90 per issue

Subscribe

All prices are NET prices.
VAT will be added later in the checkout.

Rent or Buy article

Get time limited or full article access on ReadCube.

from$8.99

Rent or Buy

All prices are NET prices.

Additional access options:

- Log in
- Access through your institution
- Learn about institutional subscriptions

Fig. 1: Female-specific vpoDNs control vaginal plate opening (VPO).

Fig. 2: Auditory inputs to vpoDNs.

Fig. 3: vpoENs and vpoDNs are tuned to conspecific courtship song.

Fig. 4: vpoDNs integrate mating status and song.

Data availability

Confocal images of the central nervous systems of split-GAL4 lines used in this study are available at http://splitgal4.janelia.org/cgi-bin/splitgal4.cgi. Other datasets generated during the current study are available from the corresponding author on reasonable request.

References

1. 1.

   Hall, J. C. The mating of a fly. *Science* **264**, 1702–1714 (1994).

   ADS CAS Article Google Scholar

2. 2.

Bussell, J. J., Yapici, N., Zhang, S. X., Dickson, B. J. & Vosshall, L. B. Abdominal-B neurons control *Drosophila* virgin female receptivity. *Curr. Biol*. **24**, 1584–1595 (2014).

CAS Article Google Scholar

3. 3.

Zhou, C., Pan, Y., Robinett, C. C., Meissner, G. W. & Baker, B. S. Central brain neurons expressing *doublesex* regulate female receptivity in *Drosophila*. *Neuron* **83**, 149–163 (2014).

CAS Article Google Scholar

4. 4.

Wang, F. et al. Neural circuitry linking mating and egg laying in *Drosophila* females. *Nature* **579**, 101–105 (2020).

ADS CAS Article Google Scholar

5. 5.

Göpfert, M. C. & Robert, D. The mechanical basis of *Drosophila* audition. *J. Exp. Biol*. **205**, 1199–1208 (2002).

PubMed Google Scholar

6. 6.

Kamikouchi, A. et al. The neural basis of *Drosophila* gravity-sensing and hearing. *Nature* **458**, 165–171 (2009).

ADS CAS Article Google Scholar

7. 7.

Lai, J. S., Lo, S. J., Dickson, B. J. & Chiang, A. S. Auditory circuit in the *Drosophila* brain. *Proc. Natl Acad. Sci. USA* **109**, 2607–2612

(2012).

ADS CAS Article Google Scholar

8. 8.

Vaughan, A. G., Zhou, C., Manoli, D. S. & Baker, B. S. Neural pathways for the detection and discrimination of conspecific song in *D. melanogaster*. *Curr. Biol*. **24**, 1039–1049 (2014).

CAS Article Google Scholar

9. 9.

Deutsch, D., Clemens, J., Thiberge, S. Y., Guan, G. & Murthy, M. Shared song detector neurons in *Drosophila* male and female brains drive sex-specific behaviors. *Curr. Biol*. **29**, 3200–3215 (2019).

CAS Article Google Scholar

10. 10.

Kubli, E. The sex-peptide. *BioEssays* **14**, 779–784 (1992).

CAS Article Google Scholar

11. 11.

Yang, C. H. et al. Control of the postmating behavioral switch in *Drosophila* females by internal sensory neurons. *Neuron* **61**, 519–526 (2009).

CAS Article Google Scholar

12. 12.

Häsemeyer, M., Yapici, N., Heberlein, U. & Dickson, B. J. Sensory neurons in the *Drosophila* genital tract regulate female reproductive behavior. *Neuron* **61**, 511–518 (2009).

Article Google Scholar

13. 13.

Feng, K., Palfreyman, M. T., Häsemeyer, M., Talsma, A. & Dickson, B. J. Ascending SAG neurons control sexual receptivity of *Drosophila* females. *Neuron* **83**, 135–148 (2014).

CAS Article Google Scholar

14. 14.

Stockinger, P., Kvitsiani, D., Rotkopf, S., Tirián, L. & Dickson, B. J. Neural circuitry that governs *Drosophila* male courtship behavior. *Cell* **121**, 795–807 (2005).

CAS Article Google Scholar

15. 15.

Kvitsiani, D. & Dickson, B. J. Shared neural circuitry for female and male sexual behaviours in *Drosophila*. *Curr. Biol*. **16**, R355–R356 (2006).

CAS Article Google Scholar

16. 16.

Rideout, E. J., Dornan, A. J., Neville, M. C., Eadie, S. & Goodwin, S. F. Control of sexual differentiation and behavior by the *doublesex* gene in *Drosophila melanogaster*. *Nat. Neurosci*. **13**, 458–466 (2010).

CAS Article Google Scholar

17. 17.

Kimura, K., Sato, C., Koganezawa, M. & Yamamoto, D. *Drosophila* ovipositor extension in mating behavior and egg deposition involves distinct sets of brain interneurons. *PLoS ONE* **10**, e0126445 (2015).

Article Google Scholar

18. 18.

Zheng, Z. et al. A complete electron microscopy volume of the brain of adult *Drosophila melanogaster*. *Cell* **174**, 730–743 (2018).

CAS Article Google Scholar

19. 19.

Ewing, A. W. & Bennet-Clark, H. C. Courtship songs of *Drosophila*. *Behaviour* **31**, 288–301 (1968).

Article Google Scholar

20. 20.

Cowling, D. E. & Burnet, B. Courtship songs and genetic-control of their acoustic characteristics in sibling species of the *Drosophila-melanogaster* subgroup. *Anim. Behav*. **29**, 924–935 (1981).

Article Google Scholar

21. 21.

Clemens, J. et al. Discovery of a new song mode in *Drosophila* reveals hidden structure in the sensory and neural drivers of behavior. *Curr. Biol*. **28**, 2400–2412 (2018).

MathSciNet CAS Article Google Scholar

22. 22.

Imhof, M., Harr, B., Brem, G. & Schlötterer, C. Multiple mating in wild *Drosophila melanogaster* revisited by microsatellite analysis. *Mol. Ecol*. **7**, 915–917 (1998).

CAS Article Google Scholar

23. 23.

Ochando, M. D., Reyes, A. & Ayala, F. J. Multiple paternity in two natural populations (orchard and vineyard) of *Drosophila*. *Proc. Natl Acad. Sci. USA* **93**, 11769–11773 (1996).

ADS CAS Article Google Scholar

24. 24.

Bath, D. E. et al. FlyMAD: rapid thermogenetic control of neuronal activity in freely walking *Drosophila*. *Nat. Methods* **11**, 756–762 (2014).

CAS Article Google Scholar

25. 25.

Inagaki, H. K. et al. Optogenetic control of *Drosophila* using a red-shifted channelrhodopsin reveals experience-dependent influences on courtship. *Nat. Methods* **11**, 325–332 (2014).

CAS Article Google Scholar

26. 26.

Auer, T. O. & Benton, R. Sexual circuitry in *Drosophila*. *Curr. Opin. Neurobiol*. **38**, 18–26 (2016).

CAS Article Google Scholar

27. 27.

Backhaus, B., Sulkowski, E. & Schlote, F. W. A semi-synthetic, general-purpose medium for *Drosophila melanogaster*. *Drosoph. Inf. Serv*. **60**, 210–212 (1984).

Google Scholar

28. 28.

Schneider-Mizell, C. M. et al. Quantitative neuroanatomy for connectomics in *Drosophila*. *eLife* **5**, e12059 (2016).

Article Google Scholar

29. 29.

Meissner, G. W. et al. Mapping neurotransmitter identity in the whole-mount *Drosophila* brain using multiplex high-throughput fluorescence in situ hybridization. *Genetics* **211**, 473–482 (2019).

CAS Article Google Scholar

30. 30.

Schindelin, J. et al. Fiji: an open-source platform for biological-image analysis. *Nat. Methods* **9**, 676–682 (2012).

CAS Article Google Scholar

Download references

Acknowledgements

We thank the Janelia FlyLight, Fly Facility, Project Technical Resources, Molecular Biology, Functional Connectome, and Experimental Technology teams and N. Chen for technical assistance; E. Lillvis, E. Behrman and D. Stern for providing courtship songs of various *Drosophila* species; and K. Svoboda, K. Feng and K. Keleman for comments on the manuscript. This work was funded by the Howard Hughes Medical Institute.

Author information

Author notes

1. These authors contributed equally: Kaiyu Wang, Fei Wang

Affiliations

1. Janelia Research Campus, Howard Hughes Medical Institute, Ashburn, VA, USA

   Kaiyu Wang, Fei Wang, Nora Forknall, Tansy Yang, Christopher Patrick, Ruchi Parekh & Barry J. Dickson

2. Queensland Brain Institute, University of Queensland, St Lucia, Queensland, Australia

   Barry J. Dickson

Authors

1. Kaiyu Wang
   View author publications

   You can also search for this author in PubMed Google Scholar

2. Fei Wang
   View author publications

   You can also search for this author in PubMed Google Scholar

3. Nora Forknall
   View author publications

   You can also search for this author in PubMed Google Scholar

4. Tansy Yang
   View author publications

   You can also search for this author in PubMed Google Scholar

5. Christopher Patrick
   View author publications

You can also search for this author in PubMed Google Scholar

6. Ruchi Parekh
   View author publications

   You can also search for this author in PubMed Google Scholar

7. Barry J. Dickson
   View author publications

   You can also search for this author in PubMed Google Scholar

Contributions

B.J.D., K.W. and F.W. conceived the study and wrote the manuscript. K.W. and F.W. performed all experiments and analysed the data. N.F., T.Y., C.P. and F.W. reconstructed selected neurons and synapses in the FAFB EM volume. R.P. managed the tracing team.

Corresponding author

Correspondence to Barry J. Dickson.

Ethics declarations

Competing interests

The authors declare no competing interests.

Additional information

Peer review information *Nature* thanks the anonymous reviewer(s) for their contribution to the peer review of this work.

Publisher's note Springer Nature remains neutral with regard to jurisdictional claims in published maps and institutional affiliations.

Extended data figures and tables

Extended Data Fig. 1 Genetic screen for neuronal activities required for female receptivity.

a, Difference in the copulation frequencies of split-GAL4 *UAS-TNTe* (tetanus toxin) and control *UAS-TNTe* virgin females within a 10-min observation period, relative to the control group. **b**, Stable-split lines (SS ID) and sample size (*n*) for the 234 split-GAL4 lines shown in **a**.

Extended Data Fig. 2 Anatomical characterization of vpoDNs.

a, Confocal images of brains and ventral nerve cords from female and male flies carrying *vpoDN-SS1*, *vpoDN-SS2*, or *vpoDN-SS3*, and *UAS-myrFLAG*, stained with anti-FLAG to reveal membranes of targeted neurons (green) and mAb nc82 to reveal all synapses (magenta). One pair of vpoDNs are labelled in females but not in males. Scale bar: 100 µm. **b**, Confocal images of female brains showing the co-labelling of vpoDNs with *dsx-LexA* but not *fru-LexA*. Scale bar: 20 µm. **c**, Confocal images of female brains showing the expression of *ChAT*, *GAD1*, and *vGluT* in vpoDN (labelled by Halo tag, arrows), as revealed by FISH. Scale bar: 10 µm. Representative images are shown from at least 5 independent samples examined in each case.

Extended Data Fig. 3 Functional characterization of vpoDNs.

a, **b**, Percentage of pairs copulating (**a**) and frequency of VPO (**b**) during 10 min of courtship between a virgin female of the indicated genotype and a wild-type male. **c**, Percentage of time wild-type males chased or extended their wings towards the virgin female during a 10-min observation period. **d**, Snapshots of female VPO induced upon photoactivation of vpoDNs (Supplementary Videos 2, 3). **e**, Percentage of isolated virgins performing VPO upon photoactivation of vpoDNs (5 s, 635 nm, 57 µW mm^{-2}). Each female was tested three times as follows: first, while intact, then with the cuticle over the posterior part of ventral nerve cord removed to expose the abdominal ganglion (sham), and finally, after the abdominal nerve trunk was severed (cut). Data in **b** and **c** shown as scatter plots with mean ± s.e.m.

P values in italics, two-sided Fisher's exact test in **a**, two-sided Wilcoxon test in **b** and **c**. See Supplementary Table 3 for details of statistical analyses.

Extended Data Fig. 4 vpoDNs are sensitive to courtship song and are postsynaptic to auditory neurons.

a, Frequency of male courtship behaviours around the onset of female VPO. *n* = 124 VPOs from 12 pairs of flies. **b**, GCaMP6s signal changes in vpoDNs of virgins with intact aristae in response to courtship song and white noise. Lines connect data points from the same fly. Error bars show mean ± s.e.m. *P* values in italics, paired two-sided Wilcoxon test. See also Supplementary Table 3. **c**, Neurons presynaptic to a single vpoDN in the FAFB EM volume, showing the number of input synapses identified (thresholded at 10).

Extended Data Fig. 5 Split-GAL4 driver lines targeting vpoENs and vpoINs and neurotransmitter types revealed by FISH.

a, Confocal images of female central nervous system carrying indicated split-GAL4 driver lines and *UAS-myrFLAG* or *UAS-Chrimson-mVenus*. Samples were stained with anti-FLAG or anti-GFP (green) to reveal membranes of targeted neurons and mAb nc82 to reveal all synapses (magenta). Arrows indicate soma. Scale bar: 100 µm. **b**, Confocal images showing the expression of *ChAT*, *GAD1*, and *vGluT* in vpoEN and vpoIN neurons (labelled by Halo tag, arrows) in female brains, as revealed by FISH. Representative images are shown from at least 5 independent samples examined in each case.

Extended Data Fig. 6 Responses of vpoDN, vpoEN, and vpoIN towards natural and synthetic courtship songs.

a, **c**, **e**, Traces of natural and artificial songs used as auditory stimuli. **b**, **d**, **f**, Sound-evoked GCaMP6s responses in vpoDNs, vpoENs and vpoINs of virgin *melanogaster* females. Darker traces indicate mean response; grey shading indicates s.e.m. Grey bars indicate stimuli (5 s). '1' and '2' in **a** and **b** indicate different audio clips from the same species. Selected data for

Drosophila elegans are reproduced in Fig. 3. Sample sizes were as indicated, except for responses to *simulans* songs, for which n = 7, 6 and 6 for vpoDN, vpoEN, and vpoIN, respectively.

Extended Data Table 1 vpoDN inputs identified by EM reconstruction
Full size table
Extended Data Table 2 Synaptic connections identified by EM reconstruction
Full size table

Supplementary information

Supplementary Information

This file contains Supplementary Notes, Supplementary Figure 1, Supplementary Tables 1-5 and Supplementary References.

Reporting Summary

Supplementary Video 1

| Vaginal plate opening A virgin female fly performs VPO while being courted by a male, shown at half speed (15 fps) and replayed once. The full arena is shown on the left; a close-up of the female's abdomen on the right.

Supplementary Video 2

| Optogenetic activation of vpoDNs elicits vaginal plate opening A montage of video clips of 4 virgin *vpoDN-SS1 UAS-Chrimson* females upon 3 s of continuous 625 nm illumination at 200 μW/mm^2), shown at normal speed (30 fps).

Supplementary Video 3

| Comparison of vaginal plate opening and ovipositor extrusion Video clips of vaginal plate opening by *vpoDN-SS1 UAS-Chrimson* virgins (left) and

ovipositor extrusion[31] by *DNp13-SS1 UAS-Chrimson* virgins (right), induced by photoactivation with 5 s of continuous 635 nm illumination at 57 μW/mm^2). Shown at normal speed (30 fps) in lateral (top) and ventral (bottom) views.

Supplementary Video 4

| vpoDN reconstructed in female brain EM volume A single vpoDN cells (red) reconstructed in the right hemisphere of the FAFB EM volume.

Supplementary Video 5

| pC1a, vpoENs and vpoINs are presynaptic to vpoDN Single pC1a (orange), vpoEN (blue) and vpoIN (purple) cells partially reconstructed in the right hemisphere of the FAFB EM volume.

Rights and permissions

Reprints and Permissions

About this article

Check for updates

Cite this article

Wang, K., Wang, F., Forknall, N. *et al.* Neural circuit mechanisms of sexual receptivity in *Drosophila* females. *Nature* **589,** 577–581 (2021). https://doi.org/10.1038/s41586-020-2972-7

Download citation

- Received: 13 January 2020

- Accepted: 30 September 2020
- Published: 25 November 2020
- Issue Date: 28 January 2021
- DOI: https://doi.org/10.1038/s41586-020-2972-7

Further reading

- **The neural basis for a persistent internal state in Drosophila females**
  - David Deutsch
  - , Diego Pacheco
  - , Lucas Encarnacion-Rivera
  - , Talmo Pereira
  - , Ramie Fathy
  - , Jan Clemens
  - , Cyrille Girardin
  - , Adam Calhoun
  - , Elise Ireland
  - , Austin Burke
  - , Sven Dorkenwald
  - , Claire McKellar
  - , Thomas Macrina
  - , Ran Lu
  - , Kisuk Lee
  - , Nico Kemnitz
  - , Dodham Ih
  - , Manuel Castro
  - , Akhilesh Halageri
  - , Chris Jordan
  - , William Silversmith
  - , Jingpeng Wu
  - , H Sebastian Seung
  - & Mala Murthy

eLife (2020)

Comments

By submitting a comment you agree to abide by our Terms and Community Guidelines. If you find something abusive or that does not comply with our terms or guidelines please flag it as inappropriate.

Access through your institution
Change institution
Buy or subscribe

This article was downloaded by **calibre** from https://www.nature.com/articles/s41586-020-2972-7

| Section menu | Main menu |

- Article
- Published: 02 December 2020

Availability of food determines the need for sleep in memory consolidation

- Nitin S. Chouhan[1,2],
- Leslie C. Griffith[3],
- Paula Haynes[1,2 na1] &
- Amita Sehgal ORCID: orcid.org/0000-0001-7354-9641[1,2 na1]

Nature **volume 589**, pages582–585(2021)Cite this article

- 8367 Accesses
- 113 Altmetric
- Metrics details

Subjects

- Cognitive neuroscience
- Neural circuits

Abstract

Sleep remains a major mystery of biology, with little understood about its basic function. One of the most commonly proposed functions of sleep is the consolidation of memory[1,2,3]. However, as conditions such as starvation require the organism to be awake and active[4], the ability to switch to a

memory consolidation mechanism that is not contingent on sleep may confer an evolutionary advantage. Here we identify an adaptive circuit-based mechanism that enables *Drosophila* to form sleep-dependent and sleep-independent memory. Flies fed after appetitive conditioning needed increased sleep for memory consolidation, but flies starved after training did not require sleep to form memories. Memory in fed flies is mediated by the anterior–posterior α′/β′ neurons of the mushroom body, while memory under starvation is mediated by medial α′/β′ neurons. Sleep-dependent and sleep-independent memory rely on distinct dopaminergic neurons and corresponding mushroom body output neurons. However, sleep and memory are coupled such that mushroom body neurons required for sleep-dependent memory also promote sleep. Flies lacking Neuropeptide F display sleep-dependent memory even when starved, suggesting that circuit selection is determined by hunger. This plasticity in memory circuits enables flies to retain essential information in changing environments.

Access through your institution
Change institution
Buy or subscribe

Access options

Subscribe to Journal

Get full journal access for 1 year

$199.00

only $3.90 per issue

Subscribe

All prices are NET prices.
VAT will be added later in the checkout.

Rent or Buy article

Get time limited or full article access on ReadCube.

from$8.99

Rent or Buy

All prices are NET prices.

Additional access options:

- Log in
- Access through your institution
- Learn about institutional subscriptions

Fig. 1: Flies fed post-training require sleep for memory consolidation.

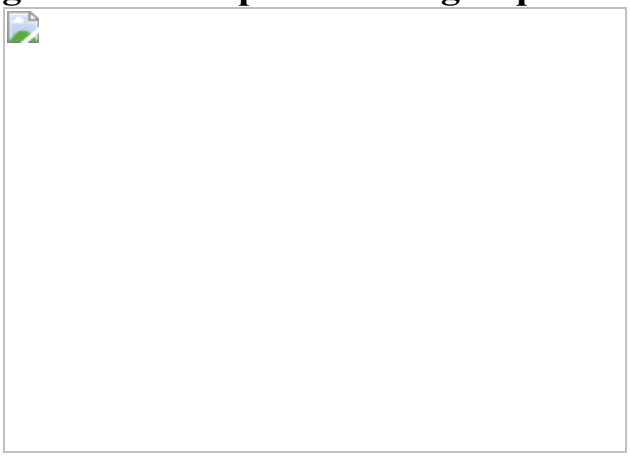

Fig. 2: Distinct α′/β′ subsets mediate sleep-dependent and sleep-independent memory.

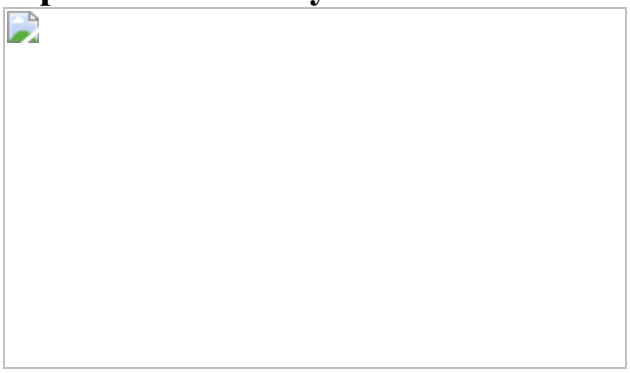

Fig. 3: Feeding drives recruitment of different DANs and MBONs for appetitive memory formation.

Data availability

Source data are provided with this paper.

References

1. 1.

   Le Glou, E., Seugnet, L., Shaw, P. J., Preat, T. & Goguel, V. Circadian modulation of consolidated memory retrieval following sleep deprivation in *Drosophila*. *Sleep* **35**, 1377–1384 (2012).

   Article Google Scholar

2. 2.

   Rasch, B. & Born, J. About sleep's role in memory. *Physiol. Rev*. **93**, 681–766 (2013).

   CAS Article Google Scholar

3. 3.

   Ganguly-Fitzgerald, I., Donlea, J. & Shaw, P. J. Waking experience affects sleep need in *Drosophila*. *Science* **313**, 1775–1781 (2006).

ADS CAS Article Google Scholar

4. 4.

Keene, A. C. et al. Clock and cycle limit starvation-induced sleep loss in *Drosophila*. *Curr. Biol*. **20**, 1209–1215 (2010).

CAS Article Google Scholar

5. 5.

Krashes, M. J. & Waddell, S. Rapid consolidation to a *radish* and protein synthesis-dependent long-term memory after single-session appetitive olfactory conditioning in *Drosophila*. *J. Neurosci*. **28**, 3103–3113 (2008).

CAS Article Google Scholar

6. 6.

Shi, M., Yue, Z., Kuryatov, A., Lindstrom, J. M. & Sehgal, A. Identification of Redeye, a new sleep-regulating protein whose expression is modulated by sleep amount. *eLife* **3**, e01473 (2014).

Article Google Scholar

7. 7.

Wigglesworth, V. B. The utilization of reserve substances in *Drosophila* during flight. *J. Exp. Biol*. **26**, 150–163 (1949).

CAS PubMed Google Scholar

8. 8.

Burke, C. J. & Waddell, S. Remembering nutrient quality of sugar in *Drosophila*. *Curr. Biol*. **21**, 746–750 (2011).

CAS Article Google Scholar

9. 9.

Wu, Q. et al. Developmental control of foraging and social behavior by the *Drosophila* neuropeptide Y-like system. *Neuron* **39**, 147–161 (2003).

CAS Article Google Scholar

10. 10.

Wu, Q., Zhao, Z. & Shen, P. Regulation of aversion to noxious food by *Drosophila* neuropeptide Y- and insulin-like systems. *Nat. Neurosci*. **8**, 1350–1355 (2005).

CAS Article Google Scholar

11. 11.

Krashes, M. J. et al. A neural circuit mechanism integrating motivational state with memory expression in *Drosophila*. *Cell* **139**, 416–427 (2009).

CAS Article Google Scholar

12. 12.

Lin, H.-H., Lai, J. S.-Y., Chin, A.-L., Chen, Y.-C. & Chiang, A.-S. A map of olfactory representation in the *Drosophila* mushroom body. *Cell* **128**, 1205–1217 (2007).

CAS Article Google Scholar

13. 13.

Strausfeld, N. J., Sinakevitch, I. & Vilinsky, I. The mushroom bodies of *Drosophila melanogaster*: an immunocytological and golgi study of Kenyon cell organization in the calyces and lobes. *Microsc. Res. Tech*. **62**, 151–169 (2003).

Article Google Scholar

14. 14.

Aso, Y. et al. The neuronal architecture of the mushroom body provides a logic for associative learning. *eLife* **3**, e04577 (2014).

Article Google Scholar

15. 15.

Yang, C.-H. et al. Additive expression of consolidated memory through *Drosophila* mushroom body subsets. *PLoS Genet*. **12**, e1006061 (2016).

Article Google Scholar

16. 16.

Haynes, P. *Functional and Anatomical Interactions of Sleep- and Memory Consolidation-Promoting Circuitry in Drosophila*. PhD thesis, Brandeis Univ. (2015).

17. 17.

Masuyama, K., Zhang, Y., Rao, Y. & Wang, J. W. Mapping neural circuits with activity-dependent nuclear import of a transcription factor. *J. Neurogenet*. **26**, 89–102 (2012).

CAS Article Google Scholar

18. 18.

Haynes, P. R., Christmann, B. L. & Griffith, L. C. A single pair of neurons links sleep to memory consolidation in *Drosophila melanogaster*. *eLife* **4**, e03868 (2015).

19. 19.

Sitaraman, D. et al. Propagation of homeostatic sleep signals by segregated synaptic microcircuits of the *Drosophila* mushroom body. *Curr. Biol*. **25**, 2915–2927 (2015).

CAS Article Google Scholar

20. 20.

Musso, P.-Y., Tchenio, P. & Preat, T. Delayed dopamine signaling of energy level builds appetitive long-term memory in *Drosophila*. *Cell Rep*. **10**, 1023–1031 (2015).

CAS Article Google Scholar

21. 21.

Aso, Y. & Rubin, G. M. Dopaminergic neurons write and update memories with cell-type-specific rules. *eLife* **5**, e16135 (2016).

Article Google Scholar

22. 22.

Aso, Y. et al. Mushroom body output neurons encode valence and guide memory-based action selection in *Drosophila*. *eLife* **3**, e04580 (2014).

Article Google Scholar

23. 23.

Berry, J. A., Phan, A. & Davis, R. L. Dopamine neurons mediate learning and forgetting through bidirectional modulation of a memory trace. *Cell Rep*. **25**, 651–662 (2018).

CAS Article Google Scholar

24. 24.

Felsenberg, J., Barnstedt, O., Cognigni, P., Lin, S. & Waddell, S. Re-evaluation of learned information in *Drosophila*. *Nature* **544**, 240–244 (2017).

ADS CAS Article Google Scholar

25. 25.

Pavlowsky, A., Schor, J., Plaçais, P.-Y. & Preat, T. A GABAergic feedback shapes dopaminergic input on the *Drosophila* mushroom body to promote appetitive long-term memory. *Curr. Biol*. **28**, 1783–1793 (2018).

CAS Article Google Scholar

26. 26.

Graves, L. A., Heller, E. A., Pack, A. I. & Abel, T. Sleep deprivation selectively impairs memory consolidation for contextual fear conditioning. *Learn. Mem*. **10**, 168–176 (2003).

Article Google Scholar

27. 27.

Weber, F. D., Wang, J.-Y., Born, J. & Inostroza, M. Sleep benefits in parallel implicit and explicit measures of episodic memory. *Learn. Mem*. **21**, 190–198 (2014).

Article Google Scholar

28. 28.

van der Helm, E., Gujar, N., Nishida, M. & Walker, M. P. Sleep-dependent facilitation of episodic memory details. *PLoS ONE* **6**, e27421 (2011).

ADS Article Google Scholar

29. 29.

Aly, M. & Moscovitch, M. The effects of sleep on episodic memory in older and younger adults. *Memory* **18**, 327–334 (2010).

Article Google Scholar

30. 30.

Colomb, J., Kaiser, L., Chabaud, M.-A. & Preat, T. Parametric and genetic analysis of *Drosophila* appetitive long-term memory and sugar motivation. *Genes Brain Behav*. **8**, 407–415 (2009).

CAS Article Google Scholar

31. 31.

Hendricks, J. C. et al. Rest in *Drosophila* is a sleep-like state. *Neuron* **25**, 129–138 (2000).

CAS Article Google Scholar

32. 32.

Shaw, P. J., Cirelli, C., Greenspan, R. J. & Tononi, G. Correlates of sleep and waking in *Drosophila melanogaster*. *Science* **287**, 1834–1837 (2000).

ADS CAS Article Google Scholar

33. 33.

Lenz, O., Xiong, J., Nelson, M. D., Raizen, D. M. & Williams, J. A. FMRFamide signaling promotes stress-induced sleep in *Drosophila*. *Brain Behav. Immun*. **47**, 141–148 (2015).

CAS Article Google Scholar

Download references

Acknowledgements

We thank the members of the Sehgal laboratory for helpful discussions, and K. Lin for input on statistics. We thank C. Stein and A. Kolesnik for their assistance in imaging experiments. This work was supported by R01 DK120757 (to A.S.) and by the HHMI. P.H. was supported by T32 MH014654. Initial studies were supported by R01 MH067284 (to L.C.G.).

Author information

Author notes

1. These authors jointly supervised this work: Paula Haynes, Amita Sehgal

Affiliations

1. Howard Hughes Medical Institute, Perelman School of Medicine at the University of Pennsylvania, Philadelphia, PA, USA

   Nitin S. Chouhan, Paula Haynes & Amita Sehgal

2. Chronobiology and Sleep Institute, Perelman School of Medicine at the University of Pennsylvania, Philadelphia, PA, USA

   Nitin S. Chouhan, Paula Haynes & Amita Sehgal

3. Department of Biology, Volen National Center for Complex Systems and National Center for Behavioral Genomics, Brandeis University, Waltham, MA, USA

   Leslie C. Griffith

Authors

1. Nitin S. Chouhan
   View author publications

You can also search for this author in PubMed Google Scholar

2. Leslie C. Griffith
   View author publications

   You can also search for this author in PubMed Google Scholar

3. Paula Haynes
   View author publications

   You can also search for this author in PubMed Google Scholar

4. Amita Sehgal
   View author publications

   You can also search for this author in PubMed Google Scholar

Contributions

N.S.C., P.H., L.C.G. and A.S. conceived the project. N.S.C. and A.S. designed all experiments. P.H. conducted pilot sleep-deprivation experiments and identified the sleep-promoting role of α′/β′ap neurons, N.S.C. conducted and analysed all behavioural experiments. N.S.C. and P.H. conducted and analysed imaging experiments. The manuscript was written by N.S.C. and A.S.

Corresponding author

Correspondence to Amita Sehgal.

Ethics declarations

Competing interests

The authors declare no competing interests.

Additional information

Peer review information *Nature* thanks Ravi Allada and the other, anonymous, reviewer(s) for their contribution to the peer review of this work.

Publisher's note Springer Nature remains neutral with regard to jurisdictional claims in published maps and institutional affiliations.

Extended data figures and tables

Extended Data Fig. 1 Sleep increases in flies fed after appetitive training.

(**a**) Flies starved for 6 h before training show no difference in sleep between trained and untrained groups. However, moving trained flies into sucrose tubes post-training resulted in a significant increase in sleep compared to untrained controls despite only 6 h of pre-training starvation. Sleep was quantified for the ZT8-12 interval (two-sided *t*-tests were performed for each condition to compare trained and untrained groups, followed by Bonferroni correction; $n = 32$). (**b**) and (**c**) Training increases sleep bout length in fed flies but not in starved flies. Flies were trained after 18 h (**b**) and 6 h (**c**) starvation (two-sided Mann–Whitney *U*-tests were performed for each condition to compare trained and untrained groups; $n = 32$). Data are represented as mean ± s.e.m. Each data point depicts a single fly. Precise 'n' and 'p' values are in the Source Data. ***$P < 0.001$; **$P < 0.01$; *$P < 0.05$. Source data

Extended Data Fig. 2 Memory in flies fed after training is sleep and protein synthesis-dependent but independent of light cycles.

(**a**) Long-term memory in fed flies is sensitive to cycloheximide based inhibition of protein-synthesis (two-sided *t*-test; $n \geq 6$). (**b**) Flies demonstrate substantial rebound sleep when sleep-deprived in a group of

about 100 flies in a vial in both fed and starved conditions. Flies were sleep-deprived from ZT12-ZT24 and then introduced individually into locomotor tubes (two-sided Mann–Whitney *U*-tests were performed for each condition to compare undisturbed and sleep-deprived groups; $n = 32$). (**c**) Starved flies were effectively sleep-deprived when exposed to a mechanical stimulus post-training ($n \geq 31$). Flies were starved for 6 h and then trained at ZT6 and subsequently introduced into agar locomotor tubes. A mechanical stimulus was applied for 6 h after training. A rebound is evident after sleep deprivation. (**d**) Flies starved for only 6 h, as opposed to 18 h, before training and then allowed to feed showed impaired memory performance when sleep-deprived for 6 h post-training (two-sided *t*-test; $n = 8$). Sleep post-training was comparable to flies depicted in Extended Data Fig. 1a. (**e**) 6 h sleep deprivation had no effect on long-term memory in flies kept starved after training. Here, flies were starved for 6 h before training (two-sided *t*-test; $n \geq 6$). Sleep post-training was comparable to flies depicted in Extended Data Fig. 1a. (**f**) Sleep deprivation initiated 6 h after training had no effect on memory in fed and trained flies (two-sided *t*-test; $n = 8$). (**g**) Long-term memory was resistant to sleep deprivation in flies that were starved after conditioning but then tested after a feeding and re-starvation period (two-sided *t*-test; $n \geq 6$). Flies were starved (and sleep-deprived) for 6 h post-training and then allowed to feed for 18 h before 30 h restarvation for memory tests. (**h**) and (**i**) 6 h sleep deprivation of flies maintained in constant light affected appetitive long-term memory when they were fed, but not starved, post-training (two-sided *t*-test; $n \geq 6$). Data are represented as mean ± s.e.m. Each data point in a memory experiment represents a group of flies and in a sleep experiment it depicts a single fly. Precise 'n' and 'p' values are in the Source Data. ***$P < 0.001$; **$P < 0.01$; *$P < 0.05$. Source data

Extended Data Fig. 3 The *rye* mutation affects sleep-dependent memory.

(**a**) Long-term memory is substantially lower in satiated short-sleeping *rye* mutants. Background *iso*[31] line was used as control (two-sided *t*-test; $n \geq 8$). (**b**) *rye* mutants form robust appetitive 24 h memory, similar to controls when kept starved (two-sided *t*-test; $n \geq 6$). (**c**) Satiated *rye* mutants demonstrate no difference in sleep between trained and untrained groups.

Total sleep in the ZT8-12 interval is depicted (two-sided *t*-tests were performed for each genotype to compare trained and untrained groups, followed by Bonferroni correction; $n \geq 31$). Data are represented as mean ± s.e.m. Each data point in a memory experiment represents a group of flies and in a sleep experiment it depicts a single fly. Precise 'n' and 'p' values are in the Source Data. $^{**}P < 0.01$; $^{*}P < 0.05$. Source data

Extended Data Fig. 4 Flies on arabinose demonstrate a significant increase in post-training sleep.

(**a**) Trained flies show a substantial increase in sleep relative to untrained flies when kept on arabinose after appetitive conditioning. Sleep was quantified for the 0–4 h interval post-training (two-sided *t*-test; $n \geq 31$). (**b**) Bout length was considerably higher in trained flies compared to untrained flies when moved to arabinose after training (two-sided Mann–Whitney *U*-test; $n \geq 31$). Data are represented as mean ± s.e.m. Each data point depicts a single fly. Precise 'n' and 'p' values are in the Source Data. $^{***}P < 0.001$; $^{**}P < 0.01$. Source data

Extended Data Fig. 5 *npf* signalling is essential for sleep-independent memory in starved flies.

(**a**) Starved *npfr* mutant flies show a substantial increase in sleep post-training compared to untrained flies. *npfr/+* was used as control. Total sleep in the 0–4 h interval post-training is depicted (two-sided *t*-tests were performed for each genotype to compare trained and untrained groups, followed by Bonferroni correction; $n \geq 32$). (**b**) Bout length was considerably higher in trained and starved *npfr* mutant flies compared to untrained flies. *npfr/+* was used as control (two-sided Mann–Whitney U-tests were performed for each genotype to compare trained and untrained groups; $n \geq 32$). (**c**) RNAi knockdown of *npfr* pan-neuronally results in sleep-dependent memory formation in hungry flies. 6 h sleep disruption post-training resulted in impaired memory performance in UAS-*npfr*-RNAi/n-syb-Gal4 flies (two-sided *t*-tests were performed for each genotype to compare undisturbed and sleep-deprived groups, followed by Bonferroni correction; $n \geq 6$). (**d**) Starved UAS-*npf*-RNAi/NPF-Gal4 flies show lower

long-term memory when sleep-deprived for 6 h post-training (two-sided *t*-tests were performed for each genotype to compare undisturbed and sleep-deprived groups, followed by Bonferroni correction; $n \geq 6$). Data are represented as mean ± s.e.m. Each data point in a memory experiment represents a group of flies and in a sleep experiment it depicts a single fly. Precise 'n' and 'p' values are in the Source Data. ***$P < 0.001$; *$P < 0.05$. Source data

Extended Data Fig. 6 α'/β' neurotransmission is essential for long-term memory under both fed and starved conditions.

(**a**) Starved UAS-*shibire*^{ts1}/MB461B flies kept at restrictive settings for 4 h immediately after training show impaired long-term memory ($n \geq 6$). Restrictive temperature 8-12 h after training had no effect (**b**) ($n = 6$) (one-factor ANOVA with Tukey post hoc test). (**c**) Long-term memory remained unchanged in experimental and control flies when kept at 25°C (one-factor ANOVA with Tukey post hoc test; $n = 6$). (**d**) and (**e**) Silencing α'/β' neurons immediately after conditioning, but not at hours 8-12, affects long-term memory in fed flies (one-factor ANOVA with Tukey post hoc test; $n \geq 6$). (**f**) Long-term memory remained intact in UAS-*shibire*^{ts1}/MB461B flies fed after training but maintained at the permissive temperature (one-factor ANOVA with Tukey post hoc test; $n \geq 6$). Data are represented as mean ± s.e.m. Each data point represents a group of flies. Precise 'n' and 'p' values are in the Source Data. **$P < 0.01$. Asterisks in (**a**, **d**) indicate a significant difference between experimental flies and genetic controls. Source data

Extended Data Fig. 7 Effects of manipulating the activity of α'/β' subset specific neurons on long-term memory.

(**a**) and (**b**) Neurotransmission from α'/β'm neurons (UAS-*shibire*^{ts1}/R26E01 and UAS-*shibire*^{ts1}/MB370B) is dispensable for long-term memory in fed flies ($n \geq 6$). Temperature controls are depicted in (**b**) ($n \geq 6$) (one-factor ANOVA with Tukey post hoc test). (**c**) and (**d**) Blocking the activity of α'/β'ap neurons (UAS-*shibire*^{ts1}/R35B12 and UAS-*shibire*^{ts1}/VT50658) for 4 h after conditioning in starved flies has no effect

on long-term memory (n = 6). Long-term memory in experimental and control flies at the permissive temperature, 25°C, is shown in (**d**) (n = 6) (one-factor ANOVA with Tukey post hoc test). (**e**) *shibire*^{ts} does not affect memory in flies maintained under starvation conditions at the permissive temperature (one-factor ANOVA with Tukey post hoc test; n = 6). Controls related to Fig. 2(a). (**f**) *shibire*^{ts} has no effect on memory in flies maintained on food at the permissive temperature (one-factor ANOVA with Tukey post hoc test; $n \geq 6$). Controls related to Fig. 2(b). (**g**) Hyperactivation of α'/β'ap neurons (UAS-*TrpA1*/R35B12) for 4 h post-training does not affect long-term memory formation in starved flies (one-factor ANOVA with Tukey post hoc test; n = 6). (**h**) Memory was not affected in UAS-*TrpA1*/R35B12 flies at permissive settings (one-factor ANOVA with Tukey post hoc test; n = 6). Data are represented as mean ± s.e.m. Each data point in a memory experiment represents a group of flies. Precise 'n' and 'p' values are in the Source Data. Source data

Extended Data Fig. 8 α'/β' subsets differentially regulate sleep.

(**a**) Thermogenetic activation of α'/β'ap neurons (UAS-*TrpA1*/VT50658) results in a considerable enhancement in sleep while flies in which α'/β'm neurons (UAS-*TrpA1*/MB370B) were activated showed a significant decrease in sleep (one-factor ANOVA with Tukey post hoc test; $n \geq 30$). (**b**) and (**c**) Disabling neurotransmission in α'/β'ap neurons (UAS-*shibire*^{ts1}/R35B12 and UAS-*shibire*^{ts1}/VT50658) or α'/β'm neurons (UAS-*shibire*^{ts1}/R26E01 and UAS-*shibire*^{ts1}/MB370B) had no effect on sleep (one-factor ANOVA with Tukey post hoc test; $n \geq 31$). Data are represented as mean ± s.e.m. Each data point depicts a single fly. Precise 'n' and 'p' values are in the Source Data. Asterisks in (**a**) indicate a significant difference between experimental flies and genetic controls. Source data

Extended Data Fig. 9 The activity of α'/β'ap, but not α'/β'm, neurons is relevant for sleep after conditioning.

(**a**) *shibire*^{ts} expression in α'/β'ap neurons has no effect on sleep post-training if flies are maintained at the permissive temperature (two-sided t-tests were performed for each genotype to compare trained and untrained

groups, followed by Bonferroni correction; $n \geq 30$). Controls related to Fig. 2(g). (**b**) and (**c**) A training-dependent increase in sleep bout length was prevented in flies in which α'/β'ap neurons were silenced ($n \geq 31$). Temperature controls are shown in (**c**) ($n \geq 30$) (two-sided Mann–Whitney *U*-tests were performed for each genotype to compare trained and untrained groups). (**d**) and (**e**) Trained flies expressing *shibire*^{ts1} in α'/β'm neurons showed an enhancement in sleep even when moved to 32°C for 4 h post-training. The total amount of sleep in 0–4 h interval after training is quantified ($n \geq 32$). Post-training sleep in experimental and control flies at the permissive temperature, 25°C, is shown in (**e**) ($n \geq 16$) (two-sided *t*-tests were performed for each genotype to compare trained and untrained groups, followed by Bonferroni correction). (**f**) and (**g**) Silencing α'/β'm neurons does not prevent an increase in sleep bout length after training ($n \geq 32$). Temperature controls are shown in (**g**) ($n \geq 16$) (two-sided Mann–Whitney *U*-tests were performed for each genotype to compare trained and untrained groups). (**h**) Calcium/GFP signal in α'/β'm neurons was comparable between control and sleep-deprived flies when kept starved post-training (two-sided Mann–Whitney *U*-test; $n \geq 11$). Representative images are shown, two independent experiments; Scale bar, 50 μm. Data are represented as mean ± s.e.m. Each data point depicts a single fly. Precise 'n' and 'p' values are in the Source Data. ***$P < 0.001$; **$P < 0.01$; *$P < 0.05$. Source data

Extended Data Fig. 10 Effects of manipulating the neurotransmission of PPL1 neurons and MBONs on long-term memory.

(**a**) and (**b**) Trained starved flies show lower long-term memory performance when the PPL1 cluster neurons (UAS-*shibire*^{ts1}/MB504B) are silenced for 4 h post-training ($n \geq 8$). Temperature controls are shown in (**b**) ($n \geq 7$) (one-factor ANOVA with Tukey post hoc test). (**c**) and (**d**) Silencing PPL1 DANs affects long-term memory performance in flies kept fed after training ($n \geq 7$). Temperature controls are shown in (**d**) ($n \geq 6$) (one-factor ANOVA with Tukey post hoc test). (**e**) Expression of *shibire*^{ts1} in MP1 and MV1 neurons at permissive temperature does not affect memory in flies starved after training (one-factor ANOVA with Tukey post hoc test; $n \geq 6$).

Controls related to Fig. 3a. (**f**) Permissive temperature control for Fig. 3b. Expression of *shibire*^{ts1} in MP1 and MV1 neurons does not affect memory in flies kept on food at 25°C after training (one-factor ANOVA with Tukey post hoc test; $n \geq 6$). (**g**) Blocking the activity of MP1 neurons (UAS-*shibire*^{ts1}/MB320C at restrictive temperature) for 6 h after conditioning has no effect on long-term memory in flies kept on food vials after training (one-factor ANOVA with Tukey post hoc test; $n = 6$). (**h**) and (**i**) Long-term memory in UAS-*shibire*^{ts1}/MB077B and UAS-*shibire*^{ts1}/MB112C flies was similar to that of genetic controls when kept starved or fed at 25°C (one-factor ANOVA with Tukey post hoc test; $n \geq 6$). Temperature controls related to Fig. 3c, d. Data are represented as mean ± s.e.m. Each data point represents a group of flies. Precise 'n' and 'p' values are in the Source Data. Asterisks in (**a**, **c**) indicate a significant difference between experimental flies and genetic controls. Source data

Supplementary information

Reporting Summary

Source data

Source Data Fig. 1

Source Data Fig. 2

Source Data Fig. 3

Source Data Extended Data Fig. 1

Source Data Extended Data Fig. 2

Source Data Extended Data Fig. 3

Source Data Extended Data Fig. 4

Source Data Extended Data Fig. 5

Source Data Extended Data Fig. 6

Source Data Extended Data Fig. 7

Source Data Extended Data Fig. 8

Source Data Extended Data Fig. 9

Source Data Extended Data Fig. 10

Rights and permissions

Reprints and Permissions

About this article

Check for updates

Cite this article

Chouhan, N.S., Griffith, L.C., Haynes, P. *et al.* Availability of food determines the need for sleep in memory consolidation. *Nature* **589,** 582–585 (2021). https://doi.org/10.1038/s41586-020-2997-y

Download citation

- Received: 09 December 2019
- Accepted: 09 October 2020
- Published: 02 December 2020

- Issue Date: 28 January 2021
- DOI: https://doi.org/10.1038/s41586-020-2997-y

Comments

By submitting a comment you agree to abide by our Terms and Community Guidelines. If you find something abusive or that does not comply with our terms or guidelines please flag it as inappropriate.

Access through your institution
Change institution
Buy or subscribe

This article was downloaded by **calibre** from https://www.nature.com/articles/s41586-020-2997-y

| Section menu | Main menu |

- Article
- Published: 09 December 2020

An SHR–SCR module specifies legume cortical cell fate to enable nodulation

- Wentao Dong ORCID: orcid.org/0000-0003-1389-2258[1,2],
- Yayun Zhu ORCID: orcid.org/0000-0002-4041-2726[1,3],
- Huizhong Chang ORCID: orcid.org/0000-0002-9925-1138[1,3],
- Chunhua Wang[4],
- Jun Yang ORCID: orcid.org/0000-0002-9834-1326[1],
- Jincai Shi ORCID: orcid.org/0000-0002-3186-4827[1,2],
- Jinpeng Gao ORCID: orcid.org/0000-0002-3221-3911[1,5],
- Weibing Yang[1],
- Liying Lan[1,2],
- Yuru Wang[1,2],
- Xiaowei Zhang[1],
- Huiling Dai ORCID: orcid.org/0000-0003-3140-6639[1],
- Yuchen Miao[5],
- Lin Xu ORCID: orcid.org/0000-0003-4718-1286[1],
- Zuhua He ORCID: orcid.org/0000-0002-6098-7893[1],
- Chunpeng Song ORCID: orcid.org/0000-0001-8774-4309[5],
- Shuang Wu[4],
- Dong Wang[6],
- Nan Yu[3] &
- Ertao Wang ORCID: orcid.org/0000-0002-5178-3530[1]

Nature **volume 589**, pages586–590(2021)Cite this article

- 7141 Accesses
- 2 Citations
- 74 Altmetric
- Metrics details

Subjects

- Evolutionary developmental biology
- Plant development
- Plant symbiosis

This article has been updated

Abstract

Legumes, unlike other plants, have the ability to establish symbiosis with nitrogen-fixing rhizobia. It has been theorized that a unique property of legume root cortical cells enabled the initial establishment of rhizobial symbiosis[1,2,3]. Here we show that a SHORTROOT–SCARECROW (SHR–SCR) stem cell program in cortical cells of the legume *Medicago truncatula* specifies their distinct fate. Regulatory elements drive the cortical expression of *SCR*, and stele-expressed SHR protein accumulates in cortical cells of *M. truncatula* but not *Arabidopsis thaliana*. The cortical SHR–SCR network is conserved across legume species, responds to rhizobial signals, and initiates legume-specific cortical cell division for de novo nodule organogenesis and accommodation of rhizobia. Ectopic activation of SHR and SCR in legumes is sufficient to induce root cortical cell division. Our work suggests that acquisition of the cortical SHR–SCR module enabled cell division coupled to rhizobial infection in legumes. We propose that this event was central to the evolution of rhizobial endosymbiosis.

Access through your institution

Change institution
Buy or subscribe

Access options

Subscribe to Journal

Get full journal access for 1 year

$199.00

only $3.90 per issue

Subscribe

All prices are NET prices.
VAT will be added later in the checkout.

Rent or Buy article

Get time limited or full article access on ReadCube.

from$8.99

Rent or Buy

All prices are NET prices.

Additional access options:

- Log in
- Access through your institution
- Learn about institutional subscriptions

Fig. 1: Two regulatory elements in the *MtSCR* promoter govern its expression in legume cortical cells and are required for nodule symbiosis.

Fig. 2: MtSHR1/2 are present in cortical cells and required for nodule symbiosis.

Fig. 3: MtSHR1/2 and MtSCR are required in cortical cells for nodule organogenesis and for normal developmental responses to cytokinins.

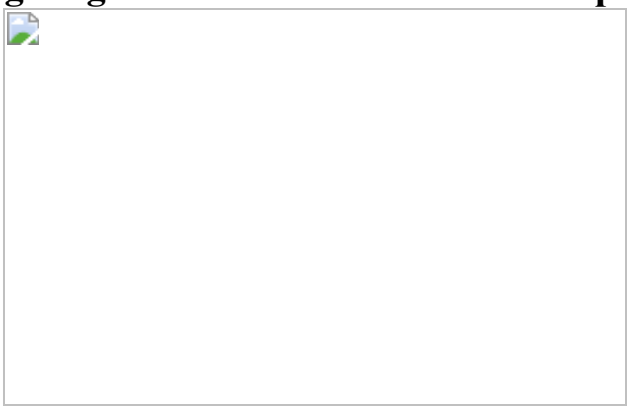

Fig. 4: Rhizobia symbiosis signal activates MtSHR–MtSCR program and overexpression of *MtSHR1* ubiquitously in *M. truncatula* hairy roots induces cortical cell division that resembles nodules.

Data availability

All data generated or analysed during this study are included in this article and its Supplementary Information. Sequencing data for gene-expression analysis (RNA-seq) reported in this study have been deposited in the publicly available NCBI BioProject database under accession PRJNA599246, Sequence Read Archive accession numbers SAMN13741852–SAMN13741857. RNA-seq data for the 24 h and 120 h post *S. meliloti* spot inoculation were obtained from Schiessl et al.[30] (Data S1). The *M. truncatula Tnt1* transposon insertion lines used in this study were obtained from the Noble Foundation *Tnt1* database (http://medicago-mutant.noble.org/mutant/database.php). The blot source data are provided in the Supplementary Information. Source data are provided with this paper.

Change history

- **11 January 2021**

  This Article was amended to correct the Peer review information, which was originally incorrect.

References

1. 1.

   Geurts, R., Xiao, T. T. & Reinhold-Hurek, B. What does it take to evolve a nitrogen-fixing endosymbiosis? *Trends Plant Sci*. **21**, 199–208 (2016).

   CAS PubMed Google Scholar

2. 2.

   Foucher, F. & Kondorosi, E. Cell cycle regulation in the course of nodule organogenesis. *Plant Mol. Biol*. **43**, 229–242 (2000).

   Google Scholar

3. 3.

Gualtieri, G. & Biselling, T. The evolution of nodulation. *Plant Mol. Biol*. **42**, 181–194 (2000).

CAS PubMed Google Scholar

4. 4.

Beijerinck, M. W. Rhizobial systematic. *Botany Zeitung* **46**, 796–804 (1888).

Google Scholar

5. 5.

Hellriegel, H. & Wilfarth, H. *Untersuchungen Über die Stickstoffnahrung der Gramineen und Leguminosen* (Buchdruckerei der 'Post' Kayssler) (1888).

6. 6.

Huisman, R. & Geurts, R. A roadmap toward engineered nitrogen-fixing nodule symbiosis. *Plant Commun* **1**, 100019 (2020).

PubMed Google Scholar

7. 7.

Oldroyd, G. E. D. & Downie, J. A. Coordinating nodule morphogenesis with rhizobial infection in legumes. *Annu. Rev. Plant Biol*. **59**, 519–546 (2008).

CAS PubMed Google Scholar

8. 8.

Timmers, A. C. J., Auriac, M. C. & Truchet, G. Refined analysis of early symbiotic steps of the *Rhizobium-Medicago* interaction in relationship with microtubular cytoskeleton rearrangements. *Development* **126**, 3617–3628 (1999).

CAS PubMed Google Scholar

9. 9.

Xiao, T. T. et al. Fate map of *Medicago truncatula* root nodules. *Development* **141**, 3517–3528 (2014).

CAS PubMed Google Scholar

10. 10.

Truchet, G. et al. Sulphated lipo-oligosaccharide signals of *Rhizobium meliloti* elicit root nodule organogenesis in alfalfa. *Nature* **351**, 670–673 (1991).

ADS CAS Google Scholar

11. 11.

Gauthier-Coles, C., White, R. G. & Mathesius, U. Nodulating legumes are distinguished by a sensitivity to cytokinin in the root cortex leading to pseudonodule development. *Front. Plant Sci* **9**, 1901 (2019).

PubMed PubMed Central Google Scholar

12. 12.

Hirsch, A. M., Larue, T. A. & Doyle, J. Is the legume nodule a modified root or stem or an organ *sui generis? Crit. Rev. Plant Sci*. **16**, 361–392 (1997).

Google Scholar

13. 13.

Cooper, J. B. & Long, S. R. Morphogenetic rescue of *Rhizobium meliloti* nodulation mutants by *trans*-Zeatin secretion. *Plant Cell* **6**, 215–225 (1994).

CAS PubMed PubMed Central Google Scholar

14. 14.

Di Laurenzio, L. et al. The *SCARECROW* gene regulates an asymmetric cell division that is essential for generating the radial organization of the *Arabidopsis* root. *Cell* **86**, 423–433 (1996).

PubMed Google Scholar

15. 15.

Datta, N. & Cashmore, A. R. Binding of a pea nuclear protein to promoters of certain photoregulated genes is modulated by phosphorylation. *Plant Cell* **1**, 1069–1077 (1989).

CAS PubMed PubMed Central Google Scholar

16. 16.

Gilmartin, P. M., Sarokin, L., Memelink, J. & Chua, N. H. Molecular light switches for plant genes. *Plant Cell* **2**, 369–378 (1990).

CAS PubMed PubMed Central Google Scholar

17. 17.

Kucho, K., Yoshioka, S., Taniguchi, F., Ohyama, K. & Fukuzawa, H. *Cis*-acting elements and DNA-binding proteins involved in CO_2-responsive transcriptional activation of *Cah1* encoding a periplasmic carbonic anhydrase in *Chlamydomonas reinhardtii*. *Plant Physiol*. **133**, 783–793 (2003).

CAS PubMed PubMed Central Google Scholar

18. 18.

Wysocka-Diller, J. W., Helariutta, Y., Fukaki, H., Malamy, J. E. & Benfey, P. N. Molecular analysis of SCARECROW function reveals a

radial patterning mechanism common to root and shoot. *Development* **127**, 595–603 (2000).

CAS PubMed Google Scholar

19. 19.

Hiratsu, K., Matsui, K., Koyama, T. & Ohme-Takagi, M. Dominant repression of target genes by chimeric repressors that include the EAR motif, a repression domain, in *Arabidopsis*. *Plant J*. **34**, 733–739 (2003).

CAS PubMed Google Scholar

20. 20.

Vernié, T. et al. The *NIN* transcription factor coordinates diverse nodulation programs in different tissues of the *Medicago truncatula* root. *Plant Cell* **27**, 3410–3424 (2015).

PubMed PubMed Central Google Scholar

21. 21.

Long, Y. et al. SCARECROW-LIKE23 and SCARECROW jointly specify endodermal cell fate but distinctly control SHORT-ROOT movement. *Plant J*. **84**, 773–784 (2015).

CAS PubMed Google Scholar

22. 22.

Cui, H. et al. An evolutionarily conserved mechanism delimiting SHR movement defines a single layer of endodermis in plants. *Science* **316**, 421–425 (2007).

ADS CAS PubMed Google Scholar

23. 23.

Helariutta, Y. et al. The *SHORT-ROOT* gene controls radial patterning of the *Arabidopsis* root through radial signaling. *Cell* **101**, 555–567 (2000).

CAS PubMed Google Scholar

24. 24.

Gallagher, K. L., Paquette, A. J., Nakajima, K. & Benfey, P. N. Mechanisms regulating SHORT-ROOT intercellular movement. *Curr. Biol*. **14**, 1847–1851 (2004).

CAS PubMed Google Scholar

25. 25.

Mathesius, U., Charon, C., Rolfe, B. G., Kondorosi, A. & Crespi, M. Temporal and spatial order of events during the induction of cortical cell divisions in white clover by *Rhizobium leguminosarum* bv. *trifolii* inoculation or localized cytokinin addition. *Mol. Plant Microbe Interact*. **13**, 617–628 (2000).

CAS PubMed Google Scholar

26. 26.

Tirichine, L. et al. A gain-of-function mutation in a cytokinin receptor triggers spontaneous root nodule organogenesis. *Science* **315**, 104–107 (2007).

ADS CAS PubMed Google Scholar

27. 27.

Murray, J. D. et al. A cytokinin perception mutant colonized by *Rhizobium* in the absence of nodule organogenesis. *Science* **315**, 101–104 (2007).

ADS CAS PubMed Google Scholar

28. 28.

Yu, Q. et al. Cell-fate specification in *Arabidopsis* roots requires coordinative action of lineage instruction and positional reprogramming. *Plant Physiol*. **175**, 816–827 (2017).

CAS PubMed PubMed Central Google Scholar

29. 29.

Henry, S. et al. *SHR* overexpression induces the formation of supernumerary cell layers with cortex cell identity in rice. *Dev. Biol*. **425**, 1–7 (2017).

CAS PubMed Google Scholar

30. 30.

Schiessl, K. et al. NODULE INCEPTION recruits the lateral root developmental program for symbiotic nodule organogenesis in *Medicago truncatula*. *Curr. Biol*. **29**, 3657–3668 (2019).

CAS PubMed PubMed Central Google Scholar

31. 31.

Soyano, T., Shimoda, Y., Kawaguchi, M. & Hayashi, M. A shared gene drives lateral root development and root nodule symbiosis pathways in *Lotus*. *Science* **366**, 1021–1023 (2019).

ADS CAS PubMed Google Scholar

32. 32.

Soltis, D. E. et al. Chloroplast gene sequence data suggest a single origin of the predisposition for symbiotic nitrogen fixation in angiosperms. *Proc. Natl Acad. Sci. USA* **92**, 2647–2651 (1995).

ADS CAS PubMed Google Scholar

33. 33.

Griesmann, M. et al. Phylogenomics reveals multiple losses of nitrogen-fixing root nodule symbiosis. *Science* **361**, eaat1743 (2018).

PubMed Google Scholar

34. 34.

Gou, J. Y., Felippes, F. F., Liu, C. J., Weigel, D. & Wang, J. W. Negative regulation of anthocyanin biosynthesis in *Arabidopsis* by a miR156-targeted SPL transcription factor. *Plant Cell* **23**, 1512–1522 (2011).

CAS PubMed PubMed Central Google Scholar

35. 35.

Zhu, Q. et al. Development of "purple endosperm rice" by engineering anthocyanin biosynthesis in the endosperm with a high-efficiency transgene stacking system. *Mol. Plant* **10**, 918–929 (2017).

CAS PubMed Google Scholar

36. 36.

Boisson-Dernier, A. et al. *Agrobacterium rhizogenes*-transformed roots of *Medicago truncatula* for the study of nitrogen-fixing and endomycorrhizal symbiotic associations. *Mol. Plant Microbe Interact*. **14**, 695–700 (2001).

CAS PubMed Google Scholar

37. 37.

Clough, S. J. & Bent, A. F. Floral dip: a simplified method for *Agrobacterium*-mediated transformation of *Arabidopsis thaliana*. *Plant J*. **16**, 735–743 (1998).

CAS PubMed Google Scholar

38. 38.

Cosson, V., Durand, P., d'Erfurth, I., Kondorosi, A. & Ratet, P. in *Agrobacterium Protocols* (ed. Wang, K.) (Humana, 2006).

39. 39.

Lauressergues, D. et al. The microRNA miR171h modulates arbuscular mycorrhizal colonization of *Medicago truncatula* by targeting *NSP2*. *Plant J*. **72**, 512–522 (2012).

CAS PubMed Google Scholar

40. 40.

Patel, R. K. & Jain, M. NGS QC Toolkit: a toolkit for quality control of next generation sequencing data. *PLoS One* **7**, e30619 (2012).

ADS CAS PubMed PubMed Central Google Scholar

41. 41.

Kim, D., Langmead, B. & Salzberg, S. L. HISAT: a fast spliced aligner with low memory requirements. *Nat. Methods* **12**, 357–360 (2015).

CAS PubMed PubMed Central Google Scholar

42. 42.

Trapnell, C. et al. Differential gene and transcript expression analysis of RNA-seq experiments with TopHat and Cufflinks. *Nat. Protocols* **7**, 562–578 (2012).

CAS PubMed Google Scholar

43. 43.

Anders, S., Pyl, P. T. & Huber, W. HTSeq—a Python framework to work with high-throughput sequencing data. *Bioinformatics* **31**, 166–169 (2015).

CAS PubMed Google Scholar

44. 44.

Anders, S. & Huber, W. *Differential Expression of RNA-Seq Data at the Gene Level—the DESeq Package* (EMBL, 2013).

45. 45.

Kurihara, D., Mizuta, Y., Sato, Y. & Higashiyama, T. ClearSee: a rapid optical clearing reagent for whole-plant fluorescence imaging. *Development* **142**, 4168–4179 (2015).

CAS PubMed PubMed Central Google Scholar

46. 46.

Coen, E. S. et al. *floricaula*: a homeotic gene required for flower development in *Antirrhinum majus*. *Cell* **63**, 1311–1322 (1990).

CAS PubMed Google Scholar

47. 47.

Paciorek, T., Sauer, M., Balla, J., Wiśniewska, J. & Friml, J. Immunocytochemical technique for protein localization in sections of plant tissues. *Nat. Protocols* **1**, 104–107 (2006).

CAS PubMed Google Scholar

48. 48.

Gietz, R. D. & Woods, R. A. Transformation of yeast by lithium acetate/single-stranded carrier DNA/polyethylene glycol method. *Methods Enzymol*. **350**, 87–96 (2002).

CAS PubMed Google Scholar

49. 49.

Chen, H. et al. Firefly luciferase complementation imaging assay for protein-protein interactions in plants. *Plant Physiol*. **146**, 368–376 (2008).

ADS CAS PubMed PubMed Central Google Scholar

50. 50.

Nozaki, M. et al. A missense mutation in the glucosamine-6-phosphate *N*-acetyltransferase-encoding gene causes temperature-dependent growth defects and ectopic lignin deposition in *Arabidopsis*. *Plant Cell* **24**, 3366–3379 (2012).

ADS CAS PubMed PubMed Central Google Scholar

51. 51.

Kumar, S., Stecher, G. & Tamura, K. MEGA7: molecular evolutionary genetics analysis version 7.0 for bigger datasets. *Mol. Biol. Evol*. **33**, 1870–1874 (2016).

CAS Google Scholar

Download references

Acknowledgements

We thank G. Oldroyd, J. Xu, X. Chen, and P. Benfey for suggestions on the manuscript; G. Oldroyd for *lbd16-1* seeds; W. Cai for confocal imaging; and Life Science Editors for editing assistance. The research was supported by the Strategic Priority Research Program ‘Molecular Mechanism of Plant Growth and Development’ of the Chinese Academy of Sciences (XDB27040207), the National Science Foundation (31825003, 31730103, 32088102 to E. W., and 31500198), the National Key R&D Program of

China (2019YFA0904703, 2016YFA0500502), the Ministry of Agriculture of China for Transgenic Research (2016ZX08009-003-001, 2016ZX08009003005-003), the Youth Innovation Promotion Association CAS (2016255) and 153D31KYSB20160074 (The Samuel Roberts Noble Foundation). The *M. truncatula Tnt1* insertion mutant lines were obtained from The Samuel Roberts Noble Foundation and were created through research funded, in part, by a grant from the National Science Foundation, NSF-0703285.

Author information

Affiliations

1. National Key Laboratory of Plant Molecular Genetics, CAS Center for Excellence in Molecular Plant Sciences, Institute of Plant Physiology and Ecology, SIBS, Chinese Academy of Sciences, Shanghai, China

   Wentao Dong, Yayun Zhu, Huizhong Chang, Jun Yang, Jincai Shi, Jinpeng Gao, Weibing Yang, Liying Lan, Yuru Wang, Xiaowei Zhang, Huiling Dai, Lin Xu, Zuhua He & Ertao Wang

2. University of Chinese Academy of Sciences, Beijing, China

   Wentao Dong, Jincai Shi, Liying Lan & Yuru Wang

3. Shanghai Key Laboratory of Plant Molecular Sciences, College of Life Sciences, Shanghai Normal University, Shanghai, China

   Yayun Zhu, Huizhong Chang & Nan Yu

4. College of Horticulture, Fujian Agriculture and Forestry University, Fuzhou, China

   Chunhua Wang & Shuang Wu

5. Collaborative Innovation Center of Crop Stress Biology, Institute of Plant Stress Biology, State Key Laboratory of Cotton Biology,

Department of Biology, Henan University, Kaifeng, China

Jinpeng Gao, Yuchen Miao & Chunpeng Song

6. Department of Biochemistry and Molecular Biology, University of Massachusetts Amherst, Amherst, MA, USA

   Dong Wang

Authors

1. Wentao Dong
   View author publications

   You can also search for this author in PubMed Google Scholar

2. Yayun Zhu
   View author publications

   You can also search for this author in PubMed Google Scholar

3. Huizhong Chang
   View author publications

   You can also search for this author in PubMed Google Scholar

4. Chunhua Wang
   View author publications

   You can also search for this author in PubMed Google Scholar

5. Jun Yang
   View author publications

   You can also search for this author in PubMed Google Scholar

6. Jincai Shi
   View author publications

You can also search for this author in PubMed Google Scholar

7. Jinpeng Gao
   View author publications

   You can also search for this author in PubMed Google Scholar

8. Weibing Yang
   View author publications

   You can also search for this author in PubMed Google Scholar

9. Liying Lan
   View author publications

   You can also search for this author in PubMed Google Scholar

10. Yuru Wang
    View author publications

    You can also search for this author in PubMed Google Scholar

11. Xiaowei Zhang
    View author publications

    You can also search for this author in PubMed Google Scholar

12. Huiling Dai
    View author publications

    You can also search for this author in PubMed Google Scholar

13. Yuchen Miao
    View author publications

    You can also search for this author in PubMed Google Scholar

14. Lin Xu
    View author publications

You can also search for this author in PubMed Google Scholar

15. Zuhua He
    View author publications

    You can also search for this author in PubMed Google Scholar

16. Chunpeng Song
    View author publications

    You can also search for this author in PubMed Google Scholar

17. Shuang Wu
    View author publications

    You can also search for this author in PubMed Google Scholar

18. Dong Wang
    View author publications

    You can also search for this author in PubMed Google Scholar

19. Nan Yu
    View author publications

    You can also search for this author in PubMed Google Scholar

20. Ertao Wang
    View author publications

    You can also search for this author in PubMed Google Scholar

Contributions

W.D. and E.W. directed the research. W.D., Y.Z., H.C., J.Y., J.S., J.G. and W.Y. performed most of the experiments. C.W., L.L., Y.W., X.Z., H.D., Y.M., L.X., Z.H., C.S., S.W. and N.Y. contributed to the analytical, molecular cloning, and transformation work. E.W. oversaw the entire study. W.D., D.W. and E.W. wrote the manuscript.

Corresponding author

Correspondence to Ertao Wang.

Ethics declarations

Competing interests

The authors declare no competing interests.

Additional information

Peer review information *Nature* thanks Kimberly Gallagher, Jan Lohmann, Takashi Soyano and Krzysztof Szczyglowski for their contribution to the peer review of this work.

Publisher's note Springer Nature remains neutral with regard to jurisdictional claims in published maps and institutional affiliations.

Extended data figures and tables

Extended Data Fig. 1 Representative images of GUS staining of transformed hairy root tips in *M. truncatula*.

The *Medicago* orthologues of pivotal genes required for plant development in other species were identified by protein similarity (double-direction BLAST). The promoter length of these genes is indicated. Roots were stained in GUS staining solution about 60 min. These experiments were repeated two times with similar results. Scale bars, 100 μm. Details of these genes are in Supplementary Table 2.

Extended Data Fig. 2 Two regulatory elements in the *MtSCR* promoter govern its cortical cell expression in *A. thaliana* and cortical expression of *SCR* in other legumes.

a, *AtSCR* promoter-specific expression in QC and endodermis of stable transformed *A. thaliana*. Promoter truncation analysis in stable transformed *A. thaliana* shows that the AT1-box (−1,604 bp to −1,615 bp) and enhancer (−1,632 bp to −1,638 bp) elements of the *MtSCR* promoter are essential, and function synergistically to govern *MtSCR* expression in cortical and epidermal cells in *A. thaliana*. *Cis*-elements were predicated by using website PlantPAN 2.0 (http://plantpan2.itps.ncku.edu.tw/). C, cortex; E, endodermis; QC, quiescent centre. **b**, Sections of GUS-stained hairy roots show *MtSCR* and *AtSCR* expression patterns in *M. truncatula*. Transverse sections were made at about 3–5 mm from the root tip. **c**, In situ hybridization shows cortical expression of *MtSCR* in wild-type *M. truncatula* but not in *Mtscr-1*. **d**, Comparative genomics analysis reveals that legume and *Parasponia SCR* gene promoters harbour closely located (less than 100 bp) enhancer and AT1-box elements, whereas larger distances (170 bp or longer) between AT1-box and enhancer, or the absence of at least one of these elements, were observed in species outside the nitrogen fixation clade. **e**, In situ hybridization shows cortical cell expression of *SCR* in *G. max*, *L. japonicus*, *C. arietinum*, *P. sativum* and *L. albus*. **f**, *PsSCR* promoter (3,257 bp) and *LaSCR2* promoter (3,162 bp) expressed in endodermis, QC and cortex of *M. truncatula* hairy root tips, whereas *StSCR* promoter (2,660 bp) shows endodermis-specific expression pattern. Note that *LaSCR2* promoter (3,162 bp) showed very weak expression in *Medicago* transgenic hairy root. These experiments were repeated two times with similar results. C, cortex; E, endodermis; QC, quiescent centre. Scale bars, 20 μm (**a**, **c**, **e**, **f**) and 100 μm (**b**).

Extended Data Fig. 3 Root development and nodule formation in *M. truncatula Mtscr* mutants.

a, Schematic representation of *MtSCR* genomic sequence (top) and identification of *Tnt1* insertion mutant of *MtSCR* (bottom). *MtSCR* genomic DNA is composed of 2 exons and 1 intron. *Tnt1* insertion sites are indicated by arrows. **b**, Relative *MtSCR* expression levels in wild-type, *Mtscr-1* and *Mtscr-2* roots ($n = 3$). Expression levels were normalized against the reference gene *EF-1*. Data are mean ± s.d. **c**, **d**, Nodule numbers of wild-type, *Mtscr-1* and *Mtscr-2* roots (**c**) and representative images of plants and nodules (**d**) at 7 dpi, 14 dpi, 21 dpi and 28 dpi. **e**, Density of lateral root

numbers (top) and nodules and primordia (bottom) in wild-type, *Mtscr-1* and *Mtscr-2* roots ($n \geq 20$). These experiments were repeated three times with similar results. **f**, Nodulation phenotype of progeny from *Mtscr-1* crossed with *Mtscr-2* is comparable with their parents at 14 dpi, indicating that the *Mtscr-1* mutation is allelic to the *Mtscr-2* mutation ($n \geq 8$). **b**, **e**, **f**, Two-sided Student's *t*-test (**P* < 0.05; ***P* < 0.01). **c**, Significance tests for nodule primordia (a/b/c/d) and nodules (a′/b′/c′/d′/e′) were performed. Conditions with different letters were significantly different (ANOVA, Duncan's multiple range tests; *P* < 0.05). **c**, **e**, **f**, Boxes show the first quartile, median and third quartile; whiskers indicate minimum and maximum values. Data points are represented by dots. *n* represents independent biological samples. Scale bars, 1 cm (plants) and 1 mm (root nodules). Source data

Extended Data Fig. 4 Developmental phenotype in *Mtscr*, *Mtscr-1Mtscl23* and complementation plants.

a, Primary and lateral root radial patterning defects in *Mtscr* and *Mtscr-1Mtscl23* mutants. Note that *M. truncatula* wild-type roots formed 4–5 layers of cortical cells whereas *Mtscr* roots formed only 3–4 layers of cortical-like cells. **b**, All of *pMtSCR:MtSCR*, *pMtSCRΔEnΔAT1:MtSCR* and *pAtSCR:MtSCR* could complement *Mtscr-1* hairy root radial patterning. **c**–**e**, Stable transgenic *Mtscr-1* mutant transformed with *pAtSCR:MtSCR* shows normal shoot gravitropism (**c**) and root radial patterning (**d**), but shows a significant reduction in nodule formation at 14 dpi (**e**) ($n \geq 23$). Letters (a/b) indicate significant differences (ANOVA Duncan's multiple range tests; *P* < 0.01). **e**, Boxes show the first quartile, median and third quartile; whiskers indicate minimum and maximum values. **f**, Relative *MtSCR* expression levels in empty vector (WT), empty vector (*Mtscr-1*) and *Mtscr-1pAtSCR:MtSCR* stable transgenic lines ($n = 6$). Expression levels were normalized against the reference gene *EF-1*. Two-sided Student's *t*-test (***P* < 0.01). Data are mean ± s.d. In **a**, **b**, **d**, transverse sections were made at about 3–5 mm from the root tip. Red represents liginin deposition stained with phloroglucinol. White arrows in *Mtscr-1*, *Mtscr-2*, *Mtscr-1Mtscl23* and empty vector (*Mtscr-1*) indicate lignin deposition between adjacent cells. Black arrows indicate endodermal cells, which are thin and long in wild-type or complementary hairy roots while in *Mtscr-1*, *Mtscr-2*

and *Mtscr-1Mtscl23* mutant they are thick and round. P, pericycle; E, endodermis; m, mutant cell layer. Scale bars, 100 μm. *n* represents independent biological samples. Data points are represented by dots. These experiments were repeated three times with similar results. Lignin is produced in association with xylem differentiation and is deposited into the secondary cell walls of tracheary elements and fibre cells[50]. Source data

Extended Data Fig. 5 *SCR* expression in cortical cells is required for nodulation symbiosis in *M. truncatula*, *L. japonicus* and *G. max*.

a, Nodulation phenotype at 21 dpi in wild-type (WT) hairy roots transformed with an empty vector (*EV*), *pLjUBQ:MtSCR-SRDX*, *pMtSCR:MtSCR-SRDX* or *pMtNRT1.3:MtSCR-SRDX* ($n \geq 21$). **b**, Representative images show that hairy roots transformed with *MtSCR-SRDX* have greatly decreased nodule numbers compared with empty vector. White arrows indicate nodules. **c**, Hairy root lengths of *M. truncatula* at 21 dpi transformed with empty vector (EV), *pLjUBQ:MtSCR-SRDX*, *pMtSCR:MtSCR-SRDX*, or *pMtNRT1.3:MtSCR-SRDX* ($n \geq 21$). **d**, Relative expression levels of *MtSCR-SRDX* in transgenic hairy roots from **a**. Expression levels were normalized against the reference gene *EF-1*. Data are mean ± s.d. **e**, Nodulation phenotype in *L. japonicus* hairy roots transformed with empty vector or *pMtNRT1.3:LjSCR-SRDX* at 21 dpi. ($n \geq 12$). **f**, Representative images of empty vector and *pMtNRT1.3:LjSCR-SRDX* transgenic hairy roots. White arrows indicate nodules. **g**, Hairy root lengths of *L. japonicus* at 21 dpi transformed with empty vector and *pMtNRT1.3:LjSCR-SRDX* ($n \geq 12$). **h**, Relative expression levels of *LjSCR-SRDX* in transgenic hairy roots from **e**. Expression levels were normalized against the reference gene *LjUb*. Data are mean ± s.d. **i**, Nodulation phenotype in *G. max* hairy roots transformed with an empty vector or *pMtNRT1.3:GmSCR-SRDX* at 21 dpi ($n \geq 35$). **j**, Representative images of empty vector and *pMtNRT1.3:GmSCR-SRDX* transgenic hairy roots. White arrows indicate nodules. **k**, Hairy root lengths of *G. max* at 21 dpi transformed with empty vector and *pMtNRT1.3:GmSCR-SRDX* ($n \geq 35$). **l**, Relative expression levels of *GmSCR-SRDX* in transgenic hairy roots from **i**. Expression levels were normalized against the reference gene *GmELF1B*. Data are mean ± s.d. **a**, **c**, Asterisks indicate significant differences from the

empty vector control (ANOVA, Dunnett's multiple tests; $^{**}P < 0.01$; ns, not significant). **e**, **g**, **i**, **k**, Asterisks indicate significant differences by two-sided Student's *t*-test ($^{*}P < 0.05$; ns, not significant). **a**, **c**, **e**, **g**, **i**, **k**, Boxes show the first quartile, median and third quartile; whiskers indicate minimum and maximum values. *n* represents independent biological samples. Data points are represented by dots. These experiments were repeated three times with similar results. Scale bars, 1 mm. Source data

Extended Data Fig. 6 MtSCL23 and MtSCR function redundantly in nodule organogenesis.

a, Maximum likelihood phylogenetic tree of SCR from *A. thaliana*; *Oryza sativa* (Q2RB59, A2ZAX5); *Zea mays* (NP_001168484); *M. truncatula* (Medtr7g074650); *Selaginella moellendorffii* (85562, 84762); *Physcomitrella patens* (Pp1s882_1V6.1, Pp1s85_139V6.1, Pp1s324_56V6.1) and its homologues from *A. thaliana* (AtSCL23, AtRGA1, AtSCL3, AtLAS/SCL18) and *M. truncatula* (Medtr4g076020, Medtr1g069725, Medtr3g065980, Medtr7g027190, Medtr8g442410). Branch support was obtained from 1,000 bootstrap repetitions. Evolutionary analyses were conducted in MEGA7[51]. **b**, GUS staining of hairy roots transformed with *pMtSCL23:EGFP-GUS* or *pMtSCL2:EGFP-GUS* shows both *MtSCL23* and *MtSCL2* expressed in the cortical cells. Transverse sections were made at about 3–5 mm from the root tip. **c**, Mutant identification (left) and relative gene expression (right) levels of *MtSCL23* (top) and *MtSCL2* (bottom). *Tnt1* insertion sites and qPCR primers are indicated. **d**, Nodulation phenotype of wild-type and *Mtscl23* roots at 14 days after *Sm1021* inoculation ($n \geq 24$). **e**–**g**, Nodule numbers (**e**), lateral root numbers (**f**) and root lengths (**g**) of wild-type, *Mtscr-1*, *Mtscl2*, and *Mtscr-1Mtscl2* roots at 14 dpi and 21 dpi ($n \geq 15$). **h**, **i**, Primary root length (**h**) and lateral root numbers (**i**) of wild-type, *Mtscr-1*, and *Mtscr-1Mtscl23* roots at 7 dpi, 14 dpi, 21 dpi and 28 dpi. *Mtscr-1Mtscl23* shows short primary root length and similar lateral root numbers compared with *Mtscr-1* ($n \geq 19$). **j**, **k**, The density of lateral roots in *Mtscr-1Mtscl23* plants is significantly increased compared with *Mtscr-1* (**j**), whereas nodule density is significantly decreased (**k**) ($n \geq 19$). **l**, Real-time RT–PCR (qPCR) analysis shows that induction of *LBD16*, *ENOD40*, *FLOT4* and *RIP* upon Nod factor treatment for 24 h is fully dependent on *MtSCR* and *MtSCL23*.

Expression of *NIN*, *ERN1*, *NSP2* and *VAPYRIN* still can be induced, but the expression level was much lower than that in wild-type plants. Data are mean ± s.d. Expression levels were normalized against the reference gene *EF-1*. **c**–**l**, Two-sided Student's *t*-test (**P* < 0.05; ***P* < 0.01; ns, not significant). **d**–**k**, Boxes show the first quartile, median and third quartile; whiskers indicate minimum and maximum values. *n* represents independent biological samples. Data points are represented by dots. These experiments were repeated three times with similar results. Scale bars, 1 mm (**b**, root tip) and 50 μm (**b**, root sections). Source data

Extended Data Fig. 7 *MtSHR1* is expressed in the stele and MtSCR interacts with MtSHR1 and MtSHR2.

a, In situ hybridization shows that *MtSHR1* is expressed in the stele. Scale bars, 100 μm. These experiments were repeated two times. **b**, Interactions between MtSCR and MtSHR1/2 in yeast two-hybrid assay. BD, binding domain; AD, activation domain. SD2, SD medium lacking leucine, tryptophan; SD4, SD medium lacking leucine, tryptophan, histidine and adenine. **c**, Split luciferase complementation indicates an in vivo interaction between MtSCR and MtSHR1/2 in *N. benthamiana* leaves. Fluorescence signal intensity is indicated. JW771 and JW772, which were derived from pCAMBIA2300 by insert *Pro35S:nLUC* or *Pro35S:cLUC* cassette, respectively, were used[34]. **d**, MtSCR co-immunoprecipitates with MtSHR1/2 in *N. benthamiana*. WB, western blot; IP, immunoprecipitation; CoIP, coimmunoprecipitation. MtSCR–HA and MtSHR1–FLAG or MtSHR2–FLAG were co-expressed in *N. benthamiana* leaves, respectively. For blot source data, see Supplementary Fig. 1. These experiments were repeated three times with similar results. **e**, Protein alignments show that two regions of SHR protein sequence show high variation.

Extended Data Fig. 8 *M. truncatula MtSHR* is required for nodule symbiosis.

a, Schematic representation of *MtSHR2* genomic sequence (top) and identification of *Tnt1* insertion mutant of *MtSHR2* (bottom). **b**, Relative expression levels of MtSHR1 and MtSHR2 in *Mtshr2* mutant ($n \geq 3$). qPCR

primer is indicated in **a**. **c**, Root length of wild-type and *Mtshr2* roots at 14dpi ($n \geq 23$). **d**, Numbers of nodules and primordia in wild-type and *Mtshr2* roots at 14 dpi. **e**, Hairy root length of *Mtshr2* at 21 dpi transformed with empty vector or *MtSHR1* RNAi ($n \geq 16$). **f**, Nodulation phenotype of *Mtshr2* transformed with empty vector or *MtSHR1* RNAi ($n \geq 16$). **g**, qPCR showing that expression of *MtSHR1* but not its homologues was significantly reduced in *MtSHR1* RNAi transgenic hairy roots at 21 dpi ($n \geq 5$). **h**, Representative images show that nodule numbers were reduced in *MtSHR1-SRDX* transgenic hairy roots of *Mtshr2* plants. White arrows indicate nodules. **i**, Hairy root length of *Mtshr2* at 21 dpi transformed with empty vector, *pLjUBQ:MtSHR1-SRDX*, *pMtSHR1:MtSHR1-SRDX*, or *pMtNRT1.3:MtSHR1-SRDX* ($n \geq 10$). **j**, Relative expression levels of *MtSHR1-SRDX* in transgenic hairy roots in **i**. **k**, GUS staining shows that MtSHR1–SRDX-2NLS–GUS is specially located in cortical cells in *pNRT1.3:MtSHR1-SRDX-2NLS-GUS* transgenic hairy roots. **l**, Nodulation phenotype of *Mtshr2* at 21 dpi transformed with empty vector or *pMtNRT1.3:MtSHR1-SRDX-2NLS* ($n \geq 10$). **m**, Hairy root length of *Mtshr2* plants at 21 dpi transformed with empty vector or *pMtNRT1.3:MtSHR1-SRDX-2NLS*. **n**, Relative expression levels of *MtSHR1-SRDX-2NLS* in transgenic hairy roots in **m**. In **b**, **g**, **j** and **n**, expression levels were normalized against the reference gene *EF-1*. Data are mean ± s.d. **b**–**g**, **i**, **l**, **m**, Two-sided Student's *t*-test (*$P < 0.05$; **$P < 0.01$; ns, not significant). **c**–**f**, **i**, **l**, **m**, Boxes show first quartile, median and third quartile; whiskers indicate minimum and maximum values. *n* represents independent biological samples. Data points are represented by dots. These experiments were repeated three times with similar results. Scale bars, 1 mm (**h**) and 50 μm (**k**). Source data

Extended Data Fig. 9 MtSHR1/2 and MtSCR are induced by cytokinins and required for NIN-induced spontaneous nodule formation, and overexpression of SHR promotes cortical cell division.

a, Immunoblotting showing that MtSHR1–GUS (~130 kDa) accumulated in *pMtSHR1:MtSHR1-GUS* transgenic hairy roots after 6-BA treatment for 4 days ($n \geq 10$). For blot source data, see Supplementary Fig. 1. **b**, 6-BA

treatment for 4 days upregulated the expression of *MtSCR* in root tips. Expression levels were normalized against the reference gene *EF-1* ($n \geq 20$). **c**, **d**, The frequency (**c**) and numbers (**d**) of spontaneous nodules induced at 10 weeks by transformation with *pLjUBQ:NIN* were significantly lower in *Mtscr-1* than in wild-type plants ($n \geq 26$). **e**, Section of spontaneous nodules formed in wild-type and *Mtscr-1* roots, in the absence of *S. meliloti* in **c**. **f**, In *A. thaliana*, cortical cell divisions were evident within 24 h after initiating conditional ectopic overexpression (*pG1090-XVE:AtSHR* stable transformed line) of *AtSHR* via oestradiol treatment (10 μM). Arrowheads indicate cortical cell divisions. En, endodermis; Co, cortex; Ep, epidermis. These experiments were repeated two times with similar results. **g**, Relative expression levels of *MtSCR* and *MtSHR1* in stable transformed rice ($n = 6$). Expression levels were normalized against the reference gene *Cyclophilin2*. **h**, Root sections of rice roots transformed with empty vector or overexpression of *MtSCR-MtSHR1* lines. These experiments were repeated two times with similar results. **i**, Cortex-specific overexpression of *MtSHR1* driven by the *MtNRT1.3* promoter is sufficient to trigger cortical cell division. Transverse sections were made at about 3–5 mm from the root tip. These experiments were repeated three times with similar results. **j**, Table showing that excessive cortical cell division induced by *MtSHR1* overexpression requires *MtSCR*, but does not require the Nod factor signalling pathway components *NFP*, *NSP1*, *NSP2* and *NIN*. **d**, Boxes show first quartile, median and third quartile; whiskers indicate minimum and maximum values. **b**, **d**, **g**, Two-sided Student's *t*-test (**$P < 0.01$). Data are mean ± s.d. *n* represents independent biological samples. Data points are represented by dots. Scale bars, 1 mm (**c**), 20 μm (**f**), 50 μm (**e**) and 100 μm (**h**, **i**). Source data

Extended Data Fig. 10 The MtSHR–MtSCR module is required for infection thread formation and can be activated by symbiotic signals.

a, Histochemical analysis of *ENOD11:GUS* expression of *pLjUBQ:MtSHR1*-transformed roots. **b**, A higher frequency of *pMtENOD11:GUS* staining sites was observed in *MtSHR1*-overexpressing hairy roots compared with the empty vector control at 7 dpi with *Sm1021*. **c**, Average numbers of infection threads (ITs) and infection foci in wild-type,

Mtscr-1, and *Mtscr-1Mtscl23* roots 7 days after inoculation with *LacZ*-marked *Sm1021* ($n \geq 12$). Different letters (a/b) indicate significant differences (ANOVA, Duncan's multiple range tests; $P < 0.05$). **d**, Average numbers of infection threads and infection foci in empty vector and *pLjUBQ:MtSHR1-SRDX* transformed hairy roots 7 days after inoculation with *LacZ*-marked *Sm1021* ($n \geq 14$). ITs includes infection threads that end in epidermis and reach cortex. **e**, Real-time RT–PCR (qPCR) analysis showing that expression of *MtSCR* but not *MtSHR1/2* is induced in wild-type plants at 7 dpi ($n = 5$). **f**, GUS staining of hairy roots shows that *pMtSCR:EGFP-GUS* and *pMtSHR1:MtSHR1-GUS* but not *pMtSHR1:EGFP-GUS* are induced in nodule primordia. These experiments were repeated three times with similar results. **g**, qPCR showing that genetic impairment of *MtSHR1/2* function significantly reduces the expression of *MtSCR* at 7 dpi ($n \geq 5$). **h**, *MtSCR* induction in *M. truncatula* requires the Nod factor signalling pathway components *NSP1*, *NSP2* and *NIN* ($n \geq 5$). **i**, GUS protein is not modified and accumulated upon *Sm1021* inoculation in *p35S:GUS* transgenic root. Actin is a loading control. These experiments were repeated two times with similar results. For blot source data, see Supplementary Fig. 1. **j**, Elevated levels of MtSHR1–GUS fusion proteins upon *Sm1021* inoculation depend on the Nod factor signalling pathway components *NSP1* and *NSP2*. These experiments were repeated three times with similar results. For blot source data, see Supplementary Fig. 1. **k**, qPCR shows that overexpression of *MtSHR1* triggers upregulation of *MtSCR* ($n = 5$). **l**, ChIP–PCR shows that MtSHR1 associated with the promoter of an *MtSCR* fragment that does not overlap with the AT1-box (−1,604 bp to −1,615 bp) and enhancer (−1,632 bp to −1,638 bp). GFP–3×FLAG-transformed hairy roots were used as control. *p35S:MtSHR1-3× FLAG* or *p35S:GFP-3× FLAG*-transformed hairy roots were collected 21 days after *Sm1021* inoculation. Fold-enrichment calculations from three replicate qPCR assays. These experiments were repeated in two independent ChIP experiments with similar results. **m**, **n**, The induction of *LBD16* upon Nod factor treatment for 24 h was abolished in *Mtscr-1Mtscl23* (**m**) and SHR1 dominant-negative transgenic roots (**n**). **o**, The induction of *MtSCR* upon *Sm1021* treatment was abolished in *lbd16-1* roots. **p**, *MtSHR–MtSCR* and *LBD16* may regulate each other to form a positive feedback loop to coordinately regulate nodule organogenesis. **b**, **d**, **e**, **g**, **h**, **k**–**o**, Two-sided Student's *t*-test (*$P < 0.05$; **$P < 0.01$; ns, not significant).

e, **g**, **h**, **k–o**, Expression levels were normalized against the reference gene *EF-1*. **b**, Boxes show first quartile, median and third quartile; whiskers indicate minimum and maximum values. *n* represents independent biological samples. Data are mean ± s.d. Data points are represented by dots. These experiments were repeated three times with similar results. Scale bars, 1 mm (**a**) and 100 μm (**f**). Source data

Extended Data Fig. 11 A proposed model of cortical cell division competence for nodule organogenesis in legumes.

a, The MtSHR–MtSCR network in cortical cells allows them to respond to symbiotic signals and cytokinins. **b**, Rhizobial signals activate the MtSHR–MtSCR module to promote cortical cell division and nodule organogenesis. **c**, SHR and SCR are not expressed in root cortical cells of *A. thaliana*. **d**, Ectopic expression of SHR–SCR network leads to cortical cell division in *A. thaliana*. Ep, epidermis; Co, cortex; En, endodermis; Vasc, vascular tissue; Lrc, lateral root cap; Col, columella.

Supplementary information

Supplementary Information

This file contains Supplementary Figure 1: Source data for images for blots. Original source images for all data obtained by western blots; Supplementary Table 2: Genes used for screening in this study; Supplementary Table 3: Promoter screening primers; Supplementary Table 4: Primers used in this study.

Reporting Summary

Supplementary Table

Supplementary Table 1: Differentially expressed genes in *M. truncatula* hairy roots overexpressing *MtSHR1 (OE).*

Source data

Source Data Fig. 1

Source Data Fig. 2

Source Data Fig. 3

Source Data Extended Data Fig. 3

Source Data Extended Data Fig. 4

Source Data Extended Data Fig. 5

Source Data Extended Data Fig. 6

Source Data Extended Data Fig. 8

Source Data Extended Data Fig. 9

Source Data Extended Data Fig. 10

Rights and permissions

Reprints and Permissions

About this article

Check for updates

Cite this article

Dong, W., Zhu, Y., Chang, H. *et al.* An SHR–SCR module specifies legume cortical cell fate to enable nodulation. *Nature* **589,** 586–590 (2021). https://doi.org/10.1038/s41586-020-3016-z

Download citation

- Received: 06 August 2019
- Accepted: 19 October 2020
- Published: 09 December 2020
- Issue Date: 28 January 2021
- DOI: https://doi.org/10.1038/s41586-020-3016-z

Further reading

- **SHR–SCR regulates cortical cell division and nodulation**
  - M. Arif Ashraf
  - & Jaimie M. Van Norman

  Molecular Plant (2021)

- **Interaction of symbiotic rhizobia and parasitic root-knot nematodes in legume roots – from molecular regulation to field application**
  - Sofia R. Costa
  - , Jason Liang Pin Ng
  - & Ulrike Mathesius

  Molecular Plant-Microbe Interactions® (2021)

Comments

By submitting a comment you agree to abide by our Terms and Community Guidelines. If you find something abusive or that does not comply with our terms or guidelines please flag it as inappropriate.

Access through your institution
Change institution
Buy or subscribe

This article was downloaded by **calibre** from https://www.nature.com/articles/s41586-020-3016-z

- Article
- Published: 23 December 2020

Nociceptive nerves regulate haematopoietic stem cell mobilization

- Xin Gao[1,2],
- Dachuan Zhang ORCID: orcid.org/0000-0002-1746-275X[1,2] na1,
- Chunliang Xu ORCID: orcid.org/0000-0002-4514-8477[1,2] na1,
- Huihui Li[1,2],
- Kathleen M. Caron[3] &
- Paul S. Frenette ORCID: orcid.org/0000-0003-0862-9922[1,2,4]

Nature **volume 589**, pages591–596(2021)Cite this article

- 12k Accesses
- 323 Altmetric
- Metrics details

Subjects

- Haematopoietic stem cells
- Somatic system
- Stem-cell research

Abstract

Haematopoietic stem cells (HSCs) reside in specialized microenvironments in the bone marrow—often referred to as ‘niches’—that represent complex regulatory milieux influenced by multiple cellular constituents, including nerves[1,2]. Although sympathetic nerves are known to regulate the HSC niche[3,4,5,6], the contribution of nociceptive neurons in the bone marrow remains unclear. Here we show that nociceptive nerves are required for enforced HSC mobilization and that they collaborate with sympathetic nerves to maintain HSCs in the bone marrow. Nociceptor neurons drive granulocyte colony-stimulating factor (G-CSF)-induced HSC mobilization via the secretion of calcitonin gene-related peptide (CGRP). Unlike sympathetic nerves, which regulate HSCs indirectly via the niche[3,4,6], CGRP acts directly on HSCs via receptor activity modifying protein 1 (RAMP1) and the calcitonin receptor-like receptor (CALCRL) to promote egress by activating the $G\alpha_s$/adenylyl cyclase/cAMP pathway. The ingestion of food containing capsaicin—a natural component of chili peppers that can trigger the activation of nociceptive neurons—significantly enhanced HSC mobilization in mice. Targeting the nociceptive nervous system could therefore represent a strategy to improve the yield of HSCs for stem cell-based therapeutic agents.

Access through your institution
Change institution
Buy or subscribe

Access options

Subscribe to Journal

Get full journal access for 1 year

$199.00

only $3.90 per issue

Subscribe

All prices are NET prices.
VAT will be added later in the checkout.

Rent or Buy article

Get time limited or full article access on ReadCube.

from$8.99

Rent or Buy

All prices are NET prices.

Additional access options:

- Log in
- Access through your institution
- Learn about institutional subscriptions

Fig. 1: Nociceptive neurons promote HSC mobilization.

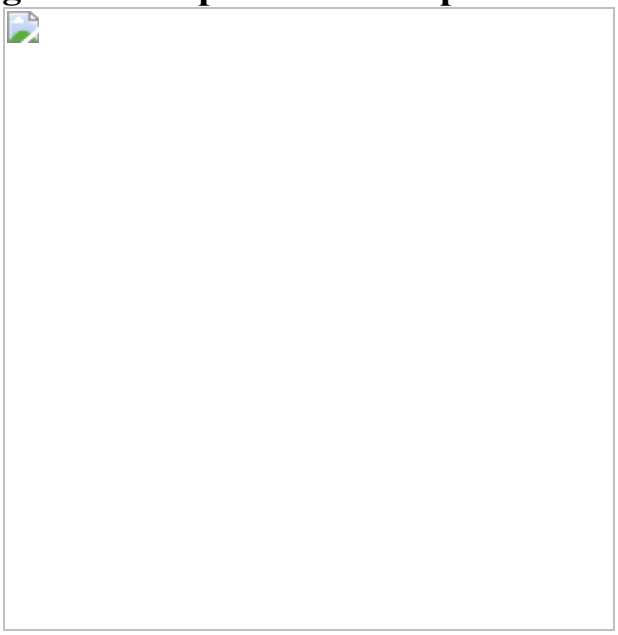

Fig. 2: Nociceptor-derived CGRP induces HSC mobilization via its cognate receptor CALCRL–RAMP1.

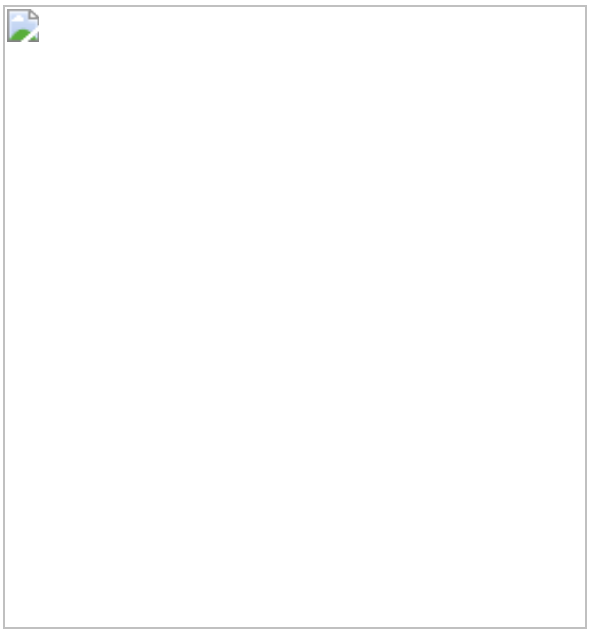

Fig. 3: RAMP1 signals directly in HSCs.

Fig. 4: CGRP amplifies HSC mobilization via the $G\alpha_s$–adenylyl cyclase–cAMP pathway.

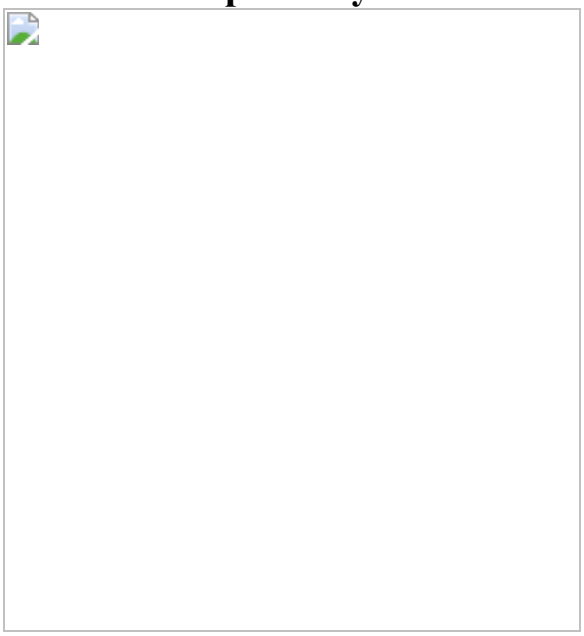

Data availability

RNA sequencing data have been deposited in the Gene Expression Omnibus under accession number GSE156449. All other data are available from the corresponding author upon reasonable request. Source data are provided with this paper.

References

1. 1.

   Gao, X., Xu, C., Asada, N. & Frenette, P. S. The hematopoietic stem cell niche: from embryo to adult. *Development* **145**, dev139691 (2018).

   Article Google Scholar

2. 2.

   Hoggatt, J., Kfoury, Y. & Scadden, D. T. Hematopoietic stem cell niche in health and disease. *Annu. Rev. Pathol*. **11**, 555–581 (2016).

   CAS Article Google Scholar

3. 3.

   Katayama, Y. et al. Signals from the sympathetic nervous system regulate hematopoietic stem cell egress from bone marrow. *Cell* **124**, 407–421 (2006).

   CAS Article Google Scholar

4. 4.

   Lucas, D. et al. Chemotherapy-induced bone marrow nerve injury impairs hematopoietic regeneration. *Nat. Med*. **19**, 695–703 (2013).

   ADS CAS Article Google Scholar

5. 5.

Maryanovich, M. et al. Adrenergic nerve degeneration in bone marrow drives aging of the hematopoietic stem cell niche. *Nat. Med*. **24**, 782–791 (2018).

CAS Article Google Scholar

6. 6.

Méndez-Ferrer, S. et al. Mesenchymal and haematopoietic stem cells form a unique bone marrow niche. *Nature* **466**, 829–834 (2010).

ADS Article Google Scholar

7. 7.

Bensinger, W., DiPersio, J. F. & McCarty, J. M. Improving stem cell mobilization strategies: future directions. *Bone Marrow Transplant*. **43**, 181–195 (2009).

CAS Article Google Scholar

8. 8.

Ordovas-Montanes, J. et al. The regulation of immunological processes by peripheral neurons in homeostasis and disease. *Trends Immunol*. **36**, 578–604 (2015).

CAS Article Google Scholar

9. 9.

Pavlov, V. A., Chavan, S. S. & Tracey, K. J. Molecular and functional neuroscience in immunity. *Annu. Rev. Immunol*. **36**, 783–812 (2018).

CAS Article Google Scholar

10. 10.

Pinho-Ribeiro, F. A., Verri, W. A. & Chiu, I. M. Nociceptor sensory neuron–immune interactions in pain and inflammation. *Trends Immunol*. **38**, 5–19 (2017).

CAS Article Google Scholar

11. 11.

Tsunokuma, N. et al. Depletion of neural crest-derived cells leads to reduction in plasma noradrenaline and alters B lymphopoiesis. *J. Immunol*. **198**, 156–169 (2017).

CAS Article Google Scholar

12. 12.

Suekane, A. et al. CGRP−CRLR/RAMP1 signal is important for stress-induced hematopoiesis. *Sci. Rep*. **9**, 429 (2019).

ADS Article Google Scholar

13. 13.

Chow, A. et al. Bone marrow CD169^{+} macrophages promote the retention of hematopoietic stem and progenitor cells in the mesenchymal stem cell niche. *J. Exp. Med*. **208**, 261–271 (2011).

CAS Article Google Scholar

14. 14.

Christopher, M. J., Rao, M., Liu, F., Woloszynek, J. R. & Link, D. C. Expression of the G-CSF receptor in monocytic cells is sufficient to mediate hematopoietic progenitor mobilization by G-CSF in mice. *J. Exp. Med*. **208**, 251–260 (2011).

CAS Article Google Scholar

15. 15.

Winkler, I. G. et al. Bone marrow macrophages maintain hematopoietic stem cell (HSC) niches and their depletion mobilizes HSCs. *Blood* **116**, 4815–4828 (2010).

CAS Article Google Scholar

16. 16.

Broxmeyer, H. E. et al. Rapid mobilization of murine and human hematopoietic stem and progenitor cells with AMD3100, a CXCR4 antagonist. *J. Exp. Med*. **201**, 1307–1318 (2005).

CAS Article Google Scholar

17. 17.

Lucas, D. et al. Norepinephrine reuptake inhibition promotes mobilization in mice: potential impact to rescue low stem cell yields. *Blood* **119**, 3962–3965 (2012).

CAS Article Google Scholar

18. 18.

Shastri, A. et al. Stimulation of adrenergic activity by desipramine enhances hematopoietic stem and progenitor cell mobilization along with G-CSF in multiple myeloma: A pilot study. *Am. J. Hematol*. **92**, 1047–1051 (2017).

CAS Article Google Scholar

19. 19.

Ford, C. D., Green, W., Warenski, S. & Petersen, F. B. Effect of prior chemotherapy on hematopoietic stem cell mobilization. *Bone Marrow Transplant*. **33**, 901–905 (2004).

CAS Article Google Scholar

20. 20.

Adams, G. B. et al. Haematopoietic stem cells depend on $G\alpha_s$-mediated signalling to engraft bone marrow. *Nature* **459**, 103–107 (2009).

ADS CAS Article Google Scholar

21. 21.

Hagedorn, E. J., Durand, E. M., Fast, E. M. & Zon, L. I. Getting more for your marrow: boosting hematopoietic stem cell numbers with PGE2. *Exp Cell Res*. **329**, 220–226 (2014).

CAS Article Google Scholar

22. 22.

Hoggatt, J. et al. Differential stem- and progenitor-cell trafficking by prostaglandin E_2. *Nature* **495**, 365–369 (2013).

ADS CAS Article Google Scholar

23. 23.

Sands, W. A. & Palmer, T. M. Regulating gene transcription in response to cyclic AMP elevation. *Cell. Signal*. **20**, 460–466 (2008).

CAS Article Google Scholar

24. 24.

Pulsipher, M. A. et al. Adverse events among 2408 unrelated donors of peripheral blood stem cells: results of a prospective trial from the National Marrow Donor Program. *Blood* **113**, 3604–3611 (2009).

CAS Article Google Scholar

25. 25.

Schweizerhof, M. et al. Hematopoietic colony-stimulating factors mediate tumor–nerve interactions and bone cancer pain. *Nat. Med*. **15**, 802–807 (2009).

CAS Article Google Scholar

26. 26.

Charles, A. & Pozo-Rosich, P. Targeting calcitonin gene-related peptide: a new era in migraine therapy. *Lancet* **394**, 1765–1774 (2019).

Article Google Scholar

27. 27.

Cui, M., Gosu, V., Basith, S., Hong, S. & Choi, S. Polymodal transient receptor potential vanilloid type 1 nocisensor: structure, modulators, and therapeutic applications. *Adv. Protein Chem. Struct. Biol*. **104**, 81–125 (2016).

CAS Article Google Scholar

28. 28.

Asada, N. et al. Differential cytokine contributions of perivascular haematopoietic stem cell niches. *Nat. Cell Biol*. **19**, 214–223 (2017).

CAS Article Google Scholar

29. 29.

Li, M. et al. Deficiency of RAMP1 attenuates antigen-induced airway hyperresponsiveness in mice. *PLoS ONE* **9**, e102356 (2014).

ADS Article Google Scholar

30. 30.

Fritz-Six, K. L., Dunworth, W. P., Li, M. & Caron, K. M. Adrenomedullin signaling is necessary for murine lymphatic vascular development. *J. Clin. Invest*. **118**, 40–50 (2008).

CAS Article Google Scholar

Download references

Acknowledgements

We thank J. Wood for providing $Na_V1.8$-Cre mice, C. Prophete for technical assistance, A. Birbrair and N. Asada for advice with the initial experiments, and D. Sun from the Human Stem Cell FACS and Xenotransplantation Facility for assistance with cell sorting. This work was supported by grants from the National Institutes of Health (U01DK116312, R01DK056638, R01DK112976 and R01HL069438) to P.S.F. H.L. is the recipient of a F32 Ruth L. Kirschstein Postdoctoral Individual National Research Service Award (HL142243-01).

Author information

Author notes

1. These authors contributed equally: Dachuan Zhang, Chunliang Xu

Affiliations

1. Ruth L. and David S. Gottesman Institute for Stem Cell and Regenerative Medicine Research, Albert Einstein College of Medicine, New York, NY, USA

   Xin Gao, Dachuan Zhang, Chunliang Xu, Huihui Li & Paul S. Frenette

2. Department of Cell Biology, Albert Einstein College of Medicine, New York, NY, USA

   Xin Gao, Dachuan Zhang, Chunliang Xu, Huihui Li & Paul S. Frenette

3. Department of Cell Biology and Physiology, University of North Carolina at Chapel Hill, Chapel Hill, NC, USA

   Kathleen M. Caron

4. Department of Medicine, Albert Einstein College of Medicine, New York, NY, USA

   Paul S. Frenette

Authors

1. Xin Gao
   View author publications

   You can also search for this author in PubMed Google Scholar

2. Dachuan Zhang
   View author publications

   You can also search for this author in PubMed Google Scholar

3. Chunliang Xu
   View author publications

   You can also search for this author in PubMed Google Scholar

4. Huihui Li
   View author publications

   You can also search for this author in PubMed Google Scholar

5. Kathleen M. Caron
   View author publications

   You can also search for this author in PubMed Google Scholar

6. Paul S. Frenette
   View author publications

You can also search for this author in PubMed Google Scholar

Contributions

X.G. designed the study, performed most of the experiments, analysed data and wrote the manuscript. D.Z. advised on experiment design, helped with flow cytometry analysis, sorting and bone marrow transplantations, and provided input on the manuscript. C.X. participated in study design and performed experiments. H.L. advised on experiment design and helped with experiments. K.M.C. provided *Ramp1*$^{-/-}$ and *Calcrl*$^{fl/fl}$ mice and commented on the manuscript. P.S.F. designed and supervised the study, interpreted data and wrote the manuscript.

Corresponding author

Correspondence to Paul S. Frenette.

Ethics declarations

Competing interests

P.S.F. serves as consultant for Pfizer, has received research funding from Ironwood Pharmaceuticals and is a shareholder of Cygnal Therapeutics. The rest of the authors declare no competing interests.

Additional information

Peer review information *Nature* thanks Iannis Aifantis, Toshio Suda and the other, anonymous, reviewer(s) for their contribution to the peer review of this work.

Publisher's note Springer Nature remains neutral with regard to jurisdictional claims in published maps and institutional affiliations.

Extended data figures and tables

Extended Data Fig. 1 Characterization of nociceptive and sympathetic innervation in the bone marrow.

a, **b**, Representative confocal *z*-stack projection montages of C57BL/6 mouse femur stained for CGRP (nociceptive nerves), TH (sympathetic nerves), and TUBB3 (all peripheral nerves), $CD31^+CD144^+$ double-positive vasculature. Scale bar, 100 µm. Femoral sensory and sympathetic innervation is quantified by the total length of all $CGRP^+$, TH^+ or $TUBB^+$ nerve fibres divided by the bone marrow (BM) area. $n = 3$ mice. **c**, Schematic illustration of the pharmacological denervation experiment using RTX and 6OHDA. **d**, **e**, Representative images of confocal *z*-stack projections from femurs of control, RTX-, 6OHDA- and dual-denervated mice stained for $CGRP^+$ nociceptive nerve fibres, TH^+ sympathetic nerve fibres, $CD31^+CD144^+$ blood vessels and DAPI. Scale bar, 100 µm. Femoral sensory and sympathetic innervation is quantified by the total length of $CGRP^+$ or TH^+ nerves divided by total bone marrow area. Data from $n = 4$, 5, 4, 4 mice, respectively. Data are mean ± s.e.m.; significance was assessed using a one-way ANOVA. Source data

Extended Data Fig. 2 Nociceptive or sympathetic nerves are dispensable for HSC maintenance, whereas the depletion of both systems expands poorly functional HSCs.

a, **b**, Bone marrow cellularity and absolute numbers of B cells ($B220^+$), T cells ($CD3e^+$) and myeloid cells ($Mac\text{-}1^+$) per femur from control, RTX, 6OHDA, or dual-denervated mice. $n = 10, 8, 8, 11$ (**a**) and 10, 9, 7, 10 (**b**) mice, respectively. **c**, Representative FACS plots showing the gating strategy for $Lin^-Sca\text{-}1^+Kit^+CD150^+CD48^-$ HSCs. The same gating strategy was used throughout. **d**, Absolute number of HSCs and LSK cells ($Lin^-Sca\text{-}1^+Kit^+$) per femur from control, RTX, 6OHDA or dual-denervated mice. $n = 10, 8, 8, 11$ mice, respectively. **e**, Peripheral blood chimerism ($CD45.2^+$) in CD45.1-recipient mice transplanted with 0.5×10^6 CD45.1 competitor bone marrow cells mixed with 0.5×10^6 donor bone marrow cells (CD45.2) from control, RTX, 6OHDA or dual-denervated mice at the indicated time points post-transplantation. $n = 4, 4, 4, 5$ mice, respectively. **f**, Bone marrow

chimerism ($CD45.2^+$) 20 weeks after transplantation. **g**, Experimental design to determine the homing efficiency of HSCs and LSK cells (CD45.2) from control- or dual-denervated mice to the bone marrow of recipients (CD45.1). **h**, Homing efficiency of donor CD45.2 HSCs and LSK cells detected in the recipient bone marrow. $n = 4$, 5 mice, respectively. Data are mean ± s.e.m.; significance was assessed using a two-tailed unpaired Student's *t*-test (**h**) or one-way ANOVA (**a**, **b**, **d**–**f**). For box plots, the box spans from the 25th to 75th percentiles and the centre line was plotted at the median. Whiskers represent minimum to maximum range. Source data

Extended Data Fig. 3 Expansion of phenotypic HSCs after dual sympathetic and nociceptive denervation is normalized by administration of CGRP or a β-adrenergic agonist.

a, Representative confocal *z*-stack projections from femurs of $Na_v1.8$-Cre^+; $iTdTomato^+$ mice stained for $CD31^+CD144^+$ vasculature and $CGRP^+$ nociceptive nerves. Nociceptive innervation quantified by the total length of all $Na_v1.8^+$ (red), $CGRP^+$ (green) and $Na_v1.8^+CGRP^+$ double positive (yellow) nerves divided by the bone marrow area. $n = 4$ mice. **b**, Schematic illustration of the dual denervation experiment with $Na_v1.8$-Cre; iDTA mice. **c**, **d**, Representative images of confocal *z*-stack projections from femurs of $Na_v1.8$-Cre^+;$iTdTomato^+$;$iDTA^-$ or $Na_v1.8$-Cre^+;$iTdTomato^+$;$iDTA^+$ mice stained for blood vessels (blue). Quantification of $TdTomato^+$ nociceptive nerves in the femurs. $n = 3$ mice per group. **e**, **f**, Absolute numbers of HSCs (Lin^-Sca-$1^+Kit^+CD150^+CD48^-$), B cells ($B220^+$), T cells ($CD3e^+$) and myeloid cells (Mac-1^+) per femur from $Na_v1.8$-Cre^-;$iDTA^+$ or $Na_v1.8$-Cre^+;$iDTA^+$ mice with or without 6OHDA treatment. Each dot represents data from individual mice. $n = 8, 7, 3, 8$ (**e**) and 6, 6, 4, 7 (**f**) mice, respectively. **g**, Absolute numbers of HSCs, B cells and myeloid cells per femur from control and dual-denervated mice implanted with osmotic pumps containing saline as control, CGRP, isoproterenol or substance P. $n = 14, 9, 5, 5, 5$ mice respectively. Data are mean ± s.e.m. Significance was assessed using a two-tailed unpaired Student's *t*-test (**d**) or one-way ANOVA (**e**–**g**). For box plots, the box spans from the 25th to 75th percentiles and the centre line

was plotted at the median. Whiskers represent minimum to maximum range. Source data

Extended Data Fig. 4 G-CSF-induced HSPC mobilization is impaired in mice that lack nociceptor neurons.

a, White blood cell counts and absolute numbers of LSK cells per ml of peripheral blood after G-CSF mobilization in vehicle-treated control and RTX-treated mice. *n* = 11, 13 mice, respectively. **b**, Spleen weight and the absolute numbers of LSK cells in the spleen after G-CSF mobilization in vehicle-treated control and RTX-treated mice. *n* = 11 mice per group. **c**, Bone marrow cellularity and the absolute numbers of LSK cells in the bone marrow after G-CSF-induced mobilization in vehicle-treated control and RTX-treated mice. *n* = 11, 13 mice, respectively. **d**, Cell cycle analysis of bone marrow HSCs ($Lin^{-}Sca\text{-}1^{+}Kit^{+}CD150^{+}CD48^{-}$) from control or RTX-treated mice determined by FACS using anti-Ki67 and Hoechst 33342 staining. *n* = 6, 4 mice, respectively. **e**, White blood cell counts and absolute numbers of LSK cells per ml of peripheral blood after G-CSF-induced mobilization in $Na_v1.8\text{-}Cre^{-};iDTA^{+}$ and $Na_v1.8\text{-}Cre^{+};iDTA^{+}$ mice. *n* = 4, 5 mice, respectively. **f**, Bone marrow cellularity and the absolute numbers of LSK cells in the bone marrow after G-CSF-induced mobilization in $Na_v1.8\text{-}Cre^{-};iDTA^{+}$ and $Na_v1.8\text{-}Cre^{+};iDTA^{+}$ mice. *n* = 4, 5 mice, respectively. **g**, Peripheral blood B-cell ($B220^{+}CD45.2^{+}$), blood T-cell ($CD3e^{+}CD45.2^{+}$), and myeloid-cell ($Mac\text{-}1^{+}CD45.2^{+}$) donor chimerism in CD45.1-recipient mice transplanted with mobilized blood (CD45.2) derived from saline or RTX-treated mice mixed with CD45.1 competitor bone marrow cells at the indicated time points post-transplantation. *n* = 9, 8 mice, respectively. **h**, Total bone marrow chimerism ($CD45.2^{+}$) and bone marrow HSC chimerism ($Lin^{-}Sca\text{-}1^{+}Kit^{+}CD150^{+}CD48^{-}CD45.2^{+}$) 20 weeks after transplantation. *n* = 9, 8 mice, respectively. Data are mean ± s.e.m. Significance was assessed using a two-tailed unpaired Student's *t*-test. For box plots, the box spans from the 25th to 75th percentiles and the centre line was plotted at the median. Whiskers represent minimum to maximum range. Source data

Extended Data Fig. 5 The neuropeptide CGRP, but not substance P, promotes G-CSF-induced HSC mobilization.

a, Absolute numbers of HSCs ($Lin^{-}Sca\text{-}1^{+}Kit^{+}CD150^{+}CD48^{-}$) and LSK cells ($Lin^{-}Sca\text{-}1^{+}Kit^{+}$) per ml of peripheral blood after G-CSF-induced mobilization in C57BL/6 mice implanted with osmotic pumps containing saline or substance P. $n = 5$ mice per group. **b**, Bone marrow cellularity and the absolute numbers of LSK cells and HSCs in the bone marrow after G-CSF administration in C57BL/6 mice implanted with osmotic pumps containing saline or substance P. $n = 5$ mice per group. **c**, Bone marrow cellularity and the absolute numbers of HSCs per femur from mice described in Fig. 2a. $n = 18, 9, 7, 7$ mice, respectively. **d**, Left, experimental design to determine the effect of CGRP on HSC mobilization of 6OHDA-denervated mice. Right, absolute number of HSCs per ml of peripheral blood after G-CSF administration in saline-or 6OHDA- treated C57BL/6 mice implanted with osmotic pumps containing saline or CGRP. $n = 6$ mice per group. Data are mean ± s.e.m.; significance was assessed using a two-tailed unpaired Student's *t*-test. Source data

Extended Data Fig. 6 *Ramp1*-deficient mice exhibit no haematopoietic defect at steady state.

a, *Ramp1* mRNA expression levels determined by quantitative PCR in total bone marrow cells derived from $Ramp1^{+/+}$ or $Ramp1^{-/-}$ mice. $n = 5$ biological samples. **b**, **c**, White blood cell counts (**b**) and the absolute numbers of B cells ($B220^{+}$), T cells ($CD3e^{+}$) and myeloid cells ($Mac\text{-}1^{+}$) (**c**) per ml of peripheral blood from $Ramp1^{+/+}$ or $Ramp1^{-/-}$ mice at steady state. $n = 5$ mice per group. **d**, **e**, Bone marrow cellularity (**d**) and the absolute numbers of LSK cells, B cells ($B220^{+}$), T cells ($CD3e^{+}$) and myeloid cells ($Mac\text{-}1^{+}$) (**e**) per femur from $Ramp1^{+/+}$ or $Ramp1^{-/-}$ mice at steady state. $n = 5$ mice per group. **f**, Left, experimental design to determine the homing efficiency of HSCs ($Lin^{-}Sca\text{-}1^{+}Kit^{+}CD150^{+}CD48^{-}$) and LSK cells from $Ramp1^{+/+}$ and $Ramp1^{-/-}$ mice (CD45.2) to the bone marrow of lethally irradiated recipients (CD45.1). Right, the percentage of donor $CD45.2^{+}$ HSCs and LSK cells detected in the recipient bone marrow. $n = 5$ mice per group. **g**, Bone marrow cellularity and the absolute number of HSCs in the

bone marrow. n = 3, 4, 3, 3 mice, respectively. Data are mean ± s.e.m. Significance was assessed using a two-tailed unpaired Student's t-test (**a**–**f**) or one-way ANOVA (**g**). Source data

Extended Data Fig. 7 Nociceptive-nerve-deficient mice exhibit no alteration of HSC niche components after G-CSF treatment.

a, Absolute numbers of mesenchymal stem cells (MSCs) ($CD45^{-}Ter119^{-}CD31^{-}CD51^{+}PDGFR\alpha^{+}$), endothelial cells (ECs) ($CD45^{-}Ter119^{-}CD31^{high}$) and macrophages ($Gr\text{-}1^{-}F4/80^{+}CD115^{int}SSC^{int/low}$) per femur from saline- or RTX-treated mice after G-CSF treatment. n = 4, 4 (left and middle), 6, 8 (right) mice, respectively. **b**, qPCR quantification of *Cxcl12* mRNA levels in total bone marrow cells, sorted MSCs and ECs from saline- or RTX-treated mice after G-CSF treatment. n = 5 mice per group. **c**, Levels of CXCL12 in bone marrow extracellular fluid (BMEF) measured by ELISA. n = 3, 5, 4 (left), 3, 4, 5 (middle), 4, 5 (right) mice. **d**, Mean fluorescence intensities (MFI) in the expression of CXCR4, VLA4 and CD44 on HSCs ($Lin^{-}Sca\text{-}1^{+}Kit^{+}CD150^{+}CD48^{-}$). n = 4 mice per group. Data are mean ± s.e.m. Significance was assessed using a two-tailed unpaired Student's t-test (**a**, **b**, **d**) or one-way ANOVA (**c**). Source data

Extended Data Fig. 8 Transcriptome analysis by RNA sequencing of HSCs from *Ramp1*$^{+/+}$ and *Ramp1*$^{-/-}$ mice.

a, Heat map shows differentially expressed genes between wild-type- and *Ramp1*$^{-/-}$-sorted HSCs (adjusted P value <0.05). **b**, Gene set enrichment analyses showing upregulated and downregulated pathways in *Ramp1*$^{-/-}$ HSCs compared to wild-type HSCs ($P < 0.01$, n = 3 biological replicates per group). **c**, Gene set enrichment analyses showing significant alterations of gene sets involved in the $G\alpha_s$/adenylyl cyclase/cAMP pathway. **d**, Schematic illustration of the dual stimulation experiment. **e**, Absolute number of HSCs ($Lin^{-}Sca\text{-}1^{+}Kit^{+}CD150^{+}CD48^{-}$) in the mobilized peripheral blood of mice treated with control saline, desipramine (DES), CGRP, or both DES and CGRP. n = 9, 4, 8, 4 mice, respectively. Data are

mean ± s.e.m. Significance was assessed using a one-way ANOVA. Source data

Extended Data Fig. 9 Ingestion of spicy food enhances HSC mobilization.

a, Scoville heat scale for chili peppers. 100 ppm = 100 mg kg^{-1}. **b**, Three pellets of standard chow (brown) and three pellets of spicy chow (red) were provided to two mice at 18:00 on day 1. Sixteen hours later (10:00 on day 2), two of the three standard pellets had been consumed whereas the spicy food pellets remained untouched. **c**, Daily food intake (left) and the body weight (right) of mice fed with standard diet or capsaicin-containing diet. *n* = 5 (left), 4 mice (right) per group. **d**, CGRP levels in the BMEF from mice fed with control diet or capsaicin diet. *n* = 9 mice per group. **e**, Left, absolute numbers of HSCs ($Lin^{-}Sca\text{-}1^{+}Kit^{+}CD150^{+}CD48^{-}$) in the bone marrow after G-CSF-induced mobilization in mice fed with standard or capsaicin-containing chow. *n* = 6, 7 mice, respectively. Right, cell cycle analysis of bone marrow HSCs was determined by FACS using anti-Ki67 and Hoechst 33342 staining. *n* = 6 mice. **f**, White blood cell (WBC) counts (left) and absolute numbers of LSK cells (right) per ml of peripheral blood after G-CSF-induced mobilization in mice fed with standard diet or capsaicin-containing diet. *n* = 6, 7 mice, respectively. **g**, **i**, Peripheral total blood donor chimerism ($CD45.2^{+}$) in CD45.1-recipient mice transplanted with 0.5×10^{6} CD45.1 competitor bone marrow cells and 250 HSCs sorted from mobilized blood (**g**) or bone marrow (**i**) from mice fed with standard or capsaicin chow. *n* = 9, 8 (**g**), 8, 8 (**i**) mice, respectively. **h**, **j**, Peripheral blood B cell ($B220^{+}CD45.2^{+}$), T cell ($CD3e^{+}CD45.2^{+}$) and myeloid cell ($Mac\text{-}1^{+}CD45.2^{+}$) donor chimerism in CD45.1-recipient mice transplanted with 250 blood HSCs (**h**) or bone marrow HSCs (**j**) with competitor bone marrow cells at 16 weeks post-transplantation. *n* = 9, 8 (**h**), 8, 8 (**j**) mice, respectively. **k**, Experimental design to determine the effects of CGRP administration on HSC competitiveness. **l**, Peripheral total blood donor chimerism ($CD45.2^{+}$) in CD45.1-recipient mice transplanted with 0.5×10^{6} CD45.1 competitor bone marrow cells and 250 HSCs sorted from mobilized blood from PBS- or CGRP-treated mice. *n* = 7, 9 mice, respectively. **m**, Peripheral blood B cell, T cell and myeloid cell donor chimerism in

CD45.1-recipient mice transplanted with 250 blood HSCs with competitor bone marrow cells at 16 weeks post-transplantation. $n = 7$, 9 mice, respectively. Data are mean ± s.e.m. Two-tailed unpaired Student's *t*-test. For box plots, the box spans from the 25th to 75th percentiles and the centre line was plotted at the median. Whiskers represent minimum to maximum range. Source data

Extended Data Fig. 10 Nociceptor-mediated HSC mobilization.

Schematic representation showing that nociceptive-nerve-derived CGRP, but not substance P, acts via CGRP receptors on HSCs to enhance their mobilization via a cAMP-mediated signalling pathway.

Supplementary information

Reporting Summary

Source data

Source Data Fig. 1

Source Data Fig. 2

Source Data Fig. 3

Source Data Fig. 4

Source Data Extended Data Fig. 1

Source Data Extended Data Fig. 2

Source Data Extended Data Fig. 3

Source Data Extended Data Fig. 4

Source Data Extended Data Fig. 5

Source Data Extended Data Fig. 6

Source Data Extended Data Fig. 7

Source Data Extended Data Fig. 8

Source Data Extended Data Fig. 9

Rights and permissions

Reprints and Permissions

About this article

Check for updates

Cite this article

Gao, X., Zhang, D., Xu, C. *et al.* Nociceptive nerves regulate haematopoietic stem cell mobilization. *Nature* **589,** 591–596 (2021). https://doi.org/10.1038/s41586-020-03057-y

Download citation

- Received: 04 November 2019
- Accepted: 19 November 2020
- Published: 23 December 2020
- Issue Date: 28 January 2021

- DOI: https://doi.org/10.1038/s41586-020-03057-y

Comments

By submitting a comment you agree to abide by our Terms and Community Guidelines. If you find something abusive or that does not comply with our terms or guidelines please flag it as inappropriate.

Access through your institution
Change institution
Buy or subscribe

Associated Content

Nature | News & Views

Pain-sensing neurons mobilize blood stem cells from bone marrow

- Anastasia N. Tikhonova
- & Iannis Aifantis

This article was downloaded by **calibre** from https://www.nature.com/articles/s41586-020-03057-y

- Article
- Published: 23 December 2020

IspH inhibitors kill Gram-negative bacteria and mobilize immune clearance

- Kumar Sachin Singh[1],
- Rishabh Sharma[1],
- Poli Adi Narayana Reddy[2],
- Prashanthi Vonteddu[1],
- Madeline Good[2],
- Anjana Sundarrajan[1],
- Hyeree Choi[1],
- Kar Muthumani ORCID: orcid.org/0000-0002-6807-2065[1],
- Andrew Kossenkov[3],
- Aaron R. Goldman ORCID: orcid.org/0000-0001-7605-9592[4],
- Hsin-Yao Tang ORCID: orcid.org/0000-0003-1838-018X[4],
- Maxim Totrov[5],
- Joel Cassel[6],
- Maureen E. Murphy[2],
- Rajasekharan Somasundaram[2],
- Meenhard Herlyn ORCID: orcid.org/0000-0003-0839-0739[2],
- Joseph M. Salvino ORCID: orcid.org/0000-0002-2184-5980[2,6] &
- Farokh Dotiwala ORCID: orcid.org/0000-0002-7387-2219[1]

Nature **volume 589**, pages597–602(2021)Cite this article

- 9183 Accesses

- 1 Citations
- 508 Altmetric
- Metrics details

Subjects

- Antimicrobial responses
- Bacterial host response
- Bacterial infection
- Drug discovery and development

Abstract

Isoprenoids are vital for all organisms, in which they maintain membrane stability and support core functions such as respiration[1]. IspH, an enzyme in the methyl erythritol phosphate pathway of isoprenoid synthesis, is essential for Gram-negative bacteria, mycobacteria and apicomplexans[2,3]. Its substrate, (*E*)-4-hydroxy-3-methyl-but-2-enyl pyrophosphate (HMBPP), is not produced in metazoans, and in humans and other primates it activates cytotoxic Vγ9Vδ2 T cells at extremely low concentrations[4,5,6]. Here we describe a class of IspH inhibitors and refine their potency to nanomolar levels through structure-guided analogue design. After modification of these compounds into prodrugs for delivery into bacteria, we show that they kill clinical isolates of several multidrug-resistant bacteria—including those from the genera *Acinetobacter*, *Pseudomonas*, *Klebsiella*, *Enterobacter*, *Vibrio*, *Shigella*, *Salmonella*, *Yersinia*, *Mycobacterium* and *Bacillus*—yet are relatively non-toxic to mammalian cells. Proteomic analysis reveals that bacteria treated with these prodrugs resemble those after conditional IspH knockdown. Notably, these prodrugs also induce the expansion and activation of human Vγ9Vδ2 T cells in a humanized mouse model of bacterial infection. The prodrugs we describe here synergize the direct killing of bacteria with a simultaneous rapid immune response by cytotoxic γδ T cells, which may limit the increase of antibiotic-resistant bacterial populations.

Access through your institution
Change institution
Buy or subscribe

Access options

Subscribe to Journal

Get full journal access for 1 year

$199.00

only $3.90 per issue

Subscribe

All prices are NET prices.
VAT will be added later in the checkout.

Rent or Buy article

Get time limited or full article access on ReadCube.

from$8.99

Rent or Buy

All prices are NET prices.

Additional access options:

- Log in
- Access through your institution
- Learn about institutional subscriptions

Fig. 1: Testing IspH as a target for the DAIA strategy.

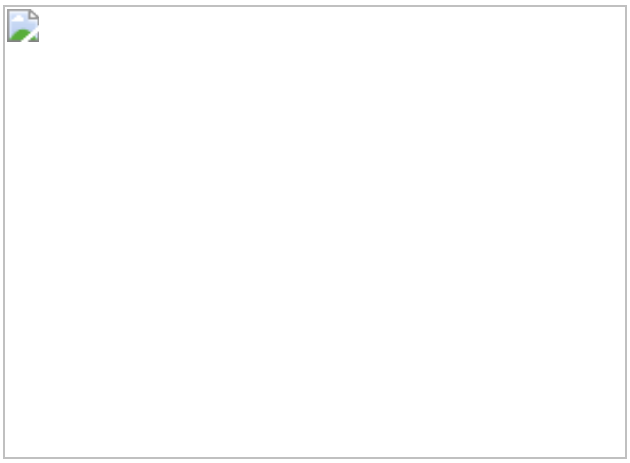

Fig. 2: Inhibition of purified IspH and the killing of bacteria by IspH inhibitors.

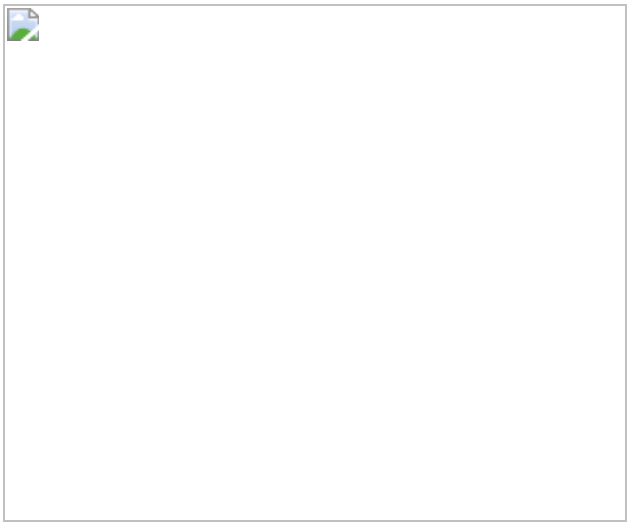

Fig. 3: Analogues of the prodrug C23 have lower MIC_{90} values against multidrug-resistant clinical isolates of Gram-negative bacteria than best-in-class antibiotics.

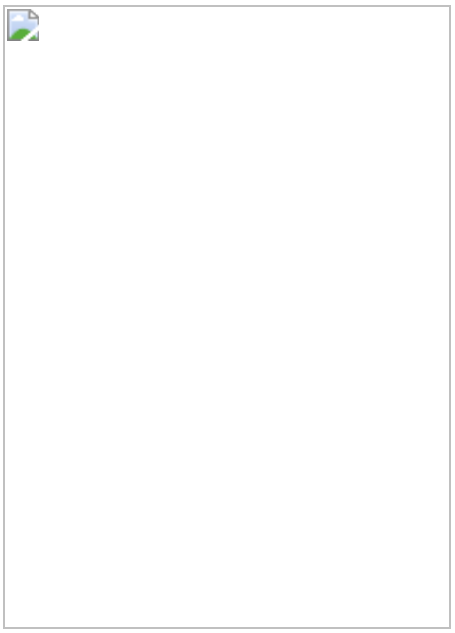

Fig. 4: γδ T cell activation in prodrug-treated, bacteria-infected PBMCs and humanized mice.

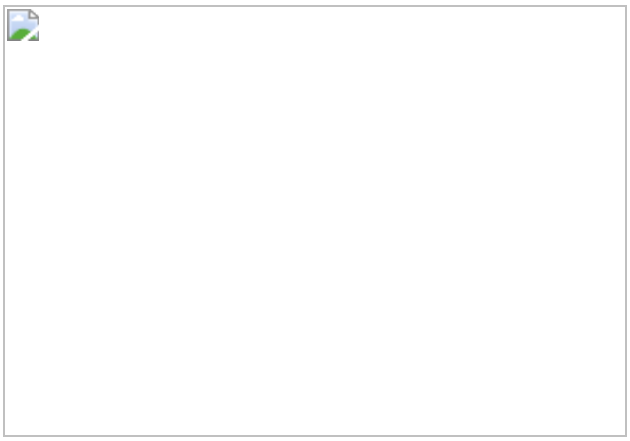

Data availability

Molecular docking studies were performed using the *E. coli* IspH structure 3KE8 from the Protein Data Bank. The atomic field property of the IspH binding pocket was mapped using the Internal Coordinate Mechanics (ICM) software (http://www.molsoft.com/icm_pro.html) from Molsoft and the molecular docking of 10 million compounds from the MolCart library (https://www.molsoft.com/molcart.html) was carried out using theVirtual Ligand Screening software (https://molsoft.com/vls.html) from Molsoft. Owing to the lack of a suitable online repository, all docking data are available upon request as an .icb file, viewable using the free ICM browser

(http://www.molsoft.com/icm_browser.html). LC–MS/MS spectra were searched against the UniProt *E. coli* (BL21-DE3) database (https://www.uniprot.org/proteomes/UP000002032). The proteomics data are available on MassIVE (https://massive.ucsd.edu/) using the accession number MSV000086359, or they can be downloaded from ftp://massive.ucsd.edu/MSV000086359/. All reagents used or generated and all data that support the findings of this study are available from the authors on reasonable request, see author contributions for contacts for specific datasets. Source data are provided with this paper.

References

1. 1.

   Odom, A. R. Five questions about non-mevalonate isoprenoid biosynthesis. *PLoS Pathog*. **7**, e1002323 (2011).

   CAS PubMed PubMed Central Google Scholar

2. 2.

   Jomaa, H. et al. Inhibitors of the nonmevalonate pathway of isoprenoid biosynthesis as antimalarial drugs. *Science* **285**, 1573–1576 (1999).

   CAS PubMed Google Scholar

3. 3.

   McAteer, S., Coulson, A., McLennan, N. & Masters, M. The *lytB* gene of *Escherichia coli* is essential and specifies a product needed for isoprenoid biosynthesis. *J. Bacteriol*. **183**, 7403–7407 (2001).

   CAS PubMed PubMed Central Google Scholar

4. 4.

   Rhodes, D. A. et al. Activation of human γδ T cells by cytosolic interactions of BTN3A1 with soluble phosphoantigens and the

cytoskeletal adaptor periplakin. *J. Immunol*. **194**, 2390–2398 (2015).

CAS PubMed PubMed Central Google Scholar

5. 5.

Chien, Y. H., Meyer, C. & Bonneville, M. γδ T cells: first line of defense and beyond. *Annu. Rev. Immunol*. **32**, 121–155 (2014).

CAS PubMed PubMed Central Google Scholar

6. 6.

Chen, Z. W. Multifunctional immune responses of HMBPP-specific Vγ2Vδ2 T cells in *M. tuberculosis* and other infections. *Cell. Mol. Immunol*. **10**, 58–64 (2013).

PubMed PubMed Central Google Scholar

7. 7.

Alberts, B. et al. *Molecular Biology of the Cell* 4th edn (Garland Science, 2002).

8. 8.

Lieberman, J. in *Fundamental Immunology* 7th edn (ed. Paul, W. E.) Ch. 37 (Lippincott, Williams & Wilkins, 2012).

9. 9.

Magill, S. S. et al. Multistate point-prevalence survey of health care-associated infections. *N. Engl. J. Med*. **370**, 1198–1208 (2014).

CAS PubMed PubMed Central Google Scholar

10. 10.

WHO. *Tuberculosis* https://www.who.int/en/news-room/fact-sheets/detail/tuberculosis (World Health Organization, 2020).

11. 11.

    WHO. *Artemisinin resistance and artemisinin-based combination therapy efficacy* https://www.who.int/docs/default-source/documents/publications/gmp/who-cds-gmp-2019-17-eng.pdf?ua=1 (World Health Organization, 2019).

12. 12.

    Wright, G. D. Bacterial resistance to antibiotics: enzymatic degradation and modification. *Adv. Drug Deliv. Rev*. **57**, 1451–1470 (2005).

    CAS Google Scholar

13. 13.

    Li, X. Z., Plésiat, P. & Nikaido, H. The challenge of efflux-mediated antibiotic resistance in Gram-negative bacteria. *Clin. Microbiol. Rev*. **28**, 337–418 (2015).

    PubMed PubMed Central Google Scholar

14. 14.

    Wilson, D. N. Ribosome-targeting antibiotics and mechanisms of bacterial resistance. *Nat. Rev. Microbiol*. **12**, 35–48 (2014).

    CAS Google Scholar

15. 15.

    Dotiwala, F. et al. Granzyme B disrupts central metabolism and protein synthesis in bacteria to promote an immune cell death program. *Cell* **171**, 1125–1137.e11 (2017).

CAS PubMed PubMed Central Google Scholar

16. 16.

Walch, M. et al. Cytotoxic cells kill intracellular bacteria through granulysin-mediated delivery of granzymes. *Cell* **157**, 1309–1323 (2014).

CAS PubMed PubMed Central Google Scholar

17. 17.

Dotiwala, F. et al. Killer lymphocytes use granulysin, perforin and granzymes to kill intracellular parasites. *Nat. Med*. **22**, 210–216 (2016).

CAS PubMed PubMed Central Google Scholar

18. 18.

Finlay, B. B. & McFadden, G. Anti-immunology: evasion of the host immune system by bacterial and viral pathogens. *Cell* **124**, 767–782 (2006).

CAS Google Scholar

19. 19.

Yang, J. H. et al. Antibiotic-induced changes to the host metabolic environment inhibit drug efficacy and alter immune function. *Cell Host Microbe* **22**, 757–765.e3 (2017).

CAS PubMed PubMed Central Google Scholar

20. 20.

Chiang, C. Y. et al. Mitigating the impact of antibacterial drug resistance through host-directed therapies: current progress, outlook, and challenges. *MBio* **9**, e01932-17 (2018).

CAS PubMed PubMed Central Google Scholar

21. 21.

Oldfield, E. & Feng, X. Resistance-resistant antibiotics. *Trends Pharmacol. Sci*. **35**, 664–674 (2014).

CAS PubMed PubMed Central Google Scholar

22. 22.

Marakasova, E. S. et al. Prenylation: from bacteria to eukaryotes. *Mol. Biol. (Mosk.)* **47**, 717–730 (2013).

CAS Google Scholar

23. 23.

Workalemahu, G. et al. Metabolic engineering of *Salmonella* vaccine bacteria to boost human Vγ2Vδ2 T cell immunity. *J. Immunol*. **193**, 708–721 (2014).

CAS PubMed PubMed Central Google Scholar

24. 24.

Dieli, F. et al. Granulysin-dependent killing of intracellular and extracellular *Mycobacterium tuberculosis* by Vγ9/Vδ2 T lymphocytes. *J. Infect. Dis*. **184**, 1082–1085 (2001).

CAS PubMed PubMed Central Google Scholar

25. 25.

Wolff, M. et al. Isoprenoid biosynthesis via the methylerythritol phosphate pathway: the (*E*)-4-hydroxy-3-methylbut-2-enyl diphosphate reductase (LytB/IspH) from *Escherichia coli* is a [4Fe-4S] protein. *FEBS Lett*. **541**, 115–120 (2003).

CAS PubMed PubMed Central Google Scholar

26. 26.

Rohdich, F. et al. The deoxyxylulose phosphate pathway of isoprenoid biosynthesis: studies on the mechanisms of the reactions catalyzed by IspG and IspH protein. *Proc. Natl Acad. Sci. USA* **100**, 1586–1591 (2003).

ADS CAS PubMed PubMed Central Google Scholar

27. 27.

Xiao, Y., Chu, L., Sanakis, Y. & Liu, P. Revisiting the IspH catalytic system in the deoxyxylulose phosphate pathway: achieving high activity. *J. Am. Chem. Soc*. **131**, 9931–9933 (2009).

CAS PubMed PubMed Central Google Scholar

28. 28.

Gräwert, T. et al. Probing the reaction mechanism of IspH protein by X-ray structure analysis. *Proc. Natl Acad. Sci. USA* **107**, 1077–1081 (2010).

ADS PubMed PubMed Central Google Scholar

29. 29.

Nazarov, P. A. et al. Mitochondria-targeted antioxidants as highly effective antibiotics. *Sci. Rep*. **7**, 1394 (2017).

ADS PubMed PubMed Central Google Scholar

30. 30.

Ortmann, R. et al. Acyloxyalkyl ester prodrugs of FR900098 with improved in vivo anti-malarial activity. *Bioorg. Med. Chem. Lett*. **13**, 2163–2166 (2003).

CAS Google Scholar

31. 31.

Søballe, B. & Poole, R. K. Microbial ubiquinones: multiple roles in respiration, gene regulation and oxidative stress management. *Microbiology* **145**, 1817–1830 (1999).

Google Scholar

32. 32.

Trnka, J., Elkalaf, M. & Anděl, M. Lipophilic triphenylphosphonium cations inhibit mitochondrial electron transport chain and induce mitochondrial proton leak. *PLoS ONE* **10**, e0121837 (2015).

PubMed PubMed Central Google Scholar

33. 33.

Wingrove, D. E. & Gunter, T. E. Kinetics of mitochondrial calcium transport. II. A kinetic description of the sodium-dependent calcium efflux mechanism of liver mitochondria and inhibition by ruthenium red and by tetraphenylphosphonium. *J. Biol. Chem*. **261**, 15166–15171 (1986).

CAS Google Scholar

34. 34.

Schwartz, A. S., Yu, J., Gardenour, K. R., Finley, R. L., Jr & Ideker, T. Cost-effective strategies for completing the interactome. *Nat. Methods* **6**, 55–61 (2009).

CAS Google Scholar

35. 35.

Wang, H. et al. Butyrophilin 3A1 plays an essential role in prenyl pyrophosphate stimulation of human Vγ2Vδ2 T cells. *J. Immunol*. **191**, 1029–1042 (2013).

CAS Google Scholar

36. 36.

Sandstrom, A. et al. The intracellular B30.2 domain of butyrophilin 3A1 binds phosphoantigens to mediate activation of human Vγ9Vδ2 T cells. *Immunity* **40**, 490–500 (2014).

CAS PubMed PubMed Central Google Scholar

37. 37.

Rigau, M. et al. Butyrophilin 2A1 is essential for phosphoantigen reactivity by γδ T cells. *Science* **367**, eaay5516 (2020).

CAS Google Scholar

38. 38.

Karunakaran, M. M. et al. Butyrophilin-2A1 directly binds germline-encoded regions of the Vγ9Vδ2 TCR and is essential for phosphoantigen sensing. *Immunity* **52**, 487–498.e6 (2020).

CAS PubMed PubMed Central Google Scholar

39. 39.

Wei, H. et al. Definition of APC presentation of phosphoantigen (*E*)-4-hydroxy-3-methyl-but-2-enyl pyrophosphate to Vγ2Vδ2 TCR. *J. Immunol*. **181**, 4798–4806 (2008).

CAS PubMed PubMed Central Google Scholar

40. 40.

Mogues, T., Goodrich, M. E., Ryan, L., LaCourse, R. & North, R. J. The relative importance of T cell subsets in immunity and immunopathology of airborne *Mycobacterium tuberculosis* infection in mice. *J. Exp. Med*. **193**, 271–280 (2001).

CAS PubMed PubMed Central Google Scholar

41. 41.

Abagyan, R., Totrov, M. & Kuznetsov, D. ICM—a new method for protein modeling and design - applications to docking and structure prediction from the distorted native conformation. *J. Comput. Chem*. **15**, 488–506 (1994).

CAS Google Scholar

42. 42.

Abagyan, R. & Totrov, M. Biased probability Monte Carlo conformational searches and electrostatic calculations for peptides and proteins. *J. Mol. Biol*. **235**, 983–1002 (1994).

CAS PubMed PubMed Central Google Scholar

43. 43.

Lam, P. C., Abagyan, R. & Totrov, M. Hybrid receptor structure/ligand-based docking and activity prediction in ICM: development and evaluation in D3R Grand Challenge 3. *J. Comput. Aided Mol. Des*. **33**, 35–46 (2019).

ADS CAS PubMed PubMed Central Google Scholar

44. 44.

Lam, P. C., Abagyan, R. & Totrov, M. Ligand-biased ensemble receptor docking (LigBEnD): a hybrid ligand/receptor structure-based approach. *J. Comput. Aided Mol. Des*. **32**, 187–198 (2018).

ADS CAS PubMed PubMed Central Google Scholar

45. 45.

Totrov, M. Atomic property fields: generalized 3D pharmacophoric potential for automated ligand superposition, pharmacophore elucidation and 3D QSAR. *Chem. Biol. Drug Des*. **71**, 15–27 (2008).

CAS PubMed PubMed Central Google Scholar

46. 46.

Chen, Q. & Chen, J. Isolation of $CD34^+$ cells from human fetal liver and cord blood. *Bio Protoc*. **3**, e991 (2013).

Google Scholar

47. 47.

Somasundaram, R. et al. Tumor-associated B-cells induce tumor heterogeneity and therapy resistance. *Nat. Commun*. **8**, 607 (2017).

ADS PubMed PubMed Central Google Scholar

48. 48.

Span, I. et al. Insights into the binding of pyridines to the iron–sulfur enzyme IspH. *J. Am. Chem. Soc*. **136**, 7926–7932 (2014).

CAS PubMed PubMed Central Google Scholar

49. 49.

Braet, F., De Zanger, R. & Wisse, E. Drying cells for SEM, AFM and TEM by hexamethyldisilazane: a study on hepatic endothelial cells. *J. Microsc*. **186**, 84–87 (1997).

CAS PubMed PubMed Central Google Scholar

50. 50.

Cox, J. et al. Accurate proteome-wide label-free quantification by delayed normalization and maximal peptide ratio extraction, termed MaxLFQ. *Mol. Cell Proteomics* **13**, 2513–2526 (2014).

CAS PubMed PubMed Central Google Scholar

51. 51.

Storey, J. D. & Tibshirani, R. Statistical significance for genomewide studies. *Proc. Natl Acad. Sci. USA* **100**, 9440–9445 (2003).

ADS MathSciNet CAS PubMed MATH Google Scholar

52. 52.

Oliveros, J. C. *Venny* v.2.1 (BioinfoGP, 2007).

Download references

Acknowledgements

This research was supported by the G. Harold and Leila Y. Mathers Charitable Foundation, Commonwealth Universal Research Enhancement Program (CURE – Pennsylvania Department of Health) and the Wistar Science Discovery Fund (F.D.). F.D. was supported by a Wistar Institute recruitment grant from The Pew Charitable Trusts. R.S.S. and M.H. were funded by the Adelson Medical Research Foundation and DOD for Hu-mice generation. We thank D. Speicher from the Proteomics Facility at the Wistar Institute, S. Molugu from the Electron Microscopy Resource Laboratory and Y. Velich from the Cell and Developmental Biology Microscopy core at UPenn. Support for the Wistar Institute Proteomics and Metabolomics and Genomics Shared Resources was provided by Cancer Center Support Grant P30 CA010815 and National Institutes of Health instrument grant S10 OD023586. We thank M. Groll, E. Oldfield, A. Odom John and C. Morita for advice on the bacterial isoprenoid synthesis pathway, IspH and γδ T cell fields.

Author information

Affiliations

1. Vaccine and Immunotherapy Center, The Wistar Institute, Philadelphia, PA, USA

   Kumar Sachin Singh, Rishabh Sharma, Prashanthi Vonteddu, Anjana Sundarrajan, Hyeree Choi, Kar Muthumani & Farokh Dotiwala

2. Program in Molecular and Cellular Oncogenesis, The Wistar Institute, Philadelphia, PA, USA

   Poli Adi Narayana Reddy, Madeline Good, Maureen E. Murphy, Rajasekharan Somasundaram, Meenhard Herlyn & Joseph M. Salvino

3. Bioinformatics Facility, The Wistar Institute, Philadelphia, PA, USA

   Andrew Kossenkov

4. Proteomics and Metabolomics Facility, The Wistar Institute, Philadelphia, PA, USA

   Aaron R. Goldman & Hsin-Yao Tang

5. Molsoft, San Diego, CA, USA

   Maxim Totrov

6. Molecular Screening and Protein Expression Facility, The Wistar Institute, Philadelphia, PA, USA

   Joel Cassel & Joseph M. Salvino

Authors

1. Kumar Sachin Singh

View author publications

You can also search for this author in PubMed Google Scholar

2. Rishabh Sharma
   View author publications

   You can also search for this author in PubMed Google Scholar

3. Poli Adi Narayana Reddy
   View author publications

   You can also search for this author in PubMed Google Scholar

4. Prashanthi Vonteddu
   View author publications

   You can also search for this author in PubMed Google Scholar

5. Madeline Good
   View author publications

   You can also search for this author in PubMed Google Scholar

6. Anjana Sundarrajan
   View author publications

   You can also search for this author in PubMed Google Scholar

7. Hyeree Choi
   View author publications

   You can also search for this author in PubMed Google Scholar

8. Kar Muthumani
   View author publications

   You can also search for this author in PubMed Google Scholar

9. Andrew Kossenkov
View author publications

You can also search for this author in PubMed Google Scholar

10. Aaron R. Goldman
View author publications

You can also search for this author in PubMed Google Scholar

11. Hsin-Yao Tang
View author publications

You can also search for this author in PubMed Google Scholar

12. Maxim Totrov
View author publications

You can also search for this author in PubMed Google Scholar

13. Joel Cassel
View author publications

You can also search for this author in PubMed Google Scholar

14. Maureen E. Murphy
View author publications

You can also search for this author in PubMed Google Scholar

15. Rajasekharan Somasundaram
View author publications

You can also search for this author in PubMed Google Scholar

16. Meenhard Herlyn
View author publications

You can also search for this author in PubMed Google Scholar

17. Joseph M. Salvino
View author publications

You can also search for this author in PubMed Google Scholar

18. Farokh Dotiwala
View author publications

You can also search for this author in PubMed Google Scholar

Contributions

F.D. conceived the study and planned the experiments. M.T. set up the atomic field property of the IspH catalytic site and performed molecular docking experiments. K.S.S., R. Sharma, P.V. and A.S. purified the proteins, performed the biochemical activity assays, bacterial killing experiments, mouse infection studies and contributed to the preparation of the manuscript. P.V. performed flow cytometry and microscopy studies. K.S.S. performed the electron microscopy studies with assistance from the UPenn electron microscopy core. A.R.G. and H.-Y.T. ran the samples for proteomics and small-molecule studies. A.K. and R. Sharma performed the bioinformatics and pathway analysis on proteomics data and helped to illustrate it in a figure. J.C. performed the surface plasmon resonance studies. J.M.S. planned the synthesis of DAIA prodrugs and P.A.N.R. synthesized them. H.C., K.M., R. Somasundaram and M.H. provided Hu-mice. M.G. and M.E.M. performed the seahorse experiments. F.D. and J.M.S. analysed the data. F.D. generated the figures and drafted the manuscript. J.M.S. and P.A.N.R. provided reagents and expertise. All authors provided critical revisions to the manuscript.

Corresponding authors

Correspondence to Joseph M. Salvino or Farokh Dotiwala.

Ethics declarations

Competing interests

The authors declare no competing interests.

Additional information

Peer review information *Nature* thanks Herman Sintim, Ben Willcox and Gerry Wright for their contribution to the peer review of this work.

Publisher's note Springer Nature remains neutral with regard to jurisdictional claims in published maps and institutional affiliations.

Extended data figures and tables

Extended Data Fig. 1 Purification of recombinant IspH proteins from multiple microbial species and measurement of their biochemical activity by methyl viologen assay.

a, Coomassie-stained gels showing IPTG induction of recombinant 6His-tagged *P. falciparum* (Pf), *E. coli* (Ec), *P. aeruginosa* (Pa) and *M. tuberculosis* (MTB) IspH. **b**, Anti-His-tag immunoblots showing the respective purified IspH proteins. Images in **a**, **b** are representative of 3 independent purification attempts. **c**, IspH uses methyl viologen (MV) as an electron donor for the reductive dehydroxylation of HMBPP. Colourless oxidized methyl viologen is restored to its reduced blue form by sodium dithionite. In the absence or inhibition of IspH activity, methyl viologen stays blue. **d**, **e**, Methyl viologen assays measuring IspH activity using different concentrations of *E. coli* IspH at 10 min in the presence of 1 mM HMBPP (**d**) and different concentrations of HMBPP (**e**) at 30 min in the presence of 50 nM *E. coli* IspH. For **d**, **e**, data are mean of 3 independent experiments ± s.e.m. ***$P < 0.001$, **$P < 0.01$, *$P < 0.05$, ns, not significant; two-tailed unpaired Student's *t*-test, relative to 0 nM IspH in **d** or 0 μM HMBPP in **e**. Source data

Extended Data Fig. 2 In silico molecular docking with the active pocket of *E. coli* IspH.

a, Crystal structure of *E. coli* IspH (PDB: 3KE8)[28] (top left) was used to generate the atomic property field (bottom left) and mimic HMBPP interactions in the active binding pocket (right). **b**, Automated virtual ligand screening (Molsoft) identified 168 out of 9.6 million compounds on the basis of predicted binding at the active site. **c**, The top 24 compounds were compared with HMBPP visually and on the basis of their predicted number of hydrogen bonds formed, hydrogen-bond energy, Van der Waals interaction energy and other interactions as mentioned. In silico docking for C1–24 is shown in Extended Data Fig. 3a.

Extended Data Fig. 3 In silico molecular docking of compounds C1–24 and their inhibitory activity on *E. coli* IspH.

a, Chemical structures and in silico docking of the top 24 candidate IspH inhibitors at the *E. coli* IspH active pocket rendered by Molsoft. Structures are shown in Supplementary Fig. 2a. **b**, Activity of *P. aeruginosa* (Pa), *M. tuberculosis* (MTB) and *P. falciparum* (Pf) IspH pretreated with DMSO (control), C10, C17 and C23 over time. Data are mean of 4 independent experiments ± s.e.m. **c**–**e**, Inhibition of *E. coli* IspH by analogues of C10 (**c**), C17 (**d**) or C23 (**e**). Structures are shown in Supplementary Fig. 2. For analogues with better activity than the parent compound, ***$P < 0.001$, **$P < 0.01$, *$P < 0.05$; two-tailed unpaired Student's *t*-test, relative to C23 ($n = 8$ technical replicates). Data are mean ± s.e.m. Source data

Extended Data Fig. 4 Drug binding assays, structure–activity relationship, testing prodrug potency with different carrier molecules and determining prodrug cleavage and *E. coli* IspH inhibition by LC–MS.

a, SPR signals (resonance units (RU)) from different concentrations of HMBPP, C23.20 and C23.21 run on *E. coli* IspH crosslinked NTA chip, plotted against concentrations to calculate K_D and R_{max} (the amount of ligand (in RU) to be immobilized) values ($n = 3$ biological and 2 technical replicates). **b**, Structure–activity guided analogue design reduced the IC_{50} values of multiple C23 analogues compared with the parent compound. Structures are shown in Supplementary Fig. 2. **c**, **d**, Prodrug ester forms of

analogue C23.47 obtained by linking ethanol, TPP or dimethylaminopropanol (synthetic reactions are shown in Supplementary Fig. 3) were tested for *E. coli* killing by dynamic growth curves (**c**) and by resazurin blue assay (**d**). For **c**, **d**, $n = 3$ biological and 8 technical replicates. **e**, *Escherichia coli* cells treated with 5 μM C23.28–TPP for 30 min were lysed and the lysates analysed by LC–MS to quantify the relative abundance of C23.28–TPP (prodrug), TPP (carrier molecule) and C23.28 (active drug). Respective molecules were identified by their respective retention times (RT) and mass:charge (m/z) ratios. Area under the respective peaks is measured in arbitrary units (AU) and is directly proportional to the abundance of the molecules. **f**, Relative abundances of C23.28–TPP (prodrug), TPP (carrier molecule) and C23.28 (active drug) found within *E. coli* treated with different concentrations (10–5,000 nM) of C23.28–TPP ($n = 3$ technical and 2 biological replicates). **g**, Methyl viologen assay performed by treating 1 mM HMBPP with 50 nM *E. coli* IspH pre-treated with 5 μM C23.28 or TPP for 30 min. Samples analysed by LC–MS to quantify relative conversion of HMBPP (IspH substrate) to DMAPP and IPP (IspH products). Respective molecules were identified by their respective retention times and mass:charge (m/z) ratios. Area under the respective peaks is measured in AU and is directly proportional to the abundance of the molecules. **h**, Conversion of 1 mM HMBPP (black) to DMAPP and IPP (grey) in 30 min by 50 nM *E. coli* IspH in the presence of different concentrations (10–5,000 nM) of TPP (dotted lines) or C23.28 (solid lines) ($n = 3$ technical and 2 biological replicates). For **f**, **h**, data are mean of 3 independent experiments ± s.e.m. Source data

Extended Data Fig. 5 C23 prodrugs specifically act on IspH and kill multidrug-resistant clinical isolates of *V. cholerae*.

a, Immunoblot shows modulation of IspH levels in CGSC 8074 (*E. coli*) achieved by altering arabinose levels in culture medium. RpoD, loading control; representative of 3 independent experiments. **b**, **c**, Sensitivity of the CGSC 8074 strain to C23.28–TPP decreases with increasing IspH levels, as shown by resazurin blue assay (**b**) and dynamic growth curves (**c**). Data are mean of 3 independent experiments ± s.e.m. ***$P < 0.001$, **$P < 0.01$, *$P < 0.05$, the remainder are not significant; two-tailed paired Student's t-test. **d**–**f**, TPP-linked prodrug esters of C23 analogues C23.7, C23.20,

C23.21, C23.28 and C23.47 (**d**) were tested for ability to kill *V. cholerae* (strain M045) by dynamic growth curves and resazurin blue assay (**e**; $n = 3$ biological and 8 technical replicates) or by CFU plating after 24 or 48 h treatment (**f**; $n = 3$ biological replicates with 3 serial dilutions). The MIC_{90} values for prodrug analogues tested on drug-resistant clinical isolates of different pathogenic bacteria are shown in Extended Data Fig. 8a. Data are mean of 3 independent experiments ± s.e.m. $^{*}P < 0.05$, $^{**}P < 0.01$, $^{***}P < 0.001$, the remainder are not significant; two-tailed unpaired Student's *t*-test. Source data

Extended Data Fig. 6 DAIA prodrugs increase oxidative stress and cause defects in bacterial respiration, membrane integrity and cell-wall architecture.

a, **b**, Respiratory changes in *E. coli* treated with TPP or with the indicated concentration of the DAIA prodrug C23.28–TPP were compared by measuring OCR (for aerobic respiration) (**a**) and ECAR (for glycolysis) (**b**). $^{***}P < 0.001$; two-tailed unpaired Student's *t*-test, relative to TPP-treated control. **c**, **d**, Superoxide (solid line, 2 h after treatment; dotted line, 4 h after treatment) (**c**) and hydrogen peroxide (**d**) levels were simultaneously measured by dihydroethidium (DHE) and Amplex red fluorescence respectively. $n = 8$ biological replicates; data are mean ± s.e.m. **e**, **f**, Changes in *E. coli* membrane integrity, upon TPP or prodrug treatment, measured by Live/Dead (SYTO 9/propidium iodide) assay using flow cytometry (**e**) or fluorescence microscopy (**f**). $n = 3$ biological replicates. Scale bar, 2 µm. **g**, **h**, Loss of *E. coli* membrane potential upon treatment with TPP or prodrug measured by BacLight ($DiOC_2$) assay using flow cytometry (**g**) or fluorescence microscopy (**h**). $n = 3$ biological replicates. Scale bar, 2 µm. **i**, Scanning electron micrographs (SEM; left) and transmission electron micrographs (TEM; right) compare the morphology of *E. coli* after 8 h of TPP or prodrug treatment to that of the conditional ispH knockdown *E. coli* strain CGSC 8074 (Δ*ispH*) kept for 8 h in 1% glucose medium. Red arrows indicate membrane blebbing. **j**, SEM (top) and TEM (bottom) compare the morphology of *V. cholerae* after 8 h of TPP or prodrug (C23.28–TPP) treatment. In **i**, **j**, images are representative of 20 fields from 3 technical replicates. Scale bar, 400 nm. Source data

Extended Data Fig. 7 DAIA prodrugs are stable in plasma and liver microsomes, non-toxic to mammalian cells, do not disrupt mitochondrial membrane potential in C2C12 myoblasts and do not disrupt hERG function.

a, **b**, Nonlinear regression curves for degradation of prodrugs C23.28–TPP and C23.21–TPP and the appearance of the parent drugs C23.28 and C23.21 in the presence of human, pig and mouse plasma (**a**) or human, monkey and mouse liver microsomes (**b**). Drug and prodrug concentration measured by LC–MS and normalized on a standard curve. The half-lives ($t_{1/2}$) are calculated from respective curves. Data are mean ± s.e.m. of 3 independent experiments. **c**, **d**, Cytotoxicity of prodrug analogues on HepG2, RAW264.7 and Vero cells (**c**) and C2C12 myoblasts (**d**) measured at 24, 48 and 72 h by LDH release (n = 3 biological and 4 technical replicates). **e**, Effect of TPP and prodrugs C23.28–TPP and C23.47–TPP on mitochondrial membrane potential of C2C12 myoblasts, measured by tetramethyl rhodamine methyl ester (TMRM) fluorescence. CCCP, positive control (n = 3 biological and 4 technical replicates). **f**, Toxicity of C23.28–TPP, the carrier (6-hydroxyhexyl)triphenylphosphonium bromide and Me-TPP to hERG channel measured by automated Q patch assay; the normalized current response is plotted using nonlinear regression curves and the IC_{50} of respective compounds is calculated. Data are mean of 3 independent experiments ± s.e.m. Verapamil was used as the positive control and DMSO as the negative control. Source data

Extended Data Fig. 8 Treating *E. coli* with an IspH inhibitor prodrug disrupts the levels of IspH and several proteins in essential bacterial metabolic and synthesis pathways.

a, Immunoblots measure relative levels of *E. coli* IspH at 8 and 24 h after C23.28–TPP treatment or after conditional knockdown in CGSC 8074 (Δ*ispH*) grown on 1% glucose. **b**, Immunoblots measure relative levels of IspH in clinical isolates of several pathogenic bacteria at 8 and 24 h after C23.28–TPP treatment. For **a**, **b**, RpoD immunoblot serves as loading control and the blots are representative of 3 technical replicates. **c**, Unsupervised hierarchical clustering of 2,346 proteins resolved indicates

that the 3 biological replicates for each condition clustered together. A total of 525 proteins were either up- or downregulated both after C23.28–TPP treatment or after conditional knockdown in CGSC 8074 (Δ*ispH*). **d**, Functions or pathways that are significantly enriched 8 and 24 h after C23.28–TPP treatment. Bars indicate the $-\log_{10}(P \text{ value})$ with the number of proteins identified in each category next to the respective bar. The bars are colour-coded for the percentage of proteins in the pathway that are up- or downregulated. **e**, Venn diagram comparing the overlap in downregulated (>2-fold) proteins at 8 or 24 h after C23.28–TPP treatment or after conditional knockdown in CGSC 8074 (Δ*ispH*). **f**, Proteins important for lipid synthesis, ribosome modification, respiration, cell division, tRNA aminoacylation, DNA/RNA synthesis, DNA repair, amino acid (AA) synthesis and lipopolysaccharide (LPS) cell-wall synthesis pathways are among those significantly downregulated. Associated with Extended Data Fig. 9a. $P < 0.05$ and FDR < 5%. **g**, Venn diagram comparing the overlap in upregulated (>2-fold) proteins at 8 or 24 h after C23.28–TPP treatment or after conditional knockdown in CGSC 8074 (Δ*ispH*). **h**, Ribosome component proteins or proteins important for multidrug efflux and oxidative defence pathways are among those significantly upregulated. Associated with Extended Data Fig. 9b. $P < 0.05$ and FDR <5%. Source data

Extended Data Fig. 9 *Escherichia coli* metabolic pathways up- or downregulated after IspH inhibition.

a, **b**, Pathway analysis of 323 downregulated (**a**) (Extended Data Fig. 8e, f) or 60 upregulated (**b**) (Extended Data Fig. 8g, h) proteins from a proteomic screen comparing Δ*ispH E. coli* and *E. coli* after C23.28–TPP treatment to untreated wild-type *E. coli*. Source data

Extended Data Fig. 10 By dual action, IspH prodrugs expand and activate Vγ9Vδ2 T cells and reduce the emergence of antibiotic resistant bacteria.

a, Top, uninfected (UI) human PBMCs or those co-infected with *E. coli* analysed for expansion of $CD3^+V\gamma9TCR^+$ (γδ) T cells and compared to untreated (UT) or TPP-, prodrug (C23.07–TPP)- or kanamycin (Kan)-

treated PBMCs. Middle, bottom, gated γδ T cell populations analysed for cytotoxic granule proteins granulysin (GNLY) and perforin (middle) or cell surface markers of T cell activation CD69 and HLA-DR (bottom). Representative of 4 independent experiments (4 donors). Percentage of $V\gamma9^+$ T cells from $CD3^+$ population and the percentage of $V\gamma9^+$ T cells with increased expression of granulysin, perforin, CD69 and HLA-DR were plotted in the respective graphs. Data are mean ± s.e.m. $^{**}P < 0.05$, $^{***}P < 0.001$, the remainder are not significant; one-way ANOVA relative to untreated sample. **b**, Uninfected human PBMCs or those co-infected with *V. cholerae* (top) or *M. smegmatis* (bottom) were analysed for expansion of $CD3^+V\gamma9TCR^+$ (γδ) T cells and compared to untreated or TPP-, prodrug (C23.07–TPP)- or kanamycin-treated PBMCs ($n = 4$ biological replicates). Percentage of $V\gamma9^+$ T cells from the $CD3^+$ population were plotted in the respective graphs. Data are mean ± s.e.m. $^{***}P < 0.001$, rest not significant, calculated by one-way ANOVA relative to untreated sample. **c**, Human PBMCs co-infected with kanamycin-resistant *E. coli* or *V. cholerae* can kill neither on their own. Addition of C23.07–TPP kills both *V. cholerae* and *E. coli* ($n = 2$ biological and 3 technical replicates). Data are mean ± s.e.m. $^{***}P < 0.001$, ns, not significant; unpaired Student's *t*-test relative to untreated samples. **d**, γδ T cell depletion from human PBMCs is verified by treating depleted ($\gamma\delta^-$) and undepleted human PBMCs treated with 10 μM HMBPP and 50 ng ml^{-1} IL-15. Representative of 4 independent experiments (4 donors). Percentage of $V\gamma9^+$ T cells from the $CD3^+$ population on different days were plotted in the respective graphs. Data are mean ± s.e.m. $^{***}P < 0.001$ comparing γδ depleted and undepleted PBMCs calculated by unpaired *t*-test. **e**, **f**, Multidrug-resistant clinical isolates of *Vibrio* (**e**) and *Klebsiella* (**f**) grown for 18 serial passages in media (RPMI+ 10% human serum) containing DAIA prodrug (C23.28–TPP) or conventional antibiotics (hygromycin (Hyg) or streptomycin (Strep)) gradually develop resistance when measured by CFU (top). Similar serial passages in presence of human PBMC inhibit the development of resistance against the DAIA prodrug but not against hygromycin or streptomycin. Passages in γδ depleted ($\gamma\delta^-$) PBMCs show higher antibiotic resistance against the DAIA prodrug. ($n = 3$ technical replicates). Data are mean ± s.e.m. $^{***}P < 0.001$, NS, not significant; unpaired Student's *t*-test. **g**, C57BL/6 mice infected with *V. cholerae* are treated with TPP or the

DAIA prodrug C23.28–TPP and monitored daily from day 2 post-infection for survival (n = 10 mice per group). **h**, *Vibrio* load in different organs at the experimental endpoint measured as CFU mg^{-1} (n = 10 mice with 3 technical replicates), comparing changes in bacterial CFU in C57BL/6b mice after C23.28–TPP treatment. Data are mean ± s.e.m. ***$P < 0.001$; unpaired Student's t-test, relative to TPP-treated mice. **i**, Hu-mice injected i.p. with HMBPP at different concentrations show dose-dependent expansion of γδ T cells but not αβ T cells in blood taken every day for a week (n = 2 mice per group). Source data

Extended Data Fig. 11 γδ T cells expand in the tissues of prodrug-treated, *E. coli*-infected humanized mice.

a, Hu-mice infected with *E. coli* (green) and treated with TPP or the prodrug C23.07–TPP are compared for expansion of Vδ2 TCR^+ T cells (red) in multiple organs at day 5 post-infection. DAPI, blue. Scale bar, 100 μm (representative of samples tested from 5–6 Hu-mice). **b**, Vδ2 antibody validated for immunofluorescence staining of formalin-fixed human PBMCs that are γδ expanded (HMBPP + IL15) or γδ depleted. HepG2 and Vero cells serve as negative controls. **c**, Anti-*E. coli* antibody validated for immunofluorescence staining of formalin-fixed HepG2 cells co-infected with *E. coli* BL21 strain. HepG2 without *E. coli* serves as a negative control. Source data

Supplementary information

Supplementary Figures

This file contains Supplementary Figures 1-3.

Reporting Summary

Supplementary Tables

This file contains Supplementary Tables 1-5.

Source data

Source Data Fig. 1

Source Data Fig. 2

Source Data Fig. 3

Source Data Fig. 4

Source Data Extended Data Fig. 1

Source Data Extended Data Fig. 3

Source Data Extended Data Fig. 4

Source Data Extended Data Fig. 5

Source Data Extended Data Fig. 6

Source Data Extended Data Fig. 7

Source Data Extended Data Fig. 8

Source Data Extended Data Fig. 9

Source Data Extended Data Fig. 10

Source Data Extended Data Fig. 11

Rights and permissions

Reprints and Permissions

About this article

Check for updates

Cite this article

Singh, K.S., Sharma, R., Reddy, P.A.N. *et al.* IspH inhibitors kill Gram-negative bacteria and mobilize immune clearance. *Nature* **589,** 597–602 (2021). https://doi.org/10.1038/s41586-020-03074-x

Download citation

- Received: 28 January 2020
- Accepted: 11 November 2020
- Published: 23 December 2020
- Issue Date: 28 January 2021
- DOI: https://doi.org/10.1038/s41586-020-03074-x

Further reading

- **A two-pronged attack on antibiotic-resistant microbes**
  - Youcef Mehellou
  - & Benjamin E. Willcox

  Nature (2021)

Comments

By submitting a comment you agree to abide by our Terms and Community Guidelines. If you find something abusive or that does not comply with our terms or guidelines please flag it as inappropriate.

Access through your institution
Change institution
Buy or subscribe

Associated Content

Nature | News & Views

A two-pronged attack on antibiotic-resistant microbes

- Youcef Mehellou
- & Benjamin E. Willcox

This article was downloaded by **calibre** from https://www.nature.com/articles/s41586-020-03074-x

COVID-19 treatments and pathogenesis including anosmia in K18-hACE2 mice
Download PDF

- Article
- Published: 09 November 2020

COVID-19 treatments and pathogenesis including anosmia in K18-hACE2 mice

- Jian Zheng[1 na1],
- Lok-Yin Roy Wong ORCID: orcid.org/0000-0002-0727-8289[1 na1],
- Kun Li[2 na1],
- Abhishek Kumar Verma[1 na1],
- Miguel E. Ortiz ORCID: orcid.org/0000-0002-3573-5416[2],
- Christine Wohlford-Lenane[2],
- Mariah R. Leidinger[3],
- C. Michael Knudson[3],
- David K. Meyerholz ORCID: orcid.org/0000-0003-1552-3253[3],
- Paul B. McCray Jr ORCID: orcid.org/0000-0002-4067-577X[1,2] &
- Stanley Perlman ORCID: orcid.org/0000-0003-4213-2354[1,2]

Nature **volume 589**, pages603–607(2021)Cite this article

- 15k Accesses
- 4 Citations
- 114 Altmetric
- Metrics details

Subjects

- Experimental models of disease
- SARS-CoV-2

Abstract

The ongoing coronavirus disease 2019 (COVID-19) pandemic is associated with substantial morbidity and mortality. Although much has been learned in the first few months of the pandemic, many features of COVID-19 pathogenesis remain to be determined. For example, anosmia is a common presentation, and many patients with anosmia show no or only minor respiratory symptoms[1]. Studies in animals infected experimentally with severe acute respiratory syndrome coronavirus 2 (SARS-CoV-2), the cause of COVID-19, provide opportunities to study aspects of the disease that are not easily investigated in human patients. Although the severity of COVID-19 ranges from asymptomatic to lethal[2], most experimental infections provide insights into mild disease[3]. Here, using K18-hACE2 transgenic mice that were originally developed for SARS studies[4], we show that infection with SARS-CoV-2 causes severe disease in the lung and, in some mice, the brain. Evidence of thrombosis and vasculitis was detected in mice with severe pneumonia. Furthermore, we show that infusion of convalescent plasma from a recovered patient with COVID-19 protected against lethal disease. Mice developed anosmia at early time points after infection. Notably, although pre-treatment with convalescent plasma prevented most signs of clinical disease, it did not prevent anosmia. Thus, K18-hACE2 mice provide a useful model for studying the pathological basis of both mild and lethal COVID-19 and for assessing therapeutic interventions.

Download PDF

Main

SARS-CoV-2 uses the same receptor as SARS-CoV, human angiotensin-converting enzyme 2 (hACE2)[5]. Mice, which are susceptible to SARS-CoV, are resistant to infection with SARS-CoV-2 because of incompatibilities between mouse ACE2 and the viral spike protein. During the 2003–2004 SARS epidemic, because infected mice developed only mild disease, we and others engineered mice that transgenically displayed hACE2[4,6,7]. K18-hACE2 mice express hACE2 driven by the cytokeratin 18 (*KRT18*) promoter, predominantly in epithelial cells[8]. K18-hACE2 mice infected with SARS-CoV developed overwhelming encephalitis, and mild virus-induced pneumonia[4]. Both SARS-CoV-2 and SARS-CoV use hACE2 but show differences in disease manifestations in patients. SARS-CoV-2 infects the upper airways to a greater extent than SARS-CoV, and has also been associated with clinical manifestations such as anosmia, ageusia, thrombosis and endothelial damage in the lung vasculature, cardiac and neurological disease, and a multisystem inflammatory disease in children and adolescents[1,9,10]. On the basis of these observations, we reasoned that SARS-CoV-2 infection of the K18-hACE2 mice might also show differences in pathogenesis. Here we demonstrate the use of K18-hACE2 mice for studies of COVID-19 disease and treatments.

Clinical and virological characterization

To assess the susceptibility of K18-hACE2 mice to SARS-CoV-2, we intranasally challenged male and female mice using inocula of 10^3, 10^4 and 10^5 plaque-forming units (PFU). We observed a dose-dependent increase in weight loss and mortality (Fig. 1a). At the 10^5 PFU inoculum, all mice succumbed, whereas all mice survived when challenged with 10^3 PFU. There was variable mortality when mice were inoculated with 10^4 PFU (2 out of 3 female mice and 3 out of 7 male mice survived). To understand the cause(s) of this morbidity and mortality better, we assessed the tissue distribution of infectious virus and viral genomic RNA at 2, 4 and 6 days post infection (dpi) in mice receiving 10^5 PFU of SARS-CoV-2. The predominant target organs were the lung at early time points and, variably, the brain at later time points. Virus replicated to high titres in lung tissue at 2 dpi and decreased at 4 and 6 dpi (Fig. 1b). In some but not all mice, brain titres gradually increased from 2 to 6 dpi. Variability in brain infection was also described in a recent study of K18-hACE2 mice infected with SARS-CoV-2[11]. Small amounts of infectious virus were detected in the kidney, small intestine and colon, perhaps signifying low level haematogenous dissemination (Fig. 1b). We also detected viral RNA in the heart, liver, spleen, kidney, intestine and colon (Extended Data Fig. 1a). These results demonstrate that SARS-CoV-2 infection of K18-hACE2 mice causes a dose-dependent lethal respiratory illness, with a subset of mice developing brain infection that also contributes to death.

Fig. 1: Clinical and pathological disease in K18-hACE2 mice infected with SARS-CoV-2.

figure1

a, Percentage of initial weight and survival of wild-type (WT) (n = 1 mouse) and K18-hACE2 mice infected with 10^3 (n = 3 mice), 10^4 (n = 10 mice), or 10^5 (n = 8 mice) PFU of SARS-CoV-2 per mouse (two independent experiments). P values determined by analysis of variance (ANOVA), two-tailed Student's t-tests without adjustments

(weight change) and log-rank (Mantel–Cox) tests (survival). Left, $P < 0.0001$ 10^3 vs 10^5 PFU inoculum; $P = 0.0842$ for 10^4 vs 10^5 PFU inoculum. NS, not significant. **b**, Infectious viral titres detected by plaque assay in different organs at 2, 4 and 6 dpi with 10^5 PFU SARS-CoV-2 (days 2, 4 $n = 4$ mice; day 6, $n = 8$ mice (brain) and $n = 4$ (other organs); three independent experiments). LOD, limit of detection. **c**–**j**, Nasal and sinus tissues were examined at days 2 (**c**–**f**) and 5 (**g**–**j**). Nucleocapsid protein immunostaining (**c**–**e**, **g**, **i**, **j**) and haematoxylin and eosin (H&E) stain (**f**, **h**). Data in **a** and **b** are mean ± s.e.m. **c**, Nucleocapsid protein immunostaining in olfactory epithelium (OE). **d**, Nucleocapsid protein immunostaining (brown) localized near the interface of olfactory epithelium and respiratory epithelium (RE). Subjacent to epithelium, nucleocapsid protein was occasionally detected in endothelial lining of vessels (left arrowhead) and Bowman's glands (right arrow) were occasionally detected. **e**, **f**, Maxillary sinus (MS) lining epithelium had extensive immunostaining for nucleocapsid protein (**e**, brown, arrows) with common sloughing and cellular debris (**f**, arrowheads). The lateral nasal glands (LNG) also had multifocal cellular and karyorrhectic debris (**f**, arrows). **g**, **h**, Olfactory epithelium at day 5 with nucleocapsid protein immunostaining (**g**, arrows) localized near interface with respiratory epithelium. At these sites, cellular sloughing and loss of cellularity (**h**, arrows) were seen. **i**, **j**, Strong immunostaining of nucleocapsid protein (arrows) was seen in tall olfactory epithelium cells with 'classic' morphology of sustentacular cells, along with the immunostain expanding to adjacent cells. Scale bars, 128 μm (**c**, **e**), 63 μm (**g**, **h**), 31 μm (**d**, **f**), 42 μm (**i**), 21 μm (**j**). Two sections of each tissue from 3–4 mice per group were evaluated.

Source data

Full size image

Extensive and progressive lung disease

In view of the early pulmonary virus replication, we stained lungs at 4 and 6 dpi for SARS-CoV-2 antigen. Using an inoculum of 10^5 PFU, we observed extensive and diffuse parenchymal localization of SARS-CoV-2 nucleocapsid protein at 4 dpi that was less intense by 6 dpi (Extended Data Fig. 1b). Uninfected tissues showed no nucleocapsid protein signal. Examination of haematoxylin and eosin-stained tissues revealed evidence of diffuse alveolar damage with progressive alveolar or interstitial lesions characterized by oedema, inflammation and focal cytomegaly in some alveolar lining cells (Extended Data Fig. 1c). We also found an accumulation of immune effector cells, including granulocytes and macrophages, evidence of cell death, haemorrhage, hyaline membranes, occasional vascular thrombi (Extended Data Fig. 1c) and rare syncytia. Pulmonary vascular thrombi are often observed in severe cases of human COVID-19[9]. These findings are summarized in Extended Data Fig. 1d.

We also surveyed liver, heart, spleen, kidney, small intestine and colon tissues for disease-associated changes (Extended Data Fig. 2). At 4 dpi, occasional vessels in the liver had evidence of fibrin thrombi adherent along the vascular wall (Extended Data Fig. 2a), suggestive of the coagulopathy observed in COVID-19 autopsies[12]. The other tissues examined showed no disease-specific changes. To further characterize the lung tissue responses to SARS-CoV-2 infection, we assessed the expression of several cytokines, chemokines and innate immune transcripts at 2, 4 and 6 dpi by quantitative PCR with reverse transcription (qRT–PCR). As shown in Extended Data Fig. 3a, there were significant increases in type I, II and III interferons, ISG-15, RIG-I, MDA5, IL-1β, IL-6, IL-8, IL-12, CCL-2, CCL-5, CCR7, CXCL-2, CXCL-9, CXCL-10 and TNF compared with uninfected lungs over the course of infection. Similar changes in the expression of pro-inflammatory molecules were observed in patients with COVID-19[13].

Inflammatory cell infiltration

To further investigate the factors that contribute to lung injury and virus clearance, we performed immunophenotyping of infiltrating cells at 4 and 6 dpi (Extended Data Fig. 3b–e). We observed a progressive increase in the numbers of macrophages, monocytes, neutrophils and CD4 and CD8 T cells (Extended Data Fig. 3e). Infiltrating inflammatory macrophages, monocytes and neutrophils may have both protective and pathogenic roles, on the basis of previous studies of SARS and Middle East respiratory syndrome (MERS)[14]. Virus-specific CD8 and CD4 T cells, which are required for optimal clearance of SARS-CoV-2, were detected in lung tissues at 6 dpi. These cells responded to pools of peptides representing the SARS-CoV-2 spike, nucleocapsid and membrane proteins to varying extents, as assessed by the expression of IFNγ and TNF (Extended Data Fig. 3c, d). Together, these results indicate that lung disease in K18-hACE2 mice shares features with severe COVID-19. Another characteristic of severe human COVID-19 is an early antibody response, consistent with plasmablast activation[13]. We detected serum-neutralizing antibodies as early as 6 dpi, consistent with such a response (Extended Data Fig. 3f).

Brain infection in some mice

Because infectious virus was detected in the brains of 5 out of 8 mice after 10^5 PFU intranasal inoculation, we immunostained tissues for viral nucleocapsid protein at 4 and 6 dpi. We observed no antigen staining at 4 dpi (4 out of 4 brains studied), but saw extensive staining at 6 dpi in several brain regions including the olfactory bulb, cerebral cortex, caudate/putamen, thalamus, hypothalamus and ventral striatum (2 out of 3 brains studied) (Extended Data Fig. 4a, Extended Data Table 1). Uninfected mice showed no nucleocapsid protein staining (3 out of 3 mice). Haematoxylin and eosin

staining showed cell death and thrombi, noted in the thalamus (Extended Data Fig. 4b, c) and foci of cell death were sometimes also detected adjacent to degenerative ependyma cells (Extended Data Fig. 4d). The thalamus is affected in many patients with COVID-19 with neurological disease[15]. Of note, although most of the affected areas are secondary or tertiary connections of the olfactory bulb, some—such as the area postrema and hypoglossal nucleus—are not directly connected. Similar results were observed in analyses of mice infected with SARS-CoV[16]. These results suggest an important role for olfactory bulb infection in spread to the brain in some mice but also indicate that virus may enter the central nervous system by other routes. Infection of the olfactory epithelium is expected to precede brain infection and could also contribute to the anosmia and ageusia observed in many patients[1], including some who were asymptomatic or mildly symptomatic.

Infection of the sinonasal epithelium

To assess virus replication in the upper respiratory tract after intranasal inoculation, we quantified viral RNA in nasal secretions by qRT–PCR at 3 dpi. SARS-CoV-2 genomic RNA (C_t = 21.5 ± 1.2, mean ± s.e.m.) was detected in secretions from 5 out of 7 mice, and 4 of these mice had evidence of subgenomic RNA (36.7 ± 1.1), consistent with active virus replication. Viral antigen was readily detected in both the respiratory and olfactory epithelium at 2 and 5 dpi. At 2 dpi, virus antigen was present at several sites, often at the interface of the olfactory and respiratory epithelium (Fig. 1c). Viral antigen was also detected in nerve bundles subjacent to the olfactory epithelium (Extended Data Fig. 4e) and occasionally in vascular endothelia (Fig. 1d, left arrow) and Bowman's glands (Fig. 1d, right arrow). At sites of antigen positivity in the olfactory epithelium and maxillary sinus, we observed cell death and cellular debris at 2 dpi (Fig. 1e, f, Extended Data Fig. 4f), which progressed to cell sloughing and loss of cellularity by 5 dpi (Fig. 1g, h). ACE2 has been detected in sustentacular cells in the olfactory epithelium[17], but not in olfactory sensory neurons, suggesting that these cells are a primary site of infection. Consistent with this, we detected SARS-CoV-2 antigen in sustentacular cells (Fig. 1i, j). Infection of sustentacular cells is not expected to result in spread to the olfactory bulb and its connections, but could still contribute to anosmia.

Anosmia in infected K18-hACE2 mice

To directly assess anosmia, we performed three sets of behavioural tests, all of which require a normal sense of smell, as described in the Methods. First, in the social scent-discrimination assays, male mice were exposed to bedding containing female or male dander in a 2-ml Eppendorf tube (Fig. 2a). Mice identify the tube visually, and then preferentially spend time with the female dander, if olfaction is normal. Because

female mice are not preferentially attracted to male dander[18], in a second experiment, female mice were exposed to bedding from their home cage ('familiar') and another, foreign cage ('novel') (Fig. 2d). Mice with normal olfaction preferentially explore the unfamiliar bedding. Third, we used a buried food test, in which mice are attracted to a food item that is hidden in the bedding that they were previously conditioned to detect (Fig. 2g). K18-hACE2 mice infected with SARS-CoV-2 performed worse than control mice in all of the tests so that at days 2 and 3 after infection, male mice spent less time in the vicinity of the female dander (Fig. 2c), female mice were not attracted to the foreign bedding (Fig. 2f) and male and female mice took longer to find buried food (Fig. 2h, i). At 2 and 3 dpi, brains were not infected (Fig. 1b, Extended Data Fig. 4a) and mice exhibited minimal weight loss (Fig. 2b, e). In addition, mobility was largely normal as there were no significant differences in the amount of time spent in exploring the tube containing male dander (Fig. 2c) or familiar bedding (Fig. 2f), when infected or uninfected mice were compared. Preference indices were calculated for the social scent-discrimination assays and confirmed hyposmia or anosmia (Extended Data Fig. 5). Together, these results suggest that hyposmia or anosmia at these times points is primarily caused by infection of the nasal epithelium and is not a consequence of generalized malaise or the spread of virus to the brain.

Fig. 2: SARS-CoV-2 infection causes anosmia in K18-hACE2 mice.

figure2

Male and female mice were treated with PBS (uninfected) or 10^5 PFU of SARS-CoV-2 intranasally. **a**, **d**, Schematic showing social scent-discrimination tests. **b**, **e**, Weights were recorded daily. **c**, Each male mouse was allowed 5 min in the cage with scents from male or female mice (bedding from male or female cages) placed at two corners

of the cage. The time that male mice spent sniffing male or female scents was recorded. *P* values were determined by two-way ANOVA. **f**, Female mice were exposed to their own bedding (familiar) or bedding from another cage (novel). The time that female mice spent exploring each bedding was recorded. *P* values were determined by two-way ANOVA. In some experiments, mice were pre-treated with undiluted convalescent plasma (CP; results on right of vertical line) (**c**, **f**). **g**–**i**, Buried food test (schematic shown in **g**). Food was buried under the bedding and each mouse was allowed 4 min in the cage to search for the food. **h**, The dotted line denotes the time limit of 4 min. *P* values were determined by two-tailed Mann–Whitney *U*-test. **i**, The percentage of mice that found the buried food within 4 min is shown. *P* values were determined by χ^2 Fisher's exact test. In some experiments, mice were pre-treated with undiluted convalescent plasma (denoted by blue bars in **h**, **i**). Male mice: uninfected: $n = 15$ mice; infected: $n = 10$ mice. Female mice: uninfected and infected: $n = 8$ mice each; infected/plasma-treated: $n = 7$ mice; analysed in four independent experiments. Data are mean ± s.e.m. Preference indices for the social scent-discrimination assays are shown in Extended Data Fig. 5.

Source data

Full size image

Human convalescent plasma therapy

Convalescent plasma from survivors of COVID-19 is being tested as a treatment in patients with clinical COVID-19[19]. Studies have shown positive effects of convalescent plasma on outcomes in several infectious diseases, if titres are sufficiently high and if the convalescent plasma is administered early in the course of disease[20]. To assess the effect of convalescent plasma on outcomes in K18-hACE2 mice infected with SARS-CoV-2, we administered undiluted and diluted human high-titre plasma (original neutralizing titre 1:1,480) intravenously 12 h before infection. Undiluted plasma administered 12 h before infection protected mice from death but not mild weight loss and reduced lung tissue titres, whereas convalescent plasma diluted 1:3 provided partial protection (Fig. 3a, b). Pre-treatment with undiluted and diluted convalescent plasma markedly inhibited the spread of infection to the brain (Fig. 3b) even in mice that died, supporting the conclusion that a lethal lung infection was the cause of death. On examination of lung tissues, levels of viral antigen and pathological changes were greatly decreased by convalescent plasma treatment (Extended Data Fig. 6a). Delivery of undiluted plasma at 24 hours after infection was partially protective (Extended Data Fig. 6b). Notably, convalescent plasma did not diminish infection of sinonasal tissues (Fig. 3c). Finally, to assess the effects of convalescent plasma treatment on SARS-CoV-2-induced anosmia, we treated infected mice with plasma at 12 h before infection and assessed mice for olfactory loss as

described above (Fig. 2). Even though mice had minimal signs of clinical disease after convalescent plasma treatment, by day 4 all mice exhibited profound anosmia (Fig. 2c, f, h, i, Extended Data Fig. 5).

Fig. 3: Effects of convalescent plasma on outcomes.

figure3

a, Percentage of initial weight (left) and survival (right) of K18-hACE2 mice receiving control serum (n = 4 mice, black), undiluted (n = 4 mice, blue), 1:3 dilution (n = 4 mice, red) and 1:9 dilution (n = 3 mice, purple) human convalescent plasma (CP) at 24 h before challenge with 10^5 PFU of SARS-CoV-2. Data are from two independent experiments. P values were determined by ANOVA, two-tailed Student's t-tests without adjustments (weight change), and log-rank (Mantel–Cox) tests (survival). **b**, Viral titres of plasma-treated mice in the lungs (left) and brains (right) at 2 and 5 dpi. n = 3 mice, except n = 2 mice at 2 dpi, 1:9 dilution; 1 independent experiment. LOD, limit of detection. *P = 0.0455, control vs undiluted CP; *P = 0.0443 control vs 1:3 diluted CP, two-tailed Student's t-tests without adjustments. **c**, Scores of nucleocapsid protein immunostaining in plasma-treated mice in the nasal cavity at 2 dpi (top) and 5 dpi (bottom). 0, none; 1, rare <1%; 2, multifocal or localized <33% cells; 3, multifocal, coalescing, 33–66%; 4, extensive >67%. Two sections of each sinonasal cavity from three mice per group were evaluated. Data are mean ± s.e.m. VMO, vomeronasal organ.

Source data

Full size image

Discussion

K18-hACE2 mice infected with SARS-CoV-2 developed dose-dependent lung disease with features that are similar to severe human COVID-19, including diffuse alveolar damage, inflammatory cell infiltration, tissue injury, lung vascular damage and death. hACE2 transgenic mice driven by other promoters have also been developed, with variable outcomes observed after SARS-CoV-2 infection[21,22]. Notably, K18-hACE2 mice also support SARS-CoV-2 replication in the sinonasal epithelium and develop anosmia, a common feature of human disease. Furthermore, the uniformly fatal disease outcome with a 10^5 inoculum was prevented by pre-treatment with convalescent plasma from a patient with COVID-19. Notably, pre-treatment with plasma did not prevent initial infection of the lungs, damage to nasal respiratory and olfactory epithelia, or anosmia. We observed greater anosmia in female mice than in male mice in the presence or absence of convalescent plasma. Similarly, anosmia is more common in women than in men with COVID-19[23,24,25]. SARS-CoV-2 infection of K18-hACE2 mice treated with convalescent plasma or, potentially, neutralizing monoclonal antibodies will be especially useful for studies of anosmia because mice do not succumb to the infection but, similar to many infected patients with mild disease, have olfactory loss as a major manifestation[1]. Anosmia appears to result from initial infection and damage to supporting sustentacular cells rather than to olfactory sensory neurons, which suggests that the resulting inflammatory milieu, rather than direct neuronal damage, is disease-causing. Therefore, we postulate that the observed

anosmia has at least two possible, non-exclusionary explanations. First, the infection of sustentacular cells may disrupt signalling from olfactory sensory neurons to the olfactory bulb. For example, sustentacular cells provide support to olfactory sensory neurons by maintaining ion balance[26], which may be altered either directly by infection to sustentacular cells or indirectly via disorganization of the olfactory epithelium, leading to loss of cilia from olfactory sensory neurons and deficient signal transduction[27,28]. The second possibility is collateral damage to olfactory sensory neurons resulting from the secretion of pro-inflammatory cytokines by sustentacular cells infected with SARS-CoV-2. These cells have been reported to secrete cytokines and chemokines such as TNF, IL-1β, IL-1α and CXCL2 in patients with chronic rhinosinusitis and COVID-19[29,30]. Together, K18-hACE2 mice infected with SARS-CoV-2, readily available from Jackson Laboratories, recapitulate many of the findings observed in patients with COVID-19 and provide a useful model to study pathogenesis and to evaluate interventions.

Methods

No statistical methods were used to predetermine sample size. The experiments were not randomized, and investigators were not blinded to allocation during experiments and outcome assessment unless stated otherwise.

Human subject approval

Written informed consent was obtained from subjects to obtain plasma for participation in this study. The study was approved by the Institutional Review Board of the University of Iowa (IRB (202003554 and 201402735).

Mice, cells and virus

Transgenic mice expressing hACE2 were previously reported[4]. hACE2 is expressed under control of the cytokeratin 18 (*KRT18*) promoter. Although the *KRT18* promoter predominantly directs gene expression to multiple epithelia-lined tissues[8], it also directs reporter gene expression in neurons[31]. The mice (7–8 weeks old, male or female) used in these studies were obtained from the Jackson Laboratory (034860-B6.Cg-Tg(K18-ACE2)2Prlman/J) and are congenic on the C57BL/6 background. Non-transgenic C57BL/6 mice were used as controls in some experiments. All protocols were approved by the Institutional Animal Care and Use Committee of the University of Iowa. The 2019n-CoV/USA-WA1/2019 strain of SARS-CoV-2 (accession number: MT985325.1) used in these studies was passaged on Calu-3 2B4 cells (ATCC HTB-55). Calu-3 2B4 cells were grown in MEM (GIBCO) supplemented

with 20% FBS. Vero E6 cells (ATCC CRL-1586) were grown in DMEM (GIBCO) supplemented with 10% fetal bovine serum (FBS).

Infection of mice

Mice were lightly anaesthetized with ketamine/xylazine and infected intranasally with the indicated amount of SARS-CoV-2 in a total volume of 50 µl DMEM. Mouse weight and health were monitored daily. All experiments with SARS-CoV-2 were performed in a Biosafety Level 3 (BSL3) Laboratory at the University of Iowa.

Nasal lavage

Mice were sedated with ketamine/xylazine (100 mg kg^{-1} ketamine/12.5 mg kg^{-1} xylazine). One-hundred microliters of carbachol (100 µg ml^{-1}) was administered intraperitoneally and after approximately 15 min, nasal secretions were recovered. Secretions of 20 µl were recovered per mouse. Nasal secretions were immediately added to 500 µl Trizol, mixed and stored at −80 °C until RNA was isolated.

Viral titre by plaque assay

Virus or tissue homogenate supernatants were serially diluted in DMEM. 12-well plates of VeroE6 cells were inoculated at 37 °C in 5% CO_2 for 1 h and gently rocked every 15 min. After removing the inocula, plates were overlaid with 0.6% agarose containing 2% FBS. After 3 days, overlays were removed, and plaques were visualized by staining with 0.1% crystal violet. Viral titres were quantified as PFU per ml tissue.

Flow cytometry

The following monoclonal antibodies were used as described by manufacturer at a dilution of 1:200: anti-mouse CD3e-BV421 (clone 145-2C11, 562600), anti-mouse CD16/32 (clone 93, cat. no.:101302), anti-mouse CD4-PercP (clone RM4-5, 550954), anti-mouse CD8-APC-Cy7 (clone 53-6.7, 100714), anti-mouse CD220-APC (clone RA3-6B2, 553092), anti-mouse Ly6C-PerCP (clone HK1.4, 128028), anti-mouse Ly6G-FITC (clone 1A8, 127606), anti-mouse CD11b-BV510 (clone M1/70, 101263), anti-mouse CD11c-BV421 (clone N418, 117343), anti-mouse CD64-PE-Cy7 (X54-5/7.1, 139314), Biolegend; anti-mouse CD103-APC (clone 2E7, 17-1031-80), anti-mouse TNF-FITC (clone MP6-XT22, 11-7321-82), anti-mouse IFNγ-APC (clone XMG1.2, 25-7311-82), eBioscience. For intracellular cytokine staining (ICS), lymphocytes were cultured in 96-well dishes at 37 °C for 5–6 h in the presence of 2 µM peptide pool and brefeldin A (BD Biosciences). Cells were then labelled for cell-

surface markers, fixed/permeabilized with Cytofix/Cytoperm Solution (BD Biosciences), and labelled with anti-IFNγ and anti-TNF antibody. All flow cytometry data were acquired using a BD FACSVerse and analysed with FlowJo software.

Histology and immunohistochemistry

Mice were anaesthetized and perfused transcardially with PBS, followed by zinc formalin. Lungs were fixed in zinc formalin. For routine histology, tissue sections (approximately 4 μm each) were stained with H&E. The following criteria were used for scoring oedema, hyaline membrane formation and necrotic cellular debris: 0, none; 1, uncommon detection in <5% lung fields (200×); 2, detectable in up to 33% of lung fields; 3, detectable in up to 33–66% of lung fields; 4, detectable in >66% of lung fields. For scoring neutrophil infiltration: 0, within normal limits; 1, scattered PMNs sequestered in septa; 2, no. 1 plus solitary PMNs extravasated in airspaces; 3, no. 2 plus small aggregates in vessel and airspaces. For scoring mononuclear infiltrates, thrombosis and haemorrhage: 0, none; 1, uncommon detection in <5% lung fields (200×); 2, detectable in up to 33% of lung fields; 3, detectable in up to 33–66% of lung fields; 4, detectable in >66% of lung fields.

For SARS-CoV-2 antigen detection, slides were incubated with blocking reagent (10% normal goat serum × 30 min) followed by rabbit monoclonal antibody against SARS-CoV-2 nucleocapsid protein (1:20,000 dilution × 60 min, 40143-R019, Sino Biological), then incubated with Rabbit Envision (Dako) and diaminobenzidine (Dako) as chromogen. Tissues were examined and scored in a post-examination method of masking by a boarded experimental pathologist[32]. Ordinal scores for lesion parameters were assigned using the following tiers: 0, within expected limits; 1, uncommon, <5%; 2, detectable in 5–33%; 3, detectable in 34–66% and 4, detectable in >66% of lung fields (200× objective magnification).

Human convalescent plasma

High-titre convalescent plasma was collected with subject consent under an IRB (202003554)-approved protocol that allows use of samples for research. The convalescent plasma donor was a 58-year-old female patient who had molecularly confirmed COVID-19 more than 4 weeks before their donation. After the donation, she tested positive for HLA antibodies so the plasma was not eligible for administration to patients and was diverted to research. Antibody testing (EUROIMMUN SARS-COV-2 ELISA (IgG)) performed on this donor was 9.8, well above the cut-off value of 1.1 for a positive result. Neutralization titre using a luciferase-expressing SARS-CoV-2 spike protein pseudovirus assay showed that the neutralization half-maximal inhibitory concentration (IC_{50}) titre was 1:1,480. Control plasma was obtained from an expired plasma unit collected before COVID-19 spread

in our area and this product was collected under an IRB (201402735) approved protocol that allows for research use of these products. Convalescent and control plasma were administered intravenously at the indicated times.

RNA isolation and qRT–PCR

Total RNA was extracted from tissues (or nasal lavage) using Trizol (Invitrogen) according to the manufacturer's protocol. After a DNase treatment step 200 ng of total RNA was used as a template for first strand cDNA. The resulting cDNA was subjected to amplification of selected genes by real-time quantitative PCR using Power SYBR Green PCR Master Mix (Applied Biosystems). Average values from duplicates of each gene were used to calculate the relative abundance of transcripts normalized to HPRT and presented as $2^{-\Delta Ct}$. The primers used for cytokines and chemokines were previously reported[33]. For detection of viral genomes, the following primers were used to amplify the genomic RNA for the nucleocapsid protein: 2019-nCoV_N1-F: 5′-GACCCCAAAATCAGCGAAAT-3′; 2019-nCoV_N1-R: 5′-TCTGGTTACTGCCAGTTGAATCTG-3′. The following primers were used to amplify the subgenomic RNA for the E protein: F: 5′-CGATCTCTTGTAGATCTGTTCTC-3′; R: 5′-ATATTGCAGCAGTACGCACACA-3′.

Pseudovirus neutralizing antibody assay

To determine neutralization activity of patient and mouse plasma, we used a luciferase reporter-based pseudovirus neutralization assay, which has a nonreplicative vesicular stomatitis virus backbone coated with the SARS-CoV-2 spike protein. Sera from K18-hACE2 mice infected with SARS-CoV-2 were collected at the indicated time points and heat inactivated by incubation at 56 °C for 30 min. Human convalescent plasma or mouse sera were serially diluted twofold in 96-well plates and incubated with the same volume of VSV pseudotyped with SARS-CoV-2 spike protein at 37 °C for 1 h. Samples were placed onto Vero E6 cells and incubated at 37 °C for 1 h to allow virus binding. After removal of the initial inoculum, cells were incubated for 24 h. Neutralization was measured with a luciferase assay kit (Promega) and plotted relative to the value for control wells.

Social scent-discrimination tests

For male mice, the social scent-discrimination task was designed to assess the capability of mice to discriminate social scents as previously described[34]. Two identical tubes were separately sealed in a Ziploc bag in a large cage (used for housing rats (31 cm × 26 cm × 22 cm)) containing bedding from female mice and from the home (male) cage overnight. Next, mice infected with SARS-CoV-2 or treated with PBS were released in a fresh cage containing the tubes placed at two different corners.

Sniffing latency (sniffing and exploring the tubes) was calculated within a 5-min period. One trial on each mouse was performed each day with the position of tubes changed daily. Data were recorded in the BSL3 facility from a distance of approximately 1 m.

For female mice, two identical 3-cm dishes were separately sealed with mouse dander from the home cage ('familiar') and another cage ('novel') overnight. The dander-containing dishes were placed at two corners of a fresh cage. Mice infected with SARS-CoV-2 or treated with PBS mice were released into the cage and sniffing latency was calculated and recorded as described for male mice. One trial on each mouse was performed each day with the position of the dishes changed daily.

We calculated a preference index for each mouse, to compensate for any differences due to decreased mobility or malaise. The preference index for male mice is calculated as: (female time − male time)/female time + male time), whereas for female mice the preference index is: (novel scent time − familiar scent time)/(novel scent time + familiar scent time). Data were analysed using Mann–Whitney *U*-tests.

Buried food test

Evaluation of odour detection was carried out by a buried food test as previously described[34]. In brief, food palatability was confirmed before initiation of the experiments. SARS-CoV-2-infected or PBS-treated mice were sensitized to the food for 10–15 min on the day of the experiment. The food pellet was then buried approximately 1 cm below the surface of bedding in a fresh cage. One trial per infected or uninfected mouse per day was performed with the position of the food changed on a daily basis. The latency to locate and uncover the buried food pellet was recorded with a stopwatch. Mice were allowed to explore the cage for 4 min and if they could not locate the food, the time was recorded as 4 min. The experiment was repeated daily.

Statistical analysis

Differences in mean values between groups were analysed by ANOVA and Student's *t*-tests and differences in survival were analysed by log-rank (Mantel–Cox) tests using GraphPad Prism 8. All results are expressed as mean ± s.e.m. and were corrected for multiple comparisons. For behavioural studies, data from the social scent-discrimination tests, and buried food test were analysed by two-way ANOVA and nonparametric (Mann–Whitney *U*-tests) tests, respectively. $P < 0.05$ were considered statistically significant. $^{*}P \leq 0.05$, $^{**}P \leq 0.005$, $^{***}P \leq 0.0005$, $^{****}P \leq 0.0001$.

Reporting summary

Further information on research design is available in the Nature Research Reporting Summary linked to this paper.

Data availability

The data supporting the findings of this study are documented within the paper and are available from the corresponding authors upon request. Source data are provided with this paper.

References

1. 1.

   Spinato, G. et al. Alterations in smell or taste in mildly symptomatic outpatients with SARS-CoV-2 infection. *J. Am. Med. Assoc*. **323**, 2089–2090 (2020).

   CAS Article Google Scholar

2. 2.

   Williamson, E. J. et al. Factors associated with COVID-19-related death using OpenSAFELY. *Nature* **584**, 430–436 (2020).

   CAS Article Google Scholar

3. 3.

   Muñoz-Fontela, C. et al. Animal models for COVID-19. *Nature* **586**, 509–515 (2020).

   ADS Article Google Scholar

4. 4.

   McCray, P. B., Jr et al. Lethal infection in K18-hACE2 mice infected with SARS-CoV. *J. Virol*. **81**, 813–821 (2006).

   Article Google Scholar

5. 5.

   Zhou, P. et al. A pneumonia outbreak associated with a new coronavirus of probable bat origin. *Nature* **579**, 270–273 (2020).

ADS CAS Article Google Scholar

6. 6.

Tseng, C. T. et al. SARS coronavirus infection of mice transgenic for the human angiotensin-converting enzyme 2 (hACE2) virus receptor. *J. Virol*. **81**, 1162–1173 (2006).

Article Google Scholar

7. 7.

Yang, X. H. et al. Mice transgenic for human angiotensin-converting enzyme 2 provide a model for SARS coronavirus infection. *Comp. Med*. **57**, 450–459 (2007).

CAS PubMed Google Scholar

8. 8.

Chow, Y. H. et al. Development of an epithelium-specific expression cassette with human DNA regulatory elements for transgene expression in lung airways. *Proc. Natl Acad. Sci. USA* **94**, 14695–14700 (1997).

ADS CAS Article Google Scholar

9. 9.

Ackermann, M. et al. Pulmonary vascular endothelialitis, thrombosis, and angiogenesis in Covid-19. *N. Engl. J. Med*. **383**, 120–128 (2020).

CAS Article Google Scholar

10. 10.

Feldstein, L. R. et al. Multisystem inflammatory syndrome in U.S. children and adolescents. *N. Engl. J. Med*. **383**, 334–346 (2020).

CAS Article Google Scholar

11. 11.

Winkler, E. S. et al. SARS-CoV-2 infection of human ACE2-transgenic mice causes severe lung inflammation and impaired function. *Nat. Immunol*. **21**, 1327–

1335 (2020).

CAS Article Google Scholar

12. 12.

Bradley, B. T. et al. Histopathology and ultrastructural findings of fatal COVID-19 infections in Washington State: a case series. *Lancet* **396**, 320–332 (2020).

CAS Article Google Scholar

13. 13.

Mathew, D. et al. Deep immune profiling of COVID-19 patients reveals distinct immunotypes with therapeutic implications. *Science* **369**, eabc8511 (2020).

CAS Article Google Scholar

14. 14.

Channappanavar, R. et al. Dysregulated type I interferon and inflammatory monocyte-macrophage responses cause lethal pneumonia in SARS-CoV-infected mice. *Cell Host Microbe* **19**, 181–193 (2016).

CAS Article Google Scholar

15. 15.

Poyiadji, N. et al. COVID-19-associated acute hemorrhagic necrotizing encephalopathy: imaging features. *Radiology* **296**, E119–E120 (2020).

Article Google Scholar

16. 16.

Netland, J., Meyerholz, D. K., Moore, S., Cassell, M. & Perlman, S. Severe acute respiratory syndrome coronavirus infection causes neuronal death in the absence of encephalitis in mice transgenic for human ACE2. *J. Virol*. **82**, 7264–7275 (2008).

CAS Article Google Scholar

17. 17.

Bilinska, K., Jakubowska, P., Von Bartheld, C. S. & Butowt, R. Expression of the SARS-CoV-2 entry proteins, ACE2 and TMPRSS2, in cells of the olfactory epithelium: identification of cell types and trends with age. *ACS Chem. Neurosci*. **11**, 1555–1562 (2020).

CAS Article Google Scholar

18. 18.

Dey, S. et al. Cyclic regulation of sensory perception by a female hormone alters behavior. *Cell* **161**, 1334–1344 (2015).

CAS Article Google Scholar

19. 19.

Joyner, M. et al. Early safety indicators of COVID-19 convalescent plasma in 5,000 patients. *J. Clin. Invest*. https://doi.org/10.1172/JCI140200 (2020).

20. 20.

Casadevall, A., Joyner, M. J. & Pirofski, L. A. SARS-CoV-2 viral load and antibody responses: the case for convalescent plasma therapy. *J. Clin. Invest*. **130**, 5112–5114 (2020).

CAS Article Google Scholar

21. 21.

Bao, L. et al. The pathogenicity of SARS-CoV-2 in hACE2 transgenic mice. *Nature* **583**, 830–833 (2020).

ADS CAS Article Google Scholar

22. 22.

Jiang, R. D. et al. Pathogenesis of SARS-CoV-2 in transgenic mice expressing human angiotensin-converting enzyme 2. *Cell* **182**, 50–58 (2020).

CAS Article Google Scholar

23. 23.

Makaronidis, J. et al. Seroprevalence of SARS-CoV-2 antibodies in people with an acute loss in their sense of smell and/or taste in a community-based population in London, UK: an observational cohort study. *PLoS Med*. **17**, e1003358 (2020).

CAS Article Google Scholar

24. 24.

Giacomelli, A. et al. Self-reported olfactory and taste disorders in patients with severe acute respiratory coronavirus 2 infection: a cross-sectional study. *Clin. Infect. Dis*. **71**, 889–890 (2020).

CAS Article Google Scholar

25. 25.

Lechien, J. R. et al. Olfactory and gustatory dysfunctions as a clinical presentation of mild-to-moderate forms of the coronavirus disease (COVID-19): a multicenter European study. *Eur. Arch. Otorhinolaryngol*. **277**, 2251–2261 (2020).

Article Google Scholar

26. 26.

Vogalis, F., Hegg, C. C. & Lucero, M. T. Ionic conductances in sustentacular cells of the mouse olfactory epithelium. *J. Physiol. (Lond.)* **562**, 785–799 (2005).

CAS Article Google Scholar

27. 27.

Bryche, B. et al. Massive transient damage of the olfactory epithelium associated with infection of sustentacular cells by SARS-CoV-2 in golden Syrian hamsters. *Brain Behav. Immun*. **89**, 579–586 (2020).

CAS Article Google Scholar

28. 28.

Zhang, A. J. et al. SARS-CoV-2 infects and damages the mature and immature olfactory sensory neurons of hamsters. *Clin. Infect. Dis*. https://doi.org/10.1093/cid/ciaa995 (2020).

29. 29.

Imamura, F. & Hasegawa-Ishii, S. Environmental toxicants-induced immune responses in the olfactory mucosa. *Front. Immunol*. **7**, 475 (2016).

Article Google Scholar

30. 30.

Torabi, A. et al. Proinflammatory cytokines in the olfactory mucosa result in COVID-19 induced anosmia. *ACS Chem. Neurosci*. **11**, 1909–1913 (2020).

CAS Article Google Scholar

31. 31.

Chow, Y. H. et al. Targeting transgene expression to airway epithelia and submucosal glands, prominent sites of human CFTR expression. *Mol. Ther*. **2**, 359–367 (2000).

CAS Article Google Scholar

32. 32.

Meyerholz, D. K. & Beck, A. P. Principles and approaches for reproducible scoring of tissue stains in research. *Lab. Invest*. **98**, 844–855 (2018).

Article Google Scholar

33. 33.

Li, K. et al. Middle East respiratory syndrome coronavirus causes multiple organ damage and lethal disease in mice transgenic for human dipeptidyl peptidase 4. *J. Infect. Dis*. **213**, 712–722 (2016).

CAS Article Google Scholar

34. 34.

Yang, M. & Crawley, J. N. Simple behavioral assessment of mouse olfaction. *Curr. Protoc. Neurosci*. **Chapter 8**, Unit 8.24 (2009)

PubMed Google Scholar

Download references

Acknowledgements

We thank M. Moye-Rowley for help with the artwork. This work is supported in part by grants from the US National Institutes of Health (NIH) (P01 AI060699 (S.P., P.B.M.) and RO1 AI129269 (S.P.)); and the Pathology Core, which is partially supported by the Center for Gene Therapy for Cystic Fibrosis (NIH grant P30 DK-54759), and the Cystic Fibrosis Foundation. P.B.M. is supported by the Roy J. Carver Charitable Trust.

Author information

Author notes

1. These authors contributed equally: Jian Zheng, Lok-Yin Roy Wong, Kun Li, Abhishek Kumar Verma

Affiliations

1. Department of Microbiology and Immunology, University of Iowa, Iowa City, IA, USA

   Jian Zheng, Lok-Yin Roy Wong, Abhishek Kumar Verma, Paul B. McCray Jr & Stanley Perlman

2. Department of Pediatrics, University of Iowa, Iowa City, IA, USA

   Kun Li, Miguel E. Ortiz, Christine Wohlford-Lenane, Paul B. McCray Jr & Stanley Perlman

3. Department of Pathology, University of Iowa, Iowa City, IA, USA

   Mariah R. Leidinger, C. Michael Knudson & David K. Meyerholz

Authors

1. Jian Zheng
   View author publications

   You can also search for this author in PubMed Google Scholar

2. Lok-Yin Roy Wong
   View author publications

You can also search for this author in PubMed Google Scholar

3. Kun Li
View author publications

You can also search for this author in PubMed Google Scholar

4. Abhishek Kumar Verma
View author publications

You can also search for this author in PubMed Google Scholar

5. Miguel E. Ortiz
View author publications

You can also search for this author in PubMed Google Scholar

6. Christine Wohlford-Lenane
View author publications

You can also search for this author in PubMed Google Scholar

7. Mariah R. Leidinger
View author publications

You can also search for this author in PubMed Google Scholar

8. C. Michael Knudson
View author publications

You can also search for this author in PubMed Google Scholar

9. David K. Meyerholz
View author publications

You can also search for this author in PubMed Google Scholar

10. Paul B. McCray Jr
View author publications

You can also search for this author in PubMed Google Scholar

11. Stanley Perlman
View author publications

You can also search for this author in PubMed Google Scholar

Contributions

Conceptualization and writing of the original draft: P.B.M., S.P. Data curation: A.K.V. Formal analysis: J.Z., L.-Y.R.W., K.L., M.E.O., A.K.V., D.K.M., P.B.M. and S.P. Investigation: J.Z., L.-Y.R.W., K.L., M.E.O., C.W.-L., A.K.V., C.M.K., D.K.M., P.B.M. and S.P. Visualization: A.K.V., M.R.L., D.K.M. Resources: D.K.M., P.B.M. and S.P. Writing, reviewing and editing: J.Z., L.-Y.R.W., S.P. and P.B.M.

Corresponding authors

Correspondence to Paul B. McCray Jr or Stanley Perlman.

Ethics declarations

Competing interests

The authors declare no competing interests.

Additional information

Peer review information *Nature* thanks Dan Barouch, Linda J. Saif, Gonzalo Otazu, and the other, anonymous, reviewer(s) for their contribution to the peer review of this work. Peer reviewer reports are available.

Extended data figures and tables

Extended Data Fig. 1 Clinical and pathological disease in K18-hACE2 mice infected with SARs-CoV-2.

Mice were infected intranasally with 10^5 PFU of SARS-CoV-2. **a**, Viral RNA detected by qPCR targeting viral nucleocapsid gene with normalization to *Hprt* for the indicated organs at 2, 4 and 6 dpi (10^3, $n = 4$; 10^4, $n = 4$; 10^5, $n = 6$, each organ was collected from an individual mouse). **b**, Lungs from uninfected ($n = 3$), and infected (4 dpi ($n = 4$) and 6 dpi ($n = 3$)) mice were immunostained to detect SARS-CoV-2 nucleocapsid protein. Scale bar, 701 µm. **c**, Infected lungs exhibited evidence of airway oedema (asterisks, bottom middle panel), alveolar hyaline membranes, vascular thrombosis (top inset and arrow, bottom right panel), dying cells with pyknotic to karyorrhectic nuclei, and proliferative alveolar epithelium (arrowhead and lower inset,

bottom right panel, arrows). Scale bar, 701 and 70 μm (top and bottom, respectively), H&E stain. **d**, Summary of lung lesion scoring, as described in Methods (uninfected, $n = 3$; day 4, $n = 4$; day 6, $n = 3$, each brain was collected from an individual mouse). Two sections of each lung from 3–4 mice per group were evaluated. Data in **a**, **d** are representative of three independent experiments. Data are mean ± s.e.m. Source data

Extended Data Fig. 2 Histological analysis of extrapulmonary tissue.

Mice were killed at 0, 4 and 6 dpi with 10^5 PFU of SARS-CoV-2 and tissues were prepared for histological examination. **a**–**e**, Liver (**a**), spleen (**b**), kidney (**c**), small intestine (**d**) and colon (**e**) were studied. Pathological changes were minor and only observed in the liver. In the liver, all mice had some blood vessels filled with clear space or aggregates variably composed of erythrocytes or platelets (insets). Rare vessels had evidence of eosinophilic fibrillar material adherent along the vascular wall consistent with fibrin thrombi (**a**, arrows, inset, middle). Scale bars, 110 μm (**a**, **c**–**e**) and 221 μm (**b**), H&E stain. Two sections of each organ from 3–4 mice per group were evaluated.

Extended Data Fig. 3 Inflammatory mediators and immune effector cells in infected lungs.

a, Cytokine and chemokine transcripts were measured by qRT–PCR after isolation of RNA from the lungs of K18-hACE2 mice infected with 10^5 PFU of SARS-CoV-2 (mock and 6 dpi, $n = 3$; 2 and 4 dpi, $n = 4$, each lung was collected from an individual mouse); one independent experiment. Statistical significance compared to results obtained at 0 dpi. *P* values were determined by two-tailed Student's *t*-tests without adjustments. **b**, Gating strategy for identification of immune cells in lungs is shown. **c**, Representative FACS plot of $IFN\gamma^+TNF^+$ CD8 and CD4 T cells (as gated in **b**) after stimulation with indicated peptide pools in the lungs of K18-hACE2 mice infected with10^5 PFU of SARS-CoV-2. **d**, Summary data are shown ($n = 3$ mice per time point). Data are representative of two independent experiments. **e**, Quantification of immune cells (as gated in **b**) in the lungs ($n = 3$ for uninfected group; $n = 4$ for 4 and 6 dpi, each lung was collected from an individual mouse). Data are representative of two independent experiments. **f**, Sera were collected from infected mice at the indicated time points and IC_{50} values were determined by neutralization of SARS-CoV-2 pseudoviruses expressing luciferase ($n = 4$, days 0, 2, 4, 6; $n = 7$, day 13, 2 independent experiments). Data are mean ± s.e.m. Source data

Extended Data Fig. 4 Brain and nasal cavity infection in SARS-CoV-2 infected K18-hACE2 mice.

a, Brains from uninfected and infected (10^5 PFU of SARS-CoV-2) mice were immunostained to detect SARS-CoV-2 nucleocapsid protein. **b**, **c**, Several sites were characterized by cellular and karyorrhectic nuclear debris (**b**, arrows). Thrombi were detected, seen here in thalamus (**c**, arrow and inset). Scale bar, 17 µm. **d**, Ependyma (arrow) at 6 dpi had focal denudation and degeneration of ependymal cells (arrowheads) overlying focal region of cellular and karyorrhectic nuclei debris (asterisks). **e**, Nerve bundles (NB) subjacent to olfactory epithelium had evidence of punctate to linear immunostaining (brown, arrows). **f**, Sites of nucleocapsid protein localization at interface of olfactory epithelium and respiratory epithelium at 2 dpi (see Fig. 1d) had evidence of cell death and cellular debris (arrows). **g**, Olfactory epithelium with sustentacular cell immunostaining for nucleocapsid protein. Scale bar, 1.3 mm (**a**), 65 µm (**b**, **c**, **e**–**g**) and 130 µm (**d**). Two sections of each tissue from 3–4 mice per group were evaluated.

Extended Data Fig. 5 Preference indices for social scent-discrimination assays.

Preferences indices were calculated as described in Methods for each mouse shown in Fig. 2. The preference index was calculated as time spent with preferred or non-preferred scent: (preferred – non-preferred)/(preferred + non preferred). **a**, For male mice, preferred scent = female dander; non-preferred = male dander (uninfected: $n = 15$ mice, other groups: $n = 10$ mice). **b**, For female mice, preferred scent = novel scent; non-preferred = familiar scent (uninfected and infected alone groups: $n = 8$ mice each; infected/plasma-treated groups: $n = 7$ mice). P values were determined by two-tailed Mann–Whitney U-tests. Data are mean ± s.e.m. Source data

Extended Data Fig. 6 Effects of convalescent plasma delivered 6 h before or 24 h after infection.

a, Immunostaining of nucleocapsid protein in the lungs of mice treated with control plasma (healthy donor) or convalescent plasma at 2 and 5 dpi with 10^5 PFU SARS-CoV-2. Scale bars, 800 µm (top) and 160 µm (bottom). Two sections of each lung from three mice per group were evaluated. Representative images are shown. **b**, Percentage of initial weight (left), and survival (right) of K18-hACE2 mice receiving control plasma ($n = 2$) or undiluted convalescent plasma ($n = 4$) at 24 h after challenge with 10^5 PFU of SARS-CoV-2. Data are mean ± s.e.m. and are representative of one independent experiment. P values were determined by ANOVA, two-tailed Student's t-tests without adjustments (weights) and log-rank (Mantel–Cox) tests (survival). Source data

Extended Data Table 1 Distribution of SARS-CoV2 antigen in brain
Full size table

Supplementary information

Reporting Summary

Peer Review File

Source data

Source Data Fig. 1

Source Data Fig. 2

Source Data Fig. 3

Source Data Extended Data Fig. 1

Source Data Extended Data Fig. 3

Source Data Extended Data Fig. 5

Source Data Extended Data Fig. 6

Rights and permissions

Reprints and Permissions

About this article

Check for updates

Cite this article

Zheng, J., Wong, LY.R., Li, K. *et al.* COVID-19 treatments and pathogenesis including anosmia in K18-hACE2 mice. *Nature* **589,** 603–607 (2021). https://doi.org/10.1038/s41586-020-2943-z

Download citation

- Received: 05 August 2020
- Accepted: 02 November 2020
- Published: 09 November 2020
- Issue Date: 28 January 2021
- DOI: https://doi.org/10.1038/s41586-020-2943-z

Further reading

- **Neuroinvasion and Encephalitis Following Intranasal Inoculation of SARS-CoV-2 in K18-hACE2 Mice**

  - Pratima Kumari
  - , Hussin A. Rothan
  - , Janhavi P. Natekar
  - , Shannon Stone
  - , Heather Pathak
  - , Philip G. Strate
  - , Komal Arora
  - , Margo A. Brinton
  - & Mukesh Kumar

  Viruses (2021)

- **Psychosocial risk factors, non-communicable diseases and animal models for COVID-19**

  - Alessandro Bartolomucci
  - & Robert M. Sapolsky

  Biological Psychiatry (2020)

- **Severe Acute Respiratory Syndrome Coronavirus 2–Induced Immune Activation and Death of Monocyte-Derived Human Macrophages and Dendritic Cells**

  - Jian Zheng

- , Yuhang Wang
- , Kun Li
- , David K Meyerholz
- , Chantal Allamargot
- & Stanley Perlman

The Journal of Infectious Diseases (2020)

- **Convalescent plasma-mediated resolution of COVID-19 in a patient with humoral immunodeficiency**
  - Kazuhito Honjo
  - , Ronnie M. Russell
  - , Ran Li
  - , Weimin Liu
  - , Regina Stoltz
  - , Edlue M. Tabengwa
  - , Yutao Hua
  - , Lynn Prichard
  - , Ashton N. Kornbrust
  - , Sarah Sterrett
  - , Marisa B. Marques
  - , Jose L. Lima
  - , Chris M. Lough
  - , Todd P. McCarty
  - , Thomas J. Ketas
  - , Theodora Hatziioannou
  - , Paul D. Bieniasz
  - , David T. Redden
  - , John P. Moore
  - , Paul A. Goepfert
  - , Sonya L. Heath
  - , Beatrice H. Hahn
  - & Randall S. Davis

  Cell Reports Medicine (2020)

Comments

By submitting a comment you agree to abide by our Terms and Community Guidelines. If you find something abusive or that does not comply with our terms or guidelines please flag it as inappropriate.

Download PDF

This article was downloaded by **calibre** from https://www.nature.com/articles/s41586-020-2943-z

- Article
- Published: 06 January 2021

In vivo base editing rescues Hutchinson–Gilford progeria syndrome in mice

- Luke W. Koblan ORCID: orcid.org/0000-0003-2814-4412[1,2,3] na1,
- Michael R. Erdos ORCID: orcid.org/0000-0002-6603-1833[4] na1,
- Christopher Wilson ORCID: orcid.org/0000-0002-8012-2440[1,2,3],
- Wayne A. Cabral ORCID: orcid.org/0000-0002-0563-5289[4],
- Jonathan M. Levy ORCID: orcid.org/0000-0002-8061-7953[1,2,3],
- Zheng-Mei Xiong[4],
- Urraca L. Tavarez ORCID: orcid.org/0000-0002-2577-5377[4],
- Lindsay M. Davison[5],
- Yantenew G. Gete[6],
- Xiaojing Mao[6],
- Gregory A. Newby[1,2,3],
- Sean P. Doherty[5],
- Narisu Narisu ORCID: orcid.org/0000-0002-8483-1156[4],
- Quanhu Sheng[7],
- Chad Krilow[4],
- Charles Y. Lin ORCID: orcid.org/0000-0002-9155-090X[8,9] nAff12,
- Leslie B. Gordon[10,11],
- Kan Cao ORCID: orcid.org/0000-0002-5806-2939[6],
- Francis S. Collins ORCID: orcid.org/0000-0002-1023-7410[4],
- Jonathan D. Brown ORCID: orcid.org/0000-0002-0359-6167[5] &
- David R. Liu ORCID: orcid.org/0000-0002-9943-7557[1,2,3]

Nature **volume 589**, pages608–614(2021)Cite this article

- 13k Accesses
- 3 Citations
- 596 Altmetric
- Metrics details

Subjects

- CRISPR-Cas9 genome editing
- Targeted gene repair

Abstract

Hutchinson–Gilford progeria syndrome (HGPS or progeria) is typically caused by a dominant-negative C•G-to-T•A mutation (c.1824 C>T; p.G608G) in *LMNA*, the gene that encodes nuclear lamin A. This mutation causes RNA mis-splicing that produces progerin, a toxic protein that induces rapid ageing and shortens the lifespan of children with progeria to approximately 14 years[1,2,3,4]. Adenine base editors (ABEs) convert targeted A•T base pairs to G•C base pairs with minimal by-products and without requiring double-strand DNA breaks or donor DNA templates[5,6]. Here we describe the use of an ABE to directly correct the pathogenic HGPS mutation in cultured fibroblasts derived from children with progeria and in a mouse model of HGPS. Lentiviral delivery of the ABE to fibroblasts from children with HGPS resulted in 87–91% correction of the pathogenic allele, mitigation of RNA mis-splicing, reduced levels of progerin and correction of nuclear abnormalities. Unbiased off-target DNA and RNA editing analysis did not detect off-target editing in treated patient-derived fibroblasts. In transgenic mice that are homozygous for the human *LMNA* c.1824 C>T allele, a single retro-orbital injection of adeno-associated virus 9 (AAV9) encoding the ABE resulted in substantial, durable correction of the pathogenic mutation (around 20–60% across various organs six months after injection), restoration of normal RNA splicing and reduction of progerin protein levels. In vivo base editing rescued the vascular pathology of the mice, preserving vascular smooth muscle cell counts and preventing

adventitial fibrosis. A single injection of ABE-expressing AAV9 at postnatal day 14 improved vitality and greatly extended the median lifespan of the mice from 215 to 510 days. These findings demonstrate the potential of in vivo base editing as a possible treatment for HGPS and other genetic diseases by directly correcting their root cause.

Access through your institution
Change institution
Buy or subscribe

Access options

Subscribe to Journal

Get full journal access for 1 year

$199.00

only $3.90 per issue

Subscribe

All prices are NET prices.
VAT will be added later in the checkout.

Rent or Buy article

Get time limited or full article access on ReadCube.

from$8.99

Rent or Buy

All prices are NET prices.

Additional access options:

- Log in

- Access through your institution
- Learn about institutional subscriptions

Fig. 1: ABE-mediated correction of the *LMNA* c.1824 C>T mutation in fibroblasts derived from patients with progeria.

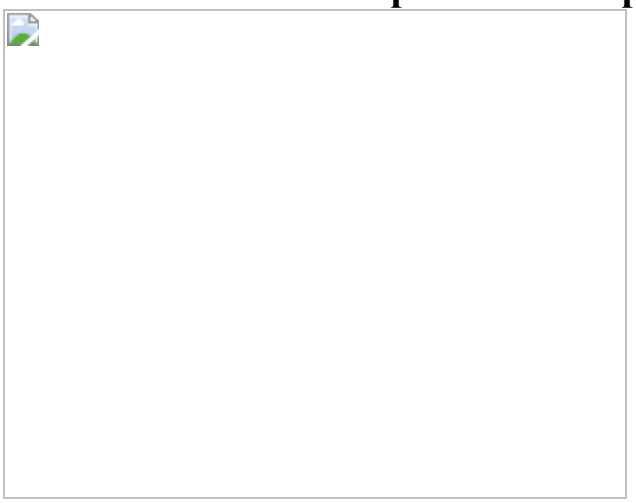

Fig. 2: Analysis of off-target DNA and RNA editing and gene expression changes after treating fibroblasts derived from patients with progeria with ABEmax-VRQR.

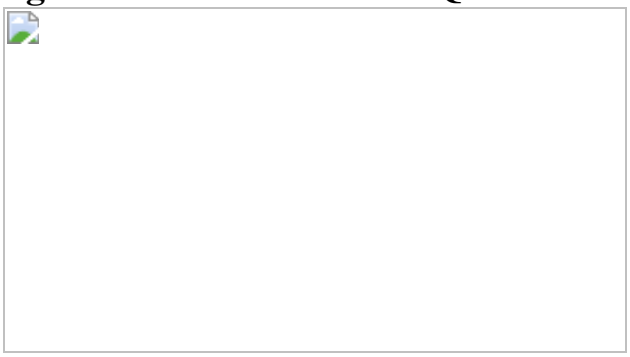

Fig. 3: DNA, RNA and protein levels after a single in vivo injection of ABE-expressing AAV9 in a mouse model of human progeria.

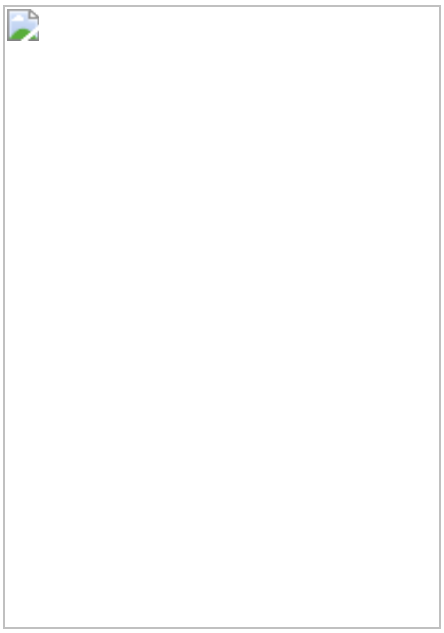

Fig. 4: Aortic histopathology and lifespan of progeria mice after a single injection of ABE-AAV9.

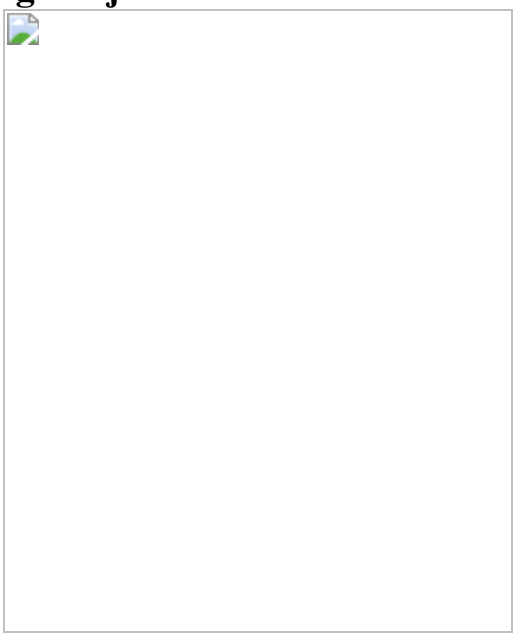

Data availability

DNA-sequencing files can be accessed at the NCBI SRA with accession code PRJNA627465. Raw data are available in Supplementary Data 1, 2, 3, 5 and 6.

Code availability

Code used in this study is available from https://github.com/CwilsonBroad/Koblan_2020_In-Vivo-Adenine-Base-Editing-Corrects-Hutchinson-Gilford-Progeria-Syndrome (Supplementary Note 3).

References

1. 1.

   Eriksson, M. et al. Recurrent de novo point mutations in lamin A cause Hutchinson–Gilford progeria syndrome. *Nature* **423**, 293–298 (2003).

   ADS CAS PubMed PubMed Central Google Scholar

2. 2.

   De Sandre-Giovannoli, A. et al. Lamin A truncation in Hutchinson–Gilford progeria. *Science* **300**, 2055 (2003).

   PubMed Google Scholar

3. 3.

   Gordon, L. B. et al. Impact of farnesylation inhibitors on survival in Hutchinson–Gilford progeria syndrome. *Circulation* **130**, 27–34 (2014).

   CAS PubMed PubMed Central Google Scholar

4. 4.

   Gordon, L. B., Brown, W. T. & Collins, F. S. *Hutchinson–Gilford Progeria Syndrome* (GeneReviews, 2019).

5. 5.

Gaudelli, N. M. et al. Programmable base editing of A•T to G•C in genomic DNA without DNA cleavage. *Nature* **551**, 464–471 (2017).

ADS CAS PubMed PubMed Central Google Scholar

6. 6.

Anzalone, A. V., Koblan, L. W. & Liu, D. R. Genome editing with CRISPR–Cas nucleases, base editors, transposases and prime editors. *Nat. Biotechnol*. **38**, 824–844 (2020).

CAS PubMed PubMed Central Google Scholar

7. 7.

Olive, M. et al. Cardiovascular pathology in Hutchinson–Gilford progeria: correlation with the vascular pathology of aging. *Arterioscler. Thromb. Vasc. Biol*. **30**, 2301–2309 (2010).

CAS PubMed PubMed Central Google Scholar

8. 8.

Gerhard-Herman, M. et al. Mechanisms of premature vascular aging in children with Hutchinson–Gilford progeria syndrome. *Hypertension* **59**, 92–97 (2012).

CAS PubMed PubMed Central Google Scholar

9. 9.

Rivera-Torres, J. et al. Cardiac electrical defects in progeroid mice and Hutchinson–Gilford progeria syndrome patients with nuclear lamina alterations. *Proc. Natl Acad. Sci. USA* **113**, E7250–E7259 (2016).

CAS PubMed PubMed Central Google Scholar

10. 10.

Prakash, A. et al. Cardiac abnormalities in patients with Hutchinson–Gilford progeria syndrome. *JAMA Cardiol*. **3**, 326–334 (2018).

PubMed PubMed Central Google Scholar

11. 11.

Stehbens, W. E., Wakefield, S. J., Gilbert-Barness, E., Olson, R. E. & Ackerman, J. Histological and ultrastructural features of atherosclerosis in progeria. *Cardiovasc. Pathol*. **8**, 29–39 (1999).

CAS PubMed PubMed Central Google Scholar

12. 12.

Gordon, L. B. et al. Clinical trial of a farnesyltransferase inhibitor in children with Hutchinson–Gilford progeria syndrome. *Proc. Natl Acad. Sci. USA* **109**, 16666–16671 (2012).

ADS CAS PubMed PubMed Central Google Scholar

13. 13.

Capell, B. C. & Collins, F. S. Human laminopathies: nuclei gone genetically awry. *Nat. Rev. Genet*. **7**, 940–952 (2006).

CAS PubMed PubMed Central Google Scholar

14. 14.

Lai, W.-F. & Wong, W.-T. Progress and trends in the development of therapies for Hutchinson–Gilford progeria syndrome. *Aging Cell* **19**, e13175 (2020).

CAS PubMed PubMed Central Google Scholar

15. 15.

Beyret, E. et al. Single-dose CRISPR–Cas9 therapy extends lifespan of mice with Hutchinson–Gilford progeria syndrome. *Nat. Med*. **25**, 419–422 (2019).

CAS PubMed PubMed Central Google Scholar

16. 16.

Santiago-Fernández, O. et al. Development of a CRISPR/Cas9-based therapy for Hutchinson–Gilford progeria syndrome. *Nat. Med*. **25**, 423–426 (2019).

PubMed PubMed Central Google Scholar

17. 17.

Suzuki, K. et al. Precise in vivo genome editing via single homology arm donor mediated intron-targeting gene integration for genetic disease correction. *Cell Res*. **29**, 804–819 (2019).

PubMed PubMed Central Google Scholar

18. 18.

Scaffidi, P. & Misteli, T. Reversal of the cellular phenotype in the premature aging disease Hutchinson–Gilford progeria syndrome. *Nat. Med*. **11**, 440–445 (2005).

CAS PubMed PubMed Central Google Scholar

19. 19.

Jiang, F. & Doudna, J. A. CRISPR–Cas9 structures and mechanisms. *Annu. Rev. Biophys*. **46**, 505–529 (2017).

CAS PubMed PubMed Central Google Scholar

20. 20.

Pattanayak, V. et al. High-throughput profiling of off-target DNA cleavage reveals RNA-programmed Cas9 nuclease specificity. *Nat. Biotechnol*. **31**, 839–843 (2013).

CAS PubMed PubMed Central Google Scholar

21. 21.

Komor, A. C., Kim, Y. B., Packer, M. S., Zuris, J. A. & Liu, D. R. Programmable editing of a target base in genomic DNA without double-stranded DNA cleavage. *Nature* **533**, 420–424 (2016).

ADS CAS PubMed PubMed Central Google Scholar

22. 22.

Varga, R. et al. Progressive vascular smooth muscle cell defects in a mouse model of Hutchinson–Gilford progeria syndrome. *Proc. Natl Acad. Sci. USA* **103**, 3250–3255 (2006).

ADS CAS PubMed PubMed Central Google Scholar

23. 23.

Huang, T. P. et al. Circularly permuted and PAM-modified Cas9 variants broaden the targeting scope of base editors. *Nat. Biotechnol*. **37**, 626–631 (2019).

CAS PubMed PubMed Central Google Scholar

24. 24.

Koblan, L. W. et al. Improving cytidine and adenine base editors by expression optimization and ancestral reconstruction. *Nat. Biotechnol*. **36**, 843–846 (2018).

CAS PubMed PubMed Central Google Scholar

25. 25.

Kleinstiver, B. P. et al. High-fidelity CRISPR–Cas9 nucleases with no detectable genome-wide off-target effects. *Nature* **529**, 490–495 (2016).

ADS CAS PubMed PubMed Central Google Scholar

26. 26.

Tsai, S. Q. et al. CIRCLE-seq: a highly sensitive in vitro screen for genome-wide CRISPR–Cas9 nuclease off-targets. *Nat. Methods* **14**, 607–614 (2017).

CAS PubMed PubMed Central Google Scholar

27. 27.

Eisenberg, E. & Levanon, E. Y. A-to-I RNA editing—immune protector and transcriptome diversifier. *Nat. Rev. Genet*. **19**, 473–490 (2018).

CAS PubMed PubMed Central Google Scholar

28. 28.

Levy, J. M. et al. Cytosine and adenine base editing of the brain, liver, retina, heart and skeletal muscle of mice via adeno-associated viruses. *Nat. Biomed. Eng*. **4**, 97–110 (2020).

CAS PubMed PubMed Central Google Scholar

29. 29.

Villiger, L. et al. Treatment of a metabolic liver disease by in vivo genome base editing in adult mice. *Nat. Med*. **24**, 1519–1525 (2018).

CAS PubMed PubMed Central Google Scholar

30. 30.

Zincarelli, C., Soltys, S., Rengo, G. & Rabinowitz, J. E. Analysis of AAV serotypes 1-9 mediated gene expression and tropism in mice after systemic injection. *Mol. Ther*. **16**, 1073–1080 (2008).

CAS PubMed Google Scholar

31. 31.

Inagaki, K. et al. Robust systemic transduction with AAV9 vectors in mice: efficient global cardiac gene transfer superior to that of AAV8. *Mol. Ther*. **14**, 45–53 (2006).

CAS PubMed PubMed Central Google Scholar

32. 32.

Bostick, B., Ghosh, A., Yue, Y., Long, C. & Duan, D. Systemic AAV-9 transduction in mice is influenced by animal age but not by the route of administration. *Gene Ther*. **14**, 1605–1609 (2007).

CAS PubMed PubMed Central Google Scholar

33. 33.

Wang, L., Wang, H., Bell, P., McMenamin, D. & Wilson, J. M. Hepatic gene transfer in neonatal mice by adeno-associated virus serotype 8 vector. *Hum. Gene Ther*. **23**, 533–539 (2012).

CAS PubMed PubMed Central Google Scholar

34. 34.

Kessler, P. D. et al. Gene delivery to skeletal muscle results in sustained expression and systemic delivery of a therapeutic protein. *Proc. Natl Acad. Sci. USA* **93**, 14082–14087 (1996).

ADS CAS PubMed PubMed Central Google Scholar

35. 35.

Nathwani, A. C. et al. Long-term safety and efficacy of factor IX gene therapy in hemophilia B. *N. Engl. J. Med*. **371**, 1994–2004 (2014).

PubMed PubMed Central Google Scholar

36. 36.

Hagan, C. When are mice considered old? *The Jackson Laboratory* https://www.jax.org/news-and-insights/jax-blog/2017/november/when-are-mice-considered-old (2017).

37. 37.

Chandler, R. J., Sands, M. S. & Venditti, C. P. Recombinant adeno-associated viral integration and genotoxicity: insights from animal models. *Hum. Gene Ther*. **28**, 314–322 (2017).

CAS PubMed PubMed Central Google Scholar

38. 38.

Nault, J.-C. et al. Wild-type AAV insertions in hepatocellular carcinoma do not inform debate over genotoxicity risk of vectorized AAV. *Mol. Ther*. **24**, 660–661 (2016).

CAS PubMed PubMed Central Google Scholar

39. 39.

Geng, D., Zhao, W., Feng, Y. & Liu, J. Overexpression of Rab25 promotes hepatocellular carcinoma cell proliferation and invasion. *Tumour Biol*. **37**, 7713–7718 (2016).

CAS PubMed PubMed Central Google Scholar

40. 40.

Donsante, A. et al. Observed incidence of tumorigenesis in long-term rodent studies of rAAV vectors. *Gene Ther*. **8**, 1343–1346 (2001).

CAS PubMed PubMed Central Google Scholar

41. 41.

Donsante, A. et al. AAV vector integration sites in mouse hepatocellular carcinoma. *Science* **317**, 477 (2007).

ADS CAS PubMed PubMed Central Google Scholar

42. 42.

Embury, J. E., Charron, C. C., Poirier, A. E. & Zori, A. Long term portal vein administration of AAV-WPRE vector results in increased incidence of neoplastic disease and hepatic pathology. *Mol. Ther*. **13**, S83 (2006).

Google Scholar

43. 43.

Sands, M. S. AAV-mediated liver-directed gene therapy. *Methods Mol. Biol*. **807**, 141–157 (2011).

CAS PubMed PubMed Central Google Scholar

44. 44.

Richter, M. F. et al. Phage-assisted evolution of an adenine base editor with enhanced Cas domain compatibility and activity. *Nat. Biotechnol*. **38**, 883–891 (2020).

CAS PubMed PubMed Central Google Scholar

45. 45.

Gaudelli, N. M. et al. Directed evolution of adenine base editors with increased activity and therapeutic application. *Nat. Biotechnol*. **38**, 892–900 (2020).

CAS PubMed PubMed Central Google Scholar

46. 46.

Osorio, F. G. et al. Splicing-directed therapy in a new mouse model of human accelerated aging. *Sci. Transl. Med*. **3**, 106ra107 (2011).

PubMed PubMed Central Google Scholar

47. 47.

Mateos, J. et al. Next-generation sequencing and quantitative proteomics of Hutchinson–Gilford progeria syndrome-derived cells point to a role of nucleotide metabolism in premature aging. *PloS One* **13**, e0205878 (2018).

PubMed PubMed Central Google Scholar

48. 48.

Doench, J. G. et al. Optimized sgRNA design to maximize activity and minimize off-target effects of CRISPR–Cas9. *Nat. Biotechnol*. **34**, 184–191 (2016).

CAS PubMed PubMed Central Google Scholar

49. 49.

Sanjana, N. E., Shalem, O. & Zhang, F. Improved vectors and genome-wide libraries for CRISPR screening. *Nat. Methods* **11**, 783–784 (2014).

CAS PubMed PubMed Central Google Scholar

50. 50.

Wu, D. & Smyth, G. K. Camera: a competitive gene set test accounting for inter-gene correlation. *Nucleic Acids Res*. **40**, e133 (2012).

CAS PubMed PubMed Central Google Scholar

51. 51.

Cao, K. et al. Rapamycin reverses cellular phenotypes and enhances mutant protein clearance in Hutchinson–Gilford progeria syndrome cells. *Sci. Transl. Med*. **3**, 89ra58 (2011).

CAS PubMed PubMed Central Google Scholar

52. 52.

Ewels, P., Magnusson, M., Lundin, S. & Käller, M. MultiQC: summarize analysis results for multiple tools and samples in a single report. *Bioinformatics* **32**, 3047–3048 (2016).

CAS PubMed PubMed Central Google Scholar

53. 53.

Frengen, E. et al. A modular, positive selection bacterial artificial chromosome vector with multiple cloning sites. *Genomics* **58**, 250–253 (1999).

CAS PubMed PubMed Central Google Scholar

54. 54.

DuBose, A. J. et al. Use of microarray hybrid capture and next-generation sequencing to identify the anatomy of a transgene. *Nucleic Acids Res*. **41**, e70

55. 55.

Li, H. & Durbin, R. Fast and accurate short read alignment with Burrows–Wheeler transform. *Bioinformatics* **25**, 1754–1760 (2009).

CAS PubMed PubMed Central Google Scholar

56. 56.

Li, H. et al. The Sequence Alignment/Map format and SAMtools. *Bioinformatics* **25**, 2078–2079 (2009).

PubMed PubMed Central Google Scholar

57. 57.

Quinlan, A. R. & Hall, I. M. BEDTools: a flexible suite of utilities for comparing genomic features. *Bioinformatics* **26**, 841–842 (2010).

CAS PubMed PubMed Central Google Scholar

58. 58.

Tarasov, A., Vilella, A. J., Cuppen, E., Nijman, I. J. & Prins, P. Sambamba: fast processing of NGS alignment formats. *Bioinformatics* **31**, 2032–2034 (2015).

CAS PubMed PubMed Central Google Scholar

59. 59.

McKenna, A. et al. The Genome Analysis Toolkit: a MapReduce framework for analyzing next-generation DNA sequencing data. *Genome Res*. **20**, 1297–1303 (2010).

CAS PubMed PubMed Central Google Scholar

60. 60.

DePristo, M. A. et al. A framework for variation discovery and genotyping using next-generation DNA sequencing data. *Nat. Genet*. **43**, 491–498 (2011).

CAS PubMed PubMed Central Google Scholar

61. 61.

Van der Auwera, G. A. et al. From FastQ data to high confidence variant calls: the Genome Analysis Toolkit best practices pipeline. *Curr. Protoc. Bioinformatics* **43**, 11.10.1–11.10.33 (2013).

Google Scholar

62. 62.

Wang, K., Li, M. & Hakonarson, H. ANNOVAR: functional annotation of genetic variants from high-throughput sequencing data. *Nucleic Acids Res*. **38**, e164 (2010).

PubMed PubMed Central Google Scholar

63. 63.

Sondka, Z. et al. The COSMIC Cancer Gene Census: describing genetic dysfunction across all human cancers. *Nat. Rev. Cancer* **18**, 696–705 (2018).

CAS PubMed PubMed Central Google Scholar

64. 64.

Buenrostro, J. D., Giresi, P. G., Zaba, L. C., Chang, H. Y. & Greenleaf, W. J. Transposition of native chromatin for fast and sensitive epigenomic profiling of open chromatin, DNA-binding proteins and nucleosome position. *Nat. Methods* **10**, 1213–1218 (2013).

CAS PubMed PubMed Central Google Scholar

Download references

Acknowledgements

This work was supported by NIH grants U01AI142756, UG3AI150551, UG3TR002636, RM1HG009490, R01EB022376, R35GM118062, Z01HG200305, R01HL146654 and R01HL126784, and by the Howard

Hughes Medical Institute. L.W.K. acknowledges an NSF GRFP fellowship; C.W. acknowledges a Damon Runyon Cancer Research Foundation fellowship (DRG-2343-18); G.A.N. acknowledges a Helen Hay Whitney postdoctoral fellowship; and L.B.G., L.W.K. and D.R.L. acknowledge support from The Progeria Research Foundation.

Author information

Author notes

1. Charles Y. Lin

   Present address: Kronos, Bio Inc., Cambridge, MA, USA

2. These authors contributed equally: Luke W. Koblan, Michael R. Erdos

Affiliations

1. Merkin Institute of Transformative Technologies in Healthcare, Broad Institute of Harvard and MIT, Cambridge, MA, USA

   Luke W. Koblan, Christopher Wilson, Jonathan M. Levy, Gregory A. Newby & David R. Liu

2. Department of Chemistry and Chemical Biology, Harvard University, Cambridge, MA, USA

   Luke W. Koblan, Christopher Wilson, Jonathan M. Levy, Gregory A. Newby & David R. Liu

3. Howard Hughes Medical Institute, Harvard University, Cambridge, MA, USA

   Luke W. Koblan, Christopher Wilson, Jonathan M. Levy, Gregory A. Newby & David R. Liu

4. National Human Genome Research Institute, National Institutes of Health, Bethesda, MD, USA

Michael R. Erdos, Wayne A. Cabral, Zheng-Mei Xiong, Urraca L. Tavarez, Narisu Narisu, Chad Krilow & Francis S. Collins

5. Division of Cardiovascular Medicine, Vanderbilt University Medical Center, Nashville, TN, USA

   Lindsay M. Davison, Sean P. Doherty & Jonathan D. Brown

6. Department of Cell Biology and Molecular Genetics, University of Maryland, College Park, MD, USA

   Yantenew G. Gete, Xiaojing Mao & Kan Cao

7. Department of Biostatistics, Vanderbilt University Medical Center, Nashville, TN, USA

   Quanhu Sheng

8. Department of Molecular and Human Genetics, Baylor College of Medicine, Houston, TX, USA

   Charles Y. Lin

9. Therapeutic Innovation Center, Department of Biochemistry and Molecular Biology, Baylor College of Medicine, Houston, TX, USA

   Charles Y. Lin

10. Hasbro Children's Hospital, Alpert Medical School of Brown University, Providence, RI, USA

    Leslie B. Gordon

11. Boston Children's Hospital, Harvard Medical School, Boston, MA, USA

    Leslie B. Gordon

Authors

1. Luke W. Koblan
   View author publications

   You can also search for this author in PubMed Google Scholar

2. Michael R. Erdos
   View author publications

   You can also search for this author in PubMed Google Scholar

3. Christopher Wilson
   View author publications

   You can also search for this author in PubMed Google Scholar

4. Wayne A. Cabral
   View author publications

   You can also search for this author in PubMed Google Scholar

5. Jonathan M. Levy
   View author publications

   You can also search for this author in PubMed Google Scholar

6. Zheng-Mei Xiong
   View author publications

   You can also search for this author in PubMed Google Scholar

7. Urraca L. Tavarez
   View author publications

   You can also search for this author in PubMed Google Scholar

8. Lindsay M. Davison
   View author publications

   You can also search for this author in PubMed Google Scholar

9. Yantenew G. Gete
View author publications

You can also search for this author in PubMed Google Scholar

10. Xiaojing Mao
View author publications

You can also search for this author in PubMed Google Scholar

11. Gregory A. Newby
View author publications

You can also search for this author in PubMed Google Scholar

12. Sean P. Doherty
View author publications

You can also search for this author in PubMed Google Scholar

13. Narisu Narisu
View author publications

You can also search for this author in PubMed Google Scholar

14. Quanhu Sheng
View author publications

You can also search for this author in PubMed Google Scholar

15. Chad Krilow
View author publications

You can also search for this author in PubMed Google Scholar

16. Charles Y. Lin
View author publications

You can also search for this author in PubMed Google Scholar

17. Leslie B. Gordon
View author publications

You can also search for this author in PubMed Google Scholar

18. Kan Cao
View author publications

You can also search for this author in PubMed Google Scholar

19. Francis S. Collins
View author publications

You can also search for this author in PubMed Google Scholar

20. Jonathan D. Brown
View author publications

You can also search for this author in PubMed Google Scholar

21. David R. Liu
View author publications

You can also search for this author in PubMed Google Scholar

Contributions

L.W.K., J.D.B., C.Y.L., M.R.E., F.S.C. and D.R.L. designed the research. L.W.K., M.R.E., C.W., W.A.C., L.D., Y.G.G., X.M., G.A.N., S.P.D., J.D.B. performed cell culture experiments. L.W.K., M.R.E., C.W., W.A.C., J.M.L., Z.X., U.L.T., L.D., S.P.D., N.N., Q.S., C.K. and J.D.B. performed in vivo experiments. L.B.G., K.C., F.S.C., J.D.B. and D.R.L. supervised the project. L.W.K. and D.R.L. wrote the manuscript with input from all other authors.

Corresponding authors

Correspondence to Francis S. Collins or Jonathan D. Brown or David R. Liu.

Ethics declarations

Competing interests

D.R.L. is a co-founder of Beam Therapeutics, Prime Medicine, Pairwise Plants and Editas Medicine, companies that use genome editing. The remaining authors declare no competing interests.

Additional information

Peer review information *Nature* thanks the anonymous reviewers for their contribution to the peer review of this work.

Publisher's note Springer Nature remains neutral with regard to jurisdictional claims in published maps and institutional affiliations.

Extended data figures and tables

Extended Data Fig. 1 Additional characterization of patient-derived cells treated with ABE7.10max-VRQR.

a, Bystander V690A editing in patient-derived HGADFN167 and HGADFN188 cells 20 days after treatment with lentiviral ABE7.10max-VRQR. **b**, Indel formation frequency at the c.1824 target locus in HGADFN167 and HGADFN188 cells 20 days after treatment with lentiviral ABE7.10max-VRQR. Data are mean ± s.d. for $n = 5$ technical replicates (individual points) for **a**, **b**. **c**, Sanger DNA sequencing traces of untreated HGADFN167 cells, 20-day treated HGADFN167 cells and unaffected control cells. The target nucleotide is boxed. **d**, qPCR-normalized progerin mRNA abundance in cells described in **c**. Data are mean ± s.d. for $n = 3$ biological replicates. **e**, Western blot analysis of HGADFN167 cells described in **c**. LMNA, progerin, and LMNC protein are all stained on the gel, A GAPDH loading control is shown below. An additional replicate is provided in Fig. 1d. Unaff. ctrl, control cells from an unaffected parent. **f**, Sanger DNA sequencing traces of untreated, non-

targeting (NT)-sgRNA-treated and ABE-treated HGADFN155 fibroblasts at a 20-day time point to ensure NT-sgRNA did not lead to DNA editing. **g**, Western blot analysis of cells described in **f** as well as treated cells at a 30-day time point. LMNA, progerin, and LMNC proteins are all stained on the gel, a β-actin loading control is shown below. Expected molecular weights: lamin A, 74 kDa; progerin, 69 kDa; lamin C, 65 kDa. Complete blots are available in Supplementary Fig. 1. Additional replication was not performed. **h**, HGADFN167 (left) and HGADFN188 (right) cell lines untreated or treated with lentiviral ABE7.10max-VRQR after 10 or 20 days show similar relative distributions of A-to-I SNVs in their transcriptomes compared with the hg38 human genome reference sequence. On average, 36 ± 3.6% of SNPs in these samples occur with around 100% frequency, suggesting they arise from genomic sequence variations; however, we cannot explicitly exclude them from consideration as no whole-genome sequence is available for these cell lines. Raw counts of 100% edited SNPs per sample are: untreated HGADFN167 cells (849), HGADFN167 10 d after treatment (883), HGADFN167 20 d after treatment (871), untreated HGADFN188 cells (488), HGADFN188 10 d after treatment (501), HGADFN188 20 d after treatment (510).

Extended Data Fig. 2 CIRCLE-seq analysis of HGADFN167 and HGADFN188 cells using Cas9-VRQR and the progeria-targeting sgRNA.

a, **b**, CIRCLE-seq read counts for Cas9-VRQR nuclease-treated genomic DNA from HGADFN167 (**a**) and HGADFN188 (**b**) cell lines. Targeted amplicon sequencing was used to assess the off-target base editing for 36 noted total loci distributed across both cell lines. DNA at 32 of 35 loci amplified efficiently from both cell lines (denoted by black check marks), DNA at 3 loci failed to amplify (denoted by red X marks). Complete CIRCLE-seq data are provided in Supplementary Data 4. **c**, SDS–PAGE gel stained with InstantBlue to follow protein purification of Cas9-VRQR. Totals of 0.5 µl clarified lysate, 0.25 µl nickel column elution or 0.1 µl of the concentrated protein stock after His-tag purification and ion-exchange chromatography were added to 5 µl NuPAGE loading buffer. Samples were denatured at 98 °C for 5 min before loading onto the 4–12% acrylamide gel. A Precision Plus Protein Kaleidoscope Pre-Stained Ladder (Bio-Rad) was

used as reference. The desired Cas9-VRQR has a predicted molecular weight of 161.9 kDa. Additional replication was not performed.

Extended Data Fig. 3 DNA on-target editing, bystander editing and indel efficiencies across tissues from in vivo injection route optimization experiments.

a, Dual AAV9 encoding split-intein ABE7.10max-VRQR base editor halves and the *LMNA*-targeting sgRNA were injected into homozygous *LMNA* c.1824 C>T mice. P3 retro-orbital (RO) injections (5×10^{10} vg of each AAV, 1×10^{11} vg total), P14 RO injections (5×10^{11} vg of each AAV, 1×10^{12} vg total) and P14 intraperitoneal (IP) injections (5×10^{11} vg of each AAV, 1×10^{12} vg total) were tested. At 6-weeks of age, mice were euthanized and heart, muscle, liver, aorta and bone were isolated for sequencing analysis. Tissues were sub-sectioned for sequencing analysis to ensure sub-sections did not show differences in editing efficiencies for downstream analyses. Each bar represents a different tissue subsection. DNA-editing efficiencies correcting *LMNA* c.1824 from T (pathogenic) to C (wild-type) for P3 RO-injected mice (left, $n = 4$), P14 RO-injected mice (middle, $n = 5$) and P14 IP-injected mice (right, $n = 5$) at 6 weeks of age are shown for five disease-relevant tissues. Data are mean ± s.d. **b**, Apparent *LMNA* c.1824 T (pathogenic) to C (wild-type) mutations from tissue samples of saline-injected P3 RO (left) and P14 RO (right) control mice at 6 months of age show background signal due to amplicon crossover during PCR between the human diseased allele and the wild-type mouse allele, which share 90% overall sequence identity within the amplified region. Similar crossover levels were observed across 11 tissues in both P3 RO and P14 RO saline-injected mice. Data are mean ± s.d. for $n = 12$ mice (6 male, 6 female). **c**, Computational filtering of same sequencing reads shown in **b** after removing any reads containing any mouse-specific sequence variations, analysing only reads containing exclusively human sequence. The script used to remove mouse-containing sequencing reads is in the link in Supplementary Note 3 and is described in the Methods ('High-throughput sequencing of in vivo samples'). **d**, DNA editing for P3- and P14-injected mice at 6 months of age across 11 tissues. Each point represents a biological replicate of a tissue taken from a unique mouse

(n = 12 for each group). **e**, V690A bystander editing frequency across eleven tissues for P3 RO and P14 RO ABE-treated mice at 6 months of age (n = 12 for each group). **f**, Indel frequencies at the c.1824 target locus across 11 tissues for P3 RO and P14 RO ABE-treated mice at 6 months of age. Data are mean ± s.d. for the indicated number of biological replicates. *$P < 0.05$, **$P < 0.01$, ***$P < 0.001$, ****$P < 0.0001$ by Student's unpaired two-sided t-test.

Extended Data Fig. 4 Quantification of *LMNA* and progerin transcript abundance by ddPCR in mice that were retro-orbitally injected with saline or ABE-AAV9 at P3 or P14.

a, ddPCR counts for *LMNA* (grey bars) and progerin (red bars) RNA transcript abundance in P3 RO saline- and ABE-AAV9-injected mice. Data are mean ± s.d. for n = 12 mice. **b**, ddPCR counts for *LMNA* (grey bars) and progerin (red bars) RNA transcript abundance in P14 RO saline- and ABE-AAV9-injected mice. Data are mean ± s.d. for n = 12 biological replicates for all samples except for saline-injected mouse skin (n = 11), WAT (n = 7), visceral fat (n = 11), tibia (n = 11) and aorta (n = 8); and ABE-AAV9-injected mouse WAT (n = 11), tibia (n = 9) and aorta (n = 10). Visc. fat, visceral fat. *$P < 0.05$, **$P < 0.01$, ***$P < 0.001$, ****$P < 0.0001$ by Student's unpaired two-sided t-test for **a**, **b**. Liver and heart values are reproduced from Fig. 3c for ease of comparison.

Extended Data Fig. 5 Quantification of western blots.

Liver, heart and aorta tissue western blots for P3-injected (top half of each tissue set) and P14-injected mice (bottom half of each tissue set) were quantified by western blot. Samples from females appear in the left column, and samples from males are in the right column. Each lane represents the tissue type specified on the left taken from a different mouse. Control mice were treated with saline instead of ABE-AAV9. WT indicates C57BL/6 mouse lacking the transgene, showing that the antibody is specific to human lamin proteins and progerin. The abundance of lamin A or progerin protein relative to β-actin in saline- or ABE-treated mouse tissues was quantified by normalizing the fluorescence signal from the secondary antibody for each

band (800 nm for progerin and lamins, and 680 nm for actin; see Methods ('Protein isolation and western blotting from mouse tissues'). The normalized protein abundance relative to saline-treated samples (set to 100) is shown in the bar graphs. Control mice were treated identically to the corresponding ABE-treated mice except injected with saline instead of ABE-AAV9. Raw fluorescent signal for progerin protein measured at the 800-nm wavelength (using IRDye-labelled antibody) is displayed under each lane. Data are mean ± s.d. for $n = 5$ or 6 biological replicates, as indicated. The n for each sample type is listed in each figure panel. $^{*}P < 0.05$, $^{**}P < 0.01$, $^{***}P < 0.001$, $^{****}P < 0.0001$ by Student's unpaired two-sided t-test. Expected molecular weights: lamin A, 74 kDa; progerin, 69 kDa; lamin C, 65 kDa. Liver and heart blots are reproduced from Fig. 3c for ease of comparison. Complete blots are available in Supplementary Fig. 1.

Extended Data Fig. 6 Aortic histology of male and female mice that were retro-orbitally injected with saline or ABE-AAV9 at P3.

a, Representative aorta cross-sections for P3 RO saline- or ABE-AAV9-injected males at 6 months of age. Left images were stained with H&E; right images were stained with Movat's pentachrome stain. **b**, Representative aorta cross-sections for P3 RO saline- or ABE-AAV9-treated females at 6 months of age. Left images were stained with H&E; right images were stained with Movat's pentachrome stain. Unaffected WT are wild-type C57BL/6 mice. WT M2, 9609M, 9177M, WT F3, 9628F and 9148F are reproduced from Fig. 4 for ease of comparison. These sections each represent replicates from different mice.

Extended Data Fig. 7 Aortic histology of male and female mice that were retro-orbitally injected with saline or ABE-AAV9 at P14.

a, Representative aorta cross-sections for P14 RO saline- or ABE-AAV9-injected males at 6 months of age. Left images were stained with H&E; right images were stained with Movat's pentachrome stain. **b**,

Representative aorta cross-sections for P14 RO saline- or ABE-AAV9-treated females at 6 months of age. Left images were stained with H&E; right images were stained with Movat's pentachrome stain. Unaffected WT are wild-type C57BL/6 mice, reproduced from Extended Data Fig. 9a, b for ease of comparison. Images from the following mice are reproduced from Fig. 4 for ease of comparison: WT M2, 9440M, 9459M, WT F3, 9536F and 9535F. These sections each represent replicates from different mice.

Extended Data Fig. 8 Immunofluorescence staining of aortas from male and female control C57BL/6 mice, untreated mice and mice that were retro-orbitally injected with saline or ABE-AAV9 at P14.

Immunofluorescence staining of C57BL/6 (n = 2), untreated P28 homozygous *LMNA* c.1824 C>T (n = 1), saline-treated homozygous *LMNA* c.1824 C>T (n = 4) and ABE-treated homozygous *LMNA* c.1824 C>T (n = 5) mouse aortas stained for human lamin A/C + DAPI or for progerin + DAPI. Scale bars, 10 μm. Images from untreated 28 day-old, WT M1, 9424M and 9464M are replicated from Fig. 4 for ease of comparison.

Extended Data Fig. 9 Skin histology of male and female mice that were retro-orbitally injected with saline or ABE-AAV9 at P3.

a, Representative skin cross-sections for P3 RO saline-injected (left), ABE-AAV9-injected (middle) and wild-type C57BL/6 males at 6 months of age. Left images were stained with H&E; right images were prepared with Masson's trichrome staining. **b**, Representative skin cross-sections for P3 RO saline-injected (left), ABE-AAV9-injected (middle) and wild-type C57BL/6 females at 6 months of age. Left images were stained with H&E; right images were prepared with Masson's trichrome staining. Unaffected WT are wild-type C57BL/6 mice. These sections each represent replicates from different mice.

Extended Data Fig. 10 Skin histology of male and female mice that were retro-orbitally injected with saline or ABE-AAV9 at P14.

a, Representative skin cross-sections for P14 RO saline-injected (left), ABE-AAV9-treated (middle) and wild-type C57BL/6 males at 6 months of age. Left images were stained with H&E; right images were prepared with Masson's trichrome staining. **b**, Representative skin cross-sections for P14 RO saline-injected (left), ABE-AAV9-treated (middle) and wild-type C57BL/6 females at 6 months of age. Left images were stained with H&E; right images were prepared with Masson's trichrome staining. Unaffected WT are wild-type C57BL/6 mice, reproduced from Extended Data Fig. 12a, b for ease of comparison. These sections each represent replicates from different mice.

Extended Data Fig. 11 Body weights of mice that were retro-orbitally injected with saline or ABE-AAV9 at P3 or P14.

Weights of homozygous *LMNA* c.1824 C>T mice taken across mouse lifespans for cohorts of P3 RO (left) and P14 RO (right) saline- and ABE-AAV9-injected cohorts. Mouse weights are shown by sex. The *x* axis shows days post-injection, rather than age. Data are mean ± s.d. for the number of surviving mice at each time point; complete data can be accessed in Supplementary Data 5.

Extended Data Fig. 12 Whole-genome sequencing analysis of SNVs and indels and quantification of *RAB25* transcript levels in mouse tissue samples.

a, Distribution of all possible SNV types in non-tumour liver tissue and liver tumour tissue samples isolated from ABE-AAV9-injected and saline-injected mice. Values from individual tissue samples are shown on the left. Aggregated values from all AAV-injected mouse tumour tissue samples, all AAV-injected mouse liver tissue samples and all saline-injected mouse liver tissue samples are shown on the right. Data are mean ± s.d. with each tissue

section treated as a different sample: AAV-injected tumour tissue (n = 7), AAV-injected liver tissue (n = 6) and saline-injected liver tissue (n = 2). **b**, Genomic classification of A•T-to-G•C SNVs. Values from individual tissue samples are shown on the left. Aggregated values from AAV-injected mouse tumour tissue samples, AAV-injected mouse liver tissue samples and saline-injected mouse liver tissue samples from all tissue types are shown on the right. Data are mean ± s.d. with each tissue section treated as a different sample: AAV-injected tumour tissue (n = 7), AAV-injected liver tissue (n = 6), saline-injected liver tissue (n = 2). **c**, A•T-to-G•C SNVs and indels found in or near genes that are recurrently mutated in human liver cancers[63,64] including introns, exons, and at ATAC-seq-defined *cis*-regulatory regions within 100-kb of each gene's transcription start site, in AAV-injected mouse tumour tissue samples, AAV-injected mouse liver tissue samples and saline-injected mouse liver tissue samples. Data are mean ± s.d. Individual data points are shown for each sample. The complete list of SNVs from ANNOVAR analysis is provided as Supplementary Data 6. Summary statistics for SNV calls are in Supplementary Data 2. **d**, RNA isolated from mouse liver tissue samples was reverse-transcribed and amplified with primer sets specific to mouse *Gapdh* (detected with Cy5), mouse *Actb* (detected with Cy5.5) and human *RAB25* (detected with TEX 615). Ct values were determined by quantitative PCR and are shown below each lane. N.D., not detected.

Supplementary information

Supplementary Information

This file contains Supplementary Notes 1-3, Supplementary Figure 1, Supplementary Tables 1-2 and Supplementary References.

Reporting Summary

Supplementary Data

Supplementary Data 1: AAV integration analysis from mouse whole-genome sequencing data.

Supplementary Data

Supplementary Data 2: Analysis of SNVs from mouse whole-genome sequencing data.

Supplementary Data

Supplementary Data 3: Liver cancer-associated SNVs and indels in mouse wholegenome sequencing data.

Supplementary Data

Supplementary Data 4: CIRCLE-seq candidate off-target loci genomic coordinates and amplification primers.

Supplementary Data

Supplementary Data 5: Raw data for *in vivo* samples.

Supplementary Data

Supplementary Data 6: All SNVs from mouse whole-genome sequencing data.

Video 1

Representative untreated male progeria mouse (not enrolled in this study), taken at 7.5 months of age.

Video 2

Representative male progeria mice injected at P14 with ABE-AAV, taken at 9.75 months of age.

Video 3

Representative female progeria mice injected at P14 with ABE-AAV, and wild-type C57BL/6 female mouse, taken at 9.75 months of age.

Video 4

Representative male progeria mice injected at P14 with ABE-AAV, and wild-type C57BL/6 male mouse, taken at 11 months of age.

Video 5

Representative female progeria mice injected at P14 with ABE-AAV, taken at 11 months of age.

Rights and permissions

Reprints and Permissions

About this article

Check for updates

Cite this article

Koblan, L.W., Erdos, M.R., Wilson, C. *et al.* In vivo base editing rescues Hutchinson–Gilford progeria syndrome in mice. *Nature* **589,** 608–614 (2021). https://doi.org/10.1038/s41586-020-03086-7

Download citation

- Received: 09 June 2020
- Accepted: 30 November 2020
- Published: 06 January 2021

- Issue Date: 28 January 2021
- DOI: https://doi.org/10.1038/s41586-020-03086-7

Further reading

- **In vivo base editing rescues progeria in mice**
  - Megan Cully

  Nature Reviews Drug Discovery (2021)

- **Base editor repairs mutation found in the premature-ageing syndrome progeria**
  - Wilbert P. Vermeij
  - & Jan H. J. Hoeijmakers

  Nature (2021)

- **Fixing an ageing mutation**
  - Katharine H. Wrighton

  Nature Reviews Genetics (2021)

Comments

By submitting a comment you agree to abide by our Terms and Community Guidelines. If you find something abusive or that does not comply with our terms or guidelines please flag it as inappropriate.

Access through your institution
Change institution
Buy or subscribe

Associated Content

Nature | News & Views

Base editor repairs mutation found in the premature-ageing syndrome progeria

- Wilbert P. Vermeij
- & Jan H. J. Hoeijmakers

This article was downloaded by **calibre** from https://www.nature.com/articles/s41586-020-03086-7

Capping pores of alphavirus nsP1 gate membranous viral replication factories
Download PDF

- Article
- Published: 16 December 2020

Capping pores of alphavirus nsP1 gate membranous viral replication factories

- Rhian Jones[1],
- Gabriel Bragagnolo[1],
- Rocío Arranz ORCID: orcid.org/0000-0001-5321-0915[2] &
- Juan Reguera ORCID: orcid.org/0000-0003-4977-7948[1,3]

Nature **volume 589**, pages615–619(2021)Cite this article

- 4313 Accesses
- 47 Altmetric
- Metrics details

Subjects

- Alphaviruses
- Cryoelectron microscopy
- Membrane proteins
- Viral proteins

Abstract

Positive-sense single-stranded RNA viruses, such as coronaviruses, flaviviruses and alphaviruses, carry out transcription and replication inside virus-induced membranous organelles within host cells[1,2,3,4,5,6,7]. The remodelling of the host-cell membranes for the formation of these organelles is coupled to the membrane association of viral replication complexes and to RNA synthesis. These viral niches allow for the concentration of metabolites and proteins for the synthesis of viral RNA, and prevent the detection of this RNA by the cellular innate immune system[8]. Here we present the

cryo-electron microscopy structure of non-structural protein 1 (nsP1) of the alphavirus chikungunya virus, which is responsible for RNA capping and membrane binding of the viral replication machinery. The structure shows the enzyme in its active form, assembled in a monotopic membrane-associated dodecameric ring. The structure reveals the structural basis of the coupling between membrane binding, oligomerization and allosteric activation of the capping enzyme. The stoichiometry—with 12 active sites in a single complex—redefines viral replication complexes as RNA synthesis reactors. The ring shape of the complex implies it has a role in controlling access to the viral organelle and ensuring the exit of properly capped viral RNA. Our results provide high-resolution information about the membrane association of the replication machinery of positive-sense single-stranded RNA viruses, and open up avenues for the further characterization of viral replication on cell membranes and the generation of antiviral agents.

Download PDF

Main

Alphaviruses generate invaginations in the plasma membrane or cytoplasmic vacuoles of host cells, creating small (around 50 nm in diameter) lipid baskets known as spherules[2]. Spherules have a small aperture that connects with the external cytosol, which is the only way out for the newly synthetized viral RNA and the only way in for the metabolites and proteins that are required for RNA synthesis. The extruded viral RNAs are capped and polyadenylated, ready for translation of the viral proteins by the host. This is achieved by viral replication complexes that assemble onto cellular membranes, promoting spherule formation and synthesizing viral RNAs in a coordinated fashion.

Alphaviruses have a replication complex that contains four non-structural proteins (nsP1, nsP2, nsP3 and nsP4), which are produced following cleavage of the viral polyprotein precursor by a viral protease in nsP2. nsP1, nsP2, nsP3 and nsP4 are essential for replication[9,10]. nsP1 is the only one of these proteins that is known to interact directly with the membrane, and it displays two activities that are necessary for the capping of viral RNA: *S*-adenosyl-l-methionine (SAM)-dependent methyltransferase (MTase) and m^7GTP transferase (GTase) activities[11,12,13,14], both of which are dependent on membrane binding[15]. Here we show the structure of the nsP1 complex, which provides a structural basis for these phenomena and challenges biochemical data that have accumulated over decades on positive-sense single-stranded RNA viruses replicating in membrane-associated viral factories.

Assembly of nsP1 into active dodecameric pores

We expressed nsP1 recombinantly in *Escherichia coli* and in insect cells[16], and recovered inactive monomeric and active membrane-associated nsP1, respectively. Detergent screening enabled us to solubilize and purify active ring-shaped complexes of nsP1 from insect cells and inactive monomeric protein, which indicates that nsP1 of chikungunya virus (CHIKV) needs to be assembled as oligomers for activity (Extended Data Fig. 1, Methods). We determined the structure of the complex using single-particle cryo-electron microscopy (cryo-EM). The sorting of particles into two-dimensional (2D) and three-dimensional (3D) class averages was consistent with two volumes, which correspond to dodecameric single and double rings of nsP1: the structures of these rings were determined at a resolution of 2.6 Å and 2.9 Å, respectively (Extended Data Figs. 2, 3, Extended Data Table 1). The absence of contacts between the interface of the double rings confirms that the single ring is the biological assembly (Extended Data Fig. 4). Twelve molecules of nsP1 assemble in the ring with C12 symmetry (Fig. 1a). The rings are 18.6 nm in diameter and 7 nm in height, and have a central aperture that is 7 nm wide (Fig. 1b, c). Three regions are well-defined in the complex: the crown, the waist and the membrane-binding skirt, which together confer a bodice-like shape to the complex (Fig. 1c). The crown is formed from the capping domains of the 12 subunits (as discussed in 'Atomic structure of CHIKV nsP1 protein'), generating a cone-shaped inner chamber that is negatively charged, about 3.7 nm in depth and has a diameter of 14 nm at the top that narrows to 7 nm at the bottom. The top of the crown is lined with positively charged pockets that correspond to the active sites of the capping domain. Under the crown, the 7-nm-wide waist region defines a pore that is 2 nm in depth as well as a positively charged region outside the complex. The inner walls of the pore have a neutral charge and would allow for the passage of globular proteins smaller than about 70–90 kDa in size. Under the waist, spikes from the membrane-binding skirt project into the detergent micelles at an angle of around 35° from the equatorial plane of the pore, generating a concave and positively charged surface that extends from the bottom of the complex to the lower external waist (with the exception of the hydrophobic tips of the spikes). Tomographic reconstructions of spherule necks, performed in a nodavirus (Flock House virus (FHV)) at low resolution, maintain dimensions and architecture similar to those shown by the nsP1 complex[9] (Fig. 1d, Extended Data Fig. 5). In conclusion, the nsP1 complex forms enzymatically active rings that are monotopically associated with the membrane within the spherule necks, and which gate access to the organelle. This is the foundation of the generation of spherule-like viral replication factories.

Fig. 1: Cryo-EM structure of the spherule–pore complex of CHIKV nsP1.

figure1

a, Ribbon representation of the nsP1 complex from its cytosolic (top) view. The 12-fold symmetry is indicated by numbering; each protomer is shown in a different colour. **b**, Surface representation of the top cytoplasmic view (top) and membrane-bound side (bottom). The surface electrostatics were calculated using APBS (https://www.poissonboltzmann.org/) from −5 kT/e to 5 kT/e, and are represented by the colour code of the bottom bar. The diameters of the ring and the pore aperture are indicated. **c**, Same representation as in **b**, of the lateral view of the complex (left) and a section through the broader part (right). The three regions (crown, waist and skirt) are delimited by black lines. The dimensions of the height, the cone upper aperture, the pore height and the bottom skirt diameter are indicated. The membrane-binding spikes are visible at the bottom of the skirt. The detergent-binding interface (substituting the membrane) is indicated by a thick dashed line. The projection angle of the spikes with respect to the pore is also indicated. **d**, Lateral view of tomographic reconstructions of FHV spherule necks[4] in which the CHIKV nsP1 complex is superposed (Extended Data Fig. 5). nsP1 is shown coloured by protomer inside the FHV volume (represented as a transparent grey surface). **e**, Schematic of the structural regions of nsP1, indicating the residues that delimit each region (CHIKV numbering). The green fragment (NT) is the N-terminal extension of the capping domain. The grey fragment corresponds to the C-terminal residues that are disordered in the structure (Extended Data Fig. 6). **f**, Two-side view of the nsP1 protomer structure, represented as a cartoon following the same colour code as in **e**. All secondary structures and the Zn atom are labelled, as are the corresponding regions of the crown, waist and skirt of the ring. The missing loop between αi and αh is indicated by blue dashed lines. The circled C and N represent the C and N termini, respectively.

Full size image

Atomic structure of CHIKV nsP1 protein

We built the atomic model of nsP1 de novo: it includes residues 3–471 out of 535, with density gaps at 364–376 and 450–458. No substantial differences were found between protomers of the double and single rings. nsP1 folds as two interconnected domains: the capping domain (located in the crown of the complex) and the ring-aperture membrane-binding and oligomerization (RAMBO) domain, which defines the waist and skirt regions of the complex (Fig. 1e, f). The capping domain (residues 1–294 and 459–472) exhibits high structural similarity with other SAM-dependent MTases: the DALI protein-structure comparison server[17]—using the complete Protein Data Bank (PDB) database—identifies MTases of *Encephalitozoon cuniculi* (PDB code 1RI1), vaccinia virus (PDB code 6RFL) and human (PDB code 5E8J) (among others) as being similar to CHIKV nsP1, with respective *Z*-scores of 10.1, 10.0 and 9.6, and root mean square deviations of 3.2 Å for all of them, including—respectively—188, 190 and 192 residues in the structural alignments (Extended Data Fig. 6). All of these MTases exhibit variations of a canonical SAM-dependent fold that comprises a core β-sheet of seven β-strands (β1 to β7) flanked by α-helices. In nsP1, the core β-sheet is modified through substitution of β3 by the α-helix αC (which forms an α-bundle with αB and αk; upper- and lower-case letters denote conserved secondary structures among MTases and specific secondary structures of CHIKV MTase, respectively), the incorporation of an additional β-strand (β6′) at the outer edge of the sheet and the inclusion of a Zn-binding site formed by the tetrahedral arrangement of the side chains of residues H79, E129, C134 and C141 (Extended Data Fig. 3a). The nsP1 N terminus is extended by a β–α–β motif (β1′–αa–β2′). An additional, smaller β-sheet insertion (β8 to β11) is conserved in vaccinia virus, human and *E. cuniculi* MTases[18,19], but is absent in other positive-stranded RNA viruses such as flavivirus MTases[20]. This insertion is involved in the binding of a GTP acceptor in the methyltransferase reaction. Within this region, nsP1 has a 35-amino-acid-long loop insertion between β9 and β10 (residues 201–236) that is critical for membrane binding and oligomerization (which we term membrane binding and oligomerization loop 1 (MBO loop 1)) (Extended Data Fig. 6a). We could assign weak density, consistent with an α-helix (αk), to residues 462–472 at the C terminus of nsP1 (Extended Data Fig. 3b). Beyond this point, density could not be resolved, which indicates that the missing C-terminal 60 residues are disordered and projected towards the top of the crown.

The RAMBO domain (residues 295–450) folds in two β-sheets of antiparallel strands (β13–β15 and β12–β16), forming the platform on which the capping domain sits. The α-bundle that follows these strands comprises three α-helices (αh, αi and αj), which form the inner walls of the pore. A loop between αh and αi (residues 365–375) is not visible, which implies that it is highly flexible and deployed towards the cone area. Infections with temperature-sensitive mutants of the Sindbis virus RNA-dependent

RNA polymerase nsP4—which prevent the synthesis of negative-strand RNA under non-permissive temperatures—could be compensated by mutations in nsP1 (T349K or T349L and N374H or N374I) (CHIKV T351 and N375) that are, respectively, located at the base and in the disordered loop at the top of the α-bundle[21,22] (Extended Data Fig. 6d). This suggests that nsP4 may interact with both the inner and the outer sides of the pore. Beneath the complex, a long loop (which we term the MBO loop 2) and a pair of long antiparallel strands (β13 and β14 (which we term the MBO β-turn)) are involved in membrane binding (as discussed in 'nsP1 oligomerization defines membrane binding').

In conclusion, the nsP1 capping enzyme is derived from a classic SAM-dependent MTase fold with modifications that allow for the capping reaction, multimerization and membrane binding. The modifications include novel insertions and extensions at the N terminus and the C terminus of the MTase fold. Sequence similarity shows that this folding is conserved among all alphaviruses (Extended Data Figs. 6d, 7).

nsP1 oligomerization defines membrane binding

The structure shows that oligomerization is mediated by contacts that involve the capping and, mainly, the RAMBO domain. Our analysis of the complex interfaces using the PISA server[23] reveals an extensive interface that engages 84 amino acid residues in contacts with the adjacent $nsP1^{n-1}$ and 92 residues in contacts with $nsP1^{n+1}$ subunits, burying 3,282 $Å^2$ and 3,213 $Å^2$ of protein surface, respectively. Each of the 12 interfaces includes 49 hydrogen bonds and 19 salt bridges, (Extended Data Figs. 7, 8, Supplementary Table 1). Altogether this network of interactions buries 29.3% of the nsP1 surface area (reaching 77,940 $Å^2$ for the whole ring), and engages most of the nsP1 secondary structures. As a consequence, oligomerization allosterically activates the enzyme by stabilizing the conformation of the capping domain and generating a bilobular catalytic pocket in which the GTP-binding lobe faces the interior, and the SAM-binding lobe faces the exterior, of the crown (Fig. 2a).

Fig. 2: nsP1 oligomerization and membrane binding are coupled processes.

figure2

a, Left, the top view of the ring is represented as a cartoon and coloured as in Fig. 1f. The active site cavities are depicted as green meshes. Access to the GTP- and SAM-binding pockets in the active site from each side of the ring is indicated. The active site (dashed box) is magnified on the right; the view is indicated by the eye icon. The

entrance of the GTP and the SAM to their respective binding pockets in the active-site cavity is indicated by arrows. The pocket is covered by the neighbouring $n - 1$ subunit (in grey). SAH and GTP molecules are superimposed from the structure of Ecm1 (PDB code 2RI1). **b**, Cartoon representation of the spike (dashed box), with magnified detail on the right. The *n* protomer is coloured as in **a**; the MBO β-turn and MBO loop 1 are coloured in red; and MBO loop 2 from the $n - 1$ protomer is coloured in green. The MBO loop residues are shown as sticks. The curved dashed line indicates the boundaries of the micelles found in the double-ring structure (Extended Data Fig. 4). A black arrow indicates the 10-Å length of the nsP1 fragment inserted into the FC12 micelles. **c**, MBO loop 2 represented as in **b**, with the density of the cryo-EM structure in blue mesh (drawn in PyMOL at 2σ). The FC12 detergent micelle boundary is indicated by a dashed line as in **b**. Details of the cysteine triad density are shown in Extended Data Fig. 3i–k. **d**, Representation of the MBO loop 1, as in **c**.

Full size image

The most notable part of the interface is generated in the vicinity of the membrane by the MBO loop 2 from the RAMBO domain, which wraps under MBO loop 1 of the capping domain and the β-turn of the RAMBO domain of the $nsP1^{n-1}$ (Fig. 2b). These elements fold together, forming amphipathic membrane-binding spikes that penetrate about 10 Å into the detergent FC12 micelle. The tip of the spike is hydrophobic and includes residues ^{225}LSIM^{228} from MBO loop 1 and ^{416}TCCCLWA^{422} from nsP^{n+1} MBO loop 2. The bases of the spikes create a positively charged belt that is continuous around the skirt, and which constitutes a platform for the binding of the negatively charged phospholipid heads. A triad of cysteines in MBO loop 2 are known to be palmitoylated[24,25] in mammalian cells, but —consistent with the very low levels of palmitoylation detected in our insect-cell-expressed nsP1 (Extended Data Fig. 1g)—we do not observe acylation in the structure (Extended Data Fig. 3i–k). However, the cysteine triad appears in the structure at the end of the tip inside the micelles, consistent with the putative insertion of the palmitoyl moieties into the cellular membrane. Thus, palmitoylation is not essential for pore formation, which suggests that other eukaryotic cell factors must be required. This is consistent with previous studies that have demonstrated that palmitoylation is a determinant of nsP1 localization within the membrane, rather than of activity or membrane binding[24]. However, in combination, the approximately 17-Å-long palmitoyl chains and the approximately 10-Å-long inserted tip can reach a depth of around 2.7 nm into the lipid bilayer (the thickness of which ranges from about 2.5 to 3.5 nm). This represents a very strong monotopic interaction with the lipid bilayer. The well-defined electron density maps in the bases of the spikes indicates that the spikes are rigidly projected from the complex (Fig. 2c, d). The strength of the membrane binding, the rigidity of the spikes and the curvature of the positively charged skirt edges—which attract the membrane phospholipid heads—can potentially induce the

marked membrane bending that is observed in spherule necks[7,9]. Thus, the structure of the spikes demonstrates the coupling between oligomerization, allosteric activation of the capping domain, membrane binding and membrane bending in the assembly of the nsP1 complex. This is likely to be conserved among alpha-like viruses[26,27].

Structural basis of the capping reaction

In contrast to conventional capping systems (which use sequential capping and methylation reactions to form the cap-1 structure (m^7GpppRNA)), alphavirus nsP1 first methylates the GTP, covalently binds m^7GMP and finally transfers m^7GMP to a 5′-end diphosphate viral RNA acceptor[13]. Our structure shows that this is achieved by a modified SAM-dependent MTase-like domain. Superposition of the nsP1 capping domain with *E. cuniculi* MTase bound to *S*-adenysol-l-homocysteine (SAH) and GTP[19] enabled us to identify residues, defining their binding sites for the guanine-N7 methylation reaction (Fig. 3, Extended Data Fig. 9a, b). The GTP-binding site is formed by residues close to the base moiety-binding position (A40, D152, Y285, Y154 and Y248) and positively charged and polar residues near the triphosphate position (K49, H45, R41, R70, R71, S44, Q151 and D152) (Fig. 3a, Extended Data Figs. 3g, 9a). The SAM-binding pocket is defined by residues shared with the GTP-binding site (R70, R71, Q151 and D152) and others that are exclusive for SAM binding (V153, G65, R92, E88, D89 and P83) (Fig. 3b, Extended Data Figs. 3h, 9b).

Fig. 3: Structure of the capping active site of nsP1.

a, Cartoon representation of the nsP1 GTP-binding-site cavity. The GTP moieties (represented as lines) are superposed in two positions, from the structures of *E. cuniculi* in complex with m^7GpppG (PDB code 2RI2) alone (red sticks), and m^7GpppG and SAH (PDB code 1RI1) (cyan sticks). Only the GTP moiety of the cap structure that was visible in these PDB entries is shown. The amino acid residues that

define the cavity and form putative contacts to the GTP are shown as sticks and labelled. The secondary structures that shape the cavity are also labelled. The catalytic histidine H37 is shown as sticks and highlighted by a transparent sphere envelope. $GTP^{(SAH+)}$ label indicates the GTP position in the structure that includes SAH. GTP label indicates the GTP position in the structure with only m^7GpppG. **b**, Cartoon representation of the nsP1 SAM-binding-site cavity. The cavity is shown as in **a**, with the carbon backbone of the SAH molecule coloured as green lines, from superposition of *E. cuniculi* MTase in complex with m^7GpppG and SAH (PDB code 1RI1). The Zn atom is represented as a shadow sphere next to P83 and behind αB (Extended Data Fig. 9).

Full size image

The nsP1–m^7GMP intermediate is formed by a covalent bond between H37 and the α-phosphate of the m^7GTP[14] (Extended Data Fig. 9a, c). In our structure, H37 is close to the GTP-binding site but about 6–9 Å away from the superposed GTP α-phosphate position. Thus, after GTP methylation, a relocation of m^7GTP in the binding pocket or a conformational change must occur to permit the formation of the covalent intermediate nsP1–m^7GTP. The diphosphate viral RNA (the acceptor of the m^7GMP moiety) could access the active site through a positively charged path that runs from the cone-shaped chamber of the ring to complete the cap transfer (Extended Data Fig. 9d). However, the cap transfer requires the generation of the diphosphate viral RNA by nsP2. Thus, coupling of the activities of the two proteins is required for capping viral RNA during infection. Further biochemical and structural studies will be necessary to understand the nsP1–nsP2 coupling and the precise role of the identified nsP1 residues in specificity and coordination for carrying out the three steps of the viral RNA capping reaction.

Conclusion

To our knowledge, our structure of the nsP1 complex is the first to define the structural basis of membrane binding for the replication complex of a positive-sense single-stranded RNA virus. The nsP1 pore reveals the architecture of replication complexes in the membranes, and controls the transit of molecules that enter and exit spherules that contain the double-stranded RNA viral genome, acting as a kind of viral nuclear pore complex. This markedly improves our view of the mechanisms of action of replication complexes (Extended Data Fig. 10). Moreover, the high oligomerization order and the unusual spike-mediated interaction with the membrane makes nsP1 the first example of a new class of membrane-bending, monotopic membrane proteins[28,29]. This class appears to be common to several positive-sense single-

stranded RNA viruses. Our results thus open up avenues for the study of these viral replication complexes in the context of their membrane association.

Methods

No statistical methods were used to predetermine sample size. The experiments were not randomized, and investigators were not blinded to allocation during experiments and outcome assessment.

Expression and purification of CHIKV nsP1 from insect cells

nsP1 was expressed in Hi5 cells (Thermo Fisher). The coding sequence of nsP1 (corresponding to residues 1–535 of the non-structural polyprotein sequence from the S27 African prototype, UniProt identifier: Q8JUX6) was synthesized by Gen9 as a codon-optimized gene and subcloned into a pFastBac vector (Thermo Fisher) with a C-terminal heptahistidine tag. Recombinant bacmids and viruses were produced in YFP-DH10 Bac cells[16] and Sf21 cells (Thermo Fisher), respectively, according to the manufacturer's protocols. For protein expression, Hi5 cells in suspension at a density of $0.5–1.0 \times 10^6$ ml^{-1} were infected with baculoviruses at 2% volume of the culture. Cells were collected at 2–3 days after cell arrest, when nsP1 expression was ascertained to be highest by western blotting.

Cells were resuspended in buffer A (35 mM Tris pH 7.6, 200 mM NaCl, 2 mM TCEP, 5% glycerol and10 mM imidazole) supplemented with 1 mM PMSF, 10 $\mu g \times ml^{-1}$ DNase, 2 $\mu g \times ml^{-1}$ RNase and 2 mM $MgSO_4$, and lysed by sonication. Lysates were centrifuged at 15,000*g* to remove unbroken cells and debris, and then again at 100,000*g* to pellet the membrane fraction. Membranes were resuspended at 50 $mg \times ml^{-1}$ in buffer A containing 1 mM PMSF using a hand-held homogenizer, and then incubated with 1% fos-choline 12 detergent (Anatrace) for 2 h at 4 °C with gentle agitation for solubilization. Solubilized membranes were then recentrifuged at 100,000*g*, and supernatants containing nsP1 incubated with Ni-NTA resin (GE Healthcare) in batch at 4 °C for 30 min. Resin was washed with 10 column volumes of buffer A containing 40 mM imidazole and 0.13% fos-choline 12, and the protein eluted over 1.5 column volumes with buffer A containing 250 mM imidazole and 0.13% fos-choline. Elution fractions containing the protein were pooled and concentrated (Amicon 100k MW cut-off) for size-exclusion chromatography. Samples were applied to a Superose 6 10/30 column (GE Healthcare) pre-equilibrated with 25 mM tris pH 7.6, 200 mM NaCl, 2 mM TCEP and 0.13% fos-choline 12. Fractions were analysed by SDS–PAGE to assess purity, and western blotting with an nsP1 antibody and matrix-assisted laser desorption/ionization–time of flight (MALDI–TOF) mass spectrometry to confirm the presence of nsP1.

Expression and purification of CHIKV nsP1 from *E. coli*

The *nsP1* gene was cloned into a pET28b vector in frame with a C-terminal heptahistidine tag for expression in *E. coli* Rosetta pLysS (DE3) cells (Novagen). Cells were grown in 2TY medium at 37 °C until reaching an optical density of 0.8 at 600 nm, when isopropyl-β-d-thiogalactopyranoside was added at 0.5 mM to induce expression at 18 °C overnight. Cells were collected by centrifugation at 4,000*g* and frozen until use. Cell pellets were resuspended in 35 mM Tris HCl pH 7.6, 0.3 M NaCl, 2 mM TCEP, 5% glycerol and 10 mM imidazole (buffer A) supplemented with 1 mM PMSF, 10 μg × ml^{-1} DNase, 2 μg × ml^{-1} RNase and 2 mM $MgSO_4$ before lysis by sonication. Following centrifugation at 15,000*g*, the soluble fraction was applied to a 5-ml HisTrap crude FF column (GE Healthcare) pre-equilibrated in buffer A. The column was washed with buffer A containing 40 mM imidazole, and then eluted in buffer A containing 250 mM imidazole. Elution fractions containing nsP1 were concentrated (Amicon 30k MW cut-off) before application on a S200 10/30 size-exclusion column pre-equilibrated in 25 mM Tris-HCl pH 7.6, 0.2 M NaCl and 2 mM TCEP. Fractions were analysed by SDS–PAGE, MALDI–TOF and western blotting with an anti-nsP1 antibody.

Electron microscopy

The central fraction of the peak corresponding to nsP1 oligomers was selected for analysis by electron microscopy. For negative staining, 6 μl of the protein at a concentration of 60 μg × ml^{-1} was applied to Cu 300 mesh carbon grids (Agar Scientific), previously glow-discharged for 1 min at 15 mA using a PELCO EasiGlow cleaning system (Ted Pella). Grids were blotted, washed twice with water and stained with 6 μl of 2% (w/v) uranyl acetate before blotting and air drying. Images were acquired using a FEI Tecnai G2 Spirit microscope operating at 120 kV and equipped with a Veleta CCD camera (Olympus).

For cryo-EM, protein was diluted to 0.25 mg × ml^{-1} in size-exclusion buffer lacking detergent to reduce the concentration of free micelles applied to grids (to 0.5× the critical micelle concentration). Four μl of protein was applied to glow-discharged carbon-coated Cu/Rh 300 mesh Quantifoil R2/2 holey grids (Quantifoil), before manual blotting and plunge-freezing in liquid ethane using a Leica EM CPC cryo-fixation unit. Data were collected with a Titan Krios microscope operated at 300kV (ESRF-CM01)[30] equipped with a post column LS/967 energy filter (Gatan) (slit width 20 eV) and K2 Summit direct electron detector (Gatan) in counting mode. Using EPU automated software (FEI), 5,626 movies were collected at a nominal magnification of 165,000× (corresponding to a sampling rate of 0.827 Å per pixel) across a defocus range of 1 to 2.5 μm. Each movie was recorded with a dose rate of 5.27 e^- per pixel

per s for an exposure time of 5 s distributed over 40 frames, yielding a total accumulated dose of 38.5 e^- per $Å^2$.

Cryo-EM data processing

All data were processed using RELION 3.0[31]. Movies were corrected for drift using MotionCorr2 with dose-weighting[32] and contrast transfer function (CTF) determination from the aligned non-dose-weighted micrographs was performed with CTFFind4[33]. All frames of the movies were included for motion correction and CTF estimation. Poor-quality micrographs were discarded, yielding a subset of 5,148 images. Around 1,000 particles were selected from 100 images and subjected to 2D reference-free alignment to yield templates for the autopicking procedure of RELION. Following autopicking across the curated micrographs, 263,415 particles were extracted from the dose-weighted micrographs and subjected to 2D classification and particle sorting for removal of bad particles. Inspection of the 2D classes indicated that both single and double rings of nsP1 were present in the data, and data processing beyond this point was optimized to separate these species.

The best 2D classes (corresponding to 180,921 particles) were selected for 3D classification, using a single ring model as a template that had been generated ab initio from 2D classes obtained from a previous dataset collected from the same grid on a TALOS Arctica microscope (CNB-CIB cryo-EM facility). The model was low-pass-filtered to 60 Å, and 3D classification was performed with coarse alignment sampling (7.5°) using a circular mask of 290 Å and 3–5 classes. Ab initio model generation and all classifications were performed without imposing symmetry. Three-dimensional classification consistently yielded one major class corresponding to single rings (105,825 particles), and one class corresponding to double rings (47,338 particles). A further round of 3D classification was performed with the separated single-ring and double-ring classes to improve homogeneity, until further classification yielded no improvement. Three-dimensional classification performed with finer angular sampling did not indicate that there were conformational differences between individual protomers. A 3D reconstruction of particles from the best 3D class corresponding to single rings (94,018 particles) was performed in C1 using 3D auto-refine to a resolution of 4.3 Å (4.0 Å after map sharpening), and inspection of maps did not reveal conformational differences between protomers. The particles were thus 3D auto-refined imposing C12 symmetry to a resolution of 3.7 Å without masking, and 3.0 Å with masking, as estimated using the gold Fourier shell correlation criterion at a threshold of 0.143. Resolution improved to 3.4 Å and 2.9 Å following map sharpening, and further to 2.6 Å following a single round of particle polishing and per-particle CTF correction. Masks to perform map sharpening or refinements were generated through low-pass-filtering of the model to 15 Å and extending the map by 8 pixels and adding 6 pixels of a soft edge.

Particles from the best 3D class corresponding to double rings (47,338 particles) were auto-refined as described for single rings. Reconstructions in C1 reached a resolution of 7.1 Å (6.8 Å after map sharpening), and reconstructions performed imposing D12 symmetry reached a resolution of 3.87 Å without masking and 3.1 Å with masking. A single round of particle polishing and per-particle CTF correction finally improved the resolution to 2.9 Å. Masks were generated as outlined for single rings. Local resolution in the 3D structures was estimated using the localres implementation in RELION.

Model building

De novo model building of nsP1 was performed though fitting the protein sequence into C12- and D12-sharpened maps in Coot[34]. The quality of the maps allowed for unambiguous assignment of all residues with the exception of the two N-terminal residues (MG), residues 365–375, residues 451–457 and C-terminal residues 473–535, for which no density was observed. Density for residues 415–420 in MBO loop 2 within the micelle and C-terminal helix 458–472 is weaker, consistent with variations in local resolution estimates. Iterative cycles of model building and real-space refinement were performed with Coot and Phenix[35] with NCS to improve the model. Validation of the model was performed using MolProbity[36], and through cross-correlation analysis of the model and maps in Phenix. Pocket dimensions in the structure were calculated using POCASA[37]. Figures were generated using Chimera[38] or PyMOL.

Sucrose gradient membrane flotation assays

Discontinuous sucrose gradients and flotation assays were adapted from a previously published method[15]. Small-scale cultures (10 ml) of *E. coli* or Hi5 cells expressing nsP1 were prepared as outlined in 'Expression and purification of CHIKV nsP1 from insect cells' and 'Expression and purification of CHIKV nsP1 from *E. coli*'. Cells were resuspended in 2 ml of lysis buffer (35 mM Tris HCl, pH 7.6, 0.3 M NaCl and 2 mM TCEP) supplemented with 1 mM PMSF, 2 $\mu g \times ml^{-1}$ RNase and DNase and lysed by sonication. Following centrifugation at 15,000*g*, the soluble fraction was diluted with a 67% sucrose solution to yield a final concentration of 60%. The gradient layers (bottom to top) were as follows; 2 ml of the 67% solution, 2.5 ml of the sample, 5 ml of a 50% sucrose solution, followed by 2.5 ml of a 10% sucrose solution. All sucrose solutions were prepared in lysis buffer. Samples were centrifuged at 100,000*g* for 18 h in a SW40 Ti swinging-bucket rotor (Beckman Coulter) to allow the membrane fractions to float to the 10–50% interface. One-ml fractions were taken from the top of the gradient and analysed by SDS–PAGE.

Activity assays and western blotting

Five μM nsP1 was incubated with 50 μM m^7GTP and 100 μM SAH or 50 μM GTP and 100 μM SAM at 30 °C for 1 h in gel filtration buffer in 20-μl reaction volumes. Two μl of the reactions were applied to 10% SDS–PAGE gels for electrophoresis at 180 mV for 1 h. Samples were transferred to nitrocellulose membranes via electroblotting at 320 mA for 1 h. Following blocking of membranes with 5% milk in TBST buffer (50 mM tris-HCl pH 7.5, 150 mM NaCl and 0.05% Tween-20) for 1 h at room temperature, membranes were incubated overnight with a primary antibody raised against nsP1 (provided by A. Merits) or an anti-m^3G/m^7G antibody (Synaptic Systems). Both antibodies were used at a 1/10,000 dilution in TBST buffer containing 0.5% milk. Membranes were subjected to four 10-min wash steps in TBST, before incubation with a secondary-HRP conjugated antibody for 1 h, repetition of the wash steps and revelation with Amersham Start ECL reagent (GE Healthcare). Chemiluminescence was detected with a Kodak DS Digital Science Image Station.

Detergent screening for solubilization of nsP1 from membranes

Membranes were prepared from Hi5 cells expressing nsP1 as outlined in 'Expression and purification of CHIKV nsP1 from insect cells'. Following resuspension at 50 mg × ml^{-1} with a hand-held homogenizer, aliquots of the suspension were incubated with 1% detergent for 3 h at room temperature or at 4 °C overnight. Following centrifugation of samples at 100,000*g* for 2 h, supernatants were analysed by SDS–PAGE and assayed for guanyltransferase activity as outlined in 'Activity assays and western blotting'. The following detergents were tested: cymal-5 (5-cyclohexyl-15-cyclohexyl-1-pentyl-β-d-maltoside), anzergent 3-10 (*N*-decyl-*N*,*N*-dimethyl-3-ammonio-1-propanesulfonate), DG (*n*-decyl-β-d-glucopyranoside), β-OG (*n*-octyl-β-d-glucoside), fos-choline 12 (*n*-dodecylphosphocholine), DM (*n*-decyl-β-d-maltoside), sodium dodecyl sulfate (SDS), DMNG (decyl maltose neopentyl glycol), LDAO (lauryldimethylamine-*N*-oxide) and DDM (*n*-dodecyl-β-d-maltopyranoside).

Acyl capture experiments

The palmitoylation states of purified nsP1 samples were assessed with an acyl capture kit (Badrilla). In brief, 150 μg of oligomeric or monomeric nsP1 was incubated at 60 °C for 4 h in a buffer to block free thiols before acetone precipitation. The precipitates were redissolved and incubated with a reagent designed to cleave any palmitoyl or acyl moieties, in the presence of resin that covalently bound the liberated thiols. Paired negative controls performed with a thiol protection reagent in place of the cleavage reagent yielded estimates of background binding to the resin. Bound samples were eluted from the resin through heating in the presence of Laemmli buffer. Monomeric nsP1 purified from *E. coli* was also included as a negative control.

Reporting summary

Further information on research design is available in the Nature Research Reporting Summary linked to this paper.

Data availability

Structure coordinates are available from the PDB with accession codes 6Z0V and 6Z0U for single and double rings, respectively. The electron density maps are available from the Electron Microscopy Data Bank (EMDB) under accession codes EMD-11024 and EMD-11023 for single and double rings, respectively. All other data generated or analysed in this study are available from the corresponding author upon reasonable request.

Viral amino acid sequences used for gene synthesis and sequence alignments were retrieved from the UniProt database with the following accession numbers: CHIKV S27 African prototype (UniProt: Q8JUX6); CHIKV (UniProt: Q5XXP4), Semliki Forest virus (UniProt: P08411), Venezuelan equine encephalitis virus (UniProt: P27282), Sindbis virus (UniProt: P03317), aura virus (UniProt: Q86924) and salmonid sleeping disease virus (UniProt: Q8QL53). MTase structures for structural superpositions were retrieved from the PDB with accession codes 2RI1 and 1RI1 for *E. cuniculi* MTase, and 1L9K for dengue virus MTase.

References

1. 1.

   Romero-Brey, I. & Bartenschlager, R. Membranous replication factories induced by plus-strand RNA viruses. *Viruses* **6**, 2826–2857 (2014).

   CAS PubMed PubMed Central Google Scholar

2. 2.

   Harak, C. & Lohmann, V. Ultrastructure of the replication sites of positive-strand RNA viruses. *Virology* **479-480**, 418–433 (2015).

   CAS PubMed Google Scholar

3. 3.

Knoops, K. et al. SARS-coronavirus replication is supported by a reticulovesicular network of modified endoplasmic reticulum. *PLoS Biol*. **6**, e226 (2008).

PubMed PubMed Central Google Scholar

4. 4.

Kopek, B. G., Perkins, G., Miller, D. J., Ellisman, M. H. & Ahlquist, P. Three-dimensional analysis of a viral RNA replication complex reveals a virus-induced mini-organelle. *PLoS Biol*. **5**, e220 (2007).

PubMed PubMed Central Google Scholar

5. 5.

Egger, D. et al. Expression of hepatitis C virus proteins induces distinct membrane alterations including a candidate viral replication complex. *J. Virol*. **76**, 5974–5984 (2002).

CAS PubMed PubMed Central Google Scholar

6. 6.

Belov, G. A. et al. Hijacking components of the cellular secretory pathway for replication of poliovirus RNA. *J. Virol*. **81**, 558–567 (2007).

CAS PubMed Google Scholar

7. 7.

Kujala, P. et al. Biogenesis of the Semliki Forest virus RNA replication complex. *J. Virol*. **75**, 3873–3884 (2001).

CAS PubMed PubMed Central Google Scholar

8. 8.

Kawai, T. & Akira, S. Innate immune recognition of viral infection. *Nat. Immunol*. **7**, 131–137 (2006).

CAS PubMed Google Scholar

9. 9.

Pietilä, M. K., Hellström, K. & Ahola, T. Alphavirus polymerase and RNA replication. *Virus Res*. **234**, 44–57 (2017).

PubMed Google Scholar

10. 10.

Frolova, E. I., Gorchakov, R., Pereboeva, L., Atasheva, S. & Frolov, I. Functional Sindbis virus replicative complexes are formed at the plasma membrane. *J. Virol*. **84**, 11679–11695 (2010).

CAS PubMed PubMed Central Google Scholar

11. 11.

Tomar, S., Narwal, M., Harms, E., Smith, J. L. & Kuhn, R. J. Heterologous production, purification and characterization of enzymatically active Sindbis virus nonstructural protein nsP1. *Protein Expr. Purif*. **79**, 277–284 (2011).

CAS PubMed PubMed Central Google Scholar

12. 12.

Li, C. et al. mRNA capping by Venezuelan equine encephalitis virus nsP1: functional characterization and implications for antiviral research. *J. Virol*. **89**, 8292–8303 (2015).

CAS PubMed PubMed Central Google Scholar

13. 13.

Decroly, E., Ferron, F., Lescar, J. & Canard, B. Conventional and unconventional mechanisms for capping viral mRNA. *Nat. Rev. Microbiol*. **10**, 51–65 (2012).

CAS Google Scholar

14. 14.

Ahola, T., Laakkonen, P., Vihinen, H. & Kääriäinen, L. Critical residues of Semliki Forest virus RNA capping enzyme involved in methyltransferase and guanylyltransferase-like activities. *J. Virol*. **71**, 392–397 (1997).

CAS PubMed PubMed Central Google Scholar

15. 15.

Ahola, T., Lampio, A., Auvinen, P. & Kääriäinen, L. Semliki Forest virus mRNA capping enzyme requires association with anionic membrane phospholipids for activity. *EMBO J*. **18**, 3164–3172 (1999).

CAS PubMed PubMed Central Google Scholar

16. 16.

Trowitzsch, S., Bieniossek, C., Nie, Y., Garzoni, F. & Berger, I. New baculovirus expression tools for recombinant protein complex production. *J. Struct. Biol*. **172**, 45–54 (2010).

CAS PubMed Google Scholar

17. 17.

Holm, L. & Laakso, L. M. Dali server update. *Nucleic Acids Res*. **44**, W351–W355 (2016).

CAS PubMed PubMed Central Google Scholar

18. 18.

De la Peña, M., Kyrieleis, O. J. P. & Cusack, S. Structural insights into the mechanism and evolution of the vaccinia virus mRNA cap N7 methyl-transferase. *EMBO J*. **26**, 4913–4925 (2007).

PubMed PubMed Central Google Scholar

19. 19.

Fabrega, C., Hausmann, S., Shen, V., Shuman, S. & Lima, C. D. Structure and mechanism of mRNA cap (guanine-N7) methyltransferase. *Mol. Cell* **13**, 77–89 (2004).

CAS PubMed Google Scholar

20. 20.

Egloff, M. P., Benarroch, D., Selisko, B., Romette, J. L. & Canard, B. An RNA cap (nucleoside-2′-*O*-)-methyltransferase in the flavivirus RNA polymerase NS5: crystal structure and functional characterization. *EMBO J*. **21**, 2757–2768 (2002).

CAS PubMed PubMed Central Google Scholar

21. 21.

Shirako, Y., Strauss, E. G. & Strauss, J. H. Suppressor mutations that allow Sindbis virus RNA polymerase to function with nonaromatic amino acids at the N-terminus: evidence for interaction between nsP1 and nsP4 in minus-strand RNA synthesis. *Virology* **276**, 148–160 (2000).

CAS PubMed Google Scholar

22. 22.

Fata, C. L., Sawicki, S. G. & Sawicki, D. L. Modification of Asn374 of nsP1 suppresses a Sindbis virus nsP4 minus-strand polymerase mutant. *J. Virol*. **76**, 8641–8649 (2002).

CAS PubMed PubMed Central Google Scholar

23. 23.

Krissinel, E. & Henrick, K. Inference of macromolecular assemblies from crystalline state. *J. Mol. Biol*. **372**, 774–797 (2007).

CAS PubMed Google Scholar

24. 24.

Laakkonen, P., Ahola, T. & Kääriäinen, L. The effects of palmitoylation on membrane association of Semliki Forest virus RNA capping enzyme. *J. Biol. Chem*. **271**, 28567–28571 (1996).

CAS PubMed Google Scholar

25. 25.

Karo-Astover, L., Sarova, O., Merits, A. & Zusinaite, E. The infection of mammalian and insect cells with SFV bearing nsP1 palmitoylation mutations. *Virus Res*. **153**, 277–287 (2010).

CAS PubMed Google Scholar

26. 26.

Rozanov, M. N., Koonin, E. V. & Gorbalenya, A. E. Conservation of the putative methyltransferase domain: a hallmark of the 'Sindbis-like' supergroup of positive-strand RNA viruses. *J. Gen. Virol*. **73**, 2129–2134 (1992).

CAS PubMed Google Scholar

27. 27.

Ahola, T. New phylogenetic grouping of positive-sense RNA viruses is concordant with replication complex morphology. *MBio* **10**, e01402-19 (2019).

CAS PubMed PubMed Central Google Scholar

28. 28.

Allen, K. N., Entova, S., Ray, L. C. & Imperiali, B. Monotopic membrane proteins join the fold. *Trends Biochem. Sci*. **44**, 7–20 (2019).

CAS PubMed Google Scholar

29. 29.

Prinz, W. A. & Hinshaw, J. E. Membrane-bending proteins. *Crit. Rev. Biochem. Mol. Biol*. **44**, 278–291 (2009).

CAS PubMed PubMed Central Google Scholar

30. 30.

Kandiah, E. et al. CM01: a facility for cryo-electron microscopy at the European synchrotron. *Acta Crystallogr. D* **75**, 528–535 (2019).

CAS Google Scholar

31. 31.

Zivanov, J. et al. New tools for automated high-resolution cryo-EM structure determination in RELION-3. *eLife* **7**, e42166 (2018).

PubMed PubMed Central Google Scholar

32. 32.

Zheng, S. Q. et al. MotionCor2: anisotropic correction of beam-induced motion for improved cryo-electron microscopy. *Nat. Methods* **14**, 331–332 (2017).

CAS PubMed PubMed Central Google Scholar

33. 33.

Rohou, A. & Grigorieff, N. CTFFIND4: fast and accurate defocus estimation from electron micrographs. *J. Struct. Biol*. **192**, 216–221 (2015).

PubMed PubMed Central Google Scholar

34. 34.

Emsley, P., Lohkamp, B., Scott, W. G. & Cowtan, K. Features and development of Coot. *Acta Crystallogr. D* **66**, 486–501 (2010).

CAS PubMed Google Scholar

35. 35.

Liebschner, D. et al. Macromolecular structure determination using X-rays, neutrons and electrons: recent developments in Phenix. *Acta Crystallogr. D* **75**, 861–877 (2019).

CAS Google Scholar

36. 36.

Williams, C. J. et al. MolProbity: more and better reference data for improved all-atom structure validation. *Protein Sci*. **27**, 293–315 (2018).

CAS PubMed PubMed Central Google Scholar

37. 37.

Yu, J., Zhou, Y., Tanaka, I. & Yao, M. Roll: a new algorithm for the detection of protein pockets and cavities with a rolling probe sphere. *Bioinformatics* **26**, 46–52 (2010).

PubMed Google Scholar

38. 38.

Pettersen, E. F. et al. UCSF Chimera—a visualization system for exploratory research and analysis. *J. Comput. Chem*. **25**, 1605–1612 (2004).

CAS PubMed Google Scholar

39. 39.

Unchwaniwala, N. et al. Subdomain cryo-EM structure of nodaviral replication protein A crown complex provides mechanistic insights into RNA genome replication. *Proc. Natl Acad. Sci. USA* **117**, 18680–18691 (2020).

CAS PubMed Google Scholar

40. 40.

Hellström, K. et al. Partially uncleaved alphavirus replicase forms spherule structures in the presence and absence of RNA template. *J. Virol*. **91**, e00787-17 (2017).

PubMed PubMed Central Google Scholar

41. 41.

Frey, T. K., Gard, D. L. & Strauss, J. H. Replication of Sindbis virus. VII. Location of 5-methyl cytidine residues in virus-specific RNA. *Virology* **89**, 450–460 (1978).

CAS PubMed Google Scholar

42. 42.

Hsuchen, C. C. & Dubin, D. T. Di-and trimethylated congeners of 7-methylguanine in Sindbis virus mRNA. *Nature* **264**, 190–191 (1976).

ADS CAS PubMed Google Scholar

43. 43.

Spuul, P. et al. Role of the amphipathic peptide of Semliki forest virus replicase protein nsP1 in membrane association and virus replication. *J. Virol*. **81**, 872–883 (2007).

CAS PubMed Google Scholar

Download references

Acknowledgements

We thank the European Synchrotron Radiation Facility for provision of beam time on CM01, and E. Kandiah for assistance; J. Martin-Benito and the CNB-CIB (CSIC) cryo-EM facility for granting us access to cryo-EM equipment through a technical support contract, and J. Chichon for technical support; INSTRUCT-Eric and R. Melero for access to the computing facilities at the CNB-CSIC (PID 7046 VID 13154); A. Goulet, S. Spinelli and the electron microscopy platform at the AFMB; I. Berger and A. Aubert for supplying material and technical advice regarding eukaryotic expression; and T. Ahola, A. Merits and F. Rico for critical reading of the manuscript. The nsP1 antibody was provided by A. Merits, and the m^7G cap antibody by B. Coutard. This work has been supported by the Bettencourt Shueller Fondation and an ATIP-Avenir grant (CNRS/INSERM).

Author information

Affiliations

1. Aix-Marseille Université, CNRS, AFMB UMR 7257, Marseille, France

   Rhian Jones, Gabriel Bragagnolo & Juan Reguera

2. National Center of Biotechnology, CSIC, Madrid, Spain

   Rocío Arranz

3. INSERM, AFMB UMR7257, Marseille, France

   Juan Reguera

Authors

1. Rhian Jones
   View author publications

   You can also search for this author in PubMed Google Scholar

2. Gabriel Bragagnolo
   View author publications

   You can also search for this author in PubMed Google Scholar

3. Rocío Arranz
   View author publications

You can also search for this author in PubMed Google Scholar

4. Juan Reguera
View author publications

You can also search for this author in PubMed Google Scholar

Contributions

R.J. performed sample production and purification, biochemical characterization and structure determination together with J.R. G.B. contributed to protein production and purification. R.A. assisted with sample preparation for cryo-EM. J.R. conceived and obtained the funding for the project. R.J. and J.R. designed the experiments and J.R. wrote the Article with the input of R.J.

Corresponding author

Correspondence to Juan Reguera.

Ethics declarations

Competing interests

The authors declare no competing interests.

Additional information

Peer review information *Nature* thanks Kyung Choi and the other, anonymous, reviewer(s) for their contribution to the peer review of this work.

Publisher's note Springer Nature remains neutral with regard to jurisdictional claims in published maps and institutional affiliations.

Extended data figures and tables

Extended Data Fig. 1 Isolation and biochemical characterization of nsP1 ring complexes.

a, Size-exclusion profile of monomeric CHIKV nsP1 expressed in *E. coli* cells after purification by affinity chromatography. The elution volume corresponds to a

molecular weight of approximately 61 kDa, corresponding to a nsP1 monomer. Fractions corresponding to the peak of the monomeric nsP1are shown in the offset SDS–PAGE with the molecular weight markers on the left. **b**, Western-blot-based activity test with CHIKV nsP1 purified from insect cells (H5) and *E. coli* with an antibody specific for m^3G and m^7G. The capping intermediate of the methylated GMP covalently bound to nsP1 is detected at 61 kDa for samples purified from insect cells when SAM and GTP are added in the reaction, and substantially more when m^7GTP is added as substrate instead of GTP. Conversely, the monomeric nsP1 produced in *E. coli* shows no activity despite a substantially higher amount of protein used in the experiments. This is shown in the SDS–PAGE gel on the right. **c**, SDS–PAGE gels of fractions derived from a sucrose gradient flotation assay (Methods), in which extracts from *E. coli* cells (top gel) and Hi5 insect cells (bottom gel) expressing CHIKV nsP1 were subjected to flotation analysis. Total samples (In) were loaded in the 60% sucrose layer of the gradient (fractions 8 and 9), and during centrifugation membrane-associated proteins float to the 10–50% sucrose interface (fractions 3 and 4) and soluble proteins remain in the 60% layer. nsP1 expressed in Hi5 cells floats and that expressed in *E. coli* is mainly soluble (arrows). The sucrose concentration along the gradient is indicated, and molecular weight markers are in the second lane from the left. The fluorescence emission of soluble YFP, used for following insect cell expression with the MultiBac system[16], was monitored as an internal control (graph below). As expected, the YFP migrates to the soluble fraction. **d**, Screening to identify a detergent suitable for solubilization of CHIKV nsP1 from Hi5 membranes. Isolated membranes were incubated with a range of detergents at 1% concentration and subjected to ultracentrifugation. The resulting soluble fractions were analysed by SDS–PAGE (top-right panel) and for nsP1 guanyltransferase activity in the presence of SAH and m^7GMP by western blotting with the m^3G and m^7G antibody (bottom-right panel). Lanes are as follows: 1, crude membrane fraction; 2–11, soluble fractions with no detergent (2), anzergent 3-10 (3), cymal 5 (orange) (4), DG (5), β-OG (purple) (6), fos-choline 12 (blue) (7), DM (green) (8), SDS (9), DMNG (yellow) (10), DDM (grey) (11). **e**, Size-exclusion chromatograms of a subset of promising detergents that were used in scaled-up purifications (same colour scheme used as in **d**). **f**, Size-exclusion chromatogram of CHIKV nsP1 purified from insect cells with SDS–PAGE of elution fractions with molecular weight markers shown on the left. Fractions corresponding to the oligomeric peak (1) and monomeric peak (2) are indicated, as well as the fractions used for subsequent biochemical experiments with the oligomeric (O) and the monomeric (M) nsP1. **g**, Acyl capture experiment to assess palmitoylation of oligomeric and monomeric nsP1. After blocking of free thiols and cleavage of acyl thioester bonds, palmitoylated samples are retained by a resin that binds free thiols (cBF, cleaved bound fraction) and non-palmitoylated samples are washed away (cUF, cleaved unbound fraction). Paired negative controls in which thiols were not cleaved are also shown (pBF, protected bound fraction; pUF, protected unbound fraction). The input for the resin is labelled IF (input fraction). Only a very small proportion of

oligomeric nsP1 is palmitoylated. **h**, Guanyltransferase activity tests of the oligomeric (O) and monomeric (M) species that were pooled after size exclusion. The top panels show a western blot with a nsP1 antibody. The lower panel shows the protein activity as monitored in **b**. Only the oligomers produce the intermediate of the guanyltransferase reaction with both GTP and m^7GTP as substrate. Molecular weight markers are shown on the left. **i**, Negative-stain electron micrograph of the central fraction from the oligomeric peak shown in **f**. The micrograph shows top views of the ring (1), side views of single rings (2) and side views of double rings (3), all indicated by arrows. The magnification is indicated by the 100-nm-long bar below. All original gels can be found in Supplementary Fig. 1. All results from activity assays (**b**, **d**, **h**), acyl-capture experiments (**g**) and negative-stain electron-microscopy experiments (**i**) were successfully reproduced at least three times. Gels for sucrose flotation assays (**c**) are representative of two repeats.

Extended Data Fig. 2 Cryo-EM reconstruction of nsP1 single and double dodecameric rings.

a, Cryo-EM micrograph of nsP1 oligomers acquired with a Titan Krios microscope (ESRF-CM01), representative of 4,948 micrographs collected. Top views and side views of the single and double rings are visible. The power spectrum of the micrograph is shown in the offset. **b**, Two-dimensional class averages of nsP1. Classes correspond to single or double rings in a range of orientations. **c**, The cryo-EM image processing workflow. The 180,981 particles selected following 2D classification and image pruning were subjected to 3D classification using an ab initio model low-pass-filtered to 60 Å. Classification with different numbers of classes consistently yielded two main classes, corresponding to single rings (pink) and double rings (gold). For the single rings, a second round of 3D classification improved homogeneity and resolution of the final reconstruction. Final 3D reconstructions were performed with masking and imposing C12 and D12 symmetry for single and double rings, respectively, following a single round of particle polishing and per-particle CTF refinement. **d**, Angular distribution plot of all particles included in the final C12 symmetry reconstruction of the single rings (pink) and D12 symmetry reconstruction of the double rings (gold). The length and colour of the cylinders correspond to the number of particles at a given Euler angle. The plots demonstrate a higher distribution of particles in side orientations in the case of the double rings, and top orientations for single rings, but sufficient coverage of the symmetry space to avoid this being detrimental to the reconstruction. **e**, Final 3D reconstructions coloured according to local resolution for single rings (left) and double (right) rings. The resolution range is relatively narrow for both reconstructions (scale indicated), where resolution is highest in the core of the complexes around the pore aperture. Resolution is lower in the top and bottom of the rings, corresponding to the region interacting with the FC12 micelles, and the C-terminal helix (αk) respectively. **f**, Fourier shell correlation curves for the single ring

(left) and double ring (right) reconstructions. Curves for the unmasked (gold), masked (pink), phase-randomized (red) and cryo-EM density maps corrected for mask convolution effects (blue) are indicated, and the inset shows the final atomic model and mask used for the reconstructions. The resolutions estimated according to the 0.143 threshold are indicated, corresponding to 2.6 Å for single rings and 2.9 Å for double rings.

Extended Data Fig. 3 Details of the density maps of the C12 nsP1 volume reconstruction.

The panels were created in PyMOL with residues represented as sticks and density as blue mesh at the indicated σ. The carbon backbone is coloured according to domains, following Figs. 1, 2. **a**–**h**, Electron densities. **a**, The Zn-binding site. Dashed black lines indicate the tetragonal coordination of the Zn atom. The amino acid side chains coordinating the Zn atom are shown as sticks. **b**, The weak electron density for the C-terminal α-helix αk. **c**, The long helix αj. **d**, Helix αZ, **e**, The α-turn of the pore-wall helices αh–αi. **f**, The β-sheet β7. **g**,The GTP-binding site. **h**, The SAM-binding site. **i**–**k**, Three decreasing contour levels of the electron density observed around the cysteine triad at the edge of the membrane-binding spikes.

Extended Data Fig. 4 nsP1–detergent interactions.

Micelle arrangement and membrane-binding regions of the double-ring structure. **a**, Lateral section of the double-ring map represented by a green mesh. A section of the map including one detergent micelle is highlighted in blue (left). The central panel shows two symmetry-related nsP1 dimers (n and $n + 1$) interacting with the FC12 micelle, as a cartoon model coloured in pink and orange. Right, the same as in central panel without the blue mesh, showing the interaction between the two neighbouring nsP1s from each ring and the three cysteines at the tip of the spike. The closest residue between the two rings is C417 from each dimer, with an approximate distance of 4.4 Å between their sulfur atoms. **b**, Same representation as in **a** of the entire map, with the view rotated by 90° about the indicated two-fold axis.

Extended Data Fig. 5 Superposition of the nsP1 complex in the FHV tomographic reconstruction of spherule necks.

a, Cytoplasmic view of the nsP1 complex (coloured by protomer) superposed into the tomography map reconstructed from FHV growing spherules (light grey surface)[4]. The volume is shown at two contour levels, 1.2 (left) and 0.9 (right), using ChimeraX. The superposition shows the 12-fold symmetry of both structures and that they are of a similar shape and size. The FHV central crown appears to be slightly larger. The panel

on the left at lower contour level allows for visualization of the membrane around the crown. **b**, Lateral view of the superposition. The nsP1 fits into the lower part of the FHV crown in contact with the membrane. In the right panel, it is possible to appreciate the membrane bending carried out by the complex together with 12 external detached volumes of unidentified origin. From this view, an extension of the crown is visible at the top of the ring. This region probably corresponds to the polymerase domain of FHV protein A, which is in the same polypeptide chain as the capping enzyme that is homologous to alphavirus nsP1. **c**, Bottom view of the superposition. In this orientation, the inner shape of the viral spherule can be seen. The FHV volume was provided by P. Ahlquist, who has since published the same structure at higher resolution[39].

Extended Data Fig. 6 Structural comparison of nsP1 with *E. cuniculi* and dengue virus MTases.

a, Left, topology diagram of CHIKV nsP1. The MTase conserved motifs are coloured in yellow. The CHIKV-specific features of the capping domain are coloured in orange. The RAMBO domain is coloured in teal. The MBO regions are coloured in red and labelled. The Zn-binding site and the SAM-binding regions are also indicated. Middle, right, two views of nsP1 as a cartoon model rotated by 180°. The same colour code is used as in the diagram on the left, and secondary structural elements are labelled. The Zn atom is shown as a grey sphere. **b**, Same representation as in **a**, for the MTase of *E. cuniculi*. (PDB code 1RI1), in which the SAH and GTP ligands are labelled. **c**, Same representation as in **b**, for the MTase of dengue virus (PDB code 1L9K). In dengue virus, the MTase and RNA-dependent RNA polymerase domain are in the same protein (NS5). The connection with the polymerase domain is indicated at the N terminus. This MTase has only one central β-sheet instead of the two β-sheet folding of *E. cuniculi* and nsP1. **d**, ConSurf representation of nsP1 sequence conservation within the alphavirus family according to the alignment of Extended Data Fig. 7. Two views of nsP1 are represented as cartoons and coloured according to the conservation score calculated by ConSurf. The lower bar indicates the conservation degree of each residue from non-conserved (blue) to fully conserved residues (purple). The GTP and SAH putative ligands are shown as red and green transparent spheres. The side chains of residues mutated in previous studies are shown as green sticks (Supplementary Information). The positions of residues suspected to bind to nsP4, T351 and N375 (missing in the structure), are shown as yellow spheres. The αg and β11 secondary structures, previously[43] thought to be an amphipathic membrane-associated helix, are labelled.

Extended Data Fig. 7 Sequence alignment of alphavirus nsP1.

The sequence alignment of nsP1 sequences of CHIKV (UniProt: Q5XXP4), Semliki Forest virus (SFV) (UniProt: P08411), Venezuelan equine encephalitis virus (VEEV) (UniProt: P27282), sindbis virus (SINV) (UniProt: P03317), aura virus (UniProt: Q86924) and salmonid sleeping disease virus (SDV) (UniProt: Q8QL53). The secondary structural elements revealed by the nsP1 structure are indicated at the top of the alignment. Below the sequences, the residues forming the GTP-binding site are highlighted by blue spots, those forming the SAM-binding site by red spots and those involved in Zn binding by red stars. Underneath, the interface line indicates the residues involved in interactions with the $n + 1$ nsP1 protomer in pink and with the $n - 1$ in brown. The blue lines indicate those residues making contacts to $n - 1$ and $n + 1$. At the bottom, rectangles indicate the domain boundaries of the nsP1 fold, coloured as described in Fig. 1e. Three motifs are conserved in the amino acid sequences of alphaviruses and similar viruses such hepatitis E virus, rubella virus and more[26,27]: (i) the catalytic histidine (H37) responsible for the cap transfer; (ii) the DXG motif (in which X stands for any residue) (^{63}DIG^{65} in CHIKV); and (iii) and the DXXR motif (^{89}DPER^{92} in CHIKV)—the last two define the SAM-binding site. This suggests that all alphavirus nsP1 have similar capping enzymes. Driven by the structural alignment of nsP1 and *E. cuniculi* MTase, we can more generally assign the DXG motif to the SAM-dependent MTases motif D/EX(G)XGXGXDL[14,18,19], which —in alphavirus—corresponds to ^{63}DIGSAPXRR^{71}.

Extended Data Fig. 8 Oligomerization interface of the nsP1 complex.

Cartoon representation of one protomer (n, coloured by the domains as outlined in Fig. 1f, Extended Data Fig. 6a) flanked by two protomers ($n + 1$ and $n - 1$, in grey) from the exterior view of the complex. The interaction interfaces are depicted as transparent surfaces. Contacts with the $n - 1$ protomer are maintained mainly with the capping domain, whereas the contacts with $n + 1$ are made mainly with the RAMBO domain. The side chains of the n protomer residues involved in $n/n - 1$ and $n/n + 1$ hydrogen bonds are represented as sticks. The Zn atom is shown as a grey sphere and labelled. The secondary structural elements involved in interactions, the active site and the MBO loops of the n protomer are labelled and indicated by arrows. MBO loop 2 folds under the $n + 1$ protomer and MBO loop 1 over the $n - 1$ protomer. The interface with nsP1^{n-1} involves the MTase main β-sheet (including β6′, β6 and β7), the helix αZ and the N-terminal extension (mainly the loop between αa and β2′). The RAMBO domain is also engaged in the interaction by the strands β12, β15, β16 and the beginning of β13, the C terminus of the long helix αj and one side of αh at the pore-forming α-bundle. The interface with nsP1^{n-1} is built by the capping domain small β-sheet (β9 to β11), αB and the C-terminal αk in the top of the ring and notably by the MBO loop 1, which builds up most of the interface in the membrane-binding region. A small

interface between nsP1^{n-1} and nsP1^{n+1}, which is sealing the ring, is formed by residues represented in blue sticks and labelled.

Extended Data Fig. 9 Structure of the nsP1 capping active site and comparison with *E. cuniculi* MTase.

a, Structural alignment of CHIKV capping domain and *E. cuniculi* MTase (PDB code 1RI1) showing the GTP-binding site. The structures are represented in cartoon model and coloured in yellow for CHIKV (left) and green for *E. cuniculi* (right). The superposed GTP visible moieties corresponding to the *E. cuniculi* MTase structures in complex with SAH and m7GpppG (PDB code 1RI1) and only m^{7}GpppG, (PDB code 1RI2) are shown in both models as thin sticks with carbon atoms coloured in blue and red, respectively, and are labelled. The residues involved in GTP binding in *E. cuniculi*, and the residues positioned to maintain contacts with the superposed GTP in CHIKV are shown as sticks and labelled. The secondary structures are also labelled. **b**, Same representation as in **a**, showing the SAM-binding site. The SAH molecule of the *E. cuniculi* structure is superposed on CHIKV. **c**, Same representation as in **a**, **b**, focusing on the catalytic histidine H37, showing in dashed lines the distances with the GTP superposed phosphate α oxygen where covalent binding would occur for the GTase reaction. **d**, Surface electrostatics of the GTP-binding site by APBS are shown from −5 kT/e in red to 5 kT/e in blue as indicated in the bar below. The superposed GTP from PDB codes 1RI1 and 1RI2 are shown as in **a**. The direction towards the pore of the ring is indicated by a black arrow.

Extended Data Fig. 10 Model of replication-complex assembly, replication and spherule formation.

a, Our results demonstrate that the nsP1 active complex can assemble in the absence of other replication complex subunits. The complex could be formed by uncleaved nsP precursors as nsP123[40]; in this case, nsP123 would stay non-cleaved until step d. **b**, The nsP2, 3 and 4 subunits of the replication complex would be recruited on the spherule pore complex together with other cellular factors for the formation of active replication complexes. The negatively charged cone walls and the exposed loop between helix αi and helix αh could serve as anchoring points. **c**, The deep insertion of the amphipathic spikes into the membrane would have a wedging effect on the membrane, and the membrane phospholipid heads would interact with the concave positively charged patches around the waist and below the complex. Altogether, these interactions are prone to induce the first negative curvature of the membrane. Coupled with the synthesis of the negative RNA intermediate by nsP123+4, the spherule could grow below the pore, while maintaining a tight attachment to the complex. The direction of RNA synthesis into the pore is indicated by arrows, as the genomic RNA

transcripts released from virions are located in the cytoplasm. **d**, After complete synthesis of the negative strand and growth of the spherule, transcription of capped viral RNAs may occur. The double-stranded RNA templates for viral RNA transcription must be read by the polymerase inside the spherule. A conformational change of the replication complex upon cleavage of nsP1 from nsP2 (for example, the internalization of the nsP4 proteins into the spherule) should allow the change of RNA product direction (indicated by arrows). Indeed, thermal-sensitive mutants at both sides of the pore α-bundle suggests that nsP4 interacts with both sides of the pore (see 'Atomic structure of CHIKV nsP1 protein'). The forced traffic of the newly synthetized viral RNAs through the pore and capping active sites would ensure their capping before reaching the cytoplasm. **e**, The stoichiometry of the complex and size of the pore suggests that up to 12 capped viral RNA molecules could be capped simultaneously. **f**, After the 5′ of the viral RNA is capped the rest of the molecule will be expelled close to the MTase-domain GTP-binding site. This could facilitate the incorporation of internal methylations, a phenomenon that has previously been described for alphavirus viral RNA[41,42], that confers stability to the RNA and prevents its recognition by the innate immune system.

Extended Data Table 1 Cryo-EM data collection, refinement and validation statistics
Full size table

Supplementary information

Supplementary Information

This file contains Supplementary Text, Supplementary Methods, Data Availability Statement and Supplementary References.

Reporting Summary

Supplementary Table 1

List of atom-atom interactions across CHIKV nsP1complex protein-protein interface. List generated by the PDBsum server.

Supplementary Figure 1

Raw data gels corresponding to Extended Data Fig. 1.

Rights and permissions

Reprints and Permissions

About this article

Check for updates

Cite this article

Jones, R., Bragagnolo, G., Arranz, R. *et al.* Capping pores of alphavirus nsP1 gate membranous viral replication factories. *Nature* **589,** 615–619 (2021). https://doi.org/10.1038/s41586-020-3036-8

Download citation

- Received: 13 April 2020
- Accepted: 21 October 2020
- Published: 16 December 2020
- Issue Date: 28 January 2021
- DOI: https://doi.org/10.1038/s41586-020-3036-8

Comments

By submitting a comment you agree to abide by our Terms and Community Guidelines. If you find something abusive or that does not comply with our terms or guidelines please flag it as inappropriate.

Download PDF

This article was downloaded by **calibre** from https://www.nature.com/articles/s41586-020-3036-8

| Section menu | Main menu |

Structures of the glucocorticoid-bound adhesion receptor GPR97–G_o complex

Download PDF

- Article
- Published: 06 January 2021

Structures of the glucocorticoid-bound adhesion receptor GPR97–G_o complex

- Yu-Qi Ping[1,2,3] na1,
- Chunyou Mao[4,5] na1,
- Peng Xiao[3] na1,
- Ru-Jia Zhao[3] na1,
- Yi Jiang ORCID: orcid.org/0000-0002-0723-1413[1] na1,
- Zhao Yang[3],
- Wen-Tao An[3],
- Dan-Dan Shen[4,5],
- Fan Yang[3,6],
- Huibing Zhang[4,5],
- Changxiu Qu[2,3],
- Qingya Shen ORCID: orcid.org/0000-0001-6602-7116[4,5],
- Caiping Tian[7,8],
- Zi-jian Li[9],
- Shaolong Li[3],
- Guang-Yu Wang[3],
- Xiaona Tao[3],
- Xin Wen[3],
- Ya-Ni Zhong[3],
- Jing Yang[7],
- Fan Yi[10],
- Xiao Yu[6],
- H. Eric Xu ORCID: orcid.org/0000-0002-6829-8144[1],
- Yan Zhang ORCID: orcid.org/0000-0003-2189-0244[4,5,11,12] &
- Jin-Peng Sun ORCID: orcid.org/0000-0003-3572-1580[2,3]

Nature **volume 589**, pages620–626(2021)Cite this article

- 8899 Accesses
- 38 Altmetric
- Metrics details

Subjects

- Cryoelectron microscopy

Abstract

Adhesion G-protein-coupled receptors (GPCRs) are a major family of GPCRs, but limited knowledge of their ligand regulation or structure is available[1,2,3]. Here we report that glucocorticoid stress hormones activate adhesion G-protein-coupled receptor G3 (ADGRG3; also known as GPR97)[4,5,6], a prototypical adhesion GPCR. The cryo-electron microscopy structures of GPR97–G_o complexes bound to the anti-inflammatory drug beclomethasone or the steroid hormone cortisol revealed that glucocorticoids bind to a pocket within the transmembrane domain. The steroidal core of glucocorticoids is packed against the 'toggle switch' residue $W^{6.53}$, which senses the binding of a ligand and induces activation of the receptor. Active GPR97 uses a quaternary core and HLY motif to fasten the seven-transmembrane bundle and to mediate G protein coupling. The cytoplasmic side of GPR97 has an open cavity, where all three intracellular loops interact with the G_o protein, contributing to the high basal activity of GRP97. Palmitoylation at the cytosolic tail of the G_o protein was found to be essential for efficient engagement with GPR97 but is not observed in other solved GPCR complex structures. Our work provides a structural basis for ligand binding to the seven-transmembrane domain of an adhesion GPCR and subsequent G protein coupling.

Download PDF

Main

The orphan receptor GPR97 is a member of the adhesion GPCR (aGPCR) family[1,2,3]. As one of the evolutionarily ancient families in the GPCR superfamily, aGPCRs are crucial molecular switches that regulate many physiological processes, including brain development, ion–water homeostasis, inflammation and cell-fate determination[2,7,8,9,10,11]. Mutations in aGPCRs have been associated with specific human diseases, including vibratory urticaria, bilateral frontoparietal polymicrogyria,

chondrogenesis, Usher syndrome and male infertility[2,7,8]. Compared with other GPCR families, aGPCRs are well-known for the presence of a large ectodomain that contains the GAIN domain, which functions together with the seven-transmembrane (7TM) bundle as a pair, and subsequent activation of the receptor through tethered agonism, mechanical force or other mechanisms[3,7,12,13,14,15,16,17,18,19,20,21]. Although substantial progress has been made in discovering the emerging functions of aGPCRs, the coupling of several aGPCR members to G proteins remains to be clarified, the structural basis for aGPCR activation is unclear and whether the 7TM bundle of aGPCR constitutes a typical pocket to recognize a small chemical ligand is uncertain. In addition, because the aGPCR family does not share the conserved residues in class A or class B GPCRs for receptor activation and G protein coupling, aGPCRs may be activated through distinct sets of residue connections and coupling to G proteins via different motifs[22]. On the basis of this, the structural characterization of aGPCRs in complex with downstream signal transducers is of great value.

In the present study, we found that glucocorticoid stress hormones acutely inhibited the levels of cAMP via the activation of one aGPCR member, GPR97, which is involved in the development of experimental autoimmune encephalomyelitis, determination of B lymphocyte fate and the progression of acute kidney injury[4,5,23,24]. We further determined the cryo-electron microscopy (cryo-EM) structures of active GPR97 in complex with the heterotrimeric G protein G_o and two glucocorticoids, the anti-inflammatory drug beclomethasone (BCM) and cortisol, without or with scFv16 stabilization, respectively. Our studies provide important structural insights into the ligand binding, receptor activation and G protein coupling of an aGPCR member.

Glucocorticoids activate GPR97

BCM dipropionate is an exogenous ligand of GPR97 (ref. [25]). In solution, BCM dipropionate may undergo hydrolysis to produce BCM, a synthetic glucocorticoid drug[6] (Supplementary Fig. 2). We therefore suspected that BCM directly activates GPR97 and then verified this effect (Extended Data Fig. 1a–e, Supplementary Fig. 3, Supplementary Table 1). Dexamethasone, another glucocorticoid drug, showed greater potency (approximately threefold higher) than BCM (Extended Data Fig. 1d, Supplementary Fig. 4a–c, Supplementary Table 1). Both of these anti-inflammatory drugs share the same steroid core as endogenous steroid hormones. On the basis of this, we screened a panel of 23 endogenous steroid hormones and derivatives for the induction of GPR97 activity (Extended Data Fig. 1b, Supplementary Fig. 3, Supplementary Table 1). Glucocorticoid hormones, including cortisol (hydrocortisone), cortisone and 11-deoxycortisol, were found to be activating ligands for GPR97.

The administration of cortisol and cortisone to HEK293 cells overexpressing wild-type GPR97 elicited a dose-dependent decrease in the levels of forskolin-induced cAMP, with half maximal effective concentration (EC_{50}) values of 800 ± 10 pM and 2.61 ± 0.14 nM, respectively (Extended Data Fig. 1c–e, Supplementary Fig. 4a–c). The activation of GPR97 by glucocorticoids was further verified by G_{qo} dissociation assays (Extended Data Fig. 1f, Supplementary Fig. 4d, e). It has long been suspected that one or several GPCRs were unidentified glucocorticoid membrane receptors[26,27,28]. Thus, G_o-coupled GPR97 was a candidate for this unidentified glucocorticoid membrane receptor. To explore this hypothesis, we administered cortisone to mouse Y-1 cells of the adrenal cortex, which resulted in an acute reduction in the cAMP-induced and adrenocorticotropic hormone-induced release of corticosterone. The knockdown of *Gpr97* expression abolished the effects of cortisone (Extended Data Fig. 1g–i). These data suggest that GPR97 may be involved in the acute effects of glucocorticoids.

Cryo-EM studies of GPR97

We set out to determine the structure of human GPR97 in complex with glucocorticoids and G_{o1} using single-particle cryo-EM. GPR97 contains a GAIN domain, which has an auto-cleavage site that produces two subunits: the α-subunit (N-terminal fragment (NTF)) and the β-subunit (C-terminal fragment) (Extended Data Fig. 1a). Initially, we attempted to form the complex that comprised wild-type GPR97 and G_o; however, the intrinsic tendency of the GPR97 α-subunit to dissociate from the β-subunit and the resulting instability of the complex during purification presented a challenge for structure determination using cryo-EM. Thus, we mutated the autoproteolysis motif ^{248}HLT^{250} of GPR97 to ^{248}ALA^{250} to produce stabilized full-length GPR97 (designated GPR97-FL-AA) and used thermostabilized miniGo[29] to facilitate structure determination (Extended Data Figs. 1a, 2a, d, Supplementary Fig. 1). GPR97-FL-AA showed comparable activity towards various agonists and therefore would not cause significant structural perturbation (Extended Data Fig. 1d, Supplementary Fig. 4a). Accumulated data have suggested that the Stachel sequence that resides in the GAIN domain has a central role in governing aGPCR activation[7,16,17,18,19,20]. The GPR97 β-subunit responded to BCM and cortisol stimulation with an 8–30-fold higher potency than GPR97-FL-AA or wild-type GPR97 (Extended Data Fig. 1d, Supplementary Fig. 4a). Removal of the Stachel sequence, which forms the tethered motif, from the N-terminal GPR97β (designated GPR97-β-T) eliminated this effect, confirming the important role of the tethered sequence[19,21] (Extended Data Fig. 1a, d, Supplementary Fig. 4a).

Using a Titan Krios microscope, a total of 2,707 and 5,871 movies were collected for the BCM–GPR97-FL-AA–G_o and the cortisol–GPR97-FL-AA–G_o–scFv16 complexes reconstituted in vitro, respectively (Extended Data Fig. 2). The 2D averages showed clear density for the GPR97 transmembrane domain and the heterotrimeric G protein; however, the density of the NTF was visible only in certain directions and was very weak (Extended Data Fig. 2b, e, Supplementary Fig. 5). We therefore improved the quality of the cryo-EM map by applying a masked classification with the alignment focused on the GPR97 7TM bundle and the G_o protein subunits. The resulting cryo-EM maps after final refinement have overall resolutions of 3.1 Å and 2.9 Å for the BCM-bound and the cortisol-bound GPR97–G_o complexes, respectively (Fig. 1, Extended Data Fig. 2c, f).

Fig. 1: Cryo-EM structure of the GPR97–G_o complex.

figure1

a, **b**, Orthogonal views of the density map for the BCM–GPR97–G_o (**a**) and the cortisol–GPR97–G_o–scFv16 (**b**) complexes. GPR97 is shown in light sea green, $G\alpha_o$ in salmon, Gβ in light blue, Gγ in yellow, scFv16 in purple, BCM in slate blue and cortisol in pink. **c**, Orthogonal views of the model of the GPR97–G_o complex and the detailed ligand positions of BCM (slate blue) and cortisol (pink) in the structure.

Full size image

The high-quality density map allowed accurate model building for receptor residues R270 to P527, the active core of BCM or cortisol, and most residues of the miniGo protein trimer (Fig. 1, Extended Data Fig. 2g, h, Extended Data Table 1). The structure of GPR97 adopted a unique 7TM bundle with several differences in both the spatial arrangement and the lengths of the transmembrane helices (see details in the following text) compared with other reported GPCR structures (Fig. 1c). Although previous experimental evidence indicated that the GAIN and 7TM domains function as a pair that serves as the hub for aGPCR activation[7,16,17,18,19,20], which leads to the hypothesis that the small-compound activator may also bind to the GAIN domain, we unexpectedly but unambiguously observed that glucocorticoids bound to a pocket within the 7TM domain of GPR97. At the cytoplasmic face, the 7TM bundle of GPR97 contains a large crevice to accommodate the G_o trimer. Unique to GPR97–G_o complexes, palmitoylation at the C terminus of G_o was observed to insert deeply into the 7TM core of GPR97, and the intracellular loop 1 (ICL1) of the receptor adopted a one-turn helical structure that formed direct contacts with Gβ (Fig. 1c).

The 7TM bundle and ECLs of GPR97

To date, the transmembrane domain structures of representative members from all GPCR families have been reported, with the sole exception of the aGPCR family. Comparison of the 7TM bundle of the GPR97–G_o complex with the structures of neurotensin receptor type 1 (NTSR1; class A), parathyroid hormone/parathyroid hormone-related peptide receptor (PTH1R; class B) and smoothened receptor (class F) in complex with their cognate G-protein-binding partners revealed similar topology (Extended Data Fig. 3a). For class C GPCRs, we used the recently reported structure of the active $GABA_B$ receptor that was determined in the presence of G protein for comparison (Protein Data Bank (PDB) ID: 7C7Q)[30]. However, structural comparison between these receptors suggested that there was greater separation between TM6 and TM7 in GPR97 than in the other four structures and that TM1 and TM7 were relatively close together (Extended Data Fig. 3a–c). In particular, GPR97 showed a relatively short TM6 (Extended Data Fig. 3d). The proximity of the extracellular portions of TM6 and TM7 provides additional space for ligand binding. Above the transmembrane bundle, an extended β-sheet in extracellular loop 2 (ECL2) created a

flap on the top of TM6 and TM7 to constitute the top cover of the ligand-binding site (Fig. 1c, Extended Data Fig. 3e). Notably, the part of ECL2 that covers ECL3 (the top of TM6 and TM7) was constituted by consecutive hydrophilic residues, namely, R409^{ECL2}DRENRT415^{ECL2} (Extended Data Fig. 3e). Cryo-EM densities were unambiguously assigned only for the main chain of this ECL2 region. ECL2 consistently exhibited a very weak interaction with ECL3 (Extended Data Fig. 3f), serving as a flexible lid for the ligand-binding pocket, and might connect the conformational changes of the NTF to the 7TM bundle.

Ligand-binding pocket

The presence of a small ligand-binding pocket within GPR97 is unusual but is consistent with the hypothesis that aGPCRs could be activated via a Stachel-independent mechanism[3,15]. The overall glucocorticoid-binding pocket of GPR97 within the 7TM bundle had a long ellipsoidal shape with a large, solvent-accessible channel that connected to the extracellular region (Fig. 2a–d). The cryo-EM maps enabled the unambiguous assignment of BCM and cortisol, with the A–B rings of the steroid core facing towards the solvent channel and the C–D rings oriented downwards against TM1, TM2 and TM7 (Fig. 2a–d, Extended Data Fig. 4a–f). The binding modes of the two glucocorticoids were further supported by molecular dynamics simulations (Extended Data Fig. 4g). The steroid cores of bound glucocorticoids were perpendicular to the plane of the plasma membrane, parallel to TM7 and at an angle of approximately 70° from the central TM3 (Extended Data Fig. 4e, f). The bound glucocorticoids fit into the centre of the pocket, which was deep and open, made up of residues from six transmembrane helices (TM1–TM3 and TM5–TM7) as well as residues from ECL2 and ECL3 (Fig. 2a–d). Compared to ligands in other ligand-bound GPCR structures (Extended Data Fig. 4h), BCM and cortisol were observed to pack relatively close to TM6 and TM7, with the bulky steroid core further pushing TM7 away from the core of the transmembrane domain, thus leading to a large separation between the extracellular ends of TM6 and TM7.

Fig. 2: The glucocorticoid-binding pocket of GPR97.

figure2

a, Vertical cross-section of the BCM-binding pocket in GPR97. **b**, Corresponding interactions that contribute to BCM binding in GPR97. The hydrogen bond is depicted as a dashed line. In contrast to cortisol, BCM interacts with I494, which is labelled in red. **c**, Vertical cross-section of the cortisol-binding (top) and the BCM-binding (bottom) pockets in GPR97. **d**, Corresponding interactions that contribute to cortisol binding in GPR97. The polar interaction is depicted as a dashed line. **e**, **f**, The effects of mutations in the ligand-binding pocket or structural motifs in GPR97 on BCM-induced (**e**) or cortisol-induced (**f**) cAMP inhibition. Values are shown as the mean ± s.e.m. from three independent experiments performed in triplicate. $^{***}P < 0.001$; NS, not significant (comparison between the wild-type full-length GPR97 (GPR97-FL-WT) and its mutant). All data were analysed by two-sided, one-way analysis of variance (ANOVA) with Tukey's test ($P < 0.0001$, $P < 0.0001$, $P < 0.0001$, $P < 0.0001$, $P < 0.0001$, $P = 0.1034$, $P < 0.0001$, $P < 0.0001$, $P < 0.0001$, $P < 0.0001$, $P < 0.0001$ and $P = 0.1233$ from top to bottom for the BCM group; $P < 0.0001$, $P < 0.0001$, $P < 0.0001$, $P < 0.0001$, $P < 0.0001$, $P = 0.5662$, $P < 0.0001$,

$P < 0.0001$, $P < 0.0001$, $P < 0.0001$, $P < 0.0001$ and $P = 0.0646$ from top to bottom for the cortisol group).

Full size image

Glucocorticoids are recognized by extensive hydrophobic contacts and only one polar interaction. The residues in contact with BCM were very similar to those in contact with cortisol, sharing ten identical residues and differing by only three hydrophobic residues (Extended Data Fig. 4i). The plane of the steroid core of these two glucocorticoids was defined by two hydrophobic patches: one side constituted by $F323^{2.64}$, $F345^{3.36}$, $Y406^{ECL2}$ and $W421^{ECL2}$, and the other side by $W490^{6.53}$, $I494^{6.57}$, $L498^{ECL3}$ and $F506^{7.42}$ (the superscript text following the receptor residues is indicated according to the Wootten numbering system for the class B subfamily of GPCRs[31]; the lowercase letter 'a' after the superscript text indicates the use of the Ballesteros–Weinstein system for the class A subfamily of GPCRs[32] (Fig. 2b, d, Extended Data Fig. 4a–d, Supplementary Table 2)). The polar contacts resided in the bottom of the pocket and were mediated by the interaction of the 18-carbonyl or the 19-hydroxyl group with the side chain of $N510^{7.46}$ in glucocorticoid-bound GPR97 structures (Fig. 2b, d, Extended Data Fig. 4c, d).

The binding of a ligand to the 7TM bundle of class A receptors has been demonstrated to couple to specific conformational alterations in the extracellular domain[33]. To exclude the constitutively bound glucocorticoids within GPR97, we used the intramolecular fluorescent arsenical hairpin bioluminescence resonance energy transfer (FlAsH-BRET) method to monitor the glucocorticoid-induced GPR97 conformational changes in the extracellular domain[34] (Extended Data Fig. 5a). The binding of BCM to GPR97 caused separation of the ECLs from the N terminus in a concentration-dependent manner, with the largest signal produced by labelling the FlAsH motif in ECL2 (Extended Data Fig. 5a–e, Supplementary Table 3). We next used both the cAMP assay and FlAsH-BRET-based extracellular conformational sensors to monitor the effects of mutations in ligand-binding pockets of GPR97. Consistent with the observations of the structures of GPR97 bound to glucocorticoids, mutations of the polar residue $N510^{7.46}$ or of any five hydrophobic pocket residues to alanine impaired both agonist-induced cAMP inhibition and extracellular conformational changes (Fig. 2e, f, Extended Data Figs. 5f–j, 6a–e, Supplementary Tables 3, 4). Notably, seven out of nine hydrophobic residues and one polar residue involved in BCM interaction are highly conserved in all aGPCR G subfamily members (Extended Data Fig. 5k), strongly implying that steroid hormones are probably ligands of other aGPCR G subfamily members.

Active structure of GPR97

Structural superimposition of the GPR97–G_o complex with other GPCR–G_o complexes corroborated the previous assignment of homologous residues at X.50 positions for each transmembrane helix by comparative studies[35]. Residue W490$^{6.53}$ of GPR97 aligned to roughly the same position as the homologous toggle switch residue W$^{6.48a}$ in class A GPCRs[29,36,37]. In GPR97, the potential toggle switch W490$^{6.53}$ sensed the binding of glucocorticoids by direct interactions (Fig. 3a, Extended Data Fig. 7a, b). Residues I$^{3.40a}$, P$^{5.50a}$ and F$^{6.44a}$ form the core triad motif[37], which is located close to the toggle switch, and these were replaced by F353$^{3.44}$, T442$^{5.46}$ and V486$^{6.49}$ in GPR97 (Fig. 3b). T442$^{5.46}$ of GPR97 did not form many interactions with F353$^{3.44}$, and these two residues were far from V486$^{6.49}$ (Fig. 3b). Thus, there are no traditional PIF core triad interactions in the active structure of GPR97. Instead, TM3, TM5 and TM6 were tethered by packing interactions mediated by F353$^{3.44}$, M356$^{3.47}$, F439$^{5.43}$ and the toggle switch residue W490$^{6.53}$ in the upper region (Fig. 3c). F353$^{3.44}$, F439$^{5.43}$, M356$^{3.47}$ and W490$^{6.53}$ served as a newly identified 'upper quaternary core' (UQC) (Fig. 3c, Extended Data Fig. 7c). In the lower region, L363$^{3.54}$ was packed against L450$^{5.54}$ and L479$^{6.42}$, forming a specific 'lower triad core' (Fig. 3c). The importance of the tight packing of TM3–TM6 by these residues was further supported by the observation that mutations in the UQC of GPR97 reduced the potency of stimulation of GPR97 by BCM (Figs. 2e, 3d, Extended Data Fig. 6, Supplementary Table 4). Residues involved in W$^{6.53}$ and the UQC were conserved in members of the G subfamily of aGPCRs (Extended Data Fig. 7d). Mutations of the UQC residues in GPR126, another aGPCR member, impaired Stachel peptide-induced activation (Extended Data Fig. 7e, f, Supplementary Table 5). These results indicated the potential structural importance of the conserved W$^{6.53}$ and UQC residues, which could be further confirmed by the solution of additional aGPCR structures.

Fig. 3: The active structure of GPR97.

figure3

a, The position of the W490 toggle switch in GPR97, which directly interacts with BCM. **b**, Superimposition of G_o-coupled GPR97 with G_o-coupled 5-$HT_{1B}R$ aligned at the 'PIF motif'. **c**, The detailed interactions of TM3–TM5–TM6 in G_o-coupled GPR97. **d**, The effects of mutations in transmembrane-helix tethering motifs in GPR97 on BCM-induced cAMP inhibition. Values are shown as the mean ± s.e.m. from three independent experiments performed in triplicate. $^{***}P < 0.001$ (comparison between GPR97-FL-WT and its mutant). All data were analysed by two-sided, one-way ANOVA with Tukey's test (from left to right: $P < 0.0001$, $P < 0.0001$, $P < 0.0001$, $P < 0.0001$, $P = 0.0961$ and $P = 0.0881$). **e**, Interactions mediated by $H(N)^{3.53}L(M)^{3.54}Y^{3.55}$. Both $H^{3.53}$ and $L^{3.54}$ of GPR97 directly interact with the G_o protein or the specific palmitoylation site. The hydrogen bond is depicted as a dashed line.

Full size image

Another notable observation is that in all aGPCR G subfamily members, TM7 lacks a conserved $N^{7.49a}P^{7.50a}XXY^{7.53a}$ motif, which mediates the packing of TM7 against TM3 in several active GPCR structures[29,36,38]. No significant packing between TM3 and TM7 was observed in the GPR97–G_o complex structures. The mutation of $I517^{7.53}$ to asparagine consistently had no significant effect on BCM-induced GPR97

activation (Fig. 3d, Supplementary Table 4). Therefore, GPR97 has a different transmembrane helix arrangement from other active class A GPCR structures.

On the cytoplasmic side, the separation of the TM3 and TM6 ends is approximately 14 Å (Extended Data Fig. 7g, h). The separation of the transmembrane ends is generally accompanied by a break in the ionic lock and the structural rearrangement of the $D^{3.49a}R^{3.50a}Y^{3.51a}$ motif in active class A GPCR structures[37]. The $D^{3.49a}R^{3.50a}Y^{3.51a}$ motif was replaced by $H(N)^{3.53}L(M)^{3.54}Y^{3.55}$ in the aGPCR family (Fig. 3e, Extended Data Fig. 7i, j). In GPR97, the conserved $Y364^{3.55}$ residue formed contacts with residues from TM5 and ICL2 and stabilized the ICL2 conformation (Fig. 3e). $H362^{3.53}$ and $L363^{3.54}$ of the $H(N)^{3.53}L(M)^{3.54}Y^{3.55}$ motif of GPR97 were shown to interact with $L348^{G.H5.20}$ and a palmitoylation on the α5 helix of G_o (the superscripts following the Gα residues are according to the Common Gα numbering system[39]) (Fig. 3e, Extended Data Fig. 7i). Mutations of any residue in the conserved HLY motif of GPR97 to alanine or mutation of $L363^{3.54}$ to the corresponding $R^{3.50a}$ in class A GPCRs significantly decreased the activation of GPR97 (Fig. 2e, f, Extended Data Figs. 6, 7k, Supplementary Table 4), suggesting the functional importance of the conserved $H(N)^{3.53}L(M)^{3.54}Y^{3.55}$ motif in the aGPCR family.

Coupling of GPR97 with G_o

The cytoplasmic side of GPR97 displayed a wide cavity. Aligning the central TM3 (GPR97–G_o, 5-HT_{1B}R–G_o and M2R–G_o) allowed us to identify a wider separation between TM5 and TM7 of GPR97 on the cytoplasmic side (Fig. 4a). This change led to an approximately 10° tilt of the α5 helix of G_o towards the plasma membrane in the GPR97–G_o complex structure (Fig. 4b). GPR97 has a significantly larger buried surface (1,116 $Å^2$) for G_o than does 5-HT_{1B}R (822 $Å^2$). The interface between GPR97 and G_o consisted of four transmembrane helices (TM3, TM5, TM6 and TM7) and three intracellular loops of GPR97 (Fig. 4c–f, Supplementary Tables 6–9). Specifically, residues of the C-terminal wavy hook of the α5 helix of G_o form hydrophobic and polar interactions with the cytoplasmic portion of TM6 (Extended Data Fig. 8a, b). $C351^{G.H5.23}$ of G_o formed a polar interaction with the side chain of $W520^{7.56}$. The N terminus of $C351^{G.H5.23}$ was the helical portion of the α5 helix of G_o, which fit into the cavity formed by residues from TM3, TM5 and TM6 (Extended Data Fig. 8a, b).

Fig. 4: General features of G_o coupling to GPR97.

figure4

a, A cytoplasmic view (left) and an orthogonal view (right) of the GPR97 7TM bundle compared with G_o-coupled 5-HT_{1B}R (PDB ID: 6G79) and M2R (PDB ID: 6OIK). GPR97 is shown in light sea green, 5-HT_{1B}R in wheat and M2R in salmon. **b**, The structures of G_o-coupled GPR97 (light sea green), 5-HT_{1B}R (wheat) and M2R (salmon) complexes were superimposed based on TM2, TM3 and TM4. This panel is shown with views at two different angles; the red arrows indicate the tilt of the α5 helix of $G\alpha_o$ from the GPR97–G_o complex compared to the 5-HT_{1B}R–G_o or M2R–G_o complexes. **c**, The residues in GPR97, 5-HT_{1B}R and M2R that contact G_o. **d**–**f**, The detailed interactions of ICL1 with Gβ (**d**), ICL2 with the α5 helix and the β1 and β3 strands of $G\alpha_o$ (**e**) and of ICL3 with the β6 strand and the α4 and α5 helices of $G\alpha_o$ (**f**). The hydrogen bonds are depicted as dashed lines.

Full size image

All three intracellular loops of GPR97 participated in direct binding to the G_o trimer. ICL1 formed both electrostatic and van der Waals interactions with the Gβ subunit

(Fig. 4d, Supplementary Table 7). Mutations of ICL1 residues significantly reduced BCM-induced GPR97 activity (Extended Data Figs. 6, 8c, Supplementary Table 4). ICL2 of GPR97 fit into the groove formed by the α5, αN, β1 and β3 strands of G_o (Fig. 4e). The hydrophobic side chains of $V370^{ICL2}$ and $F371^{ICL2}$ of GPR97 were packed against a hydrophobic cleft created by the α5 helix and β1–β3 strands of G_o (Fig. 4e, Supplementary Table 8). ICL3 is unstructured in most GPCR structures solved to date, but the complete structure was visible in the cryo-EM density in GPR97, which was probably stabilized by many direct interactions with G_o (Fig. 4f, Extended Data Fig. 9). Several GPR97 ICL3 residues (A463, T464, V466, K471 and N472) interacted directly with α4, α5 and β6 of G_o (Fig. 4f, Supplementary Table 9). Importantly, compared with all other solved GPCR structures, some of the extensive interactions of the three ICLs of GPR97 with G_o might contribute to the high basal activity observed for GPR97. Consistent with this hypothesis, mutations in key ICL1 and ICL3 residues that contact the G_o trimer not only decreased the BCM-induced cAMP reduction but also greatly decreased the basal activity of GPR97 (Extended Data Fig. 8d–f). Therefore, the interactions mediated by the ICLs could be one determinant for the high basal activity of GPR97.

Palmitoylation at the C-tail of G_o

A strong cryo-EM density was observed in the crevice between TM3, TM5 and TM6 of GPR97 and was connected to $C351^{G.H5.23}$ of the α5 helix end of G_o (Fig. 5a). Mass spectrometry enabled us to clarify this specific post-modification as a palmitoylation, which could be unambiguously assigned into the cryo-EM density (Extended Data Fig. 9a, b). Notably, the carbonyl group of the palmitoylation formed a well-defined hydrogen bond with $H362^{3.53}$ of the conserved $H^{3.53}L^{3.54}Y^{3.55}$ motif. The aliphatic chain of the palmitoylation formed contacts with 9 hydrophobic residues that were contributed by TM3 and TM5–TM7, inserting 17 Å deep into the 7TM core and finally reaching the UQC, thus further tethering the transmembrane helices in the active receptor conformation (Fig. 5a, b, Extended Data Fig. 9c). Importantly, a similar palmitoylation at $C351^{G.H5.23}$ of G_o or G_i proteins would clash with other GPCRs in all solved GPCR–G_i or GPCR–G_o complex structures (Extended Data Fig. 9d). Mutations of C351A or C351S of G_o markedly impaired G_o coupling to GPR97 but not to D2R, a prototype G_o/G_i-coupled receptor (Fig. 5c, Extended Data Fig. 9e–h). Therefore, the palmitoylation of the C terminus of the G_o protein contributed to its specific coupling to GPR97 (Supplementary Table 10).

Fig. 5: Palmitoylation of G_o mediates GPR97 coupling.

figure5

a, An unknown continuous electron density connected to C351 in the α5 helix of $G\alpha_o$ was observed in the cortisol–GPR97–G_o complex structure. A similar cryo-EM density was also observed in the BCM-bound GPR97–G_o complex structure. **b**, The detailed interactions of TM3–TM5–TM6–TM7 with palmitoylated C351 in G_o-coupled GPR97 (PDB ID: 7D77). The hydrogen bond is depicted as a dashed line. **c**, The effects of mutations of C351 in the α5 helix of $G\alpha_o$ on GPR97 or D2R activities. The bar graph represents the average pEC_{50} (that is, $-\log EC_{50}$) measured from three independent experiments. The original dose–response data are shown in Extended Data Fig. 9g, h. The data represent the mean ± s.e.m. from three independent experiments performed in triplicate. $^{***}P < 0.001$, $G\alpha_o$ C351 mutations versus $G\alpha_o$ WT in activating GPR97; NS, $G\alpha_o$ C351 mutations versus $G\alpha_o$ WT in activating D2R. All data were analysed by two-sided, one-way ANOVA with Tukey's test ($P < 0.0001$ and $P < 0.0001$ from left to right for the GPR97 group; $P = 0.0859$ and $P = 0.0744$ from left to right for the D2R group).

Full size image

Conclusion

In summary, we have provided experimental evidence that endogenous steroid hormone glucocorticoids are high-affinity agonists for GPR97, an aGPCR, and presented the structures of GPR97–G_o in complex with two glucocorticoids. Our structure highlighted that the small steroid hormone could bind to the 7TM bundle of one aGPCR member for activation of the receptor. The ligand-binding pocket of GPR97 is within the top half of the 7TM bundle and is covered by the extended ECL2. The glucocorticoids bound at the centre of this pocket with their D rings packed against the toggle switch residue $W490^{6.53}$. Furthermore, our cryo-EM structure revealed that GPR97 has a unique 7TM architecture with an extended ECL2 β-sheet and a relatively short helix TM6. Although GPR97 has neither the traditional 'PIF' core triad nor the NPXXY motif that commonly mediates the activation of class A

GPCRs, it senses ligand binding by the conserved toggle switch $W^{6.53}$ and tethers TM3–TM5–TM6 by the newly identified and sequence-conserved UQC consisting of $F353^{3.44}M356^{3.47}F439^{5.47}W490^{6.53}$ for the active receptor conformation. In the aGPCR family, the conserved D/ERY motif is replaced by H(N)L(M)Y, which forms specific interactions with the palmitoylation of G_o. In addition, all three ICLs of GPR97 are involved in direct interactions with the G_o subunits, which may contribute to the high basal activity. Several of these observed characteristics in the GPR97 structure, including the arrangement of the 7TM bundle, the ligand-binding mode[40,41], the ligand-induced receptor activation and the manner of G protein coupling, could also be shared by other aGPCR family members (Supplementary Fig. 6).

Methods

No statistical methods were used to predetermine sample size. The experiments were not randomized, and investigators were not blinded to allocation during experiments and outcome assessment.

Cell lines

HEK293 cells were obtained from the Cell Resource Center of Shanghai Institute for Biological Sciences (Chinese Academy of Sciences). *Spodoptera frugiperda* (Sf9) cells were purchased from Expression Systems (cat. 94-001S). Y-1 cells were originally obtained from the American Type Culture Collection (ATCC). The cells were grown in monolayer culture in RPMI 1640 with 10% FBS (Gibco) at 37 °C in a humidified atmosphere consisting of 5% CO_2 and 95% air.

Constructs of GPR97 and miniGo heterotrimer

For protein production in insect cells, the human GPR97 (residues 21–549) with the autoproteolysis motif mutation (H248/A and T250/A) was sub-cloned into the pFastBac1 vector. The native signal peptide was replaced with the haemagglutinin signal peptide (HA) to enhance receptor expression, followed by a Flag tag DYKDDDK (China peptide) to facilitate complex purification. An engineered human $G\alpha_{o1}$ with $G\alpha_{o1}$ H domain deletion, named mini$G\alpha_{o1}$ was cloned into pFastBac1 according to published literature[29]. Human Gβ1 with the C-terminal hexa-histidine tag and human Gγ2 were subcloned into the pFastBacDual vector. scFv16 was cloned into pfastBac1 with the C-terminal hexa-histidine tag and the N-terminal GP67 signal peptide. To examine the activities of GPR97, the GPR97-FL-WT (wild-type full-length GPR97), GPR97-FL-AA (GPR97 GPS site mutation, H248/A and T250/A), GPR97β (GPR97 with the NTF removed, residues 250–549) and GPR97-β-T

(GPR97β with the N-terminal tethered Stachel sequence removed, residues 265–549) were sub-cloned into the pcDNA3.1 plasmid. The GPR97 mutations E298A, R299A, F345A, F353A, H362A, L363A, Y364A, V370A, F371A, Y406A, W421A, W490A, A493G, I494A, L498A and N510A were generated using the Quikchange mutagenesis kit (Stratagene). The G protein BRET probes were constructed according to previous publications[42,43]. Human G protein subunits ($G\alpha_q$, Gβ1 and Gγ2) were sub-cloned into the pcDNA3.1 expression vectors. The $G\alpha_q$-RlucII subunit was generated by amplifying and inserting the coding sequence of RlucII into $G\alpha_q$ between residue L97 and K98. The G_{qo} probe, in which the six amino acids of the C-terminal of $G\alpha_q$-RlucII were substituted with those from $G\alpha_{o1}$, was constructed by PCR amplification using synthesized oligonucleotides encoding swapped C-terminal sequences. The GFP10–Gγ2 plasmid was generated by fusing the GFP10 coding sequence in frame at the N terminus to Gγ2. All of the constructs and mutations were verified by DNA sequencing.

Protein expression

High titre recombinant baculoviruses were generated using Bac-to-Bac Baculovirus Expression System. In brief, 2 μg of recombinant bacmid and 2 μl X-tremGENE HP transfection reagent (Roche) in 100 μl Opti-MEM medium (Gibco) were mixed and incubated for 20 min at room temperature. The transfection solution was added to 2.5 ml Sf9 cells with a density of 1×10^6 per ml in a 24-well plate. The infected cells were cultured in a shaker at 27 °C for 4 days. P0 virus was collected and then amplified to generate P1 virus. The viral titres were determined by flow cytometric analysis of cells stained with gp64-PE antibody (1:200 dilution; 12-6991-82, Thermo Fisher). Then, Sf9 cells were infected with viruses encoding GPR97-FL-AA, mini$G\alpha_o$, Gβγ, and with or without scFv16, respectively, at equal multiplicity of infection. The infected cells were cultured at 27 °C, 110 rpm for 48 h before collection. Cells were finally collected by centrifugation and the cell pellets were stored at −80 °C.

GPR97–G_o complex formation and purification

Cell pellets transfected with virus encompassing the GPR97-FL-AA, miniGo trimer and scFv16 (only existed in cell pellets for purifying the cortisol–GPR97-FL-AA–G_o–scFv16 complex) were resuspended in 20 mM HEPES, pH 7.4, 100 mM NaCl, 10% glycerol, 10 mM $MgCl_2$ and 5 mM $CaCl_2$ supplemented with Protease Inhibitor Cocktail (B14001, Bimake) and 100 μM TCEP (Thermo Fisher Scientific). The complex was formed for 2 h at room temperature by adding 10 μM BCM (HY-B1540, MedChemExpress) or cortisol (HY-N0583, MedChemExpress), 25 mU/ml apyrase (Sigma), and then solubilized by 0.5% (w/v) lauryl maltose neopentylglycol (LMNG;

Anatrace) and 0.1% (w/v) cholesteryl hemisuccinate TRIS salt (CHS; Anatrace) for 2 h at 4 °C. Supernatant was collected by centrifugation at 30,000 rpm for 40 min, and the solubilized complex was incubated with nickel resin for 2 h at 4 °C. The resin was collected and washed with 20 column volumes of 20 mM HEPES, pH 7.4, 100 mM NaCl, 10% glycerol, 2 mM $MgCl_2$, 25 mM imidazole, 0.01% (w/v) LMNG, 0.01% GDN (Anatrace), 0.004% (w/v) CHS, 10 μM BCM (or cortisol) and 100 μM TCEP. The complex was eluted with 20 mM HEPES, pH 7.4, 100 mM NaCl, 10% glycerol, 2 mM $MgCl_2$, 200 mM imidazole, 0.01% (w/v) LMNG, 0.01% GDN, 0.004% (w/v) CHS, 10 μM BCM (or cortisol) and 100 μM TCEP. The elution of nickel resin was applied to M1 anti-Flag resin (Sigma) for 2 h and washed with 20 mM HEPES, pH 7.4, 100 mM NaCl, 10% glycerol, 2 mM $MgCl_2$, 5 mM $CaCl_2$, 0.01% (w/v) LMNG, 0.01% GDN, 0.004% (w/v) CHS, 10 μM BCM (or cortisol) and 100 μM TCEP. The GPR97–G_o complex was eluted in buffer containing 20 mM HEPES, pH 7.4, 100 mM NaCl, 10% glycerol, 2 mM $MgCl_2$, 0.01% (w/v) LMNG, 0.01% GDN, 0.004% (w/v) CHS, 10 μM BCM (or cortisol), 100 μM TCEP, 5 mM EGTA and 0.2 mg/ml Flag peptide. The complex was concentrated and then injected onto Superdex 200 increase 10/300 GL column equilibrated in the buffer containing 20 mM HEPES, pH 7.4, 100 mM NaCl, 2 mM $MgCl_2$, 0.00075% (w/v) LMNG, 0.00025% GDN, 0.0002% (w/v) CHS, 10 μM BCM (or cortisol) and 100 μM TCEP. The complex fractions were collected and concentrated individually for EM experiments.

Cryo-EM grid preparation and data collection

For the preparation of cryo-EM grids, 3 μl of purified BCM-bound and cortisol-bound GPR97–G_o complex at approximately 20 mg/ml was applied onto a glow-discharged holey carbon grid (Quantifoil R1.2/1.3). Grids were plunge-frozen in liquid ethane cooled by liquid nitrogen using Vitrobot Mark IV (Thermo Fisher Scientific). Cryo-EM imaging was performed on a Titan Krios at 300 kV accelerating voltage in the Center of Cryo-Electron Microscopy, Zhejiang University. Micrographs were recorded using a Gatan K2 Summit direct electron detector in counting mode with a nominal magnification of ×29,000, which corresponds to a pixel size of 1.014 Å. Movies were obtained using serialEM at a dose rate of about 7.8 electrons per $Å^2$ per second with a defocus ranging from −0.5 to −2.5 μm. The total exposure time was 8 s and intermediate frames were recorded in 0.2-s intervals, resulting in an accumulated dose of 62 electrons per $Å^2$ and a total of 40 frames per micrograph. A total of 2,707 and 5,871 movies were collected for the BCM-bound and cortisol-bound GPR97–G_o complex, respectively.

Cryo-EM data processing

Dose-fractionated image stacks for the BCM–GPR97–G_o complex were subjected to beam-induced motion correction using MotionCor2.1[44]. Contrast transfer function (CTF) parameters for each non-dose-weighted micrograph were determined by Gctf[45]. Particle selection, 2D and 3D classifications of the BCM–GPR97–G_o complex were performed on a binned data set with a pixel size of 2.028 Å using RELION-3.0-beta2[46].

For the BCM–GPR97–G_o complex, semi-automated particle selection yielded 2,026,926 particle projections. The projections were subjected to reference-free 2D classification to discard particles in poorly defined classes, producing 911,519 particle projections for further processing. The map of the 5-HT_{1B}R–miniGo complex (EMDB-4358)[47] low-pass filtered to 40 Å was used as a reference model for maximum-likelihood-based 3D classification, resulting in one well-defined subset with 307,700 projections. Further 3D classifications focusing the alignment on the complex produced two good subsets that accounted for 166,116 particles, which were subsequently subjected to 3D refinement, CTF refinement and Bayesian polishing. The final refinement generated a map with an indicated global resolution of 3.1 Å at a Fourier shell correlation of 0.143.

For the cortisol–GPR97–G_o complex, particle selection yielded 4,323,518 particle projections for reference-free 2D classification. The well-defined classes with 2,201,933 particle projections were selected for a further two rounds of 3D classification using the map of the BCM-bound complex as reference. One good subset that accounted for 335,552 particle projections was selected for a further two rounds of 3D classifications that focused the alignment on the complex, and produced one high-quality subset with 75,814 particle projections. The final particle projections were subsequently subjected to 3D refinement, CTF refinement and Bayesian polishing, which generates a map with a global resolution of 2.9 Å. Local resolution for both density maps was determined using the Bsoft package with half maps as input maps[48].

Model building and refinement

For the structure of the BCM–GPR97–G_o complex, the initial template of GPR97 was generated using the module ‘map to model’ in PHENIX[44]. The coordinate of the 5-HT_{1B}R–G_o complex (PDB ID: 6G79) was used to generate the initial models for G_o (ref. [44]). Models were docked into the EM density map using UCSF Chimera[49], followed by iterative manual rebuilding in COOT[50] according to side-chain densities. BCM and lipid coordinates and geometry restraints were generated using phenix.elbow. BCM was built to the model using the ‘LigandFit’ module in PHENIX.

The placement of BCM shows a correlation coefficient of 0.81, indicating a good ligand fit to the density. The model was further subjected to real-space refinement using Rosetta[51] and PHENIX[44].

For the structure of the cortisol–GPR97–G_o complex, the coordinates of GPR97 and G_o from the BCM-bound complex and scFv16 from the human NTSR1–G_{i1} complex (PDB ID: 6OS9) were used as initial model. Models were docked into the density map and then were manual rebuilt in COOT. The agonist cortisol was built to the model using the 'LigandFit' module as described, showing a good density fit with a correlation coefficient of 0.80. The model was further refined using Rosetta[51] and PHENIX[44]. The final refinement statistics for both structures were validated using the module 'comprehensive validation (cryo-EM)' in PHENIX[44]. The goodness of the fit of the model to the map was performed for both structures using a global model-versus-map FSC (Extended Data Fig. 2). The refinement statistics are provided in Extended Data Table 1. Figures of the structures were generated using UCSF Chimera, UCSF ChimeraX[52] and PyMOL[53].

Molecular dynamics simulation of the BCM–GPR97 and cortisol–GPR97 complexes

On the basis of the favour binding poses of BCM and cortisol with the receptor GPR97, which was calculated by the LigandFit program of PHENIX, the GPR97–agonist complexes were substrate from the two GPR97–agonist–mG_o complexes for molecular dynamics simulation. The orientations of receptors were calculated by the Orientations of Proteins in Membranes (OPM) database. Following this, the whole systems were prepared by the CHARM-GUI and embedded in a bilayer that consisted of 200 1-palmitoyl-2-oleoyl-*sn*-glycero-3-phosphocholine (POPC) lipids by replacement methods. The membrane systems were then solvated into a periodic TIP3P water box supplemented with 0.15 M NaCl. The CHARMM36m Force Filed was used to model protein molecules, CHARMM36 Force Filed for lipids and salt with CHARMM General Force Field (CGenFF) for the agonist molecules BCM and cortisol.

Then, the system was subjected to minimization for 10,000 steps using the conjugated gradient algorithm and then heated and equilibrated at 310.13 K and 1 atm for 200 ps with 10.0 kcal mol^{-1} $Å^{-2}$ harmonic restraints in the NAMD 2.13 software. Next followed five cycles of equilibration for 2 ns each at 310.13 K and 1 atm, for which the harmonic restraints were 5.0, 2.5, 1.0, 0.5 and 0.1 kcal mol^{-1} $Å^{-2}$ in sequence.

Production simulations were run at 310.13 K and 1 atm in the NPT ensemble using the Langevin thermostat and Nose–Hoover method for 200 ns. Electrostatic interactions

were calculated using the particle mesh Ewald (PME) method with a cut-off of 12 Å. Throughout the final stages of equilibration and production, 5.0 kcal mol^{-1} $Å^{-2}$ harmonic restraints were placed on the residues of GPR97 that were within 5 Å of G_o in the BCM (or cortisol)–GPR97–G_o complex to ensure that the receptor remained in the active state in the absence of the G protein. Trajectories were visualized and analysed using Visual Molecular Dynamics (VMD, version 1.9.3)

cAMP ELISA detection in Y-1 cells

Y-1 cells were transfected with *Gpr97* siRNA (si-97, GUGCAGGGAAUGUCUUUAA) or control siRNA (si-Con) for 48 h. After starvation for 12 h in serum-free medium, the cells were further stimulated with cortisone (8 nM), forskolin (5 μM) (Sigma-Aldrich) or control vehicle for 10 min. Then, cells were washed three times with pre-cooled PBS and resuspended in pre-cooled 0.1 N HCl containing 500 μM IBMX at a 1:5 ratio (w/v). The samples were neutralized with 1 N NaOH at a 1:10 ratio (v/v) after 10 min. The supernatants were collected after centrifugation of the samples at 600*g* for 10 min. The supernatants were then prepared for cAMP determination using the cAMP Parameter Assay Kit (R&D Systems) according to the manufacturer's instruction. The *Gpr97* expression level under various conditions were further confirmed using quantitative real-time PCR.

Corticosterone measurements

Mouse adrenocorticotoma cell line Y-1 cells were transfected with *Gpr97* siRNA (si-97) or control siRNA (si-Con) for 48 h. Then, the cells were treated with serum-free medium for 12 h. After that, cortisone (16 nM) or ACTH (0.5 μM) were added to cells for 30 min. The supernatants of the cell culture medium were collected for measurements of corticosterone by ELISA according to the manufacturer's instructions.

Quantitative real-time PCR

Total RNA of cells was extracted using a standard TRIzol RNA isolation method. The reverse transcription and PCR experiments were performed with the Revertra Ace qPCR RT Kit (TOYOBO FSQ-101) using 1.0 μg of each sample, according to the manufacturer's protocols. The quantitative real-time PCR was conducted in the Light Cycler apparatus (Bio-Rad) using the FastStart Universal SYBR Green Master (Roche). The mRNA level was normalized to GAPDH in the same sample and then compared with the control. The forward and reverse primers for GPR97 used in the experiments were CAGTTTGGGACTGAGGGACC and GCCCACACTTGGTGAAACAC. The mRNA level of GAPDH was used as an

internal control. The forward and reverse primers for GAPDH were GCCTTCCGTGTTCCTACC and GCCTGCTTCACCACCTTC.

cAMP inhibition assay

To measure the inhibitory effects on forskolin-induced cAMP accumulation of different GPR97 constructs or mutants in response to different ligands or constitutive activity, the GloSensor cAMP assay (Promega) was performed according to previous publications[12,13]. HEK293 cells were transiently co-transfected with the GloSensor and various versions of GPR97 or vehicle (pcDNA3.1) plasmids using PEI in six-well plates. After incubation at 37 °C for 24 h, transfected cells were seeded into 96-well plates with serum-free DMEM medium (Gibco) and incubated for another 24 h at 37 °C in a 5% CO_2 atmosphere. Different ligands were dissolved in DMSO (Sigma) to a stock concentration of 10 mM and followed by serial dilution using PBS solution immediately before the ligand stimulation. The transfected cells were pre-incubated with 50 µl of serum-free DMEM medium containing GloSensor cAMP reagent (Promega). After incubation at 37 °C for 2 h, varying concentrations of ligands were added into each well and followed by the addition of forskolin to 1 µM. The luminescence intensity was examined on an EnVision multi-label microplate detector (Perkin Elmer).

The G_{qo} protein activation BRET assay

According to previous publications, the BCM dipropionate-induced GPR97 activity could be measured by chimeric G_{qo} protein assays[25]. The G_{qo} BRET probes were generated by replacing the six amino acids of the C-terminal of G_q-RlucII with those from G_{oA1}, creating a chimeric G_{qo}-RlucII subunit[47]. GFP10 was connected to Gγ. The G_{qo} protein activation BRET assay was performed as previously described[54]. In brief, HEK293 cells were transiently co-transfected with control D2R and various GPR97 constructs, plasmids encoding the G_{qo} BRET probes, incubated at 37 °C in a 5% CO_2 atmosphere for 48 h. Cells were washed twice with PBS, collected and resuspended in buffer containing 25 mM HEPES, pH 7.4, 140 mM NaCl, 2.7 mM KCl, 1 mM $CaCl_2$, 12 mM $NaHCO_3$, 5.6 mM d-glucose, 0.5 mM $MgCl_2$ and 0.37 mM NaH_2PO_4. Cells that were dispensed into a 96-well microplate at a density of 5–8 × 10^4 cells per well were stimulated with different concentrations of ligands. $BRET^2$ between RLucII and GFP10 was measured after the addition of the substrate coelenterazine 400a (5 µM, Interchim) (Cayman) using a Mithras LB940 multimode reader (Berthold Technologies). The $BRET^2$ signal was calculated as the ratio of emission of GFP10 (510 nm) to RLucII (400 nm).

Measurement of receptor cell-surface expression by ELISA

To evaluate the expression level of wild-type GPR97 and its mutants, HEK293 cells were transiently transfected with wild-type and mutant GPR97 or vehicle (pcDNA3.1) using PEI regent at in six-well plates. After incubation at 37 °C for 18 h, transfected cells were plated into 24-well plates at a density of 10^5 cells per well and further incubated at 37 °C in a 5% CO_2 atmosphere for 18 h. Cells were then fixed in 4% (w/v) paraformaldehyde and blocked with 5% (w/v) BSA at room temperature. Each well was incubated with 200 µl of monoclonal anti-FLAG (F1804, Sigma-Aldrich) primary antibody overnight at 4 °C and followed by incubation of a secondary goat anti-mouse antibody (A-21235, Thermo Fisher) conjugated to horseradish peroxide for 1 h at room temperature. After washing, 200 µl of 3,3′,5,5′-tetramethylbenzidine (TMB) solution was added. Reactions were quenched by adding an equal volume of 0.25 M HCl solution and the optical density at 450 nm was measured using the TECAN (Infinite M200 Pro NanoQuant) luminescence counter. For determination of the constitutive activities of different GPR97 constructs or mutants, varying concentrations of desired plasmids were transiently transfected into HEK293 cells and the absorbance at 450 nm was measured.

The FlAsH-BRET assay

HEK293 cells were seeded in six-well plates after transfection with GPR97-FlAsH with Nluc inserted in a specific N-terminal site. Before the BRET assay, HEK293 cells were starved with serum for 1 h. Then cells were digested, centrifuged and resuspended in 500 µl BRET buffer (25 mM HEPES, 1 mM $CaCl_2$, 140 mM NaCl, 2.7 mM KCl, 0.9 mM $MgCl_2$, 0.37 mM NaH_2PO_4, 5.5 mM d-glucose and 12 mM $NaHCO_3$). The FlAsH-EDT2 was added at a final concentration of 2.5 µM and incubated at 37 °C for 60 min. Subsequently, HEK293 cells were washed with BRET buffer and then distributed into black-wall clear-bottom 96-well plates, with approximately 100,000 cells per well. The cells were treated with a final concentration of BCM and cortisol at 10^{-5} to 10^{-11} and then coelenterazinc H was added at a final concentration of 5 µM, followed by checking the luciferase (440–480 nm) and FlAsH (525–585 nm) emissions immediately. The BRET ratio (emission enhanced yellow fluorescent protein/emission Nluc) was calculated using a Berthold Technologies Tristar 3 LB 941 spectrofluorimeter. The procedure was modified from those described previously[34,55,56].

Statistical analysis

A one-way ANOVA test was performed to evaluate the statistical significance between various versions of GPR97 and their mutant in terms of expression level, potency or efficacy using GraphPad Prism. For all experiments, the standard error of the mean of the values calculated based on the data sets from three independent experiments is shown in respective figure legends.

Reporting summary

Further information on research design is available in the Nature Research Reporting Summary linked to this paper.

Data availability

The density maps and structure coordinates have been deposited to the Electron Microscopy Database (EMDB) and the PDB with the accession codes EMD-30602 and 7D76 for the BCM–GPR97–G_o complex. The cryo-EM density map and coordinates for the cortisol–GPR97–G_o complex have been deposited to the EMDB and PDB under the accession codes EMD-30603 and 7D77. The Orientations of Proteins in Membranes database is accessible at http://opm.phar.umich.edu. All other data are available on request to the corresponding authors.

References

1. 1.

   Folts, C. J., Giera, S., Li, T. & Piao, X. Adhesion G protein-coupled receptors as drug targets for neurological diseases. *Trends Pharmacol. Sci*. **40**, 278–293 (2019).

   CAS PubMed PubMed Central Google Scholar

2. 2.

Bassilana, F., Nash, M. & Ludwig, M. G. Adhesion G protein-coupled receptors: opportunities for drug discovery. *Nat. Rev. Drug Discov*. **18**, 869–884 (2019).

CAS PubMed Google Scholar

3. 3.

Purcell, R. H. & Hall, R. A. Adhesion G protein-coupled receptors as drug targets. *Annu. Rev. Pharmacol. Toxicol*. **58**, 429–449 (2018).

CAS PubMed Google Scholar

4. 4.

Fang, W. et al. Gpr97 exacerbates AKI by mediating Sema3A signaling. *J. Am. Soc. Nephrol*. **29**, 1475–1489 (2018).

CAS PubMed PubMed Central Google Scholar

5. 5.

Hsiao, C. C. et al. The adhesion G protein-coupled receptor GPR97/*ADGRG3* is expressed in human granulocytes and triggers antimicrobial effector functions. *Front. Immunol*. **9**, 2830 (2018).

PubMed PubMed Central Google Scholar

6. 6.

Daley-Yates, P. T., Price, A. C., Sisson, J. R., Pereira, A. & Dallow, N. Beclomethasone dipropionate: absolute bioavailability, pharmacokinetics and metabolism following intravenous, oral, intranasal and inhaled administration in man. *Br. J. Clin. Pharmacol*. **51**, 400–409 (2001).

CAS PubMed PubMed Central Google Scholar

7. 7.

Piao, X. et al. G protein-coupled receptor-dependent development of human frontal cortex. *Science* **303**, 2033–2036 (2004).

ADS CAS PubMed Google Scholar

8. 8.

Boyden, S. E. et al. Vibratory urticaria associated with a missense variant in ADGRE2. *N. Engl. J. Med*. **374**, 656–663 (2016).

CAS PubMed PubMed Central Google Scholar

9. 9.

Eubelen, M. et al. A molecular mechanism for Wnt ligand-specific signaling. *Science* **361**, eaat1178 (2018).

ADS PubMed Google Scholar

10. 10.

Hochreiter-Hufford, A. E. et al. Phosphatidylserine receptor BAI1 and apoptotic cells as new promoters of myoblast fusion. *Nature* **497**, 263–267 (2013).

ADS CAS PubMed PubMed Central Google Scholar

11. 11.

Monk, K. R. et al. A G protein-coupled receptor is essential for Schwann cells to initiate myelination. *Science* **325**, 1402–1405 (2009).

ADS CAS PubMed PubMed Central Google Scholar

12. 12.

Zhang, D. L. et al. Gq activity- and β-arrestin-1 scaffolding-mediated ADGRG2/CFTR coupling are required for male fertility. *eLife* **7**, e33432 (2018).

PubMed PubMed Central Google Scholar

13. 13.

Hu, Q. X. et al. Constitutive Gαi coupling activity of very large G protein-coupled receptor 1 (VLGR1) and its regulation by PDZD7 protein. *J. Biol. Chem*. **289**, 24215–24225 (2014).

CAS PubMed PubMed Central Google Scholar

14. 14.

Kishore, A. & Hall, R. A. Disease-associated extracellular loop mutations in the adhesion G protein-coupled receptor G1 (ADGRG1; GPR56) differentially regulate downstream signaling. *J. Biol. Chem*. **292**, 9711–9720 (2017).

CAS PubMed PubMed Central Google Scholar

15. 15.

Sando, R., Jiang, X. & Südhof, T. C. Latrophilin GPCRs direct synapse specificity by coincident binding of FLRTs and teneurins. *Science* **363**, eaav7969 (2019).

CAS PubMed PubMed Central Google Scholar

16. 16.

Araç, D. et al. A novel evolutionarily conserved domain of cell-adhesion GPCRs mediates autoproteolysis. *EMBO J*. **31**, 1364–1378 (2012).

PubMed PubMed Central Google Scholar

17. 17.

Krasnoperov, V. et al. Post-translational proteolytic processing of the calcium-independent receptor of alpha-latrotoxin (CIRL), a natural chimera of the cell adhesion protein and the G protein-coupled receptor. Role of the G protein-coupled receptor proteolysis site (GPS) motif. *J. Biol. Chem*. **277**, 46518–46526 (2002).

CAS PubMed Google Scholar

18. 18.

Prömel, S. et al. The GPS motif is a molecular switch for bimodal activities of adhesion class G protein-coupled receptors. *Cell Rep*. **2**, 321–331 (2012).

PubMed PubMed Central Google Scholar

19. 19.

Liebscher, I. et al. A tethered agonist within the ectodomain activates the adhesion G protein-coupled receptors GPR126 and GPR133. *Cell Rep*. **9**, 2018–2026 (2014).

CAS PubMed PubMed Central Google Scholar

20. 20.

Scholz, N. et al. Mechano-dependent signaling by latrophilin/CIRL quenches cAMP in proprioceptive neurons. *eLife* **6**, e28360 (2017).

PubMed PubMed Central Google Scholar

21. 21.

Stoveken, H. M., Hajduczok, A. G., Xu, L. & Tall, G. G. Adhesion G protein-coupled receptors are activated by exposure of a cryptic tethered agonist. *Proc. Natl Acad. Sci. USA* **112**, 6194–6199 (2015).

ADS CAS PubMed Google Scholar

22. 22.

Hamann, J. et al. International Union of Basic and Clinical Pharmacology. XCIV. Adhesion G protein-coupled receptors. *Pharmacol. Rev*. **67**, 338–367 (2015).

CAS PubMed PubMed Central Google Scholar

23. 23.

Wang, J. J. et al. Gpr97 is essential for the follicular versus marginal zone B-lymphocyte fate decision. *Cell Death Dis*. **4**, e853 (2013).

CAS PubMed PubMed Central Google Scholar

24. 24.

Wang, J. et al. Gpr97/Adgrg3 ameliorates experimental autoimmune encephalomyelitis by regulating cytokine expression. *Acta Biochim. Biophys. Sin. (Shanghai)* **50**, 666–675 (2018).

CAS Google Scholar

25. 25.

Gupte, J. et al. Signaling property study of adhesion G-protein-coupled receptors. *FEBS Lett*. **586**, 1214–1219 (2012).

CAS PubMed Google Scholar

26. 26.

Tasker, J. G., Di, S. & Malcher-Lopes, R. Minireview: rapid glucocorticoid signaling via membrane-associated receptors. *Endocrinology* **147**, 5549–5556 (2006).

CAS PubMed PubMed Central Google Scholar

27. 27.

Popoli, M., Yan, Z., McEwen, B. S. & Sanacora, G. The stressed synapse: the impact of stress and glucocorticoids on glutamate transmission. *Nat. Rev. Neurosci*. **13**, 22–37 (2011).

PubMed PubMed Central Google Scholar

28. 28.

Horby, P. et al. Dexamethasone in hospitalized patients with Covid-19—preliminary report. *N. Engl. J. Med*. https://doi.org/10.1056/NEJMoa2021436 (2020).

29. 29.

García-Nafría, J., Nehmé, R., Edwards, P. C. & Tate, C. G. Cryo-EM structure of the serotonin 5-HT_{1B} receptor coupled to heterotrimeric G_o. *Nature* **558**, 620–623 (2018).

ADS PubMed PubMed Central Google Scholar

30. 30.

Mao, C. Y. et al. Cryo-EM structures of inactive and active $GABA_B$ receptor. *Cell Res*. **30**, 564–573 (2020).

CAS PubMed Google Scholar

31. 31.

Wootten, D., Simms, J., Miller, L. J., Christopoulos, A. & Sexton, P. M. Polar transmembrane interactions drive formation of ligand-specific and signal pathway-biased family B G protein-coupled receptor conformations. *Proc. Natl Acad. Sci. USA* **110**, 5211–5216 (2013).

ADS CAS PubMed Google Scholar

32. 32.

Visiers, I., Ballesteros, J. A. & Weinstein, H. Three-dimensional representations of G protein-coupled receptor structures and mechanisms. *Methods Enzymol*. **343**, 329–371 (2002).

PubMed Google Scholar

33. 33.

Bokoch, M. P. et al. Ligand-specific regulation of the extracellular surface of a G-protein-coupled receptor. *Nature* **463**, 108–112 (2010).

ADS CAS PubMed PubMed Central Google Scholar

34. 34.

Nuber, S. et al. β-Arrestin biosensors reveal a rapid, receptor-dependent activation/deactivation cycle. *Nature* **531**, 661–664 (2016).

ADS CAS PubMed PubMed Central Google Scholar

35. 35.

de Graaf, C., Nijmeijer, S., Wolf, S. & Ernst, O. P. 7TM domain structure of adhesion GPCRs. *Handb. Exp. Pharmacol*. **234**, 43–66 (2016).

PubMed Google Scholar

36. 36.

Maeda, S., Qu, Q., Robertson, M. J., Skiniotis, G. & Kobilka, B. K. Structures of the M1 and M2 muscarinic acetylcholine receptor/G-protein complexes. *Science* **364**, 552–557 (2019).

ADS CAS PubMed PubMed Central Google Scholar

37. 37.

Latorraca, N. R., Venkatakrishnan, A. J. & Dror, R. O. GPCR dynamics: structures in motion. *Chem. Rev*. **117**, 139–155 (2017).

CAS PubMed Google Scholar

38. 38.

Rasmussen, S. G. et al. Crystal structure of the β2 adrenergic receptor–Gs protein complex. *Nature* **477**, 549–555 (2011).

ADS CAS PubMed PubMed Central Google Scholar

39. 39.

Flock, T. et al. Universal allosteric mechanism for Gα activation by GPCRs. *Nature* **524**, 173–179 (2015).

ADS CAS PubMed PubMed Central Google Scholar

40. 40.

Zhu, B. et al. GAIN domain-mediated cleavage is required for activation of G protein-coupled receptor 56 (GPR56) by its natural ligands and a small-molecule agonist. *J. Biol. Chem*. **294**, 19246–19254 (2019).

CAS PubMed PubMed Central Google Scholar

41. 41.

Stoveken, H. M. et al. Dihydromunduletone is a small-molecule selective adhesion G protein-coupled receptor antagonist. *Mol. Pharmacol*. **90**, 214–224 (2016).

CAS PubMed PubMed Central Google Scholar

42. 42.

Galés, C. et al. Real-time monitoring of receptor and G-protein interactions in living cells. *Nat. Methods* **2**, 177–184 (2005).

PubMed Google Scholar

43. 43.

Saulière, A. et al. Deciphering biased-agonism complexity reveals a new active AT1 receptor entity. *Nat. Chem. Biol*. **8**, 622–630 (2012).

PubMed Google Scholar

44. 44.

Zheng, S. Q. et al. MotionCor2: anisotropic correction of beam-induced motion for improved cryo-electron microscopy. *Nat. Methods* **14**, 331–332 (2017).

CAS PubMed PubMed Central Google Scholar

45. 45.

Zhang, K. Gctf: real-time CTF determination and correction. *J. Struct. Biol*. **193**, 1–12 (2016).

ADS CAS PubMed PubMed Central Google Scholar

46. 46.

Scheres, S. H. RELION: implementation of a Bayesian approach to cryo-EM structure determination. *J. Struct. Biol*. **180**, 519–530 (2012).

CAS PubMed PubMed Central Google Scholar

47. 47.

Inoue, A. et al. Illuminating G-protein-coupling selectivity of GPCRs. *Cell* **177**, 1933–1947.e25 (2019).

CAS PubMed PubMed Central Google Scholar

48. 48.

Heymann, J. B. Guidelines for using Bsoft for high resolution reconstruction and validation of biomolecular structures from electron micrographs. *Protein Sci*. **27**, 159–171 (2018).

CAS PubMed Google Scholar

49. 49.

Pettersen, E. F. et al. UCSF Chimera—a visualization system for exploratory research and analysis. *J. Comput. Chem*. **25**, 1605–1612 (2004).

CAS PubMed Google Scholar

50. 50.

Emsley, P. & Cowtan, K. Coot: model-building tools for molecular graphics. *Acta Crystallogr. D* **60**, 2126–2132 (2004).

PubMed Google Scholar

51. 51.

Wang, R. Y. et al. Automated structure refinement of macromolecular assemblies from cryo-EM maps using Rosetta. *eLife* **5**, e17219 (2016).

PubMed PubMed Central Google Scholar

52. 52.

Goddard, T. D. et al. UCSF ChimeraX: meeting modern challenges in visualization and analysis. *Protein Sci*. **27**, 14–25 (2018).

CAS PubMed Google Scholar

53. 53.

The PyMOL Molecular Graphics System, Version 2.0 (Schrödinger, 2017).

54. 54.

Schrage, R. et al. The experimental power of FR900359 to study Gq-regulated biological processes. *Nat. Commun*. **6**, 10156 (2015).

ADS CAS PubMed PubMed Central Google Scholar

55. 55.

Lee, M. H. et al. The conformational signature of β-arrestin2 predicts its trafficking and signalling functions. *Nature* **531**, 665–668 (2016).

CAS PubMed PubMed Central Google Scholar

56. 56.

Yang, D. et al. Allosteric modulation of the catalytic VYD loop in Slingshot by its N-terminal domain underlies both Slingshot auto-inhibition and activation. *J. Biol. Chem*. **293**, 16226–16241 (2018).

CAS PubMed PubMed Central Google Scholar

Download references

Acknowledgements

We thank S. Chang and X. Zhang at the Center of Cryo-Electron Microscopy, Zhejiang University, for their help with cryo-EM data collection; the Core Facilities, Zhejiang University School of Medicine, for their technical support; C. Diao and C. Guo from the Core Facilities, School of Basic Medical Sciences, Shandong University, for their technical assistance; and Y. Yu and S. M. Liu from the Translational Medicine Core Facility of Advanced Medical Research Institute, Shandong University, for

their technical assistance with the luminescence counter (Envision, Perkin Elmer). This work was supported by the National Key R&D Program of China (2019YFA0904200 to J.-P.S. and P.X., 2019YFA0508800 to Y.Z. and P.X., and 2016YFA0501303 to J.Y.), the National Science Fund for Distinguished Young Scholars Grant (81825022 to J.-P.S. and 81525005 to F.Yi.), the National Natural Science Foundation of China Grant (81825022 and 81773704 to J.-P.S., 81922071 to Y.Z., 91953000 to H.E.X., 31971195 and 31700692 to P.X., 91939301 to Z.-J.L. and J.-P.S., 31770796 to Y.J. and 21922702 to J.Y.), the Zhejiang Province National Science Fund for Excellent Young Scholars (LR19H310001 to Y.Z.), the National Science Fund for Excellent Young Scholars Grant (81922071 to Y.Z. and 81822008 to X.Y.), the Strategic Priority Research Program of Chinese Academy of Sciences (XDB37030103 to H.E.X.), the Ministry of Science and Technology (China) Grant (2018YFA0507002 to H.E.X.), the Shanghai Municipal Science and Technology Major Project (2019SHZDZX02 to H.E.X.), the Shandong Provincial Natural Science Foundation Grant (ZR2016CQ07 to P.X. and ZR2019ZD40 to F.Yi.), the Shandong Key Research and Development Program (GG201709260059 to P.X.), the Rolling program of ChangJiang Scholars and Innovative Research Team in University Grant (IRT_17R68 to X.Y.), the National Science & Technology Major Project ‘Key New Drug Creation and Manufacturing Program’ (2018ZX09711002 to Y.J.), and the COVID-19 emergency tackling research program of Shandong University (2020XGB02 to J.-P.S.).

Author information

Author notes

1. These authors contributed equally: Yu-Qi Ping, Chunyou Mao, Peng Xiao, Ru-Jia Zhao, Yi Jiang

Affiliations

1. CAS Key Laboratory of Receptor Research, Center for Structure and Function of Drug Targets, Shanghai Institute of Materia Medica, Chinese Academy of Sciences, Shanghai, China

Yu-Qi Ping, Yi Jiang & H. Eric Xu

2. Department of Physiology and Pathophysiology, School of Basic Medical Sciences, Peking University, Key Laboratory of Molecular Cardiovascular Science, Ministry of Education, Beijing, China

   Yu-Qi Ping, Changxiu Qu & Jin-Peng Sun

3. Key Laboratory Experimental Teratology of the Ministry of Education, Department of Biochemistry and Molecular Biology, School of Basic Medical Sciences, Cheeloo College of Medicine, Shandong University, Shandong, China

   Yu-Qi Ping, Peng Xiao, Ru-Jia Zhao, Zhao Yang, Wen-Tao An, Fan Yang, Changxiu Qu, Shaolong Li, Guang-Yu Wang, Xiaona Tao, Xin Wen, Ya-Ni Zhong & Jin-Peng Sun

4. Department of Biophysics, and Department of Pathology of Sir Run Run Shaw Hospital, Zhejiang University School of Medicine, Hangzhou, China

   Chunyou Mao, Dan-Dan Shen, Huibing Zhang, Qingya Shen & Yan Zhang

5. Zhejiang Laboratory for Systems and Precision Medicine, Zhejiang University Medical Center, Hangzhou, China

   Chunyou Mao, Dan-Dan Shen, Huibing Zhang, Qingya Shen & Yan Zhang

6. Key Laboratory Experimental Teratology of the Ministry of Education, Department of Physiology, School of Basic Medical Sciences, Cheeloo College of Medicine, Shandong University, Shandong, China

   Fan Yang & Xiao Yu

7. State Key Laboratory of Proteomics, Beijing Proteome Research Center, National Center for Protein Sciences Beijing, Beijing Institute of Lifeomics, Beijing, China

Caiping Tian & Jing Yang

8. School of Medicine, Tsinghua University, Beijing, China

   Caiping Tian

9. Key Laboratory of Molecular Cardiovascular Science, Ministry of Education, Peking University, Beijing, China

   Zi-jian Li

10. The Key Laboratory of Infection and Immunity of Shandong Province, Department of Pharmacology, School of Basic Medical Sciences, Shandong University, Shandong, China

    Fan Yi

11. Zhejiang Provincial Key Laboratory of Immunity and Inflammatory Diseases, Hangzhou, China

    Yan Zhang

12. MOE Frontier Science Center for Brain Research and Brain-Machine Integration, Zhejiang University School of Medicine, Hangzhou, China

    Yan Zhang

Authors

1. Yu-Qi Ping
   View author publications

   You can also search for this author in PubMed Google Scholar

2. Chunyou Mao
   View author publications

   You can also search for this author in PubMed Google Scholar

3. Peng Xiao
View author publications

You can also search for this author in PubMed Google Scholar

4. Ru-Jia Zhao
View author publications

You can also search for this author in PubMed Google Scholar

5. Yi Jiang
View author publications

You can also search for this author in PubMed Google Scholar

6. Zhao Yang
View author publications

You can also search for this author in PubMed Google Scholar

7. Wen-Tao An
View author publications

You can also search for this author in PubMed Google Scholar

8. Dan-Dan Shen
View author publications

You can also search for this author in PubMed Google Scholar

9. Fan Yang
View author publications

You can also search for this author in PubMed Google Scholar

10. Huibing Zhang
View author publications

You can also search for this author in PubMed Google Scholar

11. Changxiu Qu
View author publications

You can also search for this author in PubMed Google Scholar

12. Qingya Shen
View author publications

You can also search for this author in PubMed Google Scholar

13. Caiping Tian
View author publications

You can also search for this author in PubMed Google Scholar

14. Zi-jian Li
View author publications

You can also search for this author in PubMed Google Scholar

15. Shaolong Li
View author publications

You can also search for this author in PubMed Google Scholar

16. Guang-Yu Wang
View author publications

You can also search for this author in PubMed Google Scholar

17. Xiaona Tao
View author publications

You can also search for this author in PubMed Google Scholar

18. Xin Wen
View author publications

You can also search for this author in PubMed Google Scholar

19. Ya-Ni Zhong
View author publications

You can also search for this author in PubMed Google Scholar

20. Jing Yang
View author publications

You can also search for this author in PubMed Google Scholar

21. Fan Yi
View author publications

You can also search for this author in PubMed Google Scholar

22. Xiao Yu
View author publications

You can also search for this author in PubMed Google Scholar

23. H. Eric Xu
View author publications

You can also search for this author in PubMed Google Scholar

24. Yan Zhang
View author publications

You can also search for this author in PubMed Google Scholar

25. Jin-Peng Sun
View author publications

You can also search for this author in PubMed Google Scholar

Contributions

J.-P.S., Y.Z. and H.E.X. conceived, designed and supervised the overall project. J.-P.S., Y.Z., H.E.X., Y.-Q.P., C.M., X.Y., P.X. and Y.J. participated

in data analysis and interpretation. Y.-Q.P. generated the GPR97 insect cell expression construct, established the BCM–GPR97–G_o and cortisol–GPR97–G_o–scFv16 complex purification protocol and prepared samples for the cryo-EM supervised by Y.J. Y.-Q.P., G.-Y.W., X.W., X.Y. and Y.-N.Z. generated viruses and infected Sf9 cells for large quantitative protein production. D.-D.S. and C.M. evaluated the sample by negative-stain electron microscopy. C.M. prepared the cryo-EM grids, collected the cryo-EM data with assistance from D.-D.S. and performed the cryo-EM map calculation, model building and refinement. Q.S. performed molecular dynamics simulations. H.Z. assisted in protein purification. J.-P.S., Y.Z., X.Y., J.Y., C.M. and P.X. designed all of the mutations for determination of ligand-binding sites. X.T., R.-J.Z., S.L. and F. Yang generated all of the GPR97 constructs and mutants for the cell-based G protein activity assays. R.-J.Z., P.X., S.L. C.Q. and Z.Y. performed the ELISA assays and cAMP inhibition assays. W.-T.A., X.Y., F.Yi and J.-P.S. designed the cellular functional assays for GPR97. W.-T.A. performed the cellular functional assays. J.-P.S., P.X., X.Y. and Z.-J.L. designed the FlAsH-BRET assays. R.-J.Z. performed the FlAsH-BRET experiments. C.T. and J.Y. performed the mass spectrometry experiment. J.Y. manually characterized fatty acylation on miniGo protein. Y.-Q.P., P.X., C.M., Q.S. and Y.J. prepared the figures. J.-P.S., Y.Z. and H.E.X. wrote the manuscript with input from all authors.

Corresponding authors

Correspondence to H. Eric Xu or Yan Zhang or Jin-Peng Sun.

Ethics declarations

Competing interests

The authors declare no competing interests.

Additional information

Peer review information *Nature* thanks Somnath Dutta, Bryan Roth and the other, anonymous, reviewer(s) for their contribution to the peer review of this work

Publisher's note Springer Nature remains neutral with regard to jurisdictional claims in published maps and institutional affiliations.

Extended data figures and tables

Extended Data Fig. 1 Glucocorticoids are activating ligands of GPR97.

a, Schematic diagrams showing the sequence features of GPR97 constructs used in this study. Wild-type full-length GPR97 (GPR97-FL-WT) is comprised of the conserved 7TM region and an intact GAIN domain, whereas the autoproteolysis-deficient mutant (GPR97-FL-AA) introduces two alanines to replace the autoproteolysis catalytic residues H248 and T250. **b**, The inhibition rates of steroid ligands on forskolin (1 μM)-induced cAMP accumulation in GPR97-FL-WT overexpressing HEK293 cells. Values are the mean ± SEM from three independent experiments. Statistical differences between different ligands and the control vehicle were determined by two-sided one-way ANOVA with Tukey's test. ***$P < 0.001$ (From top to bottom, $P = < 0.0001, < 0.0001, < 0.0001, < 0.0001, < 0.0001, < 0.0001, 0.0016$). The data were generated according to data shown in Supplementary Fig. 3. The original data are referred to Supplementary Table 1. **c**, Chemical structures of representative exogenous and endogenous glucocorticoids used in this study. **d**, The inhibitory effects of BCM, cortisone, cortisol, and dexamethasone (DEX) on forskolin (1 μM)-induced cAMP accumulation in GPR97-FL-WT, GPR97-FL-AA, GPR97-β and GPR97-β-T-overexpressing HEK293 cells. Values are the mean ± SEM from three independent experiments, each performed in triplicate. The potency and efficacy are summarized from data presented in Supplementary Fig. 4a. **e**, The effect of the GPR97 mediated cAMP inhibition compared with other known Gi/o coupled receptors, including AT1R and GPR120. Summarized potency and efficacy for effects of dexamethasone (DEX), Angiotensin II or TUG891 on Gi mediated cAMP level inhibition of

HEK293 cells overexpressing similar amounts of GPR97, AT1R or GPR120 (AT1R data are according to the data generated in Supplementary Fig. 4b, c). These data indicate that the potency of the dexamethasone for GPR97 is approximately 20 fold stronger than the AngII towards AT1R, the Emax of dexamethasone induced cAMP inhibition via GPR97 is similar to the AngII induced cAMP inhibition via AT1R, but is approximately 1/3 compared to the TUG891 (full agonist) induced GPR120 activity. Values are the mean ± SEM from three independent experiments, each performed in triplicate. **f**, The potency and efficacy for effects of ligand induced Gqo/Gβγ dissociation were summarized according to the data generated in Supplementary Fig. 4d, e. The Emax of the GPR97-FL-WT is similar to known Gi coupled dopamine receptor D2R. Values are the mean ± SEM from three independent experiments, each performed in triplicate. **g**, *Gpr97* knockdown in Y-1 cells abolished the acute inhibitory effects of cortisone on corticosterone. Y-1 cells were transfected with *Gpr97* siRNA (si-97) or control siRNA (si-con) for 48 h. Cells were then treated with cortisone (16 nM), ACTH (500 nM) or combined cortisone and ACTH. The level of corticosterone was measured at 30 min. Values are the mean ± SEM from three independent experiments, each performed in triplicate. ***$P < 0.001$; ns, no significance; cortisone stimulation compared with control vehicle. ###$P < 0.001$; ns, no significance; si-97 compared with si-con. All data were analysed by two-sided one-way ANOVA with Turkey test (From left to right, $P = 0.0865$, 0.0016, 0.0502, 0.1888, 0.2126, 0.0043). **h**, Knock down of *Gpr97* in neuronal cell abolished the acute effects of cortisone induced cAMP inhibition. Adrenal cortex Y-1 cells transfected with *Gpr97* siRNA (si-97) or control siRNA (si-Con) were stimulated with cortisone (16 nM) or ACTH (500 nM). The levels of cAMP for each condition were measured at 10 min after cortisone, ACTH or control vehicle stimulation. Values are mean ± SEM from three independent experiments. *$P < 0.05$, ns, no significance; Comparison between cells treated with or without cortisone; ###$P < 0.001$; Cells transfected with or without *Gpr97* siRNA were compared under cortisone stimulation. All data were analysed using by two-sided One-way ANOVA with Turkey test (From left to right, $P = 0.0108$, 0.0007, 0.0002, 0.5445, 0.2659). **i**, The expression of *Gpr97* was measured using q-PCR. Values are mean ± SEM from three independent experiments. ***$P < 0.001$. Cells transfected with or without *Gpr97* siRNA were compared under various stimulation conditions. All

data were analysed using by two-sided One-way ANOVA with Turkey test (From left to right, P = <0.0001, < 0.0001, < 0.0001, < 0.0001).

Extended Data Fig. 2 GPR97-Go complex purification, cryo-EM data processing, and overall resolution analysis of electron density of transmembrane helices, α5-helix of Gαo and the glucocorticoid ligands.

a, Representative elution profile of Flag-purified BCM-GPR97-FL-AA-miniGo complex and SDS–PAGE of the size-exclusion chromatography peak. For gel source data, see Supplementary Fig. 1. Experiments were repeated three times with similar results. **b**, Cryo-EM micrographs of BCM-GPR97-FL-AA-Go complex (scale bar: 30 nm) and 2D class averages (scale bar: 5 nm). Electron density of GPR97 N-terminal fragment (NTF) were labelled with red line. Representative cryo-EM micrograph from 2707 movies and representative two-dimensional class averages determined using approximately 2 million particles were shown. The 2D averaged electron density for NTF is significant weaker than the transmembrane helix or the G protein. The NTF is known to play important roles in aGPCR activation in many cases and also serves as a mechanosensor for extracellular force, potentially by engaging with the extracellular face of the 7TM bundle. The weak electron density of the NTF suggested high flexibility in this domain, which may be consistent with the highly dynamic nature of the mechanical stimuli, because the electrophoresis and cryo-EM experiments confirmed the integrity of the full-length receptor in our cryo-EM samples. Thus, the future determination of a high-resolution structure of full-length GPR97 by cryo-EM is important but may require additional stabilization of the receptor by additional ligands or antibodies. **c**, Flow chart of cryo-EM data processing of BCM-GPR97-FL-AA-Go complex. It is also worth noting that the 7TM structure solved by our current study closely reflects its conformational state in the context of the presence of the NTF, despite being in a static mode. **d**, Representative elution profile of Flag-purified cortisol-GPR97-FL-AA-miniGo complex and SDS–PAGE of the size-exclusion chromatography peak. For gel source data, see Supplementary Fig. 1. Experiments were repeated three times with similar results. **e**, Cryo-EM micrographs of cortisol-GPR97-FL-AA-Go complex (scale bar: 30 nm)

and 2D class averages (scale bar: 5 nm). Representative cryo-EM micrograph from 5871 movies and representative two-dimensional class averages determined using approximately 4 million particles were shown. Electron density of GPR97 N-terminal fragment (NTF) were labelled with red line. The 2D averaged electron density for NTF is significant weaker than the transmembrane helix or the G protein. **f**, Flow chart of cryo-EM data processing of cortisol-GPR97-FL-AA-Go complex. **g**, 3D density map of BCM and cortisol-bound complex colored according to local resolution (Å). Fourier shell correlation (FSC) curves of the final reconstruction and the refined model versus the final map. **h**, Cryo-EM density of transmembrane helices of GPR97, α5-helix of Gαo, the ligand of BCM and cortisol in determined BCM-GPR97-Go and cortisol-GPR97-Go cryo-EM structure respectively.

Extended Data Fig. 3 Detailed characteristics of the GPR97 7TM bundle.

a, Structural comparison of 7TM bundle (upper panel) and ECL2 (lower panel) of Go-bound GPR97 with Gi-bound NTSR1 (6OS9), Gs-bound PTH1R (6NBF), active GABAB (7C7Q) GB2 subunit and Gi-bound Smoothen receptor (6OT0) (from left to right). **b**, **c**, Plot of Cα distances of residues between the TM6 and TM7 (**b**) or between the TM1 and TM7 (**c**) of GPR97 in BCM-GPR97-Go complex structure and structures of NTSR1 (6OS9), PTH1R (PDB 6NBF), GABAB (7C7Q) and SMO (PDB 6OT0) in complex with their corresponding G proteins. Residues indicated in the X-axis were chosen based on Wootten numbering system. **d**, TM6 length of different GPCRs, including NTSR1 (6OS9), PTH1R (PDB 6NBF), $GABA_B$ (7C7Q), and SMO (PDB 6OT0). The length of TM6 were measured according to the length between the first helix turn in the cytoplasmic side and the last helix turn at the extracellular side. **e**, Consecutive polar residues in ECL2 and their interactions with the ECL3, TM6, and TM7 in GPR97. **f**, The weak association of ECL2 with ECL3 and TM1 in GPR97.

Extended Data Fig. 4 Ligand binding pocket and 7TM bundle of GPR97 and its comparison with other GPCRs.

a, **b**, High quality electron density enabled unambiguous assignment of BCM (**a**), cortisol (**b**) and several residues surrounding them in ligand binding pocket. Only one direction of BCM or cortisol could be fit correctly. **c**, **d**, Diagram of BCM (**c**) and cortisol (**d**) interaction in the ligand binding pocket of GPR97. Different interaction residues in BCM-GPR97-Go and cortisol-GPR97-Go complex were labelled with red and lemon circle respectively. In particular, F345A and I494A exhibited a more significant decrease in the potency of the BCM compared to cortisol, consistent with the observation of the stronger contacts of $F345^{3.36}$ and $I494^{6.57}$ with the chloride or B ring in BCM, respectively. **e**, **f**, The steroid core of BCM (**e**) and cortisol (**f**) are vertical relative to the plane of the plasma membrane, paralleling to TM7 and approximately 70-degree deviation from the central TM3. **g**, r.m.s.d. analysis of GPR97-Beclomethasone and GPR97-cortisol 200 ns trajectories. (Upper panel) RMSDs of GPR97 ligands Beclomethasone (purple) or cortisol (pink). (Lower panel) RMSDs of the binding sites of GPR97 towards counterpart ligands. Values were calculated based on the initial complex state after equilibration (0 ns). **h**, Vertical view of BCM binding into GPR97 binding pocket and its comparison with ligands binding in 5-HT_{1B}R (PDB 6G79), NTSR1 (PDB 6OS9) and M2R (PDB 6OIK). **i**, Interaction residues in the ligand binding pocket of the BCM–GPR97–G_o and the cortisol-GPR97–G_o–scFv16 complexes. Residues that interact with both glucocorticoids are indicated by green circles, and those that show no interaction are indicated by blank circles. The different ligand interaction residues in the two binding pockets are indicated by red and lemon circles, respectively. Wootten's residue numbers are provided for reference.

Extended Data Fig. 5 FlAsH insertion site screening and FlAsH BRET mutation experiment.

a, Schematic representation of the FlAsH-BRET assay design. The Nluc was inserted at the N terminus of wild-type GPR97-β, and the FlAsH motif were inserted in the designated positions in the figure. **b**, Detailed description of the FlAsH motif incorporation site at the extracellular loops of GPR97. FlAsH motifs are labelled in red. The specific residues that interact with the ligand are highlighted in yellow. **c**, ELISA experiments to

determine the expression levels of the wild-type GPR97 and five FlAsH motif incorporated FlAsH-BRET sensors. Values are mean ± SEM from three independent experiments performed in triplicates. ns, no significance; Comparison between GPR97-WT-Nluc and its mutant. The original data are referred to Supplementary Table 3. All data were analysed by two-sided one-way ANOVA with Turkey test (From left to right, $P = 0.5910$, 0.1912, 0.7642, 0.3076, 0.5938). **d**, The potency changes upon BCM activation by different GPR97 FlAsH-BRET sensors. These sensors were corresponding to those used in **e**. Values are mean ± SEM from three independent experiments performed in triplicates. The original data are referred to Supplementary Table 3. *$P < 0.05$, ***$P < 0.001$; ns, no significance; Comparison between site2 and other sites FlAsH-BRET sensors. All data were analysed by two-sided one-way ANOVA with Turkey test (From left to right, $P = < 0.0001$, < 0.0001, < 0.0001, < 0.0001). **e**, Representative dose response curve of the BCM-induced BRET ratio in HEK293 cells overexpressing five FlAsH-BRET sensors using FlAsH-BRET assay. Values are mean ± s.d. from three independent experiments performed in triplicates. **f**, ELISA experiments to determine the expression levels of the site2 FlAsH-BRET and corresponding mutations for glucocorticoids interaction sites. Values are mean ± SEM from three independent experiments performed in triplicates. ns, no significance; Comparison between FlAsH-BRET sensor-2 wild type and corresponding interaction sites mutations. The original data are referred to Supplementary Table 3. All data were analysed by two-sided one-way ANOVA with Turkey test (From left to right, $P = 0.5446$, 0.6579, 0.6133, 0.3484, 0.5069, 0.6488, 0.6571). **g**, The potency changes upon BCM activation by different site2 FlAsH-BRET sensor-2 mutants. These mutants were designed according to those used in **i**. The FlAsH-BRET assay and cAMP assay are two different functional assays to investigate the contribution of interaction residues observed in the cryo-EM structure. Values are mean ± SEM from three independent experiments performed in triplicates. **$P < 0.01$, ***$P < 0.001$; ns, no significance; Comparison between FlAsH-BRET sensor-2 wild type and corresponding mutant. The original data are referred to Supplementary Table 3. All data were analysed by two-sided one-way ANOVA with Turkey test (From top to bottom, $P = < 0.0001$, < 0.0001, < 0.0001, < 0.0001, < 0.0001, < 0.0001, 0.6514). **h**, The potency changes upon cortisol activation by different site2 FlAsH-BRET sensor-2 mutants. These

mutants were designed according to those used in **j**. Values are mean ± SEM from three independent experiments performed in triplicates. ***$P < 0.001$; ns, no significance; Comparison between FlAsH-BRET sensor-2 wild type and corresponding mutant. The original data are referred to Supplementary Table 3. All data were analysed by two-sided one-way ANOVA with Turkey test (From top to bottom, $P = <0.0001$, < 0.0001, < 0.0001, < 0.0001, 0.0002, 0.0005, 0.5028). **i**, **j**, Representative dose response curves of the BCM- (**i**) or cortisol-induced (**j**) BRET ratio in HEK293 cells overexpressing FlAsH-BRET sensor-2 wild type and corresponding mutant. Values are mean ± s.d. from three independent experiments performed in triplicates. **k**, Sequence alignment of residues involved in BCM and cortisol binding in GPR97 with other members of aGPCR G subfamily. The residues involved in the ligand binding of GPR97 and their counterparts in other aGPCR G subfamily members are highlight in different background. The same interaction residue in BCM-GPR97-Go and cortisol-GPR97-Go are highlight in green background. Different interaction residues are highlight in yellow or red background respectively.

Extended Data Fig. 6 Effects of mutations in the different structural motifs in GPR97 on BCM-induced cAMP inhibition.

a, ELISA experiments to determine the expression levels of the GPR97 wild type and indicated mutants in HEK293 cells. The mutant receptor expression was normalized to comparable levels as wild-type receptor expression in our ELISA assay by adjusting the amount of plasmid transfected. Values are mean ± SEM from three independent experiments performed in triplicates. ns, no significance; Comparison between GPR97-FL-WT and its mutant. The original data are referred to Supplementary Table 4. All data were analysed by two-sided one-way ANOVA with Turkey test (From left to right, $P = 0.1072$, 0.7137, 0.1804, 0.0661, 0.8105, 0.7227, 0.1521, 0.2276, 0.1118, 0.0907, 0.2280, 0.2112, 0.3975, 0.1672, 0.7230, 0.7904, 0.1302, 0.0646, 0.1433, 0.0848, 0.6376, 0.9843). **b**, The potency changes upon BCM activation by different GPR97 mutants. These mutants were corresponding to those used in Figs. 2e, 3d and Extended Data Fig. 8c. Values are mean ± SEM from three independent experiments performed in triplicates. ***$P < 0.001$; ns, no significance; Comparison between GPR97-FL-WT and its mutant. The original data are referred to

Supplementary Table 4. All data were analysed by two-sided one-way ANOVA with Turkey test. (From left to right, P = 0.8274, 0.0009, 0.0006, <0.0001, <0.0001, <0.0001, <0.0001, 0.1967, <0.0001, <0.0001, 0.0002, <0.0001, <0.0001, 0.8059, 0.0177, <0.0001, 0.0010, <0.0001, <0.0001, 0.2317, <0.0001, <0.0001). **c**, Representative dose response curve of the BCM-induced cAMP inhibition in HEK293 cells overexpressing wild type or mutant GPR97 using Glosensor assay. Values are mean ± s.d. from three independent experiments performed in triplicates. Mutation of either $V466^{ECL3}$ or $K471^{ECL3}$ reduced the potency of BCM stimulation of GPR97, indicating an essential role of ICL3-mediated GPR97-Go coupling. **d**, The potency changes upon cortisol activation by different GPR97 mutants. These mutants were corresponding to those used in Fig. 2f. Values are mean ± SEM from three independent experiments performed in triplicates. ***P < 0.001; Comparison between GPR97-FL-WT and its mutant. The original data are referred to Supplementary Table 4. All data were analysed by two-sided one-way ANOVA with Turkey test (From left to right, P = 0.0036, 0.0271, 0.0038, 0.0455, 0.0007, 0.5604, 0.0104, 0.0012, 0.0002, 0.0004, 0.0014, 0.0009). **e**, Representative dose response curve of the cortisol-induced cAMP inhibition in HEK293 cells overexpressing wild type or mutant GPR97 using Glosensor assay. Values are mean ± s.d. from three independent experiments performed in triplicates.

Extended Data Fig. 7 The structural motifs in the active state of GPR97.

a, The toggle switch $W327^{6.48a}$ in 5-HT_{1B}R (6G79) directly interacts with ligand EP5. **b**, The toggle switch $W400^{6.48a}$ in M2R (6OIK) interacts with ligand IXO. **c**, The schematic representation of quaternary motif in GPR97 tethering TM3, TM5, and TM6. **d**, The sequence alignment of adhesion GPCR ADGRG subfamily members, 5-HT_{1B}R, and M2R was created using GPCRdb (http://www.gpcrdb.org) and Jalview software. Coils represent α-helices. The conserved residues (quaternary core) tethering TM3, TM5 and TM6 in GPR97 are highlighted in green. The toggle switch W, TFV (PIF), and HLY (DRY) motifs are indicated by purple, red and blue dots, respectively. **e**, ELISA experiments to determine the expression levels of the GPR126 wild type and indicated mutants in HEK293 cells. The mutant

receptor expression was normalized to comparable levels as wild-type receptor expression in our ELISA assay by adjusting the amount of plasmid transfected. Values are mean ± SEM from three independent experiments performed in triplicates. ns, no significance; Comparison between GPR126 and its mutant. The original data are referred to Supplementary Table 5. All data were analysed by two-sided one-way ANOVA with Turkey test (P = 0.2558, 0.5436, 0.3412). **f**, Representative dose response curves of S13L (a modified stachel peptide of GPR64 functions as an agonist)-induced cAMP accumulation in HEK293 cells overexpressing GPR126 wild type or mutant using Glosensor assay. Values are mean ± s.d. from three independent experiments performed in triplicates. **g**, Comparison of TM3 and TM6 in Go-coupled GPR97, Go-coupled 5-HT_{1B}R, and inactive 5-HT_{1B}R. The Go-coupled GPR97 is in green, the inactive 5-HT_{1B}R is in grey (PDB 5V54), and Go-coupled 5-HT_{1B}R is in yellow (PDB 6G79). The toggle switch of Go-bound GPR97 is located at a position similar to that of Go-bound 5-HT_{1B}R. The separation of TM3 and TM6 in GPR97 was smaller than that in 5-HT_{1B}R-Go but larger than that in the inactive 5-HT_{1B}R structure. **h**, Plot of Cα distances of residues between the TM3 and the TM7 of GPR97 in BCM-GPR97-Go complex structure and the active structures of the M2R (6OIK) or 5-HT_{1B}R (6G79) with Go, or inactive 5-HT_{1B}R (5V54) structure. Residues indicated in the X-axis were chosen based on Wootten numbering system. **i**, Interaction of H362 in HLY motif of GPR97 with the palmitoylated C351 α5-helix of Go. **j**, Interaction of R147 in DRY motif of 5-HT_{1B}R (PDB 6G79) with the α5-helix of Go. **k**, Effects of the mutation of L363R in HLY motif of GPR97 on BCM induced cAMP inhibitory activity (mutating the key HLY motif residue in aGPCR family corresponding to DRY motif residue in other GPCR family). The original data are referred to Supplementary Table 4. Values are mean ± SEM from three independent experiments performed in triplicates. ***P < 0.001; All data were analysed by two-sided one-way ANOVA with Turkey test (P = <0.0001).

Extended Data Fig. 8 Molecular mechanisms of Go coupling to GPR97.

a, Close-up view of the interactions between the C-terminal α5 helices of Go and GPR97 (light sea green), 5-HT_{1B}R (wheat), and M2R (salmon). Hydrogen bonds were highlighted by dashed lines. **b**, Close up view of interactions between C-terminal α5 helix of Go and GPR97. **c**, Effects of mutations in ICLs of GPR97 on BCM-induced cAMP inhibition. Values are the mean ± SEM from three independent experiments performed in triplicate. *$P < 0.05$; ***$P < 0.001$; ns, no significance; Comparison between GPR97-FL-WT and its mutant. All data were analysed by two-sided one-way ANOVA with Tukey's test (From left to right, P = <0.0001, <0.0001, <0.0001, <0.0001, <0.0001, <0.0001). **d**, **e**, Effects of mutations of ICL1, ICL2 or ICL3 on the basal activities of GPR97. Inhibitory effects of forskolin (1 μM)-induced cAMP accumulation on the constitutive activities of GPR97 wild-type and its ICL region mutants were tested in HEK293 cells. All data are presented as the percentage of activities of each GPR97 mutant vs. that of wild-type GPR97 at different relative receptor expression level. Overexpression of wild-type GPR97 led to an elevated inhibitory effect on forskolin-induced cAMP accumulation, whereas mutations in either ICL1 or ICL3 significantly decreased this effect. The mutant receptor expression was normalized to comparable levels as wild-type receptor expression in our ELISA assay by adjusting the amount of plasmid transfected (see **f**). Data represent the mean ± s.d. from three independent experiments performed in triplicate. **d**, ***$P < 0.001$, ###$P < 0.001$, $$$$P < 0.001$, GPR97 mutants ICL1-R299A, ICL1-E298A or ICL1-R297S versus GPR97-FL-WT; **e**, ***$P < 0.001$, ###$P < 0.001$, ns, no significance. ICL2/V370A or ICL3-L460A versus GPR97-FL-WT. All data were analysed by two-sided one-way ANOVA with Tukey's test. (P = 0.6262, <0.0001, <0.0001, <0.0001, <0.0001 from left to right for R297S curve; P = 0.8416, <0.0001, <0.0001, <0.0001, <0.0001 from left to right for E298A curve; P = 0.9125, <0.0001, <0.0001, <0.0001, <0.0001 from left to right for R299A curve; P = >0.9999, 0.2254, 0.0014, 0.1836, 0.3143 from left to right for V370A curve; P = 0.6291, 0.0003, 0.0002, 0.0001, 0.3372 from left to right for L460A curve). **f**, ELISA experiments to determine the expression levels of GPR97 wild type and indicated mutants in HEK293 cells. Values are mean ± SEM from three independent experiments performed in triplicates. ns, no significance; Comparison between GPR97-FL-WT and its mutant. All data were analysed by two-sided one-way ANOVA with Turkey test (From left to right, P = 0.9496,

0.2058, 0.2316, 0.7907, 0.2100, 0.9558, 0.4538, 0.1063, 0.3675, 0.5311, 0.9426, 0.6767, 0.1491, 0.3360, 0.5109, 0.9700, 0.6505, 0.7398, 0.7890, 0.1970, 0.9809, 0.4458, 0.1032, 0.2440, 0.2231).

Extended Data Fig. 9 Palmitoylation of Go mediates GPR97 coupling.

a, MS-MS spectrum identified that the S-palmitoylation occurred at C351 in the α5-helix of Gαo in the cortisol-GPR97-Go complex. **b**, Table of mass to charge ratio of different ion type in mass spectrometry. The increase mz from the b14+ to b15+ is 341.24, which larger than the cysteine molecular weight and close to the palmitoylation of the C351. **c**, Cross-sectional view showing that the palmitoylation of C351 is inserted approximately 17Å deep into the 7TM bundle (PDB 7D77). **d**, Structure comparison of GPR97-Go complex (PDB 7D77) with Go-bound M2R (PDB 6OIK), Go bound $5HT_{1B}R$ (PDB 6G79), Gi -bound Mu-Opioid (PDB 6DDF), Gi bound CB2 (PDB 6PT0). A presumed palmitoylation at the C351 of Go or Gi will clash with these GPCRs in the complex structures. **e**, The potency and efficacy for effects of ligand induced Gqo/Gβγ dissociation was summarized according to the data generated in **f**–**h**. Values are the mean ± SEM from three independent experiments, each performed in triplicate. **f**, Effects of mutations in C351 in α5-helix of Gαo on GPR97 or D2R activities. The C351S and C351A mutations impaired the activation of GPR97 but not D2R. The original dose response data were shown in **g** and **h**. Bar graph represents the mean ± SEM value of Emax from three independent experiments performed in triplicates. ***$P < 0.001$; Comparison between Gαo C351 mutations and Gαo-WT in activating GPR97; ns, no significance; Comparison between Gαo C351 mutations and Gαo-WT in activating D2R. All data were analysed by two-sided one-way ANOVA with Turkey test (From left to right, $P = 0.0053$, 0.0006, 0.0795, 0.1868). **g**, **h**, Representative dose–response curves for BCM (**g**) or dopamine (**h**) induced Gαo/Gβγ dissociation from their corresponding receptors using wild type or C351 mutations of Gαo. Values are mean ± s.d. from three independent experiments performed in triplicates.

Extended Data Table 1 Cryo-EM data collection, model refinement and validation statistics

Full size table

Supplementary information

Supplementary Information

This file contains Supplementary Tables 2-4 and Supplementary Figures 1-2.

Reporting Summary

Rights and permissions

Reprints and Permissions

About this article

Check for updates

Cite this article

Ping, YQ., Mao, C., Xiao, P. *et al.* Structures of the glucocorticoid-bound adhesion receptor GPR97–G_o complex. *Nature* **589,** 620–626 (2021). https://doi.org/10.1038/s41586-020-03083-w

Download citation

- Received: 14 July 2020
- Accepted: 06 November 2020
- Published: 06 January 2021

- Issue Date: 28 January 2021
- DOI: https://doi.org/10.1038/s41586-020-03083-w

Comments

By submitting a comment you agree to abide by our Terms and Community Guidelines. If you find something abusive or that does not comply with our terms or guidelines please flag it as inappropriate.

Download PDF

This article was downloaded by **calibre** from https://www.nature.com/articles/s41586-020-03083-w

| Section menu | Main menu |

Amendments & Corrections

- **Publisher Correction: Impacts of speciation and extinction measured by an evolutionary decay clock** [13 January 2021]
  Publisher Correction •

Publisher Correction: Impacts of speciation and extinction measured by an evolutionary decay clock
Download PDF

- Publisher Correction
- Published: 13 January 2021

Publisher Correction: Impacts of speciation and extinction measured by an evolutionary decay clock

- Jennifer F. Hoyal Cuthill ORCID: orcid.org/0000-0002-3139-9750[1,2,3,4],
- Nicholas Guttenberg[3,5,6] &
- Graham E. Budd ORCID: orcid.org/0000-0001-9007-4369[7]

Nature **volume 589**, pageE10(2021)Cite this article

- 536 Accesses
- 4 Altmetric
- Metrics details

Subjects

- Machine learning
- Palaeontology

The Original Article was published on 09 December 2020

Download PDF

Correction to: *Nature* https://doi.org/10.1038/s41586-020-3003-4Published online 09 December 2020

In Fig. 2 of this Article, owing to an error during the production process, ‘C’ (for Carboniferous) was swapped with ‘Cam.’ (for Cambrian) in the timeline at the top of the figure. The original Article has been corrected online.

Author information

Affiliations

1. Institute of Analytics and Data Science, University of Essex, Colchester, UK

   Jennifer F. Hoyal Cuthill

2. School of Life Sciences, University of Essex, Colchester, UK

   Jennifer F. Hoyal Cuthill

3. Earth–Life Science Institute, Tokyo Institute of Technology, Tokyo, Japan

   Jennifer F. Hoyal Cuthill & Nicholas Guttenberg

4. Department of Earth Sciences, University of Cambridge, Cambridge, UK

   Jennifer F. Hoyal Cuthill

5. Cross Labs, Cross Compass Ltd, Tokyo, Japan

   Nicholas Guttenberg

6. GoodAI, Prague, Czech Republic

Nicholas Guttenberg

7. Department of Earth Sciences, Palaeobiology Programme, Uppsala University, Uppsala, Sweden

Graham E. Budd

Authors

1. Jennifer F. Hoyal Cuthill
   View author publications

   You can also search for this author in PubMed Google Scholar

2. Nicholas Guttenberg
   View author publications

   You can also search for this author in PubMed Google Scholar

3. Graham E. Budd
   View author publications

   You can also search for this author in PubMed Google Scholar

Corresponding author

Correspondence to Jennifer F. Hoyal Cuthill.

Rights and permissions

Reprints and Permissions

About this article

Check for updates

Cite this article

Hoyal Cuthill, J.F., Guttenberg, N. & Budd, G.E. Publisher Correction: Impacts of speciation and extinction measured by an evolutionary decay clock. *Nature* **589,** E10 (2021). https://doi.org/10.1038/s41586-020-03178-4

Download citation

- Published: 13 January 2021
- Issue Date: 28 January 2021
- DOI: https://doi.org/10.1038/s41586-020-03178-4

Comments

By submitting a comment you agree to abide by our Terms and Community Guidelines. If you find something abusive or that does not comply with our terms or guidelines please flag it as inappropriate.

Download PDF

This article was downloaded by **calibre** from https://www.nature.com/articles/s41586-020-03178-4